Composites Science and Technology

Mohammad Jawaid
Anish Khan *Editors*

Carbon Composite Catalysts

Preparation, Structural and Morphological Property and Applications

Springer

Composites Science and Technology

Series Editor

Mohammad Jawaid, Laboratory of Biocomposite Technology, Universiti Putra Malaysia, INTROP, Serdang, Malaysia

Aims and Scope

This book series publishes cutting edge research monographs comprehensively covering topics in the field of composite science and technology. The books in this series are edited or authored by top researchers and professional across the globe. The series aims at publishing state-of-the-art research and development in areas including, but not limited to:

- Composites from agricultural biomass/natural fibers include conventional composites-Plywood/MDF/Fiberboard
- Fabrication of Composites/conventional composites from biomass and natural fibers
- Utilization of biomass in polymer composites
- Wood, and Wood based materials
- Chemistry and biology of Composites and Biocomposites
- Modelling of damage of Composites and Biocomposites
- Failure Analysis of Composites and Biocomposites
- Structural Health Monitoring of Composites and Biocomposites
- Durability of Composites and Biocomposites
- Biodegradability of Composites and Biocomposites
- Thermal properties of Composites and Biocomposites
- Flammability of Composites and Biocomposites
- Tribology of Composites and Biocomposites
- Bionanocomposites and Nanocomposites
- Applications of Composites, and Biocomposites

Review Process

The proposal for each volume is reviewed by the main editor and/or the advisory board. The chapters in each volume are individually reviewed single blind by expert reviewers (at least two reviews per chapter) and the main editor.

Ethics Statement for this series can be found in the Springer standard guidelines here - https://www.springer.com/us/authors-editors/journal-author/journal-author-helpdesk/before-you-start/before-you-start/1330#c14214

More information about this series at https://link.springer.com/bookseries/16333

Mohammad Jawaid · Anish Khan
Editors

Carbon Composite Catalysts

Preparation, Structural and Morphological Property and Applications

Springer

Editors
Mohammad Jawaid
Laboratory of Biocomposite Technology
Institute of Tropical Forestry and Forest Products (INTROP)
Universiti Putra Malaysia
Serdang, Selangor, Malaysia

Anish Khan
Center of Excellence for Advanced Materials Research
King Abdulaziz University
Jeddah, Saudi Arabia

ISSN 2662-1819 ISSN 2662-1827 (electronic)
Composites Science and Technology
ISBN 978-981-19-1749-3 ISBN 978-981-19-1750-9 (eBook)
https://doi.org/10.1007/978-981-19-1750-9

This Springer imprint is published by the registered company Springer Nature Singapore Pte Ltd.
The registered company address is: 152 Beach Road, #21-01/04 Gateway East, Singapore 189721, Singapore

Preface

In early twenties, as carbon was considered earth-abundant material, its composite catalysts were found as an effective, easy, low-cost, and metal-free alternative for different industrials reactions. Carbon composite catalysts, which are pollution free, having high chemical and thermal stabilities, superior physicochemical properties over metal-based catalysts, have attracted considerable interests as a new class of catalysts that have fever or without the metal species and are considering the chemical process for high economical profit as well as readily tailorable porous structure and surface chemistry. This book provides an overview of the fundamentals and recent advances in the field of carbon composite catalysts, including graphenes, carbon nanotubes, mesoporous carbons, graphitic carbon nitrides, and related composites. Special focus is placed on their controllable preparation and applications in gas phase, liquid phase, electrochemical, and photocatalytic reactions, as well as defect and surface chemistry-related catalytic activities of carbon materials. Some perspectives are highlighted on the development of more efficient carbonaceous catalysts featuring high stability, low-cost, optimized structures, and enhanced performance, which are the key factors to accelerate the designed preparation and commercialization of carbon composite catalysts. We additionally will involve late advances in the improvement of carbon-based composite catalysts for clean energy change and storage, nature protection and essential industrial production, and storage and include the key challenges and future opportunities in this exciting field.

We have collected chapters from all around the world in this book to make it unique for the authors in the field of composite catalysts. Authors from Brazil, Turkey, Malaysia, Saudi Arabia, Iran, Japan, Russia, and Cuba contributed chapters in this book. Thank you very much for their best effort to make it possible for the readers. We are thankful to the Springer team also for working hard together to complete this book project.

Serdang, Malaysia — Dr. Mohammad Jawaid
Jeddah, Saudi Arabia — Dr. Anish Khan

Contents

Nitrogen-Doped Graphene Foam as Carbon Composites Catalysis Catalysts: Preparation, Properties and Applications

Ayşenur Öztürk and Ayşe Bayrakçeken Yurtcan

Abstract Three-dimensional (3D) graphene architectures (hydrogel, aerogel, coke, foam, sponge) have become the preferred materials in many areas, especially in electronic applications. Graphene foams, which contain both graphene and 3D macroscopic material properties, provide many advantages for material science. These structures, which have concurrently high mechanical strength and flexibility, have offered the opportunity to be used in some electronic devices that require pressure application. Its lightweight is also proper for portable and wearable applications. Graphene foam composites with high electrical conductivity are often used as catalysts in different fields. By force of a 3D interconnected graphene network, the transfer of electrons and ions within the structure occurs in a facile way. The heteroatom (nitrogen (N), boron (B), phosphorus (P), sulfur (S)) doping to carbon materials has been one of the effective ways to modify the electronic and catalytic properties of the carbon host. In this chapter, some information on the synthesis and application areas of 3D N-doped graphene foam structures were presented. Graphene foams are synthesized and N-doped simultaneously with the chemical vapor deposition (CVD) method by a majority. The applications of the 3D N-doped graphene foams as carbon composite catalysts were evaluated in the fields of fuel cells, batteries, supercapacitors and other catalytic reactions. Additionally, other applications of 3D N-doped graphene foams were also briefly mentioned.

Keywords Three-dimensional material · Graphene foam · Heteroatom · Nitrogen doping · Carbon composite catalyst

A. Öztürk · A. Bayrakçeken Yurtcan (✉)
Faculty of Engineering, Department of Chemical Engineering, Atatürk University, Erzurum 25240, Turkey
e-mail: abayrakceken@atauni.edu.tr

A. Öztürk
e-mail: aysenur.ozturk@atauni.edu.tr

A. Bayrakçeken Yurtcan
Graduate School of Science, Department of Nanoscience and Nanoengineering, Atatürk University, Erzurum 25240, Turkey

M. Jawaid and A. Khan (eds.), *Carbon Composite Catalysts*, Composites Science and Technology, https://doi.org/10.1007/978-981-19-1750-9_1

1 Properties of Graphene Foams

As is known by almost everyone, graphene is the two-dimensional (2D) structure in which carbon atoms are formed in the hexagonal plane by sp^2 hybridization. Figure 1 shows the chemical structures of all materials used for obtaining a few layers of graphene starting from the graphite. It is also possible to develop materials with tunable properties by synthesizing different derivatives of graphene structures. Graphene aerogel and graphene foam structures, which contain the properties of both graphene nanosheets and macroscopic three-dimensional (3D) structures, are being used by researchers in various applications as an alternative and advantageous forms of graphene material. Hydrogel, aerogel, coke, macroporous foam, nanoporous sponge are the popular members of these 3D graphene assemblies [1, 2]. Figure 2 shows the simple structure of these 3D graphene assemblies through the synthesis steps of heteroatom-doped 3D graphene foam.

Although the electrical, optical, catalytic, and mechanical properties gained by graphene foam materials vary according to the form of preparation technique, the general prominent features of these materials are large surface area, mechanical strength, and mass transfer capabilities. Hydrophobicity is another significant property of graphene foam structures however it limits their use for some applications in aqueous environments. Depending on the application purpose, the degree of hydrophobicity can be adjusted with some parameters like chemical composition, surface energy, and microstructure [1]. Table 1 shows the contact angle values based on application areas of 3D graphene foams/heteroatom doped graphene foams synthesized with different methods.

Tensile strength is defined as the magnitude obtained by dividing the maximum load, applied up to the final point that material can be stretched, to the cross-sectional

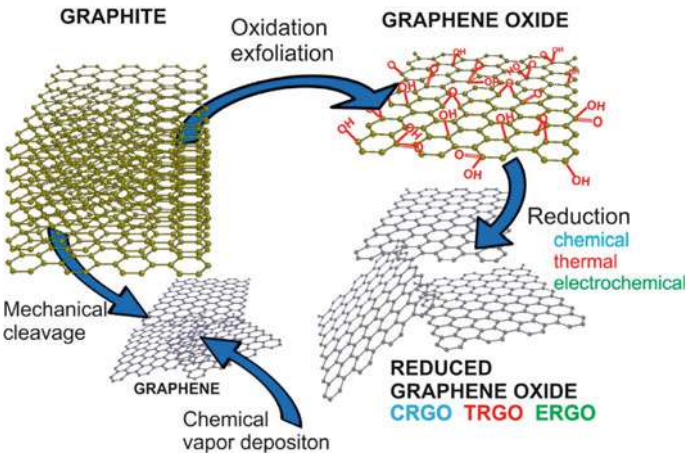

Fig. 1 Chemical structures of graphite, graphene oxide (GO), reduced graphene oxide (rGO), graphene (" Reproduced from Ref. [3] with permission from the Elsevier.")

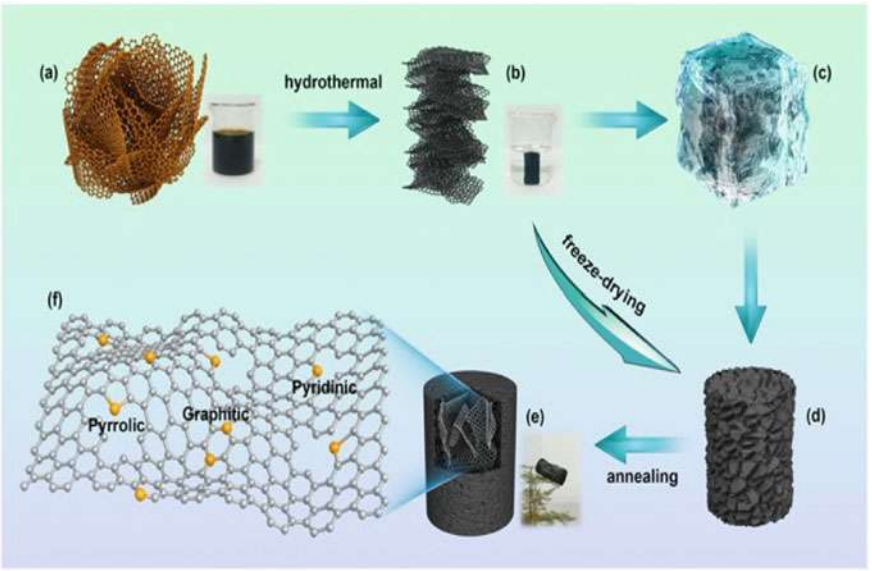

Fig. 2 3D nitrogen (N)-doped graphene foam synthesis steps **a** GO suspension **b** freeze-dried graphene hydrogel after hydrothermal reaction **c** freeze-drying treatment **d** 3D graphene aerogel **e** N-doped graphene aerogel **f** N-bonding types (" Reproduced from Ref. [4] with permission from the Springer Nature.")

area of the material. Young's modulus is another magnitude that gives us an idea about how much the material can stretch and bend. Due to their high tensile strength and Young's modulus values, 3D graphene foam structures can provide energy distribution within the material with an energy loss coefficient of 87% so they can tolerate the force loaded over them [2]. Tensile strengths of 3D graphene foam structures with bulk density between 1.5 and 110 mg cm^{-3} range from 11 kPa to 11 MPa [13]. In another study, the tensile strength of reduced graphene oxide (rGO) foam was found as 3.2 MPa while Young's modulus was found as 7 and 40 mPa for the first and last stages of tensile strength, respectively [14]. The SEM image shows the internal structure of the graphene foam in Fig. 3 [15]. In-plane and out-of-plane orientations at the junction of the branches led to the emergence of the 3D structure. The porosity of graphene foam was determined as 86.70% by Yocham et al. [16]. Thanks to these hollow tunnels of the graphene foam structures between the interconnected graphene layers, the mechanical endurance of these materials allows them to show mechanical strength at a level that can withstand 50,000 times their weight [2]. The more the synthesized graphene foam structure is free from defects, the denser the branching within the 3D graphene monolith and the higher the mechanical strength of the material [15]. Additionally, polymer composites (epoxy, polyvinyl alcohol (PVA), polydimethylsiloxane (PDMS), polyaniline (PANI), polypyrrole (PPy), polymethylmethacrylate (PMMA), polystyrene (PS), polyurethane (PU), polyvinylidene fluoride (PVDF), polyimide (PI)) of graphene foam structures provide to reinforce

Table 1 Contact angle values of some 3D graphene foams/heteroatom doped graphene foams

Material	Synthesis method	Heteroatom doping (at. %)	Contact angle (°)	Application	Refs
Porous graphene foam	Electro plating and annealing and chemical vapor deposition	–	105	Catalysts, energy storage, EMI shielding	[5]
Graphene foam	Commercial product	–	108.5	Flow fields in fuel cells	[6]
3D matrix of a graphene/polymer (PDMS) nanocomposite (GNC)	Hard template and dip-coating and thermal curing	–	126	Stretchable conductors and electrodes in different areas	[7]
Pt decorated PPy modified graphene aerogel (Pt/PPy-GA)	Hydrothermal and freeze-drying and chemical oxidative polymerization	–	137.7	Catalyst support in fuel cell	[8]
1T/2H mixed phase MoS_2 nanosheets integrated by a 3D N-doped graphene derivative (MNG-A)	Solvothermal and lyophilization and annealing	N (7.05)	124	Hydrogen evolution	[9]
3D self-assembled copolymer (P(AM-DMDAAC))/graphene aerogels (PGAs)	Hydrothermal and freeze-drying	N (8.01)	142.7	Oil/water separation	[10]
Graphene–melamine sponge (M-GS)	Impregnation and pre-heating and microwave irradiation	N/A	153.8	Removal of organic pollutants	[11]
Superhydrophobic graphene foam (SGF)	Hydrothermal and sol–gel and hydrophobic modification	N (0.9) Si (17.31)	156	Oil/water separation	[12]

the mechanical strength of the ultimate material [17, 18]. Zhang et al. [19] found that tensile strength (1.92 MPa) and Young's modulus (9.2 MPa) of PDMS/graphene foam/PPy composite (PDMS/GrF@PPy) increased compared to the tensile strength (0.73 MPa) and Young's modulus (0.79 MPa) of the pure PDMS polymer.

The flexible nature of 3D graphene foams makes these materials ideal candidates for flexible electronic devices, especially chemical sensor applications [20]. Compression is recovered by graphene foam up to 98% and 90% in air and liquids environment through the synergetic effect of cork-like and rubber-like properties.

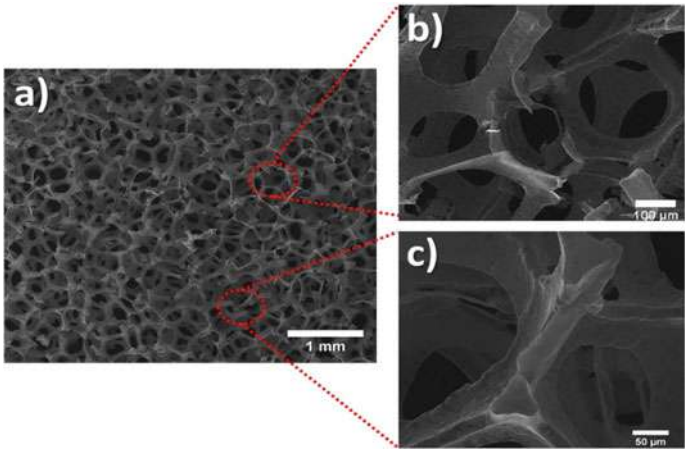

Fig. 3 **a** Low magnified SEM image showing interconnected 3D graphene networks, **b** High magnified SEM image showing typical pore size and **c** SEM image showing cross section of graphene foam walls. ("Reproduced from Ref. [15] with permission from the Elsevier.")

It maintains its structural integrity to a great extent with a 15 N m^{-1} spring coefficient and 70% deformation recovery [21]. Figure 4 shows images of the magnetic polymer-based graphene foam (MPG) synthesized by Liu et al. [22], despite severe stress, returning to its original form. Graphene foams are highly preferred for ultralight compressible applications with low-density values, although their densities vary.

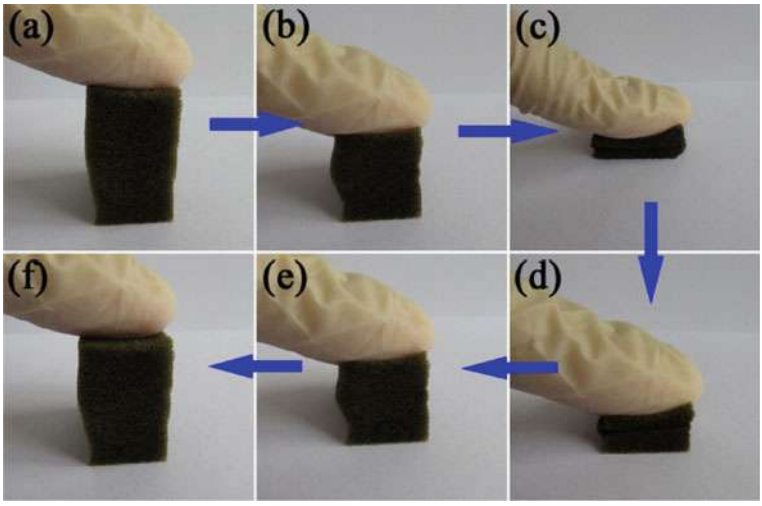

Fig. 4 Compression-recovery process of MPG (" Reproduced from Ref. [22] with permission from the Elsevier.")

Fig. 5 Advantageous properties of 3D graphene foam ("The 3D graphene foam image is adapted from Ref. [27] with permission from the Elsevier.")

Indeed, Ma et al. [23] reported the potential of ultralight interconnected graphene-amorphous carbon hierarchical foam in wearable, lightweight applications with a very low-density value (1.17×10^{-3} g cm^{-1}) of their product.

The high surface area of graphene foam structures is also utilized. Kasap et al. [24] achieved the 870 m^2 g^{-1} surface area with their graphene foam produced with the chemical vapor deposition (CVD) method under optimum experimental conditions. Chen et al. [25] stated that 3D graphene aerogels, produced with the sol–gel method, can reach a considerable high surface area up to 1200 m^2 g^{-1}. In the same study, the authors reported the high electrical conductivity of their 3D graphene foam as 125 S cm^{-1}. According to the authors, this electrical conductivity value is significantly higher than the values of graphene films (0.01–80 S cm^{-1}), doped graphene films (0.02–3 S cm^{-1}), carbon nanotubes (CNTs) or graphene papers (2–10 S cm^{-1}), graphene aerogels (0.1 S cm^{-1}) in some studies from the literature. The high electrical conductivity of the synthesized 3D graphene foam is attributed to the fast electron transfer facilitated by the interconnected graphene network. Pettes et al. [26] found the thermal conductivity values of free-standing graphene-based foams, which they synthesized using different etchants for sacrificial nickel (Ni) foam support through the CVD synthesis, in the range of 0.26–1.7 W m^{-1} K^{-1}. As a result, 3D graphene foam structures are used as ideal materials in different fields due to the many advantageous features they contain. Some of the advantageous properties of the 3D graphene foam are summarized in Fig. 5.

2 Nitrogen-Doped Graphene Foams

Doping heteroatom into the structure of carbon materials has been one of the attractive topics of recent years. The defects created in the structure by the heteroatom additive provide an extra active sites, especially for electrochemical catalytic reactions. The properties of the material vary depending on the binding types and concentrations of incorporated heteroatoms to the structure. In particular, the electronic properties of the material are highly affected by this change [28]. Nitrogen (N), boron (B),

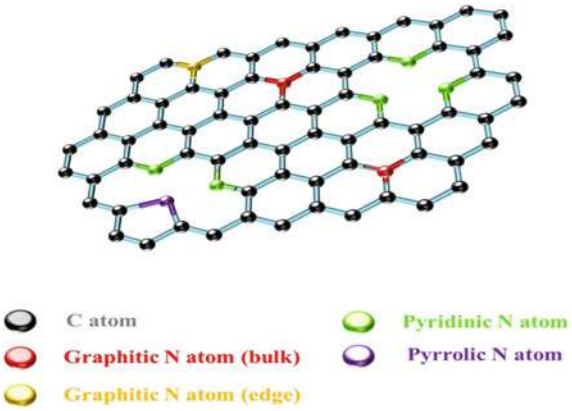

Fig. 6 Binding configurations of the N atoms inside the carbon structure (" Reproduced from Ref. [30] with permission from the Elsevier.")

phosphorus (P) and sulfur (S) are the leading heteroatoms included in carbon materials. Among these, it has been studied frequently with N as a heteroatom additive in the literature. The N element is favorable due to its atomic size comparable to carbon and its five valence electrons. The N atom adjacent to the carbon attracts the bonding electrons towards it because of its higher electronegativity and makes the carbon partially positively charged. In the presence of a partially positively charged carbon atom, the electrons in the structure are exposed to the delocalization in the sp^2 hybrid system, which facilitates the adsorption of the reacting species to the carbon atom [29]. The bonding configurations of the N atoms inside the carbon host are in different forms. Pyridinic-N, pyrrolic-N, graphitic-N are the most common types of these configurations [30]. Figure 6 shows how different nitrogen functionalities are located within the carbon structure.

Pyridinic-N is the N atom that bonds with two carbon atoms in the hexagon and contributes to the aromatic π system with one π electron, while pyrrolic-N is the N atom that bonds with two carbon atoms in the pentagon ring and provides two π electrons to the aromatic π system. As the name suggests, when graphitic (substitutional)-N gets involved in the carbon structure, it replaces one carbon atom in the sp^2 hybrid arrangement and bonds with three carbon atoms. In graphitic-N configuration, the high energy required for the displacement of one carbon atom by an N atom is supplied by the pyrolysis process at high temperatures. Pyridinic-N and pyrrolic-N species are generally located at the edge or defect sides, while the graphitic-N is located at the interior regions of the carbon matrix. Additionally, there is sp^2 hybridization both in pyridinic-N and graphitic-N and sp^3 hybridization in pyrrolic-N [31]. Apart from these, there are other types of N functionalities encountered in the carbon framework. Neighboring atoms of the N atom in a hexagon in the pyridinic-N-oxide configuration are two carbon atoms and one oxygen atom [29]. Pyridinic N-oxides subsequently convert to pyridinic-N and pyridinium cation (pyridinic-N–H) in an acidic environment [32]. The quaternary-N (quaternary ammonium cation) is the structure to which four different groups are attached to the positively charged N cation in the center. This type of N configuration can be

classified depending on attached functional groups to N cation [33]. Pyrolyzed N_4-macrocyclic complexes, abbreviated as M-Nx, mean the number of N atoms ($1 \leq x \leq 4$) coordinated with a 3d transition metal (M) such as iron (Fe) or cobalt (Co) [34]. The triazine unit (C = N) in the carbon lattice has strong covalent bonds and rich N content, which endows the chemical stability and special heteroatom effect to the material [35].

The high surface area, large pore volume, high electrical conductivity, high ion transfer capability of graphene foams make these materials attractive for electronic devices. However, graphene foams were made composite with different metals to improve further their electronic properties like electrode capacity and energy/power density. Although the use of catalytically active metals works, this case both increases the cost and brings environmental concerns such as the removal of metals. Therefore, as with many carbon derivatives, heteroatom additives with inexpensive elements (especially N) have been used for graphene foams [36]. Table 2 includes some studies in the literature on N-doped graphene foams.

Table 2 Studies on N-doped graphene foams

Method	N-content (at. %)	Application	References
Ar plasma pre-treatment	2.30	Hydrogen evolution reaction (HER)	[37]
Hydrothermal	2.57	Water splitting	[38]
Solvothermal	2.60	Electrocatalytic applications	[39]
CVD and annealing	3.49	Li/S battery	[40]
Pyrolysis	4.24	Direct methanol fuel cell (DMFC)	[41]
Freeze-drying & heat treatment	6.80	Hydrogenation reduction of p-nitrophenol	[42]
Hydrothermal and pyrolysis	7.17	Polymer electrolyte membrane (PEM) fuel cell	[43]
Hydrothermal and freeze-drying	7.23	Nitrobenzene reduction and methylene blue degradation	[44]
Hydrothermal	9.88	Supercapacitors	[45]
CVD	12.37	Energy conversion and energy storage	[46]
Hard-templating	13.12	Oxygen reduction reaction (ORR)	[47]
Hydrothermal and annealing	15.70	Supercapacitors	[48]

3 Preparation of Nitrogen-Doped Graphene Foams

N-doping of 3D graphene foam materials can be done in-situ or ex-situ during graphene foam synthesis. Moreover, a single method or more than one method can be used in any experimental procedure for the preparation of N-doped graphene foam. The methods frequently encountered in the literature are shown in Fig. 7. Each method has its advantages and limitations in terms of ease of use, special equipment requirement, production volume, protection of the 3D structural integrity of the graphene foam, N content, kind of N species, experimental time and cost. The formation of graphene foam and N-doping by CVD method takes place on-site and is one of the most preferred methods. In the hard-template technique, some template materials are used to create the 3D structure and then removed from the environment at the end of synthesis. The N-doping usually takes place ex-situ after the pyrolysis process in the presence of an N source. Although 3D graphene foam synthesis and N-doping can be done simultaneously with hydrothermal and solvothermal methods, mostly these methods are followed by pyrolysis step at high temperatures for ex-situ N-doping of the products. In 3D graphene foam synthesis, freeze-drying is rarely applied alone and is often used in conjunction with other methods to remove solvents while preserving the 3D structure. N-doping also takes place ex-situ by pyrolysis. Graphite exfoliation is usually applied to facilitate the construction of the 3D structure. In this method, N-doping is conducted through additional heat treatment. In 3D N-doped graphene foams synthesized by plasma treatment, plasma initially creates defects that promote N-doping in the structure. Then, N atoms are ex-situ doped to these defective regions by a high-temperature pyrolysis process.

CVD procedure is widely used in the synthesis of graphene foam. With this method, it is possible to obtain 3D graphene foam structures with high crystallinity and large surface area. Microporous metal templates or metal foams are used to create the 3D graphene network. The metal template used highly affects the morphology and pore size of the 3D graphene foam. Generally, commercial Ni or copper (Cu) templates with a minimum pore size of around 200 μm are preferred [49]. Other important parameters for the growth of N-doped graphene foams are gas flow rate, C/N ratio in the gas flow and temperature. Higher flow rate results in more layers, lower C/N ratio results in more N content. Temperature is effective in the formation of different N configurations [50]. In the CVD method, monolithic graphene foam synthesis is performed by decomposition of methane (CH_4) gas at ambient pressure and at 1000 °C on the Ni foam scaffold (used to build the 3D graphene architecture)

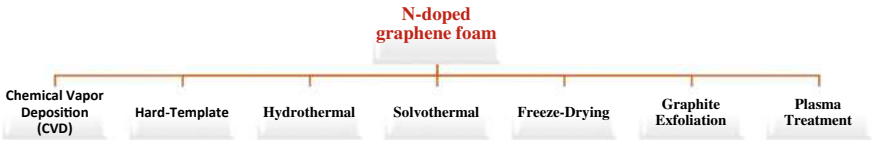

Fig. 7 N-doped graphene foam synthesis methods

to form wrinkled, intertwined graphene film and then removing the Ni substrate from the environment with etching process by using an inorganic acid [51].

Xue et al. [52] conducted the synthesis of graphene foam and N-doping simultaneously. The N-doped graphene foam was produced by heating the template Ni foam under CH_4 and ammonia (NH_3) gas flows in a quartz tube and then finally removing the Ni template from the ultimate sample. The N-doping level was reported as 3.1%. Additionally, PMMA polymer was used as a thin film on the N-doped graphene foam to protect the structural integrity of the synthesized product. Wang et al. [40] produced 3D N-doped graphene foam with the CVD method in company with Ni template and melamine. Melamine was used as a carbon and N source through the annealing process in a CVD furnace. The surface area and total pore volume of the N-doped graphene foam were respectively found as 656 $m^2\ g^{-1}$ and 3.0584 $cm^3\ g^{-1}$. It is thought as a large number of interconnected macropores will facilitate electrolyte transfer within the structure for electrochemical reactions. Mo et al. [53] designed a different nanostructure comprised of synthesized 3D N-doped graphene foam encapsulated by a yolk-shell made of germanium (Ge) and N-doped graphene. A two-step CVD method was used to create this nanostructure. The authors used this design to present a free space to the electrode during the expansion and contraction of the electrode resulting from the aggregation and leaching of lithium (Li) in Li-ion batteries. Thus, the electrochemical potential of the electrode will increase without damaging the outer shell. Other hybrid structures in which 3D graphene exists, are created with the CVD method. Li et al. [46] combined the 1D CNTs with 2D graphene in the content of a highly N-doped 3D hybrid (N-CNTs/N-graphene) structure by applying a one-step template-directed CVD process. Ni foam used (template) was mixed with melamine (carbon and N source) in a ratio of (1:5), placed in a quartz reactor, and annealed at 800 ºC under argon (Ar)/hydrogen (H_2) mixed gas flow through 0.5 h to produce N-CNTs/N-graphene. All steps of the synthesis are shown schematically in Fig. 8. N-CNTs/N-graphene yields a high graphitization degree, high N content, mesoporosity and regular 3D structure.

In the hard-template technique, the material with desired porous structure is built by using pre-formed templates such as nanoparticle aggregates, carbon, or mesoporous silica [54]. Zhou et al. [55] obtained the porous 3D N-doped graphene foam by a hard-template method using silica nanoparticles. Silica nanoparticles dissolved in ethanol were combined and mixed together with $FeCl_2.4H_2O$ and dicyandiamide. Afterward, GO suspension was added to the mixture. Subsequent to the further mixing and drying steps, the sample was pyrolyzed at 900 ºC in N_2 atmosphere. After pyrolysis, silica nanoparticles were removed and the final product was pyrolyzed again at the same conditions. Niu et al. [56] produced a sub-micrometer 3D graphene sponge using silica spheres (80 nm) by hard template-associated pyrolysis method. Chitosan was used for N-doping of the graphene sponge. First, the solution contains chitosan, glacial acetic acid and water was mixed with silica spheres and extracted under reduced pressure. The resulting solid product was separated by centrifuge and after washing and drying processes, it was pyrolyzed at 900 ºC under Ar gas flow. Subsequent to the pyrolysis process, the silica template was removed selectively by etching and a 3D N-doped graphene sponge was obtained. The authors stated that

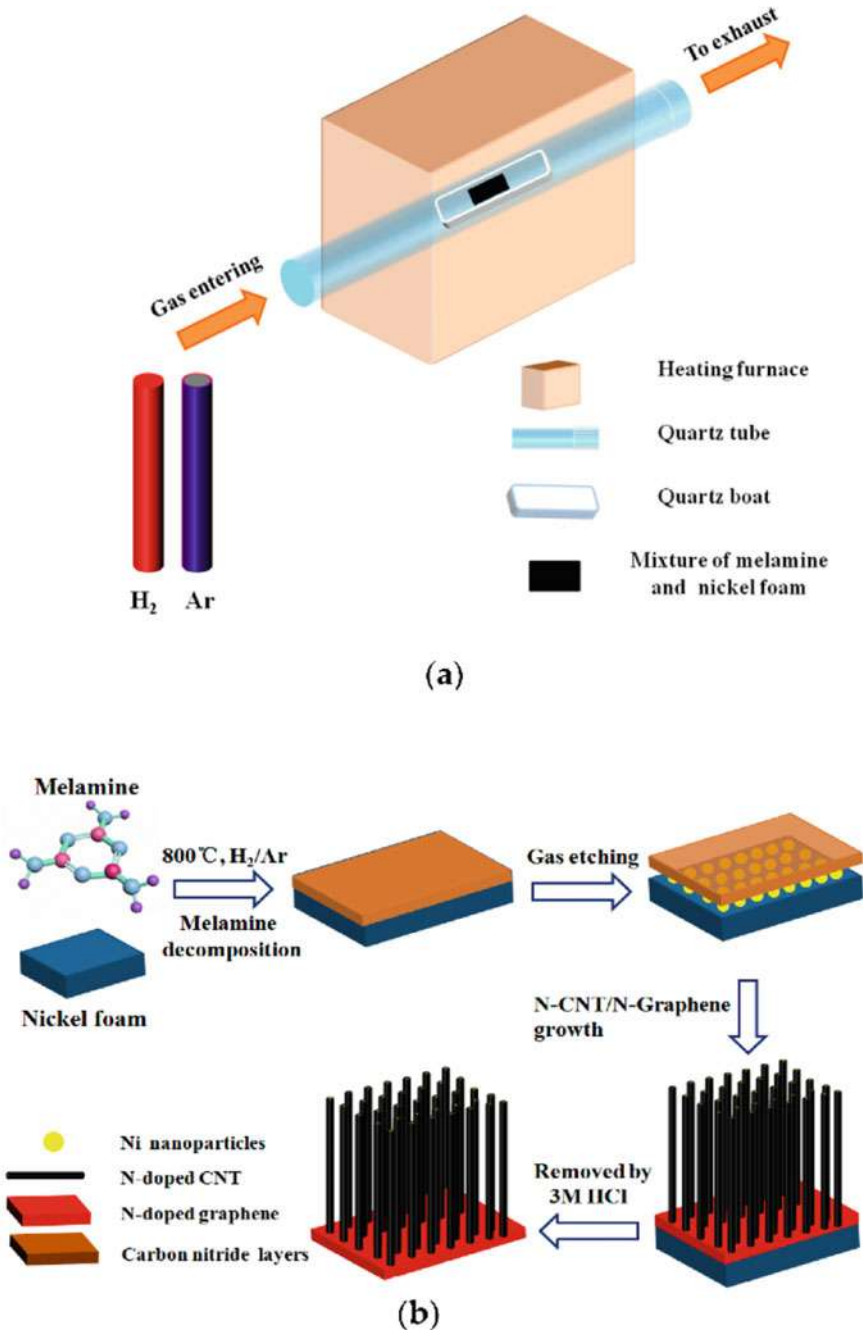

Fig. 8 Synthesis of 3D N-CNTs/N-graphene with one-step CVD method (" Reproduced from Ref. [46] with permission from the MDPI.")

adjusting the size of the silica template will control the properties of the graphene sponge such as surface area, electrical and thermal conductivity, density and pore structure.

Hydrothermal and solvothermal methods are frequently used in the synthesis of innovative materials. The chemical reactions respectively proceed in an aqueous solution (above 100 ºC) and a non-aqueous solution environment (at relatively high temperature) in the hydrothermal and solvothermal methods. Solid-state reactions occur through the diffusion of reactants at the interface, while in the hydrothermal and solvothermal methods, reactive ions or molecules react in the solution media [57]. In our previous study [8], 3D graphene aerogel synthesis was performed by the hydrothermal method. The resulting material has 265.3 m^2 g^{-1} surface area and a high hydrophobicity (145.6º). Shu et al. [58] synthesized the lightweight 3D N-doped rGO/multi-walled carbon nanotubes (MWCNTs) composite foams (NRGO/MWCNTs) as an highly efficient microwave absorbers. Acid-treated CNTs were dispersed in the GO dispersion by sonication. Ethylenediamine (EDA) was added dropwise onto the mixture. The final mixture was then treated in a Teflon-lined stainless-steel autoclave by hydrothermal method for 12 h at 120 ºC. The obtained NRGO/MWCNTs composite hydrogels were transformed into aerogels by dialysis (36 h) and freeze-drying (48 h). Finally, the aerogel structure was calcined under Ar gas flow for 1 h at different temperatures (200, 400, 500, 600 ºC). It was stated that the calcination temperature affected the microstructure. The density values of the composite foams were found in the range of 10.3–11 mg cm^{-3}. Figure 9 shows the steps of synthesis procedure of the NRGO/MWCNTs composite foams.

Xu et al. [59] synthesized the 3D N-doped porous magnetic graphene foam (MGF)-supported Ni nanocomposites via one-pot hydrothermal method. Solution B, consisting of specified amounts of nickel chloride hexahydrate ($NiCl_2 \cdot 6H_2O$) and

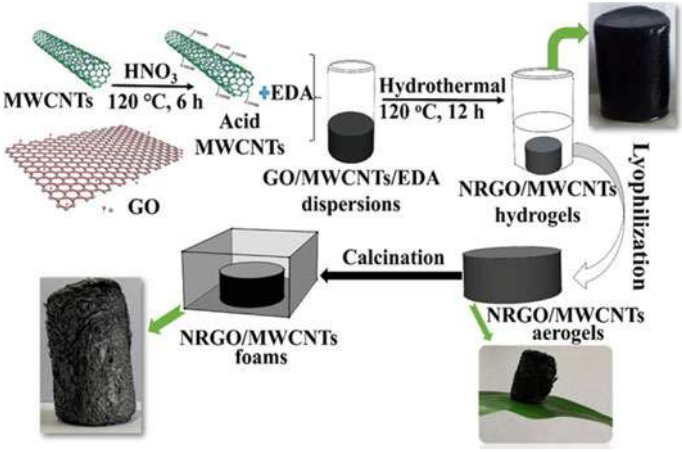

Fig. 9 Synthesis procedure of the NRGO/MWCNTs composite foams ("Reproduced with permission from [58] Copyright (2020) American Chemical Society.")

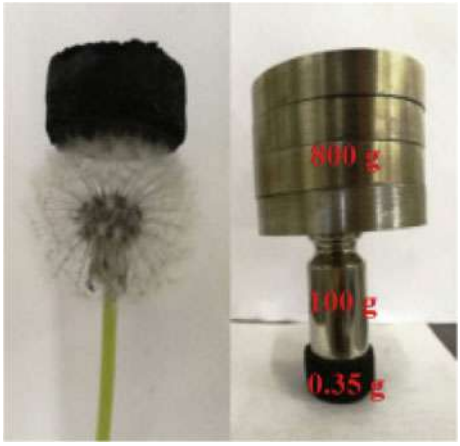

Fig. 10 Superlight and mechanically resistant 3D N-doped MGF@Ni nanocomposite (" Reproduced from Ref. [59] with permission from the Elsevier.")

hexadecyl trimethyl ammonium bromide (CTAB), was added to solution A consisting of PVA and GO, and then hydrazine hydrate ($N_2H_4{\cdot}H_2O$) was added dropwise to the final solution. This solution was heat-treated in the sealed Teflon autoclave at 180 ºC for 8 h. Afterward this step and freeze-drying, 3D N-doped MGF@Ni nanocomposite was obtained. During the hydrothermal process, the graphene layers were reduced and the 3D graphene structure spontaneously formed thanks to hydrogen bonds and π-π interactions with the driving power of PVA in the environment. The image in Fig. 10 proves that the 3D N-doped MGF@Ni nanocomposite has a very low density (0.027 g cm^{-3}) and high mechanical strength.

Moumaneix et al. [39] have synthesized 3D graphenic foam with very high surface area (2243 m^2 g^{-1}) by solvothermal method. Cyclohexanol, ethanolamine, and metallic sodium (Na) rods were mixed in an autoclave to initiate the synthesis. The sealed autoclave was filled with N_2 gas up to reach 70 bar pressure and then the reactor was heated up to 350 °C with 8 ºC min^{-1} ramp rate. Due to the increased temperature, the internal pressure of the reactor was 200 bar in its final form and it was left in this way for 72 h. Pyrolysis was conducted between the temperature range of 750–900 °C under a continuous N_2 gas flow after the solvothermal process. Graphenic foam, pyrolyzed at 850 ºC, was the best sample in terms of purity, homogeneity, and crystallinity. Pruna et al. [60] investigated the effect of parameters such as temperature, reaction time, GO concentration, GO/EDA ratio on graphene aerogel synthesized by the solvothermal method in the presence of EDA. High-temperature processing (120, 140, and 165 °C) increases the degree of GO reduction, while low-temperature processing (85 °C) increases the degree of N functionalization.

One of the traditional applications in graphene foam production is freeze-drying. The freeze-drying method enables the production of graphene foam in the desired morphology and pore size. In the freeze-drying procedure, the porous architecture of the suspended materials is obtained by initially freezing an aqueous suspension followed by sublimation of the frozen aqueous solvent at reduced pressure. Figure 11 shows the brief demonstration of porous structure formation by freeze-

drying process. Isotropic and anisotropic solidification during freeze-drying results in oriented, uniform pore size and randomly distributed, varying pore size, respectively [61]. This process is mostly used as a technique applied subsequently hydrothermal or solvothermal methods rather than solely being used in the synthesis. There is also a case where freeze-drying is applied as the fundamental method. Yu et al. [62] selected the freeze-drying method for 3D N-doped graphene foam synthesis and followed an environmentally friendly and easy path. First, they prepared a GO solution, dried this solution in liquid N_2, and then applied freeze-drying and vacuum drying for three days. They obtained GO foam with these processes. GO foams were pyrolyzed in NH_3/Ar (flow rate of 1:1) gas mixture at 800 ºC for 1 h to execute N-doping. The final product was a 3D N-doped graphene foam with a large surface area (347 m^2 g^{-1}) and uniform structure. It also exhibits the 2.71 S cm^{-1} electrical conductivity value.

Skorupska et al. [36] synthesized metal-free, 3D N-doped graphene foam in a microwave reactor by changing solvents (ethyl alcohol (EtOH) and dimethylformamide (DMF)) and microwave durations (10, 30, 60, or 90 min). Commercial expanded graphite and the natural green algae N-precursor, Chlorella Vulgaris, were sonicated together. The final dispersion was loaded into a microwave reactor and heated with the power range of 300–600 W. After washing and drying processes, the carbonization process was applied to the product under N_2 gas flow for 4 h at 900 °C. EtOH and DMF solvents both contributed to graphite exfoliation. The highest N content (2.44 at. %) belongs to the N-doped graphene foam sample prepared by

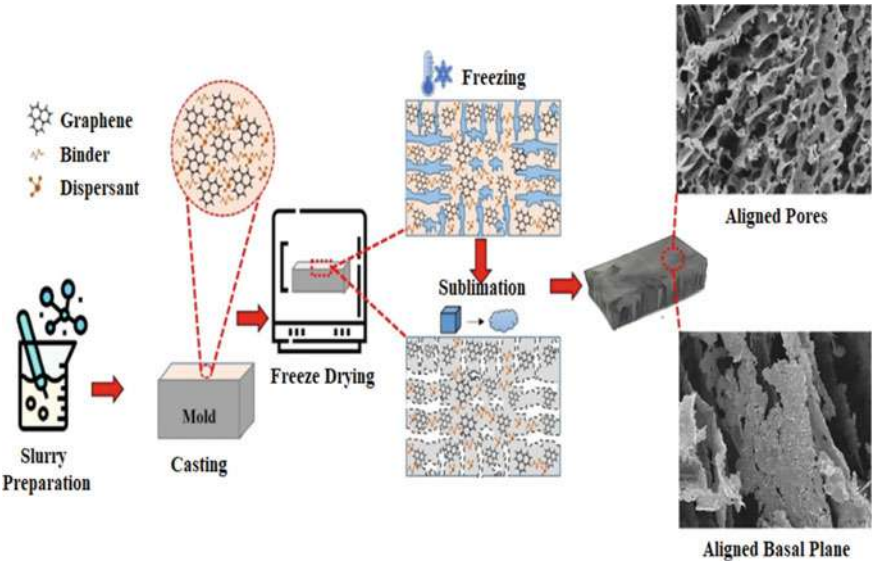

Fig. 11 A brief demonstration of porous structure formation by freeze-drying process (“ Reproduced from Ref. [61] with permission from the MDPI.”)

microwaving the exfoliated graphite in EtOH dispersion for 10 min. Zhou et al. [37] aimed at improving the electrocatalytic properties of 3D N-doped graphene foam by applying them Ar plasma pretreatment and N, S co-doping. If the experimental procedure is briefly given, a 3D graphene foam structure was created on Ni template by the CVD method. 3D N-doped graphene foam was obtained by first applying Ar plasma pretreatment to the graphene foam and then by thermal annealing in the presence of phenothiazine. The Ar plasma pretreatment and thermal annealing provided a well-organized network, which delivers the fast charge transfer within the 3D structure of the N-doped graphene foam. Additionally, Ar plasma pretreatment has created numerous nanoholes and active sites for effective heteroatom-doping.

Apart from those mentioned, there are different approaches used for 3D N-doped graphene foam synthesis. Du et al. [63] developed the classical hard-template method by pyrolyzing the commercial PU graphene foam coated with GO in the EtOH flame open to the atmosphere. The authors stated that the pyrolysis process in the EtOH flame enables the template to move away from the structure in less than 1 min and a facile way. N-doped 3D graphene foams obtained by this method have physical properties such as high flexibility, high energy dissipation ability, high hydrophobicity and ultra-low density. The visual of the applied procedure is presented in Fig. 12. Zou et al. [64] also adopted the EtOH flame annealing approach to the 3D N-doped graphene foam structure, which they created using GO-coated PU template. Liu et al. [65] synthesized N-doped graphene foam by combustion of sodium alkoxide, which they used as a low-cost N source with large-scale production. Combustion was carried

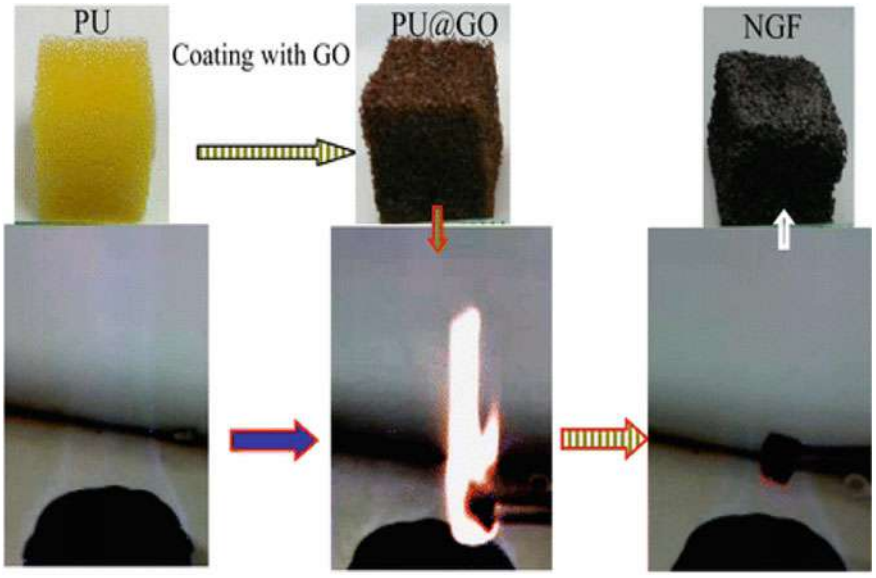

Fig. 12 Pyrolysis of PU@GO graphene foam in EtOH flame ("Reproduced with permission from [63] Copyright (2016) ACS Publications.")

out in the ignition dish and an open flame. After the burning and washing processes, the heat treatment was applied first in N_2 and then in the N_2/H_2 atmosphere. The resulting N-doped 3D graphene foam contains voids around 2 μm. Zhai et al. [66] applied water vapor treatment to adjust the hydrophobicity and adhesion of the N-doped graphene foam obtained by hydrothermal and freeze-drying methods. After 3 h of application in the environmental chamber at 85 ºC and 70% relative humidity, the structure became highly hydrophobic due to the thin hydrocarbon layer formation on the surface of the N-doped graphene foam. By the sludge flocs, which is organic waste, as both carbon and N sources, the N-doped mesocellular graphene foam was obtained by the single-step pyrolysis process by Ye et al. [67]. This method has enabled organic waste utilization and low-cost synthesis of N-doped graphene foam.

4 Applications of Nitrogen-Doped Graphene Foams

4.1 Fuel Cells

The principle of fuel cells is based on the direct conversion of chemical energy into electrical energy through electrochemical reactions taking place on the heterogeneous catalyst surface [68]. Fuel cells are more energy-efficient than other conventional systems. Various types of fuel cells (polymer electrolyte membrane (PEM), alkaline, phosphoric acid, molten carbonate, solid oxide etc.) differ from each other over fuel, electrolyte, and operating conditions [69]. Generally, platinum (Pt) or Pt alloy catalysts dispersed on carbon-based materials are favored for ensuring effective catalyst utilization in fuel cells [70–73]. Various carbon derivatives are used as support materials in fuel cell catalysts. Under this title, studies involving the use of 3D N-doped graphene foam structures in fuel cells as support material or directly as non-precious catalyst were included.

Liu et al. [65] used the N-doped graphene foam, which they obtained by combustion of N-containing sodium alkoxide, as catalyst support material in the fuel cell. The synthesized 3D N-doped graphene foam has a surface area of 700 $m^2\ g^{-1}$ and a highly defective structure. The N content is determined as 3 at. %. Linear sweep voltammetry (LSV) was applied in oxygen (O_2) saturated 0.1 $_M$ $HClO_4$ electrolyte solution for the electrochemical analysis. The onset potential, specific activity and mass activity were found as respectively 1.02 V, 13.35 μA cm^{-2} and 5.7 A $g_{Pt}{}^{-1}$ for the Pt catalyst supported with 3D N-doped graphene foam. In addition, this catalyst has less loss in electrochemical active surface area (ECSA) after 10,000 cycles in cyclic voltammetry (CV) than a pristine graphene foam supported Pt catalyst. N-doping improved the catalyst-support interaction. Ma et al. [74] prepared the bifunctional catalysts for oxygen reduction reaction (ORR) and oxygen evolution reaction (OER) from the cobalt oxide (Co_3O_4) nanocrystals supported on N, S co-doped graphene foam. The hydrothermal method was used for the synthesis of N, S-doped graphene foam.

Thiophenic S, pyridinic-N and graphitic-N atoms are desired heteroatom species for enhancement ORR catalytic activity through decreased bandgap of graphene material. Rotating disk electrode (RDE) measurements were performed in O_2 saturated alkaline 0.1 $_M$ KOH solution. Co_3O_4 catalyst supported with N-doped graphene foam gave the highest current density and 3.7 electron transfer number per O_2 molecule. The same catalyst also preserved 87% of normalized current value in an O_2 saturated 0.1 M KOH solution during the 10,000 s in the chronoamperometry experiment. N, S co-doping, Co_3O_4 (111) crystal plane and synergetic effect between the catalyst particles and graphene foam enhance the ORR catalytic activity and stability. Tang et al. [75] produced the 3D porous N-doped graphene via a facile one-step template-free method. The synthesized N-doped porous graphene provides a high specific surface area of 920 $m^2\ g^{-1}$ for the catalyst dispersion. The dominant N type in the structure was graphitic-N with a ratio of 75.85%. LSV results of electrocatalysts on RDE in O_2 saturated 0.1 M KOH electrolyte show that Pt catalyst on 3D porous N-doped graphene reaches a higher limiting current density value (7.154 mA cm^{-2}) than that of commercial Pt/C (6.077 mA cm^{-2}) catalyst. It also remarkably tolerates the destructive effect of methanol addition to the electrolyte on ORR catalytic activity according to the Pt/C. Çögenli et al. [76] prepared Pt catalysts on hydrothermally synthesized heteroatom doped (N, B) graphene aerogels to be used directly in methanol and formic acid liquid fuel cells. The doping rate for both atoms was around 8%. N-doped graphene aerogel supported Pt catalyst yielded the highest carbon monoxide (CO) tolerance for both methanol and formic acid oxidation.

In fuel cells, it is more reasonable to carry out electrochemical reactions with non-precious catalysts that provide high activity without using Pt catalysts, which are both expensive and have limited resources. In this concept, large surface area hierarchical porous N-doped graphene foams (HPGF) functionalized with a transition metal (Fe) were generated by Zhou et al. [77]. Silica spheres were used as templates. Cyanamide (HPGF-1), melamine (HPGF-2), and urea (HPGF-3) were included in the procedure as different N precursors. Graphene foams with the porous, spongy morphology, free from re-stacking of graphene sheets, were obtained. N species in HPGF-1 were detected as pyridinic-N (37.9%), graphitic-N (51.9%) and N-oxide (10.2%), so it was expected the enhanced ORR catalytic activity due to the majority of pyridinic-N and graphitic-N in the structure. According to Fig. 13, the limiting current density value (~9.90 mA cm^{-2}) of the HPGF-1 was 1.8 times higher than the value (5.40 mA cm^{-2}) given by the commercial Pt/C catalyst in acidic media. Large surface area (918.7 $m^2\ g^{-1}$) of this catalyst provides effective distribution of catalytically active sites. Hierarchical porosity accelerates the mass transfer via short diffusion pathways inside the graphene foams.

Xu et al. [52] produced N-doped, B-doped and N, B co-doped graphene foam with the CVD method. The N, B co-doping was provided by the melamine diborate precursor. Synthesized heteroatom doped graphene foams served as a non-precious catalyst for the ORR reaction. According to the ORR catalytic activity measurements with RDE, N (4.5 at. %), B (3 at. %) co-doped grapheme foam reveals the highest limiting diffusion current density value in alkaline media. 3D well-defined porous structure, high ECSA value, and co-doping of N and B atoms led to this positive

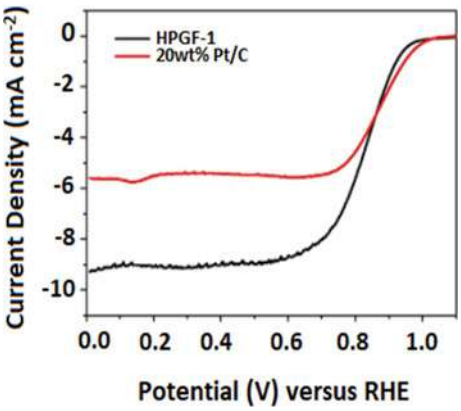

Fig. 13 ORR polarization curves of the HPGF-1 and Pt/C catalysts (O_2-saturated 0.1 M KOH electrolyte, scan rate: 50 mV s^{-1}, rotation rate: 1600 rpm) (" Reproduced from Ref. [77] with permission from the Elsevier.")

result for the related graphene foam. Dong et al. [47] also suggested that adding more than one heteroatom (N, B, P) to porous graphene foam gives the best results in terms of ORR. During the synthesis of the graphene foam, the Fe used as transition metal increased the number of heteroatoms included in the structure. As a result of the direct use of the final porous B, N, P and Fe-doped graphene foam as a non-precious catalyst, higher ORR catalytic activity was obtained compared to a single heteroatom additive.

As can be seen from the examples given, both the 3D interconnected graphene network and the heteroatom doping give positive results on the ORR, regardless of how the material is used as a support or non-precious catalyst. Table 3 gives a summary of some presented studies on ORR catalytic activities of 3D N-doped graphene foams. In-situ fuel cell performance tests should also be included in literature studies to see the actual performance of 3D N-doped graphene foams in the fuel cell catalyst concept.

4.2 Batteries

The increasing energy need has made the use of renewable energy sources more on the agenda. Continuous improvements have been made to adapt renewable energy sources to daily life. Since the intermittent energy supply of these resources are possible, energy storage systems are needed as an additional source in order to eliminate the negative effect of energy cut off. Portable electrochemical batteries are at the top of the energy storage systems. Batteries can convert the chemical energy they stored into electrical energy with high efficiency. They offer high energy density, high specific capacity, high retention rate, safe use and low cost [82]. Intensive studies have been carried out on different types of batteries and innovative electrode

Table 3 ORR catalytic activities of 3D N-doped graphene foams catalysts

Catalyst	Synthesis method	BET surface area ($m^2 g^{-1}$)	N-doping (at. %)				Catalyst loading (mg cm^{-2})	Onset potential (V)	Half-wave potential (V)	Limiting current density (mA cm^{-2}) (@1600 rpm)	Electron transfer number	Electrolyte	Refs
(B,N)-Doped 3D porous graphene–CNTs (B–N–G–CNT)	Two-step CVD	32.9	N/A				N/A	N/A	N/A	~ 8 (@rpm: N/A)	N/A	0.1 M KOH	[78]
			Pyrrolic N	Pyridinic N	Graphitic N	Pyridinic N-Oxide							
			N/A	N/A	N/A	N/A							
N-doped porous graphene foams (PNGFs)	Hard-template and Pyrolysis	670	5.07				0.485	1.02 (vs. RHE)	0.86 (vs. RHE)	~ 7	3.9	0.1 M KOH	[55]
			Pyrrolic N	Pyridinic N	Graphitic N	Pyridinic N-Oxide		0.83 (vs. RHE)	N/A	6.9 (ca.)	2.7 (ca.)	0.1 M $HClO_4$	
			–	55.9	44.1	–							
B,N-doped graphene foam (BN-GF)	CVD	N/A	3.1				N/A	−0.16 (versus. SCE)	N/A	6.5–7 (ca.)	3.4–3.8 ((−0.2)−(−0.5) V)	0.1 M KOH	[52]
			Pyrrolic N	Pyridinic N	Graphitic N	Pyridinic N-Oxide							
			–	N/A	N/A	–							
N, S co-doped 3D reduced graphene oxide (N-3DrGO) (@950ºC)	Hydrothermal and Soft template and Pyrolysis	391.9	1.69				0.2	0.895 (versus RHE)	0.732 (vs. RHE)	5.23	3.87 (0.4 V)	0.1 M KOH	[79]
			Pyrrolic N	Pyridinic N	Graphitic N	Pyridinic N-Oxide							
			12.4	34.9	39.7	13.0							
FeNi-functionalized 3D N,P-doped graphene foam (FeNi@NP-GF)	One-step pyrolysis	397.9	N/A				N/A	0.91 (versus RHE)	0.74 (vs. RHE)	4.81	3.75 (−0.55)−(−0.7)V)	0.1 M KOH	[41]
			Pyrrolic N	Pyridinic N	Graphitic N	Pyridinic N-Oxide							
			-	N/A	N/A	-							
3D-Pt@N-doped graphene foam	Hydrothermal and Carbonization	903	7.17				N/A	0.989 (vs. RHE)	0.895 (vs. RHE)	4.675	3.7 (0.4–0.7 V)	0.5 M H_2SO_4	[43]
			Pyrrolic N	Pyridinic N	Graphitic N	Pyridinic N-Oxide							
			42.7	24.6	24.8	7.8							

(continued)

Table 3 (continued)

N-doped carbon encapsulated CoFe/mesoporous N-doped graphene foam (CoFe@N–C/MNGF) (@700°C)	Hydrothermal and Freeze-drying and Pyrolysis	321.6	N/A				0.153	0.87 (vs. RHE)	N/A	4.5 (ca.)	2.1–3.6 (0.15–0.35 V)	0.1 M KOH	[80]
			Pyrrolic N	Pyridinic N	Graphitic N	Pyridinic N-Oxide							
			N/A	N/A	N/A	–							
Pt Decorated N-Doped graphene foam (Pt/GF_N)	Combustion	705	3.0				0.0173	1.02 (vs. RHE)	N/A	4.3 (ca.)	N/A	0.1 M $HClO_4$	[65]
			Pyrrolic N	Pyridinic N	Graphitic N	Pyridinic N-Oxide							
			N/A	N/A	N/A	–							
3D $Co_{1-x}S$/S, N-codoped graphene/carbon foam ($Co_{1-x}S$/SNG/CF)	Infiltration and Drying and Sulfuration	136	1.61 (wt. %)				0.15	0.99 (vs. RHE)	N/A	4.2 (ca.)	3.95 (0.1–0.6 V)	0.1 M KOH	[81]
			Pyrrolic N	Pyridinic N	Graphitic N	Pyridinic N-Oxide							
			-	N/A	N/A	N/A							
Co_3O_4 anchored N,S-doped graphene foam (Co_3O_4/NSGF)	Hydrothermal	90.2	0.6				0.212	– 0.05 V (vs. SCE)	0.034 V (vs. SCE)	4.2 (ca.)	3.7	0.1 M KOH	[74]
			Pyrrolic N	Pyridinic N	Graphitic N	Pyridinic N-Oxide							
			N/A	N/A	N/A	–							

materials that will increase the energy density in these systems. The use of 3D N-doped graphene foams as carbon composite catalysts in different battery types also appears in the literature.

Jiang et al. [83] prepared the 3D architecture comprised of TiO_2 nanoparticles embedded in N-doped graphene networks (UTO/NGF) by using hydrothermal and freeze-drying processes. TiO_2 particles anchored to rGO layers during the hydrothermal process, and at the end of the synthesis, a macroscopic 3D structure where partial overlapping appeared in the rGO sheets, was formed. The total N content of UTO/NGF sourced from cyanamide was found as 7.34 at. %. UTO/NGF as anodes in Li-ion batteries performed with high reversible capacities at different current rates (165 mA h g^{-1} after 200 cycles at 1 C rate, 143 mAh g^{-1} after 200 cycles at 5 C rate, 1 C = 168 mA g^{-1}). The electrical conductivity and electrochemical activity of the UTO/NGF enhanced with the 3D architecture of the graphene networks and N-doping. Li et al. [84] prepared 3D N-doped graphene nanomesh foam (3DNGF) by simultaneously applying N-doping (calcining the PPy) and etching (calcining the $FeCl_3 \cdot 6H_2O$ nanoparticles) and used it as the cathode electrode material in the Li–S battery. The average diameter of the nanoholes with high density 1.4 $\times$ 10^{10} holes per cm^2 on the graphene sheets ranges from 30–70 nm. Penetration of the polysulfide will be facilitated with the nanoholes and 3D macroporous structure of the foam. 3DNGF has 384 m^2 g^{-1} surface area and 4.36 at. % N-doping. In addition to 3DNGF, graphene (GE) and 3D graphene (3DGE) were synthesized to compare between them. Rate performances of the prepared materials were investigated at various rates from 0.2C to 2C. 3DNGF outperformed with the reversible specific capacities of 1062, 817, 769, 729 mAh g^{-1} at 0.2, 0.5, 1, 2 C, respectively. The 831 mAh g^{-1} specific capacitance value is shown by 3DNGF when it returns to the starting point after different cycles at various currents, reveals that 3DNGF has a good rate performance. 3DNGF also exhibited long-cycle performance with 68% retention of specific capacity (578 mAh g^{-1}) after 500 cycles at 0.5 C. Figure 14 shows some of the results obtained in the related study.

Lu et al. [85] designed the 3D graphene foams co-doped with S and N for aqueous rechargeable zinc (Zn)-iodine (I) battery. The Zn and I redox reactions are expected to be regulated with a 3D porous matrix. N, S co-doped graphene foam (NSGF) was utilized both as anodic and cathodic scaffolds in the assembly of Zn-I battery. Zn-decorated NSGF was present on the anode side to prevent the formation of zinc dendrites while, pristine NSGF was present on the cathode side to promote interfacial I^-/I_3^- redox process by its porous and doping nature. Graphitic-N doping has increased in NSGF structures with the increase of pyrolysis temperature. According to the CV profiles of iodine redox properties, the NSGF sample pyrolyzed at 900 °C provided the highest current density value with good reversibility. The specific capacities for the liquid cathode in NSGF//Zn@NSGF cell were detected as 109, 99, 88, 72, and 59 mAh g^{-1}, respectively, at 50, 80, 100, 200, and 400 mA g^{-1}. The retention rate depends on the difference between the highest and lowest specific capacitance value was found to be 46%. The authors concluded as the aqueous 3D Zn-I battery with a low decay rate of 0.042% per cycle (>500 cycles) would be complementary to Li-based batteries. Xu et al. [86] synthesized 3D N-doped graphene foam (N-GF)

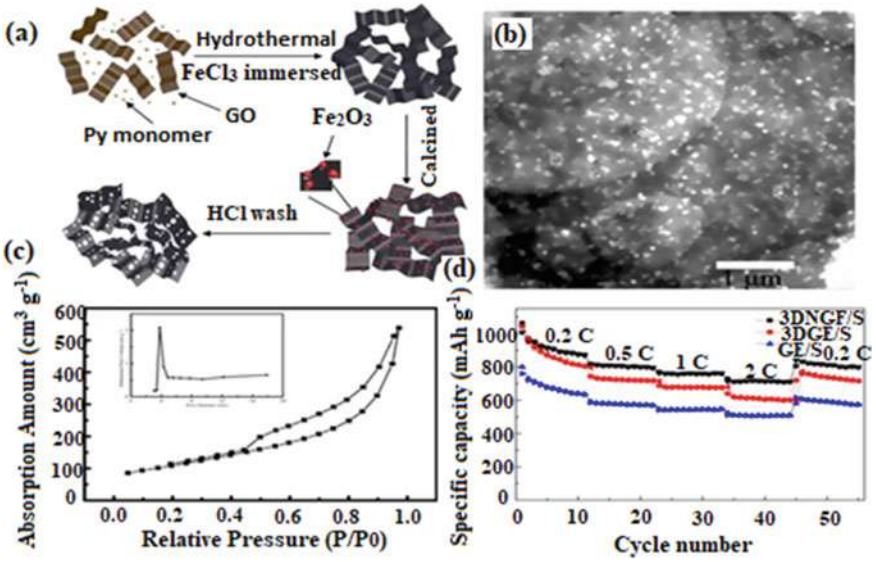

Fig. 14 **a** Preparation of 3DNGF **b** TEM image of 3DNGF **c** BET isotherm of 3DNGF **d** rate capability performance (0.2C–2C) of 3DNGF, 3DGE and GE ("Reproduced from Ref. [84] with permission from the Elsevier.").

with 6.8% N content by annealing freeze-dried GO foam in NH_3 to use as anode material in Na-ion batteries. The authors also synthesized the reduced graphene (rG), N-doped graphene (N-G), and reduced graphene foams (rGF) to compare them with N-GF. The I_D/I_G peak intensity ratio of N-GF was higher than the other samples because of edge defects and structural distortion created by 3D porous network and N-doping. 3D porous structure enables Na storage without volume expansion via available galleries to enhance the storage capacity of the ultimate material. Highly overlapped anodic peaks corresponding to partial oxidation of Na-OX groups refer to the higher Na ion insertion/extraction capability of N-GF. Average charge capacities of N-GF were recorded as 1057.1 (0.2 C), 943.5 (0.4 C), 815.2 (1 C), 467.1 (2 C), 244.7 (4 C), and 137.7 (10 C) mAh g^{-1} at different current values (1C = 500 mA g^{-1}) for 50 cycles in the voltage range of 0.02–3 V. N-GF was superior to the other samples in terms of specific capacity, charge capacity retention and Coulombic efficiency. The materials have charge transfer resistances in the decreasing order such as rG (839.8 Ω), N-G (744.8 Ω), rGF (604.1 Ω), and N-GF (502.0 Ω) in which proves the highest ionic conductivity of N-GF.

If evaluated in general, the porous matrix of 3D N-doped structures increases the charge storage capacity of electrodes for batteries in charge/discharge conditions without expansion the volume. In addition, the 3D porous structure allows ions to be transferred quickly and increases their utilization through redox reactions. Electrochemical activity improves as the N-doping promotes the formation of active sites. When all these advantages collect in one material, 3D N-doped graphene foams offer

high specific capacity, higher retention rate, high reversibility and high Coulombic efficiency when used in the electrodes of many batteries as shown in Table 4.

4.3 Supercapacitors

Supercapacitors, also known as ultracapacitors or electrochemical capacitors, are energy storage devices that are specified with their extraordinary power performance, long-cycle durability (>1,000,000 cycles), easy adaptation to electronic devices, operational ease and reversibility. Cell capacitance, operating voltage, equivalent series resistance, power density, energy density, and time constant are the key parameters that determine the performance of supercapacitors [92]. Supercapacitors are classified into three groups based on how they store energy. These are electrochemical double-layer capacitors (non-faradaic), pseudocapacitors (faradaic reactions) and hybrid capacitors (faradaic and non-faradaic reactions) [93]. The electric double layer capacitance (EDLC) originates from the electrostatically stored charge at the electrode/electrolyte interface, while the pseudocapacitance originates from the faradaically stored charge at the electrode surface [92]. Composite materials formed by combining carbon materials with conductive polymers or transition metal oxides are frequently used as electrodes of hybrid capacitors to increase both energy/power density and electrode stability [93].

Zhu et al. [94] synthesized 3D N-doped graphene (N-GE)/PANI composite foam intending to obtain supercapacitive material. The authors believe that the hierarchical porous structure of the composite foam will facilitate the penetration of the electrolyte, N-doping will increase the active sites in the foam and conductive polymer PANI will enhance the electrical conductivity of the overall material. Composite graphene foams contain different percentages of PANI polymer (20, 25, 30 wt. %), were formed by hydrothermal and freeze-drying methods. The pyridinic-N and pyrrolic-N contents of composite graphene foam containing 25% PANI polymer (N-GE/PANI-25%) by mass are respectively 4.65% and 5.50%, which will increase the pseudocapacitance of the graphene foam as electrode material. The increased amount of redox-active components in the structure provided the highest specific capacitance value of 528.4 F g^{-1} (@0.1 A g^{-1}) in acidic media with the N-GE/PANI-25% as shown in Fig. 15. The same material maintained 95.9% of its specific capacitance value after 5000 cycles. Zhang et al. [95] designed an interesting N-superdoped 3D graphene network with N content up to 15.8%. First, the graphene foam-rGO hybrid aerogel was prepared by immersing the 3D conductive graphene foam in the rGO solution and annealing the structure in this way. Subsequently, this hybrid aerogel was annealed in the presence of xenon difluoride (XeF_2) and then subjected to N-doping by annealing in the presence of NH_3. Fluorination/thermal defluorination creates defects in the GO, making the material ready for N-doping. N-superdoped 3D graphene network combined with the properties of graphene foam, rGO hydrogel, N-doping, offers a highly conductive interconnected 3D porous structure (3.33 S cm^{-1}), large surface area (583 m^2 g^{-1}), and low internal resistance (0.4 Ω). It also

Table 4 Performance results of the some 3D N-doped graphene foams based catalysts in batteries

Catalyst	Battery	Synthesis Method	BET Surface Area (m^2 g^{-1})	N-Doping (at. %)				Initial Specific Reversible Capacity (mAh g^{-1})	Coulombic Efficiency (%)	Capacity Retention Rate (%)	Rate Capability (@charge/discharge rates) (mAh g^{-1})		Ref
3D interconnected porous N-doped graphene foam with encapsulated Ge quantum dot@N-doped graphene yolk-shell nanoarchitecture (Ge-QD@NG/NGF)	Li-ion	CVD and Hydrothermal and Electroplating	392.8	N/A				1220 (charge) (0.01–1.5 V) (@ 1 C)	76.4 (initial) (0.01–1.5 V) (@1 C)	> 96 (charge) (1000 cycles) (0.01–1.5 V) (@1 C)	1 C = 1600 (mA g^{-1}) (1,2,5,10,20,40 C) (total 110 cycles)		[53]
				Pyrrolic N	Pyridinic N	Graphitic N	Pyridinic N-Oxide				Initial (@ 1 C)	1194	
				N/A	N/A	N/A	N/A				Final (@ 1 C)	1185	
3D N-doped graphene foam (NGF-700*) *annealing temperature	Li–S	Powder metallurgy template and CVD	656	3.6				987 (discharge) (@ 0.2 C)	97 (average)	82.9 (discharge) (200 cycles) (@ 0.2 C)	1 C = 1675 (mA g^{-1}) (0.1,0.2,0.5,1,2 C) (total 30 cycles)		[40]
				Pyrrolic N	Pyridinic N	Graphitic N	Pyridinic N-Oxide				Initial (@ 0.2 C)	988	
				31.4	60	8.6	–				Final (@ 0.2 C)	900 (ca.)	

(continued)

Table 4 (continued)

Catalyst	Battery	Synthesis Method	BET Surface Area (m^2 g^{-1})	N-Doping (at. %)				Initial Specific Reversible Capacity (mAh g^{-1})	Coulombic Efficiency (%)	Capacity Retention Rate (%)	Rate Capability (@charge/discharge rates) (mAh g^{-1})		Ref
N-doped carbon enwrapped Fe_3O_4 nanoparticles confined in a porous 3D N-doped graphene network (Fe_3O_4/NC/NG)	Li-ion	Hydrothermal and Calcination	215.5	2.8 (wt. %)				952 (charge) (0.01–3 V) (200 mA g^{-1})	67 (initial) (0.01–3 V) (200 mA g^{-1})	95 (charge) (100 cycles) (0.01–3 V) (200 mA g^{-1})	(100,200,500,1000 mA g^{-1}) (total 50 cycles)		[87]
				Pyrrolic N	Pyridinic N	Graphitic N	Pyridinic N-Oxide				Initial (@ 100 mA g^{-1})	970 (ca.)	
				53.8	29.7	16.5	– ara>				Final (@ 100 mA g^{-1})	894	
3D N-Doped Graphene Foam (N-GF)	Na-ion	Freeze-drying and Annealing	357	5.9				852.6 (charge) (0.02–3 V) (@ 1 C)	42.6 (initial) (0.02–3 V) (@ 1 C)	69.7 (charge) (150 cycles) (0.02–3 V) (@ 1 C)	1 C = 500 (mA g^{-1}) (0.2,0.4,1,2,4,10 C) ((0.02–3 V), total 50 cycles)		[86]
				Pyrrolic N	Pyridinic N	Graphitic N	Pyridinic N-Oxide				Initial (@ 0.2 C)	1057.1	
				N/A	N/A	–	–				Final (@ 0.2 C)	750 (ca.)	
3D N-doped graphene nanomesh foam (3DNGF)	Li–S	Hydrothermal and Freeze-drying and Pyrolysis	384	4.36				827 (1.7–2.5 V) (@ 0.5 C)	100.6 (initial) (1.7–2.5 V) (@ 0.5 C)	85.9 (200 cycles) (1.7–2.5 V) (@ 0.5 C)	1 C = 1675 (mA g^{-1}) (0.2,0.5,1,2 C) (total 30 cycles)		[84]
				Pyrrolic N	Pyridinic N	Graphitic N	Pyridinic N-Oxide				Initial (@ 0.2 C)	1062	
				N/A	N/A	N/A	–				Final (@ 0.2 C)	831	

(continued)

Table 4 (continued)

Catalyst	Battery	Synthesis Method	BET Surface Area (m^2 g^{-1})	N-Doping (at. %)				Initial Specific Reversible Capacity (mAh g^{-1})	Coulombic Efficiency (%)	Capacity Retention Rate (%)	Rate Capability (@charge/discharge rates) (mAh g^{-1})		Ref
3D N-doped graphene supported metal oxide ($NiFe_2O_4$/3DNGE)	Li–S	Hydrothermal and Freeze-drying	90	N/A				795 (charge) (1.7–2.7 V) (@ 1 C)	~ 100 (initial) (1.7–2.7 V) (@ 1 C)	79 (charge) (700 cycles) (1.7–2.7 V) (@ 1 C)	(0.2,0.5,1,2 C) (total 25 cycles)		[88]
				Pyrrolic N	Pyridinic N	Graphitic N	Pyridinic N-Oxide				Initial (@ 0.5 C)	980 (ca.)	
				N/A	N/A	N/A	–				Final (@ 0.5 C)	950 (ca.)	
Bi_2O_3 nanoparticles encapsulated by three-dimensional porous N-doped graphene (Bi_2O_3@N-G)	Li-ion	Hydrothermal and Freeze-drying and Heat treatment	112	4.4				651 (0.01–3.0 V) (200 mA g^{-1})	70 (initial) (0.01–3.0 V) (200 mA g^{-1})	64.1 (charge) (100 cycles) (0.01–3.0 V) (200 mA g^{-1})	(200,500,1000,2000, 5000,10,000 mA g^{-1}) (total 50 cycles)		[89]
				Pyrrolic N	Pyridinic N	Graphitic N	Pyridinic N-Oxide				Initial (@ 200 mA g^{-1})	650	
				N/A	N/A	N/A					Final (@ 200 mA g^{-1})	530 (ca.)	
Bi_2S_3 encapsulated within 3D N-doped graphene (Bi_2S_3/3DNG)	Na-ion	Hydrothermal and Freeze-drying and Annealing	25.7	3.24				490 (0.01–3.0 V) (125 mA g^{-1})	66 (initial) (0.01–3.0 V) (62.5 mA g^{-1})	63 (charge) (100 cycles) (125 mA g^{-1})	1 C = 625 mA g^{-1} (62.5, 125, 312.5, 625, 1250 mA g^{-1}) (total 40 cycles)		[90]
				Pyrrolic N	Pyridinic N	Graphitic N	Pyridinic N-Oxide				Initial (@ 125 mA g^{-1})	484.5	
				N/A	N/A	-	-				Final (@ 125 mA g^{-1})	447	

(continued)

Table 4 (continued)

Catalyst	Battery	Synthesis Method	BET Surface Area ($m^2 g^{-1}$)	N-Doping (at. %)				Initial Specific Reversible Capacity (mAh g^{-1})	Coulombic Efficiency (%)	Capacity Retention Rate (%)	Rate Capability (@charge/discharge rates) (mAh g^{-1})		Ref
V_2O_5 nanoparticles confined in three − dimensionally organized, porous N-Doped graphene frameworks (V_2O_5@3DNG(2.5))	Li-ion	Hydrothermal and Freeze-drying and Heat treatment	57.4	N/A				283 (100 mA g^{-1})	> 99 (initial) (100 mA g^{-1})	83 (100 cycles) (100 mA g^{-1})	(100,200,500,1000, 2000 mA g^{-1}) (total 60 cycles)		[91]
				Pyrrolic N	Pyridinic N	Graphitic N	Pyridinic N-Oxide				Initial (@ 100 mA g^{-1})	290	
				N/A	N/A	-	N/A				Final (@ 100 mA g^{-1})	275	
3D N-doped graphene foams embedded with ultrafine TiO_2 nanoparticles (UTO/NGF)	Li-ion	Hydrothermal and Freeze-drying	249.2	7.34				198 (charge) (@ 1 C)	66 (initial) (@ 0.1 C)	83.3 (charge) (200 cycles) (@ 1 C)	1 C = 168 (mA g^{-1}) (0.1,0.2,1,2,3,5,10,20 C) (total 110 cycles)		[83]
				Pyrrolic N	Pyridinic N	Graphitic N	Pyridinic N-Oxide				Initial (@ 1 C)	175 (ca.)	
				N/A	N/A	N/A	N/A				Final (@ 1 C)	170 (ca.)	

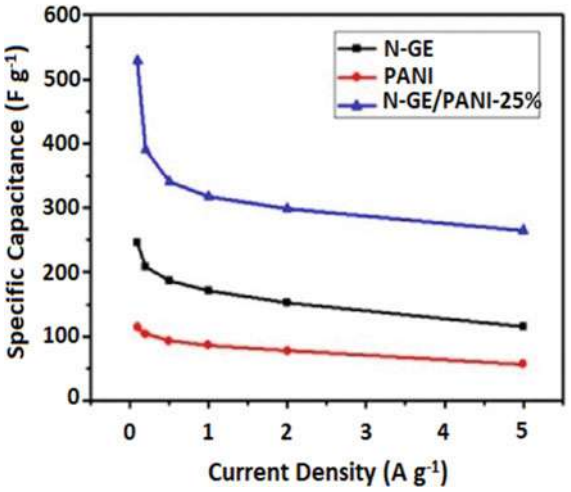

Fig. 15 The comparison of the specific capacitances of PANI, N-GE, and N-GE/PANI-25% at different current densities (" Reproduced from Ref. [94] with permission from the Elsevier.")

exhibits the 380 F g^{-1} specific capacitance in alkaline media and 93.5% retention rate after 4600 cycles.

Kwak et al. [96] fabricated the bulk-scale N-doped 3D-graphitic foams using Fe precursors in the facile one-step pyrolysis method. 3D graphitic foam has a highly interconnected structure containing micro-, meso- and macropores. Additionally, the high surface area (1509 m^2 g^{-1}) and electrical conductivity (10 S cm^{-1}) values of this material are outstanding. The high-temperature pyrolysis process promotes the formation of the graphitic-N species. In the measurements taken in the alkaline electrolyte environment (6 M KOH) in the three-electrode system, while the scanning rate was 5 m s^{-1}, the specific capacitance value of the N-doped graphitic foam was found as 330 F g^{-1}. Zou et al. [97] combined the Co_3O_4 and N-doped graphene foam for the enhanced charge storage ability. Co_3O_4 is among the materials with a high theoretical capacitance value (320 F g^{-1}) due to its stable oxidation states. Initially, N-doped graphene foam was prepared by the CVD method on a Ni template and then vertically aligned Co_3O_4 nanosheets were electrodeposited on this structure for the completion of mesoporous Co_3O_4 N-doped graphene foam. Co_3O_4 nanosheets were also built on Ni template only, without creating N-doped graphene foam on it. Co_3O_4 nanosheets electrodeposited on only Ni foam and N-doped graphene foam gave the 321 F g^{-1} and 451 F g^{-1} specific capacitance values, respectively, under the conditions 1 M KOH electrolyte at 1 A g^{-1} current density. Co_3O_4 nanosheets on N-doped graphene foam also has a 95% retention factor after 1000 cycles despite high current density (20 A g^{-1}) condition. So far, the performance improvement effect of porous 3D N-doped graphene foam as a supercapacitor electrode material is clearly understood. Table 5 shows some of the performance results of N-doped graphene foams as catalysts in supercapacitors from the literature.

Table 5 Performance results of the some 3D N-doped graphene foams based catalysts in supercapacitors

Catalyst	Synthesis method	BET surface area ($m^2 g^{-1}$)	N-doping (at. %)				Specific capacitance ($F g^{-1}$)	Coulombic efficiency (%)	Capacity retention rate (%)	Specific capacitances (@ current densities) ($F g^{-1}$)		Energy density ($Wh kg^{-1}$)	Refs
$NiCo_2S_4$ (NCS) nanotubes anchored on a 3D ultrathin N-doped graphene framework (NGF) (NCS/NGF)	Hydrothermal and Sulfurization	19	10.6				1240 (0.0–0.45 V) (@ 1 A g^{-1})	N/A	80 (5000 cycles) (0.0–0.45 V) (@ 10 A g^{-1})	(1,2,5,10,20 A g^{-1})		20.17 (@ 3000 W kg^{-1})	[98]
			Pyrrolic N	Pyridinic N	Graphitic N	Pyridinic N-Oxide				1 A g^{-1}	1240		
			N/A	N/A	N/A	-				20 A g^{-1}	861		
N-doped graphene framework supported $NiCo_2O_4$ ((NCO/NGF))	Hydrothermal and Annealing	155	10.6				1198 (0.0–0.45 V) (@ 1 A g^{-1})	N/A	97 (5000 cycles) (0.0–0.45 V) (@ 1 A g^{-1})	(1,2,4,5,8,10,15,20 A g^{-1})		32.1 (@ 188 W kg^{-1})	[99]
			Pyrrolic N	Pyridinic N	Graphitic N	Pyridinic N-Oxide				1 A g^{-1}	1198		
			N/A	N/A	N/A	-				20 A g^{-1}	634		
3D N-doped graphene/PANI composite foam (N-GE)/PANI-25%	Hydrothermal and Freeze-drying	N/A	10.15				528 (@ 0.1 A g^{-1})	N/A	95.9 (5000 cycles) (@ 5 A g^{-1})	(0.1,0.5,1,2,5 A g^{-1})		N/A	[94]
			Pyrrolic N	Pyridinic N	Graphitic N	Pyridinic N-Oxide				0.1 A g^{-1}	528		
			54.2	45.8	-	-				5 A g^{-1}	268		
Co_3O_4 Nanosheet Arrays on N-Doped Graphene Foam (Co_3O_4/NGF)	CVD and Electrodeposition	42	N/A				451 (0.0–0.45 V) (@ 1 A g^{-1})	89.2 (0.0–0.45 V) (@ 1 A g^{-1})	95 (1000 cycles) (0.0–0.45 V) (@ 1 A g^{-1})	(1,2,3,4,5,6,7,8,9,10 A g^{-1})		N/A	[97]
			Pyrrolic N	Pyridinic N	Graphitic N	Pyridinic N-Oxide				1 A g^{-1}	451		

(continued)

Table 5 (continued)

Catalyst	Synthesis method	BET surface area ($m^2 g^{-1}$)	N-doping (at. %)				Specific capacitance ($F g^{-1}$)	Coulombic efficiency (%)	Capacity retention rate (%)	Specific capacitances (@ current densities) ($F g^{-1}$)		Energy density ($Wh kg^{-1}$)	Refs
			N/A	N/A	N/A	N/A				10 A g^{-1}	397		
3D N-doped mesoporous graphene (N-3DMG)	Solvothermal (amidation) and Freeze-drying and Calcination	627	9.25				408 (0.0–0.4 V) (@ 1 A g^{-1})	N/A	90.6 (5000 cycles)	(1,2,3,5,10 A g^{-1})		N/A	[100]
			Pyrrolic N	Pyridinic N	Graphitic N	Pyridinic N-Oxide				1 A g^{-1}	408		
			N/A	N/A	N/A	N/A				10 A g^{-1}	255		
N,S co-doped graphene-enhanced hierarchical porous carbon foam (N,S-GHPCF)	Sol–gel & Freeze-drying and Calcination	2806	6.67				405 (@ 1 A g^{-1})	> 97 (@ 10 A g^{-1})	98.8 (10,000 cycles)	(1,2,5,10,20,50,100 A g^{-1})		18.4 (@ 300 W kg^{-1})	[101]
			Pyrrolic N	Pyridinic N	Graphitic N	Pyridinic N-Oxide				1 A g^{-1}	405		
			N/A	N/A	N/A	-				100 A g^{-1}	295		
3D N-doped graphene derived from poly-o-phenylenediamine (3DNGN)	Heat treatment and Acid leaching	907	7.24				345 (@ 1 A g^{-1}) (@ H_2SO_4) 312 (@ 1 A g^{-1}) (@ KOH)	N/A	96 (5000 cycles) (@ 2 A g^{-1}) (@ H_2SO_4) 98 (5000 cycles) (@ 2 A g^{-1}) (@ KOH)	(1,2,5,10,20,50,100 A g^{-1})		8.4 (@ 10,000 W kg^{-1}) (@ H_2SO_4) 9.1 (@ 10,000 W kg^{-1}) (@ KOH)	[102]
			Pyrrolic N	Pyridinic N	Graphitic N	Pyridinic N-Oxide				1 A g^{-1} (@ H_2SO_4) 1 A g^{-1} (@KOH)	345 312		
			16.7	22.1	61.2	-				50 A g^{-1} (@ H_2SO_4) 100 A g^{-1} (@KOH)	238 227		

(continued)

Table 5 (continued)

Catalyst	Synthesis method	BET surface area ($m^2 g^{-1}$)	N-doping (at. %)				Specific capacitance ($F g^{-1}$)	Coulombic efficiency (%)	Capacity retention rate (%)	Specific capacitances (@ current densities) ($F g^{-1}$)		Energy density ($Wh kg^{-1}$)	Refs
3D N&S co-doped rGO foam (3D NS-rGO)	Freeze-drying and Heat treatment	505.7	3.5				306.3 (@ 1 A g^{-1})	N/A	98 (10,000 cycles)	(1,2,3,4,5,10 A g^{-1})		N/A	[103]
			Pyrrolic N	Pyridinic N	Graphitic N	Pyridinic N-Oxide				1 A g^{-1}	306.3		
			38.7	32.6	21.4	7.3				10 A g^{-1}	206.3		
N-superdoped, graphene fiber-supported 3D graphene foam (NGF)	Hydrothermal and Fluorination and Annealing	252.2	15.7				303.5 (@ 0.5 A g^{-1})	N/A	92.8 (1000 cycles) (@ 30 A g^{-1})	(0.5,1,2.5,5,10 A g^{-1})		42.1 (@ 250 W kg^{-1})	[48]
			Pyrrolic N	Pyridinic N	Graphitic N	Pyridinic N-Oxide				0.5 A g^{-1}	303.5		
			N/A	N/A	N/A	-				10 A g^{-1}	221		
3D N-doped, steam activated, reduced graphene oxides (N-SRGO)	Freeze-drying and Heat treatment/steam activation	497	7.84				23 (0–2.5 V) (@ 0.5 A g^{-1})	97.3 (@ 5 A g^{-1})	63 (5000 cycles) (@ 5 A g^{-1})	(0.5,1,2,5 A g^{-1})		20 (@ 6190 W kg^{-1})	[104]
			Pyrrolic N	Pyridinic N	Graphitic N	Pyridinic N-Oxide				0.5 A g^{-1}	23		
			N/A	N/A	N/A	N/A				5 A g^{-1}	16 (ca.)		

4.4 Sensors

Chemical sensors generate an analytical signal based on chemical information, such as the concentration of a chemical compound. Chemical information is generated in connection with a chemical reaction or a determinant physical property of the system. In biosensors, specific biochemical reactions detect the chemical compounds via an electrical, thermal or optical signal. Basically, a working electrode, a counter electrode, and a reference electrode construct a chemical sensor. However, potentiometry measurements were conducted with only two electrodes [105]. Among the new generation electronic systems, especially in the flexible and wearable electronic devices, the properties of carbon materials such as high electrical conductivity, lightweight, structural flexibility, high chemical and thermal stability, mass production, ease of functionalization are frequently used [106]. As a carbon-based material, the adaptation of 3D N-doped graphene foams in electrochemical or biochemical sensors will also serve the purpose with their advantageous physical properties.

Feng et al. [107] fabricated the 3D N-doped graphene foam using the CVD method as an electrode material for the electrochemical detection of dopamine (DA). Free-standing, 3D N-doped graphene foam has the 2.71 at. % N content. Depending on CV experiments, 3D N-doped graphene foam showed the highest current value due to its high electrocatalytic activity towards the detection of DA. It is considered that the 3D porous structure and N atoms in the structure improve the transfer of electrons, thus electrocatalytic activity. The developed sensor is capable of detecting DA concentration in the range of (3×10^{-6} M)−(1×10^{-4} M). Although there were interfering compounds with DA in the media such as glucose, ascorbic acid and, urea, the 3D N-doped graphene foam sensor responded with a significant peak only towards DA addition. This case reveals the high selectivity of 3D N-doped graphene foam for DA. Chen et al. [108] developed the 3D N-doped graphene foam for sensitive detection of specific sequences of DNA. 3D N-doped graphene foam was created on Ni foam by the CVD method. DNA electrochemical biosensor was prepared after the stages of immersing the 3D N-doped graphene foam into chitosan solution, ultrasonication, washing, drying, drop-casting the 5 μL of ssDNA (1×10^{-6} M) solution on the electrode and incubation. DNA hybridization was monitored with differential pulse voltammetry along with methylene blue indicator. 3D N-doped graphene foam electrode showed the increasing peak currents linearly increasing with the logarithm of the concentrations of ssDNA. The electrode has an approximately 2.38×10^{-15} M detection limit. 3D N-doped graphene foam electrode provided high reproducibility, good selectivity, and high stability in the human blood serums as a DNA biosensor. Huang et al. [109] stated that heteroatom doping gives graphene a piezoelectric effect to be used in flexible electronic devices. For this purpose, the authors produced 3D N-doped graphene foam sensor material to monitor human motions. The graphene foam produced has many advantageous properties such as low density, large elasticity, good electrical conductivity (1.4 S m^{-1}), fine sensitivity (1.33 kP^{-1}), long-term stability (3000 cycles) and fast response (72.4 ms) that will serve its intended use. The 3D N-doped graphene foam-based piezoelectric sensor is

sensitive even up to detect finger bending with the bending degree of approximately 30° and the tiny pulse perturbation of the wrist joint. This positive result was attributed to the excellent piezoelectric properties of the structure with a tunneling-resistance-dominated conduction mechanism running on pyridinic-N and pyrrolic-N species in a 3D N-doped graphene foam. Consequently, 3D N-doped graphene foams are promising candidates for sensing applications due to the positive effects of porous interconnected networks and N-doping on the detection sensitivity shown by the material.

4.5 Other Catalytic Reactions

3D N-doped graphene foam structures have also served as catalysts for other catalytic reactions. In the study conducted by Liu et al. [42], hydrogenation reduction of p-nitrophenol to p-aminophenol was performed with a 3D N-doped graphene foam metal-free catalyst along with sodium borohydride ($NaBH_4$) aqueous solution. The purpose of this reaction is the conversion of p-nitrophenol, which is an organic pollutant, to p-aminophenol as an intermediate for valuable products in the pharmaceutical industry. It was stated that the graphene foam catalyst would provide a good interface for this reduction reaction with more accessible active sites. 3D N-doped graphene foam was prepared by freeze-drying and pyrolysis processes. The specific reaction constant and activation energy of the 3D N-doped graphene foam were found as 4.94×10^{-4} mol L^{-1} s^{-1} g^{-1} and 44.3 kJ mol^{-1}, respectively. These values found for 3D N-doped graphene foam catalyst, are close to those of metal-based catalysts. Released electrons from BH_4^- can be concentrated on the graphene foam surface via electron delocalization powered by N-doping. In this way, the reduction reaction is facilitated with the effective uptake of electrons by p-nitrophenol molecules. Wu et al. [110] developed 3D graphene foam incorporated with N defects as a metal-free catalyst for the electrochemical conversion of carbon dioxide (CO_2) to CO without using gold (Au) or silver (Ag) noble metal catalysts. In recent years, carbon materials have been considered catalysts for the CO_2 reduction reaction due to their high surface area, adjustable heteroatom doping and low cost. It was assumed that the 3D hierarchical skeleton in the graphene foam would facilitate the electrolyte penetration to the material and thus increase the interfacial interaction required for the reaction to take place. The graphene foam, synthesized by the widely known CVD method and pyrolyzed at 800 °C, has the highest N-doping and pyridinic N-type. The highest catalytic activity for CO_2 reduction belongs to N-doped graphene foam (@800 °C) which manages to catalyze CO production with the lowest overpotential (-0.19 V). As the N-doped graphene foam (@800 °C) catalyst lowers the energy barrier that the COOH* reaction intermediate has to overcome to adsorb to the catalyst surface, it promotes the CO formation and shows high selectivity for this, due to the highest pyridinic N-type.

Water splitting is another kind of reaction in which N-doped graphene foam is used as a catalyst. Hydrogen evolution reaction (HER) and OER, which are half-reactions of water splitting, are usually carried out with noble metal-based catalysts such as Pt, RuO_2 and IrO_2. Kuang et al. [111] proposed the MoS_2-NiS_2 decorated 3D N-doped graphene foam composite catalyst for water splitting because of the high cost and limited resources of noble metal catalysts. Bimetallic metal sulfides, which are in strong interaction with each other, will accelerate the dissociation of water. On the other hand, the 3D porous structure provided by graphene foam will facilitate the transfer of electrons and mass and release of the gas products. It was anticipated that the composite catalyst that contains these positive effects would exhibit high catalytic activity for water splitting. First of all, N-doped graphene foam was produced by burning GO-absorbed melamine sponge in alcohol flame. MoO_2-$Ni(OH)_2$ composite was formed on this N-doped graphene foam by hydrothermal method. Finally, this triple structure was converted to the ultimate MoS_2-NiS_2/N-doped graphene foam composite catalyst by the CVD method. In the three-electrode cell system, the significant cathodic current density with increasing overpotential and bubble formation due to the high amount of H_2 gas release were observed at the HER measurements of the composite catalyst. In addition, the low Tafel loss (70 mV dec^{-1}) of this catalyst showed that the HER kinetics proceeded through a Volmer-Heyrovsky pathway in which water molecules are initially adsorbed on the catalyst's surface and subsequently, H_{ads} coupled with another H atom and electron to form and release H_2. The 97% faradaic efficiency of the same catalyst for OER reaction indicated that the resulting oxidative current was related to the OER reaction running through the four-electron mechanism. The authors suggested the MoS_2-NiS_2/N-doped graphene foam composite catalyst loaded on a Ni foam as a bifunctional catalyst to be used in HER and OER reactions for performing overall water splitting economically and efficiently in an alkaline environment.

4.6 Other Applications

This section briefly presented a few studies on 3D N-doped graphene foams used for different purposes. Liu et al. [112] synthesized the ultra-lightweight N-doped graphene foams via hydrothermal and freeze-drying methods. They believed that the electromagnetic wave attenuation capability of the graphene foam enhances with the heteroatom doping. The material gains a strong electromagnetic wave absorption feature with the reticulated walls formed by N atoms in the structure. Zhang et al. [113] investigated the electromagnetic interference (EMI) shielding properties of the polydopamine (PDA) decorated 3D rGO foam. First, PDA-GO suspension was filtered with a special membrane to form PDA-GO film. This film was peeled off from the membrane and treated with hydrazine monohydrate in an autoclave for building 3D porous N-doped PDA-rGO foam. PDA increased the reduction of GO and supplied the N atoms to the structure for N-doping. EMI shielding effectiveness strongly correlates with the electrical conductivity of the material. Results showed

that the EMI shielding effectiveness of PDA-rGO foam (26.5 dB) was approximately 15% higher than that of the rGO-foam (23.1 dB). Fang et al. [114] fabricated the N-doped graphene nanoscroll foam for the removal of organic pollutants. Graphene nanoscroll allows continuous diffusion of organic impurities without any restrictions, thanks to its adjustable inner layer distance. The developed material showed a high affinity for the removal of organic impurities. N atoms in the structure enable the material to adhere better to organic pollutants through stronger π-π interactions, making it a super adsorbent. As can be seen from these sample studies, it is possible to exploit 3D N-doped graphene foams in other ways.

5 Conclusions

Synthesis of materials with desired features has become popular to satisfy any needs or expand the comfort zone. In this direction, the materials offer many advantageous features in one package are preferred options. 3D graphene assemblies which have both the characteristics of graphene and macroscopic porous structure, have been used in many different applications. Electron/ion mobility occurs in a facile way by the interconnected graphene network in these 3D structures such as hydrogel, aerogel, foam or sponge forms. Thanks to their high mechanical strength and flexibility at the same time, these materials are suitable for use under pressure and in applications requiring flexibility. Ultralight and high electrical conductivity 3D graphene structures are also attractive for portable or wearable sensor applications. Heteroatom doping (N, B, P, S) is used to modify the electronic and catalytic properties of these materials further. N-doped graphene foams were taken into account in this chapter. N atoms are included in different configurations in the carbon plane. Although the methods for synthesizing 3D N-doped graphene foams vary, the most commonly used ones are CVD, hard-template, and hydrothermal methods. Pyrolysis process performed in parallel with these methods is quite common. The pyrolysis temperature and N-containing precursors affect the N species included in the structure, which ultimately affects the catalytic activity of the material. Since different methods and experimental conditions affect the N-doping percentages of the materials, they show various degrees of catalytic activity towards any specified reaction. Different N-types in the carbon plane such as pyridinic-N, pyrrolic-N, graphitic-N differ from each other by structural regularity, the neighboring atoms to which they are attached and their affinity for interaction with other reactive species in the media. Therefore, the degree of catalytic activity enhancement of N-doped materials depends on what type N species is dominant in the graphene structure. In fuel cell applications, graphitic-N generally provides better catalytic activity for ORR on the other side in battery and capacitor applications, pyridinic-N and pyrrolic-N improve the pseudocapacitance of the material. As a result, 3D N-doped graphene foam materials give positive results concerning catalytic activity for fuel cells, batteries, supercapacitors, sensors, and some electrochemical reactions by means of the interconnected porous 3D architecture, N content, and different N species included in the structure. Apart

from these, they are also used for different purposes in other fields. Consequently, 3D N-doped graphene foams continue to be used and developed in different applications as promising materials with their many favorable properties.

References

1. Huang GH et al (2020) Study of the effect of chemical composition on the surface wettability of three-dimensional graphene foams. Chin Chem Lett 31(7):1839–1842
2. Nautiyal P et al (2018) In-situ mechanics of 3D graphene foam based ultra-stiff and flexible metallic metamaterial. Carbon 137:502–510
3. Rowley-Neale SJ et al (2018) An overview of recent applications of reduced graphene oxide as a basis of electroanalytical sensing platforms. Appl Mater Today 10:218–226
4. Zhang J et al (2017) 3D free-standing nitrogen-doped reduced graphene oxide aerogel as anode material for sodium ion batteries with enhanced sodium storage. Sci Rep 7
5. Huang M et al (2020) CVD growth of porous graphene foam in film form. Matter 3(2):487–497
6. Park JE et al (2018) Enhancement of mass transport in fuel cells using three-dimensional graphene foam as flow field. Electrochim Acta 265:488–496
7. Chun S et al (2020) A hierarchical 3d graphene nanocomposite foam for extremely tough, non-wettable, and elastic conductor. Adv Mater Interfaces 7(14)
8. Oner E, Ozturk A, Yurtcan AB (2020) Utilization of the graphene aerogel as PEM fuel cell catalyst support: effect of polypyrrole (PPy) and polydimethylsiloxane (PDMS) addition. Int J Hydrogen Energy 45(60):34818–34836
9. Zang XB et al (2020) 1T/2H mixed phase MoS2 nanosheets integrated by a 3D nitrogen-doped graphene derivative for enhanced electrocatalytic hydrogen evolution. ACS Appl Mater Interfaces 12(50):55884–55893
10. Zhang SM et al (2019) A facile approach to ultralight and recyclable 3D self-assembled copolymer/graphene aerogels for efficient oil/water separation. Sci Total Environ 694
11. Liu WL et al (2018) Conductive graphene-melamine sponge prepared via microwave irradiation. ACS Appl Mater Interfaces 10(29):24776–24783
12. Yang SD et al (2017) Surface roughness induced superhydrophobicity of graphene foam for oil-water separation. J Colloid Interface Sci 508:254–262
13. Qin Z et al (2017) The mechanics and design of a lightweight three-dimensional graphene assembly. Sci Adv 3(1)
14. Niu ZQ et al (2012) A leavening strategy to prepare reduced graphene oxide foams. Adv Mater 24(30):4144–4150
15. Nieto A, Boesl B, Agarwal A (2015) Multi-scale intrinsic deformation mechanisms of 3D graphene foam. Carbon 85:299–308
16. Yocham KM et al (2018) Mechanical properties of graphene foam and graphene foam-tissue composites. Adv Eng Mater 20(9)
17. Kausar A (2019) Scientific worth of polymer and graphene foambased nanomaterial. J Chinese Adv Mater Soc 779–800
18. Li Y et al (2015) Polyimide/graphene composite foam sheets with ultrahigh thermostability for electromagnetic interference shielding. RSC Adv 5(31):24342–24351
19. Zhang BX et al (2021) Interfacial engineering in PDMS/graphene composites via anchoring polypyrrole nanowires to enhance its electro-photo thermal performance. Carbon 174:10–23
20. Yang G, Lee C, Kim J (2013) Three-dimensional graphene network-based chemical sensors on paper substrate. J Electrochem Soc 160(9):B160–B163
21. Pan DX, Wang C, Wang XJ (2018) Graphene foam: hole-flake network for uniaxial supercompression and recovery behavior. ACS Nano 12(11):11491–11502

22. Liu C et al (2015) Versatile fabrication of the magnetic polymer-based graphene foam and applications for oil-water separation. Colloids Surfaces A-Physicochem Eng Aspects 468:10–16
23. Ma YX et al (2017) Ultralight interconnected graphene-amorphous carbon hierarchical foam with mechanical resiliency for high sensitivity and durable strain sensors. ACS Appl Mater Interfaces 9(32):27127–27134
24. Kasap S, Acar MB, Cakiroglu D (2019) Optimization of CVD parameters on 3D graphene foam structures with response surface methodology (RSM). Mater Res Express 6(9)
25. Chen GQ et al (2014) Fabrication of three-dimensional graphene foam with high electrical conductivity and large adsorption capability. Appl Surf Sci 311:808–815
26. Pettes MT et al (2012) Thermal transport in three-dimensional foam architectures of few-layer graphene and ultrathin graphite. Nano Lett 12(6):2959–2964
27. Sagar RUR et al (2020) Large magnetotransport properties in mixed-dimensional van der Waals heterostructures of graphene foam. Carbon 159:648–655
28. Ozturk A, Yurtcan AB (2018) Synthesis of polypyrrole (PPy) based porous N-doped carbon nanotubes (N-CNTs) as catalyst support for PEM fuel cells. Int J Hydrogen Energy 43(40):18559–18571
29. Ozturk A, Yurtcan AB (2021) Preparation and characterization of melamine-led nitrogen-doped carbon blacks at different pyrolysis temperatures. J Solid State Chem 296
30. Feng YJ et al (2021) Graphene family for hydrogen peroxide production in electrochemical system. Sci Total Environ 769
31. Inagaki M et al (2018) Nitrogen-doped carbon materials. Carbon 132:104–140
32. Liu G et al (2010) Studies of oxygen reduction reaction active sites and stability of nitrogen-modified carbon composite catalysts for PEM fuel cells. Electrochim Acta 55(8):2853–2858
33. Gerba CP (2015) Quaternary ammonium biocides: efficacy in application. Appl Environ Microbiol 81(2):464–469
34. Masa J et al (2015) On the role of metals in nitrogen-doped carbon electrocatalysts for oxygen reduction. Angewandte Chemie-International Edition 54(35):10102–10120
35. Liu MY et al (2019) Covalent triazine frameworks: synthesis and applications. Journal of Materials Chemistry A 7(10):5153–5172
36. Skorupska M, Ilnicka A, Lukaszewicz JP (2021) N-doped graphene foam obtained by microwave-assisted exfoliation of graphite. Sci Rep 11(1)
37. Zhou JH et al (2017) Significantly enhanced electrocatalytic properties of three-dimensional graphene foam via Ar plasma pretreatment and N, S co-doping. Int J Hydrogen Energy 42(44):27004–27012
38. Zhou J et al (2020) NiSe2 anchored N, S-doped graphene/ni foam as free-standing bi functional electrocatalyst for efficient water splitting. Nanoscale 12(7):9866–9872
39. Moumaneix L et al (2020) Nitrogen-doped graphenic foam synthesized by solvothermal-based process: Effect of pyrolysis temperature on the material properties. Microporous Mesoporous Mater 300
40. Wang Y et al (2018) Powder metallurgy template growth of 3D N-doped graphene foam as binder-free cathode for high-performance lithium/sulfur battery. Carbon 137:368–378
41. Shi CJ, Maimaitiyiming X (2021) FeNi-functionalized 3D N, P doped graphene foam as a noble metal-free bifunctional electrocatalyst for direct methanol fuel cells. J Alloys Compounds 867
42. Liu JY et al (2017) Three-dimensional nitrogen-doped graphene foam as metal-free catalyst for the hydrogenation reduction of p-nitrophenol. J Colloid Interface Sci 497:102–107
43. Karuppanan KK et al (2019) 3D-porous electrocatalytic foam based on Pt@N-doped graphene for high performance and durable polymer electrolyte membrane fuel cells. Sustain Energy Fuels 3(4):996–1011
44. Wang ZY et al (2020) Nitrogen-doped graphene foam as a metal-free catalyst for reduction reactions under a high gravity field. Engineering 6(6):680–687
45. Liu DQ et al (2019) A confinement strategy to prepare N-doped reduced graphene oxide foams with desired monolithic structures for supercapacitors. Nanoscale 11(10):4362–4368

46. Li HF et al (2018) One-step chemical vapor deposition synthesis of 3D N-doped carbon nanotube/N-doped graphene hybrid material on nickel foam. Nanomaterials 8(9)
47. Dong F et al (2018) Heteroatom (B, N and P) doped porous graphene foams for efficient oxygen reduction reaction electrocatalysis. Int J Hydrogen Energy 43(28):12661–12670
48. Ke WG et al (2020) Synthesis of nitrogen-superdoped and graphene fiber-supported three-dimensional graphene foam for supercapacitors. J Mater Sci 55(16):6952–6962
49. Drieschner S et al (2016) High surface area graphene foams by chemical vapor deposition. 2d Materials 3(4)
50. Fan MM et al (2016) Recent progress in 2D or 3D N-doped graphene synthesis and the characterizations, properties, and modulations of N species. J Mater Sci 51(23):10323–10349
51. Li C, Shi G (2012) Three-dimensional graphene architectures. Nanoscale 4:5549–5563
52. Xue YH et al (2013) Three-dimensional B, N-doped graphene foam as a metal-free catalyst for oxygen reduction reaction. Phys Chem Chem Phys 15(29):12220–12226
53. Mo RW et al (2017) 3D nitrogen-doped graphene foam with encapsulated germanium/nitrogen-doped graphene yolk-shell nanoarchitecture for high-performance flexible Li-ion battery. Nature Commun 8
54. Marcos-Hernandez M, Villagran D (2019) Mesoporous composite nanomaterials for dye removal and other applications. Compos Nanoadsorbents 265–293
55. Zhou XJ et al (2015) 3-Dimensional porous N-doped graphene foam as a non-precious catalyst for the oxygen reduction reaction. Journal of Materials Chemistry A 3(7):3343–3350
56. Niu JA et al (2019) Uniform nanoporous graphene sponge from natural polysaccharides as a metal-free electrocatalyst for hydrogen generation. RSC Adv 9(1):99–106
57. Feng SH, G-H L (2017) Hydrothermal and solvothermal syntheses. In: Modern inorganic synthetic chemistry, Elsevier, pp 73–104
58. Shu RW et al (2020) Facile design of three-dimensional nitrogen-doped reduced graphene oxide/multi-walled carbon nanotube composite foams as lightweight and highly efficient microwave absorbers. ACS Appl Mater Interfaces 12(4):4689–4698
59. Xu DW et al (2019) 3D nitrogen-doped porous magnetic graphene foam-supported Ni nanocomposites with superior microwave absorption properties. J Alloy Compd 782:600–610
60. Pruna AI et al (2019) The effect of solvothermal conditions on the properties of three-dimensional N-doped graphene aerogels. Nanomaterials 9(3)
61. Thomas T, Agarwal A (2021) A facile and scalable approach in the fabrication of tailored 3D graphene foam via freeze drying. Materials 14(4)
62. Yu H et al (2016) Green synthesis of porous three-dimensional nitrogen-doped graphene foam for electrochemical applications. ACS Appl Mater Interfaces 8(4):2505–2510
63. Du XS, Liu HY, Mai YW (2016) Ultrafast synthesis of multifunctional N-doped graphene foam in an ethanol flame. ACS Nano 10(1):453–462
64. Zou HY et al (2018) NixSy nanowalls/nitrogen-doped graphene foam is an efficient trifunctional catalyst for unassisted artificial photosynthesis. Adv Funct Mater 28(13).
65. Liu J et al (2014) Platinum-decorated nitrogen-doped graphene foam electrocatalysts. Fuel Cells 14(5):728–734
66. Zhai P et al (2015) Tuning surface wettability and adhesivity of a nitrogen-doped graphene foam after water vapor treatment for efficient oil removal. Adv Mater Interfaces 2(14)
67. Ye DX et al (2015) Facile preparation of N-doped mesocellular graphene foam from sludge flocs for highly efficient oxygen reduction reaction. J Mater Chem A 3(29):15171–15176
68. Daş E, Öztürk A, Bayrakçeken Yurtcan A (2021) Electrocatalytical application of platinum nanoparticles supported on reduced graphene oxide in pem fuel cell: effect of reducing agents of dimethlyformamide or hydrazine hydrate on the properties. Electroanalysis 33:1721–1735
69. Öztürk A et al (2020) Introduction to fuel cells. Direct liquid fuel cells fundamentals, advances and future. Academic Press, pp 1–47
70. Bozkurt G, Memioglu F, Yurtcan AB (2016) Durability of carbon/conducting polymer composite supported Pt catalysts prepared by supercritical carbon dioxide deposition. Turk J Chem 40(1):117–124

71. Ozturk A, Ozcelik N, Yurtcan AB (2021) Platinum/graphene nanoplatelets/silicone rubber composites as polymer electrolyte membrane fuel cell catalysts. Mater Chem Phys 260
72. Öztürk A, Bayrakçeken Yurtcan A (2021) Raw and pyrolyzed (with and without melamine) graphene nanoplatelets with diferent surface areas as PEM fuel cell catalyst supports. Carbon Lett
73. Das E, Gursel SA, Yurtcan AB (2020) Pt-alloy decorated graphene as an efficient electrocatalyst for PEM fuel cell reactions. J Supercritical Fluids 165
74. Ma XX, He XQ (2016) Cobalt oxide anchored on nitrogen and sulfur dual-doped graphene foam as an effective oxygen electrode catalyst in alkaline media. Appl Mater Today 4:1–8
75. Tang S et al (2016) Template-free synthesis of three-dimensional nanoporous N-doped graphene for high performance fuel cell oxygen reduction reaction in alkaline media. Appl Energy 175:405–413
76. Cogenli MS, Yurtcan AB (2020) Heteroatom doped 3D graphene aerogel supported catalysts for formic acid and methanol oxidation. Int J Hydrogen Energy 45(1):650–666
77. Zhou XJ et al (2016) Hierarchical porous N-doped graphene foams with superior oxygen reduction reactivity for polymer electrolyte membrane fuel cells. Appl Energy 175:459–467
78. Gao P et al (2018) (B, N)-Doped 3D porous graphene–CNTs synthesized by chemical vapor deposition as a bi-functional catalyst for ORR and HER. RSC Adv 8:26934–26937
79. Li Y et al (2017) Soft template-assisted method for synthesis of nitrogen and sulfur co-doped three-dimensional reduced graphene oxide as an efficient metal free catalyst for oxygen reduction reaction. Carbon 122:237–246
80. Jeong DI et al (2021) Complementary performance improved crystalline N-doped carbon encapsulated CoFe/mesoporous N-doped graphene foam as bifunctional catalyst. Appl Surface Sci
81. Liang H et al (2018) Facile preparation of three-dimensional Co1-xS/sulfur and nitrogen-codoped graphene/carbon foam for highly efficient oxygen reduction reaction. J Power Sources 378:699–706
82. Scrosati B, Hassoun J, Sun YK (2011) Lithium-ion batteries. A look into the future. Energy Environ Sci 4(9):3287–3295
83. Jiang X et al (2014) 3D nitrogen-doped graphene foams embedded with ultrafine TiO2 nanoparticles for highperformance lithium-ion batteries. Journal of Materials Chemistry A 2(29):11124–11133
84. Li C et al (2017) 3D N-doped graphene nanomesh foam for long cycle life lithium-sulfur battery. Chem Eng J 326:265–272
85. Lu K et al (2019) Sulfur and nitrogen enriched graphene foam scaffolds for aqueous rechargeable zinc-iodine battery. Electrochim Acta 296:755–761
86. Xu JT et al (2015) High-performance sodium ion batteries based on a 3d anode from nitrogen-doped graphene foams. Adv Mater 27(12):2042–2048
87. Luo HL et al (2017) An ultralight and highly compressible anode for Li-ion batteries constructed from nitrogen-doped carbon enwrapped Fe3O4 nanoparticles confined in a porous 3D nitrogen-doped graphene network. Chem Eng J 326:151–161
88. Li C et al (2018) One-step synthesis of 3D N-doped graphene supported metal oxide for high performance Li-S battery. Ceram Int 44(11):13419–13425
89. Fang W et al (2016) Bi2O3 nanoparticles encapsulated by three-dimensional porous nitrogen-doped graphene for high-rate lithium ion batteries. J Power Sources 333:30–36
90. Lu C et al (2018) Nanostructured Bi2S3 encapsulated within three-dimensional N-doped graphene as active and flexible anodes for sodium-ion batteries. Nano Res 11(9):4614–4626
91. Gao XT et al (2018) V2O5 nanoparticles confined in three-dimensionally organized, porous nitrogen-doped graphene frameworks: flexible and free-standing cathodes for high performance lithium storage. Carbon 140:218–226
92. Zhang SL, Pan N (2015) Supercapacitors performance evaluation. Adv Energy Mater 5(6)
93. Samanci M, Das E, Yurtcan AB (2021) Carbon aerogel and their polypyrrole composites used as capacitive materials. Int J Energy Res 45(2):1729–1747

94. Zhu J et al (2018) Three-dimensional N-doped graphene/polyaniline composite foam for high performance supercapacitors. Appl Surf Sci 428:348–355
95. Zhang WL et al (2017) Nitrogen-superdoped 3d graphene networks for high-performance supercapacitors. Adv Mater 29(36)
96. Kwak MJ et al (2017) Single-step synthesis of n-doped three-dimensional graphitic foams for high-performance supercapacitors. Acs Sustain Chem Eng 5(8):6950–6957
97. Zou YQ, Kinloch IA, Dryfe RAW (2015) Mesoporous vertical Co3O4 nanosheet arrays on nitrogen-doped graphene foam with enhanced charge-storage performance. ACS Appl Mater Interfaces 7(41):22831–22838
98. Chen YY et al (2019) NiCo2S4 nanotubes anchored 3d nitrogen-doped graphene framework as electrode material with enhanced performance for asymmetric supercapacitors. Acs Sustain Chem Eng 7(13):11157–11165
99. Chen YY et al (2019) N-doped graphene framework supported nickel cobalt oxide as supercapacitor electrode with enhanced performance. Appl Surf Sci 484:135–143
100. Wang BH et al (2017) Smartly designed 3D N-doped mesoporous graphene for high-performance supercapacitor electrodes. Electrochim Acta 241:1–9
101. Ma LY et al (2019) Scalable one-step synthesis of N, S co-doped graphene-enhanced hierarchical porous carbon foam for high-performance solid-state supercapacitors. J Mater Chem A 7(13):7591–7603
102. Deng WF et al (2017) Three-dimensional nitrogen-doped graphene derived from poly-o-phenylenediamine for high-performance supercapacitors. J Electroanal Chem 787:103–109
103. Hao JN et al (2019) Synthesis of three dimensional N&S co-doped rGO foam with high capacity and long cycling stability for supercapacitors. J Colloid Interface Sci 537:57–65
104. Kota M, Jana M, Park HS (2018) Improving energy density of supercapacitors using heteroatom-incorporated three-dimensional macro-porous graphene electrodes and organic electrolytes. J Power Sources 399:83–88
105. Bahadir EB, Sezginturk MK (2016) Applications of graphene in electrochemical sensing and biosensing. Trac-Trends Anal Chem 76:1–14
106. Wang CY et al (2019) Advanced carbon for flexible and wearable electronics. Adv Mater 31(9)
107. Feng XM et al (2015) Three-dimensional nitrogen-doped graphene as an ultrasensitive electrochemical sensor for the detection of dopamine. Nanoscale 7(6):2427–2432
108. Chen M et al (2018) Highly sensitive electrochemical DNA sensor based on the use of three-dimensional nitrogen-doped graphene. Microchimica Acta 185(1)
109. Huang JX et al (2019) Extremely elastic and conductive N- doped graphene sponge for monitoring human motions. Nanoscale 11(3):1159–1168
110. Wu JJ et al (2016) Incorporation of nitrogen defects for efficient reduction of CO_2 via two-electron pathway on three-dimensional grapheme foam. Nano Lett 16(1):466–470
111. Kuang PY et al (2019) 0D/3D MoS2-NiS2/N-doped graphene foam composite for efficient overall water splitting. Appl Catalysis B-Environ 254:15–25
112. Liu PB et al (2019) Synthesis of lightweight N-doped graphene foams with open reticular structure for high-efficiency electromagnetic wave absorption. Chem Eng J 368:285–298
113. Zhang LY et al (2017) Polydopamine decoration on 3D graphene foam and its electromagnetic interference shielding properties. J Colloid Interface Sci 493:327–333
114. Fang QL et al (2017) Nitrogen-doped graphene nanoscroll foam with high diffusion rate and binding affinity for removal of organic pollutants. Small 13(14)

Nano Carbon-Based Carbon Catalysts: Types, Preparation, and Characterization

Tulin Avci Hansu, Aykut Caglar, Anish Khan, and Hilal Kivrak

Abstract Carbon-based nanomaterials are widely used in the chemical industry, as catalysts or catalyst supports in energy and ecological applications, due to their different properties. High surface areas, porosity, sizes and shapes are considered important because they increase the catalytic performance of carbon-based materials. Especially graphene and carbon nanotube-based nanocomposites from carbon-based materials have shown exceptional catalytic activity in organic reactions. It has been observed that catalytic products prepared using carbon nanocomposites are very important in many fields including medicine, biomedical, agricultural and material sciences. Therefore, the demand for carbon nanocomposites is increasing rapidly. The development of new preparation methods and the increase in application areas make this subject special. In this section, researches on the types, preparation methods and application areas of carbon-based nanocomposite materials in recent years were carried out.

Keywords Carbon materials · Characterization · Preparation methods

T. A. Hansu
Faculty of Engineering, Department of Chemical Engineering, Siirt University, SİİRT, Turkey

A. Caglar
Faculty of Engineering, Department of Chemical Engineering, Van Yuzuncu Yil University, Van, Turkey

A. Caglar · H. Kivrak (✉)
Faculty of Engineering and Architectural Sciences, Department of Chemical Engineering, Eskisehir Osmangazi University, ESKİŞEHİR, Turkey
e-mail: hilaldemir.kivrak@ogu.edu.tr; hilalkivrak@gmail.com

A. Khan
Center of Excellence for Advanced Materials Research, King Abdulaziz University, Jeddah 21589, Saudi Arabia

M. Jawaid and A. Khan (eds.), *Carbon Composite Catalysts*, Composites Science and Technology, https://doi.org/10.1007/978-981-19-1750-9_2

1 Introduction

Versatile and interesting, carbon is an indispensable element in our world. Carbon is the sixth most abundant element in the universe, the fourth element in the solar system, and the 17th most common element in the Earth's crust [1]. Although elemental carbon is rarely found in the earth's crust with only 0.2% of the total mass of this planet [1, 2], its function is extremely important as it can form bonds with other light elements and with itself due to its chemical structure. With the particle sizes reaching the nanometer level, interactions at the interface in the material increase and their properties develop perfectly. Materials consisting of carbon atoms; It exhibits different physical and chemical properties due to the bonding geometry of the electrons of the carbon atoms involved in bonding among themselves. Nanocarbon materials generally have a high and accessible open surface. Nanocarbon materials also have many theoretical study and application areas from basic sciences as well as engineering to health applications, thanks to their durability, different electrical and mechanical properties [3–5]. Nano carbon-based materials have electrical and thermal conductivity, as well as mechanical strength and lightness that conventional materials cannot match. Because of these properties, these materials have found a wide application area [6, 7]. High surface areas, very porosity are considered crucial to improving the catalytic performance of carbon-based materials. Nano carbon-based catalysts generally have a large surface area, thus facilitating fast reaction kinetics by shortening the diffusion paths. These nanomaterials are more resistant to oxidation than conventional carbons when used as catalysts for high temperature reactions or in electrocatalysis in the presence of oxygen [8].

Nano carbon-based catalyst have been obtained using different methods. These nanomaterials obtained were applied in different areas. This is why many researchers want to investigate the key role nano-carbon-based catalyst play in the new advanced technology. In this chapter, research has been done on the types, preparation and characterization of nano carbon based catalysts.

2 Carbon-Based Catalysts

Carbon materials are one of the versatile members of the periodic table, which is non-metallic, forms 4 e^- form covalent chemical bonds, and has an atomic number of 6, making important contributions to science [9]. Carbon is one of the few elements known since ancient times, constituting 0.025% of the Earth's crust. It is the 4th element by mass in the universe after H_2, O_2, and He, and the 15^{th} most abundant element on earth. Carbon is found as graphite, which is known for its soft structure, and as diamond, which is naturally hard in structure. Diamond is a carbon material with sp3 hybridization, tetrahedral crystal structure, and each carbon atom is four covalently bonded by four other carbon atoms. C–C bonds, and a cubic elementary cell. Unlike diamond, graphite is a material that has a soft structure, consists of

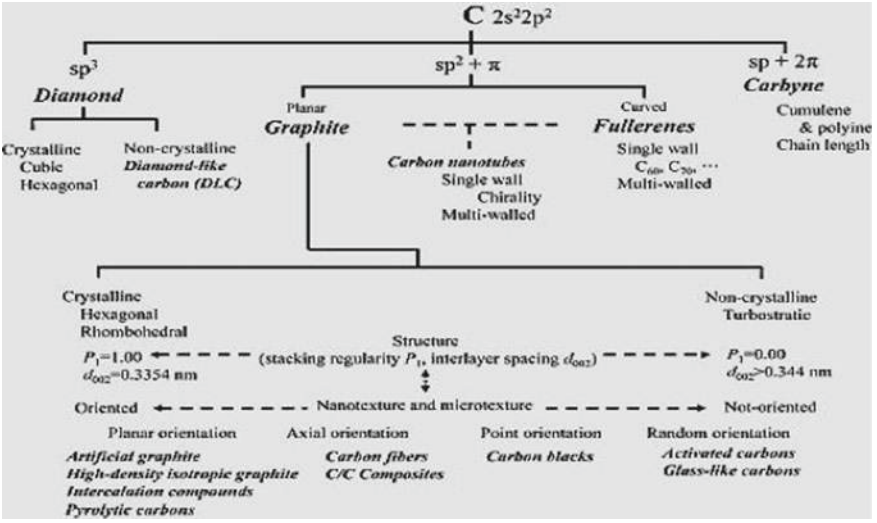

Fig. 1 Classification of carbon materials according to carbon–carbon bond structure [9] (Reprinted with permission, Elsevier, 2016)

many overlapping layers of carbon rings, and is a very good conductor of heat and electricity due to its zero band gap [10]. Figure 1 shows the carbon–carbon bonds of sp^3, $sp^2 + \pi$, and $sp + 2\pi$ hybrid orbitals of carbon materials. Carbon materials such as graphite, graphene, fullerene, and carbon nanotubes formed from one of these hybrid orbitals fall into the carbon family [11]. Carbon materials are very important for areas such as hydrogen production, fuel cell, supercapacitor due to their high surface area and good electrical conductivity.

2.1 Activated Carbon

Activated carbon (AC) is one of the porous carbon materials that increase the surface area for adsorption and chemical reactions such as water purification and air purification. In addition, it is a wide variety of adsorbent material with high porosity and surface area consisting of up to 90% carbon. AC has a high surface area of about 3000 m^2/g [12]. The powdered AC (PAC) and granular AC (GAC) are commonly used in adsorption processes [13, 14]. PAC is an adsorbent that is used effectively to treating persistent/non-biodegradable organic compounds with a fine particle size of approximately 44 μm and to remove seasonal taste and odor in the wastewater treatment plant [14]. GAC is used in hard, abrasion-resistant, and typically fast filters with a particle size of 0.6–4.0 mm. Although it is more expensive than PAC, it can be easily regenerated [15, 16]. AC can be obtained by physical and chemical activation methods [17]. AC obtained from carbonaceous sources such as coconut, charcoal,

nuts, and wood is commonly used in adsorption processes to control taste and odor in drinking water. The preparation of activated carbon from lignocellulosic precursors such as hazelnut shell, coconut shell, almond shell, pistachio shell is carried out by physical, chemical, and physicochemical methods [18]. The physical activation process produces AC between 800 and 1000 °C under CO_2 or steam [19]. In the chemical activation process, by using various chemicals such as KOH, NaOH, H_3PO_4, $ZnCl_2$ are performed at a lower temperature (300–500 °C) than physical activation [20]. Dastgheib et al. [21] reported that they obtained AC from pecan shells with a surface area of 1071 m^2/g for the removal of copper ions from aqueous solutions. The activation process was carried out with phosphoric acid after being kept under air at 450 °C using a chemical activation process. Cosnier et al. [22] activated the coconut shells under 850 °C and steam to obtain AC. They investigated the effect of water on the adsorption of volatile organic compounds on AC with a surface area of approximately 2400 m^2/g.

2.2 Graphite and Graphene Materials

Graphite, which has many basic superior properties such as large surface area, high thermal conductivity, and heat resistance, is a form of carbon element having a planar sp^2. Moreover, according to the stacking regularity of the sequence ABAB… and ABCABC… of the carbon hexagonal layers, it belongs to the hexagonal crystallographic and rhombic systems, respectively. The main difference between graphite, which turns into diamond at high pressures and temperatures, is that the carbon bond is sp^3 hybridization in diamond and sp^2 hybridization in graphite [23, 24]. Graphene has attracted attention with its high specific surface area and high performance, with a single graphite layer attached to a two-dimensional hexagonal cage. Graphene, which has achieved great success in the field of technology since 2004, was awarded the single-layer graphene Physics Nobel Prize obtained by Novoselov et al. in 2010 [25]. There are many graphene synthesis methods in the literature such as chemical vapor deposition, Hummers method, electrochemical reduction, and mechanical exfoliation [26, 27]. The synthesis methods of graphene are shown in Fig. 2. Graphene is used in many fields such as sensors, fuel cells, biomedical, hydrogen storage, supercapacitor [28]. Caglar et al. reported that they coated both few-layer graphene [29] and N, B, S-doped graphene [30] on indium tin oxide by chemical vapor deposition method. They examined the catalytic activities of the obtained electrodes on glucose electro-oxidation. Wang et al. [31] reported that they used graphene oxide as supercapacitor electrode material, which was synthesized by modification of Hummers method. They achieved a maximum specific capacitance of 205 F/g with a power density of 10 kW/kg at an energy density of 28.5 Wh/kg with graphene oxide electrode material.

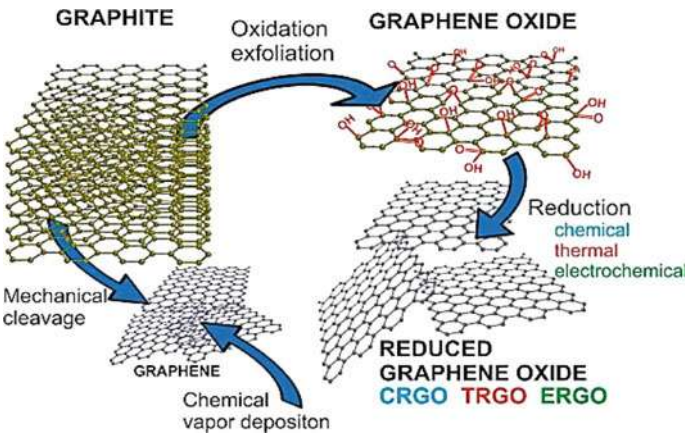

Fig. 2 The schematic illustration of synthesis for graphene and rGO [32] (Reprinted with permission, Elsevier, 2018)

2.3 Glass-Like Carbon

Glass-like carbon (GC), also referred to as glassy carbon, vitreous or polymeric is a unique carbon material with glassy and ceramic properties that attract attention in industry and science. GC is produced by thermal degradation of phenol–formaldehyde, cellulose, polyfurfuryl alcohol, and other selected polymer resins [33]. Its physical properties are generally dependent on the heat treatment temperature, which can vary between 600–300 °C. It also has a relatively low density of 1.4–1.5 g cm^{-3} and very little accessible surface area [34]. GC was first developed by Yamada and Sato in 1962 [35]. It consists of two-dimensional structural elements and sp^2-bonded atoms [36, 37]. The GC structure consists of sp^2-hybridized carbon atoms that form fullerene-like fragments of different sizes depending on the intensity of the heat treatment used during the synthesis. It has many superior properties such as high-temperature resistance, low thermal resistance, low electrical resistance, hardness, high resistance to chemical corrosion. It is also used as electrode materials and crucibles [38]. Jovanović et al. [39] investigated the electrocatalytic activity for methanol oxidation by depositing Pt particles on oxidized GC. They reported that Pt/GC_{OX} electrode exhibited better catalytic activity than others in the study.

2.4 Carbon Nanostructures

Carbon nanostructures such as carbon black (CB), carbon fiber (CF), carbon nanotubes (CNTs), carbon nanofibers (CNFs), fullerene continue to be used efficiently in many areas such as nanoscale electronics and electron transport (Fig. 3). CB is produced by the reaction of hydrocarbons such as coal tar, oil, or gas with the

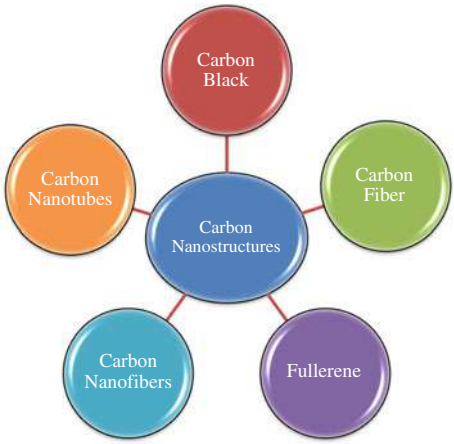

Fig. 3 Classification of carbon nanostructures

combustion air source at temperatures of 1300–1600 °C [40]. Although CB has a lower surface area than AC, it is a carbon with a high surface-area-to-volume ratio. CB is produced by three important parameters such as the furnace, the channel, thermal, lamp black, and the acetylene process [41]. It has a particle size of less than 100 nm, a medium-specific surface area, and good electrical conductivity [42]. CFs can be obtained using any fibrous precursor containing a carbon backbone. It is produced by stabilization and carbonization of organic fibers with lower carbon content, such as polyacrylonitrile between 5to 10 μm in diameter, up to 1300 °C [43, 44]. CNFs and CNTs are obtained by the catalytic decomposition of certain hydrocarbons [45]. In recent years, there is increasing attention in using these materials as support materials for catalysis due to their low electrical resistance and high porosity [46]. CNTs offer an interesting alternative as support, thanks to alternatives such as (I) high purity, (II) high electrical properties, impressive mechanical properties, and thermal stability, (III) eliminate diffusion and intraparticle mass transfer in the reaction medium due to the absence of any microporosity and high accessibility of the active phase, (IV) the possibility of shaping, (V) increase in catalytic activity and selectivity due to metal support interactions, and (VI) possibility of holding effects in the spaces contained within [47]. CNTs are single-walled CNTs (SWCNTs) and multi-walled CNTs (MWCNTs) with diameters in the range of 1 nm. CNFs, MWCNTs, and SWCNTs have a specific surface area of 10–250 $m^2\ g^{-1}$ (125–150 nm diameter), 50–500 $m^2\ g^{-1}$ (5–100 nm diameter), and 400–900 $m^2\ g^{-1}$ (0.4–2 nm diameter), respectively. Fullerene was discovered by Richard Smalley and Robert Curl at Rice University in Houston in 1985 and by Harry Kroto, who shared the Nobel Prize for the discovery in 1996 [48]. Fullerenes have icosahedral symmetry with carbon atoms such as C_{60}, C_{70}, C_{80} etc. and C_{60} has an electronic structure similar to that of graphene [49]. The most common fullerene structure, C_{60}, has 12 regular pentagons and 20 regular hexagons with 60 carbon atoms. Carbon structures with unique chemical, physical, and mechanical properties are used in

many areas such as biochemical sensors, electrochemical applications, conductive materials, electronics detection [50].

3 Preparation and Characterization Methods

3.1 Preparation Methods

Certain methods have emerged as a result of years of work to produce carbon-based nanomaterials. Each of the synthesis methods is shaped according to different application areas. Many different methods have been put forward with studies on high purity production desire, synthesis at low temperatures and increasing production capacity [51]. The main ones can be listed as laser etching, arc discharge, solar furnace method, chemical vapor deposition, vapor phase amplification and hydrothermal synthesis methods. Many methods have been researched and developed for the preparation of fullerenes from carbon-based nanomaterials. Arc discharge method is one of the most popular and widely used wide plasma methods in the preparation of fullerenes compared to other techniques [52]. The use of fullerenes is limited due to the high cost of their preparation and the low productivity of the methods available [53]. The main methods for CNT synthesis are arc discharge, laser ablation, and chemical vapor deposition (CVD) [54]. CVD is one of the most widely used and most researched methods in the literature for CNT preparation. Unlike arc discharge and laser ablation methods, the CVD method requires simpler equipment and more mild conditions. In addition, the large-scale production of CNTs is provided by this method, since the conditions in terms of temperature and pressure can also be reached [55, 56]. There are many methods for preparing graphene or graphite. These methods are based on splitting nanomaterials such as graphite or nanotubes to produce nanoscale graphene sheets using a range of physical or chemical methods. Graphene sheets are prepared by CVD method or laser ablation methods [57, 58]. Activated carbon (AC) is usually prepared in two stages. These steps are the carbonization of the starting raw materials followed by the carbon activation by chemical or physical methods. In the carbonization step, the raw material is burned at high temperatures and all non-carbon species are removed from the structure. The second step, the activation method, is usually carried out to increase the pore volume and pore diameter of the carbon mass obtained [59]. Preparation methods will be presented in detail fort he final version of this chapter.

3.1.1 Chemical Vapour Deposition Method

The schematic representation of the Chemical Vapor deposition method is given in Fig. 4. Chemical Vapor Deposition (CVD) [60] method is defined as the deposition of a solid on a heated surface from a chemical reaction in the vapor phase. In this

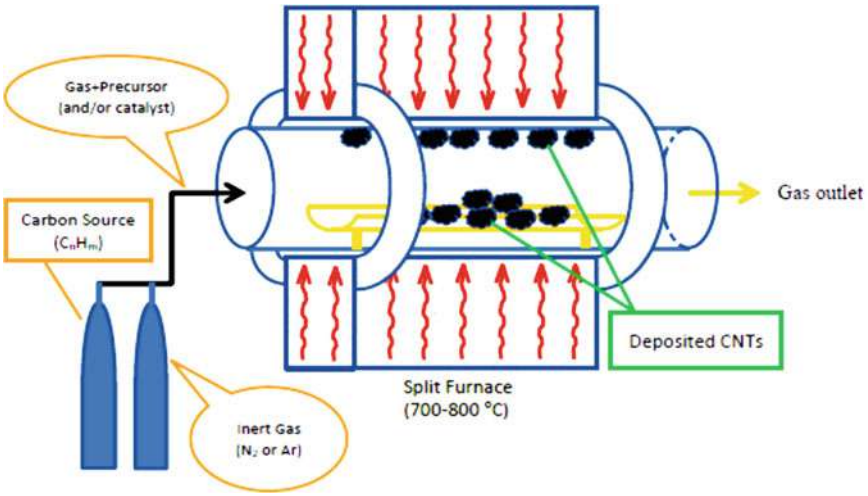

Fig. 4 Schematic diagram of chemical vapor deposition method

method, the material to be produced is loaded into the system in gaseous form and deposited as chemical vapor on a substrate specified as a heated catalyst. In the CVD technique, hydrocarbons such as methane, carbon monoxide or acetylene are used as the carbon source, while a coated metal filament is used as the catalyst (such as nickel, cobalt, iron or combinations thereof) [61]. In general, the temperature values required for CVD production are in the range of 200 to 1600 °C. The CVD method includes process steps such as gases flowing into the reactor, reacting, and then removing the by-products from the reactor. CVD production method steps are as follows:

- With pressurized gas lines, precursor gases are sent to vacuum chambers where the reaction will take place,
- The gases to be reacted move from the main flow region to the substrate via the boundary layer on the substrates used as catalysts,
- Adsorption of gases reacting on the substrate,
- Chemical reaction takes place on the surface and is divided into growth zones,
- Desorption of the by-products of the reactions and their removal from the vacuum chamber.

3.1.2 Lazer Ablation Method

Carbon-based material is synthesized as a result of using the graphite piece as a target by bombarding it with a laser unit in an oven operating at a temperature of approximately 1200 °C under 500 Tor pressure [62]. Figure 5 shows the schematic diagram of carbon-based material production by laser ablation method. As seen in the figure, the carbon particles that come out of the laser-evaporated graphite in this

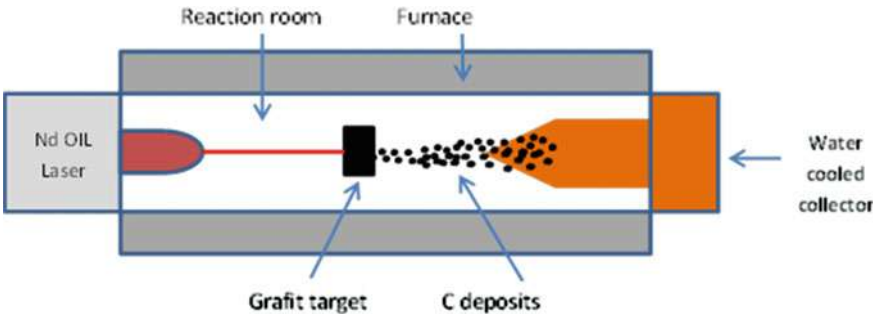

Fig. 5 Schematic diagram of laser ablation

method are deposited on the water-cooled copper collector in an inert gas environment containing helium or argon. Obtained as a result of bombardment using pure graphite nanotubes turn into a multi-walled structure. When materials containing catalysts such as Co, Ni, Fe are used, the nanotubes obtained are in a single-walled structure [51]. The laser ablation method is the most accepted technique for the production of high purity carbon nanotubes [63]. It is not preferred because it requires high energy per nanoparticle and is also very costly and has a low production capacity [64].

3.1.3 Arc-Discharge Method

The arc discharge process is the oldest technique used in nanomaterial production methods and is remarkable with its many versions. Figure 6 shows the schematic representation of the arc discharge method. As can be seen in the figure, arc discharge

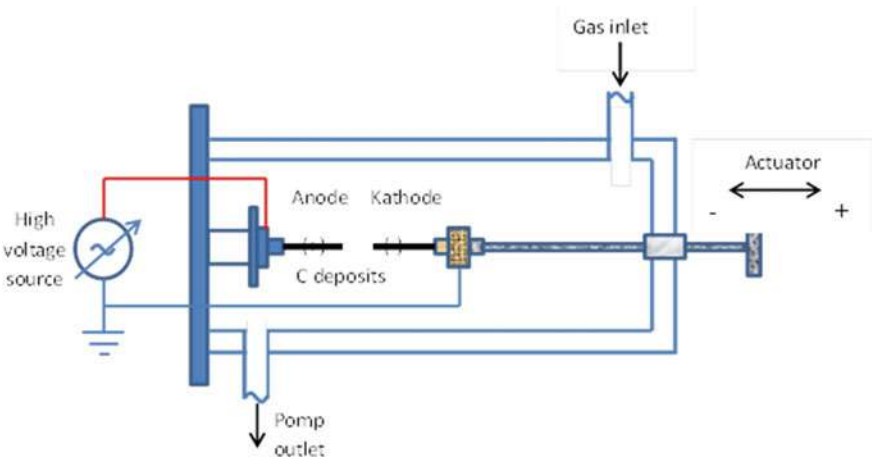

Fig. 6 Schematic diagram of Arc-discharge

is carried out between the graphite electrodes with direct current in an inert gas environment to the environment where the production takes place [65, 66]. The electric arc vaporizes the hollow graphite anode coated with a mixture of transition metals such as Fe, Co, Ni, and graphite powder. As a result of the applied current, some of the carbon evaporated from the anode is recondensed cylindrically at the cathode. Both nanotubes and nanoparticles form at the center of this cylindrical deposit.

The parameters for the arc between the two electrodes are as follows [67]:

- Voltage: 20–30 V
- Current: 60–120A(DC and AC)
- Pure or doped graphite electrode
- Distance between electrodes: 1–3 mm
- Inert gas: Helium and/or argon (Pressure is controlled during production and vacuum is applied to prevent oxidation of electrodes after production.)
- Discharge time: 10–60 s.

The disadvantages of the arc discharge process are the difficulty of managing a continuous process and the formation of amorphous carbon structures, carbon-coated metal groups and fullerenes with carbon nanotubes. In addition, another disadvantage of this method is that the efficiency of single-walled carbon nanotube production does not exceed 20–40%.

3.2 Characterization Tecnhiques

Nuclear magnetic resonance (NMR), transmission electron microscopy (TEM), X-ray diffraction (XRD), fourier transform infrared spectroscopy (FTIR), photoluminescence, UV spectroscopy and Raman spectroscopy such characterization methods surface of prepared carbon-based nanomaterials to get information about the structure are used. These characterization methods will be presented in detail for the final version of this chapter.

The X-Ray Diffraction method (XRD) is based on the principle that each crystal phase refracts X-rays in a characteristic pattern depending on their unique atomic arrangement. With the help of this method, the crystal shape and phase structure of nano carbon-based catalysts are determined. A high resolution Graphite Monochromator is used in the device, which enables monochromatized X-ray to be obtained. Measurements are made with the standard $\Theta/2\Theta$ scanning method (between $2\Theta =$ 20–90°).Generally in the literature, graphite reveals a sharp diffraction peak at 26.5 in relation to the C(0 0 2) plane and a small diffraction peak at 54.3 in the (0 0 4) plane [68].

With the transmission electron microscope (TEM), the crystal structure of the sample can be determined by diffraction of electrons passing through the sample. Crystal structure analysis and cross-section of the sample with TEM image is obtained

[69]. Due to the nanoscale effect, "high resolution TEM" (HRTEM) should be used for imaging carbon-based nanomaterials with TEM. With HRTEM, the inner wall diameter and number of walls of multi-walled nanomaterials can be determined [67].

Raman spectroscopy is based on the determination of the structure based on the difference in energy level between molecules. After the discovery of surface enhanced Raman scattering (SERS), the use of surface Raman spectroscopy has increased exponentially [70]. Identification of amorphous and crystalline regions, metal addition, shape and size of nanomaterials have been extensively studied by scientists using Raman spectroscopy [71, 72]. Raman bands for carbon-based nanostructured materials have been used in the literature to distinguish different allotropes and to examine their conductivity, structural and compositional properties [73]. Raman signals originating from lattice vibrations (phonons) of graphite materials are very sensitive due to their structural irregularity [73]. The first of the Raman band is located at about 43 cm^{-1} and corresponds to the translational motions between the carbon atoms [74]. The second band, called the G band, is located at 1581 cm^{-1} and corresponds to the region center vibration of carbon atoms against each other in the layer planes [74]. The G band is a common feature of all graphene and carbon graphite materials [74]. The presence of irregularity in the graphite lattice is due to the D band around 1350 cm^{-1} (D for defect) and the band called D' around 1620 cm^{-1} [75]. The Radial Breathing Mode (RBM) band is a band unique to carbon nanotubes and is seen in a single-walled structure and is not seen in other sp^2 hybridized structures such as the G-band [67]. In Table 1, the frequency range of the descriptive peaks of carbon-based nanomaterials is given.

Fourier transform infrared spectrometry (FTIR) is used to understand how much energy corresponds to each wavelength and the peak that appears after the beam is absorbed. In the FTIR spectrum of pure graphite, there is no significant peak associated with any functional group. But weak bands of adsorbed water molecules may appear [76]. FTIR spectroscopy is used for the characterization of functional groups in graphene oxide (GO) samples and characteristic peaks for carbon–oxygen bonds are approximately 1230–1215 cm^{-1}, 1120–1110 cm^{-1} (from epoxy), 1415 cm^{-1}, 1160 cm^{-1} (carbonyl or from carboxyl) and appears at 1080–1040 [76]. Hydroxyl (H–H) groups are defined by the stretching frequency in the range of 4000–3000 cm^{-1} and the bending frequency between 1640 cm^{-1} and 1620 cm^{-1} [76]. For carbon nanotubes, the peaks appearing in the spectra in the 400–4000 cm^{-1} frequency range

Table 1 Descriptive band and frequency range of carbon-based nanomaterials [67]

Band	Frequency (cm^{-1})
G-band	1580–1600
D-band	1290–1350
G'-band	2600–2700
D'-band	1620–1700
RBM	50–300

1026, 1250, 1372, 1445, 1736, 2362, 2851, 2925 cm^{-1} are Si–O, C–N, N–CH_3, CNT, C–O originates from C–Hx [77].

4 Conclusion

Carbon-based nanomaterials can be produced on a large industrial scale for a wide range of products and can be used in many application areas, including environment, agriculture, chemical, pharmaceutical and energy. However, there are still some difficulties in the preparation of carbon-based nanomaterials. Methods should be developed to overcome the difficulties in this preparation stage.

Carbon-based nanomaterials, which are a part of the production of high-tech materials, are among the most studied materials due to their superior properties. It is synthesized by many methods and finds wide usage area. Chemical vapor deposition method is the best method used in the production of carbon-based nanomaterials. While obtaining high purity material in CVD process, the disadvantage is that the process is slow. In the arc discharge method, as in the laser ablation method, the nanoparticles were obtained as a result of bombardment with a pure graphite target. The tubes are multi-walled. Containing catalysts such as Co, Ni, Fe, Y the nanotubes obtained as a result of bombardment from the targets are in a single-walled structure. Since single-walled carbon structures are obtained with a low yield of 20–40%, these methods are not preferred.

In the structure of molecules $-C=C-$:$-C\equiv C-$, $-N=N-$, $-S-S-$, $-C-O-C-$ type vibrations cause very intense Raman bands to be observed. Thus, these bands, which have low intensity in the infrared spectrum, can be easily measured with the Raman method. Therefore, Raman spectroscopy is more useful than IR spectroscopy in determining the structure of carbon nanotubes.

It is possible to say that these small structures have an important place in our daily life, although carbon-based nanomaterials contain many problems that are still not clear in terms of their usage areas. Knowing the development of nanomaterials is very important in terms of participating in the development in the world.

References

1. Zhang Y, Yin Q-Z (2012) Carbon and other light element contents in the Earth's core based on first-principles molecular dynamics. Proc Natl Acad Sci 109(48):19579–19583
2. Allègre C, Manhès G, Lewin É (2001) Chemical composition of the Earth and the volatility control on planetary genetics. Earth Planet Sci Lett 185(1–2):49–69
3. Ahmadi M, Elmongy H, Madrakian T, Abdel-Rehim M (2017) Nanomaterials as sorbents for sample preparation in bioanalysis: a review. Anal Chimica Acta 958:1–21
4. Chou JC, Chen JS, Liao YH, Lai CH, Yan SJ, Huang MS et al (2017) Fabrication and characteristic analysis for enzymatic glucose biosensor modified by graphene oxide and magnetic beads based on microfluidic framework. IEEE Sens J 17(6):1741–1748

5. Dasgupta A, Rajukumar LP, Rotella C, Lei Y, Terrones M (2017) Covalent three-dimensional networks of graphene and carbon nanotubes: synthesis and environmental applications. Nano Today 12:116–135
6. Ampelli C, Perathoner S, Centi G (2014) Carbon-based catalysts: opening new scenario to develop next-generation nano-engineered catalytic materials. Chin J Catal 35(6):783–791
7. Serp P, Corrias M, Kalck P (2003) Carbon nanotubes and nanofibers in catalysis. Appl Catal A 253(2):337–358
8. Figueiredo JL, Pereira MFR (2010) The role of surface chemistry in catalysis with carbons. Catal Today 150(1–2):2–7
9. Inagaki M, Kang F (2016) Chapter 1—introduction. In: Inagaki M, Kang F (eds) Materials science and engineering of carbon, Butterworth-Heinemann, pp 1–6
10. Chapter 10—Nanocarbon (2008) . In: Nayfeh M (ed) Fundamentals and applications of nano silicon in plasmonics and fullerines, Elsevier, pp 287–309
11. Inagaki M, Kang F (2014) Materials science and engineering of carbon: fundamentals, Butterworth-Heinemann
12. Dillon EC, Wilton JH, Barlow JC, Watson WA (1989) Large surface area activated charcoal and the inhibition of aspirin absorption. Ann Emerg Med 18(5):547–552
13. Heidarinejad Z, Dehghani MH, Heidari M, Javedan G, Ali I, Sillanpää M (2020) Methods for preparation and activation of activated carbon: a review. Environ Chem Lett 18(2):393–415
14. Chavoshani A, Hashemi M, Mehdi Amin M, Ameta SC (2020) Chapter 1—introduction. In: Chavoshani A, Hashemi M, Mehdi Amin M, Ameta SC (eds) Micropollutants and Challenges, Elsevier, pp 1–33.
15. Chavoshani A, Hashemi M, Mehdi Amin M, C. Ameta S (2020) Chapter 3—personal care products as an endocrine disrupting compound in the aquatic environment. In: Chavoshani A, Hashemi M, Mehdi Amin M, Ameta SC (eds) Micropollutants and Challenges, Elsevier, pp 91–144
16. Soni R, Bhardwaj S, Shukla DP (2020) Chapter 14—various water-treatment technologies for inorganic contaminants: current status and future aspects. In: Devi P, Singh P, Kansal SK (eds) Inorganic Pollutants in Water, Elsevier, pp 273–95
17. Danish M, Ahmad T (2018) A review on utilization of wood biomass as a sustainable precursor for activated carbon production and application. Renew Sustain Energy Rev 87:1–21
18. Mohamad Nor N, Lau LC, Lee KT, Mohamed AR (2013) Synthesis of activated carbon from lignocellulosic biomass and its applications in air pollution control—a review. J Environ Chem Eng 1(4):658–666
19. Gupta VK, Suhas (2009) Application of low-cost adsorbents for dye removal—a review. J Environ Manage 90(8):2313–2342
20. Şayan E (2006) Ultrasound-assisted preparation of activated carbon from alkaline impregnated hazelnut shell: an optimization study on removal of Cu2+ from aqueous solution. Chem Eng J 115(3):213–218
21. Dastgheib SA, Rockstraw DA (2001) Pecan shell activated carbon: synthesis, characterization, and application for the removal of copper from aqueous solution. Carbon 39(12):1849–1855
22. Cosnier F, Celzard A, Furdin G, Bégin D, Marêché JF (2006) Influence of water on the dynamic adsorption of chlorinated vocs on active carbon: relative humidity of the gas phase versus pre-adsorbed water. Adsorpt Sci Technol 24(3):215–228
23. Cuhadaroğlu AD, Erdal K (2018) Grafit: bir genel değerlendirme. Teknik Bilimler Dergisi 8(1):14–33
24. Chung DDL (2002) Review graphite. J Mater Sci 37(8):1475–1489
25. Tiwari SK, Sahoo S, Wang N, Huczko A (2020) Graphene research and their outputs: status and prospect. J Sci: Adv Mater Devices 5(1):10–29
26. Bhuyan MSA, Uddin MN, Islam MM, Bipasha FA, Hossain SS (2016) Synthesis of graphene. Int Nano Lett 6(2):65–83
27. Whitener KE, Sheehan PE (2014) Graphene synthesis. Diam Relat Mater 46:25–34
28. Feng W, Long P, Feng Y, Li Y (2016) Two-dimensional fluorinated graphene: synthesis, structures, properties and applications. Adv Sci 3(7):1500413

29. Caglar A, Ulas B, Sahin O, Kivrak HD (2019) Few-layer graphene coated on indium tin oxide electrodes prepared by chemical vapor deposition and their enhanced glucose electrooxidation activity. Energy Storage 1(4):e73
30. Caglar A, Ulas B, Sahin O, Kıvrak H (2019) Synthesis of in situ N-, S-, and B-doped few-layer graphene by chemical vapor deposition technique and their superior glucose electrooxidation activity. Int J Energy Res 43(14):8204–8216
31. Wang Y, Shi Z, Huang Y, Ma Y, Wang C, Chen M et al (2009) Supercapacitor devices based on graphene materials. J Phys Chem C 113(30):13103–13107
32. Rowley-Neale SJ, Randviir EP, Abo Dena AS, Banks CE (2018) An overview of recent applications of reduced graphene oxide as a basis of electroanalytical sensing platforms. Appl Mater Today 10:218–226
33. Bhatia G, Aggarwal R, Malik M, Bahl O (1984) Conversion of phenol formaldehyde resin to glass-like carbon. J Mater Sci 19(3):1022–1028
34. Serp P. 7.13—Carbon. In: Reedijk J, Poeppelmeier K (eds) (2013). Comprehensive inorganic chemistry II (Second Edition). Amsterdam, Elsevier, pp 323–69
35. Yamada S, Sato H (1962) Some physical properties of glassy carbon. Nature 193(4812):261–262
36. Fitzer E, Kochling K-H, Boehm HP, Marsh H (1995) Recommended terminology for the description of carbon as a solid (IUPAC Recommendations 1995). Pure Appl Chem 67(3):473–506
37. Harris † PJF (2004) Fullerene-related structure of commercial glassy carbons. Philosophical Magazine 84(29):3159–67
38. Romero P, Postigo PA, Baquedano E, Martínez J, Boscá A, Guzman de Villoria R (2016) Controlled synthesis of nanocrystalline glass-like carbon thin films with tuneable electrical and optical properties. Chem Eng J 299:8–14
39. Jovanović VM, Terzić S, Tripković AV, Popović KD, Lović JD (2004) The effect of electrochemically treated glassy carbon on the activity of supported Pt catalyst in methanol oxidation. Electrochem Commun 6(12):1254–1258
40. MartÍN-MartÍNez JM (2002) Chapter 13—rubber base adhesives. In: Dillard DA, Pocius AV, Chaudhury M (eds) Adhesion science and engineering. Elsevier Science B.V, Amsterdam, pp 573–675
41. Song K. 2—Micro- and nano-fillers used in the rubber industry. In: Thomas S, Maria HJ (eds) (2017) Progress in rubber nanocomposites. Woodhead Publishing, pp 41–80
42. Krebsz M, Pasinszki T, Tung TT, Losic D (2017) 14—development of vapor/gas sensors from biopolymer composites. In: Sadasivuni KK, Ponnamma D, Kim J, Cabibihan JJ, AlMaadeed MA (eds) Biopolymer composites in electronics. Elsevier, pp 385–403
43. Pusch J, Wohlmann B. Chapter 2 - Carbon Fibers. In: Mahltig B, Kyosev Y, editors. Inorganic and Composite Fibers: Woodhead Publishing; 2018. p. 31–51.
44. Inagaki M (2000) Chapter 4—carbon fibers. In: Inagaki M (ed) New carbons—control of structure and functions. Elsevier Science, Oxford, pp 82–123
45. Rodriguez NM (2011) A review of catalytically grown carbon nanofibers. J Mater Res 8(12):3233–3250
46. Serp P, Castillejos E (2010) Catalysis in carbon nanotubes. Chem Cat Chem 2(1):41–47
47. Serp P (2009) Carbon nanotubes and nanofibers in catalysis. Carbon materials for catalysis. Wiley, Hoboken, NJ, 309–72
48. Rogers R (2015) Chapter one—introduction. In: Rogers R (ed) Offshore gas hydrates. Gulf Professional Publishing, Boston, pp 1–20
49. Ramsden JJ (2016) Chapter 9—carbon-based nanomaterials and devices. In: Ramsden JJ (ed) Nanotechnology, 2nd edn. William Andrew Publishing, Oxford, pp 231–244
50. Poothanari MA, Pottathara YB, Thomas S (2019) Chapter 8—carbon nanostructures for electromagnetic shielding applications. In: Thomas S, Grohens Y, Pottathara YB (eds) Industrial applications of nanomaterials. Elsevier, pp 205–23
51. Küçükyıldırım BO, Eker AA (2012) Karbon nanotüpler, sentezleme yöntemleri ve kullanım alanları. Engineer and the Machinery Magazine 630

52. Churilov G (2008) Synthesis of fullerenes and other nanomaterials in arc discharge. Fullerenes Nanotubes Carbon Nanostruct 16(5–6):395–403
53. Zaytseva O, Neumann G (2016) Carbon nanomaterials: production, impact on plant development, agricultural and environmental applications. Chem Biol Technol Agricult 3(1):1–26
54. Gore JP, Sane A (2011) Flame synthesis of carbon nanotubes. Carbon Nanotubes-Synthesis Characterization Appl 1:16801
55. Kumar M, Ando Y (2010) Chemical vapor deposition of carbon nanotubes: a review on growth mechanism and mass production. J Nanosci Nanotechnol 10(6):3739–3758
56. Zhang Q, Huang JQ, Zhao MQ, Qian WZ, Wei F (2011) Carbon nanotube mass production: principles and processes. Chemsuschem 4(7):864–889
57. Novoselov KS, Fal V, Colombo L, Gellert P, Schwab M, Kim K (2012) A roadmap for graphene. Nature 490(7419):192–200
58. Jiao L, Zhang L, Wang X, Diankov G, Dai H (2009) Narrow graphene nanoribbons from carbon nanotubes. Nature 458(7240):877–880
59. Nasir S, Hussein MZ, Zainal Z, Yusof NA (2018) Carbon-based nanomaterials/allotropes: a glimpse of their synthesis, properties and some applications. Materials 11(2):295
60. Doğan F (2011) Kimyasal buhar biriktirme yöntemiyle SnO_2 ince filmlerin üretilmesi
61. Khan W, Sharma R, Saini P (2016) Carbon nanotube-based polymer composites: synthesis, properties and applications. Carbon Nanotubes-Current Progress of their Polymer Composites
62. Bhushan B, Bhushan B, Baumann (2007)Springer handbook of nanotechnology, Springer
63. Zhang M, Yudasaka M, Iijima S (2001) Single-wall carbon nanotubes: a high yield of tubes through laser ablation of a crude-tube target. Chem Phys Lett 336(3–4):196–200
64. Hakan A, Bahçeci E (2015) Nano malzemeler için üretim yöntemleri. Gazi Üniversitesi Fen Bilimleri Dergisi Part C: Tasarım ve Teknoloji. 3(2):483–499
65. Kiang C-H, Goddard WA III, Beyers R, Bethune DS (1995) Carbon nanotubes with single-layer walls. Carbon 33(7):903–914
66. Takikawa H, Kusano O, Sakakibara T (1999) Graphite cathode spot produces carbon nanotubes in arc discharge. J Phys D Appl Phys 32(18):2433
67. Yuca N (2010) Karbon Nanotüplerin Çesitli Yöntemlerle Saflaştırılması. Enerji Enstitüsü
68. Rivera-Gavidia LM, de la Puente IF, Hernández-Rodríguez MA, Celorrio V, Sebastián D, Lázaro M et al (2020) Bi-functional carbon-based catalysts for unitized regenerative fuel cells. J Catalysis 387:138–44
69. Ajayan P, Charlier J-C, Rinzler A (1999) Carbon nanotubes: from macromolecules to nanotechnology. Proc Natl Acad Sci 96(25):14199–14200
70. Roy D, Kanojia S, Mukhopadhyay K, Prasad NE (2021) Analysis of carbon-based nanomaterials using Raman spectroscopy: principles and case studies. Bull Mater Sci 44(1):1–9
71. Popović Z, Dohčević-Mitrović Z, Šćepanović M, Grujić-Brojčin M, Aškrabić S (2011) Raman scattering on nanomaterials and nanostructures. Ann Phys 523(1–2):62–74
72. Drescher D, Kneipp J (2012) Nanomaterials in complex biological systems: insights from Raman spectroscopy. Chem Soc Rev 41(17):5780–5799
73. Bokobza L, Bruneel J-L, Couzi M (2014) Raman spectroscopy as a tool for the analysis of carbon-based materials (highly oriented pyrolitic graphite, multilayer graphene and multiwall carbon nanotubes) and of some of their elastomeric composites. Vib Spectrosc 74:57–63
74. Ferrari AC, Basko DM (2013) Raman spectroscopy as a versatile tool for studying the properties of graphene. Nat Nanotechnol 8(4):235–246
75. Sadezky A, Muckenhuber H, Grothe H, Niessner R, Pöschl U (2005) Raman microspectroscopy of soot and related carbonaceous materials: spectral analysis and structural information. Carbon 43(8):1731–1742
76. Ţucureanu V, Matei A, Avram AM (2016) FTIR spectroscopy for carbon family study. Crit Rev Anal Chem 46(6):502–520
77. Misra A, Tyagi PK, Singh MK, Misra D (2006) FTIR studies of nitrogen doped carbon nanotubes. Diam Relat Mater 15(2–3):385–388

Carbon Based Perovskite Composite Catalysts and Their Structural, Morphological and Photocatalytic Performances

Özlem Tuna and Esra Bilgin Simsek

Abstract Recently, perovskite materials have shown excellent promise for efficient photodegradation and water splitting processes, on account of their unique crystal structure and electronic properties. The crystal structure of perovskite offers an excellent framework to tune the band gap values to enable visible light absorption and band edge potentials, meeting the requirement of specific photocatalytic features. Nevertheless, fast recombination rate, long-term stability as well as large-scale production still limit their applications especially in light driven processes. Carbon materials, scoping from one-dimensional nanostructures to three-dimensional carbon aerogels, have been successfully utilized in improving structural and optical properties as well as catalytic activities of perovskites. In particular, the recombination rates can be remarkably hindered with the introduction of carbon materials upgrading the catalytic degradation performance. Various perovskite-carbon composites have been discussed, emphasizing their synthesis method, specific improvements on their characteristics related with enhanced activities in the photocatalytic-driven systems. This review provides a broad overview of perovskite coupled with carbonaceous photocatalysts, summarizing developments, and offering useful insights for their future studies.

Keywords Carbon materials · Composite · Perovskite · Photocatalysis · Photocatalytic degradation

1 Introduction

In the past decades, perovskite oxides have received considerable interest owing to their well crystalline structure, unique physical and electrochemical features leading excellent catalytic efficiencies in many reactions. Perovskites generally exist in the form of cubic crystal ABO_3 stoichiometry where, A and B are rare-earth or alkaline earth metal cation with large atomic radii and first row transition metals (e.g.,

Ö. Tuna · E. B. Simsek (✉)
Department of Chemical Engineering, Faculty of Engineering, Yalova University, 77100 Yalova, Turkey
e-mail: ebilgin.simsek@yalova.edu.tr

M. Jawaid and A. Khan (eds.), *Carbon Composite Catalysts*, Composites Science and Technology, https://doi.org/10.1007/978-981-19-1750-9_3

Co, Fe, Ni, Mn, Ti) with small atomic radii, respectively [1]. The doping or substitution on A or B site can easily allow the basic perovskite structure to change its properties resulting formation of third-generation perovskites including binary metal oxides ($A_xB_yO_z$: $A^{3+}B^{3+}O_3$, $A^{2+}B^{4+}O_3$ or $A^{3+}B^{5+}O_4$). The flexible crystal structure and the presence of transition metals in the oxidation states make perovskites to have high stability under aggressive conditions [2]. The related interactions driven by the type of the cations can be altered to yield the different lattice distortion in perovskite compounds that strongly influences their electronic, magnetic, and optical properties. In terms of titanate perovskites group, $SrTiO_3$, $BaTiO_3$, and $PdTiO_3$ have great ferroelectric and piezoelectric properties, whereas $CaTiO_3$ is responsible for ion conductivity. Ferrite perovskites has gained attention their ferroelectrics features ($LaFeO_3$, and $BiFeO_3$, etc.) and lanthanate-based perovskites ($LaMnO_3$, $LaCoO_3$ and $LaNiO_3$) shows attractive electrical conductivity and magnetic property [3]. Tuning the structural and physicochemical properties of perovskites by changing their chemical compositions can lead them to be applied in many areas such as solar cell, gas sensor, magnetic materials and heterogeneous photocatalysts for H_2 production and degradation of organic pollutants.

The photocatalytic efficiencies of perovskites have been widely investigated due to the advantages of similar and basic structures, tunable valences and stoichiometry as well as surface properties [4]. The optical features of light absorption and scattering coefficients and refractive index are crucial for the photocatalytic efficiencies of perovskites as they specify the pathway of light transfer [5]. The band gap and band edge potentials of perovskites can be easily changed to extend the absorption in the visible region. Moreover, abundant oxygen vacancies and valence metal ions in the structure yields excellent photocatalytic performance in water splitting reactions [6]. Besides, the electronic structure of perovskites plays a crucial role on the photocatalytic activity since it affects the lifetime of photo-excited electron–hole (e^-/h^+) pairs; subsequently arranges the thermodynamic feasibility of oxidation and reduction reactions during photocatalytic process. The photocatalytic reaction mainly follows photoexcitation, separation of charge carries and redox of catalyst surface. When the light energy was equivalent or larger than the band gap of catalyst, electrons in valence band (VB) are induced and move towards the conduction band (CB) while the holes are produced in VB creating robust oxidizing and reducing agents, respectively. In the absence of electron scavengers, these photoinduced electrons can quickly recombine with holes [1].

Despite these special properties, perovskites still face some challenges as high recombination rate of charge pairs can result in a low quantum yield [7]. Moreover, titanate-based perovskites suffer from weak light response range which they absorb only ~5% of solar energy, limiting their utilization in the solar spectrum as well as inhibiting photocatalytic performances. Another major bottleneck is the low specific surface area of them caused by high calcination temperature limiting the ability to capture reactants as well as lowering the photocatalytic efficiency [8, 9]. Thus, application of perovskites in photocatalytic processes requires new routes to enlarge their surface area. In addition, low-cost fabrication of perovskites should be considered in order to utilize in large-scale processes [7]. Several strategies have been developed

including metal/non-metal doping, supporting on larger matrices, heterostructure formation and or coupling with carbonaceous materials to overcome these limitations for enhanced photocatalytic performance. The incorporation of conductive carbon materials (i.e., graphene, graphitic carbon nitride, carbon nanotubes) into the structure can reduce the band gap energy, suppress the photo-induced charge carriers and effectively improve the photocatalytic performances of pristine perovskites.

Carbon is one of the most abundant material with an excellent capability to tune its sp-hybridization to form different allotropes with several carbon bonding such as sp, sp^2 and sp^3 characters [10]. Carbonaceous materials possess several excellent features such as low-cost, conductivity, chemical stability and tunable porosity leading them a hot topic of interest. Graphite and diamond as crystalline carbon forms were first recognized by researchers while fullerene and carbon nanofibers have gained interest in 1960–1970s [11]. The most common carbon-based materials used in the photocatalytic reactions are graphene, graphene oxide, graphitic carbon nitride (g-C_3N_4), carbon nanotubes (CNTs), fullerenes and carbon fibers. Graphene and its derivatives, graphene oxide (GO) and reduced graphene oxide (rGO), are regarded as an important class of carbon materials which have the benefits of low-cost, unique conjugated π structure, high conductivity, good carrier transport ability which significantly accelerates the separation and migration of charge carriers in the photocatalyzed reaction [12, 13]. Also, 2-dimensional sheet structure of graphene have oxygen-containing carbonyl, carboxyl, and hydroxyl functional groups. Graphitic carbon nitride (g-C_3N_4), a metal-free polymeric semiconductor, was first discovered in 2009 for photocatalytic H_2 generation [14]. The narrow band gap (~2.7 eV) and chemical stability features allow g-C_3N_4 a popular material in the field of photocatalysis photocatalyst. Under ambient conditions, carbon nanotubes (CNTs) display p-type semiconducting characteristics and the excellent conductivity of MWCNT structure endorses a tight contact with perovskite interface resulting great efficiency and stability [15]. Besides, high electron transport features of fullerenes allow them to be used as ideal electron transport materials in the composite structure [16]. Moreover, new carbon materials such as carbon/graphene quantum dots and carbon aerogels have been risen as an alternative for conventional carbons. The roles of carbon materials in the photocatalytic reactions are generally listed as (i) broadening adsorptive surface sites, (ii) co-catalyst, (iii), supporting network (iv), lowering band gap (v) electron acceptor and transfer channel and (vi) photosensitization [17]. Several reports discussed the nature of perovskite-carbon interaction as well as its effects on the optical and photocatalytic properties. With this in mind, this paper aimed to review relevant advances in perovskite/carbon composite photocatalysts and a comprehensive discussion was given about the effects of carbon texture and content on the photocatalyzed reactions.

To the best of our knowledge, there has been no compilation of literature reported about perovskites-based carbon composite catalysts. In this review, we attempted to deliver detailed information on the structural and morphological changes of perovskites composited with carbon materials including graphene, g-C_3N_4, CNTs, fullerenes, carbon fibers and quantum dots. The utilization of perovskite/carbon composites in the photocatalytic reactions were reported mainly focusing on the

hydrogen production and catalytic degradation of pollutants. The review can guide the readers get helpful information about development of carbon-based perovskite materials in the field of photocatalysis.

2 Carbon Based Perovskite Composite Photocatalysts

2.1 Graphene Based Perovskite Composites

Graphene is a two-dimensional allotrope of carbon consisting of a single layer of sp^2–hybridized carbon atoms. The reduced graphene oxide (rGO) can be formed through exfoliation or oxidation followed by thermal, chemical or electrochemical processes to extend the interplanar spaces by functionalizing basal planes of graphene oxide (GO). The π conjugation structure of graphene leads it having superior electrical conductivity and the hydrophilic nature enables excellent catalytic performances in many fields. The graphene and its derivatives also exhibit unique features such as high chemical stability, fast electron mobility, and large surface area [18]. Meanwhile, the adsorption sites on its surface can contribute to obtain high efficiency in water remediation for organic pollutants through synergetic effect of adsorption and photocatalytic degradation. The aromatic rings of organic molecules can be adsorbed on graphene through π–π interaction owing to its large localized π-electron systems [19]. There have been intense efforts to utilize graphene materials in many fields including sensors, electronic, optoelectronic, capacitor, energy storage and photocatalytic applications. Many researchers have focused on the combination of semiconductor catalysts with graphene materials for improved photocatalytic performance. The main role of graphene and its derivatives in the composite semiconductor systems has been stated as delocalization of the photo-induced electron through its π network, which hinders the recombination rate and thereby enhances the photocatalytic efficiency. The two-dimensional reduced graphene oxide (rGO) can act as an electron mediator for effective charge separation, and it can be also utilized as a cocatalyst in photocatalytic H_2 evolution reactions by improving charge transfer rate.

In this regard, various graphene-based perovskite composites have been developed via several methods such as hydrothermal, solvothermal, sol–gel, ultrasonication, electrospinning etc. and the photocatalytic activities have been investigated especially for degradation and water splitting reactions. Table 1 summarizes literature survey of graphene-based titanate perovskites.

For instance, the photocatalytic activity of $CaTiO_3$ which is titanate-based perovskite having wide-band energy has been increased via compositing with graphene sheets [20–26]. Xian et al. [20] reported that the photocatalytic degradation of methyl orange dye was highly improved by $CaTiO_3$/graphene composite deduced from the hindered recombination rate owing to the migration of excited electrons from the conduction band of $CaTiO_3$ to graphene sheets. Kumar et al. [21]

Table 1 Graphene based titanate perovskite catalysts reported in literature

Carbon source	Perovskite	Carbon amount	Synthesis method of composite	Photocatalytic reaction	Efficiency	Ref.
GO	$CaTiO_3$	9:1 wt	Polyacrylamide gel route	MO degradation	97.5% removal	[20]
rGO	N-$CaTiO_3$	1–20 wt.%	Hydrothermal	MB, Thiabendazole degradation	95% MB removal	[21]
rGO	$CaTiO_3/Pr^{3+}$–Y_2SiO_5	1–5 mg rGO	Sol–gel	H_2 evolution	0.77 μmol g^{-1}	[23]
rGO	$CaTiO_3/MoS_2$	5–30 wt.%	Hydrothermal	H_2 evolution	222.5 μmol $h^{-1} g_{cat}{}^{-1}$	[25]
rGO	$CaTiO_3/Ni_2FeO_4$	15 mg rGO	Hydrothermal	MB, RhB degradation	83% MB, 74% RhB	[26]
rGO	$SrTiO_3$	0.5–2 wt.%	Photoreduction	RhB, Ciprofloxacin, Ibuprofen Degradation	%99 for RhB 74.1% for CIPRO 68.4% for IBP	[27]
rGO	$SrTiO_3$	1 wt.%	Hydrothermal	Toluen degradation	100% (0.3 L/min)	[28]
rGO	$SrTiO_3$	0.4–1 wt.%	Hydrothermal	H_2 evolution	363.79 mmol/g h	[29]
GO	$SrTiO_3$	–	Heat treatment	Azo dye, phenolics degradation	>95% dye, ~70% phenol, BPA removal	[30]
GO	$SrTiO_3$	–	Electrospinning	H_2 evolution	170 mmol/g	[31]
rGO	$SrTiO_3$ /$BiVO_4$/Ru/Rh	5 wt%	Photoreduction	H_2 evolution	21.25 μmol h^{-1} g^{-1}	[32]
rGO	$NiTiO_3$	5 wt%	Microwave-assisted	RhB degradation	91.2% removal	[33]
GO	$NiTiO_3$	1–7 wt%	Microwave-ignition	H_2 evolution	8383 μmol h^{-1} g^{-1}	[34]
GO	$ZnTiO_3$	0.5–5 wt%	Hydrothermal	MB degradation	95.2% removal	[35]
GO	$ZnTiO_3$	–	Ball milling	–	–	[36]
GO	$ZnTiO_3$	–	Chemical precipitation	RhB degradation	98% removal	[37]

(continued)

Table 1 (continued)

Carbon source	Perovskite	Carbon amount	Synthesis method of composite	Photocatalytic reaction	Efficiency	Ref.
GO	$ZnTiO_3$	5–29%	Hydrothermal	Norfloxacin (NOR) MO degradation	99% NOR removal 97% MO removal	[38]
GO	$ZnTiO_3$	–	Chemical precipitation	MB degradation	~100% removal	[39]
GO	$BaTiO_3$	20–80 wt%	Freeze-drying	MB degradation	67% removal	[41]
rGO	$BaTiO_3$	10 wt%	Hydrothermal	RhB degradation MO degradation	82.4% RhB removal 78.2% MO removal	[42]
GO	$BaTiO_3$	20–80 wt%	Thermal treatment	MB degradation	95% removal	[43]
GO	$BaTiO_3$	2–8 wt%	Hydrothermal	MB degradation	–	[44]
rGO	$BaTiO_3$	10 wt.%	Solvothermal	MB, MO, RhB degradation	>87% removal	[45]
rGO	$BaTiO_3NiFe_2O_4$	7 wt.%	Mixing-thermal treatment	–	–	[46]
rGO	$CdTiO_3$	25 mg	Electrospinning /calcination	MB degradation	80% removal	[49]
rGO	$PbTiO_3$	3–12 wt.%	Self-assembling	Thiophene photooxidation	~100%	[50]
rGO	$PbTiO_3$	0.15–1.20 wt%	Hydrothermal	H_2 evolution RhB degradation	23.8 μmol 93% RhB removal	[51]
rGO	$La_2Ti_2O_7$	–	Photoreduction	RhB degradation	~100% removal	[53]
GO	$LaTiO_2$-N		Solvothermal	TC degradation	96.4% removal	[54]

demonstrated the photocatalytic performance of $CaTiO_3$/graphene composite for the degradation of methylene blue and thiabendazole increased by adsorption and photosensitization effect of graphene. Gao and co-workers [23] introduced $CaTiO_3/Pr^{3+}$–Y_2SiO_5/RGO as a visible light-driven catalyst for H_2 evolution and explored that rGO greatly accelerated the electron migration from Pr^{3+}–CTO to Pt and limited the back transfer of electrons resulting remarkably higher photocatalytic H_2 production. Analogously, a significant improvement in H_2 evolution reaction was obtained with $CaTiO_3$ mesocrystals composited with MoS_2/rGO and the nanocomposite catalyst displayed nearly 33-times higher activity when compared with pristine $CaTiO_3$ [25]. In the case of composite catalyst, the conduction band potential was more negative than the reduction potential of H^+/H_2 which was comprised of negative CB potentials of $CaTiO_3$ and MoS_2. Therefore, after light irradiation, the electrons could transfer from conduction band of perovskite to the MoS_2/rGO where rGO acted as a well electron transporter to the reaction sites in order to promote hydrogen production (Fig. 1a). Chen et al. [26] designed magnetic and ternary composite $CaTiO_3/NiFe_2O_4$/rGO through assembling nanoparticles on the graphene surface. The interfacial chemical bonding between graphene and semiconductor materials were confirmed by Ti–C, C–C, C–O and C=O chemical states from XPS spectra which greatly enhanced the stability and photocatalytic performance of the composite structure.

Strontium titanate ($SrTiO_3$) which is an important n-type perovskite has high conduction band energy level (1.4 V, pH 13) which accelerates charge migration of the electron acceptor resulting high photocatalytic efficiency. However, the band gap of $SrTiO_3$ is high (~3.2 eV) so it absorbs only 3–5% of the solar spectrum in the UV range [27]. Therefore, the composite forms of $SrTiO_3$ with graphene materials have been developed [27–32]. Ahmadi et al. [27] coupled $SrTiO_3$ (STO) with rGO through photocatalytic reduction method with varying the weight ratio of GO from 0.5 to 2%. The UV–vis diffuse reflectance spectroscopy analysis indicated that the addition of GO did not significantly change the band gap energy of STO while the photoluminescence spectrum of STO/rGO (1%) composite showed increased intensity than pristine STO. The improved photocatalytic performance of the composite was attributed to the fast transfer of photo-induced electrons/holes. The photocatalytic performance of STO/rGO nanocomposite was examined for the degradation of RhB, Ciprofloxacin and Ibuprofen pollutants and it was found that the RhB decomposition increased from 38 to 100% with increasing of rGO amount from 0.5 to 1% while higher amounts decreased the catalytic efficiency. Moreover, the transient photocurrent response analysis showed that the photocurrent of STO/rGO composite was significantly higher than that of raw STO under visible light irradiation demonstrating enhanced charge transfer from rGO toward the perovskite. In another study, toluene degradation was investigated with $SrTiO_3$/rGO which were prepared by hydrothermal method and the degradation was found remarkably higher in the composite system [28]. He and co-workers [29] evaluated $SrTiO_3$–rGO composites in the photocatalytic H_2 production process and reported that the composites exhibited higher photocatalytic performance under UV light irradiation compared

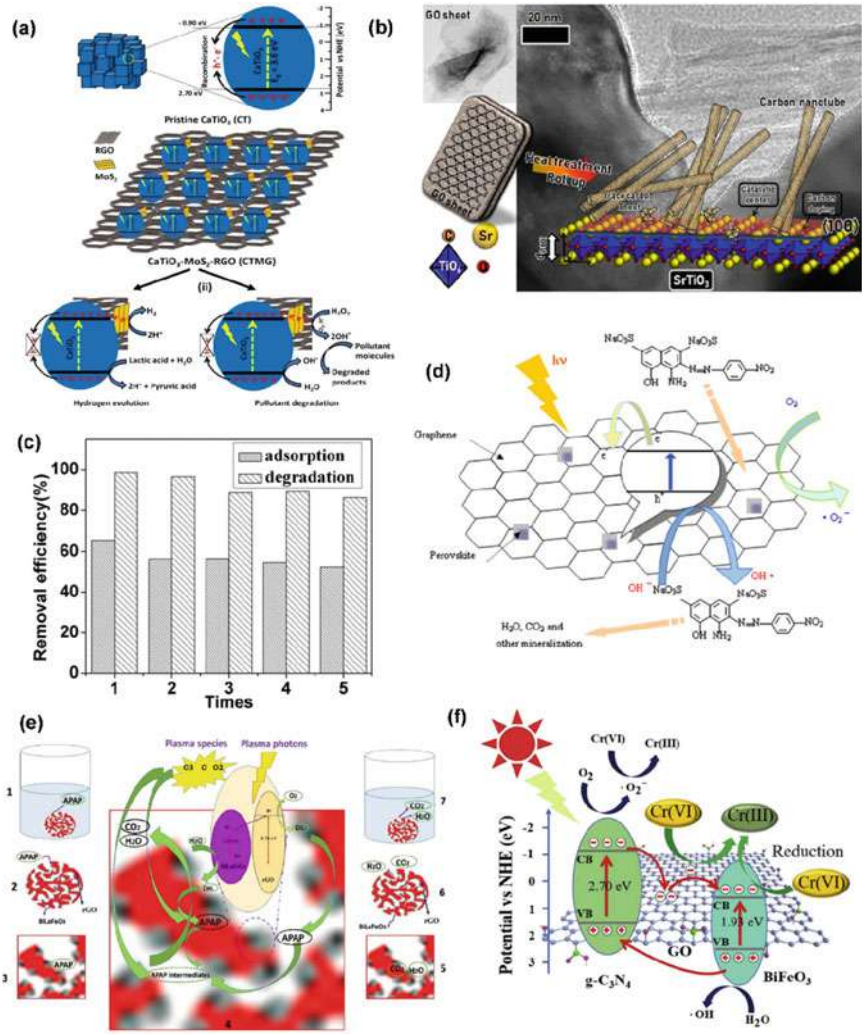

Fig. 1 **a** Schematic illustration of band edge potentials, photocatalytic reaction mechanism of $CaTiO_3/MoS_2$/rGO composites (Reprinted from Ref. [25], Copyright 2020, with permission from Wiley); **b** TEM image and formation of CNTs and carbon-doped $SrTiO_3$ (Reprinted from Ref. [30], Copyright 2019, with permission from Elsevier); **c** Reusability of MZT–GR-8 catalyst for NOR adsorption and photodegradation (Reprinted from Ref. [38], Copyright 2016, with permission from Royal Society of Chemistry); **d** Photocatalytic degradation mechanism of diamine green B over $LaMn_{1-x}Co_xO_3$/graphene composite (Reprinted from Ref. [56], Copyright 2014, with permission from Elsevier); **e** Plasma photocatalytic decomposition of APAP by $BiLaFeO_3$/rGO nanocomposite (Reprinted from Ref. [61], Copyright 2021, with permission from Elsevier); **f** Cr(VI) photoreduction mechanism over g-C_3N_4/GO/$BiFeO_3$ heterojunction (Reprinted from Ref. [67], Copyright 2019, with permission from Elsevier)

to raw $SrTiO_3$ which was ascribed to the hindered recombination rate of photo-excited electron_hole pairs. They also underlined the fact that the RGO served as a charge acceptor as well as good scaffold for homogenous dispersion of $SrTiO_3$. In an interesting work [30] with GO/$SrTiO_3$, it was discovered that the graphene sheets were decomposed and diffused into the $SrTiO_3$ lattice and substituted its inter-layer O_2–sites, resulting the formation of carbon nanotubes (Fig. 1b). Recently, bio-waste-derived layered graphene/$SrTiO_3$/PAN composite photocatalyst was synthesized via electrospinning technique and it was stated that the presence of the graphene decreased the band gap energy and also accelerated the separation of photoinduced charges resulting higher hydrogen evolution from the photocatalytic water splitting when compared with pristine $SrTiO_3$ [31].

Other titanate-based perovskites such as $NiTiO_3$ [33, 34], $ZnTiO_3$ [35–39], $BaTiO_3$ [40–48], $CdTiO_3$ [49], $PbTiO_3$ [50–52], $La_2Ti_2O_7$ [53], $LaTiO_2$–N [54] have been coupled with graphene oxide which improved both efficiency of transferring charges as well as promoted the mobilities of photo-induced e^-/h^+ in photocatalysts. Kang et al. [35] explored that the methylene blue degradation of $ZnTiO_3$ (63.9%) was greatly enhanced with increasing weight ratio of GO (95.2%) to a certain value of 0.5 wt% which was attributed to the enhanced agglomeration, generation of Ti–O–C chemical bonds which improved the transmission of interface charge. When the graphene amount increased from 0.5 to 5 wt%, the degradation rate significantly decreased owing to the blocking of active surface sites by absorbed dye molecules and decreased contact surface of $ZnTiO_3$ with sunlight irradiation. On the other hand, a facile precipitation method was carried out to prepare rGO decorated cubic ZnTiO3 rods and the RhB degradation rates were found as 71% and 98% for bare ZnTiO3 and rGO/ZTO3, respectively [37]. Mashkouri et al. [36] applied a facile mechanochemical method for the preparation of multilayer $ZnTiO_3$/GO nanocomposites and stated that the in-situ ball-milling route was effective without requiring high temperature conditions. Besides, hydrothermal process was conducted by Wu and co-workers [38] in order to synthesize mesoporous $ZnTiO_3$/rGO composites and the Raman analysis showed the two characteristic graphene oxide peaks indicating successful reduction of GO during the thermal preparation of composites. The photocatalytic performances were tested towards norfloxacin (NOR) and MO degradation and the NOR adsorption percentage of composite was 66% while the degradation rate was determined as 99% revealing that adsorption played a role in the removal process (Fig. 1c).

$BaTiO_3$ has been considered as a promising ferroelectric perovskite which have great potential capability used in optoelectronic devices. The crystal structure of $BaTiO_3$ directly affects the band gap energies which the cubic and tetragonal phases exhibit a lower band gap than the other orthorhombic or rhombohedral phases [40]. One of the most essential features of $BaTiO_3$ is its original polarization effect mechanism which increases the lifetime photogenerated carriers improving photocatalytic efficiency. A freeze-drying approach was applied to prepare $BaTiO_3$/GO hybrids applied in MB degradation and the composite catalysts displayed 1.19 times higher activity than that of bare $BaTiO_3$ which was attributed to the suitable energy band structure as well as adsorption function of graphene [41]. Rastogi et al. [42]

confirmed the role of reduced graphene oxide as macromolecular photosensitizer in enhanced charge separation which further facilitated the catalytic degradation. Mengting and co-workers [43] stated that the graphene oxide doping on $BaTiO_3$ remarkably enlarged the surface area as 62 m^2/g providing additional active surface sites for reacting with the target pollutant. Wang et al. [44] observed an intimate interfacial connection between $BaTiO_3$ and GO nanolayers and proposed that the role of graphene was acting like an organic dye-like photosensitizer for $BaTiO_3$. Jiang et al. [45] systematically examined the ferroelectric polarization properties of $BaTiO_3$/rGO nanocomposites and found that synergetic effect of polarization of $BaTiO_3$ and fast charge migration role of rGO was crucial for boosting the separation and transport of photo-excited electrons and holes. A ternary nanocomposite including $BaTiO_3$ and $NiFe_2O_4$ nanoparticles were supported on rGO nanosheets by three-step method and the increased rGO amount enhanced the impedance match as well as enforced energy attenuation derived from electronic and interfacial polarization in the composite structure [46].

Besides, lanthamide titanate ($La_2Ti_2O_7$) has layered perovskite structure with a wide band gap energy (3.8 eV). Wu and co-workers [53] prepared graphene–$La_2Ti_2O_7$ nanocomposites via UV-induced photocatalytic reduction method and the composites displayed greater photo-degradation performance for rhodamine B (RhB) dye compared to bare $La_2Ti_2O_7$. Raman analysis showed that the ratio of intensity of D to G band (I_D/I_G) remarkably decreased in the spectrum of composites revealing that chemical reduction caused a re-established conjugated graphene network (sp^2 domains) and more graphitization occurred during UV light assisted thermal treatment. On the other hand, oxynitride type perovskites such as $LaTiO_2N$, $CaTaO_2N$, TaON have narrow band gap energies while they suffer from low electric conductivity which hinders the charge transfer and promotes the recombination. Recently, a Z-scheme $LaTiO_2N/Bi_2S_3$@rGO composite catalyst was developed for enhanced performance in tetracycline (TC) degradation under visible light illumination [54]. It was stated that the reduced graphene oxide enabled a strong interfacial contact between $LaTiO_2N$ and Bi_2S_3, created new active adsorption sites, hindered the recombination rate, and improved incorporation of heterojunction structure. The photocatalytic mechanism was explained by Z-scheme transfer compared with conventional type-II junction and the enhanced degradation rate towards tetracycline was ascribed to the Z-scheme charge transfer between $LaTiO_2N$ and Bi_2S_3 accelerated by rGO.

Hu et al. [55] observed a significant red shift in the light absorption range for $LaMnO_3$/graphene composites which exhibited greater photocatalytic degradation of acid red A under visible light irradiation. In their other work [56], they prepared $LaMn_{1-x}Co_xO_3$/graphene via sol–gel method and investigated the diamine green B degradation. They hypothesized that the graphene sheets would serve as charge transfer channel on $LaMnO_3$ perovskite and hinder the charge pair recombination. The photocatalytic mechanism was explained as the photo-induced electrons transferred from perovskite to GO and temporarily stored on the graphene surface of GO, retarding the recombination of charge carriers (Fig. 1d). On the other hand,

a self-assembly photocatalytic reduction method was employed in order to encapsulate $LaNiO_3$ in rGO sheets [57]. Authors approved that the meso-macroporous skeleton of graphene enabled efficient adsorption and diffusion of methanol which subsequently boosted the capture of photo-excited holes during H_2 evolution. The hindered recombination rate of electrons/holes endorsed the migration of electrons from the surface of $LaNiO_3$ to rGO through Ni–C bond.

Ferrite perovskites ($AFeO_3$) have narrow band gap energies with higher visible light photoactivity as well as they can be used as photo-Fenton catalysts in advanced oxidation processes (Table 2). However, they have low conduction band potential, poor electron conductivity, short diffusion of exciton and low surface area [58]. Among the ferrite perovskites, $BiFeO_3$ (BFO) has high photocatalytic activity towards many organics while it shows negligible H_2 evolution performance. Thus, coupling of $BiFeO_3$ [59–73] with graphene derivatives have resulted to overcome these limitations. An et al. [59] employed graphene-$BiFeO_3$ nanocomposite as a photo-Fenton catalyst which showed fivefold larger surface area in comparison with bare $BiFeO_3$. The composite catalyst exhibited fast tetrabromobisphenol A degradation ($k = 1.19\ min^{-1}$) which was 5.43 times higher than that of $BiFeO_3$. The enhanced photo-Fenton activity was attributed to the larger surface area, enhanced adsorption capacity with increasing graphene ratio and robust electron mobility of graphene. Similarly, Li et al. [60] illustrated three dimensional $BiFeO_3$ submicron cubes composited with graphene oxide and reported better photocatalytic activity towards MB degradation compared with bare $BiFeO_3$ nanoparticles. In a recent work, Farhadi et al. [61] examined the effect of gel agents of ethylene glycol (E), citric acid (C), and mixture of citric acid-ethylene glycol (CE) for the synthesis of $BiFeO_3$/rGO nanocomposite. When compared with citric acid, higher negative combustion heat of ethylene glycol resulted in obtaining more intense peaks in the XRD spectra of $BiFeO_3$/rGO composite. The acetaminophen (APAP) adsorption in dark conditions was found as $BiFeO_3$/rGO-CE > $BiFeO_3$/rGO-E > $BiFeO_3$/rGO-C. Similarly, the degradation percentages were obtained as 89.6%, 77.9%, and 65.1% for $BiFeO_3$/rGO-CE, $BiFeO_3$/rGO-E, and $BiFeO_3$/rGO-C catalysts, respectively. It was concluded as the interaction of ethylene glycol and citric acid as gel agents allowed formation of bigger $BiFeO_3$ crystals, stronger interaction between heterojunctions, higher hydrophilic features, lower particle agglomeration, as well as higher light harvesting properties. Moreover, lanthanum was found as the optimum dopant for $BiFeO_3$/rGO-CE structure among the other metal salts (Mn, Ba and Zn) and the as-obtained $BiLaFeO_3$/rGO showed well dispersion of $BiLaFeO_3$ on rGO surface and high surface area and porosity endorsed the available active sites for APAP adsorption. Authors underlined the fact that the plasma and photocatalytic oxidation steps occurred simultaneously in which air was converted to plasma species of O_3, $^{\bullet}O_2$, and O in plasma reactor. Then, the plasma-generated photons might come across with $BiLaFeO_3$ surface and produced induced e^-/h^+ pairs. Meanwhile, the electrons migrated to the graphene structure hindering the recombination rate and prolonging the charges life (Fig. 1e). In another work [62], Sm doped $BiFeO_3$ nanoparticles were successfully anchored on rGO surface through two-step ultrasonication process and as-obtained composites had higher hydrogen conversion efficiency which reached

Table 2 Graphene based ferrite perovskite composite catalysts

Carbon source	Perovskite	Carbon amount	Synthesis method of composite	Photocatalytic Reaction	Efficiency	Ref
GO	$BiFeO_3$	0.2 wt%	Sol–gel	TBMPA degradation	$k = 1.19\ min^{-1}$	[59]
GO	$BiFeO_3$	1–3 mg/mL	Hydrothermal	MB degradation	92% degradation	[60]
rGO	SnS_2-$BiFeO_3$	0.1–0.2 wt%	Hydrothermal	MB, MO degradation	> 95% removal	[69]
rGO	$BiFeO_3$	0.5 mg rGO	One-step etching process	Electromagnetic absorption analysis	Reflection loss up to − 46.7 dB	[70]
N-GO	Sn/Gd- $BiFeO_3$	1–6% N-GO	Ultrasonication	MO degradation	~ 60% degradation	[71]
rGO	$BiFeO_3$	2–4 wt%	Ultrasonication	BPA degradation	> 99% degradation	[72]
rGO	$BiFeO_3$	0.04:0.96	Sol–gel combustion	APAP degradation	90% degradation	[61]
rGO	$Bi_{1-x}Sm_xFeO_3$	5 mg rGO	Ultrasonication	H_2 evolution	$6.54\ mmol\ h^{-1}\ cm^{-2}$	[62]
GO	$Bi_{25}FeO_{40}$	5–30 wt%	Hydrothermal	MB degradation	64.9% degradation	[63]
GO	$BiFeO_3$	5–20%	Ultrasonication	CIP degradation	98% removal	[64]
GO	$BiFeO_3$	~4 wt%	Hydrothermal	NH_3 degradation	91.2% removal	[65]
N-GO	$BiFeO_3$	–	Hydrothermal	Congo Red degradation	92% degradation	[66]
rGO/g-C_3N_4	$BiFeO_3$	–	Ultrasonication	Cr(VI) photoreduction	> 99% removal	[67]
rGO	Ag_2CrO_4/Ag/$BiFeO_3$	5–11 wt%	Ultrasonication	CIP degradation BrO_3^- reduction CO_2 reduction	96.% CIP degradation 99.6% BrO_3^- reduction 184 μmol g^{-1} CH_4 evolution	[73]
rGO	$LaFeO_3$	0.5–3 wt%	Ultrasonication	H_2 evolution	$611.3\ mmol\ h^{-1}\ g^{-1}$	[74]
rGO	$LaFeO_3$	–	Citrate auto-compulsion	–	–	[75]

(continued)

Table 2 (continued)

Carbon source	Perovskite	Carbon amount	Synthesis method of composite	Photocatalytic Reaction	Efficiency	Ref
GO	$LaFeO_3$	3 wt%	Ultrasonication	BPA degradation	($k = 0.1074\ min^{-1}$)	[77]
GO	$LaFeO_3$	5 wt%	Ultrasonication	MB degradation	91.2% removal	[78]
GO	$LaFeO_3$	20 wt%	Ultrasonication	H_2 evolution	3388 μmol g^{-1}	[79]
rGO	$LaFeO_3$/NiO	1 wt%	Solid-state	H_2 evolution Congo-Red degradation	939 μmol $h^{-1\ g-1}$ 96.5% Removal	[80]
rGO	$LaFeO_3/TiO_2$	5 wt%	Ultrasonication	H_2 evolution	0.893 mmol $h^{-1\ g-1}$	[81]
GO	$ZnFe_2O_4$	15–30 wt%	Hydrothermal	MB degradation	99% removal	[91]

to 2.45%. Moreover, the composite photoanode yielded the highest photocurrent density (1.96 mA/cm^2) owing to the extended absorption of photons in the visible region. Hu et al. [67] constructed a ternary heterojunction including g-C_3N_4, GO and $BiFeO_3$ materials which displayed high catalytic activity, narrower band gap, extended visible-light response and the stabile composites were easily separated from the reaction. Authors demonstrated that the fitted band structures of $BiFeO_3$ and g-C_3N_4 resulted in producing efficient photo-excited charge transfer from the conduction band of g-C_3N_4 to that of $BiFeO_3$, accelerating the electron bridging and collecting effects of graphene oxide. Meanwhile, the holes migrated from VB of $BiFeO_3$ to that of g-C_3N_4, allowing the effective separation of photo-induced charge pairs and subsequently improved the photocatalytic reduction of Cr(VI) (Fig. 1f).

Kumar et al. [73] constructed a highly active Ag_2CrO_4/Ag/$BiFeO_3$@rGO and applied in photo-reduction of BrO_3^-, CO_2 and Ciprofloxacin (CIF) decomposition under visible light irradiation. Z-scheme mechanism was based on a theory that $BiFeO_3$ and Ag_2CrO_4 played role in photo-reduction and photo-oxidation systems, respectively, while metallic Ag was electron mediator and rGO acted as adsorbent support and matrix electron mediator (rGO). It was hypothesized that combining these features had a triggering effect and would accelerate the reduction and oxidation reactions. The composite catalyst displayed excellent photocatalytic activity as 99.6% BrO_3^- photo-reduction, 96.3% CIF degradation and 180 μmol g^{-1} selective CH_4 generation which were higher than that of bare $BiFeO_3$. The successful formation of Z-scheme structure yielded boosted fast charge migration, suppressed recombination, and enhanced optical response. Due to its large surface area and functionality of graphene, more ciprofloxacin molecules were adsorbed on its surface and reacted with trapped radicals, electrons and holes resulting enhanced catalytic removal. Under light irradiation, both Ag_2CrO_4 and $BiFeO_3$ generated e^-/h^+ pairs owing to narrow band gap energy. The photo-induced electrons migrated from conduction band of $BiFeO_3$ (-0.35_{eV}) to more positive CB of Ag_2CrO_4 (0.80 eV). Analogously, the holes from valence band of Ag_2CrO_4 (2.5 eV) transferred to lesser positive of $BiFeO_3$ (2.08 eV). Meanwhile, metallic Ag particles captured electrons from surface and decreased the recombination rate. The photocatalytic mechanism was also supported from electron spin resonance (ESR) measurements which showed high intensity signal of $^{\bullet}O_2^-$ while the intensity of $^{\bullet}OH$ significantly increased. Therefore, the double charge transfer mechanism was tuned into an effective Z-scheme with incorporation of Ag^0 (Fig. 2a).

Studies demonstrated that the heterojunction of $LaFeO_3$ (LFO) with graphene oxide significantly enhanced optical and photocatalytic properties [74–81]. Abdel-Aal and co-workers [75] explored that citrate auto-compulsion method was effective for the synthesis of $LaFeO_3$/rGO nanocomposites which displayed a ferromagnetic behavior and extended visible light absorption with addition of rGO. Sphere-shaped $LaFeO_3$ nanoparticles were first synthesized by sol–gel method and then incorporated on reduced graphene oxide surface via ultrasonication, resulting well distribution of perovskite on graphene layers (Fig. 2b) [74]. It was emphasized that graphene acted as a cocatalyst under visible light irradiation and enhanced the H_2 evolution reaction through decreasing the recombination rate of photogenerated charge pairs. The lowest

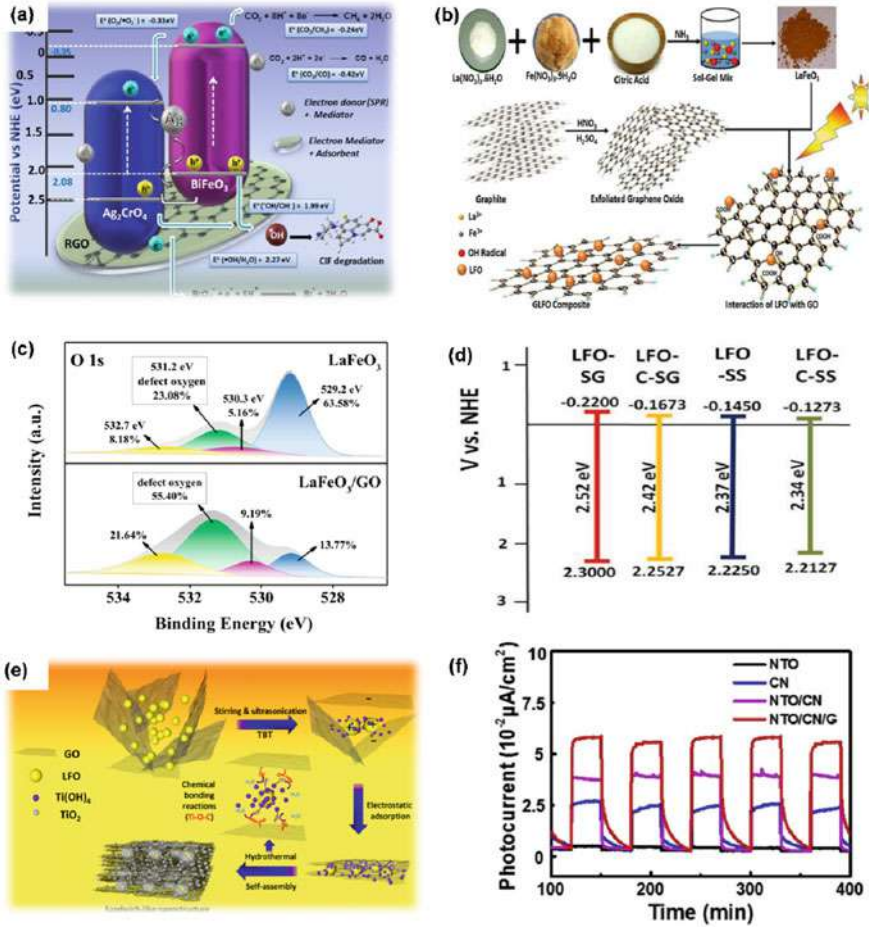

Fig. 2 **a** Transfer of charge carriers over Ag_2CrO_4/Ag/$BiFeO_3$@RGO heterojunction (Reprinted from Ref. [73], Copyright 2019, with permission from Elsevier); **b** Synthesis of RGO/LFO nanosphere composite (Reprinted from Ref. [74], Copyright 2020, with permission from Elsevier); **c** XPS spectra of O1s for $LaFeO_3$ and $LaFeO_3$/GO (Reprinted from Ref. [77], Copyright 2020, with permission from Elsevier); **d** Schematic band edge diagram of LFO prepared via sol–gel (SG) and solid-state (SS) method and their graphene composited forms (LFO-C-SG, LFO-C-SS) (Reprinted from Ref. [80], Copyright 2020, with permission from Elsevier); **e** Illustration of preparation of sandwich-like ternary TiO_2/RGO/LFO (Reprinted from Ref. [81], Copyright 2019, with permission from Elsevier); **f** Photocurrent response of $NaTaO_3$/g-C_3N_4/G composite (Reprinted from Ref. [84], Copyright 2019, with permission from Elsevier)

H_2 generation as 247.5 mmol $h^{-1\,g-1}$ was obtained by bare LFO while it increased to 490.6 mmol h^{-1} g^{-1} and 611.3 mmol h^{-1} g^{-1} by the addition of 0.5 wt% and 1 wt% of rGO, respectively. During catalytic reaction, electrons were excited from the valance band to the conduction band of LFO while the holes were created in the valence band. Then, the photo-induced electrons were moved from CB of LFO to rGO sheets where they joined the photocatalytic reaction (Eqs. 1–4).

$$\mathrm{LFO} + h\nu \rightarrow \mathrm{LFO_{CB}(e)^-} + \mathrm{LFO_{VB}(h)^+} \tag{1}$$

$$\mathrm{LFO/rGO} + h\nu \rightarrow \mathrm{rGO(e)^-} + \mathrm{LFO_{VB}(h)^+} \tag{2}$$

$$\mathrm{H_2O} + 2h^+ \rightarrow {}^1/_2\mathrm{O_2} + 2\mathrm{H^+} \tag{3}$$

$$2\mathrm{rGO(e)^-} + 2\mathrm{H^+} \rightarrow 2\mathrm{rGO} + \mathrm{H_2} \tag{4}$$

Jing and co-workers [77] investigated the performance of $LaFeO_3$/GO composites for bisphenol A (BPA) degradation from food wastewater. The hybrid samples in persulfate activated system displayed complete BPA decomposition ($k = 0.1074\,min^{-1}$) which was 18.2-folds premier than raw LFO. From the O 1 s XPS spectral analysis, the defect oxygen percentages were found as 23.1% and 55.4% for LFO and $LaFeO_3$/GO, respectively (Fig. 2c). It was hypothesized that the greater amount of defect oxygen in hybrid structure yielded high dispersion of photocatalysts in solution, improved the reactive sites and facilitated the transfer of radical oxygen species to BPA. Moreover, the hydrophobicity of benzene rings in GO promoted the enrichment of hydrophobic BPA molecules among the other hydrophilic substances in the complex wastewater. In another research [80], solid-state method was conducted for combining $LaFeO_3$, rGO and NiO materials and the resultant composite exhibited enhanced photocatalytic efficiency for Congo-red degradation and H_2 generation. It was found that the presence of NiO and rGO affected the band structure of LFO and narrower bandgaps with suitable band edge potentials (VB > 1.23 eV; CB < 0 eV) were obtained ensuring improved photocatalytic activity (Fig. 2d). Lv et al. [81] constructed a sandwich-like ternary TiO_2/rGO/LFO structure via two-step including adsorption of $LaFeO_3$ on graphene sheets followed by growth of TiO_2 over LFO-GO framework (Fig. 2e). The reduced graphene oxide acted as a solid electron mediator between TiO_2 and LFO heterojunction while the formation of chemical Ti–O–C bonds endorsed robust linked sandwich-like structure.

Other types of perovskite have been composited with graphene derivatives, as depicted in Table 3. Tantalate based perovskites exhibit outstanding photocatalytic and dielectric properties since they have conduction bands with Ta 5d orbital located at a more negative position than that of titanates (Ti 3d) [82–86]. Among them, potassium tantalate ($KTaO_3$) which has a wide band gap energy was functionalized with reduced graphene oxide via solvothermal technique and the as-prepared composites showed highly enhanced photocatalytic activity for phenol degradation

Table 3 Other types of perovskites with their graphene composites reported in literature

Carbon source	Perovskite	Carbon amount	Synthesis method of composite	Photocatalytic reaction	Efficiency	Ref.
ABO_3 type						
GO	$LaMnO_3$	–	Sol–gel	Acid Red A degradation	99.8% removal	[55]
GO	$LaMn_{1-x}Co_xO_3$	–	Sol–gel	Diamine green B degradation	98.8% removal	[56]
rGO	$LaNiO_3$	1–10 wt%	Hydrothermal	H_2 evolution	3220 μmol h^{-1} g^{-1}	[57]
GQDs	$LaCoO_3$/attapulgite	1–4 wt%	Impregnation	TC degradation	> 90% removal	[92]
GO	$YInO_3$	0.5 wt%	Solvothermal	H_2 evolution	400.4 μmol h^{-1} g^{-1}	[93]
Tantalates						
rGO	$KTaO_3$	5–30 wt%	Solvothermal	Phenol degradation	43% removal	[82]
rGO	$KTaO_3$	–	Hydrothermal	MB degradation, RhB degradation	96% MB removal 98% RhB removal	[83]
GO/g-C_3N_4	$NaTaO_3$	10–30 wt%	Photoreduction	RhB degradation	99% removal	[84]
rGO	N-$Sr_2Ta_2O_7$	–	–	H_2 evolution	194 μM h^{-1}	[85]
rGO	$NaTaO_3$	1.5 wt%	Hydrothermal	MB degradation	95% removal	[86]
Niobates						
GO	$NaNbO_3$		–	–	–	[87]
rGO	$KNbO_3$	2–4 C/O	-	–	–	[88]
rGO	$K_4Nb_6O_{17}$	5 wt%	Mixing	H_2 evolution	1530 μmol h^{-1} g^{-1}	[89]
rGO	$K_4Nb_6O_{17}$	1–5 wt%	Dispersion	H_2 evolution	106.8 μmol h^{-1} g^{-1}	[90]

which was ascribed to the formation of p–n heterojunctions between $KTaO_3$ and rGO sheets as well as to the photosensitization effect of graphene [82]. Similarly, Meng et al. [83] modified $KTaO_3$ nanotubes with rGO by hydrothermal method and the photocurrent tests verified effective transfer rate of photo-excited electrons which proved the heterojunction between materials. Besides, $NaTaO_3$ is a stable perovskite with highly positive valance band (E_{VB} ~ 3.01 eV) and suitable conduction band edge (E_{CB} ~ −0.99 eV) revealing that it can match well with other materials to form heterojunction. A ternary $NaTaO_3$/g-C_3N_4/GO catalyst were prepared by in-situ calcination followed by photo-reduction process [84]. Firstly, g-C_3N_4 sheets were grown on $NaTaO_3$ nanocubes; and then, graphene was incorporated to $NaTaO_3$/g-C_3N_4 by photochemical reduction. The resultant composite exhibited greater charge transportation efficiency and extended the optical absorbance range. According to the photocurrent response tests, the photocurrent of composite was remarkably enhanced when compared with bare $NaTaO_3$ which showed weakly photoelectric response owing to its wide band gap (Fig. 2f). The Rhodamine B photo-degradation was tested to investigate the catalytic performances of ternary catalyst which showed up to 100% decomposition under visible light irradiation.

$Sr_2Ta_2O_7$ is a layered perovskite type with a wide band gap energy (~4.2 eV) indicating it is only active under UV illumination. Mukherji et al. [85] improved the photocatalytic hydrogen production by using graphene-based N-doped $Sr_2Ta_2O_7$. The doped catalyst exhibited a strong photoreduction ability for exfoliated graphene oxide to graphene sheets which were then used as co-catalyst for Pt. The optical spectrum of GO-$Sr_2Ta_2O_{7-x}N_x$ composite shifted to the visible light region verified from the color change from canary yellow to brown/black owing to the partial restoration of π bonds within the GO structure. The composite catalyst displayed nearly 80% increase in H_2 generation and yielded higher quantum efficiency (6.45%) thank to the high charge carrier separation provided by graphene.

Moreover, niobates including $NaNbO_3$ (3.08 eV) and $KNbO_3$ (3.14 eV) have been coupled with graphene oxide in order to boost their photocatalytic activity [87–90]. Opoku and co-workers [87] developed bifunctional graphene oxide (GO)/V-doped $NaNbO_3$ heterostructure photocatalyst which showed enhanced photocatalytic performance and high stability. The heterostructure between $NaNbO_3$ and GO presented fast electron transfer which hinders the electron/hole recombination rate. Authors underlined that the GO sheets contributed as conductive electron channels for efficient charge separation and enhance the photo response of perovskite. The composite structure with narrower band gap energy showed a type-II band alignment which would further enhance its ability towards photocatalytic reactions. Besides, the effect of rGO reductivity on the photocatalytic efficiency of $KNbO_3$ was systematically investigated by using density functional theory (DFT) calculations and it was found that the increased rGO reductivity improved the photoactivity of rGO/$KNbO_3$ while the oxygen atoms of graphene greatly limited the C 2p states of rGO/CeO_2 composite which hindered its catalytic performance [88].

2.2 Graphitic Carbon Nitride-Based Perovskite Composites

Graphitic carbon nitride (g-C_3N_4) has been presented as a promising candidate to complement carbon in photocatalysis field due to its excellent thermal and chemical stability with unique optoelectronic properties [94]. The polymeric carbon nitride is constructed by the building blocks of triazine or tri-s-triazine (heptazine) rings bridged with the conjugated N atoms to the 2D layer structure (Fig. 3a). The tectonic structures depict different stability behavior depending on the different electronic environment of N atom and the sizes of the nitride pores. The tri-s-triazine allotrope is the most stable pattern of g-C_3N_4 because of its high condensation degree [95]. g-C_3N_4 acts as an n-type semiconductor due to presence of free electrons at valence band edge. The free electrons are attributed to sp^2 orbital electrons (lone pairs) of N atoms in the triazine, resulting in a band gap energy of ~2.7 eV between VB and CB. Thus, g-C_3N_4 has been regarded as visible-light active sample. However, the pristine g-C_3N_4 exhibits low photocatalytic efficiency due to its high recombination rate of the photo-induced charge carriers. In order to improve the separation rate of the electron–hole pairs, one of the most know way is to couple g-C_3N_4 with perovskites to develop composite photocatalysts. In this way, the band alignment of the as-obtained heterojunction photocatalytic composites present the staggered band structure, which are attributed to Z-type heterojunction systems (Fig. 3b) [96]. In this system, the difference of the position between the two type materials provides strong electrostatic interaction, resulting in shifting the conduction band (CB) of the g-C_3N_4 to more negative potential and widening the valence band (VB) width of the n-type carbon material. Due to the increasing the number of photogenerated electrons in the CB, the efficiencies of the photoinduced reduction reactions evolve. Furthermore, the enlargement of the VB promotes the mobility of holes, resulting more effective oxidation reactions [7]. Thus, the recombination rate of the photoinduced sites can be greatly inhibited and the photoactivity will be improved.

The main perovskite structure is presented as ABO_3, which is assigned to complex metal oxides. The most common perovskite families are lanthanate and titanate perovskite oxides to form heterostructured photocatalyst with the graphitic carbon nitride and the related studies are summarized in Table 4. In terms of lanthanate, the perovskite oxide group represents as $LaAO_3$ whereby A is attributed to a 3d transition metal such as Fe, Mn, Ni, Co and Cu. This kind of perovskite structure leads to the formation of p-type photocatalytic materials, in which the M constitute can be found in octahedral structure as MO_6 sites and the sites are stabilized by La^{+3} [97]. The construction of g-C_3N_4 with the p-type semiconductors has gained significant attention as a promising method to enhance the photocatalytic activity of the carbon structure due to their narrow band gap of about 1.89–2.71 eV, electronic and magnetic properties. The combination is attributed to the formation of p-n heterojunction photocatalysts. $LaFeO_3$ has been widely used to design the p-n type composites. Wu et al. [98] prepared a p-n heterostructured $LaFeO_3$/g-C_3N_4 photocatalyst by quasi-polymeric calcination method in which the perovskite microsphere with the nanosheets graphitic carbon nitride was coated. The Z-scheme photocatalyst

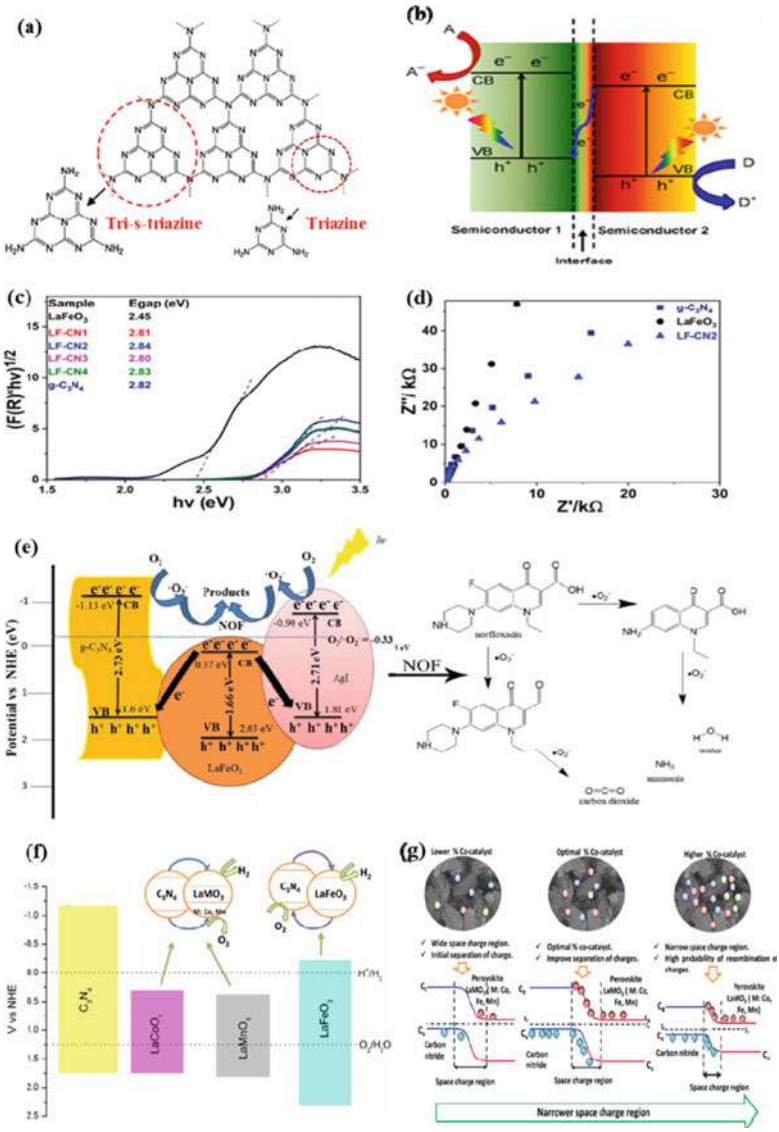

Fig. 3 **a** Chemical structures of g-C_3N_4 (Reprinted from Ref. [95], Copyright 2016, with permission from American Chemical Society); **b** Z-scheme mechanism (Reprinted from Ref. [96], Copyright 2020, with permission from Elsevier); **c** Tauc plots and resulting band gaps of $LaFeO_3$, g-C_3N_4,$LaFeO_3$/ g-C_3N_4 mechanism (Reprinted from Ref. [99], Copyright 2019, with permission from Royal Society of Chemistry); **d** Nyquist plots of $LaFeO_3$, g-C_3N_4,$LaFeO_3$/g-C_3N_4 (Reprinted from Ref. [99], Copyright 2019, with permission from Royal Society of Chemistry); **e** Degradation process of norfloxacin on AgI-incorporated $LaFeO_3$/g-C_3N_4 (Reprinted from Ref. [105], Copyright 2020, with permission from Elsevier); **f** Schematic band diagram of $LaFeO_3$, $LaMnO_3$, $LaCoO_3$, g-C_3N_4 (Reprinted from Ref. [109], Copyright 2019, with permission from Elsevier); **g** Surface saturation diagram (Reprinted from Ref. [109], Copyright 2019, with permission from Elsevier)

Table 4 Lanthanate and titanate perovskite oxide modified g-C_3N_4 photocatalysts

Photocatalyst	Band gap (eV)	Synthesis method	Light (irradiation type)	Performance	Ref.
$LaFeO_3$/g-C_3N_4		Quasi-polymeric calcination	Visible	100% BB degradation	[98]
$LaFeO_3$/g-C_3N_4		Simple calcination	Visible	98% of RhB 50% 4-CP degradation	[99]
$LaFeO_3$/g-C_3N_4		Solvothermal	Visible	90% RhB degradation	[8]
$LaFeO_3$/g-C_3N_4	2.85–2.83	Heat treatment	Visible	97.4% RhB degradation (H_2O_2)	[101]
$LaFeO_3$/g-C_3N_4	1.94–1.70	Ultrasonication-drying	Visible	1152.34 μmol/g h H_2 evolution	[102]
$LaFeO_3$/g-C_3N_4		Simple calcination	Visible	95% MB degradation	[103]
$LaFeO_3$/g-C_3N_4	–	Solid-state	Visible	35% MO degradation	[104]
AgI/$LaFeO_3$/g-C_3N_4		Ultrasound-assisted hydrothermal	Visible	95% NOF degradation	[105]
Ag/$LaFeO_3$/g-C_3N_4	–	Hydrothermal	Visible	97.9% RhB degradation 0.00423 min^{-1} phenol degradation	[106]
$LaMnO_3$/g-C_3N_4		Quasi-polymeric calcination	Visible	61.4% TC degradation	[107]
$LaCoO_3$/g-C_3N_4	2.68–2.62	Mixed calcination	Visible	35% MO degradation	[108]
$LaMO_3$ (Co, Fe, Mn)/g-C_3N_4	2.83–2.88	Sol–gel and solid-state	Visible	140 μmol/g h H_2 evolution for $LaFeO_3$/g-C_3N_4	[109]
$LaNiO_3$/g-C_3N_4	–	Heat treatment	Visible	30% TC degradation	[110]
$LaNiO_3$/g-C_3N_4	–	Mixing and solvothermal	UV	3392.50 μmol/g h H_2 evolution	[111]
$LaTiO_3$/g-C_3N_4		Sol–gel Polymerized Complex	Visible	90% RhB 84% 2,4-DCP degradation	[112]

(continued)

Table 4 (continued)

Photocatalyst	Band gap (eV)	Synthesis method	Light (irradiation type)	Performance	Ref.
$SrTiO_3$/g-C_3N_4	–	Sonication mixing	UV–Vis	90% MB degradation	[113]
$SrTiO_3$/g-C_3N_4	2.5	Thermal	Sunlight	100% BPA degradation	[114]
$SrTiO_3$:N/g-C_3N_4	3.02	Calcination	Visible	100% RhB degradation	[115]
$SrTiO_3$/ g-C_3N_4	2.92	Decomposition of urea in the presence of $SrTiO_3$	Visible	440 μmol/g h H_2 evolution	[116]
$SrTiO_3$/ g-C_3N_4	–	Ball milling and calcination	Visible	966.8 μmol/g h H_2 evolution	[117]
$SrTiO_3$/ g-C_3N_4:Rh	2.30–2.75	Calcination	Visible	223.3 μmol/g h H_2 evolution	[118]
$SrTiO_3$/ g-C_3N_4:Pt	–	Calcination	Sun light	552 μmol/g h H_2 evolution	[119]
$SrTiO_3$/ g-C_3N_4:Pt		Thermal	Solar light	93% AR degradation 471 μmol/g h H_2 evolution	[120]
$SrTiO_3$/ g-C_3N_4:Cr	2.5	Ball milling and calcination	Visible	100% RhB degradation	[121]
$SrTiO_3$/ g-C_3N_4:Cr	2.30–2.71	Sol–gel Hydrothermal	Visible	100% MO degradation	[122]
$CaTiO_3$/g-C_3N_4	–	Hydrothermal co-deposition	Visible	189.38 μmol/g h H_2 evolution	[123]
$CaTiO_3$/g-C_3N_4	2.40–2.50	Solvothermal-calcination	Sunlight	99.76% CV degradation 95.02% MG degradation	[124]
$CaTiO_3$/g-C_3N_4	2.79	Mixing	UV, visible and natural sunlight	50% RhB degradation (UV) 72% RhB degradation (Vis) 97% RhB degradation (SL) 47% BP degradation (SL)	[125]
$CaTiO_3$/g-C_3N_4/AgBr	–	Thermal	Sunlight	99.6% RhB degradation	[126]
$BaTiO_3$@g-C_3N_4	–	Mixing-calcination	Sunlight	76% MO degradation	[127]

(continued)

Table 4 (continued)

Photocatalyst	Band gap (eV)	Synthesis method	Light (irradiation type)	Performance	Ref.
$NiTiO_3$/g-C_3N_4	2.22–2.70	Calcination	LED light	0.0309×10^{-2} min^{-1} degradation rate	[128]
$NiTiO_3$/g-C_3N_4	2.34	Calcination	Visible	80% NB degradation	[129]
$CoTiO_3$/g-C_3N_4	2.78	In-situ rowth	Sunlight	858 μmol h^{-1}/g t H_2 evolution	[130]
$MnTiO_3$/g-C_3N_4	2.71	Hydrothermal	Visible	100% MB degradation	[131]

exhibited superior photocatalytic activity for Brilliant Blue (BB) degradation under visible light irradiation. The elevated performance was ascribed to enhanced separation rate of photoinduced species. $LaFeO_3$/g-C_3N_4 was also fabricated through simple calcination method to investigate the photodegradation of Rhodamine B (RhB) and 4-chlorophenol (4-CP) [99]. By doping effect, the electronic properties of g-C_3N_4 got modulated, the band gap value shifted to more narrow potential (Fig. 3c), thus the ability of visible light absorption was improved. The semiconducting nature of the heterostructure material was further analyzed by using the EIS Nyquist plot (Fig. 3d. The smallest circle size was observed for the composite and this demonstrated an effective separation of photogenerated electron–hole pairs and the effective photocatalytic degradation of RhB and 4-CP.

Another efficient $LaFeO_3$-incorporated g-C_3N_4 was fabricated by Liang et al. and the photocatalyst depicted 19.1 times higher activity on RhB degradation than that of bare perovskite under visible light illumination [100]. Moreover, the activity of $LaFeO_3$/g-C_3N_4 on RhB decomposition was improved by adding H_2O_2 as fenton agent in the reaction environment [101]. Due to its superior redox efficiency, the composite structure also showed remarkable water reduction, as well as methylene blue (MB) and methyl orange (MO) dye degradation performances under visible light [102–104]. To further enhance separation of photoinduced e^-/h^+ pairs, AgI-incorporated $LaFeO_3$/g-C_3N_4 was prepared by ultrasound-assisted hydrothermal technique [105]. In the dual Z-scheme photocatalyst, the silver compound showed high electron capture capacity, resulting that it decreased the recombination ratio between the electrons excited in the CB of $LaFeO_3$ and the photogenerated holes at the VB of g-C_3N_4. The retained electrons on the CB of g-C_3N_4 can convert O_2 to $^{\bullet}O_2^-$, resulting excellent photo-activity on norfloxacin (NOR) degradation (Fig. 3e). The great effect of Ag on charge transfer in the heterostructure was also observed for visible light driven-RhB and phenol removal in aqueous environment [106].

$LaMnO_3$ should be also considered as the other feasible lanthanate perovskite material that improves the physiochemical properties of graphitic carbon nitride. Luo et al. [107] employed $LaMnO_3$ and graphitic carbon nitride for the fabrication of Z-scheme photocatalyst that fascinatingly enhanced tetracycline degradation under visible light irradiation. The heterojunction possessed high photo-current density and surface area, enhancing lifetime of charge species and the number of the active sites. Luo et al. [108] fabricated $LaCoO_3$/g-C_3N_4 by performing mixed calcination method and the perovskite incorporated- carbon structure showed lower band gap energy than that of pristine g-C_3N_4, resulting enhanced MO degradation. In case of water splitting, the effects of $LaFeO_3$, $LaMnO_3$ and $LaCoO_3$ on the properties of g-C_3N_4, were compared to obtain the boosted photocatalytic activity. The efficiency of hydrogen production was related to the band alignment formed during the synthesis of the composite. As seen in Fig. 3f, type I heterostructure between $LaMnO_3$ or $LaCoO_3$ with g-C_3N_4 was formed that causes the accumulation of the photoinduced sites on the perovskite oxide. In terms of $LaFeO_3$, the formation of the type II heterostructure was observed, which greatly suppressed the recombination of photogenerated electron_hole pairs. The results supported that $LaFeO_3$/g-C_3N_4 exhibited the highest hydrogen evolution (140 μmol/g h). Also, the study emphasized

that the addition of 5% and 10% perovskites saturated the active surface of the g-C_3N_4, causing decreased the activity driven by lower light absorption ability and higher recombination rate of the active centers (Fig. 3g) [109]. In addition, $LaNiO_3$ and $LaTiO_3$ have been conjoined with g-C_3N_4 to obtain attractive heterojunction photocatalyst. Zhou et al. [110] synthesized $LaNiO_3$/g-C_3N_4 Z-scheme nanosheet, and the hybrid with 30 wt% $LaNiO_3$ loading exhibited intimate attachment of $LaNiO_3$ on the surface of g-C_3N_4, leading to formation of abundant heterojunctions at the interface, which were favorable for isolation of photogenerated charge carriers in comparison with the single component. The $LaNiO_3$/g-C_3N_4 sample was also utilized as a stable photocatalyst for hydrogen production from water including methanol due to large light-response area and high separation rate of photogenerated species [111]. $LaTiO_3$/g-C_3N_4 was fabricated by Rakibuddin et al. [112] and the heterojunction sample depicted sustainable organic matter degradation for three cycle in the photocatalytic process.

Another significant perovskite group is titanate, representing as $ATiO_3$ (A = Ca, Sr, Ba, etc.), which have been studied to improve the efficiency of graphitic carbon nitride in photocatalytic applications (Table 4). $SrTiO_3$ is categorized as a n-type photocatalyst with wide band gap energy. Konstas et al. [113] observed that the MB degradation significantly affected by the ratio of the carbon nitride in the hybrid structure. The amalgamation of $SrTiO_3$ and g-C_3N_4 was successfully achieved and the as-prepared photocatalyst could attain 100% of bisphenol (BPA) degradation under solar light irradiation [114]. The composite showed high photogenerated electron and hole capture capacity due to the sufficient mobility of charge carrier, resulting the formation of binary photocatalyst driven by staggered band structure. Kumar et al. [115] enhanced the activity of $SrTiO_3$/g-C_3N_4 by doping the titanate perovskite with N atom; thus the visible-light adsorption capacity of the $SrTiO_3$ phase increased and the composite showed almost 100% RhB degradation. Furthermore, $SrTiO_3$ based polymeric carbon nitride promoted hydrogen evolution by degrading water including oxalic acid under visible light illumination [116]. Hybrid nanocomposites with strong interaction were fabricated by wrapping $SrTiO_3$ in g-C_3N_4 structure with ball-milling followed by calcination method [117]. The interaction was examined by calculating the electron density variation of the composite material. Figure 4a showed that the electron accumulation was occurred on the carbon nitride phase, while the charge depletion was observed on the perovskite oxide phase. Based on the transfer of the electrons, the charge density was distributed in the interface. The active composite was doped with Rh and Pt to further improve H_2 formation rate [118–120]. Lee et al. [119] proposed three mechanisms for the movement of the charge species in the heterostructure depending on the sequence of the active materials during the synthesis procedure, as depicted in Fig. 4b. Beside the noble metal, the non-noble metals especially Cr could be utilized as a dopant to enhance photocatalytic efficiency [121, 122].

The other common titanate perovskite, $CaTiO_3$ exhibits wide band gap energy (around 3.6 eV). When it is incorporation with a narrow band gap g-C_3N_4, the charge transfer across heterojunction occurs in an effective way, resulting enhanced

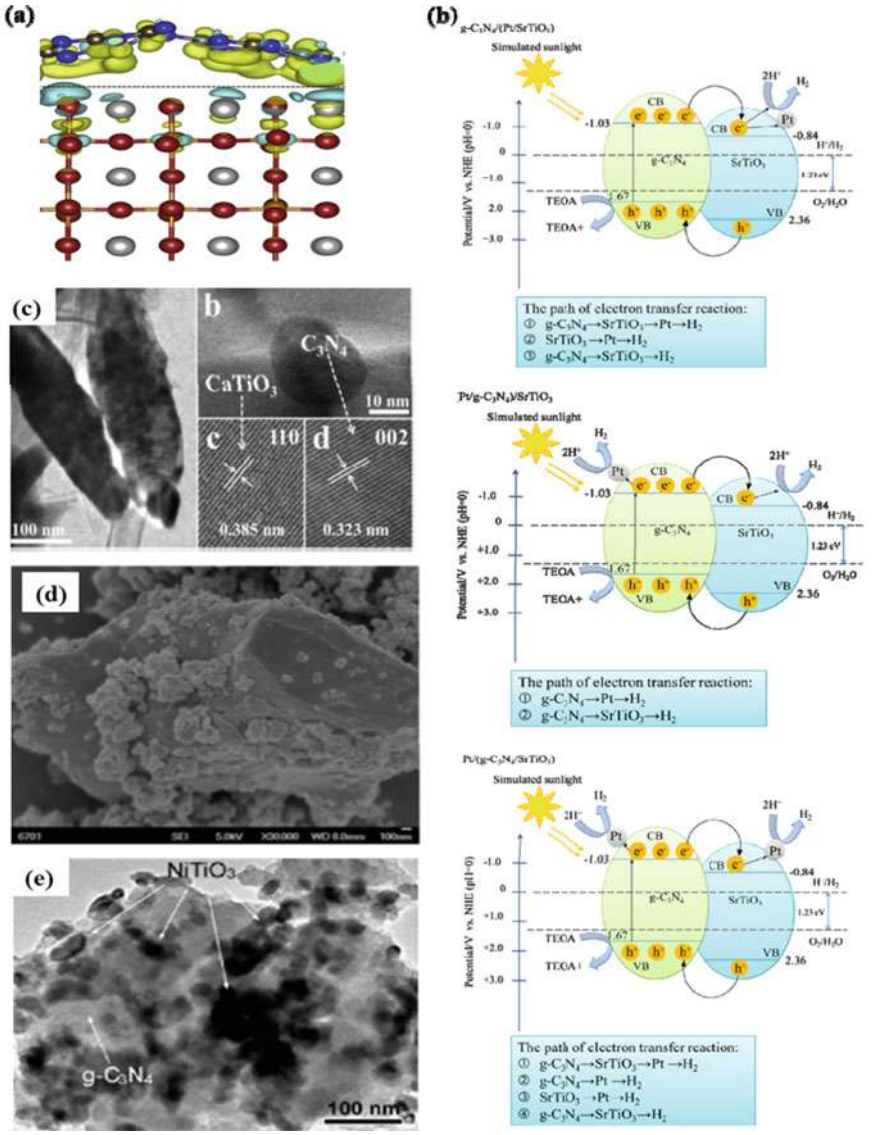

Fig. 4 **a** Charge density differences for $SrTiO_3$/g-C_3N_4. The cyan and yellow regions represent the electron depletion and accumulation, respectively. The C, N, O, Ti and Sr atoms are represented as brown, blue, red, yellow and sliver, respectively (Reprinted from Ref. [117], Copyright 2019, with permission from Elsevier); **b** Charge transfer mechanisms of the different synthetic sequences for Pt/$SrTiO_3$/g-C_3N_4 (Reprinted from Ref. [119], Copyright 2019, with permission from Elsevier); **c** TEM and HRTEM images of $CaTiO_3$/g-C_3N_4 (Reprinted from Ref. [123], Copyright 2018, with permission from Elsevier); **d** SEM image of $BaTiO_3$/g-C_3N_4 (Reprinted from Ref. [127], Copyright 2015, with permission from Elsevier); **e** TEM image of and $NiTiO_3$/g-C_3N_4 (Reprinted from Ref. [128], Copyright 2017, with permission from American Chemical Society)

photo-induced activity. Pan et al. [123] prepared $CaTiO_3$/g-C_3N_4 by hydrothermal co-deposition method. The formation of the heterostructure was characterized HRTEM images (Fig. 4c); observing the specific lattice spaces of the carbon nitride (0.323 nm) and $CaTiO_3$ (0.385 nm). The incorporation promoted the H_2 production rate of the perovskite due to prolonged lifetime of the photoinduced electrons and holes. Chen et al. [124] examined the performance of the $CaTiO_3$/g-C_3N_4 in crystal violet (CV) and malachite green (MG) degradation under sunlight illumination. The composite showed an excellent photocatalytic activity in degrading CV and MG with a degradation rate of 99.76% and 95.02% respectively. This enhancement rate was about 2.5 and 1.5 times greater than that of g-C_3N_4 and $CaTiO_3$, respectively. Kumar and co-workers [125] reported $CaTiO_3$ nanoflakes installed graphitic carbon nitride nanosheets (CTCN) for sufficient degradation of RhB and BPA. CTCN displayed significant reduction in band gap (2.79 $_{eV}$) and formed energy interfaces allowing good excitation dissociation for photogenerated charge species that facilitated enhanced $O_2^{-\bullet}$ formation. Further recyclability results showed that the composite was stable even after three successive cycles under sunlight illumination. In addition, AgBr was added to ternary Z-scheme heterostructure photocatalyst system of $CaTiO_3$/g-C_3N_4 [126]. The photocatalytic activity of the composite towards the degradation of RhB under sunlight irradiation was explored and 99.6% removal rate was attained after 30 min light-induced reaction. The improvement could be due to the fact that Ag particles acted as electron sinks by capturing the photogenerated electrons from the $CaTiO_3$ leading to efficient electron/hole pairs separation.

$BaTiO_3$-included graphitic carbon nitride composite prepared via a facile mixing and calcining method was found efficient in degrading methyl orange (MO) [127]. In case of the heterostructure, the availability of more active sites increased with well-distribution of titanate particles on carbon structure, promoting the contact between the photoactive composite and the organic pollutant. The uniform dispersion was observed via SEM technique, as depicted in Fig. 4d. Photoactive $NiTiO_3$/g-C_3N_4 composite was also constructed by Huang and co-workers and was utilized for the photocatalytic removal of RhB from wastewater [128]. In the synthesis procedure, sonication was applied to interact g-C_3N_4 with the titanate perovskite. TEM studies showed that the g-C_3N_4 was exfoliated and well-dispersion of $NiTiO_3$ was obtained (Fig. 4e). Similar heterojunction material also exhibited superior photocatalytic performance for nitrobenzene removal [129]. The great applicability of the titanate perovskite in the modification of the graphitic carbon nitride was also observed with $CoTiO_3$ [130] and $MnTiO_3$ [131] perovskites.

Regarding the heterojunction g-C_3N_4 photocatalysts, bismuth and sodium included-ABO_3 perovskites have been also presented as a recent photoactive material due to suitable band gap (Table 5). The utilization of $BiFeO_3$ in the g-C_3N_4 based heterostructure and the $BiFeO_3$/g-C_3N_4-assisted photocatalytic and photo-Fenton processes in the degradation of organic pollutant [132–135], metal removal [67] and hydrogen production [136] were also elucidated. Wang et al. [132] decorated g-C_3N_4 with $BiFeO_3$ particles by a facile ultrasound-assisted method. During the

Table 5 Bi and Na included-perovskite oxide modified g-C_3N_4 photocatalysts

Photocatalyst	Photocatalytic application	Remarks	Ref.
$BiFeO_3$/g-C_3N_4	MO degradation	After the incorporation, the morphology of $BiFeO_3$ was changed	[132]
$BiFeO_3$/g-C_3N_4	Guaiacol degradation	High surface area resulted efficient photofenton degradation	[133]
$BiFeO_3$/g-C_3N_4	RhB degradation	Z-Scheme band alignment improved transfer and separation of active species	[134]
$BiFeO_3$/g-C_3N_4	RhB degradation	The activity was driven by $\bullet O_2^-$ radicals	[135]
$BiFeO_3$/g-C_3N_4/GO	Cr(VI) degradation	The enhanced removal rate was observed at acidic condition	[67]
$BiFeO_3$/g-C_3N_4	H_2 evolution	The composite was successfully synthesized by a simple calcination method	[136]
$AgBiO_3$/g-C_3N_4	MO.TC and phenol degradation	Enhanced surface area and fast electron transfer rate improved the activity	[137]
Ag_3BiO_3/g-C_3N_4	MO degradation	Degradation efficiency was ~78% within 180 min	[138]
Ag_3BiO_3/g-C_3N_4	RhB, MG, MO and phenol degradation	The efficiencies were 52.5, 49.1, 49.0, and 32.7 times for RhB, MG, MO and phenol, respectively as compared to g-C_3N_4	[139]
$NaNbO_3$/g-C_3N_4	OFL degradation	Type II heterojunction was obtained with narrowed band gap	[140]

synthesis stage, micro cubes $BiFeO_3$ particles transformed to spindle-like nanostructure, resulting uniform perovskite distribution in the composite. In another study, Hu et al. [67] found that $BiFeO_3$/g-C_3N_4/GO heterojunction sample was able to degrade up to ~100% of the Cr(VI) contaminant after 100 min exposure to visible irradiation. They reported that the superior activity was attributed to the band-bending process during the formation of the ternary material. The different band edge positions of the components created additional pathways for the transportation of photogenerated e^-/h^+ at the photocatalyst-dye interface region, resulting in the reduction of charge carrier recombination and thus improved photocatalytic activity. On the other side, $AgBiO_3$/g-C_3N_4 promoted heterocyclic constitute degradation under visible light; the removal efficiencies were found as 95%, 80% and 97.2% for MO, TC and phenol removal, respectively [137]. However, the composite showed low reusability after four catalytic runs due to the release of the oxygen species from the perovskite part by time.

Fabrication of Ag_3BiO_3/g-C_3N_4 by hydrothermal method was reported by Song et al. [138]. The as-obtained composite displayed superior photocatalytic activity for

degradation of methyl orange (MO) under visible light irradiation and the performance could be driven by significantly enhanced amount of $^{\bullet}O_2^-$ and h^+ generation. Similar study was also conducted by using nanosized graphitic carbon nitride and excellent reduction performance was observed to remove RhB, MO, MG and phenol in aqueous environment [139]. In terms of Na-based perovskite oxide, $NaNbO_3$ [140] and $NaTaO_3$ [84] were coupled with the g-C_3N_4 to accomplish light-driven reactive catalyst for organic matter removal. Zhang et al. [140] demonstrated that $NaNbO_3$/g-C_3N_4 significantly degraded third-generation fluoroquinolone antibiotic (ofloxacin) under simulated solar light. The antibiotic degradation pathway was described by identifying the reaction intermediates with LC_MS/MS. The photodegradation of OFL could be followed by four reaction pathways. Pathway 1 and 2 was driven by oxidation and the breakage of piperazine ring. Then, the aromatic ring was ruptured by dealkylation and the leaving of some groups (–CO, $–C_2H_4$, $–CH_3$, etc.) to form low molecular weight substrates. In Pathway 3, the substitution of fluorine followed by the dealkylation was occurred. Pathway 4 started with the hydroxylation of the aromatic rings, and the oxidation was formed as further degradation step.

In case of the heterostructure construction, spinel-type perovskites are another well-known material, which are presented as AB_2O_4. In this case, the ferrites (AFe_2O_4) have been studied intensively to obtain remarkable active composite in photocatalytic processes (Table 6). Shen et al. [141], $CuFe_2O_4$/g-C_3N_4 composites were synthesized by a hydrothermal method using NaOH as mineralizer. In dye removal, the photocatalytic activity of the heterostructure was facilitated by suppressing the recombination of the photogenerated species. The composite also showed the magnetically separation ability from the aqueous reaction environment. The performance of the $CuFe_2O_4$/g-C_3N_4 composite was improved by adding peroxydisulfate (PDS) into the contaminant solution [142]. PDS was transformed to $SO_4^{\bullet-}$ in the presence of $CuFe_2O_4$ and the reactive phase enhanced the oxidization ability, resulting higher destruction of organic molecules. The reaction mechanism was presented as:

$$\text{g - } C_3N_4/CuFe_2O_4 \rightarrow h^+ + e^- \tag{5}$$

$$O_2 + e^- \rightarrow O_{2\bullet}^- \tag{6}$$

$$O_{2\bullet}^- + H^+ \rightarrow HO_2 \tag{7}$$

$$2HO_{2\bullet} \rightarrow H_2O_2 + {}^1O_2 \tag{8}$$

$$H_2O_2 + e^- \rightarrow {}^{\bullet}OH + OH^- \tag{9}$$

$$S_2O_8^{2-} + e^- \rightarrow 2SO_4^- \tag{10}$$

Table 6 Spinel type-perovskite oxide modified g-C_3N_4 photocatalysts

Photocatalyst	Synthesis method	Photocatalytic activity	Ref.
$CuFe_2O_4$/g-C_3N_4	Hydrothermal method	RhB degradation under visible light	[141]
$CuFe_2O_4$/g-C_3N_4	Ultrasonic assisted-thermal method	PRO degradation under visible light (PDS)	[142]
$NiFe_2O_4$/g-C_3N_4	Coprecipitation route	MO degradation under visible light	[143]
$NiFe_2O_4$/g-C_3N_4	Sol–gel method	MB and RhB degradation under visible light	[144]
$NiFe_2O_4$/g-C_3N_4/G	Hydrothermal method	MO degradation under visible light	[145]
$CoFe_2O_4$/g-C_3N_4	Thermal decomposition	MG, MB, AO7 and RhB degradation under UV light	[146]
$CoFe_2O_4$/g-C_3N_4	Calcination route	RhB degradation under UV light (PMS)	[147]
$ZnFe_2O_4$/g-C_3N_4	Reflux method	OII degradation under visible light (H_2O_2)	[148]
$ZnFe_2O_4$/g-C_3N_4	Coprecipitation route	RhB degradation under visible light (H_2O_2)	[149]
$ZnFe_2O_4$/g-C_3N_4	Sol–gel method	MB degradation under visible light (H_2O_2)	[150]
$ZnCr_2O_4$/g-C_3N_4	Ultrasound assisted-thermal method	Phenol and TC degradation under visible light	[151]
Bi_2MoO_6/g-C_3N_4	Hydrothermal method	MB degradation under LED light	[152]
$Ca_2Nb_2TaO_{10}$/g-C_3N_4	Exfoliation-reassembly method	H_2 evolution under visible light	[153]
$KCa_2Ta_3O_{10}$/g-C_3N_4	Hydrothermal method	H_2 evolution under visible light	[154]

$$SO_{4\bullet}^{-} + OH^{-} \rightarrow OH + SO_4^{2-} \tag{11}$$

$$\equiv Cu^{I} + S_2O_8^{2-} + e^{-} \rightarrow Cu^{II} + SO_{4\bullet}^{-} + SO_4^{2-} \tag{12}$$

$$\equiv Fe^{II} + S_2O_8^{2-} + e^{-} \rightarrow Fe^{III} + SO_{4\bullet}^{-} + SO_4^{2-} \tag{13}$$

$$O_{2\bullet}^{-}/{}^{\bullet}OH/h^{+}/SO_{4\bullet}^{-} + PRO \rightarrow \text{products} \tag{14}$$

$NiFe_2O_4$/g-C_3N_4 was synthesized by performing coprecipitation [143], sol–gel [144] and hydrothermal methods [145]. The suitability of the coprecipitation method

was examined by using XPS analysis [143]. The related spectrums clarified the presence of Ni, Fe, O, C, and N elements, as well as the peaks were attributed to N–C=N, C–N–C, C–N–H and C=N–C coordination. The sol–gel route was also successfully applied to fabrication the ferrite-based carbon nitrite, resulting from XRD, FESEM, FTIR and Raman analyses [54]. The $NiFe_2O_4$/g-C_3N_4/GO showed strong ferromagnetic behaviors at room temperature, which was associated to the characteristic magnetization value belongs to super paramagnetic materials as verified using vibrational sample magnetometer [145].

On the other side, Hassani et al. successfully fabricated $CoFe_2O_4$/g-C_3N_4 composites via thermal decomposition route and they examined their activities in visible-light driven dye removal process [146]. They examined the effect of catalyst dosage, dye concentration and solution pH on the photocatalytic maleic green (MG) removal rate. It was found that the catalyst dosage increased the decolorization rate, whereas the contaminant amount negatively affected the removal yield. In terms of pH, the low value promoted to enhance MG degradation since the acidic environment MG could be ionized with high reaction rate. The $CoFe_2O_4$/g-C_3N_4 heterostructure accomplished satisfactory photocatalytically assisted-Fenton like RhB removal [147]. In an interesting finding, the activity significantly was affected by Cl^-, NO_3^-, HCO_3^-, and PO_4^{3-} anions. HCO_3^-, and PO_4^{3-} constituents decreased the RhB degradation rate. This could be due to the competition with the organic molecules for the interaction of the active sites and the transformation of the radicals to low active centers. On the contrary, Cl^- provided the formation of the oxidizing species from the Fenton agent (peroxymonosulfate: PMS). In addition, the N-included anion showed minor inhibiting effect on the decomposition system.

As another spinel perovskite structure, $ZnFe_2O_4$ has gained attraction for the incorporation with g-C_3N_4 [148–150]. Yao et al. [148] demonstrated that while the addition of hydrogen peroxide up to 0.15 M boosted the photocatalytic degradation of OII in the presence of $ZnFe_2O_4$/g-C_3N_4, the further peroxide addition inhibited the performance. The enhancement was attributed to the formation of new radials with the reaction between Fe species and H_2O_2, resulting higher reducing effect; however, the high H_2O_2 concentration caused the consumption of ·OH radicals, which was the most important specie for OII decomposition. Brothers et al. [149] also depicted that the $ZnFe_2O_4$/g-C_3N_4 composite had excellent RhB reduction ability under visible light illumination. In order to determine the main active center for the degradation, they examined the effect of trapping agents, which were assigned to ·OH and h^+ scavengers. It was implied that the OII degradation with $ZnFe_2O_4$/g-C_3N_4 was driven by hydroxyl radical and holes at the similar rate. In addition, a novel Zn-based spinel structure, $ZnCr_2O_4$ was incorporated with g-C_3N_4 via ultrasound assisted-thermal method [151]. The elemental composition of the $ZnFe_2O_4$/g-C_3N_4 was monitored with EDX analysis and all related atoms were observed within good distribution behavior, indicating successful composite preparation. The heterostructure displayed 98.2% phenol and 98.9% TC degradation efficiency.

Graphitic carbon nitride materials have been coupled with another perovskite such as Bi_2MoO_6/g-C_3N_4 [152], $Ca_2Nb_2TaO_{10}$/g-C_3N_4 [153], and $KCa_2Ta_3O_{10}$/g-C_3N_4 [154]. Lv et al. [152] proposed that the conventional heterojunction mechanism was

not occurred in the presence of Bi_2MoO_6/g-C_3N_4 composite under LED light illumination. That is, the transfer of the photogenerated electrons from g-C_3N_4 to Bi_2MoO_6 between the related conduction bands and the movement of the photogenerated holes in the valence bands from the perovskite to the carbon structure did not observed. Instead of the traditional way, Z-scheme mechanism was formed, which provided high separation rate of the photoinduced species. $Ca_2Nb_2TaO_{10}$/g-C_3N_4 was fabricated by performing ultrasound-assisted mixing of the layered perovskite and g-C_3N_4 particles followed by freeze-drying [153]. The composite achieved 2.8 times higher hydrogen production rate than that of the pristine graphitic carbon nitride. Jiang et al. [154] designed $KCa_2Ta_3O_{10}$/g-C_3N_4 heterojunction via one-step process for visible light induced-water splitting process and the photocatalyst attained the H_2 production rate of 647.19 μmol/g, which was significantly higher than that of the bare components and the material showed stable behavior in four-cycle experiment.

2.3 Carbon Nanotube-Based Perovskite Composites

One dimensional carbon nanotubes (CNTs) are one of the most promising carbon materials with outstanding chemical, electrical, mechanical and optical features. The excellent properties such as (i) excellent electrical conductivity (>10^5 S/m); (ii) great aspect ratio; (iii) high tensile strength (≈60 GPa); (iv) high Young's modulus (≈1 TPa); and (v) thermal conductivity (>3000 W/mK) [155]. Carbon nanotubes are classified as single-walled carbon nanotubes (SWCNT), double-walled carbon nanotubes (DWCNT) and multiwalled carbon nanotubes (MWCNT). The specific surface area of the CNTs generally decreases as SWCNT (1000 $m^{2/}$g) > DWCNT (500 m^2/g) > MWCNT (110 m^2/g) and the conductivity follow the same trend (ca. 3390, 1880 and 1530 S/m, respectively). Moreover, the diameter increases with increasing wall number as 1.2–1.7, 3.5 and 20–30 nm for SWCNT, DWCNT and MWCNT, respectively [156].

CNTs have been used in the construction of several semiconductors owing to their enhanced light emission, effective transport of photoinduced electrons enhancing catalytic performances [157]. Generally, CNTs initiate the electron transfer, hole transport or play role in electrodes in optoelectronic devices and the one-dimensional charge transfer channel of CNTs enable them to be applied as superior conductors [16, 158, 159]. These changes in the composite structure induced by the presence of CNTs can directly contribute to the final photocatalytic efficiency. Whereas the direct introduction of CNTs into the perovskite layer sometimes can cause aggregation of CNTs into bundles due to robust intra-tube van der Waals interactions [158]. For this, CNTs were composited with forms of bulk, mesoporous or nanosheets through in-situ or two-step synthesis procedures [156]. Many research works have proven that coupling perovskites such as $LaNiO_3$ [160, 161], $BaTiO_3$ [162–164], $SrTiO_3$ [165, 166], $CaCu_3Ti_4O_{12}$ [167], $LaFeO_3$ [168], $GdFeO_3$ [169], PbI_2 [170], $MAPbI_3$ [171] with CNTs to improve their structural and catalytic performances. The reduction of

charge recombination rate of perovskite/CNT composites was systematically investigated by using impedance spectroscopy and computation techniques [170]. The incorporation of MWCNTs with perovskite layers not only accelerated the charge transport rate, but also significantly decreased the recombination rate of lead halide-based perovskite (PbI_2) (at least 87%) which was ascribed to selective charge transfer. The hole mobility was found 4-folds greater than the electron mobility for solar cells including 0.01% MWCNTs.

$BaTiO_3$@MWCNT nanocomposites were effectively applied in the photocatalytic oxidation of atrazine (AT) herbicide [164]. The amount of MWCNT in the structure increased the photooxidation percentages from 50% (1 wt% MWCNT) to 80% (2 wt% MWCNT) after 1 h of visible light irradiation while complete decomposition was accomplished with 3 and 4 wt% MWCNT containing samples (Fig. 5a). The upgrading performance was deduced from increased surface area, hindered recombination and extended light emission range of $BaTiO_3$/MWCNT sample. Opoku et al. [165] designed porous Zr-doped $SrTiO_3$/MWCNT catalyst which showed efficient activity for H_2 generation under visible light irradiation. Revealed from

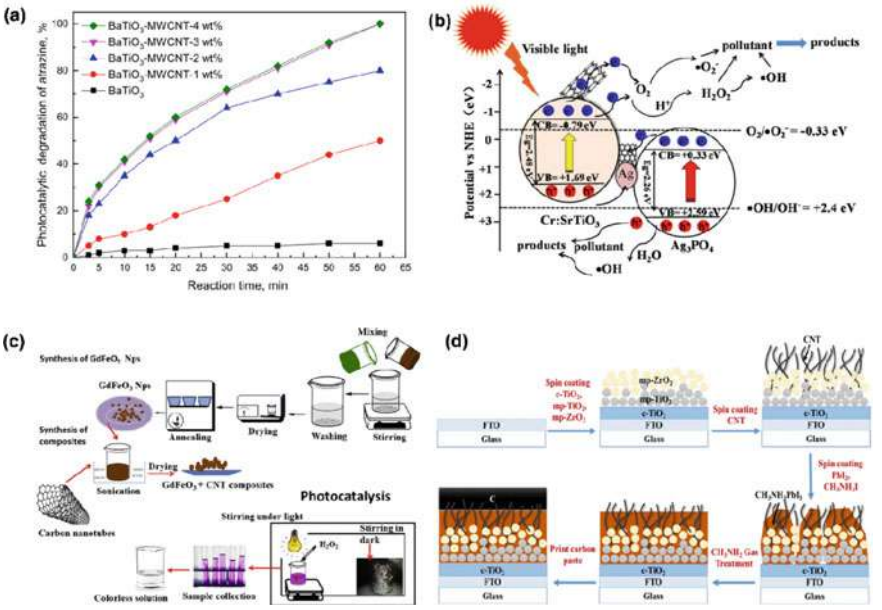

Fig. 5 **a** Photooxidation percentages of AT over $BaTiO_3$@MWCNTs (Reprinted from Ref. [164], Copyright 2021, with permission from Elsevier); **b** Presentation of Z-scheme transfer mechanism over Cr-$SrTiO_3$-Ag_3PO_4-MWCNTs (Reprinted from Ref. [166], Copyright 2018, with permission from Elsevier) (c) Synthesis procedure of $GdCr_xFe_{1-x}O_3$-CNT composites (Reprinted from Ref. [169], Copyright 2020, with permission from Elsevier). **d** Schematic illustration of $MAPbI_3$−MWCNT perovskite films (Reprinted from Ref. [171], Copyright 2019, with permission from Elsevier)

hybrid density functional theory with long-range van der Waals correction, type-II band alignment and the polarized electric field were observed facilitating the separation of charge carriers as well as photocatalytic performances. The presence of zirconium mediated the transfer of photo-excited electrons to the $SrTiO_3$ surface and the generated hydrogen atoms were effectively adsorbed on the catalyst surface owing to its negative adsorption energy (-2.03_{eV}) confirming that it could be applied as hydrogen-storage material. Furthermore, a Z-scheme photocatalytic system including Ag_3PO_4/MWCNTs/Cr:$SrTiO_3$ was developed for the degradation of malachite green [166]. The introduction of MWCNTs into the composite structure remarkably affected both morphology and particle size Ag_3PO_4 which turned from polyhedron shape (~ 30 μm) to spherical-like one crystal (0.28–0.69 μm). Revealed from ESR measurements and photo-activity tests, the generation of $^{\bullet}O_2^-$ and h^+ radicals were detected confirming the Z-scheme transfer mechanism. Due to higher Schottky barriers at the interfaces, the conduction band potentials of Ag_3PO_4 were more negative while the valence band potentials of Cr:$SrTiO_3$ were more positive than that of Ag^o. Hence, under visible light irradiation, both photogenerated electrons in the CB of Ag_3PO_4 and the holes from the VB of Cr:$SrTiO_3$ transferred to metallic Ag, resulting efficient separation and transfer of photo-induced charge pairs (Fig. 5b).

On the other hand, carbon nanotubes have very high surface area so when their composites with perovskites are prepared, both their surface area and photocatalytic efficiencies can be improved significantly. Calcium copper titanate ($CaCu_3Ti_4O_{12}$) is a titanate-based perovskite was designed with MWCNTs through ultrasonic and mixing steps and the resultants materials showed increased surface area from 1.22 to 11 m^2/g allowing more active reaction sites for dye molecules whereas the band gap energies reduced from 3.5 to 3.0 eV endorsing facile migration of electrons from conduction to valence band [167]. Similar results with surface area were also obtained by Daud et al. [169] who discussed the photocatalytic degradation performances of carbon nanotubes incorporated $GdFeO_3$ and Cr-substituted $GdCr_xFe_{1-x}O_3$ materials. At first, $GdFeO_3$ perovskites were synthesized by co-precipitation method and then the composites were obtained by sonication (Fig. 5c). The specific surface area of $GdFeO_3$–CNTs composites was determined as 30.9 m^2/g while that of bare $GdFeO_3$ was 8.66 m^2/g. It was attributed to the fact that CNTs had surface polar groups that enabled formation of bond linkages with the oxygen (O site) of perovskite while hydrogen in the structure allowed bonding of GdFe–O–CNTs providing greater adsorption sites as well as extended light absorption range in visible region.

In 2019, Chen and co-workers [171] designed a photoelectrocatalytic device including MWCNTs modified $CH_3NH_3PbI_3$ perovskite solar cells induced by methylamine as the power source while CNT/TiO_2 was applied as photoanodes. The compact TiO_2 and ZrO_2 layers were primarily coated on FTO substrates via spin-coating and then perovskite layer was immobilized via two-steps. At first, PbI_2 layer was deposited into scaffolds by spin coating, then CH_3NH_3I isopropanol solution was added onto the PbI_2 layer to obtain $CH_3NH_3PbI_3$ ($MAPbI_3$). After thermal heating, methylamine (CH_3NH_2) gas was passed through the films until they were almost bleached. Finally, the carbon electrode layer was deposited by printing carbon paint.

The schematic illustration of synthesis was shown in Fig. 5d. The carbon nanotubes in the structure acted as a charge transport pathway among perovskite nanoparticles to accelerate the collection of photo-excited holes from the carbon electrode. The incorporation of CNTs into the solar cell yielded 10.39% efficiency of power conversion. Moreover, the photoelectrocatalytic degradation efficiency towards RhB dye was obtained as 100% after 80 min of irradiation (Table 7).

2.4 Other Carbon Types-Based Perovskites Composites

Carbon fibers, carbon-based quantum dots, fullerene and carbon-aerogel have been also recognized as suitable candidates for the fabrication of perovskite-based composite photocatalysts. Carbon fibers (CFs) have been utilized in the fabrication of heteroarchitectures photocatalyst due to their excellent conductivity, promoting the electron transfer property of the catalyst. $BaTiO_3$ was coupled with carbon fiber via hydrothermal method to examine the photocatalytic performance for antibiotic degradation [172]. The promising photocatalyst displayed excellent tetracycline degradation under both visible and UV-A light irradiation. Moreover, the amount of the carbon fiber played an important role on the activity; the 5% incorporation of CF improved the decomposition rate, whereas higher amount inhibited the removal efficiencies. Xie et al. [173] synthesized $ZnFe_2O_4/Fe_3O_4/Ag$ incorporated with mesoporous carbon fibers via sol–gel method followed by electrospinning. The multicomponent composite with uniform fiber structure and a moderate specific surface area (324 m^2/g) demonstrated the degradation rates of 100% and 75% and for MB and MO, respectively under visible light irradiation. Furthermore, the photocatalyst showed high ferromagnetic property, indicating easy recovery feature to obtain sustainable photocatalytic-driven processes.

Carbon-based quantum dots have been another newsy emerging carbon nanomaterial due to their optical and electro-optical properties. Carbon quantum dots (CQDs) mainly include carbon nanoparticles of less than 10 nm size, whereas graphene quantum dots (GQDs) comprise of the graphene nanosheets with a size less than 100 nm [174]. Li et al. [175] developed $SmFeO_3$/ATP/CQDs by adsorption of $SmFeO_3$ on the mineral clay through sol–gel method and then the introduction of the carbon structure via impregnation. The material provided NO oxidation under sunlight in a continuous-flow system. The activity was related to the amount of CQDs, since the carbon-based material significantly affected the photo-driven properties of the photocatalyst. In the UV–vis spectra, the visible light absorption ability improved with the increasing carbon quantity, resulting 90% NO removal with the Z-scheme heterojunction combining 5% of CQDs. To extend the research on promising perovskite-coupled with quantum dot photocatalyst, Paszkiewicz-Gawron et al. [176] investigated the efficiency of $SrTiO_3$, $SrSnO_3$ and $AgTaO_3$ incorporated with carbon quantum dots (CQDs) or graphene quantum dots (GQDs) co-modified with erbium for the transformation of organic molecules into smaller molecules in both and aqueous environments. According to XRD analysis, the perovskite nanophases were

Table 7 CNT-based perovskite composites

Composite catalyst	Application	Remarks	Ref.
$LaNiO_3$–MWCNTs	H_2 evolution CH_4 decomposition	80% of CH_4 conversion was obtained at 700 °C. The yield of CNT and H_2 were 2.2 g_{CNT} $g^{-1}\,h^{-1}$ and 8.2 L $g^{-1}\,h^{-1}$, respectively	[160]
$LaNiO_3$–MWCNTs	CH_4 decomposition	37% carbon yield was obtained with 0.5–2 μm particle size	[161]
$BaTiO_3$–MWCNTs	–	Composite films displayed high-k and relatively low dielectric loss simultaneously	[162]
$BaTiO_3$–MWCNTs	–	Core–shell heterostructures could absorb microwave at a relatively broad frequency	[163]
$BaTiO_3$–MWCNTs	AT photo-oxidation	~100% AT oxidation yield was calculated	[164]
Zr–$SrTiO_3$–MWCNTs	H_2 evolution	Type-II band alignment and the polarized electric field were observed	[165]
Cr–$SrTiO_3$–Ag_3PO_4–MWCNTs	MG degradation	100% MG removal in 6 and 10 min under natural solar radiation and visible light irradiation were obtained	[166]
$CaCu_3Ti_4O_{12}$–MWCNT	RhB degradation	RhB decomposition was more effective with CCTO–MWCNT nanocomposites (85%) rather than bare sample (44%)	[167]
$GdCr_xFe_{1-x}O_3$–CNT	RhB degradation	Surface area of composite was 30.9515 m_2/g than that of pure $GdFeO_3$ (8.667 m_2/g); Higher degradation rate (94%) was observed	[169]
$MAPbI_3$–MWCNT	Photoelectrocatalytic RhB degradation	RhB decomposition was almost 100% after 80 min	[171]

successfully anchored to the carbon network. As compared to the corresponding GQDs-included composites, $SrSnO_3$ and $AgTaO_3$-based CQDs samples showed higher intensity, whereas $SrTiO_3$/GQDs displayed sharper peak than that of CQDs. This could be due to fact that the calcination step performed during the interaction of the two structures ($SrTiO_3$ and GQDs) was beneficial to form titanate phase. The blockage of the carbon-porosity with perovskite was more prevalent in the presence of quantum dots, observing lower specific surface area. On the other hand, it was observed that the GQDs with erbium exhibited lower photoluminescence intensity, resulting lower recombination rate for the excited electrons and holes. It could be indicated that the graphene structure promoted the transfer of the photoinduced species and for this the erbium also acted as a driving force reflecting higher toluene and phenol degradation rates for GQDs-coupled with perovskites.

Another way to synthesize the perovskite-based complex system has been the interaction of the metal structures with carbon allotrope (fullerenes: C_{60}), which shows excellent electron-accepting property due to its delocalized structure. A novel heterostructured photocatalyst was fabricated by integrating $CsPbBr_3$ with fullerene in-situ self-assembly synthesis method [177]. As compared to the bare halide perovskite, the optical absorption intensity of the composite increased, indicating the establishment of good electronic integration between $CsPbBr_3$ and C_{60}. Thus, the ability to harness visible light and charge transport were improved, creating excellent photocatalytically CO_2 reduction ability. Behera et al. [178] designed $ZnFe_2O_4$ with different carbon-based substrate (carbon nanotube, graphene oxide and fullerene) to compare the photocatalytic norfloxacin and Cr (VI) reduction. The most favorable interaction was observed between the perovskite and CNT, generating defective band structure that resulted the narrowest band gap and the fastest charge separation. In case of norfloxacin degradation, the highest activity was calculated as 91.3%, whereas the activities were observed as 85.1% and 78.3 for $ZnFe_2O_4$/Fullerene and $ZnFe_2O_4$/GO. The similar trend was obtained for the removal of the colorful contaminant.

Towards the development of carbon-coupled with perovskite composite for wastewater treatment, Wang et al. [179] designed a promising strategy to fabricate 3D hierarchically $LaFe_{0.5}$ $M_{0.5}O_3$ (M = Mn, Cu) deposited on carbon aerogel (CA) by using templating method. A superior adsorption ability was observed for the composite pertaining to high surface oxygen vacancies on the surface, resulting high catalytic decomposition rate. Under microwave irradiation, the degradation performance of fuchsin base was 100% and the cyclic adsorption runs demonstrated a stable organic dye removal. In another approach, graphene aerogel (rGO) was interacted with $ZnSnO_3$ for ciprofloxacin degradation under simulated sunlight irradiation [180]. The composites were fabricated by performing sonication-assisted hydrothermal method and the success of the method was observed XRD, FTIR, FESEM and XPS analyzes. XRD patterns of the composites showed the identical peaks of rGO and $ZnSnO_3$ and the intensity of the peak poisoned at 26.50° increased depending on the amount of the oxide samples in the as-prepared photocatalysts. Further FTIR and XPS analyzes confirmed the heterostructure formation, resulting from its functional groups and chemical bonds such as C–O, C–O–C, O=C–O, C=O, Zn–O and Sn–O. FESEM images depicted the perovskite deposition on the rGO

structure. The as-prepared magnetic composite containing ZnSn:rGO=1:1 displayed almost 100% photocatalytic antibiotic degradation. In similar synthesis manner, rGO decorated with $LaFeO_3$ and it was observed that after the photocatalysis, the composite remarkably decreased the absorption peak of MO, indicating excellent decomposition rate [181]. In further approach, Hu et al. deposited Ag-promoted $LaMnO_3$ on graphene aerogel via templating method followed silver mirror reaction-assisted method. In the heterostructure, the limited recombination rate of the photo-generated active species was observed, resulting visible light-assisted degradation of direct green BE with high efficiency (100%) (Table 8).

Table 8 Other carbon types -based perovskites composites reported in literature

	Photocatalyst	Synthesis method	Photocatalytic application	Ref.
Carbon fiber				
	$BaTiO_3$/CF	Hydrothermal	96% TC degradation	[172]
	$ZnFe_2O_4$/Fe_3O_4/Ag/CF	Sol–gel and electrospinning	100% MB degradation 75% MO degradation	[173]
Carbon quantum dots				
	$SmFeO_3$/ ATP/ CQDs	Sol–gel and impregnation	90% NO removal	[175]
	$SrTiO_3$, $SrSnO_3$ and $AgTaO_3$/ CQDs or GQDs-Er	Calcination	48–57% Toluene degradation (GQDs) 26–41%Toluene degradation (CQDs)	[176]
Fullerene				
	$CsPbBr_3/C_{60}$	In-situ self-assembly	90.2 μmol/g h consumption	[177]
	$ZnFe_2O_4$/CNT, Fullerene or GO	Hydrothermal followed by calcination	91.3% Norfloxacin degradation 80% Cr(VI) reduction	[178]
Carbon-aerogel				
	$LaFe_{0.5}$ $M_{0.5}O_3$/CA	PMMA-templating	100% FB degradation	[179]
Graphene-aerogel				
	$ZnSnO_3$/RGO	Sonication-assisted hydrothermal	100% CIP degradation	[180]
	$LaFeO_3$/RGO	Sonication-assisted hydrothermal	100% MO degradation	[181]
	Ag-$LaMnO_3$/RGO	CTAB-templating and silver mirror	100% GBE degradation	[182]

3 Conclusion

Many perovskite/carbon composite photocatalysts have been studied for visible and UV light driven photocatalytic applications. The most attractive perovskite groups, namely titanates and ferrites have depicted satisfactorily photocatalytic performances for water treatment and water splitting processes, however, the pristine perovskites exhibit relatively weak photogenerated charge separation rate and low surface area. In order to modify the negative features, the promising approach is to interact perovskites with carbon-based structures due to their outstanding characteristics such as large surface area, excellent corrosion resistance and good electronic properties. Besides, in photocatalytic process, carbonaceous materials usually act as electron scavengers due to their large electron storage capacity. Relevant studies have demonstrated that carbon-based materials such as graphene oxide and its derivatives, graphitic carbon nitride and carbon aerogel coupled with perovskite lead to the formation of heterojunctions, which enhances adsorption capacity of the compounds towards organic pollutants can also contribute to higher efficiency of water remediation. For specific application area in the photocatalysis systems, the formation of suitable cocatalysts has been performed via several synthesis methods such as hydrothermal, solvothermal, calcination and coprecipitation that promotes designing appropriate band alignment. Recent advances in the formation of perovskite/carbon composite have been yielded desired photocatalytic performances.

References

1. Wang H, Zhang Q, Qiu M, Hu B (2021) Synthesis and application of perovskite-based photocatalysts in environmental remediation: a review. J Mol Liq 334:116029. https://doi.org/10.1016/j.molliq.2021.116029
2. Shu L, Sunarso J, Hashim SS, Mao J, Zhou W, Liang F (2019) Advanced perovskite anodes for solid oxide fuel cells: a review. Int J Hydrogen Energy 44:31275–31304. https://doi.org/10.1016/j.ijhydene.2019.09.220
3. Assirey EAR (2019) Perovskite synthesis, properties and their related biochemical and industrial application. Saudi Pharm J 27:817–829. https://doi.org/10.1016/j.jsps.2019.05.003
4. Tasleem S, Tahir M (2020) Recent progress in structural development and band engineering of perovskites materials for photocatalytic solar hydrogen production: a review. Int J Hydrogen Energy 45:19078–19111. https://doi.org/10.1016/j.ijhydene.2020.05.090
5. Wang J, Nilsson AM, Barrios D, Vargas WE, Wäckelgård E, Niklasson GA (2019) Light scattering materials for energy-related applications: determination of absorption and scattering coefficients. Mater Today Proc 33:2474–2480. https://doi.org/10.1016/j.matpr.2020.01.339
6. Li CQ, Yi SS, Liu Y, Niu ZL, Yue XZ, Liu ZY (2021) In-situ constructing S-scheme/Schottky junction and oxygen vacancy on $SrTiO_3$ to steer charge transfer for boosted photocatalytic H_2 evolution. Chem Eng J 417:129231. https://doi.org/10.1016/j.cej.2021.129231
7. Kong J, Yang T, Rui Z, Ji H (2019) Perovskite-based photocatalysts for organic contaminants removal: current status and future perspectives. Catal Today 327:47–63. https://doi.org/10.1016/j.cattod.2018.06.045

8. Kéranguéven G, Ulhaq-Bouillet C, Papaefthimiou V, Royer S, Savinova E (2017) Perovskite-carbon composites synthesized through in situ autocombustion for the oxygen reduction reaction: the carbon effect. Electrochim Acta 245:156–164. https://doi.org/10.1016/j.electacta.2017.05.113
9. Xiao P, Xu X, Zhu J, Zhu Y (2020) In situ generation of perovskite oxides and carbon composites: a facile, effective and generalized route to prepare catalysts with improved performance. J Catal 383:88–96. https://doi.org/10.1016/j.jcat.2020.01.007
10. Milani A, Bassi AL, Russo V, Tommasini M, Casari C (2019) Linear carbon: from 1D carbyne to 2D hybrid sp-sp^2 nanostructures beyond grapheme. In: Handbook of graphene, Vol. 3 Graphene-like 2D materials, p 297
11. Yang Y, Chiang K, Burke N (2011) Porous carbon-supported catalysts for energy and environmental applications: a short review. Catal Today 178:197–205. https://doi.org/10.1016/j.cattod.2011.08.028
12. Mamba G, Gangashe G, Moss L, Hariganesh S, Thakur S, Vadivel S, Mishra AK, Vilakati GD, Muthuraj V, Nkambule TTI (2020) State of the art on the photocatalytic applications of graphene based nanostructures: from elimination of hazardous pollutants to disinfection and fuel generation. J Environ Chem Eng 8:103505. https://doi.org/10.1016/j.jece.2019.103505
13. Meng C, Zhao K, Yang M, Liang Y (2021) Hydrothermal preparation of novel rGO-KTaO 3 nanocubes with enhanced visible light photocatalytic activity. Spectrochim Acta Part A Mol Biomol Spectrosc 250:119352. https://doi.org/10.1016/j.saa.2020.119352
14. Liang J, Jiang Z, Wong PK, Lee C-S (2020) Recent progress on carbon nitride and its hybrid photocatalysts for CO_2 reduction. Solar RRL 5:2000478.https://doi.org/10.1002/solr.202000478
15. Meng F, Zhou Y, Gao L, Li Y, Liu A, Zhang, Fan M, Wei G, Ma T (2021) Environmental risks and strategies for the long-term stability of carbon-based perovskite solar cells. Mater Today Energy 19.https://doi.org/10.1016/j.mtener.2020.100590
16. Hu R, Chu L, Zhang J, Li X, Huang W (2017) Carbon materials for enhancing charge transport in the advancements of perovskite solar cells. J Power Sources 361:259–275. https://doi.org/10.1016/j.jpowsour.2017.06.051
17. Cao S, Yu J (2016) Carbon-based H_2-production photocatalytic materials. J Photochem Photobiol C Photochem Rev 27:72–99. https://doi.org/10.1016/j.jphotochemrev.2016.04.002
18. Chang CJ, Wang CW, Wei YH, Chen CY (2018) Enhanced photocatalytic H_2 production activity of Ag-doped Bi_2WO_6-graphene based photocatalysts. Int J Hydrogen Energy 43:11345–11354. https://doi.org/10.1016/j.ijhydene.2018.03.091
19. Wang X, Liu B, Lu Q, Qu Q (2014) Graphene-based materials: fabrication and application for adsorption in analytical chemistry. J Chromatogr A 1362:1–15. https://doi.org/10.1016/j.chroma.2014.08.023
20. Xian T, Yang H, Huo YS (2014) Enhanced photocatalytic activity of $CaTiO_3$-graphene nanocomposites for dye degradation. Phys Scr 89.https://doi.org/10.1088/0031-8949/89/11/115801
21. Kumar A, Kumar S, Bahuguna A, Kumar A, Sharma V, Krishnan V (2017) Recyclable, bifunctional composites of perovskite type N-$CaTiO_3$ and reduced graphene oxide as an efficient adsorptive photocatalyst for environmental remediation. Mater. Chem. Front. 1:2391–2404. https://doi.org/10.1039/c7qm00362e
22. Ramkumar R, Jagan G, Nivedha AK, Krishna Priya S, Selvi A (2021) Amalgamation and characterization of graphene-calcium titanate composite for electrochemical studies. Mater Today Proc. https://doi.org/10.1016/j.matpr.2020.11.112
23. Gao W, Zhang W, Tian B, Zhen W, Wu Y, Zhang X, Lu G (2018) Visible light driven water splitting over $CaTiO_3/Pr^{3+}$-Y_2SiO_5/RGO catalyst in reactor equipped artificial gill. Appl Catal B Environ 224:553–562. https://doi.org/10.1016/j.apcatb.2017.10.072
24. Mohammed J, Abubakar BF, Yerima KU, Hamisu H, Ismail UT, Muhammad A, Zulfatu UF, Abubakar A, Salihu NM, Abubakar MS, Saidu Y, Tchouank Tekou Carol T, Srivastava AK (2018) Biodegradable polymer modified rGO/PANI/CCTO nanocomposites: structural and dielectric properties. Mater Today Proc 5:28462–28469.https://doi.org/10.1016/j.matpr.2018.10.133

25. Kumar A, Navakoteswara Rao V, Kumar A, Venkatakrishnan Shankar M, Krishnan V (2020) Interplay between mesocrystals of $CaTiO_3$ and edge sulfur atom enriched MoS_2 on reduced graphene oxide nanosheets: enhanced photocatalytic performance under sunlight irradiation. ChemPhotoChem 4:427–444. https://doi.org/10.1002/cptc.201900267
26. Chen X, Di L, Yang H, Xian T (2019) A magnetically recoverable $CaTiO_3$/reduced graphene oxide/$NiFe_2O_4$ nanocomposite for the dye degradation under simulated sunlight irradiation. J Ceram Soc Japan 127:221–231. https://doi.org/10.2109/jcersj2.18168
27. Ahmadi M, Seyed Dorraji MS, Rasoulifard MH, Amani-Ghadim AR (2019) The effective role of reduced-graphene oxide in visible light photocatalytic activity of wide band gap $SrTiO_3$ semiconductor. Sep Purif Technol 228:115771. https://doi.org/10.1016/j.seppur.2019.115771
28. Mohammadi P, Ghorbani-Shahna F, Bahrami A, Rafati AA, Farhadian M (2020) Plasma-photocatalytic degradation of gaseous toluene using $SrTiO_3$/rGO as an efficient heterojunction for by-products abatement and synergistic effects. J Photochem Photobiol A Chem 394.https://doi.org/10.1016/j.jphotochem.2020.112460
29. He GL, Zhong YH, Chen MJ, Li X, Fang YP, Xu YH (2016) One-pot hydrothermal synthesis of $SrTiO_3$-reduced graphene oxide composites with enhanced photocatalytic activity for hydrogen production. J Mol Catal A Chem 423:70–76. https://doi.org/10.1016/j.molcata.2016.05.025
30. Chang CW, Hu C (2020) Graphene oxide-derived carbon-doped $SrTiO_3$ for highly efficient photocatalytic degradation of organic pollutants under visible light irradiation. Chem Eng J 383:123116. https://doi.org/10.1016/j.cej.2019.123116
31. Daulbayev C, Sultanov F, Korobeinyk AV, Yeleuov M, Azat S, Bakbolat B, Umirzakov A, Mansurov Z (2021) Bio-waste-derived few-layered graphene/$SrTiO_3$/PAN as efficient photocatalytic system for water splitting. Appl Surf Sci 549:149176. https://doi.org/10.1016/j.apsusc.2021.149176
32. Suzuki TM, Iwase A, Tanaka H, Sato S, Kudo A, Morikawa T (2015) Z-scheme water splitting under visible light irradiation over powdered metal-complex/semiconductor hybrid photocatalysts mediated by reduced graphene oxide. J Mater Chem A 3:13283–13290. https://doi.org/10.1039/c5ta02045j
33. Pham TT, Nguyen-Huy C, Shin EW (2016) $NiTiO_3$/reduced graphene oxide materials synthesized by a two-step microwave-assisted method. Mater Lett 184:38–42. https://doi.org/10.1016/j.matlet.2016.07.136
34. El-Maghrabi HH, Nada AA, Diab KR, Youssef AM, Hamdy A, Roualdes S, Abd El-Wahab S (2018) Facile fabrication of $NiTiO_3$/graphene nanocomposites for photocatalytic hydrogen generation. J Photochem Photobiol A Chem 365:86–93. https://doi.org/10.1016/j.jphotochem.2018.07.040
35. Kang C, Xiao K, Yao Z, Wang Y, Huang D, Zhu L, Liu F, Tian T (2018) Hydrothermal synthesis of graphene-$ZnTiO_3$ nanocomposites with enhanced photocatalytic activities. Res Chem Intermed 44:6621–6636. https://doi.org/10.1007/s11164-018-3512-z
36. Mashkouri S, Arsalani N, Hossienzadeh A, Shahryari E, Safavi M (2020) Green synthesis of nanocomposite multilayer graphene-$ZnTiO_3$ at one step under mechanochemical method and investigation of band gap. J Mater Sci Mater Electron 31:4582–4586. https://doi.org/10.1007/s10854-020-03009-2
37. Li J, Cui H, Mu D, Liu Y, Guan T, Xia Z, Jiang L, Zuo J, Tan C, You H (2019) Synthesis and characterization of rGO decorated cubic $ZnTiO_3$ rods for solar light-induced photodegradation of rhodamine B. New J Chem 43:3374–3382. https://doi.org/10.1039/C8NJ01971A
38. Wu H, Min Y, Zhang Q, Li W, Yuan J, Wu Z, Wang S (2016) Low-temperature synthesis of mesoporous $ZnTiO_3$-graphene composite for the removal of norfloxacin in aqueous solution. RSC Adv 6:103822–103829. https://doi.org/10.1039/c6ra17556b
39. Gayathri S, Jayabal P, Kottaisamy M, Ramakrishnan V (2015) Synthesis of the graphene-$ZnTiO_3$ nanocomposite for solar light assisted photodegradation of methylene blue. J Phys D Appl Phys 48:415305. https://doi.org/10.1088/0022-3727/48/41/415305
40. Ray SK, Cho J, Hur J (2021) A critical review on strategies for improving efficiency of $BaTiO_3$-based photocatalysts for wastewater treatment. J Environ Manage 290:112679. https://doi.org/10.1016/j.jenvman.2021.112679

41. Zhao Y, Zhang X, Liu J, Wang C, Li J, Jin H (2018) Graphene oxide modified nano-sized $BaTiO_3$ as photocatalyst. Ceram Int 44:15929–15934. https://doi.org/10.1016/j.ceramint.2018.06.013
42. Rastogi M, Bowen C, Kushwaha HS, Vaish R (2016) First principles insights into improved catalytic performance of $BaTiO_3$-graphene nanocomposites in conjugation with experimental investigations. Mater Sci Semicond Process 51:33–41. https://doi.org/10.1016/j.mssp.2016.04.008
43. Mengting Z, Kurniawan TA, Fei S, Ouyang T, Othman MHD, Rezakazemi M, Shirazian S (2019) Applicability of $BaTiO_3$/graphene oxide (GO) composite for enhanced photodegradation of methylene blue (MB) in synthetic wastewater under UV–vis irradiation. Environ Pollut 255.https://doi.org/10.1016/j.envpol.2019.113182
44. Wang RX, Zhu Q, Wang WS, Fan CM, Xu AW (2015) $BaTiO_3$-graphene nanocomposites: synthesis and visible light photocatalytic activity. New J Chem 39:4407–4413. https://doi.org/10.1039/c4nj02272f
45. Jiang S, Zhao R, Ren Z, Chen X, Tian H, Wie X, Li X, Shen G, Han G (2016) A reduced graphene oxide (rGO)-ferroelectrics hybrid nanocomposite as high efficient visible-light-driven photocatalyst. ChemistrySelect 1:6020–6025. https://doi.org/10.1002/slct.201601505
46. Zuo Y, Luo J, Cheng M, Zhang K, Dong R (2018) Synthesis, characterization and enhanced electromagnetic properties of $BaTiO_3$/$NiFe_2O_4$-decorated reduced graphene oxide nanosheets. J Alloys Compd 744:310–320. https://doi.org/10.1016/j.jallcom.2018.02.071
47. Ma Y, Luo H, Guo R, Zhou K, Zhang D (2018) Enhanced performance in multilayer-structured nanocomposites using $BaTiO_3$ and $Ba_{0.8}Sr_{0.2}TiO_3$ decorated graphene hybrids. Ceram Int 44:20871–20876. https://doi.org/10.1016/j.ceramint.2018.08.092
48. Dash T, Palei BB, Mohanty N, Mohapatra SS, Mishra RK, Biswal SK, Behera D (2021) Study on microstructural influence of graphene on synthesis of $BaTiO_3$. Mater Today Proc 43:447–450. https://doi.org/10.1016/j.matpr.2020.11.968
49. Pant B, Park M, Park SJ (2018) Synthesis, characterization, and photocatalytic performances of electrospun cadmium titanate nanofibers immobilized into the reduced graphene oxide sheets. Mater Lett 228:365–368. https://doi.org/10.1016/j.matlet.2018.06.036
50. Alhaddad M, Shawky A, Zaki ZI (2021) Reduced graphene oxide-supported $PbTiO_3$ nanospheres: Improved ceramic photocatalyst toward enriched photooxidation of thiophene by visible light. Mol Catal 499:111301. https://doi.org/10.1016/j.mcat.2020.111301
51. Wang C, Shan L, Song D, Xiao Y, Suriyaprakash J (2019) Hydrothermal synthesis of rGO/$PbTiO_3$ photocatalyst and its photocatalytic H_2 evolution activity. J Nanomater (2019).https://doi.org/10.1155/2019/4869728
52. Peng Q, Weng X, Xie W, Ying M, Lin X, Dai Y, Yu Q, Pan H, Liu J, Du M (2020) Photocatalytic reduction for graphene oxide by $PbTiO_3$ with high polarizability and its electrocatalytic application in pyrrole detection. J Colloid Interface Sci 560:502–509. https://doi.org/10.1016/j.jcis.2019.10.022
53. Wu CH, Zhang YZ, Li S, Zheng HJ, Wang H, Liu JB, Li KW, Yan H (2011) Synthesis and photocatalytic properties of the graphene-$La_2Ti_2O_7$ nanocomposites. Chem Eng J 178:468–474. https://doi.org/10.1016/j.cej.2011.10.062
54. Sharma SK, Kumar A, Sharma G, Stadler FJ, Naushad M, Ghfar AA, Ahamad T (2020) $LaTiO_2N$/Bi_2S_3 Z-scheme nano heterostructures modified by rGO with high interfacial contact for rapid photocatalytic degradation of tetracycline. J Mol Liq 311:113300. https://doi.org/10.1016/j.molliq.2020.113300
55. Hu J, Ma J, Wang L, Huang H (2014) Synthesis and photocatalytic properties of $LaMnO_3$-graphene nanocomposites. J Alloys Compd 583:539–545. https://doi.org/10.1016/j.jallcom.2013.09.030
56. Hu J, Ma J, Wang L, Huang H, Ma L (2014) Preparation, characterization and photocatalytic activity of Co-doped $LaMnO_3$/graphene composites. Powder Technol 254:556–562. https://doi.org/10.1016/j.powtec.2014.01.071

57. Lv T, Wu M, Guo M, Liu Q, Jia L (2019) Self-assembly photocatalytic reduction synthesis of graphene-encapusulated $LaNiO_3$ nanoreactor with high efficiency and stability for photocatalytic water splitting to hydrogen. Chem Eng J 356:580–591. https://doi.org/10.1016/j.cej.2018.09.031
58. Tasleem S, Tahir M (2020) Current trends in strategies to improve photocatalytic performance of perovskites materials for solar to hydrogen production. Renew Sustain Energy Rev 132:110073. https://doi.org/10.1016/j.rser.2020.110073
59. An J, Zhu L, Wang N, Song Z, Yang Z, Du D, Tang H (2013) Photo-Fenton like degradation of tetrabromobisphenol A with graphene$BiFeO_3$ composite as a catalyst. Chem Eng J 219:225–237. https://doi.org/10.1016/j.cej.2013.01.013
60. Li J, Wang Y, Ling H, Qiu Y, Lou J, Hou X, Bag SP, Wang J, Wu H, Chai G (2019) Significant enhancement of the visible light photocatalytic properties in 3D $BiFeO_3$/graphene composites. Nanomaterials 9.https://doi.org/10.3390/nano9010065
61. Farhadi ARK, Rahemi N, Allahyari S, Tasbihi M (2021) Metal-doped perovskite $BiFeO_3$/rGO nanocomposites towards the degradation of acetaminophen in aqueous phase using plasma-photocatalytic hybrid technology. J Taiwan Inst Chem Eng 120:77–92. https://doi.org/10.1016/j.jtice.2021.03.021
62. Vishwakarma AK, Hussain M, Verma SK, Shukla V, Shaz MA, Srivastava ON (2021) Synthesis and characterizations of graphene/Sm doped $BiFeO_3$ composites photoanode for efficient photo-electrochemical water splitting. Int J Hydrogen Energy. https://doi.org/10.1016/j.ijhydene.2021.02.115
63. Sun A, Chen H, Song C, Jiang F, Wang X, Fu Y (2013) Magnetic $Bi_{25}FeO_{40}$-graphene catalyst and its high visible-light photocatalytic performance. RSC Adv 3:4332–4340. https://doi.org/10.1039/c3ra22626c
64. Kadi MW, Mohamed RM, Ismail AA (2020) Facile synthesis of mesoporous $BiFeO_3$/graphene nanocomposites as highly photoactive under visible light. Opt Mater 104:109842. https://doi.org/10.1016/j.optmat.2020.109842
65. Zou CY, Liu SQ, Shen Z, Zhang Y, Jiang NS, Ji WC (2017) Efficient removal of ammonia with a novel graphene-supported $BiFeO_3$ as a reusable photocatalyst under visible light. Cuihua Xuebao/Chinese J Catal 38:20–28. https://doi.org/10.1016/S1872-2067(17)62752-9
66. Li P, Li L, Xu M, Chen Q, He Y (2017) Enhanced photocatalytic property of $BiFeO_3$/N-doped graphene composites and mechanism insight. Appl Surf Sci 396:879–887. https://doi.org/10.1016/j.apsusc.2016.11.052
67. Hu X, Wang W, Xie G, Wang H, Tan X, Jin Q, Zhou D, Zhao Y (2019) Ternary assembly of g-C_3N_4/graphene oxide sheets/$BiFeO_3$ heterojunction with enhanced photoreduction of Cr(VI) under visible-light irradiation. Chemosphere 216:733–741. https://doi.org/10.1016/j.chemosphere.2018.10.181
68. Zhou Q, Lin Y, Zhang K, Li M, Tang D (2018) Reduced graphene oxide/$BiFeO_3$ nanohybrids-based signal-on photoelectrochemical sensing system for prostate-specific antigen detection coupling with magnetic microfluidic device. Biosens Bioelectron 101:146–152. https://doi.org/10.1016/j.bios.2017.10.027
69. Bagherzadeh M, Kaveh R (2018) A new SnS_2-$BiFeO_3$/reduced graphene oxide photocatalyst with superior photocatalytic capability under visible light irradiation. J Photochem Photobiol A Chem 359:11–22. https://doi.org/10.1016/j.jphotochem.2018.03.031
70. Gao X, Wang Y, Wang Q, Wu X, Zhang W, Zong M, Zhang L (2019) Facile synthesis of a novel flower-like $BiFeO_3$ microspheres/graphene with superior electromagnetic wave absorption performances. Ceram Int 45:3325–3332. https://doi.org/10.1016/j.ceramint.2018.10.243
71. Kiani M, Kiani AB, Khan SA, ur Rehmana S, Khan QU, Mahmood I, Saleemi AS, Jalil A, Sohail M, Zhu L (2019) Facile synthesis of Gd and Sn co-doped $BiFeO_3$ supported on nitrogen doped graphene for enhanced photocatalytic activity. J Phys Chem Solids 130:222–229.https://doi.org/10.1016/j.jpcs.2019.01.032
72. Soltani T, Lee BK (2016) Sono-synthesis of nanocrystallized $BiFeO_3$/reduced graphene oxide composites for visible photocatalytic degradation improvement of bisphenol A. Chem Eng J 306:204–213. https://doi.org/10.1016/j.cej.2016.07.051

73. Kumar A, Sharma G, Naushad M, Ahamad T, Veses RC, Stadler FJ (2019) Highly visible active Ag_2CrO_4/Ag/$BiFeO_3$@RGO nano-junction for photoreduction of CO_2 and photocatalytic removal of ciprofloxacin and bromate ions: the triggering effect of Ag and RGO. Chem Eng J 370:148–165. https://doi.org/10.1016/j.cej.2019.03.196
74. Acharya S, Padhi DK, Parida KM (2020) Visible light driven $LaFeO_3$ nano sphere/RGO composite photocatalysts for efficient water decomposition reaction. Catal Today 353:220–231. https://doi.org/10.1016/j.cattod.2017.01.001
75. Abdel-Aal SK, Aly AE, Chanduví HHM, Gil Rebaza AV, Atteia E, Shankar A (2020) Magnetic and optical properties of perovskite-graphene nanocomposites $LaFeO_3$-rGO: experimental and DFT calculations. Chem Phys 538:110874. https://doi.org/10.1016/j.chemphys.2020.110874
76. Rezanezhad A, Rezaie E, Ghadimi LS, Hajalilou A, Abouzari-Lotf E, Arsalani N (2020) Outstanding supercapacitor performance of Nd–Mn co-doped perovskite $LaFeO_3$@nitrogen-doped graphene oxide nanocomposites. Electrochim Acta 335:135699. https://doi.org/10.1016/j.electacta.2020.135699
77. Jing J, Cao C, Ma S, Li Z, Qu G, Xie B, Jin W, Zhao Y (2021) Enhanced defect oxygen of $LaFeO_3$/GO hybrids in promoting persulfate activation for selective and efficient elimination of bisphenol A in food wastewater. Chem Eng J 407:126890. https://doi.org/10.1016/j.cej.2020.126890
78. Mutalib MA, Aziz F, Jamaludin NA, Yahya N, Ismail AF, Mohamed MA, Yusop MZM, Salleh WNW, Jaafar J, Yusof N (2018) Enhancement in photocatalytic degradation of methylene blue by $LaFeO_3$-GO integrated photocatalyst-adsorbents under visible light irradiation. Korean J Chem Eng 35:548–556. https://doi.org/10.1007/s11814-017-0281-0
79. Orak C, Yüksel A (2021) Graphene-supported $LaFeO_3$ for photocatalytic hydrogen energy production. Int J Energy Res, 1–17.https://doi.org/10.1002/er.6620
80. Vijayaraghavan T, Althaf R, Babu P, Parida KM, Vadivel S, Ashok AM (2020) Visible light active $LaFeO_3$ nano perovskite-RGO-NiO composite for efficient H_2 evolution by photocatalytic water splitting and textile dye degradation. J Environ Chem Eng 9:104675. https://doi.org/10.1016/j.jece.2020.104675
81. Lv T, Wang H, Hong W, Wang P, Jia L (2019) In situ self-assembly synthesis of sandwich-like TiO_2/reduced graphene oxide/$LaFeO_3$ Z-scheme ternary heterostructure towards enhanced photocatalytic hydrogen production. Mol Catal 475:110497. https://doi.org/10.1016/j.mcat.2019.110497
82. Bajorowicz B, Reszczyńska J, Lisowski W, Klimczuk T, Winiarski M, Słoma M, Zaleska-Medynska A (2015) Perovskite-type $KTaO_3$-reduced graphene oxide hybrid with improved visible light photocatalytic activity. RSC Adv 5:91315–91325. https://doi.org/10.1039/c5ra18124k
83. Meng C, Zhao K, Yang M, Liang Y (2021) Hydrothermal preparation of novel rGO-$KTaO_3$ nanocubes with enhanced visible light photocatalytic activity. Spectrochim Acta Part A Mol Biomol Spectrosc 250:119352. https://doi.org/10.1016/j.saa.2020.119352
84. Yang F, Yan L, Zhang B, He X, Li Y, Tang Y, Ma C, Li Y (2019) Fabrication of ternary $NaTaO_3$/g-C_3N_4/G heterojunction photocatalyst with enhanced activity for Rhodamine B degradation. J. Alloys Compd 805:802–810
85. Mukherji A, Seger B, Lu GQ, Wang L (2011) Nitrogen doped $Sr_2Ta_2O_7$ coupled with graphene sheets as photocatalysts for increased photocatalytic hydrogen production. ACS Nano 5:3483–3492. https://doi.org/10.1021/nn102469e
86. Fu Z, Zhang S, Fu Z (2019) Hydrothermal preparation of $NaTaO_3$/rGO composite photocatalyst to enhance UV photocatalytic activity. Results Phys. 15:102669. https://doi.org/10.1016/j.rinp.2019.102669
87. Opoku F, Govender KK, van Sittert CGCE, Govender PP (2018) Tuning the electronic structures, work functions, optical property and stability of bifunctional hybrid graphene oxide/V–doped $NaNbO_3$ type–II heterostructures: a promising photocatalyst for H_2 production. Carbon NY 136:187–195. https://doi.org/10.1016/j.carbon.2018.04.076

88. Zhang P, Shen Y, Wu W, Li J, Zhou Z (2018) Enhanced photocatalytic performance of $KNbO_3$(100)/reduced graphene oxide nanocomposites investigated using first-principles calculations: RGO reductivity effect. Appl Surf Sci 434:932–939. https://doi.org/10.1016/j.apsusc.2017.10.239
89. Hong Z, Li X, Kang SZ, Qin L, Li G, Mu J (2014) Enhanced photocatalytic activity and stability of the reduced graphene oxide loaded potassium niobate microspheres for hydrogen production from water reduction. Int J Hydrogen Energy 39:12515–12523. https://doi.org/10.1016/j.ijhydene.2014.06.075
90. Hong Z, Li X, Kang SZ, Qin L, Li G, Mu J (2015) Modifications of morphology and hydrogen evolution activity for the potassium niobate nanoscrolls by introducing reduced graphene oxide. Int J Hydrogen Energy 40:14297–14304. https://doi.org/10.1016/j.ijhydene.2015.04.102
91. Fu Y, Wang X (2011) Magnetically separable $ZnFe_2O_4$–graphene catalyst and its high photocatalytic performance under visible light irradiation. Ind Eng Chem Res 50:7210–7218. https://doi.org/10.1021/ie200162a
92. Zhu W, Li X (2017) Graphene quantum dots /$LaCoO_3$/attapulgite heterojunction photocatalysts with improved photocatalytic activity. Appl Phys A Mater Sci Process 123:1–10. https://doi.org/10.1007/s00339-017-0907-4
93. Ding J, Yan W, Xie W, Sun S, Bao J, Gao C (2014) Highly efficient photocatalytic hydrogen evolution of graphene/$YInO_3$ nanocomposites under visible light irradiation. Nanoscale 6:2299–2306. https://doi.org/10.1039/c3nr05984g
94. Nasir MS, Yang G, Ayub I, Wang S, Wang L, Wang X, Yan W, Peng S, Ramakarishna S (2019) Recent development in graphitic carbon nitride based photocatalysis for hydrogen generation. Appl Catal B Environ 257:117855. https://doi.org/10.1016/j.apcatb.2019.117855
95. Ong WJ, Tan LL, Ng YH, Yong ST, Chai SP (2016) Graphitic carbon nitride (g-C_3N_4)-based photocatalysts for artificial photosynthesis and environmental remediation: are we a step closer to achieving sustainability? Chem Rev 116:7159–7329. https://doi.org/10.1021/acs.chemrev.6b00075
96. Song T, Yu X, Tian N, Huang H (2020) Preparation, structure and application of g-C_3N_4/BiO_X composite photocatalyst. Int J Hyd Energy 46:1857–1878. https://doi.org/10.1016/j.ijhydene.2020.10.136
97. Pushkar Kanhere ZC, Nisar J, Tang Y, Pathak B, Ahuja R, Zheng J (2012) Electronic structure, optical properties, and photocatalytic activities of $LaFeO_3$–$NaTaO_3$ solid solution. J Phys Chem C 116:22767–22773. https://doi.org/10.1021/jp307857h
98. Wu Y, Wang H, Tu W, Liu Y, Tan YZ, Yuan X, Chew JW (2018) Quasi-polymeric construction of stable perovskite-type $LaFeO_3$/g-C_3N_4 heterostructured photocatalyst for improved Z-scheme photocatalytic activity via solid p-n heterojunction interfacial effect. J Hazard Mater 347:412–422. https://doi.org/10.1016/j.jhazmat.2018.01.025
99. Ismael M, Y. Wu (2019) A facile synthesis method for fabrication of $LaFeO_3$/g-C_3N_4 nanocomposite as efficient visible-light-driven photocatalyst for photodegradation of RhB and 4-CP. New J Chem, 13783–13793. https://doi.org/10.1039/c9nj03376a
100. Liang Q, Jin J, Liu C, Xu S, Li Z (2017) Constructing a novel p-n heterojunction photocatalyst $LaFeO_3$/g-C_3N_4 with enhanced visible-light-driven photocatalytic activity. J Alloys Compd 709:542–548. https://doi.org/10.1016/j.jallcom.2017.03.190
101. Ye Y, Yang H, Wang X, Feng W (2018) Photocatalytic, Fenton and photo-Fenton degradation of RhB over Z-scheme g-C_3N_4/$LaFeO_3$ heterojunction photocatalysts. Mater Sci Semicond Process 82:14–24. https://doi.org/10.1016/j.mssp.2018.03.033
102. Acharya S, Mansingh S, Parida KM (2017) The enhanced photocatalytic activity of g-C_3N_4-$LaFeO_3$ for the water reduction reaction through a mediator free Z-scheme mechanism. Inorg Chem Front 4:1022–1032. https://doi.org/10.1039/c7qi00115k
103. Xu K, Feng J (2017) Superior photocatalytic performance of $LaFeO_3$/g-C_3N_4 heterojunction nanocomposites under visible light irradiation. RSC Adv 7:45369–45376. https://doi.org/10.1039/c7ra08715b

104. Jin L, Zhou X, Ning X, Zhan L, Kong M, Tan K, Li J, Lin Z (2018) Boosting visible light photocatalytic performance of g-C_3N_4 nanosheets by combining with $LaFeO_3$ nanoparticles. Mater Res Bull 102:353–361. https://doi.org/10.1016/j.materresbull.2018.02.057
105. Zhang J, Zhu Z, Jiang J, Li H (2020) Fabrication of a novel AgI/$LaFeO_3$/g-C_3N_4 dual Z-scheme photocatalyst with enhanced photocatalytic performance. Mater Lett 262:127029. https://doi.org/10.1016/j.matlet.2019.127029
106. Gao X, Shang Y, Liu L, Nie W (2019) A plasmonic Z-scheme three-component photocatalyst g-C_3N_4/Ag/$LaFeO_3$ with enhanced visible-light photocatalytic activities. Opt Mater (Amst) 88:229–237. https://doi.org/10.1016/j.optmat.2018.11.030
107. Luo J, Chen J, Guo R, Qiu Y, Li W, Zhou X, Ning X (2019) Rational construction of direct Z-scheme $LaMnO_3$/g-C_3N_4 hybrid for improved visible-light photocatalytic tetracycline degradation. Sep Purif Technol 211:882–894. https://doi.org/10.1016/j.seppur.2018.10.062
108. Luo J, Zhou X, Ning X, Zhan L, Ma L, Xu X, Li S, Sun S (2018) Utilization of $LaCoO_3$ as an efficient co-catalyst to boost the visible light photocatalytic performance of g-C_3N_4. Sep Purif Technol 201:309–317. https://doi.org/10.1016/j.seppur.2018.03.016
109. Ibarra-Rodriguez LI, Huerta-Flores AM, Torres-Martínez LM (2019) Facile synthesis of g-C_3N_4/$LaMO_3$ (M: Co, Mn, Fe) composites for enhanced visible-light-driven photocatalytic water splitting. Mater Sci Semicond Process 103.https://doi.org/10.1016/j.mssp.2019.104643
110. Zhou X, Chen Y, Li C, Zhang L, Zhang X, Ning X, Zhan L (2019) Construction of $LaNiO_3$ nanoparticles modi fi ed g-C_3N_4 nanosheets for enhancing visible light photocatalytic activity towards tetracycline degradation. Sep Purif Technol 211:179–188. https://doi.org/10.1016/j.seppur.2018.09.075
111. Ye C, Wang R, Wang H, Jiang F (2020) The high photocatalytic efficiency and stability of $LaNiO_3$/g-C_3N_4 heterojunction nanocomposites for photocatalytic water splitting to hydrogen. BMC Chem 14:1–13. https://doi.org/10.1186/s13065-020-00719-w
112. Rakibuddin M, Kim H, Ehtisham Khan M (2018) Graphite-like carbon nitride (C_3N_4) modified N-doped $LaTiO_3$ nanocomposite for higher visible light photocatalytic and photoelectrochemical performance. Appl Surf Sci 452:400–412. https://doi.org/10.1016/j.apsusc.2018.05.018
113. Konstas P, Konstantinuo I, Petrakis D, Albanis T (2018) Synthesis, characterization of g-C_3N_4/$SrTiO_3$ heterojunctions and photocatalytic activity for organic pollutants degradation. Catalys 8(11):554. https://doi.org/10.3390/catal8110554
114. Separationdr C, Hon K, Tan Z, Sim C (2017) Symbiotic interaction of amalgamated photocatalysts with improved day light utilisation. ChemistrySelect 2:84–89. https://doi.org/10.1002/slct.201601490
115. Kumar S, Tonda S, Baruah A, Kumar B, Shanker V (2014) Synthesis of novel and stable g-C_3N_4/N-doped $SrTiO_3$ hybrid nanocomposites with improved photocurrent and photocatalytic activity under visible light irradiation. Dalton Trans 42:16105–16114. https://doi.org/10.1039/c4dt01076k
116. Xu X, Liu G, Randorn C, Irvine JTS (2011) g-C_3N_4 coated $SrTiO_3$ as an efficient photocatalyst for H_2 production in aqueous solution under visible light irradiation. Int J Hydrogen Energy 36:13501–13507. https://doi.org/10.1016/j.ijhydene.2011.08.052
117. Luo Y, Deng B, Pu Y, Liu A, Wang J, Ma K, Gao F (2019) Interfacial coupling effects in g-C_3N_4/$SrTiO_3$ nanocomposites with enhanced H_2 evolution under visible light irradiation. Appl Catal B Environ 247:1–9. https://doi.org/10.1016/j.apcatb.2019.01.089
118. Kang HW, Lim SN, Song D, Bin Park S (2012) Organic-inorganic composite of g-C_3N_4 e $SrTiO_3$: Rh photocatalyst for improved H_2 evolution under visible light irradiation. Int J Hydrogen Energy 37:11602–11610. https://doi.org/10.1016/j.ijhydene.2012.05.020
119. Lee JT, Chen YJ, Su EC, Wey MY (2019) Synthesis of solar-light responsive Pt/g-C_3N_4/$SrTiO_3$ composite for improved hydrogen production: investigation of Pt/g-C_3N_4/$SrTiO_3$ synthetic sequences. Int J Hydrogen Energy 44:21413–21423. https://doi.org/10.1016/j.ijhydene.2019.06.178

120. Tan CE, Lee JT, Su EC, Wey MY (2020) Facile approach for Z-scheme type Pt/g-C_3N_4/$SrTiO_3$ heterojunction semiconductor synthesis via low-temperature process for simultaneous dyes degradation and hydrogen production. Int J Hydrogen Energy 45:13330–13339. https://doi.org/10.1016/j.ijhydene.2020.03.034
121. Chen X, Tan P, Zhou B, Dong H, Pan J, Xiong X (2015) A green and facile strategy for preparation of novel and stable Cr-doped $SrTiO_3$/g-C_3N_4 hybrid nanocomposites with enhanced visible light photocatalytic activity. J Alloys Compd 647:456–462. https://doi.org/10.1016/j.jallcom.2015.06.056
122. Yang M, Jin X (2016) Improvement of visible light-induced photocatalytic performance by Cr-doped $SrTiO_3$−carbon nitride intercalation compound (CNIC) composite. J Cent South Univ 23:310–316.https://doi.org/10.1007/s11771-016-3075-3
123. Pan J, Jiang Z, Feng S, Zhao C, Dong Z, Wang B, Wang J, Song C, Zheng Y (2018) The enhanced photocatalytic hydrogen production. Int J Hydrogen Energy 43:19019–19028. https://doi.org/10.1016/j.ijhydene.2018.08.102
124. Chen X, He X, Yang X, Wu Z, Li Y (2020) Construction of novel 2D/1D g-C_3N_4/$CaTiO_3$ heterojunction with face-to-face contact for boosting photodegradation of triphenylmethane dyes under simulated sunlight. J Taiwan Inst Chem Eng 107:98–109. https://doi.org/10.1016/j.jtice.2019.12.002
125. Kumar A, Schuerings C, Kumar S, Kumar A, Krishnan V (2018) Perovskite-structured $CaTiO_3$ coupled with g-C_3N_4 as a heterojunction photocatalyst for organic pollutant degradation. Beilstein J Nanotechnol 9:671–685. https://doi.org/10.3762/bjnano.9.62
126. Yan Y, Yang H, Yi Z, Li R, Xian T (2020) Design of ternary $CaTiO_3$/g-C_3N_4/AgBr Z-scheme heterostructured photocatalysts and their application for dye photodegradation. Solid State Sci 100:106102. https://doi.org/10.1016/j.solidstatesciences.2019.106102
127. Xian T, Yang H, Di LJ, Dai JF (2015) Enhanced photocatalytic activity of $BaTiO_3$ @ g-C_3N_4 for the degradation of methyl orange under simulated sunlight irradiation. J Alloys Compd 622:1098–1104. https://doi.org/10.1016/j.jallcom.2014.11.051
128. Huang Z, Zeng X, Li K, Gao S, Wang Q, Lu J (2017) Z-Scheme $NiTiO_3$/g-C_3N_4 heterojunctions with enhanced photoelectrochemical and photocatalytic performances under visible LED light irradiation. ACS Appl Mater Interfaces 9:41120–41125. https://doi.org/10.1021/acsami.7b12386
129. Wang H, Yuan X, Wang H, Chen X, Wu Z, Jiang L, Xiong W, Zhang Y, Zeng G (2015) One-step calcination method for synthesis of mesoporous g-C_3N_4/$NiTiO_3$ heterostructure photocatalyst with improved visible light photoactivity. RSC Adv 5:95643–95648. https://doi.org/10.1039/c5ra18117h
130. Ye R, Fang H, Zheng YZ, Li N, Wang Y, Tao X (2016) Fabrication of $CoTiO_3$/g-C_3N_4 hybrid photocatalysts with enhanced H_2 evolution: Z-scheme photocatalytic mechanism insight. ACS Appl Mater Interfaces 8:13879–13889. https://doi.org/10.1021/acsami.6b01850
131. Li X, Zhang H, Luo J, Feng Z, Huang J (2017) Hydrothermal synthesized novel nanoporous g-C_3N_4/$MnTiO_3$ heterojunction with direct Z-scheme mechanism. Electrochim Acta 258:998–1007. https://doi.org/10.1016/j.electacta.2017.11.151
132. Wang X, Mao W, Zhang J, Han Y, Quan C, Zhang Q, Yang T (2015) Facile fabrication of highly efficient g-C_3N_4/$BiFeO_3$ nanocomposites with enhanced visible light photocatalytic activities. J Colloid Interface Sci 448:17–23. https://doi.org/10.1016/j.jcis.2015.01.090
133. An J, Zhang G, Zheng R, Wang P (2016) Removing lignin model pollutants with $BiFeO_3$–g-C_3N_4 compound as an efficient visible-light-heterogeneous Fenton-like catalyst. J Environ Sci 48:218–229. https://doi.org/10.1016/j.jes.2016.01.024
134. Deng XZ, Song C, Tong YL, Yuan G, Gao F, Liu DQ, Zhang ST (2018) Enhanced photocatalytic efficiency of C_3N_4/$BiFeO_3$ heterojunctions: the synergistic effects of band alignment and ferroelectricity. Phys Chem Chem Phys 20:3648–3657. https://doi.org/10.1039/c7cp06274e
135. Fan T, Chen C, Tang Z, Ni Y, Lu C (2015) Synthesis and characterization of g-C_3N_4/$BiFeO_3$ composites with an enhanced visible light photocatalytic activity. Mater Sci Semicond Process 40:439–445. https://doi.org/10.1016/j.mssp.2015.06.054

136. Sepahvand H, Sharifnia S (2019) Photocatalytic overall water splitting by Z-schemeg-C_3N_4/$BiFeO_3$ heterojunction. Int J Hydrogen Energy 44:23658–23668. https://doi.org/10.1016/j.ijhydene.2019.07.078
137. Wu W, Xu C, Shi X, Zhao J, An X, Ma H, Tian Y (2020) Effective degradation of organic pollutants and reaction mechanism with flower-like $AgBiO_3$/g-C_3N_4 composite. Colloids Surfaces A 599:24901. https://doi.org/10.1016/j.colsurfa.2020.124901
138. Song Z, Lin P, Wang F, Huang G, Chen L, Qiu N (2019) Ag_3BiO_3/g-C_3N_4 Nanocomposite as efficient visible-light photocatalyst for degradation of methyl orange. Russ J Phys Chem A 93:1603–1609. https://doi.org/10.1134/S003602441908034X
139. Nguyen V, Mousavi M, Ghasemi JB, Van Le Q, Shokouhimehr M, Won H, Mohammadi M (2021) g-C_3N_4 nanosheet adorned with Ag_3BiO_3 as a perovskite: an effective photocatalyst for efficient visible-light photocatalytic processes. Mater Sci Semicond Process 125:105651. https://doi.org/10.1016/j.mssp.2020.105651
140. Zhang D, Qi J, Ji H, Li S, Chen L, Huang T, Xu C, Chen X, Liu W (2020) Photocatalytic degradation of ofloxacin by perovskite-type $NaNbO_3$ nanorods modified g-C_3N_4 heterojunction under simulated solar light: theoretical calculation, ofloxacin degradation pathways and toxicity evolution. Chem Eng J 400.https://doi.org/10.1016/j.cej.2020.125918
141. Shen JY, Cui ZS, Wu ZW, Wang JX, Ning Q, Lu XM (2015) Simple preparation of $CuFe_2O_4$/C_3N_4 composites: characterisation and enhanced photocatalysis. Mater Res Innov 19:187–191. https://doi.org/10.1179/1433075X14Y.0000000240
142. Li R, Cai M, Xie Z, Zhang Q, Zeng Y, Liu H, Liu G, Lv W (2019) Construction of heterostructured $CuFe_2O_4$/g-C_3N_4 nanocomposite as an efficient visible light photocatalyst with peroxydisulfate for the organic oxidation. Appl Catal B Environ 244:974–982. https://doi.org/10.1016/j.apcatb.2018.12.043
143. Liu Y, Song Y, You Y, Fu X, Wen J, Zheng X (2018) $NiFe_2O_4$/g-C_3N_4 heterojunction composite with enhanced visible-light photocatalytic activity. J Saudi Chem Soc 22:439–448. https://doi.org/10.1016/j.jscs.2017.08.002
144. Palanivel B, Ayappan C, Jayaraman V, Chidambaram S, Maheswaran R, Mani A (2019) Inverse spinel $NiFe_2O_4$ deposited g-C_3N_4 nanosheet for enhanced visible light photocatalytic activity. Mater Sci Semicond Process 100:87–97. https://doi.org/10.1016/j.mssp.2019.04.040
145. Gebreslassie G, Bharali P, Chandra U, Sergawie A, Boruah PK, Das MR, Alemayehu E (2019) Novel g-C_3N_4/graphene/$NiFe_2O_4$ nanocomposites as magnetically separable visible light driven photocatalysts. J Photochem Photobiol A Chem 382:111960. https://doi.org/10.1016/j.jphotochem.2019.111960
146. Hassani A, Eghbali P, Ekicibil A, Metin Ö (2018) Monodisperse cobalt ferrite nanoparticles assembled on mesoporous graphitic carbon nitride ($CoFe_2O_4$/mpg-C_3N_4): a magnetically recoverable nanocomposite for the photocatalytic degradation of organic dyes. J Magn Magn Mater 456:400–412. https://doi.org/10.1016/j.jmmm.2018.02.067
147. Guo X, Ai S, Yang D, Zhao L, Ding H (2019) Synergistic photocatalytic and Fenton-like degradation of organic contaminants using peroxymonosulfate activated by $CoFe_2O_4$@g-C_3N_4 composite. Environ Technol (United Kingdom), 1–14.https://doi.org/10.1080/09593330.2019.1697378
148. Yao Y, Cai Y, Lu F, Qin J, Wei F, Xu C, Wang S (2014) Magnetic $ZnFe_2O_4-C_3N_4$ hybrid for photocatalytic degradation of aqueous organic pollutants by visible light. Ind Eng Chem Res 53(44):17294–17302. https://doi.org/10.1021/ie503437z
149. Borthakur S, Saikia L (2019) $ZnFe_2O_4$@g-C_3N_4 nanocomposites: an efficient catalyst for Fenton-like photodegradation of environmentally pollutant Rhodamine B. J Environ Chem Eng 7.https://doi.org/10.1016/j.jece.2019.103035
150. Palanivel B, Devi Mudisoodum Perumal S, Maiyalagan T, Jayarman V, Ayyappan C, Alagiri M (2019) Rational design of $ZnFe_2O_4$/g-C_3N_4 nanocomposite for enhanced photo-Fenton reaction and supercapacitor performance. Appl Surf Sci 498:143807.https://doi.org/10.1016/j.apsusc.2019.143807

151. Nguyen V, Delbari SA, Mousavi M, Namini AS, Ghasemi JB, Van Le Q, Asl MS, Mohammadi M, Shokouhimehr M (2021) g-C_3N_4-nanosheet/$ZnCr_2O_4$ S-scheme heterojunction photocatalyst with enhanced visible-light photocatalytic activity for degradation of phenol and tetracycline. Sep Purif Technol, 118511. https://doi.org/10.1016/j.seppur.2021.118511
152. Lv J, Dai K, Zhang J, Geng L, Liang C, Liu Q, Zhu G, Chen C (2015) Facile synthesis of Z-scheme graphitic-C_3N_4/Bi_2MoO_6 nanocomposite for enhanced visible photocatalytic properties. Appl Surf Sci 358:377–384. https://doi.org/10.1016/j.apsusc.2015.06.183
153. Thaweesak S, Lyu M, Peerakiatkhajohn P, Butburee T, Luo B, Chen H, Wang L (2017) Two-dimensional g-C_3N_4/$Ca_2Nb_2TaO_{10}$ nanosheet composites for efficient visible light photocatalytic hydrogen evolution. Appl Catal B Environ 202:184–190. https://doi.org/10.1016/j.apcatb.2016.09.022
154. Jiang D, Ma W, Yao Y, Xiao P, Wen B, Li D, Chen M (2018) Dion-Jacobson-type perovskite $KCa_2Ta_3O_{10}$ nanosheets hybridized with g-C_3N_4 nanosheets for photocatalytic H_2 production. Catal Sci Technol 8:3767–3773. https://doi.org/10.1039/c8cy00930a
155. Michálek M, Sedláček J, Parchoviansky M, Michálková M, Galusek D (2014) Mechanical properties and electrical conductivity of alumina/MWCNT and alumina/zirconia/MWCNT composites. Ceram Int 40:1289–1295. https://doi.org/10.1016/j.ceramint.2013.07.008
156. Christoforidis KC, Syrgiannis Z, La Parola V, Montini T, Petit C, Stathatos E, Godin R, Durrant JR, Prato M, Fornasiero P (2018) Metal-free dual-phase full organic carbon nanotubes/g-C_3N_4 heteroarchitectures for photocatalytic hydrogen production. Nano Energy 50:468–478. https://doi.org/10.1016/j.nanoen.2018.05.070
157. Sudhaik A, Raizada P, Thakur S, Saini RV, Saini AK, Singh P, Kumar Thakur V, Nguyen VH, Khan AAP, Asiri AM (2020) Synergistic photocatalytic mitigation of imidacloprid pesticide and antibacterial activity using carbon nanotube decorated phosphorus doped graphitic carbon nitride photocatalyst. J Taiwan Inst Chem Eng 113:142–154. https://doi.org/10.1016/j.jtice.2020.08.003
158. Xu WL, Niu MS, Yang XY, Xiao J, Yuan HC, Xiong C, Hao XT (2018) Carbon nanotubes as the effective charge transport pathways for planar perovskite photodetector. Org Electron 59:156–163. https://doi.org/10.1016/j.orgel.2018.05.004
159. Ding F, Zhao Z, Yang D, Zhao X, Chen Y, Jiang Z (2019) One-pot fabrication of g-C_3N_4/MWCNTs nanocomposites with superior visible-light photocatalytic performance Ind. Ind Eng Chem Res 58:3679–3687. https://doi.org/10.1021/acs.iecr.8b05293
160. Sierra Gallego G, Barrault J, Batiot-Dupeyrat C, Mondragón F (2010) Production of hydrogen and MWCNTs by methane decomposition over catalysts originated from $LaNiO_3$ perovskite. Catal Today 149:365–371. https://doi.org/10.1016/j.cattod.2009.06.004
161. Kuras M, Zimmermann Y, Petit C (2008) Reactivity of perovskite-type precursor in MWCNTs synthesis. Catal Today 138:55–61. https://doi.org/10.1016/j.cattod.2008.04.030
162. Huang X, Pu Z, Feng M, Tong L, Liu X (2013) $BaTiO_3$@MWCNTs core/shell nanotubes embedded PEN nanocomposite films with high thermal stability and highpermittivity. Mater Lett 96:139–142. https://doi.org/10.1016/j.matlet.2013.01.022
163. Huang X, Chen Z, Tong L, Feng M, Pu Z, Liu X (2013) Preparation and microwave absorption properties of $BaTiO_3$@MWCNTs core/shell heterostructure. Mater Lett 111:24–27. https://doi.org/10.1016/j.matlet.2013.08.034
164. Sobahi TR, Amin MS (2021) Photocatalytic oxidation of atrazine using $BaTiO_3$-MWCNT nanocomposites under visible light. Ceram Int 47:14366–14374. https://doi.org/10.1016/j.ceramint.2021.02.015
165. Opoku F, Govender KK, Catharina Elizabeth van Sittert CG, Govender PP (2018) Hybrid DFT study of MWCNT/Zr-doped $SrTiO_3$ heterostructure: Hydrogen production, electronic properties and charge Carrier mediator role of Zr^{4+} ion. Int J Hydrogen Energy 43:22253–22264. https://doi.org/10.1016/j.ijhydene.2018.10.072
166. Lin Y, Wu S, Li X, Wu X, Yang C, Zeng G, Peng Y, Zhou Q, Lu L (2018) Microstructure and performance of Z-scheme photocatalyst of silver phosphate modified by MWCNTs and Cr-doped $SrTiO_3$ for malachite green degradation. Appl Catal B Environ 227:557–570. https://doi.org/10.1016/j.apcatb.2018.01.054

167. Ahmadipour M, Hamzah AA, Pang AL, Le Thi A, Chiam SL, Ahmad ZA, Rajitha B, Pung SY (2021) Photodegradation of rhodamine B-dye pollutant using $CaCu_3Ti_4O_{12}$-multiwall carbon nanotube nanocomposites. J Environ Chem Eng 9:105185. https://doi.org/10.1016/j.jece.2021.105185
168. Mitra A, Mahapatra AS, Mallick A, Chakrabarti PK (2017) Enhanced microwave absorption and magnetic phase transitions of nanoparticles of multiferroic $LaFeO_3$ incorporated in multiwalled carbon nanotubes (MWCNTs). J Magn Magn Mater 435:117–125. https://doi.org/10.1016/j.jmmm.2017.03.066
169. Daud A, Warsi MF, Zulfiqar S, Agboola PO, Ur Rehman A, Shakir I (2020) Fabrication of $GdFO_3$-carbon nanotubes nanocomposites for enhanced photocatalytic applications. Ceram Int 46:12884–12890. https://doi.org/10.1016/j.ceramint.2020.01.205
170. Bag M, Renna LA, Jeong SP, Han X, Cutting CL, Maroudas D, Venkataraman D (2016) Evidence for reduced charge recombination in carbon nanotube/perovskite-based active layers. Chem Phys Lett 662:35–41. https://doi.org/10.1016/j.cplett.2016.09.004
171. Chen D, Lu Y, Wu J, Li N, Zheng YZ, Tao X (2019) Perovskite solar cells-TiO_2 tandem assembly for photoelectrocatalytic degradation of organic pollutants. J Phys Chem Solids 132:204–212. https://doi.org/10.1016/j.jpcs.2019.03.025
172. Demircivi P, Gulen B, Bilgin E, Berek D (2020) Enhanced photocatalytic degradation of tetracycline using hydrothermally synthesized carbon fiber decorated $BaTiO_3$. Mater Chem Phys 241:122236. https://doi.org/10.1016/j.matchemphys.2019.122236
173. Xie J, Qingsheng Wua DZ (2012) Electrospinning synthesis of $ZnFe_2O_4$_Fe_3O_4_Ag nanoparticle-loaded mesoporous carbon fibers with magnetic and photocatalytic properties. Carbon 50(3):800–807. https://doi.org/10.1016/j.carbon.2011.09.036
174. Li X, Rui M, Song J, Shen Z, Zeng H (2015) Carbon and graphene quantum dots for optoelectronic and energy devices: a review. Adv Funct Mater 25(31):4929–4947. https://doi.org/10.1002/adfm.201501250
175. Li X, Shi H, Wang T, Zhang Y, Zuo S, Luo S (2018) Photocatalytic removal of NO by Z-scheme mineral based heterojunction intermediated by carbon quantum dots. Appl Surf Sci 456:835–844. https://doi.org/10.1016/j.apsusc.2018.06.133
176. Paszkiewicz-gawron M, Kowalska E, Endo-kimura M, Zwara J, Pancielejko A, Wang K, Lisowski W, Justyna Ł, Zaleska-medynska A, Grabowska-musia E (2021) Stannates, titanates and tantalates modified with carbon and graphene quantum dots for enhancement of visible-light photocatalytic activity. Appl Surf Sci 541:148425. https://doi.org/10.1016/j.apsusc.2020.148425
177. Zhang Z, Shu M, Jiang Y, Xu J (2021) Fullerene modified $CsPbBr_3$ perovskite nanocrystals for efficient charge separation and photocatalytic CO_2 reduction. Chem Eng J 414:128889. https://doi.org/10.1016/j.cej.2021.128889
178. Behera A, Mansingh S, Das KK, Parida K (2019) Synergistic $ZnFe_2O_4$-carbon allotropes nanocomposite photocatalyst for norfloxacin degradation and Cr (VI) reduction. J Colloid Interface Sci 544:96–111. https://doi.org/10.1016/j.jcis.2019.02.056
179. Wang Y, Wang J, Du B, Wang Y, Xiong Y, Yang Y, Zhang X (2018) Synthesis of hierarchically porous perovskite-carbon aerogel composite catalysts for the rapid degradation of fuchsin basic under microwave irradiation and an insight into probable catalytic mechanism. Appl Surf Sci 439:475–487. https://doi.org/10.1016/j.apsusc.2017.12.196
180. Dong S, Xia L, Chen X, Cui L, Zhu W, Lu Z, Sun J, Fan M (2021) Interfacial and electronic band structure optimization for the adsorption and visible-light photocatalytic activity of macroscopic $ZnSnO_3$/graphene aerogel. Compos Part B 215:108765. https://doi.org/10.1016/j.compositesb.2021.108765
181. Kumar RD, Thangappan R, Jayavel R (2017) Facile preparation of—with enhanced visible light photocatalytic activity. J Inorg Organomet P 27:892–900. https://doi.org/10.1007/s10904-017-0534-8
182. Hu J, Liu Y, Men J, Zhang L, Huang H (2016) Ag modi fi ed $LaMnO_3$ nanorods-reduced graphene oxide composite applied in the photocatalytic discoloration of direct green. Solid State Sci 61:239–245. https://doi.org/10.1016/j.solidstatesciences.2016.10.008

Carbon Composite Catalysts for Oxygen Reduction Reactions

Haslinda Mohd Sidek, Nurul Asikin-Mijan, Mohd Razali Shamsuddin, and Yun Hin Taufiq-Yap

Abstract There is a growing interest for the development of various kind of catalysts to overcome the sluggish kinetics reaction of ORR at the cathode. Therefore, a lot of research have been done to search for promising catalysts that can speed up the ORR kinetics, hence enhance the performance. Carbon-based materials such as carbon black, carbon nanotube, and graphene derivatives hold the greatest promise as potentially ideal alternatives for ORR electrocatalyst owing to their abundance, low-cost, high surface area, and outstanding electronic conductivity. This chapter mainly focuses on research interest and activity on carbon composite catalysts for ORR, including hybridization with platinum group metal (PGM) and non-PGM. The role of carbon-based materials as support in the composite has also been discussed. Additionally, heteroatom-doping carbon composite catalyst was highlighted with an aim to enhance the catalytic performance by altering the electronic properties of carbon. To assist readers, we first provide an overview of the following background information of ORR, the reaction pathway, and the role of electrocatalyst in ORR, respectively.

Keywords Carbon composite · Electrocatalyst · ORR · Hybridization · Support

H. M. Sidek (✉) · Y. H. Taufiq-Yap
Catalysis Science and Technology Research Centre (PutraCAT), Faculty of Science, Universiti Putra Malaysia, 43400 UPM Serdang, Selangor, Malaysia
e-mail: lindasidek89@gmail.com

Department of Chemistry, Faculty of Science, Universiti Putra Malaysia, 43400 UPM Serdang, Selangor, Malaysia

N. Asikin-Mijan
Department of Chemistry, Faculty of Science and Technology, Universiti Kebangsaan Malaysia, 43600 UKM Bangi, Selangor, Malaysia

M. R. Shamsuddin
Preparatory Centre of Science and Technology, Universiti Malaysia Sabah, 88400 Kota Kinabalu, Sabah, Malaysia
e-mail: razalishamsuddin@ums.edu.my

Y. H. Taufiq-Yap
Chancellery Office, Universiti Malaysia Sabah, 88400 Kota Kinabalu, Sabah, Malaysia

M. Jawaid and A. Khan (eds.), *Carbon Composite Catalysts*, Composites Science and Technology, https://doi.org/10.1007/978-981-19-1750-9_4

1 Introduction

Oxygen reduction reaction (ORR) is an essential reaction in living processes including biological respiration and energy transformations such as in fuel cell or metal-air batteries. In electrochemical reaction, ORR take placed at the cathode, where O_2 molecules are reduced by electrons [1]. Generally, ORR could be occurred either in aqueous solution or in non-aqueous aprotic solvents and/or in alkaline solutions. There are two main pathways in aqueous solutions: the direct 4-electron reduction (formation of H_2O), and the indirect 2-electron reduction (hydrogen peroxide, H_2O_2 is formed). Subsequently, in non-aqueous aprotic solvents and/or in alkaline solutions, 1-electron reduction pathway by the formation of superoxide (O^{2-}) occurred. However, it has been claimed that ORR is sluggish kinetic reaction due to strong bond energy of 498 kJ mol^{-1} to break the O=O bond electrochemically [1, 2]. Therefore, in aqueous solutions the slower ORR at the cathode is more than six orders than hydrogen oxidation at the anode. This phenomenon can be related to the varied adsorption/desorption and reaction pathways, which involve different O-containing intermediates (e.g., OOH^*, O^*, and OH^*). Several typical ORR processes are listed in Table 1 with their thermodynamic electrode potentials value at standard conditions. The ORR mechanism is quite complicated electrochemical reaction that involves many intermediates which is really depending on the electrode material properties, catalyst, and electrolyte. The reaction pathways are discussed in detail in the next subtopic.

Noted that ORR processes by 1-, 2-, and 4-electron reduction pathways (Table 1) primally depending on its applications. The 4-electron direct pathway is highly preferred in fuel cell processes. On the contrary, for H_2O_2 production industry the

Table 1 ORR thermodynamic electrode potentials on different electrolytes [3]

Electrolyte	ORR reactions	Thermodynamic electrode potential at standard conditions, V
Acidic aqueous solution	$O_2 + 4H^+ + 4e^- \rightarrow H_2O$ (1) $O_2 + 2H^+ + 2e^- \rightarrow H_2O_2$ (2) $H_2O_2 + 2H^+ + 2e^- \rightarrow 2H_2O$ (3)	1.229 0.70 1.76
Alkaline aqueous solution	$O_2 + H_2O + 4e^- \rightarrow 4OH$ (4) $O_2 + H_2O + 2e^- \rightarrow HO_2^- + OH$ (5) $HO_2^- + H_2O + 2e^- \rightarrow 3OH$ (6)	0.401 −0.065 0.867
Non-aqueous aprotic solvents	$O_2 + e^- \rightarrow O_2^-$ (7) $O_2^- + e^- \rightarrow O_2^{2-}$ (8)	a b

a, b: The thermodynamic potentials for 1-electron pathway by superoxide formation, followed by reduction to O_2^{2-}. The value not listed due to it highly dependent on the solvent used

2-electron reduction pathway much preferable. Meanwhile, in the study of the ORR mechanism the 1-electron reduction pathway is more suitable.

1.1 Reaction Pathway

The reaction pathway of ORR processes in aqueous electrolyte occurred by the following steps: (i) Diffusion and adsorption of O_2 molecules at the surface of electrocatalysts, (ii) adsorption of O_2 molecules by electron transfer from anode, (iii) bond weakening and breaking of O=O bindings, and (iv) elimination of OH^- ions to solutions [4, 5]. As previously mentioned, the ORR could be occurred either in a highly efficient one step 4-electron pathway or a sluggish two steps of 2-electron pathway. In a direct 4-electron pathway, the reactions in alkaline follow Eq. 1 or Eq. 4 in acidic electrolyte. Thus, for indirect 2-electron two steps, after the first two-electron oxygen reduction in both acidic solution (Eq. 2) and alkaline (Eq. 5), either a further two electron reduction of H_2O_2 (Eq. 3) or the chemical disproportionation of H_2O_2 (Eq. 6).

1.2 Role of Electrocatalysts in ORR Processes

The contribution of electrocatalysts become crucial role to lower down the energy barrier for the bond activation and cleavage. As a result, the usage of catalyst for the cathode is usually ten times more than that for the anode. Industrially, 36–56% from the cost of commercial electrocatalysts for proton-exchange membrane fuel cells (PEMFC) are precious Pt-based nanomaterials. The widely application of commercial platinum group metals (PGMs) based electrocatalysts due to high activity on ORR. Pt is believed as the best electrocatalyst for the 4-electron ORR due to lowest overpotentials and the highest stability in acidic environments [3]. However, they still require more than 300 mV of overpotential to overcome thermodynamic potential of ORR due to competing water activation and sluggish kinetics reaction [1]. Furthermore, side reaction occurred on oxygen which undergoes non-dissociative adsorption on Pt surface metals, which results in Pt oxidation. Altogether, most importantly Pt remains as an expensive metal of low abundance.

2 Electronically Conductive Carbon-Based Material for ORR

Carbon materials have been widely used for catalyst support in a diverse application owing to its abundance, potential economical, availability in a variety of forms with

different properties, outstanding electronic conductivity, high surface area and relatively inert surface [6, 7]. In ORR, an efficient electrocatalyst can be achieved by using catalytic supports that are able to promote the dispersion of the nanoparticles properly. In addition to high stability in acidic or alkaline electrolytes, high potentials, and highly oxidizing environments, the electrocatalyst materials should possess an adequate conductivity especially to be applied in electrochemical applications because insufficient conductivity of the materials will lead to the increasing of resistance of the system resulting to loss of electrical efficiency. In this case, carbon-based materials are commonly used because of their high electronically conductive properties, making them feasible for being applied as a promising ORR electrocatalyst. There are few carbon-based materials that are usually utilized as ORR electrocatalyst such as carbon black, carbon nanotubes (CNT) including single-walled (SWCNT) or the most common multi-walled (MWCNT) forms, and graphene. Each of these materials will be discussed in detail in the following sections.

2.1 Carbon Black

Thanks to its high mesoporous distribution, good electrical properties, as well as low cost, carbon black has gained a lot of interest for being implemented in the field of electrochemistry [8]. This material is one of the first and the most common electrocatalyst support for polymeric electrolyte fuel cells, owing to its high electrical conductivity and corrosion resistance, porous structure and specific surface area. Moreover, carbon black has high availability as it is usually produced by thermal decomposition of hydrocarbons derived from petroleum sources [9, 10]. There are different types of carbon blacks that are mostly used as electrodes in supercapacitors or catalyst support in electrochemical applications such as acetylene black, Ketjen black, Black Pearl, and Vulcan XC-72, respectively. These materials can be differentiated in terms of their properties which depend on the manufacturing process, including porosity, electrical conductivity, surface functionalities, and specific surface area [11]. Compared to other conductive carbon black, commercially available Vulcan CX-72R has its own merits, for example high surface area (~250 $m^2\ g^{-1}$), generating from the aggregation of 30–60 nm particle size, and delivering high electrical conductivity (~2.77 S cm^{-1}) at relatively low loading level [12]. There are so many studies that have been reported for the usage of carbon black as catalyst support for ORR, including both platinum group metal (PGM) as well as non PGM. To date, platinum and carbon black have been a standard electrocatalyst for fuel cell due to their prominent electrocatalytic activity.

2.2 Carbon Nanotubes (CNT)

Carbon nanotubes (CNTs) have been extensively studied since their discovery by Iijima in 1991. CNTs are hollow nanometer-sized graphitic carbon tubes that can be pictured as a graphene sheet wrapped into a smooth cylinder. Additionally, the CNTs are carbon allotropes with a unique structure that provide superior mechanical capabilities [13]. The CNT can be classified as single-walled carbon nanotube (SWCNT) and multi-walled carbon nanotubes (MWCNTs) [14]. A SWCNT is defined as a single graphene sheet wrapped into a tube, whereas a MWCNT is defined as a series of concentric SWCNTs with varying diameters. These are typically made in diameters ranging from 0.4 to 2 mm. The sizes of SWCNTs are determined by the temperature range at which they are synthesized. As the temperature rises, larger-sized (wider) SWCNTs are integrated. However, in contrast to SWCNTs, MWCNTs contain many more cylindrical walls. MWCNTs are made up of multiple concentric walls with progressively increasing diameters that are formed by carbon molecules. Even though MWCNTs have several walls, each wall is simply an atom-thick structure. In particular, all of these types of CNTs have outstanding electrocatalytic properties. Indeed, their activity is greatly influenced by size and doping promoters [15]. The following procedures are commonly employed for the manufacturing of SWNTs and MWNTs: (i) arc discharge synthesis, (ii) laser ablation, and (iii) chemical vapour deposition (CVD). For CNT synthesis, high-temperature techniques such as arc discharge and laser ablation are being substituted by low-temperature preparative processes such as CVD (800 °C). The CVD method greatly control the purity of synthesized CNTs, whereby, the nanotube orientation, length, diameter, and density can be achieved. It has the ability to bring CNT production to a commercial level.

Utilization of CNT for ORR is highly promising since its application as a composite will promote surface chemistry stabilization, increase the graphitic domains and to accelerate electron transfer. A recent paper demonstrated the advantages of including carbon nanotubes (CNT) during the polymerization of glucose, as well as determining the optimum dose of CNT to maximize the composites' performance in supercapacitor applications [16–18]. Similarly, impressive ORR activity also has been observed when the CNT mixed with carbide-derived carbons, graphene, chitosan, carbonized metal–organic frameworks (MOF), and activated carbons to produce composites [18, 19]. Indeed, all of these CNT composites exhibited ORR activity, yet the activity still low, hence it is necessary to modify their surfaces in order to create active centers [20]. Functionalization (oxidation) of the CNT surface using acids or bases, as well as doping with heteroatoms, are the most prevalent methods. Functionalization promotes formation of functional oxygen-containing groups on the surface of CNTs that provide an increase in activity in ORRs [21, 22]. Among these approaches, it is believed that addition of dopant on CNT exhibited promising result in ORR activity [23]. Indeed, according to former study, addition of more metal or dopant on carbon and CNTs will result in higher ORR activity than addition of single metal, owing to the strong interaction between two metals [24]. Consequently, the ORR activity also strongly influenced by the metal: metal molar ratio. Unluckily,

the present of metal may reduce the CNT's actual influence on the composites' characteristics and moreover, the durability of its still need to be improved.

2.3 Graphenes

Graphene is a honeycomb lattice with a single layer with charge carrier mobility of 2–3 orders of magnitude greater than that of semiconducting silicon. Recent trends on the exploration of catalyst support have been focused on graphene derivatives, attributable to its unique properties such as exceptionally high electronic and thermal conductivity, very high surface area of 2630 $m^2\ g^{-1}$, and high mechanical strength [25]. In the outer shell of graphene, there are free electrons that can flow freely along the surface for electrical conduction. These electrons, known as pi electrons, are overlapped in graphene to facilitate bonding between carbon atoms. Indeed, for good electrical conductivity in composite material, graphene sheets must be evenly dispersed throughout the matrix [26].

Graphene can be synthesized via several approaches including micromechanical exfoliation, epitaxial growth or chemical vapor deposition and chemical vapor deposition (CVD) methods. Noted, among those methods, CVD is the best and proven technology for producing high-quality graphene. The CVD process typically includes the high-temperature breakdown of precursors, the adsorption and deposition of gaseous atoms on the substrate, and the surface chemical reaction to form a continuous layer [27]. This procedure, however, is difficult to accomplish since it requires a high temperature of more than 900 °C, and it is also harmful to the environment (producing corrosive and toxic gases).

Therefore, two graphene derivatives which are graphene oxide (GO) and reduced graphene oxide (rGO) has gained a great attention recently and these materials can be easily produced from abundant graphite crystal by common oxidation methods [7], followed by a reduction step for rGO [28]. GO lost its electronic conductivity due to partial transition from sp2 to sp3 carbon atoms, meanwhile during reduction of GO π-network will be partially restored, hence recover part of the characteristic conductivity of graphene [29]. In ORR, graphene is said to be the most promising as an electrocatalytic support among all carbonic morphologies. Taking into account its unique properties, the use of graphene for catalyst composite gave significant impact on the catalyst improvements especially on the stability, activity and the efficient use of metallic nanoparticles [30].

2.4 Heteroatom-Doped Carbon

Extensive studies have been done to explore highly efficient electrocatalyst, including functionalized carbon-based materials due to their earth abundance, facile fabrication, highly stable, exceptionally good activity, fuel immunity, and environmental

friendliness [31–33]. One of carbon functionalization which is heteroatom-doping has aroused great interest in developing promising carbon-based electrocatalyst. Heteroatom doping is a surface engineering of carbon materials with nitrogen (N), sulfur (S), phosphorus (P), and boron (B) with the aim of enabling better tuning of the electron donor properties with enhanced electrical conductivity, hence improves the catalytic activity. In the field of ORR, N-doped carbon materials is the most studied doping method and it was all started by Dai's group in 2009. The work is related to studies on nitrogen-doped vertically aligned nanotubes (N-doped VA-CNTs) for ORR [34], until a lot of studies on various heteroatom single/dual/multiple doped carbon-based electrocatalysts have been done. Generally, by introducing heteroatoms with different electronegativity, the local charge and spin density of the carbon matrix will be significantly modified. This will enhance the electrocatalytic ORR activity of heteroatom-doped carbon by facilitating the oxygen adsorption, reduce the reaction energy barrier, and afterwards break the O–O bond [35–37].

In a similar way to N (same electron configuration of valence electron), phosphorus atoms also act as electron donors for carbon to induce a shift in the Fermi level to the conducting band. Nevertheless, the larger size of P as compared to N, make it difficult to be substituted into graphitic honeycomb lattice. In order to overcome this, P atoms are always being bonded with O and/or C in the heteroatom incorporated frameworks. The introduction of P-containing functional group is said to significantly enhances the thermal stability of the carbon matrix [38, 39]. Nevertheless, the studies on P-doped carbon materials for ORR is not as much as N-doping due to insignificant improvement of the catalytic activity.

Boron is another heteroatom doping element that can be integrated into carbon materials to produce a promising carbon-based catalyst. Similar to the phosphorus, boron has lower electronegativity than nitrogen and carbon atoms and it is a unique element that has been utilized as doping material in carbon framework to boost the electrochemical capacitance [40]. The uniqueness of Boron doped (B-doped) lies on its ability to transform the electron-deficient to electron-donating site. The transformation occurred by taking advantage of the rich π-electrons in the carbon conjugated system. The active electrons from C–C π^* antibonding orbital is transferred to vacant $2p_z$ orbital of boron resulted to this beneficial property [41]. Due to this property, it has been attracted for some researcher to study on B-doped carbon composite electrocatalyst for ORR.

Besides that, there are tremendous attention towards sulphur, S-doping due to its close electronegativity value (2.58) to carbon (2.55) compared to N (3.04), B (2.04) or P (2.19) [42]. The advantageous of S-doped either as metal sulphides or sulphur atom contributed by ability to modify spin density distributions around the metal centres. Furthermore, the synergistic effect between S and other doped heteroatoms together with the S–C bond and metal sulphides are beneficials to the superior ORR performance. Besides, the S-doped hybrid electrocatalyst exhibit a small charge-transfer resistance which enhanced ORR activity [43].

Also, excellent electrochemical performance can be achieved by F-doped heteroatom due to high electronegativity property of fluorine (3.98) which can easily formed F–C bonds with high polarity and stability. Besides, not only ORR, other

application suit with this superiority such as lithium-ion battery, sodium-ion battery, supercapacitor and CO_2 reduction reaction [44]. However due to some limitation on preparation method, this electrocatalysts is still underutilized. Noted, the formation of C–F bond using F_2 gas is too dangerous for laboratory synthesize. Thus, the available method such as gas-phase techniques or plasma dissociation as reported by Panomsuwan et al. [45] are too expensive compared to more simple synthesis method which is difficult to get F-doped carbon with excellent electrochemical performance [46].

The next sections of this book chapter will highlight more on the roles of each carbon-based materials in the composite catalysts and its influence on the ORR performance.

3 Noble Metal–Carbon Composite Catalyst

3.1 Pt on Carbon-Based Material

Pt is a well-known noble metal catalysts that has been used for many ORR application [47]. However, the commercialization of Pt as catalyst is still hindered by their high cost and limited supply. Thus, major effort has been done to overcome this problem. Selection of support material needs to be highly emphasized because this will affect physicochemical properties and catalytic performance of the catalyst, which attributed to lifecycle of a Pt-catalyst [48]. The synthesis method, physicochemical properties and performance of Pt-based supported carbon-based done by group of researchers are discussed in detail in the next subtopics.

3.1.1 Carbon Black

Carbon black (CB) is repeatedly applied as support for electrocatalysts due to high surface area and porosity properties, which make it convenient for PEMFCs and direct-methanol fuel cells (DMFCs) catalyst layer as described in literatures. Wang et al. [49] investigated effect of different types of carbon black on Pt electrocatalysts. Vulcan XC-72R, Ketjen Black EC 300 J and Black Pearls 2000 has been used as the additive in Pt black cathode on direct methanol fuel cell (DMFC). Ketjen Black EC 300 J shows higher potential compared to Vulcan XC72R and Black Pearls 2000 by expanding the electrochemical surface area and DMFC performance. The stability test of Pt/Ketjen Black EC 300 J shows its stable binding with the Nafion membrane up to 360 h on air-breathing DMFC. Karousos et al. [50] prepared Pt/C electrocatalysts from Vulcan XC-72 carbon black by using novel one-step-process which is combination of galvanostatic pulsed electrodeposition and high power, low-frequency (20 kHz) pulsed ultrasonication with ultrasound. Poly(N-vinyl-2- pyrrolidone) (PVP) act as stabilizing agent to hinder nanoparticle aggregation, ensuring

narrow size distributions and postulated to prevent the establishment of a strong metal-substrate interaction. By controlling current pulse amplitude, small size particles, under 10 nm, appeared to be attached to carbon black. Meanwhile, Sattler and Ross [51] reported that carbon support promotes the change in size and/or shape of Pt crystallites. Pt particles on Pt/C electrocatalyst ranging in size (0.8 to 50 nm). The ORR rate decreased for catalysts having a particle size < 3.5 nm. The observation suggested that the dominating (111) surfaces and rough (110) regions on these small particles are less active than (100) and (100) vicinal planes.

3.1.2 Carbon Nanotube (CNT), Multiwalled-CNT (MWCNT) and Single Walled-CNT (SWCNT)

CNT become a preference as support material due to high surface area, great electrical conductivity, outstanding chemical and electrochemical stabilities, quasi one-dimensional structure with beneficial morphology in enhancing the ORR performance. In addition, CNT promotes tremendous effect on particles size and metal distribution which is essential to the electrocatalysts to achieve high catalytic activity of ORR. Jeng et al. [52] synthesized Pt–Ru supported on carbon nanotubes (Pt–Ru/CNT) which prepared via modified polyol approach. Excellent performance of Pt–Ru/CNT electrocatalyst with composition ratio of 1:1 towards (methanol oxidation reaction) MOR. High conductivity of CNT, good catalyst morphology and suitable catalyst composition of the prepared Pt–Ru/CNT electrocatalyst are some of the key factors leading to enhanced cell performance. Moreover, Show et al. [53], and Matsuda et al. [54] reported good dispersion of Pt particles on a CNT surface prepared by in-liquid plasma method. This method promotes small sized of Pt catalyst less than 10 nm. Thus, excellent catalytic performance of the catalyst recorded by the electrical power achieving 108 mW cm^{-2}.

Application of MWCNT as support material was reported by Jha et al. [55] prepared by chemical vapor deposition technique using Pt and AB_3 alloy hydride catalyst (Pt/MWNT and Pt–Ru/MWNT) electrocatalysts. Dispersion and accessibility of MWCNT on Pt-Ru/MWCNT catalyst is the key-point to high power density (39.3 mW cm^{-2}) at a current density of 130 mA cm^{-2} for the DMFC. Meanwhile, Wang et al. [56] prepared Pt-Au/CNT@TiO_2 catalysts by a deposition-UV-photoreduction method for DMFC. The results obtained shows PtAu/MWCNT@TiO_2 exhibited high performance on ORR activity and high CO tolerance due to strong interaction between the Pt–Au alloy which lowered oxidation overpotential. Furthermore, addition of Ti ions enhanced dissociation of H_2O to form adsorbed-OH species, which then strongly reacts with bound adsorbed-CO species to form CO on the Pt surface. Concurrently, Wu and Xu [57] compared the performance of MWNT and SWNT in Pt electrocatalysts for DMFC. Better performance of Pt/SWCNT due to great contact between Pt particles and SWNT network which produce highly exposed sphere shape. Furthermore, electrodeposition technique enhanced Pt particle dispersion for the higher utilization during ORR activity.

All in all, good quality of SWCNT as support material due to high degree of graphitization, great mesoporous 3D structure, and extra oxygen-containing groups at its surface sites attributed to the higher electrochemically accessibility and rapid charge of transfer rate.

3.1.3 Graphene Derivatives

Extraordinary properties of graphene and its derivatives attract the researcher's attention towards application of this material on Pt electrocatalyst for ORR. Therefore, Table 2 summarized the literatures for graphene and its derivatives.

3.2 Other Noble Metal–Carbon Composite Catalysts

Pt is considered as the best choice catalyst for ORR. Nevertheless, several significant limitations such as overprice, and lack of availability comprise the major drawbacks of the catalyst commercialization. Moreover, Pt/C catalyst still suffers from sluggish kinetics reaction which triggered in low catalytic performance [65]. In addition, Pt electrocatalyst suffered for poor long-term stability under operational conditions due to dissolution, sintering and particles agglomeration [66]. Thus, utilization of other novel metal such as Pd, Rh, Au and Ir to some extent can promotes higher activity in ORR. Pd-supported on carbon composite reported by several group researchers [67–71]. Matseke et al. [67] reported Pd/PANI/C catalytic activity depends on PANI/C ratio which contributed by synergistic effect between PANI and carbon; 1:2 ratio shows higher performance, followed by 1:1 and 1:3. The Pd/PANI/C (1:2) obeyed 4-electron pathway than other catalysts. Incorporation of correct amounts of PANI into the Pd/C catalyst can avoid agglomerations of Pd nanoparticle and sustain catalytic activity for ORR in alkaline medium. Meanwhile, Bao et al. [68] suggested that synergistic effect of SiO_2 and Pd in Pd/SiO_2@C changed the electronic structure of Pd by producing electron-rich Pd NPs and proves by DFT calculations. Thus, incorporation of SiO_2 enhanced ORR activity of Pd-based catalyst. Besides, preparation method such as immiscible ionic liquid (IL)/water interface as reported by An et al. [70] caused distortion of crystal lattice and surface roughness. The implanted Pd nanoparticles onto Co nanofilms enhanced activity Pdx/Co-nanofilms/C for ORR. The highest ORR catalytic performance showed by Pd_3/Co-nanofilms/C due to synergistic effect of Pd atoms on the surface and the 2D Co nanofilm substrate. The ORR activity is highly affected by Pd/Co atom ratio and varies in different electrolytes. In additional, proper heat-treatment improves cycling stability of Pdx/Co-nanofilms/C compared to pure Pd/C. Wang et al. [71] suggested boron doping on Pd/C catalysts. The B-doping on Pd-B/C increased ORR electrocatalytic activity compared to Pd/C: the ca. factors of. 2.0 and 2.7 higher in acidic media; and ca. factor of 1.3 and 1.6 in alkaline media at 0.85 V and 0.90 V. DFT calculations proves B-doped weakened

Table 2 The synthesis method, physicochemical properties, and catalytic performance of Pt-based on graphene, graphene oxide (GO) and reduced graphene oxide (rGO)

Pt catalysts	Method	Physicochemical properties and catalytic performance	Ref.
Pt/MV–rGO	Wet chemical	Pt/MV–RGO shows higher ORR activity due to the synergetic effect between MV and rGO	[58]
Pt/ NCL–rGO Pt/rGO	Hummer's method, polymerization	Nitrogen-doped carbon layer (NCL) decreased aggregation and agglomeration between separated graphene sheets. Thus, Pt/ NCL-RGO shows better electroactivity and stability towards MOR compared to Pt/RGO due to better dispersion of Pt particles	[59]
Nanometer-sized Pt/graphene	Chemical reduction	Pt loading on graphene plays an important role by enhancing Pt dispersion. Thus, higher performance of Pt/graphene electrocatalyst towards MOR activity id achieved by controlling Pt percentages	[60]
Pt–Co/G/GC		Pt–Co/G/GC shows excellent performance and stability toward MOR. The cobalt core–platinum shell nanoparticles supported on surface functionalized graphene enhanced catalytic activity contributed by dispersion and stabilization of Co@Pt catalyst by using poly (diallyl dimethylammonium chloride) (PDDA). Thus, PDDA-functionalized graphene provided the greater electrochemical active surface area	[61, 62]
Pt/rGO	microwave-assisted polyol	Pt/rGO exhibited excellent performance with high electrochemical active surface area and high CO tolerance compared to commercial Pt/C on the MOR	[63]

(continued)

Table 2 (continued)

Pt catalysts	Method	Physicochemical properties and catalytic performance	Ref.
Pt/C/graphene aerogel (Pt/C/GA)		Pt/C/graphene aerogel shows higher stability compared to commercial Pt/C for MOR activity in an acidic solution. The results obtained shows at the initial stage, Pt/C decreased approximately 40% after 1000 CV cycles. Contrarily, Pt/C/graphene aerogel only decreased 16% of the initial catalytic activity. Therefore, after 200 cycles of CV, Pt/C/graphene aerogel show much higher current density and stability compared to Pt/C	[64]

O-containing species adsorption on Pd surfaces and supported by the XPS and CO stripping analysis.

Lin et al. [72] prepared Rh nanoparticles supported on ultrathin carbon nanosheets (Rh/C nanosheet) by using scalable salt-templated approach for ORR and hydrogenation reaction. The higher current density and durability of Rh/C nanosheets (~93% activity) are observed compared to commercial Pt/C and commercial Rh/C (~74% and ~85% activities) after 20,000 s. In addition, Rh/C nanosheets showed the kinetic constant (k) 4.5 times higher than the commercial Rh/C catalyst in 4-nitrophenol reduction (3.1×10^{-3}). Yuan et al. [73] applied Au and Ir novel in synthesizing AuIr/C, Au/C and Ir/C for ORR and OER. The potential cycling from 0.12 to 1.72 V improves Au surface roughness for the Au/C, thus enhanced the ORR activity. However, irreversible oxidation of the Ir/C degrades ORR activity but not affected on OER activity. Thus, combining Au and Ir in AuIr/C resulted in higher catalytic activity or ORR and OER (up to 50-cycle accelerated aging test) due to Au protection by Ir because of lower electronegativity of Ir. In addition, Bonakdarpour et al. [74] prepared Se/Ru/C electrocatalyst using wet chemical method. The ORR activity of Se/Ru/C electrocatalyst occurs through a H_2O_2 intermediate and highly depends on the amount of the catalyst deposited on the electrode. Thus, low catalyst loading led to a larger fraction of H_2O_2 released into the electrolyte which decrease the ORR activity dramatically. In contrast, increasing the amount of the catalyst on the disk, enhanced H_2O_2 reduction to H_2O.

4 Non-platinum–Carbon Composite Catalyst

In order to achieve high performance of fuel cells, there is a pressing need for the rational design and development of highly efficient cathode catalyst for the ORR [75, 76]. To date, Pt nanoparticles supported on carbon materials (Pt/C) is well-known as the state-of-the-art cathode catalysts in fuel cells owing to excellent ORR catalytic activity. However, due to high cost and severe scarcity of noble metal, the preparation of cheaper, environmentally-friendly, and stable non-precious catalyst for ORR is crucial as an alternative in electrochemical fields [31, 77, 78]. In order to achieve good ORR performance, the electrocatalyst should have considerable specific surface area to provide rich active sites, suitable porous structure for efficient mass transport, and good conductivity for efficient electron transport. The non-precious materials that are commonly used for ORR catalyst including transition metal oxides, metal organic frameworks, etc. However, these materials exhibit poor conductivity cause them often required to be combined with other conductive materials such as carbon for an efficient electron transport.

4.1 Transition Metal Oxides (TMOs)

Transition metal oxides (TMOs) are one of the highly promising alternatives for Pt-based electrocatalyst [79] owing to their low-cost, easier to obtain and control. TMOs are believed to be able to shift the oxidation state in order to facilitate and better tolerate repeated charge transfer [80]. Moreover, they exist in various crystallographic structures to provide ample room for improving their catalytic activities. However, due to their low electrical conductivity, TMOs has been often incorporated onto an electronically conducting material such as carbon-based materials.

Among them, Co_3O_4 is widely studied for ORR electrocatalyst due to the low cost, earth abundance and good stability in alkaline media. Qian et al. reported the fabrication of Co_3O_4 nanoparticles on porous bio-carbon substrate as a promising ORR catalyst, which demonstrated outstanding performance close to commercial 20 wt% Pt/C [81]. The simple and easy method was implemented to prepare Co_3O_4 nanoparticles on the carbon substrate which is by hydrothermal method. The enhanced performance of the ORR reaction is mainly attributable to the synergistic effect of the composite catalyst with unique porous structure, large specific surface area, and good electrical conductivity. Each characteristic plays important roles in facilitating the rapid diffusion of electrolyte ions and oxygen, providing a rich of active sites and efficiently improve charge transfer.

Similarly, Ahmad et al. also reported on the immobilization of Co_3O_4 but with different structure of nanocactus-like on another type carbon-based materials which is CNT (Co_3O_4/CNTs) [82]. These composites are not just promising for ORR, but for oxygen evolution reaction (OER) as well on account of strong interaction between

Co_3O_4 nanoparticles and CNTs, good electron transfer properties and abundant active sites.

Mn oxides also have attained an immense interest due to their high stability, widely available, inexpensive, variable oxidation states and possess effective catalytic properties that are capable to catalyze ORR reaction. Nevertheless, it requires carbon-based materials to accelerate the ORR pathway because of high electrical resistance of Mn [83, 84]. For instance, Hazarika et al. have prepared mesoporous cubic Mn_2O_3 nanoparticles grown on carbon (Vulcan XC 72-R) (Mn_2O_3/C) as highly promising catalyst for both ORR and OER [85]. The synthesized Mn_2O_3/C demonstrate vastly superior ORR activity compared to those of commercially available Pt/C and Pd/C in alkaline media. Taking into account the vital role of carbon-based materials in increasing the electronic conductivity, unsupported Mn_2O_3 shows lower ORR activity compared to Mn_2O_3/C, Pt/C and Pd/C. The synergistic effect of Mn_2O_3 and carbon interface not only resulted in the enhanced catalytic activity, but also on the stability of the catalyst up to 1000 cycles.

4.2 Metal–Organic Framework (MOF)

Metal–organic frameworks (MOFs) are another class of crystalline porous materials that formed from hybridization between organic ligands and metallic ions. A great deal of research has been devoted for MOFs due to their large surface areas with tailorable pore structures and their excellent functionalities as gas adsorbents, gas separators, catalysts, and sensor [86–88]. Currently the application of MOFs has been extended to emerging electrochemistry-related areas such as electrocatalysts and electrodes for supercapacitors and secondary batteries [89, 90]. It has also been reported that MOFs demonstrated good electrocatalytic activities for ORR and/ or OER in alkaline solution [91, 92]. However, similar to the other materials that have been mentioned in previous section, the poor conductivity of most MOFs hinders them to be widely applied as electrocatalyst. Hence, carbon-based materials are highly needed to provide the electrical conductivity of the prepared catalysts.

In example, Fan et al. has prepared bifunctional electrocatalyst with an enhanced performance towards ORR and OER in alkaline media, respectively. The catalyst was prepared by integrating Co–OBA (OBA=4,4′-Oxybis (benzoic acid) MOF and carbon black via hydrothermal reaction [93]. Besides an effective method that has been used, the presence of carbon black (Vulcan XC-72) in the composite greatly enhanced the electrocatalytic activities in terms of their conductivity. The synergistic effect between Co–OBA and carbon black is highly responsible for the promising electrocatalytic performance of the prepared composite catalyst.

Another work done by Jahan et al. shows the assembly of graphene oxide (GO) and copper centered MOF (GO–MOF) as a promising electrocatalyst for tri-functionality including hydrogen evolution reaction (HER), oxygen evolution reaction (OER), and ORR, respectively [94]. This GO–MOF catalyst demonstrated the enhanced electrocatalytic activity as well as stability in acidic media resulted from the uniqueness of

the porous scaffold structure, enhancement of charge transport and the most important is the synergistic interactions between the GO and MOF. The catalytic activity of GO–MOF is higher than that of only Cu-MOF and GO, indicating the importance of synergistic effect of framework porosity, a larger bond polarity caused by oxygen ligand in the GO, and also the catalytically active copper in the hybrid. Moreover, the GO itself plays an important role as a charge sink in order to allow rapid charge transfer in redox reaction, especially at the covalently bonded interface between the Cu-MOF and GO.

5 Heteroatom-Doped Carbon Composite Catalyst

Chen and coworkers prepared nitrogen doped graphene to be hybridized with MnO nanoparticle as high-performance catalyst for ORR [95]. It is believed that electronic properties of graphene can be intrinsically modified by chemical doping with foreign atoms. This novel three-dimensional nitrogen doped reduced graphene/manganese monoxide composite (3D-N-RGO/MnO) catalyst has been developed by incorporating covalent assembly and nitrogen doping. The catalytic performance is enhanced by the synergistic effect of three-dimensional nitrogen doped graphene (3D-N-RGO) and MnO. The importance of using graphite oxide as a growth site has been proven by the morphological study showing a regularly shaped and good dispersion of MnO in comparison to the pure MnO particles which exhibit irregularly shape and aggregation. This nanostructured composite of carbon materials with MnO nanoparticles provide abundant active sites for enhanced electrocatalytic ORR activity. The nitrogen doping site of graphene mainly serve as an active catalytic center for ORR.

In another work by Panomsuwan et al., a composite of nitrogen-doped carbon nanoparticle-carbon nanofiber (NCNP–CNF) as highly efficient and stable ORR catalyst has been developed through solution plasma process-assisted method [96]. The synergistic effects of good electron transport from highly graphitized CNFs, abundance of exposed catalytic sites and meso/microporosity from NCNPs are mainly responsible for the enhancement in ORR activity of this composite catalyst originating from high surface area of the composite. Besides that, NCNP–CNF composite also demonstrates an excellent stability.

Using similar approach to improve the electrocatalytic activity of the catalysts, Xiong and co-workers prepared nitrogen doped on reduced graphene oxide (RGO) to enhance the electrical conductivity, which then further fabricated with carbon microtubes (CMT) [97]. Despite of its attractiveness as a potential electrocatalyst material, the stacking of graphene makes it far from being fully exploited as an electrocatalyst [98, 99]. Therefore, the introduction of CMT as spacers in this hybrid materials is crucial to avoid the graphene restacking. Moreover, CMT also serve as a bridge to transmit the electrons between N-RGO sheets. The fabrication of CMT and N–RGO is achieved by simple combining dipping and chemical vapor deposition methods, which is further used as an outstanding carbonaceous scaffold for PANI nanorod loading via electrodeposition method. The composite material was

then tested for ORR in O_2-saturated 0.1 M KOH solution and demonstrate excellent ORR performance with a larger positive onset potential of −0.12 V and half-wave potential of −0.21 V, which is comparable to that of commercial Pt/C electrode. The synergistic effect between those carbon materials with incorporation of N atoms, as well as PANI plays an important role to contribute towards an excellent performance of ORR.

Xing et al. reported on the preparation of N, S-doped multi-walled carbon nanotubes (MWCNTs) to be functionalized with bimetallic manganese as an efficient electrocatalyst [100]. MWCNTs were chosen as carbon-based supports owing to their high surface area and robust chemical structure [101, 102]. As has been mentioned before, the aim of N doping is to increase the electrical conductivity of carbon materials, hence to limit resistive losses which contribute to the enhancement of electrocatalytic activity. In this work, the electronic structure of the MWCNTs has also been optimized by co-doping with S that has resulted to outstanding ORR performance due to the synergistic effect of dual-doping [103, 104]. The introduction of bimetallic doping of transition metals on MWCNTs has been proven to serve more active electrocatalytic sites and can also successfully tune the electronic properties of the metal centers for optimizing the binding energies for oxygen-based reaction intermediates.

Tavakol and Keshavarzipour [105] investigated the potential of S-doped carbon nanotube (SCNT) by theoretical DFT calculation method. The results obtained agreed that the electrocatalytic ORR of SCNT followed a 4-electron pathway with all reaction species, intermediates and the related transition states were optimized with their energy profile. Thus, the higher efficiency of SCNT towards ORR was recorded by releasing 15.22 eV energy. Concurrently, Macias et al. [42] described potential of S-doped heteroatom towards carbon nanohorns (SCHNs) which synthesized via a modified chemical vapor deposition method (mCVD). The obtained material shows tubular structures with conical and horn-like shapes (sulphur and carbon formed thiophene type bonds). Therefore, ORR carried out by linear sweep voltammetry obtained an acceptable activity for non-Pt electrocatalyst. In addition, S-doped heteroatom exhibited better catalytic activity towards ORR compared to commercialized Pt/C catalysts as reported by Yang et al. [106]. The obtained results from CV test displayed the onset potential for S-doped graphene is close to the Pt/C catalyst and its current density is higher at −0.8 V. Furthermore, this electrocatalyst comply with four-electron-transfer pathway in which oxygen directly reduced to OH^- and calculated n-value to be 3.82 at −0.30 V.

Wang et al. [107] suggested the potential of B-doped graphene nanoribbon (BGNR) as an excellent electrocatalyst for ORR with minimum overpotential (0.36 V) compared to commercialized Pt-based electrocatalyst (0.45 V) in an acidic medium. The DFT calculation on BGNR proves that this electrocatalysts proceed through a 4-electron pathway with para-B distribution leads to high affinity for O_2 adsorption which enhanced ORR activity. Meanwhile, Bo et al. [40] synthesized ordered mesoporous boron-doped carbons (BOMCs) via co-impregnation method followed by carbonization of sucrose and 4-hydroxyphenylboronic acid on SBA-15 silica template. The results show an ordered mesoporous structure with high surface

area and uniform pore size which enhanced ORR catalytic performance in alkaline solution. Thus, synergetic effect between B content and high surface area is the key factor to this excellent performance. Similar work on B-doped carbon composite also reported by Yang et al. [41] which produced metal-free electrocatalysts of boron-doped carbon nanotubes via chemical vapour deposition (CVD) method. The catalytic performance of B-doped/CNT electrocatalyst increased progressively towards ORR with significant B loading. Therefore, they have concluded that B-doped facilitate ORR by creating CNT charged sites favourable to adsorption of O_2 by breaking its electroneutrality properties and effective utilization of carbon π electrons.

Besides that, Qiu et al. [108] studies the effect of P-doping into graphitic carbon nitride (g-C_3N_4) with NH_2-functionalized carbon black (NH_2-CB) composite for efficient electrocatalytic ORR activity. These two materials were mixed together via a novel self-assembly approach driven by the electrostatic interaction between the oppositely charged P–g–C_3N_4 and NH_2–CB, forming three-dimensional porous composite (P–g–C_3N_4@NH_2–CB). This composite demonstrates high surface area with highly exposed ORR active sites. The integration of P into tri-s-triazine rings of g–C_3N_4 further improves the ORR performance, which is much higher than that of g–C_3N_4 precursor and even comparable to Pt/C catalyst in alkaline media.

Chang et al. [46] prepared two-dimensional porous F-doped carbon (FC) nanosheets via scalable salt-templated synthesize method. FC-900 (pyrolyzed at 900 °C) displays excellent ORR activity due to larger spherical surface area (1031 $m^2\ g^{-1}$) and high availability of active sites. Thus, the findings suggested that the synergetic effect between F-doping and material defects offer higher density of active sites in these nanosheets. Furthermore, A–F site obtained 50 time higher in catalytic performance due to bulk-F and zigzag-F total contribution. Similar hard-template method also reported by Wang and Kong [109] in preparation of F-doped mesoporous carbons (F/Cs) from polytetrafluoroethylene (PTFE) supported on SBA-15 silica at 1000 °C. The obtained mesoporous structures contain high surface area (504 $m^2\ g^{-1}$) with graphitic pore walls. Hence, F/Cs exhibited comparable ORR catalytic activity to commercial Pt/C catalysts with better stability and methanol-tolerance in alkaline solutions. Meanwhile, simple preparation method of FG sheet also reported by Guo et al. [110] using thermal pyrolysis of graphene oxide (GO) with zinc fluoride (ZnF_2). The results show that pyrolysis temperature is the key point for controlling F-doped amount and morphology of catalyst. Therefore, FG-1100 (pyrolyzed at 1100 °C) electrocatalyst indicates outstanding performance with more positive onset potential, higher current density and better 4-electron pathway for ORR in the alkaline medium. Furthermore, durability and methanol tolerance ability of FG-1100 much higher than commercial Pt/C catalyst. All in all, the low-cost FG catalyst shows efficient and durable in electrocatalytic performance and suitable replacement for the Pt/C catalyst in promoting the commercialization of fuel cells.

6 Conclusions and Perspective

The interest in developing a promising catalyst for ORR in order to overcome the sluggish kinetic reaction which occurs at the cathode has continuously growth among the research community. In order to attain good ORR performance, the electrocatalyst should have considerable specific surface area to provide rich active sites, suitable porous structure for efficient mass transport, and good conductivity for efficient electron transport. Therefore, this chapter mainly highlights the importance of carbon-based materials as a potentially available candidates to the enhancement of their functionalities for being implemented in the field of electrochemical, specifically on ORR application. Through the unique properties of carbon, the effective composite formation between the carbon and other materials as has been discussed earlier, contributes to the enhancement of electrocatalytic ORR performance through the synergistic effect between both materials. To date, the use of commercial Pt/C catalyst has become the benchmark to efficiently enhanced the ORR performance. Taking into account the relatively high cost and limited supply of Pt, the presence of carbon support in the commercially available platinum-based catalyst is crucial. In addition to that, carbon support plays and important role in enhancing the morphology, structure, and activity of the catalyst, and correspondingly the whole lifetime of a Pt-catalyst. As mentioned before, the high cost of Pt hinders the use of this noble metal as catalyst. Thus, to overcome this problem, the composite formation of carbon and other materials from non-noble metal group has also been discussed in this chapter. From economical point of view, the non-PGM-carbon composite is ideal as an alternative for expensive noble-metal catalyst. The works however not only focusing on that matter, but another modification (functionalization) of carbon materials that has been considered as an effective strategy to tailor the properties of materials for enhancing the catalytic activity, was also highlighted. This strategy has been extensively studies, especially for nitrogen-doped carbon.

Despite all the effort done and the cost of the catalyst that can be significantly reduce as compared to those of commercially available Pt/C catalyst, the reported works are remain far behind in terms of onset potential and reaction current. Since the promising properties of carbon-based materials mostly because of their high surface area, highly conductive, and the unique physicochemical properties, therefore the functionalities of carbon-based materials, can be further developed especially in fundamental studies for transformation of future energy technology.

References

1. Ma R, Lin G, Zhou Y et al (2019) A review of oxygen reduction mechanisms for metal-free carbon-based electrocatalysts. NPJ Comput Mater 5. https://doi.org/10.1038/s41524-019-0210-3
2. Wu G, Santandreu A, Kellogg W et al (2016) Carbon nanocomposite catalysts for oxygen reduction and evolution reactions: from nitrogen doping to transition-metal addition. Nano

Energy 29:83–110. https://doi.org/10.1016/j.nanoen.2015.12.032
3. Song C, Zhang J (2008) Electrocatalytic oxygen reduction reaction. In: PEM fuel cell electrocatalysts and catalyst layers: fundamentals and applications, pp 1–1137
4. Wang ZL, Xu D, Xu JJ, Zhang XB (2014) Oxygen electrocatalysts in metal-air batteries: from aqueous to nonaqueous electrolytes. Chem Soc Rev 43:7746–7786. https://doi.org/10.1039/c3cs60248f
5. Cao R, Lee JS, Liu M, Cho J (2012) Recent progress in non-precious catalysts for metal-air batteries. Adv Energy Mater 2:816–829. https://doi.org/10.1002/aenm.201200013
6. Lam E, Luong JHT (2014) Carbon materials as catalyst supports and catalysts in the transformation of biomass to fuels and chemicals. ACS Catal 4:3393–3410. https://doi.org/10.1021/cs5008393
7. Molina-García MA, Rees NV (2016) Effect of catalyst carbon supports on the oxygen reduction reaction in alkaline media: a comparative study. RSC Adv 6:94669–94681. https://doi.org/10.1039/c6ra18894j
8. Pérez-Rodríguez S, Pastor E, Lázaro MJ (2018) Electrochemical behavior of the carbon black Vulcan XC-72R: influence of the surface chemistry. Int J Hydrogen Energy 43:7911–7922. https://doi.org/10.1016/j.ijhydene.2018.03.040
9. Auer E, Freund A, Pietsch J, Tacke T (1998) Carbons as supports for industrial precious metal catalysts. Appl Catal A Gen 173:259–271. https://doi.org/10.1016/S0926-860X(98)00184-7
10. Noked M, Soffer A, Arubach D (2011) The electrochemistry of activated carbonaceous materials: past, present, and future. J Solid State Electrochem 15:1563–1578. https://doi.org/10.1007/s10008-011-1411-y
11. Fic K, Frackowiak E, Béguin F (2012) Unusual energy enhancement in carbon-based electrochemical capacitors. J Mater Chem 22:24213–24223. https://doi.org/10.1039/c2jm35711a
12. Tang S, Sun G, Qi J et al (2010) Review of new carbon materials as catalyst supports in direct alcohol fuel cells. Chinese J Catal 31:12–17. https://doi.org/10.1016/s1872-2067(09)60034-6
13. Asikin-Mijan N, Lee HV, Abdulkareem-Alsultan G et al (2017) Production of green diesel via cleaner catalytic deoxygenation of *Jatropha curcas* oil. J Clean Prod 167:1048–1059. https://doi.org/10.1016/j.jclepro.2016.10.023
14. Hersam MC (2013) Chem Soc Rev, 2824–2860. https://doi.org/10.1039/c2cs35335k
15. Yang K, Zaffran J, Yang B (2020) Fast prediction of oxygen reduction reaction activity on carbon nanotubes with a localized geometric descriptor. Phys Chem Chem Phys, 890–895. https://doi.org/10.1039/c9cp04885e
16. Borghei M, Lehtonen J, Liu L, Rojas OJ (2017) Advanced biomass-derived electrocatalysts for the oxygen reduction reaction. Adv Mater, 1703691:1–27.https://doi.org/10.1002/adma.201703691
17. Rey-Raap N, Enterría M, Martins JI et al (2019) Influence of multiwalled carbon nanotubes as additives in biomass-derived carbons for supercapacitor applications. ACS Appl Mater Interfaces. https://doi.org/10.1021/acsami.8b19246
18. Ratso S, Käärik M, Kook M et al (2019) High performance catalysts based on Fe/N co-doped carbide-derived carbon and carbon nanotube composites for oxygen reduction reaction in acid media. Int J Hydrogen Energy 44:12636–12648. https://doi.org/10.1016/j.ijhydene.2018.11.080
19. Morais RG, Rey-Raap N, Costa RS et al (2020) Hydrothermal carbon/carbon nanotube composites as electrocatalysts for the oxygen reduction reaction. J Compos Sci 4:6–8. https://doi.org/10.3390/jcs4010020
20. Bogdanovskaya V, Vernigor I, Radina M et al (2020) Carbon nanotube modified by (O, n, p) atoms as effective catalysts for electroreduction of oxygen in alkaline media. Catalysts 10:1–10. https://doi.org/10.3390/catal10080892
21. Sang Y, Fu A, Li H et al (2016) Experimental and theoretical studies on the effect of functional groups on carbon nanotubes to its oxygen reduction reaction activity. Colloids Surfaces A Physicochem Eng Asp 506:476–484. https://doi.org/10.1016/j.colsurfa.2016.07.008

22. Wang X, Ouyang C, Dou S et al (2015) Oxidized carbon nanotubes as an efficient metal-free electrocatalyst for the oxygen reduction reaction. RSC Adv 5:41901–41904. https://doi.org/10.1039/c5ra05172j
23. Maity S, Samanta M, Roychowdhury T et al (2020) Polypyrrole decorated amorphous CNT: a potential ORR electrocatalyst in alkaline medium. In: 3RD international conference on condensed matter and applied physics (ICC-2019), p 080039
24. Chen S, Huang Q, Yang W et al (2018) Pt–CoN supported on TiN-modified carbon nanotubes (Pt–CoN/TiN–CNT) as efficient oxygen reduction reaction catalysts in acidic medium. Int J Hydrogen Energy 43:14337–14346. https://doi.org/10.1016/j.ijhydene.2018.06.003
25. Aleksandrzak M, Mijowska E (2015) Graphene and its derivatives for energy storage
26. Alemour B, Yaacob MH, Lim HN, Hassan MR (2018) Review of electrical properties of graphene conductive composites. Int J Nanoelectron Mater 11:371–398
27. Bin WJ, Ren Z, Hou Y et al (2020) A review of graphene synthesis at low temperatures by CVD methods. Xinxing Tan Cailiao/New Carbon Mater 35:193–208. https://doi.org/10.1016/S1872-5805(20)60484-X
28. Pei S, Cheng HM (2012) The reduction of graphene oxide. Carbon N Y 50:3210–3228. https://doi.org/10.1016/j.carbon.2011.11.010
29. Dreyer DR, Park S, Bielawski CW, Ruoff RS (2010) The chemistry of graphene oxide. Chem Soc Rev 39:228–240. https://doi.org/10.1039/b917103g
30. Shahgaldi S, Hamelin J (2015) Improved carbon nanostructures as a novel catalyst support in the cathode side of PEMFC: a critical review. Carbon N Y 94:705–728. https://doi.org/10.1016/j.carbon.2015.07.055
31. Liu X, Dai L (2016) Carbon-based metal-free catalysts. Nat Rev Mater 1.https://doi.org/10.1038/natrevmats.2016.64
32. Hu C, Dai L (2019) Doping of carbon materials for metal-free electrocatalysis. Adv Mater 31:1–17. https://doi.org/10.1002/adma.201804672
33. Daems N, Sheng X, Vankelecom IFJ, Pescarmona PP (2014) Metal-free doped carbon materials as electrocatalysts for the oxygen reduction reaction. J Mater Chem A 2:4085–4110. https://doi.org/10.1039/c3ta14043a
34. Gong K, Du F, Xia Z, et al (2009) Nitrogen-doped carbon nanotube arrays with high electrocatalytic activity for oxygen reduction. Science (80-) 323:760–764. https://doi.org/10.1126/science.1168049
35. Zhao S, Wang D, Amal R, Dai L (2019) Carbon-based metal-free catalysts for key reactions involved in energy conversion and storage. Adv Mater, 1801526:1–22. https://doi.org/10.1002/adma.201801526
36. Yang L, Shui J, Du L et al (2019) Carbon-based metal-free ORR electrocatalysts for fuel cells. Past, Present, and Future 1804799:1–20. https://doi.org/10.1002/adma.201804799
37. Li J, Hou P, Liu C (2017) Heteroatom-doped carbon nanotube and graphene-based electrocatalysts for oxygen reduction reaction. Small, 1702002:1–13. https://doi.org/10.1002/smll.201702002
38. Strelko VV, Kuts VS, Thrower PA (2000) On the mechanism of possible influence of heteroatoms of nitrogen, boron and phosphorus in a carbon matrix on the catalytic activity of carbons in electron transfer reactions. Carbon N Y 38:1499–1503. https://doi.org/10.1016/S0008-6223(00)00121-4
39. Guo MQ, Huang JQ, Kong XY et al (2016) Hydrothermal synthesis of porous phosphorus-doped carbon nanotubes and their use in the oxygen reduction reaction and lithium-sulfur batteries. Xinxing Tan Cailiao/New Carbon Mater 31:352–362. https://doi.org/10.1016/S1872-5805(16)60019-7
40. Bo X, Guo L (2013) Ordered mesoporous boron-doped carbons as metal-free electrocatalysts for the oxygen reduction reaction in alkaline solution. Phys Chem Chem Phys 15:2459–2465. https://doi.org/10.1039/c2cp43541a
41. Yang L, Jiang S, Zhao Y et al (2011) Boron-doped carbon nanotubes as metal-free electrocatalysts for the oxygen reduction reaction. Angew Chemie 123:7270–7273. https://doi.org/10.1002/ange.201101287

42. Montiel Macias E, Valenzuela-Muñiz AM, Alonso-Núñez G et al (2020) Sulfur doped carbon nanohorns towards oxygen reduction reaction. Diam Relat Mater 103:107671. https://doi.org/10.1016/j.diamond.2019.107671
43. Xu D, Duo WuW (2019) The role of sulfur-related species in oxygen reduction reactions. Chalcogen Chem. https://doi.org/10.5772/intechopen.78647
44. Zhou J, Lian J, Hou L, et al (2015) Ultrahigh volumetric capacitance and cyclic stability of fluorine and nitrogen co-doped carbon microspheres. Nat Commun 6. https://doi.org/10.1038/ncomms9503
45. Panomsuwan G, Saito N, Ishizaki T (2015) Simple one-step synthesis of fluorine-doped carbon nanoparticles as potential alternative metal-free electrocatalysts for oxygen reduction reaction. J Mater Chem A 3:9972-9981A. https://doi.org/10.1039/c5ta00244c
46. Chang Y, Chen J, Jia J et al (2021) The fluorine-doped and defects engineered carbon nanosheets as advanced electrocatalysts for oxygen electroreduction. Appl Catal B Environ 284:119721. https://doi.org/10.1016/j.apcatb.2020.119721
47. Ramli ZAC, Kamarudin SK (2018) Platinum-based catalysts on various carbon supports and conducting polymers for direct methanol fuel cell applications: a review. Nanoscale Res Lett 13.https://doi.org/10.1186/s11671-018-2799-4
48. Mirabile Gattia D, Antisari MV, Giorgi L et al (2009) Study of different nanostructured carbon supports for fuel cell catalysts. J Power Sources 194:243–251. https://doi.org/10.1016/j.jpowsour.2009.04.058
49. Wang G, Sun G, Wang Q et al (2010) Effect of carbon black additive in Pt black cathode catalyst layer on direct methanol fuel cell performance. Int J Hydrogen Energy 35:11245–11253. https://doi.org/10.1016/j.ijhydene.2010.07.045
50. Karousos DS, Desdenakis KI, Sakkas PM et al (2017) Sonoelectrochemical one-pot synthesis of Pt–carbon black nanocomposite PEMFC electrocatalyst. Ultrason Sonochem 35:591–597. https://doi.org/10.1016/j.ultsonch.2016.05.023
51. Sattler ML, Ross PN (1986) The surface structure of Pt crystallites supported on carbon black. Ultramicroscopy 20:21–28. https://doi.org/10.1016/0304-3991(86)90163-4
52. Jeng KT, Chien CC, Hsu NY et al (2006) Performance of direct methanol fuel cell using carbon nanotube-supported Pt-Ru anode catalyst with controlled composition. J Power Sources 160:97–104. https://doi.org/10.1016/j.jpowsour.2006.01.057
53. Show Y, Hirai A, Almowarai A, Ueno Y (2015) Platinum catalyst formed on carbon nanotube by the in-liquid plasma method for fuel cell. Thin Solid Films 596:198–200. https://doi.org/10.1016/j.tsf.2015.08.053
54. Matsuda N, Nakashima T, Kato T, Shiroishi H (2014) Synthesis of multiwall carbon nanotube-supported platinum catalysts by solution plasma processing for oxygen reduction in polymer electrolyte fuel cells. Electrochim Acta 146:73–78. https://doi.org/10.1016/j.electacta.2014.07.127
55. Jha N, Leela Mohana Reddy A, Shaijumon MM et al (2008) Pt-Ru/multi-walled carbon nanotubes as electrocatalysts for direct methanol fuel cell. Int J Hydrogen Energy 33:427–433. https://doi.org/10.1016/j.ijhydene.2007.07.064
56. Wang X, Zhang J, Zhu H (2011) Pt-Au/CNT@TiO_2 as a high-performance anode catalyst for direct methanol fuel cells. Cuihua Xuebao/Chinese J Catal 32:74–79. https://doi.org/10.1016/s1872-2067(10)60163-5
57. Wu G, Xu BQ (2007) Carbon nanotube supported Pt electrodes for methanol oxidation: a comparison between multi- and single-walled carbon nanotubes. J Power Sources 174:148–158. https://doi.org/10.1016/j.jpowsour.2007.08.024
58. Ma J, Wang L, Mu X, Cao Y (2015) Enhanced electrocatalytic activity of Pt nanoparticles supported on functionalized graphene for methanol oxidation and oxygen reduction. J Colloid Interface Sci 457:102–107. https://doi.org/10.1016/j.jcis.2015.06.031
59. Zhang X, Yuan W, Duan J et al (2015) Graphene nanosheets modified by nitrogen-doped carbon layer to support Pt nanoparticles for direct methanol fuel cell. Microelectron Eng 141:234–237. https://doi.org/10.1016/j.mee.2015.03.061

60. Qiu JD, Wang GC, Liang RP et al (2011) Controllable deposition of platinum nanoparticles on graphene as an electrocatalyst for direct methanol fuel cells. J Phys Chem C 115:15639–15645. https://doi.org/10.1021/jp200580u
61. Zhang M, Li Y, Yan Z et al (2015) Improved catalytic activity of cobalt core-platinum shell nanoparticles supported on surface functionalized graphene for methanol electro-oxidation. Electrochim Acta 158:81–88. https://doi.org/10.1016/j.electacta.2015.01.160
62. Félix-Navarro RM, Beltrán-Gastélum M, Reynoso-Soto EA et al (2016) Bimetallic Pt-Au nanoparticles supported on multi-wall carbon nanotubes as electrocatalysts for oxygen reduction. Renew Energy 87:31–41. https://doi.org/10.1016/j.renene.2015.09.060
63. Sharma S, Ganguly A, Papakonstantinou P et al (2010) Rapid microwave synthesis of CO tolerant Reduced graphene oxide-supported platinum electrocatalysts for oxidation of methanol. J Phys Chem C 114:19459–19466. https://doi.org/10.1021/jp107872z
64. Wang F, Xu L, Yang J et al (2017) Enhanced catalytic performance of Ir catalysts supported on ceria-based solid solutions for methane dry reforming reaction. Catal Today 281:295–303. https://doi.org/10.1016/j.cattod.2016.03.055
65. Tang Z, Wu W, Wang K (2018) Oxygen reduction reaction catalyzed by noble metal clusters. Catalysts 8.https://doi.org/10.3390/catal8020065
66. Chen W, Chen S (2009) Oxygen electroreduction catalyzed by gold nanoclusters: strong core size effects. Angew Chemie 121:4450–4453. https://doi.org/10.1002/ange.200901185
67. Matseke MS, Munonde TS, Mallick K, Zheng H (2019) Pd/PANI/C nanocomposites as electrocatalysts for oxygen reduction reaction in alkaline media. Electrocatalysis 10:436–444. https://doi.org/10.1007/s12678-019-00536-3
68. Bao Z, Zhou H, Song X et al (2019) Enhanced oxygen reduction activity on carbon supported Pd nanoparticles via SiO_2. ChemCatChem 11:1278–1285. https://doi.org/10.1002/cctc.201801511
69. Xiao W, Liutheviciene Cordeiro MA, Gong M et al (2017) Optimizing the ORR activity of Pd based nanocatalysts by tuning their strain and particle size. J Mater Chem A 5:9867–9872. https://doi.org/10.1039/c7ta02479g
70. An LL, Chen Y, Shi J et al (2018) Oxygen reduction activity and stability of composite Pdx/Co-nanofilms/C electrocatalysts in acid and alkaline media. Front Chem 6:1–10. https://doi.org/10.3389/fchem.2018.00596
71. Wang M, Qin X, Jiang K et al (2017) Electrocatalytic activities of oxygen reduction reaction on Pd/C and Pd-B/C catalysts. J Phys Chem C 121:3416–3423. https://doi.org/10.1021/acs.jpcc.6b12026
72. Lin C, Wu G, Li H et al (2017) Rh nanoparticles supported on ultrathin carbon nanosheets for high-performance oxygen reduction reaction and catalytic hydrogenation. Nanoscale 9:1834–1839. https://doi.org/10.1039/c6nr09739a
73. Yuan L, Yan Z, Jiang L et al (2016) Gold-iridium bifunctional electrocatalyst for oxygen reduction and oxygen evolution reactions. J Energy Chem 25:805–810. https://doi.org/10.1016/j.jechem.2016.04.013
74. Bonakdarpour A, Delacote C, Yang R et al (2008) Loading of Se/Ru/C electrocatalyst on a rotating ring-disk electrode and the loading impact on a H_2O_2 release during oxygen reduction reaction. Electrochem commun 10:611–615. https://doi.org/10.1016/j.elecom.2008.02.004
75. Shao Y, Cheng Y, Duan W et al (2015) Nanostructured electrocatalysts for PEM fuel cells and redox flow batteries: a selected review. ACS Catal 5:7288–7298. https://doi.org/10.1021/acscatal.5b01737
76. Shui J, Wang M, Du F, Dai L (2015) N-doped carbon nanomaterials are durable catalysts for oxygen reduction reaction in acidic fuel cells. Sci Adv 1:1–8. https://doi.org/10.1126/sciadv.1400129
77. Chen L, Xu X, Yang W, Jia J (2020) Recent advances in carbon-based electrocatalysts for oxygen reduction reaction. Chinese Chem Lett 31:626–634. https://doi.org/10.1016/j.cclet.2019.08.008
78. Li W, Wang D, Zhang Y et al (2020) Defect engineering for fuel-cell electrocatalysts. Adv Mater 32:1–20. https://doi.org/10.1002/adma.201907879

79. Wang Y, Liang Z, Zheng H, Cao R (2020) Recent progress on defect-rich transition metal oxides and their energy-related applications. Chem Asian J 15:3717–3736. https://doi.org/10.1002/asia.202000925
80. Toh RJ, Sofer Z, Pumera M (2015) Transition metal oxides for the oxygen reduction reaction: influence of the oxidation states of the metal and its position on the periodic table. ChemPhysChem 16:3527–3531. https://doi.org/10.1002/cphc.201500483
81. Qian C, Guo X, Zhang W et al (2019) Co_3O_4 nanoparticles on porous bio-carbon substrate as catalyst for oxygen reduction reaction. Microporous Mesoporous Mater 277:45–51. https://doi.org/10.1016/j.micromeso.2018.10.020
82. Ahmed MS, Choi B, Kim YB (2018) Development of highly active bifunctional electrocatalyst using coon carbon nanotubes for oxygen reduction and oxygen evolution. Sci Rep 8:1–10. https://doi.org/10.1038/s41598-018-20974-1
83. Goswami C, Hazarika KK, Bharali P (2018) Transition metal oxide nanocatalysts for oxygen reduction reaction. Mater Sci Energy Technol 1:117–128. https://doi.org/10.1016/j.mset.2018.06.005
84. Zhao A, Masa J, Xia W et al (2014) Spinel Mn-Co oxide in N-doped carbon nanotubes as a bifunctional electrocatalyst synthesized by oxidative cutting. J Am Chem Soc 136:7551–7554. https://doi.org/10.1021/ja502532y
85. Hazarika KK, Goswami C, Saikia H et al (2018) Cubic Mn_2O_3 nanoparticles on carbon as bifunctional electrocatalyst for oxygen reduction and oxygen evolution reactions. Mol Catal 451:153–160. https://doi.org/10.1016/j.mcat.2017.12.012
86. Wu D, Guo X, Sun H, Navrotsky A (2016) Interplay of confinement and surface energetics in the interaction of water with a metal-organic framework. J Phys Chem C 120:7562–7567. https://doi.org/10.1021/acs.jpcc.5b12239
87. Decoste JB, Peterson GW, Schindler BJ et al (2013) The effect of water adsorption on the structure of the carboxylate containing metal-organic frameworks Cu-BTC, Mg-MOF-74, and UiO-66. J Mater Chem A 1:11922–11932. https://doi.org/10.1039/c3ta12497e
88. Chen L, Zhang X, Cheng X et al (2020) The function of metal-organic frameworks in the application of MOF-based composites. Nanoscale Adv 2:2628–2647. https://doi.org/10.1039/d0na00184h
89. Meng J, Liu X, Niu C et al (2020) Advances in metal-organic framework coatings: versatile synthesis and broad applications. Chem Soc Rev 49:3142–3186. https://doi.org/10.1039/c9cs00806c
90. Xu X, Liu J, Liu J et al (2018) A general metal-organic framework (MOF)-derived selenidation strategy for in situ carbon-encapsulated metal selenides as high-rate anodes for Na-ion batteries. Adv Funct Mater 28:1–12. https://doi.org/10.1002/adfm.201707573
91. Ma X, Zhao X, Sun J et al (2016) A versatile strategy to fabricate MOFs/carbon material integrations and their derivatives for enhanced electrocatalysis. RSC Adv 6:7728–7735. https://doi.org/10.1039/c5ra21998a
92. Gadipelli S, Zhao T, Shevlin SA, Guo Z (2016) Switching effective oxygen reduction and evolution performance by controlled graphitization of a cobalt-nitrogen-carbon framework system. Energy Environ Sci 9:1661–1667. https://doi.org/10.1039/c6ee00551a
93. Fan T, Yin F, Wang H et al (2017) A metal–organic-framework/carbon composite with enhanced bifunctional electrocatalytic activities towards oxygen reduction/evolution reactions. Int J Hydrogen Energy 42:17376–17385. https://doi.org/10.1016/j.ijhydene.2017.02.063
94. Jahan M, Liu Z, Loh KP (2013) A graphene oxide and copper-centered metal organic framework composite as a tri-functional catalyst for HER, OER, and ORR. Adv Funct Mater 23:5363–5372. https://doi.org/10.1002/adfm.201300510
95. Chen R, Yan J, Liu Y, Li J (2015) Three-dimensional nitrogen-doped graphene/MnO nanoparticle hybrids as a high-performance catalyst for oxygen reduction reaction. J Phys Chem C 119:8032–8037. https://doi.org/10.1021/acs.jpcc.5b00306
96. Panomsuwan G, Saito N, Ishizaki T (2016) Nitrogen-doped carbon nanoparticle-carbon nanofiber composite as an efficient metal-free cathode catalyst for oxygen reduction reaction. ACS Appl Mater Interfaces 8:6962–6971. https://doi.org/10.1021/acsami.5b10493

97. Xiong C, Yang Q, Dang W et al (2020) Fabrication of eco-friendly carbon microtubes @ nitrogen-doped reduced graphene oxide hybrid as an excellent carbonaceous scaffold to load MnO_2 nanowall (PANI nanorod) as bifunctional material for high-performance supercapacitor and oxygen reduction react. J Power Sources 447:227387. https://doi.org/10.1016/j.jpowsour.2019.227387
98. Oh SM, Patil SB, Jin X, Hwang SJ (2018) Recent applications of 2D inorganic nanosheets for emerging energy storage system. Chem Eur J 24:4757–4773. https://doi.org/10.1002/chem.201704284
99. Mohd Sidek HB, Jo YK, Kim IY, Hwang SJ (2016) Stabilization of layered double oxide in hybrid matrix of graphene and layered metal oxide nanosheets: an effective way to explore efficient CO_2 adsorbent. J Phys Chem C 120:23421–23429. https://doi.org/10.1021/acs.jpcc.6b08065
100. Xing X, Liu R, Anjass M et al (2020) Bimetallic manganese-vanadium functionalized N, S-doped carbon nanotubes as efficient oxygen evolution and oxygen reduction electrocatalysts. Appl Catal B Environ 277:119195. https://doi.org/10.1016/j.apcatb.2020.119195
101. Lu X, Zhao C (2013) Highly efficient and robust oxygen evolution catalysts achieved by anchoring nanocrystalline cobalt oxides onto mildly oxidized multiwalled carbon nanotubes. J Mater Chem A 1:12053–12059. https://doi.org/10.1039/c3ta12912h
102. Gao T, Jin Z, Zhang Y et al (2017) Coupling cobalt-iron bimetallic nitrides and N-doped multi-walled carbon nanotubes as high-performance bifunctional catalysts for oxygen evolution and reduction reaction. Electrochim Acta 258:51–60. https://doi.org/10.1016/j.electacta.2017.07.172
103. Wang D, Zhang K, Liao L et al (2019) Synthesis of nitrogen and sulfur co-doped sisal fiber carbon and its electrochemical performance in lithium-ion battery. Int J Electrochem Sci 14:102–113. https://doi.org/10.20964/2019.01.53
104. Su Y, Zhang Y, Zhuang X et al (2013) Low-temperature synthesis of nitrogen/sulfur co-doped three-dimensional graphene frameworks as efficient metal-free electrocatalyst for oxygen reduction reaction. Carbon N Y 62:296–301. https://doi.org/10.1016/j.carbon.2013.05.067
105. Tavakol H, Keshavarzipour F (2016) A sulfur doped carbon nanotube as a potential catalyst for the oxygen reduction reaction. RSC Adv 6:63084–63090. https://doi.org/10.1039/c6ra11447d
106. Yang Z, Yao Z, Li G et al (2012) Sulfur-doped graphene as an efficient metal-free cathode catalyst for oxygen reduction. ACS Nano 6:205–211
107. Wang L, Dong H, Guo Z et al (2016) Potential application of novel boron-doped graphene nanoribbon as oxygen reduction reaction catalyst. J Phys Chem C 120:17427–17434. https://doi.org/10.1021/acs.jpcc.6b04639
108. Qiu Y, Xin L, Jia F et al (2016) Three-dimensional phosphorus-doped graphitic-C_3N_4 self-assembly with NH_2-functionalized carbon composite materials for enhanced oxygen reduction reaction. Langmuir 32:12569–12578. https://doi.org/10.1021/acs.langmuir.6b02498
109. Wang H, Kong A (2014) Mesoporous fluorine-doped carbon as efficient cathode material for oxygen reduction reaction. Mater Lett 136:384–387. https://doi.org/10.1016/j.matlet.2014.08.081
110. Guo J, Zhang J, Zhao H et al (2018) Fluorine-doped graphene with an outstanding electrocatalytic performance for efficient oxygen reduction reaction in alkaline solution. R Soc Open Sci 5.https://doi.org/10.1098/rsos.180925

Carbon Composites as Metal-Free Catalysts

Sefika Kaya, Aykut Caglar, Tulin Avci Hansu, Berdan Ulas, Anish Khan, and Hilal Kivrak

Abstract In recent years, carbon-based metal-free composites have come to the fore with their superior properties. Carbon-based materials attract the attention of researchers with porous structure, high surface areas, catalytic activity, high selectivity, thermal stability, mechanical strength, and chemical stability. Surface areas of these materials can be developed by functionalizing with various groups. They are widely used with these features in many fields such as electronics, energy, and materials science. In addition, they are preferred as an adsorbent as they provide high adsorption efficiency for heavy metal and dye removal from wastewater. In this study, recent studies in which carbon-based materials are used in hydrogen production and solar cell systems as catalysts have been investigated. The carbon-based materials used as adsorbents have been also researched and compared.

Keywords Carbon-based composite · Metal-free · Hydrogen production · Solar cell · Wastewater treatment

1 Introduction

Industry developments and increasing population increased energy consumption. With the danger of extinction of fossil fuels, renewable energy sources have come

S. Kaya · A. Caglar · H. Kivrak (✉)
Department of Chemical Engineering, Faculty of Engineering and Architectural Sciences, Eskisehir Osmangazi University, Eskişehir, Turkey
e-mail: hilalkivrak@gmail.com; hilaldemir.kivrak@ogu.edu.tr

A. Caglar · B. Ulas
Department of Chemical Engineering, Faculty of Engineering, Van Yuzuncu Yil University, Van, Turkey

T. A. Hansu
Department of Chemical Engineering, Faculty of Engineering, Siirt University, Siirt, Turkey

A. Khan
Center of Excellence for Advanced Materials Research, King Abdulaziz University, Jeddah 21589, Saudi Arabia

M. Jawaid and A. Khan (eds.), *Carbon Composite Catalysts*, Composites Science and Technology, https://doi.org/10.1007/978-981-19-1750-9_5

to the fore [1]. Hydrogen is an environmentally friendly type of energy which is non-toxic because it does not release harmful gases to the environment. Since this energy has high efficiency and power, it is the most important energy source of the next century [2]. In the studies so far, hydrogen production has been carried out with many different technologies such as hydrogen production from fossil fuels, photocatalyst, water splitting, and biomass conversion [3].

Increasing energy consumption has led to the demand for energy conversion and storage devices to store energy produced by renewable energy sources and to use energy whenever we want [4]. Solar cells, metal-air batteries, fuel cells, and electrolysis cells stand out as energy storage and conversion technology. Catalytic reactions (oxygen reduction reaction (ORR) and oxygen evolution reaction (OER)) are of great importance in the development of many renewable energy conversion and storage technologies. Platinum, palladium, ruthenium, and iridium based electrocatalysts, which are frequently used for catalytic reactions, have high cost and limited reserve as well as good catalytic activation [5, 6]. In addition, metal-based catalysts generally have poor durability, low selectivity, and harmful environmental effects [7]. Carbon-based metal-free materials as catalyst support have properties such as high selectivity, high activity, thermal, and chemical stability. It has attracted the attention of researchers with its large surface area, pore size developed with functional groups, alkali, and acid resistance [8].

Water resources are polluted due to the discharge of wastewater from domestic, industrial, and agricultural activities without treatment. Non-biodegradable, dangerous, and toxic pollutants in wastewater are heavy metals and dyes. These pollutants cause adverse effects on human health and ecosystem due to their toxic, mutagenic, and carcinogenic effects. Adsorption is the most widely used method for removing heavy metals and dyes from wastewater and many different adsorbents (activated carbons, clay minerals, zeolites, silica etc.) have been used in studies so far. Today, carbon-based adsorbents provide effective adsorption with their porous structure, large surface areas, and high metal selectivity [9, 10]. In this study, carbon-based metal-free composites used as catalysts and adsorbents have been investigated in recent years.

2 Hydrogen Production

2.1 Introduction

Today, due to the development of technology, the increasing demand for energy is increasing rapidly. Increasing population density and increasing needs in recent years has also increased the interest in energy. The fact that fossil resources are limited and not environmentally friendly has led researchers to tend towards new energy resources [11]. Hydrogen energy is the energy of the future due to its high energy efficiency, easy usability, safe storage and outstanding advantages such as being

environmentally friendly as well as being environmentally friendly [12]. Hydrogen can be found as an abundant element in many substances in nature (i.e. freshwater and seawater, biomass, hydrogen sulfide, and fossil fuels). Hydrogen cannot be used directly as energy since it is generally found in various compounds. In order to be used as energy, it is used by separating from its compounds, that is, it must be transformed. There are many studies in the literature on hydrogen production. There are two types of hydrogen production methods: hydrogen production from fossil sources and hydrogen production from renewable resources, respectively. Firstly, it includes methods such as hydrocarbon reforming and pyrolysis from fossil fuels. In the hydrocarbon reforming method is the conversion of hydrogen-containing chemicals with steam, autothermal steam reform and chemical oxidation. Secondly, it involves hydrogen production methods from renewable sources from water and biomass [13]. The concept of storage, which is the next stage of hydrogen production, is also important in terms of hydrogen energy. Because the storage of hydrogen is as important as its production. Due to its reliability and ease of portability, one of the most preferred methods in this regard is the method of storage by attaching to chemical (hydride) compounds by reaction [14–16].

Since many types of catalysts are used in hydrogen production, it is important in catalyst production and materials used in production. Carbon materials are considered metal-free catalysts due to their very good physical and chemical properties and abundance. In this section, various hydrogen production methods will be examined in the literature. The advantages, disadvantages and energy efficiency of carbon-based metal-free catalysts used in hydrogen production will be compared. Hydrogen production methods are given in Fig. 1.

2.2 Metal-Free Catalysts for Hydrogen Production

In addition to the different methods used in hydrogen production, there are many types of hydrogen production in the presence of a catalyst. Since many types of catalysts are used in hydrogen production in practice, it can be said that studies on catalyst production have a wide range of fields. Therefore, the interest in the production of the catalyst, which has a key role in hydrogen production, is also on a large scale and it is increasing day by day. There are various renewable energy technologies in alternative energy sources. These are energy sources such as fuel cells, supercapacitors, lithium ion batteries, hydrogen production [14, 17, 18]. The catalyst is a fundamental process and important in most of these energy technologies. In this section, recent developments in the literature on the use of carbon-based metal-free catalysts used in energy technologies are given.

Carbon-containing materials can be prepared from wood derivatives by chemical processes and hydrothermal methods. Here, Demirci et al. [19] prepared porous carbon (PC) particles by removing silica. Later, PC particles were modified with polyethyleneimine (PEI) and amine functional PC-PEI particles were prepared. Hydrochloric acid is protonated with PC-PEI + and its activity is increased.

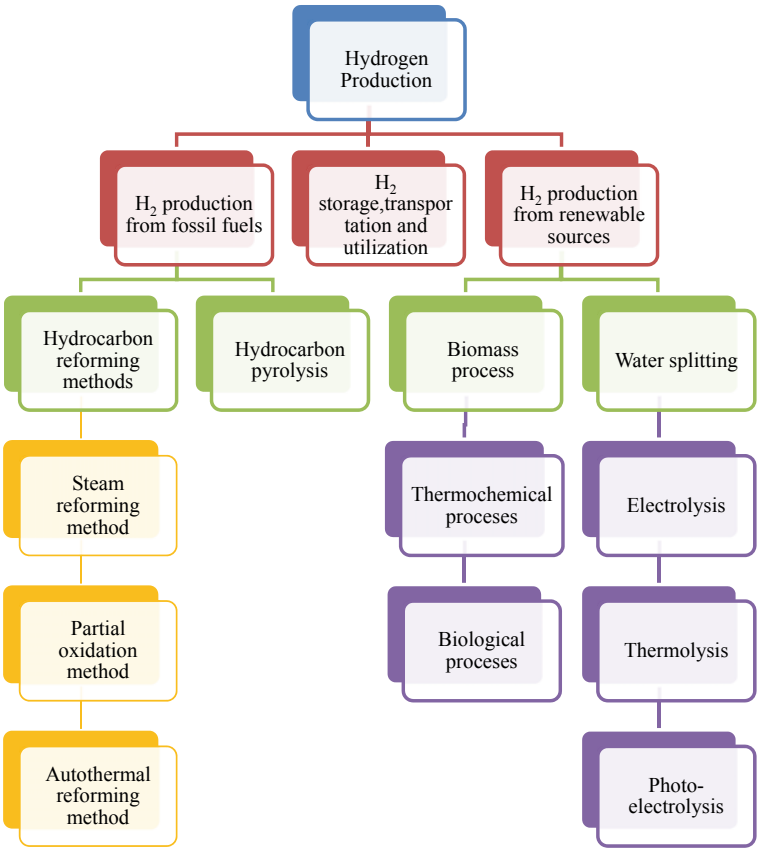

Fig. 1 Hydrogen production methods

These carbon-based particles prepared were used as metal-free catalysts to produce hydrogen from $NaBH_4$ methanolysis. In the methanolysis experiments conducted at 25 °C, the initial rate of the reaction was found to be 4040 $_{ml}$ $H_2 g_{cat} min^{-1}$. In the kinetic calculations made, the activation energy of the reaction was calculated as 23.9 kJ/mol. This study investigated the catalytic ozonation of a model naphthenic acid (NA) compound (1,3-Adamantanedicarboxylic acid; ADA) using carbon-based metal-free materials as a catalyst [20].

When hydrogen is produced from non-fossil sources, it is the emission-free fuel of the future. Biomass gasification or electrolysis of water are environmentally friendly ways. Here, the production of a carbon-based electrode from biomass for hydrogen production is presented [21]. The theoretical and technical feasibility of using carbon to produce hydrogen has been shown in the study. It has also been shown that chemical modification can further improve performance characteristics for the catalytic process. In short, this study proposes a chemical energy conversion concept for the use of carbon electrodes to convert electricity from the sun into hydrogen by splitting

water. Here, a carbon-based metal-free catalyst has been proposed as an alternative to noble metal catalysts for the oxygen reduction reaction (ORR), which is important for fuel cell performance [22]. Efficient carbon-based nitrogen-doped electrocatalysts derived from waste biomass are considered promising in fuel cell applications. In this study, coconut palm leaves were used as a carbon source. The carbon-based material was prepared by an easy and light ultrasound-assisted method. The carbon material obtained showed good catalytic activity compared to the commercial Pt/C catalyst when different starting potentials were applied. This work provided a prediction to support an environmentally friendly approach to design and use metal-free carbon-based catalysts.

Carbon-based metal-free catalysts (C-MFCE) are widely used as electrocatalysts, as they consist of nanostructured carbon allotropes of different sizes [23]. C-MFEC is used to produce electrodes with high energy storage, as they have low density and can bind to catalytically active sites. Efficient electrocatalysts are essential for the development of fuel cells and metal-air cells. In this review article, the importance of carbon-based metal-free catalysts in energy storage and production is emphasized. Electrocatalysts are important for the development of renewable energy technologies and other technologies. Metal-based catalysts are generally not preferred in new technologies because of their high cost, low selectivity, poor durability, impurity poisoning and negative effects on the environment. In this review article, a review of recent developments in the field of carbon-based metal-free catalysts is presented [24]. A brief overview of the various reactions involved in renewable energy conversion and storage, including the oxygen reduction reaction, hydrogen evolution reaction, hydrogen production, multifunctional electrocatalysis, is presented.

Catalysts are also used to obtain hydrogen from the splitting of water. Using solar energy to split water in H_2 production is an environmentally friendly method. Photocatalyst properties to be used in hydrogen production are given in Fig. 2. As can be seen in the figure, carbon-based metal-free catalysts are preferred because of

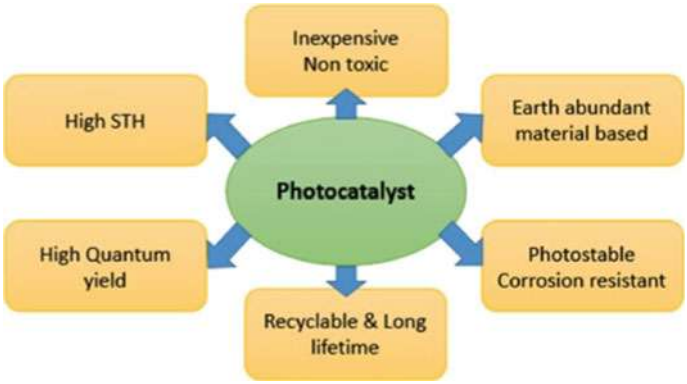

Fig. 2 Properties of photocatalysts to be used in hydrogen production (reproduced with permission from Elsevier) [25]

Table 1 Comparison of hydrogen production in the presence of a carbon-based metal-free catalyst

Catalyst	Activation energy (Ea) (kj/mol)	HGR ml $H_2 g_{cat} min^{-1}$	References
DSCG-1 M CH_3COOH	25.23	3171.4	[27]
Organik waste-100%H_3PO_4	9.81	8335.5	[28]
PC-PEI+	23.9	4040	[19]
MWCNT-COOH	20.1	8776	[29]
Polymeric microgels	30.17	3018	[30]
SPM-H_3PO_4-H	17.79	3975	[31]
DSCG-Zn	7.87	8510.1	[32]

their non-toxicity, stability and recyclability. This review article investigates the latest developments in carbon-based metal-free photocatalysts in photocatalytic water splitting for H_2 production [25]. As a result of the investigations, the importance of photocatalyst design and photocatalytic reactor was emphasized, comparing the efficiency of photocatalysts for economically viable H_2 production.

In this study, hydrogen was rapidly produced from the methanolysis of $NaBH_4$ in the presence of a carbon-based metal-free catalyst [26]. Polyethyleneimine (PEI) microgels were prepared by microemulsion polymerization. Prepared microgels are protonated with hydrochloric acid treatment (p-PEI). It is then converted to quaternized (q-PEI) -bromobutane, 1-bromohexane and 1-bromooctane by modification reaction with bromo alkanes with different alkyl chain lengths such as methyl iodide and 1-bromoethane, 1. The carbon-based metal-free catalyst prepared in this way was used in the methanolysis of $NaBH_4$. In the presence of this catalyst obtained in optimum conditions, the methanolysis reaction was completed in 1.5 min. As a result of kinetic calculations, the activation energy of the reaction was found to be 20.9 kJ/mol, and the initial rate as 8013 ml $H_2 g_{cat} min^{-1}$. A comparison of the activities of some carbon-based metal-free catalysts used in the production of hydrogen from $NaBH_4$ in the literature is given in Table 1. As can be seen from the table, it has been proven that catalysts obtained without the use of metals have good catalytic activity.

3 Metal-Free Catalysts for Dye Sensitized Solar Cells

A significant part of the energy need is met by energy conversion systems based on fossil fuels. Recent studies indicate that fossil fuels will run out in about 20 years [33, 34]. Solar cells, on the other hand, are a good alternative to fossil fuels and studies on this subject have been going on since 1954 [35]. Monocrystalline and polycrystalline silicon materials are seen as the starting point of first generation solar cells [36, 37]. The difficulty and high cost of the production processes of the first generation solar cells prevented their commercialization [38]. Second generation

solar cells made of amorphous silicon have a low power conversion efficiency of 10–15% [39]. Second generation solar cells are more acceptable than first generation solar cells in terms of cost and production methods. Studies on third generation solar cells such as organic tandem solar cells, quantum dot solar cells, organic/inorganic perovskite solar cells, dye-sensitized solar cells (DSSCs) and inorganic solar cells continue for the commercialization of these solar cells [40]. Among these solar cells, DSSCs have recently received a great deal of attention. DSSCs offer diversity in terms of used materials and have low light performance [41]. This diversity allows DSSCs to be produced at a lower cost with a high mechanical strength. The ability of DSSCs to work in cloudy environments allows for more widespread use [42]. Despite some problems to be overcome, DSSC technology has very high potential for commercialization. One of these problems is the low power conversion density (PCE) of DSSCs. Researchers have developed innovative and inexpensive materials for use in the photoanode and counter electrode components of DSSC for a higher PCE. Researchers aim to increase the electron transfer rate and reduce the interface resistance with innovative electrode materials. In addition to these parameters, the high light collection efficiency of the electrode has a positive effect on PCE [43].

DSSCs consist of four main components namely photoanode, counter electrode, dye sensitizing layer, and electrolyte [44]. The surface of the counter electrode is coated with catalyst such as Pt, Pd or carbon [45]. As seen in Fig. 3, illuminating the surface of TiO_2 causes the excitation of electrons in the dye molecules and allows the absorption of the dye molecules. The excited electrons are transferred from the conduction band of TiO_2 to the external circuit and complete the circuit by moving towards the counter electrode. Oxidized dye molecules, on the other hand, gain electrons during the redox reaction and become stable [46]. As with other electrochemical phenomena, the area of the working electrode is an important parameter

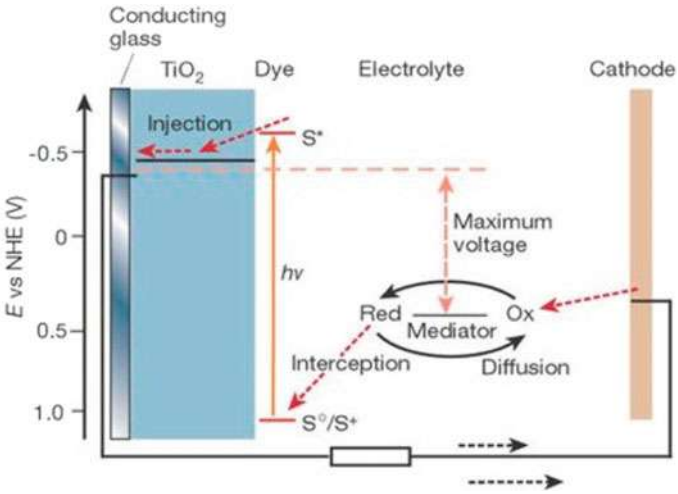

Fig. 3 Schematic represantation of a DSSC [60]

for high-performance electron transport [47]. Another factor that determines the performance of the working electrode is the amount of dye molecule that it can adsorb on its surface [44]. Semiconductor metal oxides are the main component of the photoanode, and the adsorption of dye molecules takes place in this section of the DSSC [48]. Generally, TiO_2 [49] has been used as photoanode in the literature, but the photoanode performance of metal oxides such as WO_3 [50], Au-TiO_2-SiO_2 [51], ZnO [52], Fe_2O_3 [53], Ag_2O [54], SnO_2 [55], and Nb_2O_5 [56] have also been investigated. The dye sensitizer is covalently bonded to the photoanode composed of metal oxide [57]. The main task of the dye sensitizer is to absorb the sunlight and make the dye molecule excited [58]. Electrolyte provides regeneration of oxidized dye by redox reactions [59].

The performances of DSSCs are determined and compared with the power conversion efficiency (PCE). V_{OC}, J_{SC}, FF and P_{in} in Eq. (1) symbolize open circuit voltage (mV), photocurrent density (mA/cm^2), fill factor, and power density, respectively. Iqbal et al. researched the working principle of DSSCs, reactionally and the mentioned reactions are given in Eqs. (1–7) [61, 62] where S is sensitizer and S^* is photoexcited.

$$PCE = \frac{V_{OC} J_{SC} FF}{P_{in}} \times 100 \tag{1}$$

$$TiO_2 - S + hv \rightarrow TiO_2 - S^* \quad Photoexciation \tag{2}$$

$$TiO_2 - S^* + hv \rightarrow TiO_2 - S^+ + e^- CB(TiO_2) \quad ChargeInjection \tag{3}$$

$$TiO_2 - S^* \rightarrow TiO_2 - S + hv + \Delta \quad Relaxation \tag{4}$$

$$TiO_2 - S^+ + 2I^- \rightarrow TiO_2 - S + I_2^* \quad Regeneration \tag{5}$$

$$TiO_2 - S^+ + e^-(TiO_2) \rightarrow TiO_2 - S \quad Recombination \tag{6}$$

$$e^-(TiO_2) + I_2 \rightarrow I_2^* \quad BackReaction \tag{7}$$

3.1 Composite of TiO_2 with Carbonaceous Materials for Photoanode

TiO_2 has very good properties for use in DSSCs and outperforms other metal oxides reported above. However, the photoanode performance of TiO_2 is still not sufficient for high energy demand applications. Previously, TiO_2 could be prepared in

various morphologies such as nanotube [63], film [64], nanowire [65], and nanocube [66], and improvements in DSSC performances were observed with these morphologies of TiO_2. However, DSSC performance of composites consisting of TiO_2 and carbonaceous materials has been investigated due to the limitations arising from the synthesis procedures of TiO_2 in these different morphologies. Carbonaceous compounds, together with TiO_2, are suitable composite components for photoanodes in DSSCs because they increase electron mobility [67], have high chemical stability [68], and are electrically conductive.

CNT/TiO_2 composites have been frequently used in DSSCs as they reduce the effects of recombination [69, 70]. CNT contributes to this composite photoanode system by both increasing electron mobility [71] and providing electron conduction path [72]. The positive effect of electron mobility on PCE is due to the reduction of recombination between the injected electrons and the electrolyte [73]. The distribution of CNTs is also an important factor affecting the performance of the photoanode [74]. TiO_2/MWCNTs photoanode were prepared by Mehmood et al., and researchers emphasized that power conversion efficiency of 0.03 wt% MWCNT including TiO_2 exhibited 30% greater than bare TiO_2 containing photoanode. The researchers explained the increased power conversion efficiency by increasing the surface area in the presence of CNT and by binding more dye molecules to the surface. Another reason for the increase in photoanode performance is that CNT increases the injection efficiency of electrons [69]. Yu et al. synthesized films from composites of hollow sphere TiO_2/CNT and investigated the DSSC photoanode performance. The researchers claimed that the CNT/TiO_2 ratio has a significant effect on the power conversion efficiency. While it was emphasized that dye adsorption was negatively affected at high CNT loadings, it was found that electron transport increased at low CNT loadings. In addition, it has been stated that the hollow morphological structure of TiO_2 facilitates the diffusion of the electrolyte [75]. In another study, Ho et al. coated the surface of CNT with TiO_2 by solgel method and confirmed the TiO_2 coating with SEM images. It is stated that the prepared photoanode system has 41% higher power conversion efficiency than pristine TiO_2 [76]. Cai et al., on the other hand, obtained CNT/TiO_2 composite by treating CNT with acid. The power conversion efficiency of the CNT/TiO_2 composite was reported as 6.23%, and it was emphasized that this performance was 63% higher than that of commercial TiO_2. This increase in power conversion efficiency has been attributed to the increased electron mobility with existence of CNT [77].

Graphene has a higher surface area than CNT, and its bandgap could be modified with several modifications. These properties cause the electron mobility of graphene to be high, and thus it is a good candidate for photoanode for DSSC [78]. The performance of two-dimensional graphene sheets is higher than that of CNT in terms of transport of injected electrons [79]. Therefore, strong interaction of graphene with TiO_2 results in lower recombination at the electrolyte resulting in higher PCE [80]. Kazmi et al. reported that the DSSC performance of the Graphene/TiO_2 composite was higher than that of pure TiO_2. The photoconversion efficiency of Graphene/TiO_2 was found to be 7.68%. The researchers attributed the improved power conversion efficiency to increased light absorption, shortened charge transfer distance, and

reduced charge recombination with the incorporation of graphene into the structure [81]. Song et al. also investigated the effect of the ratios of the components of the Graphene/TiO_2 composite on DSSC performance. The researchers reported the energy conversion efficiency as 6.29%, emphasizing the positive contribution of graphene to electron transfer as in previous studies [82].

Apart from graphene and CNT as photoanode in DSSCs, carbon derivatives such as CNF, activated carbon, mesoporous carbon have also been reported. The photoanode performances of metal oxides such as Nb_2O_5, SnO_2, ZnO, Zn_2SnO_4, CdS, and GaAs instead of TiO_2 have been studied in detail, but the literature on the composite performance of these metal oxides with carbon-based materials is limited, and more studies are needed.

3.2 Carbonaceous Material-Based Composites for Counter Electrode

The counter electrode is also a crucial component of DSSCs, and precious metal-free alternative counter electrode materials are of interest to researchers. As mentioned before, CE acts as a catalyst in the reduction of I^{-3} and gains the electron from the external circuit to the electrolyte. Therefore, the design of conductive CEs with high catalytic activity is a vital issue for the continuity of DSSCs. Previously, Pt with high catalytic activity was used in DSSCs like other electrochemical power conversion devices [83]. However, because Pt does not perform well in all electrolyte types, being difficult to find, and being expensive, researchers first turned to Pt-containing alloys and then to Pt-free composite materials and carbon-based materials.

A high amount of carbon is required to achieve the performance of Pt-based CE containing DSSCs [81]. The high catalytic activity, low cost, and high stability of carbon-based materials make carbon-based materials suitable candidates as CE materials in DSCCs [84]. Carbon derivatives such as CNTs, activated carbon, graphene, CNF, graphite, carbon black have been investigated previously as CE materials. It is known that the electrocatalytic activities of these carbon derivatives increase with the introduction of heteroatoms such as sulfur, phosphorus, oxygen and nitrogen into the carbon structure [85]. The heteroatoms in the structure allow the formation of active sites on the carbon surface for the reactants to interact [86].

Carbon black is spherical and amorphous [87]. Carbon black-based composites are of interest due to their high conductivity and electrocatalytic activity [88]. Particle size and charge transfer resistance are the main factors affecting the electrocatalytic activity of carbon black. Liu et al. have developed a Graphite/Carbon black composite for use as CE in DSSCs. Researchers reported that with 0.5% Pt loading, the electrochemically active surface area increased to 109.37 m^2/g. It has been reported that increased electrochemical surface area causes enhanced energy conversion efficiency of 7.61% [89]. Don et al. also prepared a CE from Graphite/Carbon black composite and reported the power conversion efficiency as 5.06% for a 3:1 Carbon

black/Graphite ratio. Researchers have reported that it has a significant effect on electron transfer kinetics of components of composite materials [88]. Narudin et al. also prepared a Graphite/Carbon black composite, but the researchers used TTIP and ZrO_2 to increase interparticle bonding. While the FF and PCE values of the Graphite/Carbon black composite without binder were reported as 42.4% and 3.67%, these values increased to 56.9% and 5.74%, respectively, in the presence of TTIP binder. Researchers claimed that TTIP facilitates charge transfer at the CE and electrolyte interface by lowering the charge transfer resistance [90]. Jaafar et al., who prepared the Carbon black/TiO_2 composite with the solid state method, investigated the effect of annealing temperature on DSSC performance, and the photovoltaic properties namely J_{SC}, V_{OC}, FF and PCE of the annealed composite at 525 °C were determined as 6.10 mA/cm^2, 0.51 V, 0.89, and 2.77%, respectively. Researchers reported that annealing treatment at optimum temperature reduces the charge transfer resistance and allows a better catalytic activity. In other words, annealing caused an increase in electron transfer between the counter electrode and the electrolyte [91].

Apart from Carbon black/Graphite, another carbon derivative that is frequently reported as CE material in DSSCs is graphene. The untreated graphene surface does not contain any functional groups and behaves as inert in catalytic reactions [92]. But with surface modifications, active sites can be created and the bandgap opens, and graphene becomes catalytically active. The most common reported method for activating graphene is the introduction of one or more heteroatoms into the structure of composite [93]. Tang et al. investigated the counter electrode photovoltaic performance of 3DGN/RGO composite material for DSSC. It was emphasized that 3DGN has suitable channels for electron transport and that RGO provides good contact at the electrolyte/CE interface. The power conversion efficiency of 3DGN/RGO composite has been reported as 9.79% [94]. In another study conducted by Sahito et al., rGO was coated on cotton fabric (GCF) and its performance as CE was investigated. The composite material in question exhibited 2.52% PCE, and the performance was found to be insufficient according to the CEs prepared with Pt. But this composite was found to be important in terms of being flexible and light. In addition, other photovoltaic properties of GCF such as J_{SC}, V_{OC}, FF have been reported as 9.08 mA/cm^2, 0.64 V and 42.97%, respectively. Although the photovoltaic properties of Pt coated FTO (J_{SC} = 14.88 mA/cm^2, V_{OC} = 0.66 V, FF = 71.18% and PCE = 7.2%) were higher than GCF, the researchers emphasized that the electrode they obtained was better in terms of cost [95]. In the study conducted by Battumur et al., the CE performance of the Graphene/CNT composite was investigated, and the power conversion efficiency was reported as 4.0%. In addition, photovoltaic properties such as J_{SC}, V_{OC}, and FF are reported as 8.8 mA/cm^2, 0.77 V, and 0.58, while these parameters are reported as 0.74 V, 0.67 and 5.0% for Pt. From these results, it is seen that the Graphene/CNT metal-free composite is competitive with Pt based CE for DSSC [96].

Contrary to graphene, CNTs are used as CE material in DSSCs with their bare state because of their electrocatalytic activity caused defects in their structure [97]. Besides the structural defects, metal impurities in the CNT are also one of the causes of a good electrocatalytic activity. The conductivity and catalytic properties of CNTs can

Table 2 Literature on carbon-based metal-free catalyst for DSSC

Materials	J_{SC} (mA/cm^{-2})	V_{oc} (V)	FF (%)	PCE (%)	References
Carbon from sugar	17.10	0.66	71	6.72	[104]
Carbon derived from Bpy	13.10	0.65	61	5.24	[105]
Graphite-like composite	10.11	0.69	68	4.73	[106]
Graphene-SWNT	12.7	0.7	56.5	5.17	[107]
N-CNOs/mGr	23.19	0.763	58	10.28	[108]
Carbon black/polymer	10.94	0.668	0.632	4.62	[109]
Gr/PANI	16.28	0.67	0.67	7.17	[110]
GnP/AC	15.8	0.767	69.994	8.478	[111]
WC/C-NF	13.96	0.63	0.66	5.85	[112]
MWCNTs/Ppy	14.83	0.77	0.65	7.42	[113]
TiN–CCB	14.29	0.791	0.70	7.92	[114]
GMWNTs	5.6	0.76	0.70	3.0	[115]
Graphite/CNT/CB	14.81	0.65	0.71	6.94	[116]
TiC/CNF	13.43	0.62	53.66	4.47	[103]

also be improved by incorporating conductive polymers into composite structures [98]. Kurokawa et al. increased the electron conductivity of CNT by introducing Poly (diallyl dimethylammonium chloride) (PDDA) into the composite structure. The power conversion efficiency of the 15 μm thick CE electrode was reported as 4.12%. Other photovoltaic properties of CNT/PDDA such as FF, V_{OC}, and J_{SC} have been reported as 45.64%, 0.7 V, and 12.82 mA/cm^2, and it has been emphasized that all these parameters affecting performance are higher than those of CNT (J_{SC} = 10.31 mA/cm^2, V_{OC} = 0.67 V, FF = 40.62 and PCE = 2.78%) [99]. Leu et al. prepared CNT/B composite and reported that boron significantly increased the thermal stability. The power conversion efficiency of CNT/B was stated to be 7.91%, and a power conversion efficiency close to that of Pt CE was obtained (PCE = 8.03%). The increase in the catalytic activity of CNT/B (relative to pristene CNT) has been attributed to the defects that boron creates on the CNT [100].

CNFs have similar properties to CNTs in terms of surface area, catalytic activity and mechanical properties. The most reported sythesis method for obtaining CNFs is the CVD method [101]. Similar to other types of carbon, DSSC performance is strongly dependent on surface defects and surface area, as well as graphitization [102]. Therefore, researchers apply carbonization at around 1000–1500 °C to increase the degree of graphitization. Xie et al. prepared TiC/CNF films by electrospinning and emphasized that the increase in the amount of TiC increases the electrical conductivity. They also stated that TiC/CNFs are competitive with Pt-based CEs in terms of power conversion efficiency. The increased DSSC performance has been attributed to the flexibility, high electrochemically active surface area, conductivity and electrocatalytic activity of the CNF film [103]. As can be seen from the studies reported above, the performance of carbon-based and metal-free CEs can

compete with those made of precious metals. Table 2 summarizes a brief literature about the performances of carbon-based metal-free catalysts for DSSCs.

4 Wastewater Treatment

Water is the most important resource for life and development of alive. In addition, it has great importance in subjects such as energy production, food security, ecosystem, biodiversity [117]. In recent years, industrialization, rapid population growth, and urbanization have negatively affected the clean water resources, causing them to decrease rapidly. However, global water demand increases every year, various types of pollution pose a threat to potential water resources [118]. Water pollution is one of the biggest environmental problems in the world. The water pollution is caused by the discharge of used water into the environment (lake, river, and ocean, etc.) without any treatment [119]. As a result, the physical, chemical, and biological properties of the water resources change and become harmful to animals, humans, and the environment [120].

Industrial, domestic, and agricultural wastewater are the main sources of the water pollution. All these sources contain high amounts of toxic pollutants. The wastewater discharged into the environment without treatment creates serious problems for surface and groundwater [121, 122]. Domestic wastewater includes many persistent organic pollutants such as polycyclic aromatic hydrocarbons, polychlorinated biphenyls, nitrogen, phosphorus, heavy metals, and pathogenic microorganisms [123, 124]. Chemical fertilizers and pesticides used in agricultural activities mix into water resources and create pollution. In case these pollutants enter the food chain, they create serious danger to the ecosystem and human health [121, 125]. Large quantities of water are used in many industries. Therefore, industrial wastewater constitutes the majority of the water pollution. Dye, textile, mining, paper, medicine, leather, food, and petroleum industries are the leading industries where water is used excessively [118, 126]. Compared to domestic and agricultural wastewater sources, the most important pollutants from industrial wastewater are heavy metals and dyes. Since heavy metals are not metabolized in the body, they accumulate in tissues and cause a toxic effect [127]. Dyes are toxic, mutagenic, and carcinogenic for all living things. Dyes in wastewater form a layer on the water surface, preventing the passage of sunlight and the ecosystem deteriorates since photosynthetic activity decreases [128, 129].

All wastewater must be treated before discharging to the environment. Many physical, chemical, and biological treatment methods have been examined in studies so far [121]. In this context, wastewater treatment methods such as precipitation, filtration, coagulation-flocculation, biological treatment, electrochemical methods, ion exchange, membrane, and adsorption have been investigated [130, 131]. Adsorption among these methods, it stands out due to its advantages such as simple equipment requirement, low energy consumption, ability to be combined with many treatment

methods, effective adsorption process with fast kinetics and ability to purify a wide variety of pollutants [132, 133].

4.1 Heavy Metal Removal

Heavy metals are elements in the third or higher period of the periodic table with an atomic density greater than 4 ± 1 g/cm^3 an atomic weight between 63.5 and 200.6 [134, 135]. Heavy metals such as Cu, Cd, Pb, Zn, Sn, Fe, Al, Hg, Mn, Ag, Co, Ni, As, Cr are generally the most common toxic heavy metals in soil and water systems. Heavy metals pass into animal and human bodies by the way of discharging industrial wastewater to drinking water and inhalation from the air as aerosol. However, heavy metals often mix with the soil, combining stronger with organic substances in the soil. Heavy metals in the soil pollute surface water with erosion, as well as pass into underground waters depending on soil properties. Plants and agricultural products grown in these regions contain heavy metals. Heavy metals in the soil pass from plants to animals and humans through the food chain. Heavy metals accumulate in the tissues of animals, which feed on plants in order to survive, and cause health problems. Heavy metals reach people through food, respiration, and skin contact. Living organisms normally need some heavy metals (such as Co, Fe, Cu, Mn, Mo, V, Se, and Zn) up to certain limits. However, the accumulation of heavy metals in the human body causes many health problems such as organ and nervous system damages, carcinogenic, mutagenic, and allergic effects since they have high toxicity [136–139]. The health effects and sources contaminations of some toxic heavy metals are reported in Table 3 [140, 141].

Among the heavy metal removal methods, adsorption comes to the fore in terms of being able to develop, ease of application, efficiency, and low cost. With the adsorption method, toxic organic and inorganic contaminants are easily separated from the aqueous environment and the separated toxic materials can be disposed of without affecting the biological structures [142, 143].

Adsorption is a type of phase transfer process used to remove atoms, ions or molecules from liquid phases (gas or liquid), in which substances form a surface and inter-surface film on the adsorbent surface [144]. Adsorbents are porous organic or inorganic materials and many different materials can be used in the adsorption process. Materials used as adsorbents should have high adsorption capacity against target pollutants in order to provide efficient treatment in wastewater. Many materials such as activated carbons, clay minerals, zeolites, silica, industrial, and agricultural wastes and biological materials have been used as adsorbents in the studies so far [135, 145]. These materials are low-cost, but they cannot provide the desired adsorption efficiency in removing heavy metals from wastewater. Therefore, the development of novel and effective adsorbents is one of the most active research topics in recent years.

Table 3 The health effects and sources of various heavy metals

Heavy metal	Health effects	Sources
Copper	Wilson's disease, stomachache, liver damage, insomnia, mental disorder, inflammation, cramps	Mining, refining ores, electroplating, smelting operations, fertilizer industries, battery, paper, tannery industries
Lead	Anaemia, diseases of the kidneys, damage the nervous system and circulatory system, mental retardation, cancer	Lead acid batteries, metal plating, mining, paints, thermal power plants
Nickel	DNA damage, chronic bronchitis, cancer of the lungs, chronic asthma, dermatitis, coughing	Electroplating, metal plating, nickel–cadmium battery industries, paper, textile, pesticides, petrochemical, smelting operations
Mercury	Rheumatoid arthritis, damage to kidneys, circulatory system and nervous system, headache, cerebral disorders	Chlor-alkali plants, coal-fired power stations, mineral deposits, industrial processes
Chromium	Lung and sinus cancer, severe diarrhea, nausea and vomiting, headache, kidney damage, dermatitis	Mining, electroplating, metal plating, leather tanning, dyeing, fertilizer, cement, plastic
Arsenic	Carcinogenic, dermatological, internal organ tumors, diabetes, neurological diseases, vascular diseases	Mining, metallurgy, smelting operations, thermal power plants, geogenic and natural processes, pesticides
Cadmium	Kidney damage, carcinogenic, bronchiolitis, skeletal damage, testicular degeneration	Waste batteries, metal plating, paint industries, mining, fuel combustion
Zinc	Stomach cramps, anemia, depression, neurological signs, skin irritations, respiratory disorders	Pharmaceuticals, smelting, paints, galvanizing, cosmetics, pigments

4.1.1 Carbon Composite Materials Employed for the Removal of Heavy Metal

Carbon-Mesoporous Silica Composite

Mesoporous silicas are preferred for the removal of contaminants due to their properties such as large surface area, equal sized pores, chemical, and thermal stability, and high pore volumes. In addition, they are effective adsorbents for certain types of contaminants as they can be developed by adding functional groups to the surface [146].

In 1990, porous silica particles were produced by Kuroda et al. using cationic surfactants and the mesoporous silica, called FSM-16 (Folded Sheet Mesoporous Material) with uniform pore distribution, was synthesized. In 1992, scientists at Mobil Oil Corporation developed MCM (Mobile Crystal Material) silica particles with similar properties and named M41S. The three most important structures of the

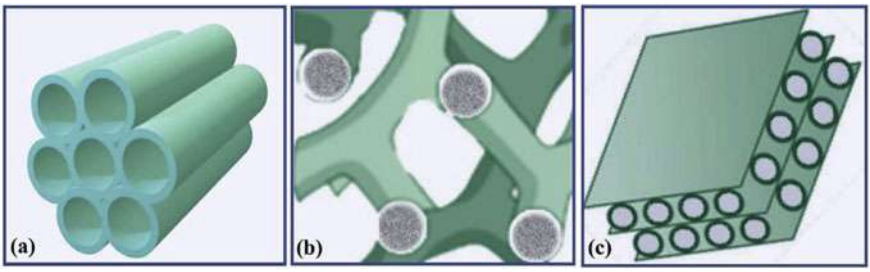

Fig. 4 Structure of MCM-41 (**a**), MCM-48 (**b**), and MCM-50 (**c**) mesoporous silica materials (reproduced with permission from Elsevier) [147]

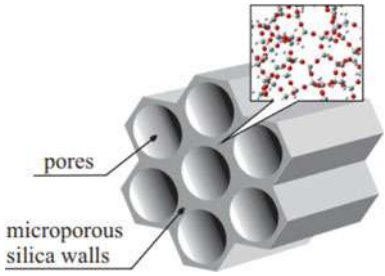

Fig. 5 Structure of SBA-15 mesoporous silica material [151]

M41S family, MCM-41 (two-dimensional (2D), hexagonal P6mm), MCM-48 (three-dimensional (3D), cubic Ia3d), and MCM-50 (layered (1D)), were synthesized under basic conditions in the presence of ionic surfactants (Fig. 4).

In 1995, HMS (Hexagonal Mesoporous Silica) was synthesized by Tanev and Pinnavaia via neutral templates. In 1998, Stucky et al. completed the synthesis of SBA-15 (Santa Barbara Amorphous). SBA-15 has a hexagonal structure with uniform pore size of up to 30 nm (Fig. 5). Since its pores can be improved with different applications, it is often preferred in studies [147–150].

In recent studies, mesoporous silicas have been functionalized with various functional groups. Thus, the active areas on the surface for the adsorption process increased and effective adsorbents were formed. Table 4 summarizes of recent studies for the adsorption of heavy metal by functionalized mesoporous silica composites. Lachowicz et al. have used functionalized SBA-15 with triethylenetetramine chelating (TETA) for Cu(II) and Zn(II) removal. In adsorption processes, the results revealed that the adsorption capacities were achieved as 23.9 mg/g for Cu(II) and 13.6 mg/g for Zn(II) [146]. Chen et al. have developed a new adsorbent NH_2/MCM-41/NTAA which has functionalized with amine and nitrilotriacetic acid anhydride (NTAA). They emphasized that the synthesized adsorbent was effective for adsorption Pb(II) and MnO_4^- from wastewater, reusable and recyclable [152]. Wang et al. have synthesized magnetic mesoporous silica and graphene oxide (MMSP-GO) composite and used the composite in the removal of Pb(II) and Cd(II) heavy metals. It is found that functionalization with PEI molecules provides large surface areas

Table 4 Adsorption of heavy metal by functionalized mesoporous silica composites

Adsorbents	Adsorbates	Surface area, m^2/g	Pore volume, cm^3/g	Pore size, nm	Adsorption capacity, mg/g	References
MDA-magMCM-48 Magnetic MCM-48 with amine and melamine-based dendrimer amines (MDA)	Pb(II) Cu(II) Cr(VI) Cd(II)	511	0.44	3.46	127.24 125.80 115.60 114.08	[157]
NH_2/MCM-41/NTAA	Pb(II) MnO_4^-	627	0.46	2.13	147 156	[152]
s-MCM-41-NH l-MCM-41-NH_2	Cr(VI)	774 517	0.4 0.3	2.5 2.4	86.4 63.3	[158]
Chitosan-MCM-41-A	Pb(II)	738.3	0.92	3.40	90.91	[159]
Chitosan/MCM-48 β-cyclodextrin/MCM-48	Cd(II)	587 544	0.73 0.68	5.71 5.52	122.4 152.2	[160]
SDS-MCM-41 MCM-41 with sodium dodecyl sulfate (SDS)	Cd(II) Cu(II) Zn(II)	285	0.22	3.14	8.61 9.37 5.90	[161]
SBA-15/TETA	Cu(II) Zn(II)	373	0.60	–	23.9 13.6	[146]
SBA-16-G SBA-16 with guanine (G)	Pb(II) Hg(II) Cd(II)	524	0.77	9.2	289.9 259.9 228.8	[162]
NH_2-SBA-15	Pb(II)	457.8	0.65	5.93	131	[163]
NZVI-SH-HMS Magnetic HMS with with thiol (SH) and nanometer zero-valent iron (NZVI)	Pb(II) Cd(II)	312.84	–	2.56	487.8 330.0	[164]
MCS Mesoporous calcium silicate	Ni(II) Cu(II) Zn(II) Pb(II) Mn(II) Cd(II)	239.42	–	11.74	278.35 389.85 402.46 452.42 200.88 437.42	[165]
MMS Magnetic mesoporous silica	Cu(II) Co(II)	298.7	–	–	132 99.1	[166]
A-SBA-15 SBA-15 with 2-acetylthiophene (A)	Cr(III)	335.6	0.68	8.1	111.73	[167]
GO-SBA-15	Pb(II)	–	–	–	255.10	[168]
MMSP-GO	Pb(II) Cd(II)	–	–	–	333 167	[153]

(continued)

Table 4 (continued)

Adsorbents	Adsorbates	Surface area, m^2/g	Pore volume, cm^3/g	Pore size, nm	Adsorption capacity, mg/g		References
NN-mSiO_2@MWCNTs	Cu(II) Ni(II) Pb(II) Zn(II)	100.554	0.420	1.674	74.627 – – –		[154]
GO-SiO_2	Pb(II) As(III)	858	0.389	5.3	527 30		[155]
M-O-MC	Cu(II)	179	0.18	2.9	59.4		[156]
GO-OMS-20 Graphene oxide-ordered mesoporous silica	Cd(II) Cr(III) Hg(II) Pb(II)	872.90	1.28	6.32	– – – –		[169]
C_{KIT-6} C_{KIT-6}-70-5 C_{KIT-6}-100-5 C_{ST} C_{ST}-70-5 C_{ST}-100-5 Oxidized mesoporous carbon (C)	Co(II) Ni(II)	821 643 23 426 221 0.66	1.10 0.73 0.02 0.44 0.20 0.002	5.41 5.18 10.70 4.12 3.60 14.60	Co(II) 72.99 90.09 156.25 69.44 88.49 140.85	Ni(II) 49.51 92.59 149.25 62.11 81.97 129.87	[170]
CKD-ox Silica–carbon sample (CKD) with acidic oxygen groups (ox)	Cu(II9 Pb(II) Zn(II)	350	0.46	7.6	61 82 87		[171]
PGOSBA SBA-15 with polyamidoamine (P) and graphene oxide (GO)	Cd(II) As(III) Tetracycline Ciprofloxacin Ivermectin	97.3	0.271	0.10	92.4 22.3 29.2 24.6 0.292		[172]

for chemical reaction with graphene oxide layers and activates surface functions. In adsorption studies, the adsorption capacities for Pb(II) and Cd(II) were obtained as 333 and 167 mg/g, respectively [153]. Yang et al. have synthesized a new adsorbent (NN-mSiO_2@MWCNTs) of mesoporous silica functionalized with diamine on multi-walled carbon nanotubes. The removal of Cu(II), Ni(II), Pb(II), and Zn(II) from aqueous solution was examined by using NN-mSiO_2@MWCNTs as adsorbent. In this study, in which the advantages of both carbon nanotube and mesoporous silica material are combined, it is reported that the synthesized adsorbent is effective for heavy metal removal [154]. Barik et al. have synthesized mesoporous silica-graphene oxide nanocomposite (GO-SiO_2). The nanocomposite synthesized using ionic liquid (IL) assisted solvothermal method was applied for removal of Pb(II) and As(III). In the study, they reported that a high surface area (858 m^2/g) mesoporous composite was obtained by using IL as a template [155]. Yi et al. have investigated adsorption

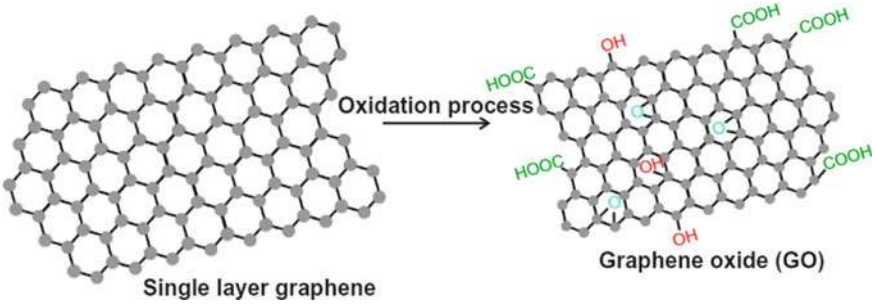

Fig. 6 Structure of graphene and graphene oxide (reproduced with permission from Elsevier) [175]

of Cu(II) by using oxidized mesoporous carbon-based magnetic composite (M-O-MC). The composite has surface area of 179 m^2/g and average particle size of 232 ± 63 nm. The analyzes showed that carboxyl functional groups on the composite surface were effective in the adsorption of Cu(II). The adsorption capacity of Cu(II) was reported as 51.4 mg/g [156].

Graphene and Graphene Oxide Composites

Carbon-based materials have attracted attention as new adsorbents in heavy metal removal from wastewater in recent years. Graphene (G) stands out with its large surface area, interconnected porous structure, small particle size, functionalized derivatives and high adsorption efficiency.

Graphene is an atomically thin, 2-dimensional (2D) honeycomb leaf of sp^2 carbon atoms. Graphene has high mechanical strength, electrical conductivity, large surface area, very good mechanical, and chemical properties. They are used as adsorbents in areas such as sensors, structural composites, capacitors, battery electrodes, polymers, and in adsorption processes [173].

Graphene oxide (GO) has a hexagonal carbon structure similar to graphene. It is formed as a result of the combination of graphene with single-layer oxygen-based functional groups by chemical oxidation. It is one of the graphene derivatives containing hydroxyl, carboxyl, epoxide, ketone, and other oxygen containing functional groups. Graphene oxides have large surface areas (approximately 2620 m^2/g) [174]. Structure of graphene and graphene oxide are shown in Fig. 6.

The recent studies for the adsorption of heavy metal by graphene and graphene oxide composites summarizes in Table 5. He et al. have synthesized graphene hydrogel (rGO) by reducing graphene oxide (GO) with ascorbic acid for U(VI) removal from aqueous solutions. In adsorption process, the maximum adsorption capacity was obtained as was 134.23 mg/g at pH 4.0. It is reported that rGO hydrogel has good mechanical stability, can be easily removed from solution and reusable [176]. Jiang et al. have used polyacrylamide graphene oxide hydrogel (SA-PAM/GO) as an adsorbent for removal Cu(II) and Pb(II). The composite, which grafted with

Table 5 Adsorption of heavy metal by graphene and graphene oxide composites

Adsorbents	Adsorbates	Surface area, m^2/g	Pore volume, cm^3/g	Pore size, nm	Adsorption capacity, mg/g		References
Chitosan/GO	Cu(II)	132.9	4.03	15	217.4		[177]
rGO	U(VI)	162.92	–	–	134.23		[176]
GO GO-G Graphene oxide with glycine (G)	Ni(II)	–	–	–	38.61 36.63		[178]
GO	Cs(I)	139.5	–	–	40.00		[179]
GONRs Graphene oxide nanoribbons (NRs)	As(V) Hg(II)	–	–	–	155.61 33.02		[180]
GO	Cu(II) Cd(II) Ni(II)	–	–	–	72.6, 83.8 62.3		[181]
GO	Cs(I)	93.7	–	–	95.46		[182]
GO-TETA-DAC Graphene oxide with triethylenetetramine (TETA) and dialdehyde cellulose (DAC)	Cu(II) Pb(II)	762	–	–	65.1 80.9		[183]
M-GO M-rGO Magnetite (M) reduced graphene oxide (rGO)	As(III) As(V)	–	–	–	As(III) 85 57	As(V) 38 12	[184]
MGO-IL Magnetic graphene oxide with ionic liquid (IL)	As(III) As(V)	–	–	–	160.65 104.13		[185]
CMGO Chitosan-magnetic graphene oxide	As(III)	152.38	0.28	7.30	45		[186]
SAGO	Cu(II) Pb(II)	–	–	–	267.4 98.0		[187]
GO/CMC	Ag(II) Cu(II) Pb(II)	–	–	–	151.30 95.37 249.38		[188]

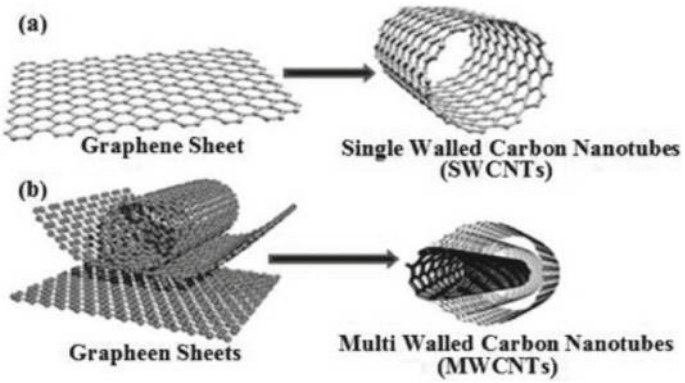

Fig. 7 Structure of SWCNT (**a**) and MWCNT (**b**) [192]

sodium alginate, was prepared by free radical polymerization. Thus, they obtained the surface area increased three times [160]. Jiao et al. have developed a novel adsorbent sodium alginate graphene oxide aerogel (SAGO). The aerogel was synthesized with cross-linking and freeze-drying method was used for adsorption of Cu(II) and Pb(II). According to the results, the maximum adsorption capacities were acquired as 267.4 mg/g for Pb(II) and 98.0 mg/g for Cu(II). The addition of graphene oxide as a filler improved the porous structure of the aerogel. It is emphasized that the prepared aerogel has very good flexibility and mechanical strength compared to pure sodium alginate (Jiao et al. 2016). Luo et al. have investigated the adsorption of Ag(II), Cu(II) and Pb(II) by using a novel composite aerogels. The graphene oxide/carboxymethyl chitosan (GO/CMC) composite aerogels were synthesized with vacuum-assisted self-assembly and freeze-drying method. It is reported that the GO/CMC aerogels have properties such as 3D porous structure, high thermal stability, and compressive strength (Luo et al. 2019).

Carbon Nanotube Composites

The carbon nanotube (CNT) materials discovered by Iijima (1991), have been widely used as effective adsorbents for removal heavy metals in adsorption process. Carbon nanotubes are thermally stable, have abundant pore structure and large surface area. The surfaces of these materials can be developed with functional groups to provide active areas for chemical modification [189]. CNTs are hollow cylinders formed from one or more graphene sheets. CNTs are divided into single-walled carbon nanotube (SWCNT) and multi-walled carbon nanotube (MWCNT) (Fig. 7). A single sheet of rounded graphene is defined as SWCNT. MWCNT is consisted of rolling two or more concentric cylindrical graphene sheets into a single cylinder [190]. According to SWCNT, MWCNT has superior properties such as synthesis without catalyst, high purity, and easy functionalization [191].

Table 6 Adsorption of heavy metal by carbon nanotube composites

Adsorbents	Adsorbates	Surface area, m^2/g	Pore volume, cm^3/g	Pore size, nm	Adsorption capacity, mg/g	References
SWCNT-SH	Hg(II)	–	–	–	131	[199]
OH-MWCNT COOH-MWCNT	Hg(II)	–	–	–	120.1 127.6	[193]
MWCNTs MWCNTs-OCH_2CO_2H	As(V) Mn(VII)	1250 1172	–	–	As(V): 200, 250 Mn(VI): 192, 236	[200]
F-MWCNTs Functionalized (F)-MWCNTs	Cu(II)	–	–	–	118.41	[201]
Sugarcane bagasse/MWCNT	Pb(II)	–	–	–	56.6	[195]
DTC-MWCNT Dithiocarbamate (DTC)-MWCNT	Cd(II) Cu(II) Zn(II)	–	–	–	167.2 98.1 11.2	[202]
MWCNT-HAP MWCNT-hydroxyapatite (HAP)	Co(II)	–	–	–	16.26	[198]
O-MWCNTs Oxidized (O)-MWCNTs	Pb(II) Cu(II) Zn(II) Cd(II)	–	–	–	76.7 15.3 13.6 32.2	[203]
MWCNTs O-MWCNTs	Cu(II)	–	–	–	45.16 61.11	[204]
O-MWCNTs	U(VI)	197	–	–	33.32	[205]
PAMAM/CNT Poly-amidoamine dendrimer/CNT	As(III) Co(II) Zn(II)	–	–	–	432 494 470	[206]

Some heavy metal adsorption studies with carbon nanotube composites are listed in Table 6. Chen et al. have used multi-walled carbon nanotubes (MWCNTs) with –OH and –COOH functional groups. Adsorption capacities of functionalized MWCNTs were compared for removal Hg(II). The results reveal that modification of MWCNTs with –OH and –COOH groups improves adsorption capacity [193]. Hamouz et al. have developed melamine-based polyamine/CNT composite via a single step polycondensation reaction. Carbon nanotubes in different weight percentages (0.01, 0.02, 0.05 and 0.1%) were functionalized and used in adsorption of Pb(II). The composites synthesized in different weight percentages (0.01, 0.02, 0.05 and 0.1%) of carbon nanotube were used to removal of Pb (II). The adsorption efficiency was achieved of ~99% for Pb(II) removal from wastewater with 0.1% CNT [194]. Hamza et al. have investigated adsorption of Pb(II) by using a sugarcane bagasse multi-walled carbon nanotube (MWCNT) composite. Adsorption capacity

was provided as 56.6 mg/g for Pb(II). It is reported that the adsorbent synthesized with carbon nanotube has mechanically more durable and better metal binding properties in adsorption processes [195]. Huang et al. have synthesized magnetic multi-wall carbon nanotubes with wet chemical treatments. They have investigated adsorption kinetics and thermodynamics for removal Cr(VI) in aqueous solutions. The results showed that the efficiency of Cr (VI) adsorption increased with magnetic MWCNT [196]. Yadav et al. have studied removal of Mn(VII) ions from wastewater. In experimental studies where they used CNT as an adsorbent, a very high adsorption efficiency (~98%) was obtained [197]. Liu et al. have developed multi-walled carbon nanotube-hydroxyapatite composites as a novel adsorbent and investigated removal of Co(II) in adsorption process. Adsorption experiments reveal that MWCNT-HAP composites are suitable materials for the removal of Co (II) ions from large volume aqueous solutions [198].

4.2 Dye Removal

In many different industries where dyes are used, large amounts of water and chemicals are consumed. Wastewater from many industries such as paper, plastic, leather, food, cosmetics, especially the textile industry, contains high concentrations of dyes [207]. Wastewater containing dyes not only cause visual pollution, but also threaten human health and the life of the aquatic flora and fauna due to non-biodegradable dyes [208]. Dyes prevent photosynthesis by reducing the light transmission in water. This situation causes oxygen deficiency and the biological cycle is disrupted. Because they are toxic, mutagenic, and carcinogenic, even low concentrations are dangerous for the living organisms. In the event that dyes leak into the soil, it damages the living flora by changing the physical and chemical structure of the soil, beneficial microorganisms disappear and soil efficient decreases [209]. Dyes are generally divided into two as natural and synthetic. Natural dyes can be obtained from plants and minerals and are widely used in the food industry. The dye type used in all other industries are synthetic dyes and there are varieties such as azo, acid, reactive, disperse, indigo, cationic, direct, pigment, solvent [210]. These pollutants cause skin irritation, allergies, nausea and vomiting, developmental problems, reproductive problems, laryngitis, and various cancers [211]. It is extremely inconvenient to discharge wastewater containing dyes without treatment, so they must be removed from wastewater. Different wastewater treatment methods such as flocculation, precipitation, ion exchange, membrane, adsorption, and electrochemical techniques are used for dyes removal so far. Among these methods, adsorption is as an efficient treatment method with its advantages such as low energy requirement, simple operation, and low cost [208, 212]. The development of adsorbents with high porosity, large surface area, and good adsorption capacity in adsorption processes has been the main subject of researchers.

4.2.1 Carbon Composite Materials Employed for the Removal of Dye

Carbon-Mesoporous Silica Composite

Dyes containing wastewater is very difficult to treat due to the inability of dyes to biodegrade and their complex molecular structure [213]. In recent years, mesoporous silicas with high pore properties are frequently used as catalyst support and adsorbents in the treatment of these organic pollutants. Mesoporous silicas are excellent materials with homogeneous pore size as well as large surface area, thermal stability, and high pore diameter [214, 215]. Mesoporous silicas are effective adsorbents which form active sites in dye removal due to the negative charges (–OH groups) on their surfaces. Surface properties can be improved by being activated with various functional groups (such as carboxyl, hydroxyl, and amino groups) [214]. The recent studies of mesoporous silicas functionalized with various groups are shown in Table 7.

Mirzaie et al. have synthesized mesoporous SBA-15 functionalized with polyamidoamine (PAMAM) via plain solgel technique. The adsorption capacity of Acid Blue 62 was obtained as 1428.57 mg/g in the adsorption process [216]. Rizzi et al. have developed amino grafted MCM-41 composite for removal the Direct Blue from wastewater. The development of mesoporous silica with amino groups positively affected the adsorption efficiency [217]. Galan et al. have studied adsorption of Naphthol Blue Black (NBB) Remazol Brilliant Blue R (RBBR) and Reactive Black 5 (RB5) by using a new composite (MCSG60) developed with mesoporous carbon and mesoporous silicagel. The results reveal that the composite is an effective adsorbent for the removal of these reactive dyes (Galan et al. 2013). Liou et al. have studied the removal of cationic dyes from wastewater using graphene oxide/SBA-15 nanocomposite as an adsorbent. The nanocomposite was synthesized by grafting graphene oxide onto the surface of mesoporous silica. The highest surface area (891 m^2/g) and adsorption capacity (138 mg/g) were achieved with the composite calcined at 550 °C [218]. Yuan et al. have synthesized coal fly ash-derived mesoporous silica material (CFA-MS) and used removal of methylene blue. It is reported that the composite, which is synthesized without using any extra commercial silica source, is promising due to its high adsorption capacity (323.62 mg/g) and cheap adsorbent [219]. Mahmoudi et al. have investigated removal of Congo Red from aqueous solutions. They synthesized a multifunctional adsorbent silica-graphene oxide composite (SGO). It is presented that combining the functional groups of silica and graphene oxide increases the adsorption capacity and is effective for various contaminants [220]. Farias et al. have developed porous N-carbon/silica nanofibers (PN-CSN) using one-step carbonizing method for adsorption methylene blue. It is said that the synthesized nanofiber with ~100% removal efficiency is an effective adsorbent in the adsorption process and will also be effective in removing other contaminants from wastewater [221]. Hennin et al. have investigated a novel adsorbent formed by the synthesis of graphene oxide with mesoporous silica (COK-12) for removal of methylene blue. It is concluded that functionalization with graphene oxide creates

Table 7 Adsorption of dyes by functionalized mesoporous silica composites

Adsorbents	Adsorbates	Surface area, m^2/g	Pore volume, cm^3/g	Pore size, nm	Adsorption capacity, mg/g	References
NH_2-MCM-41	Remazol Red	215.5	0.52	1.808	45.9	[223]
SBA-15/PAMAM	Acid Blue 62	165.94	0.36	4.1	1428.57	[216]
Polypyrrole/SBA-15	Methylene blue Methyl orange	554	0.491	–	41.66 58.82	[224]
MCM-41-NH_2	Direct blue	–	–	–	300	[217]
MCSG60	NBB RB5 RBBR	651	1.35	–	270 270 280	[225]
GO/SBA-16	Malachite green Methyl violet	1039	5.27	0.83	358.72 536.63	[226]
GO/SBA-15	Methylene blue	891	1.035	6.50	138	[218]
CFA-MS	Methylene blue	497	0.49	–	323.62	[219]
G-PMS Graphene-periodic mesoporous silica	Acid blue	452.86	–	–	21	[227]
COK-12-GO-2*	Methylene blue	298	0.48	8.5	197.5	[222]
SGO	Congo red	–	–	–	333.33	[220]
PN-CSN	Methylene blue	364	0.18	6.1	397.5	[221]

(*) represents the upscaling

a negatively charged surface area, increasing the surface area and the adsorption capacity of methylene blue [222].

Graphene and Graphene Oxide Composites

Graphene material is widely used in electronics, materials, environment, and energy fields due to its superior properties. These superior properties can be listed as large surface area, optical permeability, chemical stability, conductivity and good mechanical strength. Graphene and graphene oxide are carbon-based materials that can adsorb many different dyes [228, 229]. Especially graphene oxide (GO) has high

Table 8 Adsorption of dyes by functionalized graphene and graphene oxide composites

Adsorbents	Adsorbates	Surface area, m^2/g	Pore volume, cm^3/g	Pore size, nm	Adsorption capacity, mg/g	References
G–CNT	Methylene blue	78.9	–	–	81.97	[231]
GO-TSC-GO	Methylene blue	70.211	0.1958	11.16	596.642	[228]
GO/HCS	Reactive Black 5	–	–	–	638.93	[232]
GRGO	Rhodamine B	–	–	–	280.8	[233]
N/S-GHs Nitrogen/Sulphur-Graphene hydrogels	Malachite green	41.40	0,095	–	738.1	[236]
GA Graphene aerogel	Methylene blue Methyl orange	1099.43	–	–	221.77 166.66	[237]
PPGA	Methyl orange	–	–	–	202.8	[234]
rGO	Malachite green	931	–	–	476.2	[238]
EG Exfoliated graphene	Methylene blue	139.11	–	–	511.7	[239]
GO-SA GO-sodium alginate RGO-SA	Methylene blue	18.98 23.59	–	–	833.3 192.3	[240]
GOA	Methylene blue	42	4.379	29.52	416.667	[235]

adsorption capacity with containing carboxylic, epoxy, and hydroxy groups. Negatively charged graphene oxides bind positively charged cationic dyes and remove them from wastewater [230]. Some studies in this area are listed in Table 8.

As a novel adsorbent, graphene-carbon nanotube hybrid (G-CNT) has synthesized via a simple one-step hydrothermal process by Ai et al. The hybrid was used for methylene blue removal and an adsorption capacity of 81.97 mg/g was obtained [231]. Bu et al. have studied removal of methylene blue with a new adsorbent (GO-TSC-GO). In this study, graphene oxide was functionalized with thiosemicarbazide which was containing sulfur and nitrogen. The results revealed that the adsorbent synthesized was effective and reusable in dye removal [228]. Lai et al. have developed a new adsorbent, graphene oxide/high molecular weight chitosan (GO/HCS), for adsorption of Reactive Black 5. They reported that the adsorbent had high adsorption performance and high regeneration efficiency of ~90% [232]. Liu et al. have investigated of removal rhodamine B with three-dimensional reduced

graphene oxide (GRGO) aerogel. It is concluded that GRGO aerogel is an effective adsorbent with an adsorption capacity of 280.8 mg/g [233]. Xu et al. have synthesized graphene oxide aerogels (PPGA) co-functionalized with polydopamine (PDA) and polyethylenimine (PEI) for removal methyl orange. They said that the synthesized PPGA had high adsorption capacity in anionic dyes removal with abundant nitrogen containing functional groups [234]. Zamani et al. have used graphene oxide aerogel for adsorption of methylene blue. The graphene oxide aerogel (GOA) was synthesized with ice segregation induced self-assembly method. The experimental results revealed that GOA was an effective adsorbent for methylene blue removal with an adsorption capacity of 416.667 mg/g [235].

Carbon Nanotube Composites

Carbon nanotubes (single-walled carbon nanotubes (SWCNTs) and multi-walled carbon nanotubes (MWCNTs)) are hollow cylindrical structures composed of carbon atoms in sp^2. Carbon nanotubes (CNTs) stand out with their large surface area, hydrophobic wall, easily modified surfaces, superior thermal, mechanical, and electrical properties. Carbon-based materials such as carbon nanotubes have been involved in many studies as highly effective adsorbents for the adsorption of dyes from wastewater. The adsorption mechanism of dyes on carbon nanotubes depends on the properties of the nanomaterial and the chemical structure of the paint. The adsorption efficiency of carbon nanotubes is increased by chemical modification and synthesis of carbon nanotube-based composites [241, 242]. Table 9 includes the recent studies using carbon nanotubes as adsorbents in recent years.

Ge et al. have studied removal of methyl blue and methyl orange with single-wall carbon nanotubes. AO-Fe-SWCNTs composite was synthesized by arc discharge method with iron oxide particles. They said that loading iron oxide in the SWCNTs composite improved the properties of the nanotube and increased the adsorption efficiency [242]. Multi-walled carbon nanotubes (MWCNTs) functionalized with hypochlorite groups (–OCl) were used adsorption of acid orange 7 from wastewater by Jia et al. It is reported that on the surfaces of the functionalized nanotubes, many reactive sites suitable for adsorption have been formed [243]. Carbon nanotubes (CNTs) were functionalized with deep eutectic solvent for removal of crystal violet dye by Lawal et al. in their studies. They assigned that the modification process with DES was easier than many other solvents and did not require purification. The experimental results for adsorption showed that the adsorption capacity was 312 mg/g [244]. Machado et al. have compared adsorption capacities of multi-walled carbon nanotube (MWCNT) and powdered activated carbon (PAC) for removal of Reactive Red M-2BE dye. They reported that multi-walled carbon nanotube provided higher adsorption capacity than powdered activated carbon. The adsorption capacities for MWCNT and PAC were obtained as 335.7 and 260.7 mg/g, respectively [245]. Saxena et al. have used functionalized multiwalled carbon nanotubes with L-tyrosine for removal of methylene blue. They said that tyrosine was an environmentally friendly and inexpensive aromatic amino acid and provided additional

Table 9 Adsorption of dyes by functionalized carbon nanotube composites

Adsorbents	Adsorbates	Surface area, m^2/g	Pore volume, cm^3/g	Pore size, nm	Adsorption capacity, mg/g	References
AO-Fe-SWCNTs	Methylene blue Methyl orange	117	–	–	256.69 93.58	[242]
MWCNTs	Acid Orange 7	–	–	–	47.72 ± 0.79	[243]
CNT-DES	Crystal violet	36.13	0.352	–	312	[244]
MWCNT PAC	Reactive Red M-2BE	180.9 728.7	0.345 0.641	7.62 3.52	335.7 260.7	[245]
MWCNT PAC	Direct Blue 53	–	–	–	409.4 135.2	[247]
CNT-TYR	Methylene blue	–	–	–	440	[246]
MWCNTs–OH MWCNTs–COOH	Crystal violet	–	–	–	988 1011	[248]
MWCNT	Methylene blue Acid Red 183	217	–	–	59.7 45.2	[249]
MWNTs	Congo red Reactive green Golden yellow	91.96	–	–	148.0 152.0 141.0	[250]

carboxylic and hydroxyl sites on nanotubes to incease adsorption capacity. The results showed that the CNT-TYR composite was an effective adsorbent for dye removal with high adsorption capacity [246].

5 Conclusions

The decrease in fossil fuels and increasing environmental pollution have brought renewable energy systems to the fore. Hydrogen is one of the important energy resources in the future due to its abundance in nature, clean, and sustainable. In addition, it is important to develop low cost and environmentally friendly energy conversion and storage systems. It has emphasized that carbon-based materials used as catalysts in these areas are environmentally friendly materials that provide high catalytic activity. Carbon-mesoporous silica, graphene and graphene oxide, carbon nanotube composites used as adsorbents for heavy metal and dye adsorption studies

have been investigated. These materials with unique physical and chemical properties provide high adsorption efficiency. The carbon-based materials have been promising compared to traditional adsorbents with its easy removal from the aqueous environment and its reusability.

References

1. Zhang WP et al (2019) Sizing a stand-alone solar-wind-hydrogen energy system using weather forecasting and a hybrid search optimization algorithm. Energy Convers Manage 180:609–621
2. Tao K et al (2017) Enhanced hydrogen production from steam reforming of vegetable oil over bimodal ZrO_2-SiO_2 supported Ni catalyst. ChemistrySelect 2(1):527–532
3. Bechara R, Azizi F, Boyadjian C (2021) Process simulation and optimization for enhanced biophotolytic hydrogen production from green algae using the sulfur deprivation method. Int J Hydrogen Energy 46(27):14096–14108
4. Jayababu N, Kim D (2021) ZnO nanorods@conductive carbon black nanocomposite based flexible integrated system for energy conversion and storage through triboelectric nanogenerator and supercapacitor. Nano Energy 82
5. Yin MM et al (2021) Manganese dioxides for oxygen electrocatalysis in energy conversion and storage systems over full pH range. J Power Sour 494
6. Kumar A, Vashistha VK, Das DK (2021) Recent development on metal phthalocyanines based materials for energy conversion and storage applications. Coord Chem Rev 431
7. Hu CG, Dai LM (2017) Multifunctional carbon-based metal-free catalysts for efficient energy conversion and storage. In: Abstracts of papers of the American Chemical Society, 254
8. Ouyang LZ et al (2014) Enhanced high-rate discharge properties of La11.3Mg6.0Sm7.4Ni61.0Co7.2Al7.1 with added graphene synthesized by plasma milling. Int J Hydrogen Energy 39(24):12765–12772
9. Abdullah NH et al (2019) Solid matrices for fabrication of magnetic iron oxide nanocomposites: synthesis, properties, and application for the adsorption of heavy metal ions and dyes. Compos Part B-Eng 162:538–568
10. Burakov AE et al (2018) Adsorption of heavy metals on conventional and nanostructured materials for wastewater treatment purposes: a review. Ecotoxicol Environ Saf 148:702–712
11. Gao ZT et al (2019) Cobalt nanoparticles packaged into nitrogen-doped porous carbon derived from metal-organic framework nanocrystals for hydrogen production by hydrolysis of sodium borohydride. Int J Hydrogen Energy 44(16):8365–8375
12. Ulas B et al (2019) Carbon monoxide and formic acid electrooxidation study on Au decorated Pd catalysts prepared via microwave assisted polyol method. Fullerenes, Nanotubes, Carbon Nanostruct 27(7):545–552
13. Nikolaidis P, Poullikkas A (2017) A comparative overview of hydrogen production processes. Renew Sustain Energy Rev 67:597–611
14. Akdemir M et al Ruthenium modified defatted spent coffee catalysts for supercapacitor and methanolysis application. Energy Storage
15. Hansu TA et al (2021) Untangling the cobalt promotion role for ruthenium in sodium borohydride dehydrogenation with multiwalled carbon nanotube-supported binary ruthenium cobalt catalyst. Int J Energy Res 45(4):6054–6066
16. Hansu TA et al (2020) Hydrolysis and electrooxidation of sodium borohydride on novel CNT supported CoBi fuel cell catalyst. Mater Chem Phys 239
17. Caglar A et al (2020) Effective carbon nanotube supported metal (M=Au, Ag Co, Mn, Ni, V, Zn) core Pd shell bimetallic anode catalysts for formic acid fuel cells. Renew Energy 150:78–90

18. Caglar A et al (2019) Synthesis of in situ N-, S-, and B-doped few-layer graphene by chemical vapor deposition technique and their superior glucose electrooxidation activity. Int J Energy Res 43(14):8204–8216
19. Demirci S et al (2020) Porous carbon particles as metal-free superior catalyst for hydrogen release from methanolysis of sodium borohydride. Renew Energy 147:69–76
20. Messele SA, Chelme-Ayala P, El-Din MG (2021) Catalytic ozonation of naphthenic acids in the presence of carbon-based metal-free catalysts: performance and kinetic study. Catal Today 361:102–108
21. Ding Y et al (2020) A metal-free electrode: from biomass-derived carbon to hydrogen. Chemsuschem 13(16):4064
22. Wang H et al (2020) Ultrasound-assisted transformation from waste biomass to efficient carbon-based metal-free pH-universal oxygen reduction reaction electrocatalysts. Ultrason Sonochem 65:105048
23. Paul R et al (2019) Ten years of carbon-based metal-free electrocatalysts. Carbon Energy 1(1):19–31
24. Zhao S et al (2019) Carbon-based metal-free catalysts for key reactions involved in energy conversion and storage. Adv Mater 31(9):1801526
25. Tentu RD, Basu S (2017) Photocatalytic water splitting for hydrogen production. Curr Opin Electrochem 5(1):56–62
26. Sahiner N, Demirci S (2017) Very fast H2 production from the methanolysis of NaBH4 by metal-free poly (ethylene imine) microgel catalysts. Int J Energy Res 41(5):736–746
27. Kaya M (2020) Production of metal-free catalyst from defatted spent coffee ground for hydrogen generation by sodium borohyride methanolysis. Int J Hydrogen Energy 45(23):12731–12742
28. Kaya M (2020) Evaluating organic waste sources (spent coffee ground) as metal-free catalyst for hydrogen generation by the methanolysis of sodium borohydride. Int J Hydrogen Energy 45(23):12743–12754
29. Sahiner N (2017) Modified multi-wall carbon nanotubes as metal free catalyst for application in H2 production from methanolysis of NaBH4. J Power Sources 366:178–184
30. Sahiner N, Sengel SB (2016) Quaternized polymeric microgels as metal free catalyst for H2 production from the methanolysis of sodium borohydride. J Power Sources 336:27–34
31. Saka C, Kaya M, Bekiroğullari M (2020) Spirulina microalgal strain as efficient a metal-free catalyst to generate hydrogen via methanolysis of sodium borohydride. Int J Energy Res 44(1):402–410
32. Bekirogullari M (2020) Hydrogen production from sodium borohydride by $ZnCl_2$ treated defatted spent coffee ground catalyst. Int J Hydrogen Energy 45(16):9733–9743
33. Höök M, Tang X (2013) Depletion of fossil fuels and anthropogenic climate change—a review. Energy Policy 52:797–809
34. Hook M, Tang X (2013) Depletion of fossil fuels and anthropogenic climate change—a review. Energy Policy 52:797–809
35. Tao M (2008) Inorganic photovoltaic solar cells: silicon and beyond. The Electrochem Soc Interface 17(4):30
36. Arjunan AT, Senthil T (2013) Dye sensitised solar cells. Mater Technol 28(1–2):9–14
37. Bagher AM, Vahid MMA, Mohsen M (2015) Types of solar cells and application. Am J Opt Photonics 3(5):94–113
38. Imamzai M et al (2012) A review on comparison between traditional silicon solar cells and thin-film CdTe solar cells. In: Proceedings of national graduate conference (Nat-Grad. 2012)
39. Green MA (2013) Silicon solar cells: state of the art. Philos Trans R Soc A: Math, Phys Eng Sci 371(1996):20110413
40. Ajayan J et al (2020) A review of photovoltaic performance of organic/inorganic solar cells for future renewable and sustainable energy technologies. Superlattices Microstruct 143:106549
41. Ghernaout D, Boudjemline A, Elboughdiri N (2020) Electrochemical engineering in the core of the dye-sensitized solar cells (DSSCs). Open Access Lib J 7(3):1–12

42. Jarka P et al (2020) Influence of screen printed nanowires/nanoparticles TiO_2 nanocomposite layer on properties of dye-sensitized solar cells. Acta Phys Pol A 138:312–316
43. Zhu K et al (2007) Enhanced charge-collection efficiencies and light scattering in dye-sensitized solar cells using oriented TiO_2 nanotubes arrays. Nano Lett 7(1):69–74
44. Younas M et al (2019) Efficient and cost-effective dye-sensitized solar cells using MWCNT-TiO_2 nanocomposite as photoanode and MWCNT as Pt-free counter electrode. Sol Energy 188:1178–1188
45. Tsai C-H et al (2012) Influences of textures in Pt counter electrode on characteristics of dye-sensitized solar cells. Org Electron 13(1):199–205
46. Gong J, Liang J, Sumathy K (2012) Review on dye-sensitized solar cells (DSSCs): fundamental concepts and novel materials. Renew Sustain Energy Rev 16(8):5848–5860
47. Zhang Y et al (2020) Highly efficient bio-based porous carbon hybridized with tungsten carbide as counter electrode for dye-sensitized solar cell. Ceram Int 46(10):15812–15821
48. Sirohi R et al (2012) Novel di-anchoring dye for DSSC by bridging of two mono anchoring dye molecules: a conformational approach to reduce aggregation. Dyes Pigm 92(3):1132–1137
49. Hwang K-J et al (2010) Analysis of adsorption properties of N719 dye molecules on nanoporous TiO_2 surface for dye-sensitized solar cell. Appl Surf Sci 256(17):5428–5433
50. Yong S-M et al (2013) One-dimensional WO3 nanorods as photoelectrodes for dye-sensitized solar cells. J Alloy Compd 547:113–117
51. Fadhilah N et al (2019) Preparation of Au@ TiO_2@SiO_2 core-shell nanostructure and their light harvesting capability on DSSC (dye sensitized solar cells). In: AIP conference proceedings, 2019. AIP Publishing LLC
52. Giannouli M et al (2018) Factors affecting the power conversion efficiency in ZnO DSSCs: nanowire versus nanoparticles. Materials 11(3):411
53. Kılıç B et al (2015) Band gap engineering and modifying surface of TiO_2 nanostructures by Fe_2O_3 for enhanced-performance of dye sensitized solar cell. Mater Sci Semicond Process 31:363–371
54. Ahamad T et al (2021) Enhanced photovoltaic performance of dye-sensitized solar cells based Ag_2O doped $BiFeO_3$ hetrostructures. Sol Energy 220:758–765
55. Pari B et al (2014) Recent advances in SnO_2 based photo anode materials for third generation photovoltaics. In: Materials science forum, 2014. Trans Tech Publ
56. Jamil M et al (2017) Studies on solution processed Graphene-Nb_2O_5 nanocomposite based photoanode for dye-sensitized solar cells. J Alloy Compd 694:401–407
57. Luitel T, Zamborini FP (2013) Covalent modification of photoanodes for stable dye-sensitized solar cells. Langmuir 29(44):13582–13594
58. Mohammadi N, Mahon PJ, Wang F (2013) Toward rational design of organic dye sensitized solar cells (DSSCs): an application to the TA-St-CA dye. J Mol Graph Model 40:64–71
59. Nath NCD, Lee J-J (2019) Binary redox electrolytes used in dye-sensitized solar cells. J Ind Eng Chem 78:53–65
60. Highfield J (2015) Advances and recent trends in heterogeneous photo(electro)-catalysis for solar fuels and chemicals. Molecules 20(4):6739–6793
61. Asbury JB et al (2001) Ultrafast electron transfer dynamics from molecular adsorbates to semiconductor nanocrystalline thin films. J Phys Chem B 105(20):4545–4557
62. Iqbal MZ, Ali SR, Khan S (2019) Progress in dye sensitized solar cell by incorporating natural photosensitizers. Sol Energy 181:490–509
63. Akita T et al (2005) Transmission electron microscopy observation of the structure of TiO_2 nanotube and Au/TiO2 nanotube catalyst. Surface and Interface Analysis: An International Journal devoted to the development and application of techniques for the analysis of surfaces, interfaces and thin films 37(2):265–269
64. Hattori A, Tada H (2001) High photocatalytic activity of F-doped TiO2 film on glass. J Sol-Gel Sci Technol 22(1):47–52
65. Sahu G, Gordon SW, Tarr MA (2012) Synthesis and application of core-shell Au–TiO2 nanowire photoanode materials for dye sensitized solar cells. RSC Adv 2(2):573–582

66. Huang Y et al (2018) Plasmon-enhanced self-powered UV Photodetectors assembled by incorporating Ag@SiO_2 core–shell nanoparticles into TiO_2 nanocube photoanodes. ACS Sustain Chem Eng 6(1):438–446
67. Kilic B et al (2016) Preparation of carbon nanotube/TiO 2 mesoporous hybrid photoanode with iron pyrite (FeS 2) thin films counter electrodes for dye-sensitized solar cell. Sci Rep 6(1):1–9
68. Hadadian M, Smått J-H, Correa-Baena J-P (2020) The role of carbon-based materials in enhancing the stability of perovskite solar cells. Energy Environ Sci 13(5):1377–1407
69. Mehmood U et al (2015) Hybrid TiO_2–multiwall carbon nanotube (MWCNTs) photoanodes for efficient dye sensitized solar cells (DSSCs). Sol Energy Mater Sol Cells 140:174–179
70. Yen C-Y et al (2008) Preparation and properties of a carbon nanotube-based nanocomposite photoanode for dye-sensitized solar cells. Nanotechnology 19(37):375305
71. Dang X et al (2011) Virus-templated self-assembled single-walled carbon nanotubes for highly efficient electron collection in photovoltaic devices. Nat Nanotechnol 6(6):377–384
72. Yen M-Y et al (2011) Preparation of graphene/multi-walled carbon nanotube hybrid and its use as photoanodes of dye-sensitized solar cells. Carbon 49(11):3597–3606
73. Fabregat-Santiago F et al (2005) Influence of electrolyte in transport and recombination in dye-sensitized solar cells studied by impedance spectroscopy. Sol Energy Mater Sol Cells 87(1–4):117–131
74. Bakhshayesh AM et al (2013) Improved electron transportation of dye-sensitized solar cells using uniform mixed CNTs–TiO_2 photoanode prepared by a new polymeric gel process. J Nanopart Res 15(9):1–10
75. Yu J, Fan J, Cheng B (2011) Dye-sensitized solar cells based on anatase TiO_2 hollow spheres/carbon nanotube composite films. J Power Sour 196(18):7891–7898
76. Chang H et al (2010) Application of TiO_2 nanoparticles coated multi-wall carbon nanotube to dye-sensitized solar cells. J Nanosci Nanotechnol 10(11):7671–7675
77. Cai J et al (2015) Enhanced conversion efficiency of dye-sensitized solar cells using a CNT-incorporated TiO2 slurry-based photoanode. AIP Adva 5(2):027118
78. Sun S, Gao L, Liu Y (2010) Enhanced dye-sensitized solar cell using graphene-TiO_2 photoanode prepared by heterogeneous coagulation. Appl Phys Lett 96(8):083113
79. Yang N et al (2010) Two-dimensional graphene bridges enhanced photoinduced charge transport in dye-sensitized solar cells. ACS Nano 4(2):887–894
80. Yadav HM, Kim J-S (2016) Solvothermal synthesis of anatase TiO_2-graphene oxide nanocomposites and their photocatalytic performance. J Alloy Compd 688:123–129
81. Kazmi SA et al (2017) Electrical and optical properties of graphene-TiO_2 nanocomposite and its applications in dye sensitized solar cells (DSSC). J Alloy Compd 691:659–665
82. Song C et al (2014) Dye-sensitized solar cells based on graphene–TiO_2 nanoparticles/TiO_2 nanotubes composite films. Int J Electrochem Sci 9(12):8090–8096
83. Wang H, Hu YH (2012) Graphene as a counter electrode material for dye-sensitized solar cells. Energy Environ Sci 5(8):8182–8188
84. Ahmad I et al (2014) Carbon nanomaterial based counter electrodes for dye sensitized solar cells. Sol Energy 102:152–161
85. Xu X et al (2015) Heteroatom-doped graphene-like carbon films prepared by chemical vapour deposition for bifacial dye-sensitized solar cells. Chem Eng J 267:289–296
86. Hu C et al (2018) Functionalization of graphene materials by heteroatom-doping for energy conversion and storage. Prog Natural Sci: Mater Int 28(2):121–132
87. Fabry F, Flamant G, Fulcheri L (2001) Carbon black processing by thermal plasma. Analysis of the particle formation mechanism. Chem Eng Sci 56(6):2123–2132
88. Don MF et al (2019) Acetylene carbon black-graphite composite as low-cost and efficient counter electrode for dye-sensitized solar cells (DSSCs). Ionics 25(11):5585–5593
89. Liu G et al (2012) A mesoscopic platinized graphite/carbon black counter electrode for a highly efficient monolithic dye-sensitized solar cell. Electrochim Acta 69:334–339
90. Narudin N et al (2021) Enhanced properties of low-cost carbon black-graphite counter electrode in DSSC by incorporating binders. Sol Energy 225:237–244

91. Jaafar H, Ain MF, Ahmad ZA (2020) Performance of dye-sensitized solar cell (DSSC) using carbon black-TiO_2 composite as counter electrode subjected to different annealing temperatures. Opt Quant Electron 52(4):221
92. Roy-Mayhew JD et al (2010) Functionalized graphene as a catalytic counter electrode in dye-sensitized solar cells. ACS Nano 4(10):6203–6211
93. Ngidi NP, Ollengo MA, Nyamori VO (2019) Heteroatom-doped graphene and its application as a counter electrode in dye-sensitized solar cells. Int J Energy Res 43(5):1702–1734
94. Tang B et al (2019) Three-dimensional graphene networks and RGO-based counter electrode for DSSCs. RSC Adv 9(28):15678–15685
95. Sahito IA et al (2015) Graphene coated cotton fabric as textile structured counter electrode for DSSC. Electrochim Acta 173:164–171
96. Battumur T et al (2012) Graphene/carbon nanotubes composites as a counter electrode for dye-sensitized solar cells. Curr Appl Phys 12:e49–e53
97. Yan J et al (2013) Carbon nanotubes (CNTs) enrich the solar cells. Sol Energy 96:239–252
98. Meer S, Kausar A, Iqbal T (2016) Trends in conducting polymer and hybrids of conducting polymer/carbon nanotube: a review. Polym-Plast Technol Eng 55(13):1416–1440
99. Kurokawa Y, Nguyen DT, Taguchi K (2018) The impact of PDDA in CNT counter electrode on the conversion efficiency of DSSC. Int J Chem Eng Appl 9(6):184–188
100. Leu Y-A et al (2017) Thermally stable Boron-doped multiwalled carbon nanotubes as a Pt-free counter electrode for dye-sensitized solar cells. ACS Sustain Chem Eng 5(1):537–546
101. Jiang X (2014) CVD growth of carbon nanofibers. Phys Status Solidi (A) 211(12):2679–2687
102. Sebastián D et al (2014) Carbon nanofiber-based counter electrodes for low cost dye-sensitized solar cells. J Power Sources 250:242–249
103. Xie X et al (2018) The preparation of highly flexible mesoporous TiC/CNF film for flexible dye-sensitized solar cells. J Solid State Electrochem 22(4):1185–1195
104. Kumar R et al (2017) Synthesis and characterization of carbon based counter electrode for dye sensitized solar cells (DSSCs) using sugar free as a carbon material. Sol Energy 144:215–220
105. Kumar R, Bhargava P (2018) Synthesis and characterization of carbon based counter electrode for dye sensitized solar cells (DSSCs) using organic precursor 2–2′Bipyridine (Bpy) as a carbon material. J Alloy Compd 748:905–910
106. Yen M-Y et al (2009) A novel carbon-based nanocomposite plate as a counter electrode for dye-sensitized solar cells. Compos Sci Technol 69(13):2193–2197
107. Kim H et al (2012) Fabrication and characterization of carbon-based counter electrodes prepared by electrophoretic deposition for dye-sensitized solar cells. Nanoscale Res Lett 7(1):53
108. Pang B et al (2020) Nitrogen-doped carbon nano-onions decorated on graphene network: a novel all-carbon composite counter electrode for dye-sensitized solar cell with a 10.28% power conversion efficiency. Solar RRL 4(9):2000263
109. Zhang X et al (2013) Carbon/polymer composite counter-electrode application in dye-sensitized solar cells. J Appl Polym Sci 128(1):75–79
110. Liu C-Y et al (2012) Graphene-modified polyaniline as the catalyst material for the counter electrode of a dye-sensitized solar cell. J Power Sources 217:152–157
111. Sun KC et al (2018) Electrocatalytic porous nanocomposite of graphite nanoplatelets anchored with exfoliated activated carbon filler as counter electrode for dye sensitized solar cells. Sol Energy 167:95–101
112. Jeong I et al (2014) Low-cost electrospun WC/C composite nanofiber as a powerful platinum-free counter electrode for dye sensitized solar cell. Nano Energy 9:392–400
113. Yue G et al (2014) Fabrication of high performance multi-walled carbon nanotubes/polypyrrole counter electrode for dye-sensitized solar cells. Energy 67:460–467
114. Li GR et al (2012) TiN-conductive carbon black composite as counter electrode for dye-sensitized solar cells. Electrochim Acta 65:216–220
115. Choi H et al (2011) Dye-sensitized solar cells using graphene-based carbon nano composite as counter electrode. Sol Energy Mater Sol Cells 95(1):323–325

116. Yue G et al (2016) Carbon nanotubes hybrid carbon counter electrode for high efficiency dye-sensitized solar cells. J Mater Sci: Mater Electron 27(5):4736–4743
117. Liao ZT et al (2021) Wastewater treatment and reuse situations and influential factors in major Asian countries. J Environ Manage 282:8
118. Nidheesh PV et al (2020) Treatment of mixed industrial wastewater by electrocoagulation and indirect electrochemical oxidation. Chemosphere 251
119. Shah NH et al (2018) Optimal control for transmission of water pollutants. Int J Math Eng Manag Sci 3(4):381–391
120. Crini G, Lichtfouse E (2019) Advantages and disadvantages of techniques used for wastewater treatment. Environ Chem Lett 17(1):145–155
121. Hina H, Nafees M, Ahmad T (2021) Treatment of industrial wastewater with gamma irradiation for removal of organic load in terms of biological and chemical oxygen demand. Heliyon 7(2)
122. Malik OA et al (2015) A global indicator of wastewater treatment to inform the sustainable development goals (SDGs). Environ Sci Policy 48:172–185
123. Chung NJ et al (2008) Polycyclic aromatic hydrocarbons in soils and crops after irrigation of wastewater discharged from domestic sewage treatment plants. Bull Environ Contam Toxicol 81(2):124–127
124. Deng LY et al (2021) Enhanced simultaneous nitrogen and phosphorus removal from low COD/TIN domestic wastewater through nitritation-denitritation coupling improved anammox process with an optimal anaerobic/oxic/anoxic strategy. Bioresource Technol 322
125. Soule MEZ et al (2020) Montmorillonite- hydrothermal carbon nanocomposites: Synthesis, characterization and evaluation of pesticides retention for potential treatment of agricultural wastewater. Colloids Surf A: Physicochem Eng Aspects 586
126. Ismail M et al (2019) Pollution, toxicity and carcinogenicity of organic dyes and their catalytic bio-remediation. Curr Pharm Des 25(34):3645–3663
127. Sankaran R et al (2020) Feasibility assessment of removal of heavy metals and soluble microbial products from aqueous solutions using eggshell wastes. Clean Technol Environ Policy 22(4):773–786
128. Hussein FH (2013) Chemical properties of treated textile dyeing wastewater. Asian J Chem 25(16):9393–9400
129. Singh K, Arora S (2011) Removal of synthetic textile dyes from wastewaters: a critical review on present treatment technologies. Crit Rev Environ Sci Technol 41(9):807–878
130. Teh CY et al (2016) Recent advancement of coagulation-flocculation and its application in wastewater treatment. Ind Eng Chem Res 55(16):4363–4389
131. Kastali M et al (2021) Removal of turbidity and sludge production from industrial process wastewater treatment by a rejection of steel rich in $FeCl_3$ (SIWW). Biointerface Res Appl Chem 11(5):13359–13376
132. Liu CK et al (2017) Preparation of the porphyrin-functionalized cotton fiber for the chromogenic detection and efficient adsorption of Cd2+ ions. J Colloid Interface Sci 488:294–302
133. Zhou SX et al (2020) Selective adsorption of Au(III) with ultra-fast kinetics by a new metal-organic polymer. J Mol Liq 319
134. Aslam B et al (2011) Uptake of heavy metal residues from sewerage sludge in the milk of goat and cattle during summer season. Pak Vet J 31(1):75–77
135. Barakat MA (2011) New trends in removing heavy metals from industrial wastewater. Arab J Chem 4(4):361–377
136. Garg UK et al (2008) Removal of Nickel(II) from aqueous solution by adsorption on agricultural waste biomass using a response surface methodological approach. Biores Technol 99(5):1325–1331
137. Srivastava NK, Majumder CB (2008) Novel biofiltration methods for the treatment of heavy metals from industrial wastewater. J Hazard Mater 151(1):1–8
138. Tian Y et al (2011) Electrospun membrane of cellulose acetate for heavy metal ion adsorption in water treatment. Carbohyd Polym 83(2):743–748

139. Liu L et al (2018) Effects of wood vinegar on properties and mechanism of heavy metal competitive adsorption on secondary fermentation based composts. Ecotoxicol Environ Saf 150:270–279
140. Sherlala AIA et al (2018) A review of the applications of organo-functionalized magnetic graphene oxide nanocomposites for heavy metal adsorption. Chemosphere 193:1004–1017
141. Uddin MK (2017) A review on the adsorption of heavy metals by clay minerals, with special focus on the past decade. Chem Eng J 308:438–462
142. Qurat Ul A, Farooq MU, Jalees MI (2020) Application of magnetic graphene oxide for water purification: heavy metals removal and disinfection. J Water Process Eng 33
143. Bao SY et al (2020) PEI grafted amino-functionalized graphene oxide nanosheets for ultrafast and high selectivity removal of Cr(VI) from aqueous solutions by adsorption combined with reduction: behaviors and mechanisms. Chem Eng J 399
144. Worch E (2012) Adsorption technology in water treatment fundamentals, processes, and modeling introduction. In: Adsorption technology in water treatment: fundamentals, processes, and modeling, pp 1–9
145. Aftab K et al (2017) Fungal strains isolation, identification and application for the recovery of Zn (II) ions. J Photochem Photobiol B-Biol 175:282–290
146. Lachowicz JI, et al (2019) Adsorption of $Cu2^{+}$ and $Zn2^{+}$ on SBA-15 mesoporous silica functionalized with triethylenetetramine chelating agent. J Environ Chem Eng **7**(4)
147. Costa JAS et al (2020) Recent progresses in the adsorption of organic, inorganic, and gas compounds by MCM-41-based mesoporous materials. Microporous Mesoporous Mater 291
148. El-Safty SA, Hanaoka T (2003) Monolithic nanostructured silicate family templated by lyotropic liquid-crystalline nonionic surfactant mesophases. Chem Mater 15(15):2892–2902
149. Gommes CJ et al (2009) Quantitative characterization of pore corrugation in ordered mesoporous materials using image analysis of electron tomograms. Chem Mater 21(7):1311–1317
150. Da'na E (2017) Adsorption of heavy metals on functionalized-mesoporous silica: a review. Microporous Mesoporous Mater 247:145–157
151. Laskowski L et al (2019) Mesoporous silica-based materials for electronics-oriented applications. Molecules 24(13)
152. Chen FY et al (2015) Simultaneous efficient adsorption of Pb2+ and MnO4- ions by MCM-41 functionalized with amine and nitrilotriacetic acid anhydride. Appl Surf Sci 357:856–865
153. Wang YL et al (2013) Synergistic removal of Pb(II), Cd(II) and humic acid by Fe_3O_4@mesoporous silica-graphene oxide composites. Plos One 8(6)
154. Yang WJ et al (2013) Preparation of diamine modified mesoporous silica on multi-walled carbon nanotubes for the adsorption of heavy metals in aqueous solution. Appl Surf Sci 282:38–45
155. Barik B et al (2020) Ionic liquid assisted mesoporous silica-graphene oxide nanocomposite synthesis and its application for removal of heavy metal ions from water. Mater Chem Phys 239
156. Yi IG et al (2019) Synthesis of an oxidized mesoporous carbon-based magnetic composite and its application for heavy metal removal from aqueous solutions. Microporous Mesoporous Mater 279:45–52
157. Anbia M, Kargosha K, Khoshbooei S (2015) Heavy metal ions removal from aqueous media by modified magnetic mesoporous silica MCM-48. Chem Eng Res Des 93:779–788
158. Fellenz N et al (2017) Chromium (VI) removal from water by means of adsorption-reduction at the surface of amino-functionalized MCM-41 sorbents. Microporous Mesoporous Mater 239:138–146
159. Guo YG et al (2017) Synthesis of chitosan-functionalized MCM-41-A and its performance in Pb(II) removal from synthetic water. J Taiwan Inst Chem Eng 71:537–545
160. Jiang YL et al (2020) Synthesis of chitosan/MCM-48 and beta-cyclodextrin/MCM-48 composites as bio-adsorbents for environmental removal of $Cd2^{+}$ ions; kinetic and equilibrium studies. React Funct Polym 154
161. Kaewprachum W et al (2020) SDS modified mesoporous silica MCM-41 for the adsorption of Cu2+, Cd2+, Zn2+ from aqueous systems. J Environ Chem Eng 8(1)

162. Gupta R, Gupta SK, Pathak DD (2019) Selective adsorption of toxic heavy metal ions using guanine-functionalized mesoporous silica SBA-16-g from aqueous solution. Microporous Mesoporous Mater 288
163. Li G et al (2017) Adsorption of lead ion on amino-functionalized fly-ash-based SBA-15 mesoporous molecular sieves prepared via two-step hydrothermal method. Microporous Mesoporous Mater 252:105–115
164. Li SL et al (2021) Highly effective removal of lead and cadmium ions from wastewater by bifunctional magnetic mesoporous silica. Sep Purif Technol 265
165. Liu LH et al (2020) Surface charge of mesoporous calcium silicate and its adsorption characteristics for heavy metal ions. Solid State Sci 99
166. Shah SM et al (2019) Synthesis of sulphonic acid functionalized magnetic mesoporous silica for Cu(II) and Co(II) adsorption. Microchemical Journal, 2019. **151**.
167. Wu HM et al (2020) Functionalization of SBA-15 mesoporous materials with 2-acetylthiophene for adsorption of Cr(III) ions. Microporous Mesoporous Mater 292
168. Li XH et al (2015) Preparation, characterization, and application of mesoporous silica-grafted graphene oxide for highly selective lead adsorption. Chem Eng J 273:630–637
169. Wang XM et al (2015) Highly efficient adsorption of heavy metals from wastewaters by graphene oxide-ordered mesoporous silica materials. J Mater Sci 50(5):2113–2121
170. Marciniak M et al (2019) Optimal synthesis of oxidized mesoporous carbons for the adsorption of heavy metal ions. J Mol Liq 276:630–637
171. Valle-Vigon P, Sevilla M, Fuertes AB (2013) Carboxyl-functionalized mesoporous silica-carbon composites as highly efficient adsorbents in liquid phase. Microporous Mesoporous Mater 176:78–85
172. Xikhongelo RV et al (2021) Polyamidoamine-functionalized graphene oxide-SBA-15 mesoporous composite: adsorbent for aqueous arsenite, cadmium, ciprofloxacin, ivermectin, and tetracycline. Ind Eng Chem Res 60(10):3957–3968
173. Chowdhury S, Balasubramanian R (2014) Recent advances in the use of graphene-family nanoadsorbents for removal of toxic pollutants from wastewater. Adv Coll Interface Sci 204:35–56
174. Wang H et al (2014) Adsorption characteristics and behaviors of graphene oxide for Zn(II) removal from aqueous solution (vol 279, pg 432, 2013). Appl Surf Sci 301:585–585
175. Szostak R et al (2018) Application of graphene and graphene derivatives/oxide nanomaterials for solar cells. In: Future of semiconductor oxides in next-generation solar cells, 2018, pp 395–437
176. He YR et al (2018) Graphene (rGO) hydrogel: a promising material for facile removal of uranium from aqueous solution. Chem Eng J 338:333–340
177. Hosseinzadeh H, Ramin S (2018) Effective removal of copper from aqueous solutions by modified magnetic chitosan/graphene oxide nanocomposites. Int J Biol Macromol 113:859–868
178. Najafi F et al (2015) Thermodynamics of the adsorption of nickel ions from aqueous phase using graphene oxide and glycine functionalized graphene oxide. J Mol Liq 208:106–113
179. Tan LQ et al (2016) Effect of water chemistries on adsorption of Cs(I) onto graphene oxide investigated by batch and modeling techniques. Chem Eng J 292:92–97
180. Sadeghi MH, Tofighy MA, Mohammadi T (2020) One-dimensional graphene for efficient aqueous heavy metal adsorption: rapid removal of arsenic and mercury ions by graphene oxide nanoribbons (GONRs). Chemosphere, 253
181. Tan P et al (2015) Adsorption of Cu2+, Cd2+ and Ni2+ from aqueous single metal solutions on graphene oxide membranes. J Hazard Mater 297:251–260
182. Xing M, Zhuang ST, Wang JL, Efficient removal of Cs(I) from aqueous solution using graphene oxide. Prog Nuclear Energy 119
183. Yao MJ et al (2019) Preparation of dialdehyde cellulose graftead graphene oxide composite and its adsorption behavior for heavy metals from aqueous solution. Carbohyd Polym 212:345–351

184. Yoon Y et al (2016) Comparative evaluation of magnetite-graphene oxide and magnetite-reduced graphene oxide composite for As(III) and As(V) removal. J Hazard Mater 304:196–204
185. Zhang MY et al (2019) Enhanced removal of As(III) and As(V) from aqueous solution using ionic liquid-modified magnetic graphene oxide. Chemosphere 234:196–203
186. Sherlala AIA et al (2019) Adsorption of arsenic using chitosan magnetic graphene oxide nanocomposite. J Environ Manage 246:547–556
187. Jiao CL et al (2016) Sodium alginate/graphene oxide aerogel with enhanced strength-toughness and its heavy metal adsorption study. Int J Biol Macromol 83:133–141
188. Luo JQ et al (2019) Novel graphene oxide/carboxymethyl chitosan aerogels via vacuum-assisted self-assembly for heavy metal adsorption capacity. Colloids Surf A-Physicochem Eng Aspects 578
189. Hadavifar M et al (2014) Adsorption of mercury ions from synthetic and real wastewater aqueous solution by functionalized multi-walled carbon nanotube with both amino and thiolated groups. Chem Eng J 237:217–228
190. Duan CY et al (2020) Removal of heavy metals from aqueous solution using carbon-based adsorbents: a review. J Water Process Eng 37
191. Rahman G et al (2019) An overview of the recent progress in the synthesis and applications of carbon nanotubes. C-J Carbon Res 5(1)
192. Zuru DU (2019) Theoretical model for the design and preparation of a CNT-ursonic acid drug matrix as HIV-gp120 entry inhibitor. Sci Afr 6
193. Chen PH et al (2014) Adsorption of mercury from water by modified multi-walled carbon nanotubes: adsorption behaviour and interference resistance by coexisting anions. Environ Technol 35(15):1935–1944
194. Al Hamouz OCS, Adelabu IO, Saleh TA (2017) Novel cross-linked melamine based polyamine/CNT composites for lead ions removal. J Environ Manag 192:163–170
195. Hamza IAA et al (2013) Adsorption studies of aqueous Pb(II) onto a sugarcane bagasse/multi-walled carbon nanotube composite. Phys Chem Earth 66:157–166
196. Huang ZN, Wang XL, Yang DS (2015) Adsorption of Cr(VI) in wastewater using magnetic multi-wall carbon nanotubes. Water Sci Eng 8(3):226–232
197. Yadav DK, Srivastava S (2017) Carbon nanotubes as adsorbent to remove heavy metal ion (Mn+7) in wastewater treatment. Mater Today-Proc 4(2):4089–4094
198. Liu ZJ et al (2013) Synthesis of multi-walled carbon nanotube-hydroxyapatite composites and its application in the sorption of Co(II) from aqueous solutions. J Mol Liq 179:46–53
199. Bandaru NM et al (2013) Enhanced adsorption of mercury ions on thiol derivatized single wall carbon nanotubes. J Hazard Mater 261:534–541
200. Egbosiuba TC et al (2020) Enhanced adsorption of As(V) and Mn(VII) from industrial wastewater using multi-walled carbon nanotubes and carboxylated multi-walled carbon nanotubes. Chemosphere 254
201. Gupta VK et al (2017) Adsorption mechanism of functionalized multi-walled carbon nanotubes for advanced Cu (II) removal. J Mol Liq 230:667–673
202. Li Q et al (2015) Synthesis and characterization of dithiocarbamate carbon nanotubes for the removal of heavy metal ions from aqueous solutions. Colloids and Surf A-Physicochem Eng Aspects 482:306–314
203. Ma X et al (2015) Competitive adsorption of heavy metal ions on carbon nanotubes and the desorption in simulated biofluids. J Colloid Interface Sci 448:347–355
204. Zhou YY et al (2019) Single and simultaneous adsorption of pefloxacin and Cu(II) ions from aqueous solutions by oxidized multiwalled carbon nanotube. Sci Total Environ 646:29–36
205. Sun YB et al (2012) The removal of U(VI) from aqueous solution by oxidized multiwalled carbon nanotubes. J Environ Radioact 105:40–47
206. Hayati B et al (2018) Heavy metal adsorption using PAMAM/CNT nanocomposite from aqueous solution in batch and continuous fixed bed systems. Chem Eng J 346:258–270
207. Natarajan S, Bajaj HC, Tayade RJ (2018) Recent advances based on the synergetic effect of adsorption for removal of dyes from waste water using photocatalytic process. J Environ Sci 65:201–222

208. Chen B et al (2020) Magnetic chitosan biopolymer as a versatile adsorbent for simultaneous and synergistic removal of different sorts of dyestuffs from simulated wastewater. Chem Eng J 385
209. Jadhav SA et al (2019) Recent advancements in silica nanoparticles based technologies for removal of dyes from water. Colloid Interface Sci Commun 30
210. Pereira L, Alves M (2012) Dyes-environmental impact and remediation. In: Environmental protection strategies for sustainable development, p 111
211. Kadhom M et al (2020) Removal of dyes by agricultural waste. Sustain Chem Pharm 16
212. Liu L et al (2012) The removal of dye from aqueous solution using alginate-halloysite nanotube beads. Chem Eng J 187:210–216
213. Alardhi SM, Albayati TM, Alrubaye JM (2020) Adsorption of the methyl green dye pollutant from aqueous solution using mesoporous materials MCM-41 in a fixed-bed column. Heliyon 6(1)
214. Akpotu SO, Moodley B (2016) Synthesis and characterization of citric acid grafted MCM-41 and its adsorption of cationic dyes. J Environ Chem Eng 4(4):4503–4513
215. Bahalkeh F et al (2020) Removal of Brilliant Red dye (Brilliant Red E-4BA) fromwastewater using novel Chitosan/SBA-15 nanofiber. Int J Biol Macromol 164:818–825
216. Mirzaie M et al (2017) Removal of Anionic dye from aqueous media by adsorption onto SBA-15/polyamidoamine dendrimer hybrid: adsorption equilibrium and kinetics. J Chem Eng Data 62(4):1365–1376
217. Rizzi V et al (2019) Amino grafted MCM-41 as highly efficient and reversible ecofriendly adsorbent material for the Direct Blue removal from wastewater. J Mol Liq 273:435–446
218. Liou TH, Lin MH (2019) Preparation of mesoporous graphene oxide/SBA-15 hybrid nanoparticles as a potential adsorbent for removal of cationic dyes. Desalin Water Treat 155:285–295
219. Yuan N et al (2019) Adsorptive removal of methylene blue from aqueous solution using coal fly ash-derived mesoporous silica material. Adsorpt Sci Technol 37(3–4):333–348
220. Mahmoudi E et al (2020) Simultaneous removal of Congo red and cadmium(II) from aqueous solutions using graphene oxide-silica composite as a multifunctional adsorbent. J Environ Sci 98:151–160
221. Farias RMD et al (2020) Green synthesis of porous N-Carbon/Silica nanofibers by solution blow spinning and evaluation of their efficiency in dye adsorption. J Mater Res Technol-Jmr&T 9(3):3038–3046
222. Henning LM et al (2019) Grafting and stabilization of ordered mesoporous silica COK-12 with graphene oxide for enhanced removal of methylene blue. RSC Adv 9(62):36271–36284
223. Santos DO et al (2013) Investigating the potential of functionalized MCM-41 on adsorption of Remazol Red dye. Environ Sci Pollut Res 20(7):5028–5035
224. Boukoussa B et al (2018) Adsorption behaviors of cationic and anionic dyes from aqueous solution on nanocomposite polypyrrole/SBA-15. J Mater Sci 53(10):7372–7386
225. Galan J et al (2013) Reactive dye adsorption onto a novel mesoporous carbon. Chem Eng J 219:62–68
226. Chaudhuri H et al (2017) Room-temperature in-situ design and use of graphene oxide-SBA-16 composite for water remediation and reusable heterogeneous catalysis. ChemistrySelect 2(5):1835–1842
227. Tabani H et al (2019) Introduction of graphene-periodic mesoporous silica as a new sorbent for removal: experiment and simulation. Res Chem Intermed 45(4):1795–1813
228. Bu JQ et al (2020) High-efficiency adsorption of methylene blue dye from wastewater by a thiosemicarbazide functionalized graphene oxide composite. Diam Relat Mater 101
229. Bano Z et al (2020) Water decontamination by 3D graphene based materials: a review. J Water Process Eng 36
230. Lai KC et al (2019) Environmental application of three-dimensional graphene materials as adsorbents for dyes and heavy metals: review on ice-templating method and adsorption mechanisms. J Environ Sci 79:174–199

231. Ai LH, Jiang J (2012) Removal of methylene blue from aqueous solution with self-assembled cylindrical graphene-carbon nanotube hybrid. Chem Eng J 192:156–163
232. Lai KC et al (2020) Utilisation of eco-friendly and low cost 3D graphene-based composite for treatment of aqueous Reactive Black 5 dye: characterisation, adsorption mechanism and recyclability studies. J Taiwan Inst Chem Eng 114:57–66
233. Liu CY et al (2017) In situ reduced and assembled three-dimensional graphene aerogel for efficient dye removal. J Alloy Compd 714:522–529
234. Xu J et al (2020) Graphene oxide aerogels co-functionalized with polydopamine and polyethylenimine for the adsorption of anionic dyes and organic solvents. Chem Eng Res Des 154:192–202
235. Zamani S, Tabrizi NS (2015) Removal of methylene blue from water by graphene oxide aerogel: thermodynamic, kinetic, and equilibrium modeling. Res Chem Intermed 41(10):7945–7963
236. Shi YC et al (2016) Green-assembly of three-dimensional porous graphene hydrogels for efficient removal of organic dyes. J Colloid Interface Sci 484:254–262
237. Trinh T et al (2021) Preparing three-dimensional graphene aerogels by chemical reducing method: investigation of synthesis condition and optimization of adsorption capacity of organic dye. Surf Interfaces 23
238. Gupta K, Khatri OP (2017) Reduced graphene oxide as an effective adsorbent for removal of malachite green dye: plausible adsorption pathways. J Colloid Interface Sci 501:11–21
239. Xue ZS et al (2016) Thermodynamics of dye adsorption on electrochemically exfoliated graphene. J Mater Sci 51(10):4928–4941
240. Ma TT et al (2014) Fabrication of ultra-light graphene-based gels and their adsorption of methylene blue. Chem Eng J 240:595–600
241. Ferreira GMD et al (2017) Adsorption of red azo dyes on multi-walled carbon nanotubes and activated carbon: a thermodynamic study. Colloids Surf A-Physicochem Eng Aspects 529:531–540
242. Ge YL et al (2019) Enhanced adsorption and catalytic degradation of organic dyes by nanometer iron oxide anchored to single-wall carbon nanotubes. Appl Surf Sci 488:813–826
243. Jia L et al (2020) Modified multi-walled carbon nanotubes assisted foam fractionation for effective removal of acid orange 7 from the dyestuff wastewater. J Environ Manag 262
244. Lawal IA et al (2019) Theoretical and experimental adsorption studies of phenol and crystal violet dye on carbon nanotube functionalized with deep eutectic solvent. J Molecular Liquids 288
245. Machado FM et al (2011) Adsorption of Reactive Red M-2BE dye from water solutions by multi-walled carbon nanotubes and activated carbon. J Hazard Mater 192(3):1122–1131
246. Saxena M, Sharma N, Saxena R (2021) Highly efficient and rapid removal of a toxic dye: adsorption kinetics, isotherm, and mechanism studies on functionalized multiwalled carbon nanotubes. Surfaces and Interfaces 21
247. Prola LDT et al (2013) Adsorption of Direct Blue 53 dye from aqueous solutions by multi-walled carbon nanotubes and activated carbon. J Environ Manage 130:166–175
248. Sellaoui L et al (2017) New insights into the adsorption of crystal violet dye on functionalized multi-walled carbon nanotubes: experiments, statistical physics and COSMO-RS models application. J Mol Liq 248:890–897
249. Wang SB et al (2012) Synergistic and competitive adsorption of organic dyes on multiwalled carbon nanotubes. Chem Eng J 197:34–40
250. Mishra AK, Arockiadoss T, Ramaprabhu S (2010) Study of removal of azo dye by functionalized multi walled carbon nanotubes. Chem Eng J 162(3):1026–1034

Carbon Nanotubes-Based Mixed Matrix Membranes in Separation Technology

Anahita Soleimani and Mohammad Mahdi Doroodmand

Abstract Detail study has been focused on carbon nanotubes-based mixed matrix membranes (MMMs) in separation technology. The MMMs due to possessing significant properties such as high permeability, acceptable selectivity, enough flexibility, etc. have been considered as good candidate for the separation purposes. These properties are attributed to the presence and synergistic effects of three independent phases including organic, inorganic and filler ones with adequate and compatible work function. Consequently, the MMMs have great applications in different parts of science, especially at the separation field. Also about the carbon-nanotube-based MMMs, presence of multiple basal/edge planes in their matrices make them appropriate support with enough active surface area and plenty of O–H and –COOH functional groups. In this book chapter the MMMs have been evaluated from some different experimental and modeling aspects and have been introduced based on the researches published on the academic journals during the last decades. To the best of knowledge, there is no reports on the application of MMM in the separation science.

Keywords Carbon nanotube · Mixed matrix membranes · Separation · Modeling · Analytical science

List of Abbreviates

Abbreviate	Phrase
CNSs	Carbon nanostructures
PAN	Polyacrylonitrile
CMSMs	Carbon molecular sieve membranes

A. Soleimani
Department of Nanochemical Engineering, Shiraz University, 71454 Shiraz, Iran

M. M. Doroodmand (✉)
Department of Chemistry, College of Sciences, Shiraz University, 71454 Shiraz, Iran
e-mail: doroodmand@shirazu.ac.ir

Nanotechnology Research Institute, Shiraz University, 71454 Shiraz, Iran

M. Jawaid and A. Khan (eds.), *Carbon Composite Catalysts*, Composites Science and Technology, https://doi.org/10.1007/978-981-19-1750-9_6

MF	Metal frame
MFI	Metal frame inorganic
PSD	Pore size distribution
CVD	Chemical vapor deposition
PECVD	Plasma-enhanced CVD
MACVD	Microwave-assisted CVD
PEG	Polyethylene glycol
HDS	Hydrodesulfurization
MMMs	Mixed matrix membranes
MOF	Metal organic framework
CMS	Carbon molecular sieve
NBR	Butadiene rubbers
EPDM	Ethylene propylene rubber
PCP	Polychloroprene
PDMS	Polydimethylsiloxane
PMP	poly (4-methyl-2-pentyne)
CNTs	Carbon nanotubes
SWCNTs	Single-walled CNTs
MWCNTs	Multi-walled CNTs
APDEMS	Silane coupling agent, (3-aminopropyl)-diethoxymethylsilane
CD	Cyclodextrin
IPDI	Isophoronediisocyanate
MD	Molecular dynamic
PES	Polyethersulfone
PBNPI	Poly (bisphenol A-co-4-nitrophthalic anhydride-co-1,3-phenylene diamine
PVA	Poly (vinyl alcohol)
PSF	Polysulfone
PS	Polystyrene
SPU	Segmented polyurethane
BM	Platelet boehmite
PE	Polyethylene
BM	Platelet boehmite
MAA	Methacrylic acid
MAO	Metallocene
SBR	Styrene-butadiene rubber
BM	Boehmite
1-D, 2-D, 3-D	One-, two-, three- dimensional (1-D or 2-D)
Φ	Volume fraction
P_r	Permeability
$P_{r,Cal}$	Calculated permeability
Ψcal	Calculated Ψ function
Φ_m	Volume fraction
Φ_{Cal}	Calculated volume fraction
Φ_{Exp}	Experimental volume fraction

1 Membrane Technology

Membrane separation is considered as one of the most important fields during the last decades [1–18]. This is owing to the significant application of this technology in various fields such as chemistry, environment, pharmacy, etc. [2–19]. Basically, membrane-based separation process in found on selective transition of an analyte from a feed combination followed by separation of the feed matrix during a fixed and reproducuible time scale[4–20]. Consequently, membrane technology has been considered as one of the most important topic [21–25]. The importance of membrane technology is attributed to some fundamental capabilities and characteristics of membranes such as: satisfactory capacity for highly effective separation of a number of complex combinations from gas species to the solid mixtures [8, 14], large mechanical and high chemical stability of membranes [26–30], etc. [26–30].

For instance, permeation and selectivity are considered as two important factors in comparison with the basic performance characteristic [31–33]. Permeability is defined as the capability of the permeants to transmit through a membrane. Selectivity of membrane is also defined as the ratio of permeability of the more permeable component to that of the less permeable [31]. In another word, as the higher the permeability of a membrane, the smaller is the membrane area required, on the other hand, the higher the selectivity, the lower the driving force required. Such ideal conditions thus lower the capital and operating cost of the separation system. Robeson was the first researcher who approved the "inverse permeability/selectivity" correlation [34]. Based on his proposal, there is a theoretical "upper bound" in the relationship between permeability and selectivity [34]. Therefore, for economic consideration, selectivity and permeation rate are important parameters that should be maximized in order to provide commercially attractive outcome and achieve more efficient separation in all applications. However among these effective factors, parameters such as permeability and selectivity play significant role during evaluation of the performance of any membrane [24, 25, 32, 35, 36].

Development of high efficient membranes based on significant physicochemical properties for separation and purification of different gas and liquid molecules as well as separation processes has attracted a great deal of interest during the last two decades [37, 38]. Factors such as membrane stability and durability, high permeation flux and selectivity and low production cost are therefore considered as the most important criteria during developing a membrane for a specific separation [39, 40]. These properties make membranes to be considered as a semi-permeable blockade throughout the selective permeation across the membrane [8, 25, 41]. For instance, these characteristics correspondingly are dependent to the separation mechanism of separation for having an appropriate efficiency during the separation process [42–51]. Consequently, to enhance the selectivity as well as to promote the permeation flux, knowledge about the physicochemical properties of membranes is important [52].

Table 1 Feature of different mechanisms during the separation process

Mechanism	Feature	Application	References
Molecular sieving process	Filtration	H_2, CO_2, N_2 separation	[24]
Adsorption	Surface adsorption on supports with high active surface are	Purification of hydrogen	[58]
Surface diffusion	Diffusion to from surfaces to the bulk of any support	H_2 separation	[59, 60]
Capillary condensation	Condensation based on capillary effect	CO_2 purification	[61, 62]

2 Separation Mechanism in Membranes

Separation through a permeable membrane is initiated on a small number of processes including molecular sieving, adsorption, surface diffusion, and capillary condensation processes [53]. Through the molecular sieving process, minor fragments dispatch through the pores of these molecular sieves [54]. This process results to permit the superior species inside the feed matrix [31, 53]. Occasionally, an individual component may selectively be permeated along the pores [55]. This event may lead to have selective surface diffusion across these membrane [56, 57]. This separation process also takes place via partial or capillary condensation of one component inside the pores of the membrane based on different mechanisms [53]. Feature of each mechanism is reported in Table 1 in detail.

3 Membrane Materials

To have membrane with acceptable efficiency and capability, choice of membrane seems to be very important [24]. Often selection of suitable membrane materials for a specific separation intensely depends on the application of the membrane. The importance of this topic is so high that, this subject has been accepted as considerable challenge among the scientists [24, 63]. The significance of the selection of appropriate materials majorly affects the separation mechanism of any membrane [64]. This phenomenon is related to the significant effect the membrane's materials on some membrane-based separation factors such as producibility, durability, selectivity, permeability, and/or mechanical integrity [32]. Because of the effective role of membranes in the separation process, selection of appropriate membrane's materials is important during the fabrication of membranes [31, 65].

Through the last decades, various materials such as polymers [66], metal [67], silica [66] and activated carbon as well as different types of molecular sieves like zeolite [68] and carbon nanostructures (CNSs) [24] have been used as membranes. In the membrane technology, depending on the materials adopted to generate

membranes as well as based on relationship between permeability and selectivity, membranes are classified into two independent categories including (i) organic (polymeric), and (ii) inorganic membranes [12, 69–72].

3.1 Organic-Based (Polymeric) Membranes

In the polymer-based (polymeric) membranes, polymers such as polyimides and polysulfone are used [73–75]. Polymeric membranes are widely used in the membrane separation process due to their processability, and their flexibility [76–78]. Polymers have advantages such as high separation properties and chemical stability [24, 79]. Polymers also have special capabilities such as high selectivity [24]. However compared to porous materials, polymeric membranes often have low throughput [32, 79]. This is related to low free volume of polymers [32]. In addition polymers are not stable at high temperatures and harsh chemical conditions [32, 78, 80–83]. Besides high cost and breakable structure restrict of the polymers, the reverse behavior of permeation and selectivity of these membranes is also considered as another shortcoming of the polymeric membranes [39, 52].

A major fouling of polymer-based membranes is that, polymers are prone to aging effects and show a decrease in permeability over time. These phenomena are related to relaxation of the polymer chains and presence of impurities in the polymer matrix [84]. These shortcomings significantly limit large scale applications of polymer membranes [48, 49].

Polymeric membranes are categorized based on rubbery or glassy polymers. Rubbery polymers are often soft and elastic [24]. These properties are originated from high flexibility of the polymer backbone segments that provide the capability to rotate freely around their axis [24]. Whereas owing to the steric hindrance along the polymer matrix (backbone), glassy polymer is often rigid and tough polymer [24]. These properties cause deformation of polymer segments [24, 82].

Generally, chain rigidity is often found in glassy polymers, resulting to have an increased selectivity but lower permeability whereas high permeability can be obtained with a greater inter-segmental distance as in rubbery polymer [31].

The investigation of polymer membranes for gas separation was firstly reported in 1970s with the discovery of a delayed diffusion time lag effect for CO_2 and CH_4 using zeolite (5A)-based rubbery polymer membranes as "*Mixed Matrix Membranes*" (MMMs) [83]. In this study, Paul and Kemp found that the addition of 5A$^{\circ}$ in to the polymer matrix caused very large increases in the diffusion time lag but had only minor effects on the steady-state permeation [83]. These polymeric membranes are available in a wide array of chemistries that can be used to for particular applications.

3.2 Inorganic-Based (Mineral) Membranes

Inorganic membranes are fabricated using inorganic amorphous materials such as metals, ceramics, pyrolysisd carbon, etc. [39, 54, 84–91]. In these membranes, high thermal and physical stability as well as acceptable selectivity are considered as their main advantages [23, 92]. Compared to the polymeric membrane, the cost of the inorganic membrane fabrication is few orders of magnitude higher [24]. However these membranes are seriously suffered from low permeability [23]. Inorganic membranes are also categorized as dense and porous [23, 24, 92]. Macro porous (dense) membranes are often made of materials such as alumina, zirconia, glass, or stainless steel, resulting to provide the acceptable mechanical strength [64]. Whereas, porous inorganic membranes such as zeolite and carbon molecular sieve have significant advantages such as excellent selectivity, which are not comparable with that of polymeric membranes [24, 93, 94]. Significant challenges in the amorphous inorganic materials are that, porous inorganic membranes do not intrinsically have the inherent mechanical strength to form self-supported membranes [24, 93, 94].

Carbon and zeolite membranes have attracted great research efforts and significant progress has been made to expand this type of membrane via improving the membrane quality in selectivity, fabrication methodology and energy-production application [93–96].

3.2.1 Zeolite Membranes

Zeolite membranes, owing to possessing intrinsic characteristics such as high active surface area, presence of cages in the matrix of zeolite, as well as their selective gas separation behavior have been selected as appropriate gas-separating material [24]. In these membranes, zeolite is often supported in a metal frame (MF) [24]. The generated membrane is named as "*Metal Frame Inorganic*" (MFI) [24]. MFI-type zeolite is commonly used in the preparation of zeolite membrane due to its promising pore size and ease of preparation [24].

3.2.2 Carbon-Based Membranes

Due to the excellent properties of carbon-based membranes for separation process, carbon membranes have attracted much attention [30, 43, 46]. The separation properties of carbon membranes is based on various gas transport mechanisms such as molecular sieve carbon membranes and adsorption-selective carbon membranes [30, 43, 44].

3.2.3 Carbon Molecular Sieve Membranes

Carbon molecular sieve membranes (CMSM) are obtained from the carbonization of polymeric precursors under a controlled inert atmosphere [97]. The main feature of CMSMs is that their pore size distribution (PSD) can be tailored to suit a desired application by optimizing the pyrolysis conditions and chemical composition of the precursor [88]. Compared to other types of inorganic membranes, CMSMs possess fantastic advantages such as higher permeability, better selectivity, as well as higher thermal and chemical stability [89]. However these membranes majorly suffer from challenges such as brittle, lack mechanical stability and low reproducibility [90].

3.2.4 Adsorption-Selective Carbon Membranes

Depending on the procedure used to fabricate carbon-based membranes, these membranes can be considered as selective gas separation membranes with adsorption mechanism [43, 44, 46]. In these membranes, carbon as the main part of this membrane is often synthesized using methods such as chemical vapor deposition (CVD), electrical arc/discharge, plasma-enhanced CVD (PECVD), microwave-assisted CVD (MACVD), disproportionation reaction of CO, etc. [43]. These types of carbon membranes can separate specific gas pairs depending on adsorption mechanism during the gas transport [30].

4 Challenges Related to Organic and Inorganic Membranes

The advantages and disadvantages of both polymeric and inorganic membranes have been explained in detail in the previous sections (Sects. 3.2.3 and 3.2.4). As clearly explained, reverse correlation between selectivity and permeability is considered as the main challenge in the membrane technology [98]. This phenomenon is named as “inverse permeability/selectivity” behavior of the membrane [30, 43, 44]. This problem often leads to have low selectivity during the separation process [35, 98]. To solve this problem, scientists have focused on various factors affecting the performance of the membranes [24]. Major physicochemical factors affecting the permeability and selectivity of membrane are (i) the mobility of polymer chains, (ii) the inter-segmental spacing that is indicated by the means free volume of the polymer, (iii) the penetrant–polymer interactions [99] and (iv) swelling the membrane materials by certain feed components [98]. These factors lead to have membrane with lower thickness [24]. The membranes are named as integrally skinned membranes [30, 44, 55].

5 Integrally Skinned Membranes

In the membrane technology, for having high efficient separation, the most desirable polymers are those that provide both high permeability and selectivity [36]. As with inorganic membranes, it is aimed to form the polymer layer with minimum possible thickness. To promote the permeability of any membrane, the membrane's thickness should be quite small such as order of microns [24, 32, 54, 93, 100]. For this purpose, polymeric membranes are often casted on supports to form "*Integrally Skinned Membranes, ISMs*" [32, 53, 64, 101]. To synthesize these membranes, phase inversion is considered as one of the commonly used processes to form ISMs. In this process, briefly a soul is often inverted to form a porous three-dimensional macro molecular network [31, 32, 35, 64]. In these membranes, however some improvements have been observed in the performance and characteristics of the membranes but, the faults related to these membranes have been still existed [93, 94]. These problems seriously point to the significant importance of the modification of membranes materials.

5.1 Membranes Material Modifications

The intrinsic physical properties of the membrane's materials can significantly be improved during modification with some extra structures [12]. The modifying material plays role as coupling agent (an integral chain linker) [12]. For instance, as zeolite surface usually has hydroxyl groups; therefore introduction of a suitable functional group such as carboxylic acid (–COOH) in the polymer chains can chemically react with hydroxyl group [12]. This modification is effective during prevention from any interface void during the polymer chain shrinkage [12, 39, 52]. By the modification process, modifying agents such as organic/inorganic species (phases) are combined with each other [12, 39, 52]. Due to the combination of these two phases, these membranes are named as "Hybrid Membranes".

During the last decades, different types of hybrids such as organic/organic, inorganic/inorganic, and organic/inorganic phases have been introduced to enhance membrane performance [32]. Among the introduced hybrid membranes, organic/inorganic membranes due to the possessing the properties of both organic and inorganic membranes are more common [32].

5.1.1 Organic/Inorganic Hybrid Membranes

Organic/inorganic hybrid membrane is based on combination of both polymeric and porous inorganic materials [64]. This membrane is fabricated via incorporation of inorganic particles (phase) into a polymer (organic) matrix [102–109]. This process leads to modify a porous substrate with organic/inorganic-based materials [102–109].

Layers of polymeric material are simply immobilized on the surface of a porous substrate via some physic/chemical interactions [102–109]. Fabricated membrane has therefore significant characteristics specially as simultaneous properties of both organic and inorganic phases [64].

Based on the literature, common methods for membrane modification during filling additives for having high selectivity or high flux include crosslinking, blending, filling, and copolymerization [110]. Each process is explained in detail in the following sections.

Cross-Linking

Cross-linking of the polymers in the membrane technology significantly reduces the solubility of the membrane [110, 111]. This process reduces the solubility of the membrane during contacting with sophisticated feed mixture without swelling [110, 111]. All these properties majorly promote the selectivity of the membrane during the separation process [111]. In these membranes, promotion of the swelling resistance of the membrane during contacting with various organic and inorganic species depends on the formation of reticular spatial structure by cross-linking agent [112]. In another word, cross-linking often prevents from the swelling of the polymer-modified layers [113]. This process therefore leads to have better compatibility and maximum adhesion of layers [113].

Cross-linking is often performed via either chemical reaction or physical processes [98]. These processes lead to provide a cross-linking agent to connect two polymer chains [98]. The modification can also be achieved using a physical process called "*pervaporation*" [114, 115]. For instance it has been reported that, pervaporation performance of the cross-linked polyethylene glycol (PEG) membrane with ~20-μm thickness during long time operation of 500 h has been initially investigated by Lin et al. [115]. However physical cross-linking process has serious problems such as formation of brittle and low stable membrane [111] that majorly limits the capability of this membrane especially for pervaporation [111].

Factor affecting the quality of cross-linking performance includes the cross-linking degree [116, 117]. Cross-linking degree is strongly dependent to parameters such as the thickness of the membranes i.e. the amount of cross-linking agent and cross-linking time [117]. During this process, some figures of merit such as stability, flux and gas enrichment factor are improved [98, 116].

However, during physical cross-linking process, it should be avoided from excessive cross-linking [111]. It has been reported that, the mobility of macromolecules and chain segments are significantly decreased during the physical cross-linking process [118–120]. This challenge may effectively diminish the inter-chain free volume, as well as discouraging the permeation of small molecules [118–120]. Therefore, the cross-linking degree should be controlled and optimized [118–120].

Blending

Blend process is defined as the physical mixture of two phases such as two kinds of polymers that are not covalently bonded [98]. This technique significantly controls the permeability and selectivity of the membrane [111]. The blends can be classified in two types [111]:

(1) A homogeneous blend, in which the two phases are miscible on a molecular scale for all ratios. In this type, various distributions are observed during physical mixing of two phases [111].
(2) A heterogeneous blend, in which the two phases are not totally miscible [98]. In this type, the ratio of two phases should be controlled to prevent from loss of mechanical strength in the membrane matrix [111].

Basically this technique is considered as an ideal methodology in which the hydrophobicity of a hydrophobic membrane is promoted during optimizing the blending ratio at optimum condition and vice versa [98].

Filling

Modification of any membrane during filling another phase is based on the solution-diffusion theory that is achieved via three steps including [98]:

(1) Sorption of permeating molecules (adsorptive filler),
(2) Diffusion,
(3) Desorption from the membrane.

During these steps, adsorptive fillers are incorporated into the membrane matrix [121]. This process majorly promotes the capacity of any membrane for separation purposes. In the literature, different kinds of commercial adsorbents including zeolite, activated carbon, and metal oxide have been reported for separation purposes such as gasoline desulfurization [122–124]. Also to improve the gas removal efficiency of the membranes, selective sorbents such as transition-metal ion exchanged zeolites have been bonded to hydrodesulfurization (HDS) catalysts through π-complexation bonds [125–127].

Copolymerization

Similar to the blending process, copolymerization methodology can be adopted to control the hydrophilicity of the membrane [98]. Copolymerization is achieved via covalent bonding the two phases during the copolymerization process [98]. This process often leads to increase the mechanical stability of the membrane [98]. Using this technique, three kinds of copolymers include [98]:

– Block, in which the degree of crystallinity is considered as one of the most important feature [98],

Table 2 Modifications of membranes by various technical methods

Method	Characteristics	Advantages/disadvantages	Example	References
Cross-linking	Cross-linking materials	– Insolubility of the membrane – Promotion of selectivity – Better compatibility between membrane and feed solution – Weak mobility of macromolecules through the membrane	Sulfur-containing materials	[120, 131]
Blending	Polymer blend via mixing two polymers through via homogeneous or heterogeneous process	– Control of the hydrophobicity of the membrane – High mechanical stability, especially during homogeneous mixing	Hydrophilic and hydrophobic polymers	[110, 111, 117]
Filling	Adsorptive fillers	– Filler acts as facilitators or enhancers separation properties of the membrane – Enhancing the sorption capacity of the membrane	Adsorbents such as zeolite, activated carbon, and metal oxide	[122–124]
Copolymerization	Copolymer materials	– Increasing the mechanical stability of the membrane	Various kinds of block, random, and grafted copolymers	[114, 130]

– Random, in which the random copolymers might be completely amorphous,
– And grafted copolymers, which contain a certain degree of crystallinity.

During these processes, factors such as permeability and selectivity are controlled by changing the contents of different chain segments [98, 128]. It has been reported that, copolymerization process can make the membrane suitable for effective separation of organic components [129, 130]. According to the literature, grafting copolymer with polymers such as polyacrylonitrile (PAN) as supporting role and modified cellulose as mechanical stabilizer have been introduced for gasoline desulfurization [131].

Modifications of membranes are often achieved by various technical methods summarized in Table 2. As shown, all of these modifications result to have hybrid of organic/inorganic membranes.

6 Comparison Between Organic, Inorganic and Hybrid Membranes

In the membrane technology, in spite of great advantages of the modification of polymer and inorganic membranes, but these membranes still suffer from challenges such as weak mobility, high cost, rigidity, short life time, swelling of the membrane, reverse behavior of selectivity and permeability, etc. [125–127, 132]. Advantages and disadvantages of various types of membranes have been summarized in Table 3. These properties were firstly identified by Robeson and later were characterized more fully by Freeman [34, 133].

As shown (Table 3), despite of the advantages demonstrated by the inorganic membranes, the realization of their application is still hindered by high cost of membrane fabrication, the complication of managing the membrane technology to form continuous and defect-free membrane [51, 127, 135].

All these limitations majorly point to the strong demand for modification of hybrid materials and introduction of new types of hybrid membranes. One current trend that has been emerged in the membrane-based separation is a move to the fabrication of new type of hybrid membranes called MMMs [94, 136]. To have membrane with outstanding characteristics, inorganic membranes are regularly filled with polymers to form MMMs.

Table 3 Comparison between various types of membranes

Membrane	Characteristics		References
	Advantageous	Disadvantageous	
Polymer membrane	• Cheap • Mass production (larger scale) • Good quality control	• Structurally weak, not stable, temp. limited • Prone to denature & be contaminated (short life)	[125]
Inorganic membrane	• Long term durability • High thermal stability (>200 °C) • Chemical stability in wide pH • High structural integrity	• Brittle (Pd) • Expensive • Some have low hydrothermal stability	[125, 134]
Hybrid membrane	• Good permeability • High selectivity • High mechanical strength • Large thermal and chemical stability • High performance of gas separation	• Reverse correlation between selectivity and permeability	[133]

7 Mixed Matrix Membranes

To improve polymeric and inorganic membrane performance, a considerable research effort should be focused on the formation of membranes via addition of inorganic materials such as zeolites or carbon molecular sieves (as inorganic filler) to a continuous polymers [2, 69, 90, 97, 136–143]. This process provides new kind of hybrid membrane called MMMs. MMMs are therefore defined as the incorporation of a solid phase into a continuous polymer matrix [144]. In another word, MMM is a heterogeneous membrane in which an inorganic filler is embedded in a polymer matrix [144].

In the MMM technology, selection of membrane configuration is greatly dependent on the application [68, 145, 146]. Production of MMMs in useful configuration is certainly essential to render the progress of utilizing this material [147]. Often, the inorganic fillers used in MMMs are mostly porous molecular-sieve type materials, including zeolites [2, 136, 137, 141–143] and carbon molecular sieves [68, 145, 146]. Therefore, MMMs combine processability and cost effective of the polymer materials with excellent separation performance of molecular sieve materials [69].

8 Comparison Between MMMs and Others Membranes

The objective of MMMs is to use the solid phase in a composite membrane to provide a means to overcome the tradeoff performance based on higher selectivity and/or higher permeability of solid phase than the polymer matrix [144]. The concept of MMM combines the advantages of two different phases including:

(1) High selectivity of the dispersed fillers with desirable mechanical properties,
(2) And economic advantages of polymers.

The intelligent incorporation of inorganic fillers within a continuous polymeric matrix represents a promising approach to attain superior separation performance that surpasses the Robeson trade-off line for permeability and permselectivity [37, 139, 141]. Many studies have reported that, MMMs may exhibit substantially increased permeability and selectivity that are far beyond the intrinsic properties of pure polymer membranes [148–151]. Consequently, an interesting approach improves the separation properties of MMMs because they possess properties of both organic and inorganic membranes such as good permeability, selectivity, mechanical strength, as well as thermal and chemical stability [133, 152].

MMMs have therefore great potential to achieve higher selectivity, and permeability, compared to both currently existed polymer and inorganic membranes [153–155]. At the same time, the fragility inherent in the inorganic membranes may be avoided by using a flexible polymer as the continuous matrix. Upon these comparisons, it is obviously noted that MMMs possess very promising properties that have remarkably surpassed that of polymeric and inorganic membranes [24]. During the

last decade, MMMs have been accepted as a promising solution to the inherent permeability/selectivity trade-off of pure polymer membranes [153–155]. Consequently, MMM has been rapidly researched and is an attractive candidate for membrane-based separations in today's market [24].

9 Phases in the MMMs

In the MMM structure, this membrane consists of organic polymer and inorganic particle phases, schematically as shown in Fig. 1 [156]. Based on this schematic (Fig. 1) the existing phases in the MMM matrix includes:

- Bulk phase (phase A) is typically a polymer (organic phase),
- Fillers (phase B), i.e. interface (dispersed) morphology (inorganic phase),
- And metal organic framework (MOF, phase C).

Detail of each phase has been explained in detail in Table 4.

Combination in MMM leads to have a synergistic effect in which the rigid adsorptive porous type inorganic phase provides superior separation properties, whereas presence of flexible polymer enables the ideal membrane forming consequently solving the problem off rigidity inherent found in the inorganic membranes [6, 141, 147]. The application of MMMs for separation has attracted worldwide interest due to the potentially synergetic effects of these two phases [147].

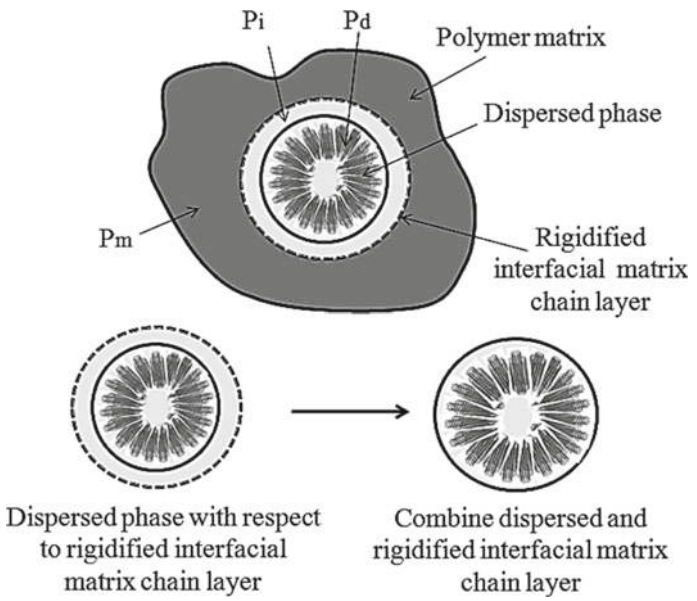

Fig. 1 Schematic representing the different phases in the MMMs [156]

Table 4 Characteristics of various phases in MMMs

Phase	Factors affecting the performance of phase	Commercially available phase	References
Polymer (organic phase, phase A)	Flexibility, Low Tg, high selectivity, large permeability	Polyhexafluorodianhydrideisopropylidenedianiline, polyhexafluorodianhydride methylene dianiline, poly hexafluorodianhydride 4,40-hexafluoro diamine, poly hexafluorodianhydride 3,30-hexafluoro diamine, tetramethylhexafluoropolysulfone, bisphenol-A polycarbonate, polyvinyl alcohol, sodium alginate, chitosan, polyimides, etc.	[12]
Filler (inorganic phase, phase B)	Compatibility between organic and inorganic phases, Formation of void in polymer matrix	Zeolite, silica, molecular sieves, activated carbon, Carbon molecular sieves such as carbon particles and carbon nanostructures, etc.	[12, 141]
Metal organic frameworks (phase C)	High surface area, controlled porosity, low density, thermal and mechanical stability, high selectivity, pore diameter	–	[24]

10 Types of MMMs

During the last decades, various forms of MMM have been introduced. This introduction is based on the materials, size, morphology and compatibility of different phases in the MMMs [157–161]. Detail of each type of MMMs has been summarized in Table 5.

Compared to the polymeric, inorganic and hybrid membranes, MMMs possess significant advantages such as flexibility, high permeability, acceptable selectivity, low cost, etc. [175–182].

Table 5 Characteristics of various types of MMMs

Membrane type	Characteristics	Properties	References
Conventional MMMs	Compatibility between organic and inorganic phases	– Separation based on selective adsorption and/or surface diffusion of more condensable components – Significant enhancement in the selectivity coefficient during gas separation process	[12, 157–162]
Unconventional MMMs	Combination between porous fillers and polymeric matrices	– Formation of membrane with inherent chain packing characteristic – Formation of intrinsically high free volume – Enhancement in factors like diffusivity, and selectivity – Diminanting the solubility coefficient during separation process	[157, 163, 164]
Asymmetric and composite MMMs or multi-layer composite membranes	– Having high productivity in industrial application – Ultra thin membrane	High selectivity	[12]

(continued)

Table 5 (continued)

Membrane type	Characteristics	Properties	References
Flat sheet asymmetric MMMs	– In-order sheets for the synthesized MMM – Asymmetric morphology	– Membranethickness varied from 5 to 25 μm – Offering negligible resistance to gas flow – Maximum efficiency for gas separation at membrane thickness lower than 18 mm – Preparations via solution deposition on top of a porous ceramic support – Filler thickness between 200 and 2000 A° Membrane thickness between 5 and 25 μm Use of ultrafine particles (0.2–0.5 μm) Prepolymerization of the suspension on supports such as silicalite, two-component Polydimethylsiloxane (PDMS) polymer and iso-octane	[163–165]

(continued)

Table 5 (continued)

Membrane type	Characteristics		Properties	References
Hollow fiber asymmetric MMMs	Based on single layer spinning		Sub-microsizedparticles must be used in order to be fit inside the ultra-thin skin layer Polymer phase defects and polymer/particle interface defects must be suppressed	[166–170]
	Based on dual-layer spinning	Formation of asymmetric membranes is the result of the micro phase separation step and/or quench step of an initially thermodynamically stable polymer solution	Great mechanical strength The use of fillers such as carbon black, vapor grown carbon fibers, andTiO_2 Including single-layer and dual-layer hollow fibers Distinctions can be drawn with regard to the conditions under which the microphase separation process occurs to generate the final membrane morphology	[166–174]

Table 6 Reason for advantages low cost of dual-layer membrane, compared to single-layer membrane [12, 180–185]

Parameter	Reasons
(1) The dual-layer fibers can reduce material costs by about 95% or even more	This property depends on the ratio of the inner layer to outer layer thickness; by means of choosing different materials for the two-layer and co-extrusion, it is possible to employ brittle (engineering infeasible), but high-performance material as the outer layer to form the composite membrane
(2) The cost reduces via choosing appropriate inner layer and adjusting the dope solution concentration	The porosity in the resultant membrane can be controlled and the dual-layer hollow fibers can withstand high pressures
(3) The cost of MMM is attributed to the formation of composite membranes	The simultaneous co-extrusion makes the formation of composite membranes more straightforward and cost-effective compared to other preparation approaches
(4) The cost of MMM is related to the quantity of materials needed for having appropriate Flux through the membrane	Higher fluxes can be obtained in the single-step production, since pore penetration, a common problem in the subsequent dip-coating process is avoided

11 Layers in MMMs

Depending on kind, polarity, morphology and homogeneity of each organic and inorganic phase in the MMMs, these membranes can be divided in to single- and dual-layer MMMs [181–185]. In the MMMs, controlling the number of layers in MMM matrix has significant advantageous such as enough compatibility, flexibility, stability and morphology of void volumes in the MMMs [180–185]. This control is often dependent to the procedure adopted for fabrication of MMMs [184, 185]. Compacted to the single-layer, lower cost is needed for synthesis of dual-layer MMMs. Economic characteristic of both single- dual- layer MMMs have been summarized in Table 6 [12, 180–185].

12 Fabrication of MMMs

To fabricate MMMs, polymeric layer is generally packed with a molecular sieve such as zeolite or carbon molecular sieve (CMS) to procedure a compact region of mixed matrix layer [171, 179–185]. MMMs are therefore fabricated via addition of porous inorganic fillers to the polymer matrices [12, 51, 66, 145]. In another word, MMMs combine the superior permeability and selectivity of inorganic membranes with the processability of polymeric membranes [24]. To fabricate MMM with novel properties, various factors such as [12]:

(1) Preparation of homogeneous polymer/inorganic filler/solvent mixture,
(2) Casting the solution on a smooth plate,
(3) Evaporation of the solvent, and sometimes,
(4) And annealing the membranes at high temperatures to remove the residual solvent, should be attended [12]. These factors can simply approve the advantage of MMM [12].

During the fabrication process, factors such as shape and size selective nature of the MMMs significantly depend on the morphology of the nonporous materials [183, 185]. These phenomena therefore control the molecular sieving discrimination based on selective passage of smaller sized species for penetration and diffusion at higher rate in comparison with that of larger sized membranes [24, 184, 185]. These factors are important during formation of controllable adhesion between the polymer phase and the external surface in the MMMs [186].

In the literature, various preparing methods have been introduced to make MMM membranes. These mythologies are based on verifying the dry and wet-phase inversion preparation method with different coating techniques [35]. Detail of these methodologies is as follows.

12.1 Dry-Phase Inversion Process

In the MMMs, when the solvent and nonsolvent components are removed exclusively by evaporation, membranes formation is defined as "*Dry-Phase Inversion Process*" or "*Slide Casting/Vacuum Process*" [35].

12.2 Wet-Phase Inversion Process

When the phase separation process is based on the solvent/nonsolvent exchange during quench step, the structure formation process is therefore named as "*Wet-Phase Inversion Process*" [35].

12.3 Comparison Between Dry-Phase and Wet-Phase Inversion Processes

Compared to the wet technique, dry method exhibit excellent gas permselectivity comparable to other coating methods [35, 176]. Detail of these preparation methods is shown in Table 7.

In this Table, the effects of different kinds of coating techniques such as slide casting/vacuum, spin coating/vacuum (dry-phase method), spin coating/isopropyl

Table 7 Various technical methods for generation of MMMs

No	Method	Detail and examples	References
1	Ultrasonic deposition	Nanoporous carbon membranes	[168, 169]
2	Dip coating	Carbonized BPTA-pp' ODA polyimide membranes	[170]
3	Vapor deposition	Supported carbon membranes from furfuryl alcohol	[187]
4	spin coating	Carbon molecular sieve membranes	[38, 188]
5	Spray coating	Nanoporous carbon membranes for air separation	[189]

alcohol (IPA; wet-phase method), and pyrolysis temperature on the gas separation performance of the membrane has been explained in detail according to the review reported in Ref. [35]. In these preparing methods, a relatively open structure like a "*Sponge-Type Structure*" is formed when the polymer concentration is scarcely changed [35].

13 Variables Tailoring MMMs' Performance

Among all the studies on MMMs, various effects control the performance of MMMs. These parameters include: the compatibility between both organic and inorganic phases, particle size of inorganic phase, the degree of particle sedimentation and aggregation, pore blockage and chain rigidification, voids between organic and inorganic phases, and addition of inorganic fillers [12, 24, 83, 157, 164, 190–195]. Detail of these variables has been summarized in Table 8. All the parameters reported in Table 8, clearly point to the performance of MMM for separation process during modification process.

14 Molecularly Engineered MMMs

To improve the characteristics of MMMs, selection of organic and inorganic phases is considered as effective role in the performance of MMMs [141, 196]. Often among various types of inorganic and organic phases, metal nanoparticles and CMS seems to be appropriate candidates for fabrication of new version of MMMs called "*Molecularly Engineered MMMs, MEMMMs*" [49, 139, 141, 171–173, 197].

The structure and performance of MEMMMs are generally a function of the physical and chemical properties of the organic/inorganic phases as well as the method of nanoparticle incorporation [142]. In the following sections, these membranes are investigated in detail.

During the last decade, numerous research groups have focused on the capability of some types of MEMMMs in flat and dense forms using different kinds of inorganic particles like zeolites, carbon molecular sieves and others [49, 139, 141, 171–173,

Table 8 Effect of variables tailoring MMMs' performance

Variables	Effective parameter	Example	References
Suitable combination of polymer/inorganic filler	– Physical properties of the inorganic fillers (e.g., particle size and particle agglomerations) – Polymer/particle interface morphologies – Selection of appropriate inorganic filler – Choice of a suitable polymer as the matrix	Combination of zeolite with various silicone rubbers of nitrile butadiene rubbers (NBR), ethylene propylene rubber (EPDM), polychloroprene (PCP), and PDMS	[196]
Particles size of inorganic phase	– Good dispersion of inorganic phase in the polymer matrix – Smaller particles are also helpful and essential in the formation of thinner MMMs – Formation of enhanced polymer/inorganic phase interface contact – Higher permeability and selectivity	Investigation of the effect of different particle sizes (0.1, 0.4, 0.7, 0.8, 8.0 mm) of silicalite in PDMS	[169]
Particle sedimentation and agglomeration	Agglomeration of zeolites will cause the pin holes that cannot be reached by polymer segments, forming as non-selective defects in the MMM	– Dispersion of fumed silica particles in PMP(poly (4-methyl-2-pentyne))	[159]

(continued)

Table 8 (continued)

Variables	Effective parameter	Example	References
Pore blockage and chain rigidification	Blockage of the pores by polymer chains may completely eliminate the function of the inorganic filler	Silane coupling agent, (3-aminopropyl)-diethoxymethylsilane (APDEMS) to modify zeolite surface for MMMs	[190]
Oxidation etching of inorganic phase	Oxidation etching is commonly utilized to purify and create open end termini in the structure to produce shorter, distinct and one-end uncapped carbon nanotubes (CNTs)	Plasma etching, mechanical polishing and acid treatment	[191]
Voids between polymer and inorganic in MMMs	– Due to the presence of van der Waals force, CNTs tend to form stabilized bundles which in turn result in the formation of tight bundles and hollow ropes – Formation of along the length and at the tips of CNTs – Significantly enhancement in the surface area and interfacial adhesion between the polymer matrix and CNTs	– Acid modified CNTs to form OH and COOH functional groups – Functionalization of CNTs with cyclodextrin (CD) or isophoronediisocyanate (IPDI), phenylamine, chlorobenzoic acid and acyl chloride, etc.	[192–195]
Addition of inorganic fillers	– Generation of strong interaction between polymer chains segment and nanofillers – Disrupting the polymer chain packing and increase the void and thus significantly enhance the gas diffusion; -formation of functional groups on the surface of inorganic filler phase for interaction with some gases to improve the solubility in the MMMs	SiC, CNTs, graphite, zeolite, molecular sieve, etc.	[24]

197]. However the industrial applications of these membranes are attributed to the intrinsic behavior of some organic/inorganic hybrids such as hollow fibers in various forms like continuous, defect-free, flat, and asymmetry [160, 173, 174]. Therefore, a significant breakthrough on fabricating MMMs in useful configurations is undoubtedly essential and this signifies one immediate challenge for membrane researchers [147].

14.1 CNT-Based MMMs

The intrinsic characteristics of CNTs such as high porosity and surface area have fascinated the interest of scientists in the preparation of membranes [131]. CNTs-based membranes not only have been used to distinguish molecules based on their size but also via modification of membranes with CNTs, molecules transport can also be influenced [128, 132]. The great capability of CNTs in the synthesis of MMMs is related to the unique properties of CNTs such as high active surface area, extreme aspect ratio, strong mechanical strength and high gas transport rates [198–200] that make functionalized CNT-based MMM suitable as an attractive candidate for separation technology [198–200]. However selectivity coefficient of CNTs as inorganic fillers seems to be much higher than the neat polymer [125], but selectivity of CNT-based MMM for separation process is related to the contribution of both inorganic fillers and polymer phases [5, 201]. Compared to other membranes, CNT-based MMMs merge various advantages including high processability, high flexibility, specific mechanical properties, low cost, thermal stability and high selectivity [201–203]. The applications of nanostructures such as CNTs as filler in the fabrication of MMMs have been recognized by different research groups. Significant role of CNTs in the performance of MMMs has been reported in Table 9.

As clearly evaluated in Table 9, the increasing performance of CNTs in membrane application can be attributed to their unique properties for separation such as high aspect ratio and surface area, frictionless surfaces, simple functionalization and dispersion in organic polymer, capability to enhance mechanical strength with small filler content and also the potentially good control of pore dimension at the nanometer scale [211, 212].

14.2 Aligned and Filling CNTs in MMMs

Since CNTs have found their potential for fluid transport, there has been continuous interest in developing methods for nanotube fillings and decoration [24]. Although the existing simulation and experimental studies have provided extensive proof that can be beneficially adopted to produce high flux and high selectivity membranes, it is difficult to synthesize CNTs with well-controlled length below 100 nm [213]. It has been found that, there are many different properties which can be manipulated in

Table 9 Effective role of CNTs in the performance of MMMs

Effective role	Detail	References
Providing high flux during separation process	Based on molecular dynamic (MD) computational simulations	[24]
Providing good interface interaction	Proper fabrication controls such as alignment, filling and functionalization of CNTs	[204]
Enhancement in the transport properties	Via good compatibility between CNTs and polymer matrix (Homogeneous dispersion of CNTs inside a polymer matrix)	[205]
Improving the compatibility between the polymers and inorganic phase	Encapsulation of polymers into CNTs may	[206]
Formation of strong CNT array–polymer interface adhesion between the surrounding polymerchains	Interfacial wetting and bonding between CNTs and polymer matrix	[24]
Control of pore dimension at the nanometer scale	Use of CNTs with various diameter and morphology	[207–209]
Simulation results of extremely high transport rate and high permeability of light gases	Use of aligned CNTs	[210]
CNT/PAN composite	Theoretical study based on gas adsorption process	[201]

different ways depending on the dispersion and alignment of CNTs in the polymer matrix when processing these nanocomposites. Effective roles of aligned CNTs in the performance of MMMs have been reported in Table 10.

Table 10 Effective role of aligned CNTs in the performance of MMMs

Effective role	Detail	References
Prevent aggregation of MMMs	Because of compatibility of aligned CNTs with polymer matrix	[206]
Formation of homogeneous MMMs	Owing to the individually dispersion of CNTs throughout the matrix	[214]
Formation of normal MMMs with close-packed structure	Possibility to synthesis chemically opened nanotubes	[214]
Control of chemical selectivity and flux of MMMs	Control of the size and morphology of CNTs during formation of aligned CNT arrays	[215]
Formation of flexible MMMs	During control of assembly of the oriented CNTs during the synthetic process	[216]
Formation of swellable MMMs	Control of the wettability and hydrophobicity of CNTs	[24, 217]

14.3 Effect of Loaded CNTs in MMMs

In the manufacture of CNT-based membranes, the mechanical resistance of the memerane depends on the kind and morpholgy of the CNTs adopted as inorganic filler [132]. It has been reported that, CNTs can significantly increase the mechanical resistance of the polymer materials even at low concentration (< ~5.0%, w/w) [132].

The amount of CNTs dispresed in the MMM also affects the peremability of membrane towards various gases. The quantity of CNT bundles provides different voids in the MMM matrix as is schematically shown in Fig. 2 [156].

As shown (Fig. 2), presence of void volume in the MMMs strongly affects the selectivity of membrane towards special gaseous mixture such as H_2 or CO_2. To study the effect of multi-walled CNTs (MWCNT)% loaded on MMMs, different percentages of MWCNTs has been loaded on the MWCNT matrix [156]. For instance, the correlation between the adsorption perentage of H_2 and CO_2 versus the amount of MWCNT loaded in the MMM matrix has been shown in Fig. 3. According to the results (Fig. 3), maximum difference between the adsorption percentages of H_2 and CO_2 is obtained for 0.3 g of MWCNTs loaded to the MMM matrix [156].

All these effective roles of CNTs point to the importance of the introduction of new synthetic process for generation of CNTs.

15 Fabrication of CNT-Based MMMs

In the literature, CNTs-based MMMs have been fabricated using several matrix polymers like polyethersulfone (PES) [213–217], poly (bisphenol A-co-4-nitrophthalic anhydride-co-1,3-phenylene diamine (PBNPI) [128], poly (vinyl alcohol) (PVA) [218], polysulfone (PSF), polystyrene (PS) [219], and polyamide [220].

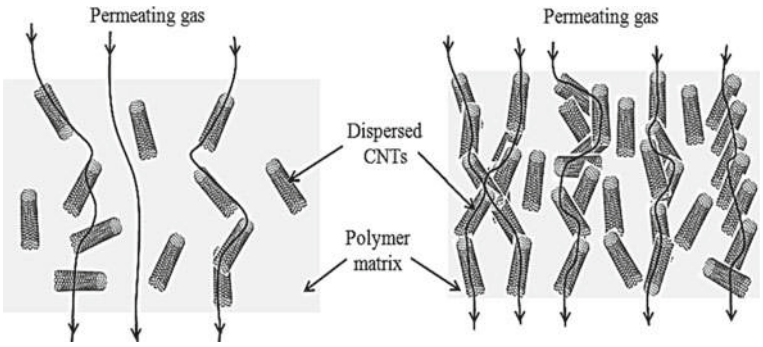

Fig. 2 Schematic representing the effect of CNTs in the permeation of gases through the CNT-based MMMs [156]

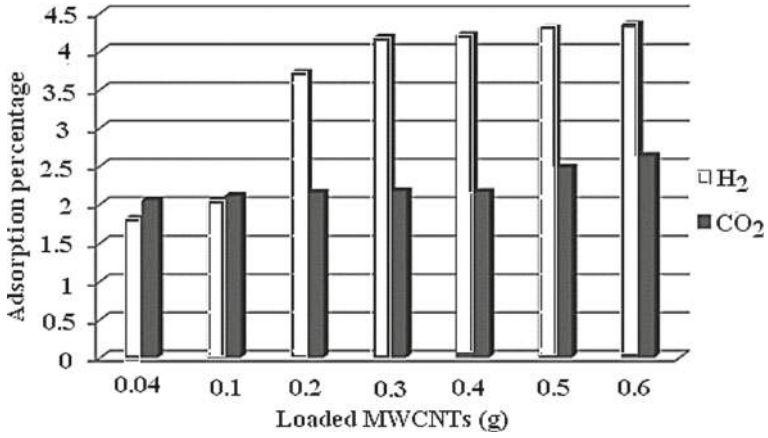

Fig. 3 Histogram representing the effect of MWCNT loaded in MMM matrix for selective separation of H_2 and CO_2 [156]

Among these polymer matrix, PS has been experimentally proven to have high wettability with CNTs [24]. As it is expected, the CNT arrays can freely be impregnated with PS [204, 206, 217, 221]. The first report on the filling of CNTs with PS was related to Liu et al. [205] via focusing on supercritical CO_2 for the encapsulation of MWCNTs (diameter: 40–50 nm)and controlling the filling fraction by changing the releasing time [24].

Similarly, Mi et al. [217] reported an alignment method using a porous alumina support to fabricate CNT-based MMM [24]. In this study, vertically aligned MWCNT, synthesized with CVD method were grown supported using a multi-step method. For this purpose, the vertically aligned MWCNTs were filled with PS by spin coating to form PS-filled CNTs (thickness: ~ 20 μm) [24]. Using this procedure, the PS was entirely covered without deeply penetration into the alumina support [24]. This phenomenon is attributed to the hydrophobic affinity of CNTs, which allow PS to stay mainly within the CNT layer [24].

16 Challenges Related to the Synthesis of CNT-Based MMMs

During the fabrication of CNT-based MMMs, it is impossible to synthesize CNT-based membranes during filling inside the CNTs without formation of any inter-tube gaps in the CNT morphology [204, 216, 217, 221]. This phenomenon is related to both the unique structures of CNTs and their growth mechanism [204, 216, 217, 221]. Consequently, this phenomenon is majorly unlike the synthesis of other types of MMMs such as zeolite-based MMM [204, 216, 217, 221]. Filling inter-CNT gaps as well as removal of the polymer over-layer is important in the synthesis of

CNT-based MMMs [204, 216, 217, 221]. Consequently, the fabrication of CNTs-MMMs is still under development in order to prevent the CNTs from aggregation and dispersion of CNTs in the polymer matrix homogeneously [222]. Experimentally, as synthesized CNTs are not often conveniently dispersed, therefore frequently weak interactions are often existed between CNTs and polymer matrix [222]. Therefore, some treatments are needed to facilitate and enhance their adhesion between CNTs and polymer matrix [219, 223, 224].

17 Effect of the Structure of CNTs During Synthesis of CNT-Based MMMs

Alignment of carbon nanostructures and adhesion between the CNTs and the substrate are considered as other important factors during the generation of CNT-based MMMs [24]. These phenomena are attributed to the characteristics of CNTs that should firmly be anchored to surface with uniform lengths and diameters [24]. For synthesis of CNT-based MMMs, filling a suitable polymer such as PS is strongly dependent to the structure of CNTs. For example, the bamboo-like CNT structure with closed compartment can majorly serve as barrier that prohibits the penetration of monomer molecules [24]. Consequently, selective filling of CNTs can be carried out through the controlling of the size of the flexible polymer molecules [24]. In these membranes, low molecular weight polymers are selectively permitted to pass through the CNT channels [24, 225]. Whereas the transport of high molecular weight polymers are restricted by their size to enter the cavities of CNTs [225].

18 Functional Groups in the CNT Matrix

In the CNT-based MMMs, CNTs functionalization has been shown to vary the flux of the transported particles [24]. For functionalization, raw CNTs should initially be purified by acid treatment to obtain open-ended CNTs and subsequent functionalized organic compounds. Detail of functionalization of CNTs has been discussed in detail in Table 11.

To study the effect of carbon nanostructure as filter for selective separation and filteration of gaseous species such as CO_2 and H_2, the permeability gradients of various carbon nanostructures were investigated in detail [156]. The results (Fig. 4) reveal that, MWCNT-based MMMs has maximum permeability gradient for this purpose [156].

For more confidence about this phenomenon, this modification has been used to evaluate the selective filteration of H_2 and CO_2 on MWCNT-based MMMs, as shown in Table 12 [156].

Table 11 CNT-based polymer

Function group	Detail	References
Bond formation between COOH and 3-aminopropyltriethoxylsilane	Grafting of functionliaed CNTs on silicone	[222, 226]
COOH-, OH- MWCNTs	Loading of CNTs in the polymer matrix	[128]
COOH-, OH- MWCNTs	Formation of MWCNTs/PBNPI membrane to separate H_2, CH_4 and CO_2	[128]
Chemically functionalized CNT membrane	For controlling the flow and selectivity of chemical transport	[227]
Functionalized MWCNTs incorporated into segmented polyurethane (SPU)	-Studying the water vapor transport properties during wastewater treatment process – Mitigation of membrane fouling through the inhibition of bacterial growth	[228]
Immobilization of CNTs in MMM matrix	Fabrication of CNT composite films with unusual antimicrobial properties against S. aureus and S. warneri bacteria	[229]
MWCNT-polysulfone composites	Evaluation of the antibacterial properties of ultrafiltration membranes	[230]
C_2H_5O-MWCNTs combined with a PES membrane	Evaluation of the selectivity of the membrane to CO_2/CH_4 and O_2/N_2	[226]
CNT-MMMs	Permeation of CH_4/H_2 mixture through the membrane (theoretical study)	[231]
CNT-MMMs based on open-ended CNTs	Evaluation of the in the diffusion coefficient for gases such as O_2, N_2 and CH_4	[232]
Single-walled CNT (SWCNT)-based MMMs	Appling atomistic simulations to study the adsorption CO_2 in SWCNTs at room temperature	[233]

As shown, synthetic method for fabriaction of CNTs is considered as another important factor during controling the physico/chemical properties of the CNT-based MMMs [156].

19 Role of Inorganic Nanoparticles as Filler

The dispersion of inorganic nanoparticles (nanocomposites) in polymer matrices also affords novel materials with improved mechanical properties, thermal stability, flame retardancy, chemical resistance, high barrier properties, scratch resistance and ion conductivity [235]. Complete potential of nanocompositesis is exploited when (i) nanofillers are homogeneously dispersed within the polymer matrix [235, 236] and (ii) there is strong interfacial bonding between the filler and rubber matrix [237]. For

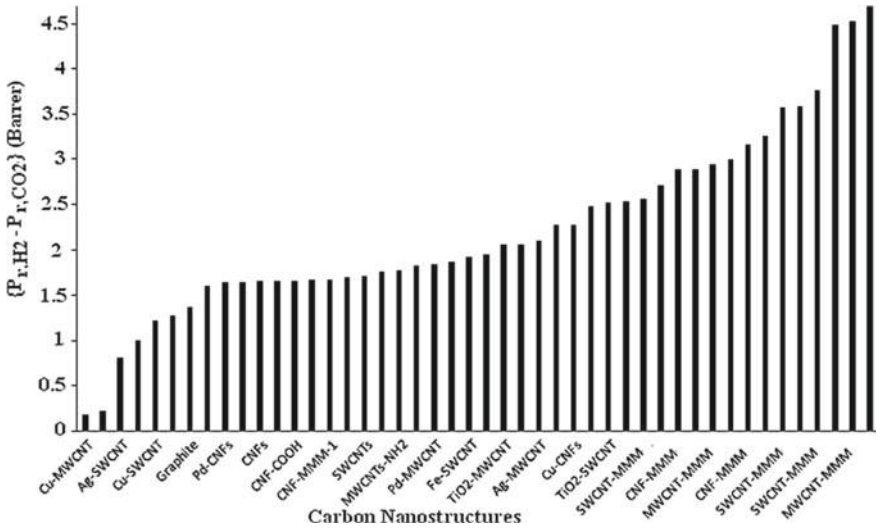

Fig. 4 Histogram revealing the performance of CNT-based MMM for selective separation of H_2 and CO_2 [156]

instance, platelet boehmite (BM) is a novel kind of nanofiller which can be potentially used for rubber reinforcement. Unlike silicate clay that shows Lewis acidic surface, surface aluminols of boehmite exhibit basicity [235].

Compared to conventional micrometer-scaled fillers, the same volume fraction of nanometer-scaled fillers contains nine orders of magnitude higher content of filler particles with much higher surface area [235]. Strong interactions between nanoparticles are common to cause formation of nanoparticle agglomerates which can initiate premature mechanical failure when nanocomposites are exposed to external mechanical stresses.

20 Permeation Models for Mixed Matrix Membrane

Besides the unique properties of MMM technology, it is necessary to have enough information about physical characteristics of MMM, especially when requiring desirable procedure and applicable design process for separation techniques [51]. For this purpose, researchers have attempted to predict the performance of MMMs using different theoretical models [156].

During the last decades, various theoretical models such as Maxwell [238], Bruggeman [239], Lewis-Nielson [240], Pal [6] and Felske [241] have been introduced for prediction of the permeability of MMMs. However, these models are used to estimate parameters such as permeability [240], selectivity coefficient [6], etc. [7, 240, 241]. Consequently, developed modification is applied to the mentioned

Table 12 Effects on various synthetic processes on gas separation factors [156]

Synthetic method	Active surface area[a] ($m^2\ g^{-1}$)	Defect[b]	Adsorption percentage[c] (%)	Kinetic diffusion coefficient[d] (mL t^{-1})	Selectivity coefficient of H_2[e] (mL t^{-1})	AARE (%)			
			CO_2	H_2	CO_2	H_2		Before correction	After correction
CVD	573	4.16	2.16	4.21	0.214	0.241	89	73.05	0.09
Arc-discharge	435	3.05	1.19	3.08	0.052	0.083	63	68.11	0.18
HiPco	468	3.42	2.05	3.46	0.126	0.162	78	39.62	0.13

[a]BET isotherm [234]
[b]Calculated according Raman spectrometry
[c]Calculated using TG analyzer
[d]Calaulated according to the slope of gas adsorption trace
[e]Calculated according to the ratio of kinetic diffusions of H_2/CO_2

models often based on the prediction of some physio/chemical properties such as the gas adsorption behavior of some various carbon nanostructure-based MMMs. There are some theoretical models to evaluate the permeability of MMMs. Presented models are almost predicted the permeability of the MMMs via evaluation of the permeability of both continuous and the dispersed phases [238].

20.1 Review on the Present Models

Present models are usually utilized to evaluate the permeability of three-dimensional (3-D) MMMs such as zeolite, resulting in that, theoretical parameters such as permeability are not compatible with one or two-dimensional (1-D or 2-D) nanomaterials such as CNT-based MMMs [239]. These models are almost focused on prediction of the permeability of the MMMs, via evaluation of the permeability of both continuous and the dispersed phases [238]. However, these models have not been significantly developed to predict the morphology of MMMs for specific gas adsorption and separation. Detail of some of these models is as follows [156].

20.1.1 Maxwell Model

Maxwell introduced a valuable model in 1873 [238]. This was initially extended to predict the permittivity of a dielectric. This model has been considered as an effective tool to evaluate some of MMM's properties using Maxwell equation [238]. Besides the importance of the Maxwell model, this model has some significant limitations [238]. For example, this model is suitable to evaluate correct amount of the permeability of 3-D MMMs, when Φ is less than 0.2, i.e. at condition at which $0 < \Phi < 0.2$ [238]. Conclusion is that, Maxwell model is suitable just for simple relations. These shortcomings provide the demand to introduce more developed models.

20.1.2 Bruggeman Model

Bruggeman model was initially derived to estimate the dielectric constant of composites [239]. Then, this model was adapted to estimate the permeability of 3-D spherical materials [156]. Significant advantageous of Bruggeman model over Maxwell model is that, this model can cover an extensive range of Φ for 3-D membranes [239].

20.1.3 Lewis-Nielsen Model

Lewis–Nielsen model was originally suggested for the elastic modulus of particulate composites [240]. This model, besides covering a broad range of Φ, extending from zero to Φ_m, can solve some of limitations of Maxwell and Bruggeman models such

as the effects of particle size distribution, the morphology of nanomaterial, and coagulation of materials through the Φ_m factor [238]. Nevertheless, this model has limitations that cannot precisely predict the physical or chemical properties of some kinds of MMMs such as CNT-based MMMs.

20.1.4 Pal Model

Pal model was originally developed for thermal conductivity [242]. This model, from one side is similar to the Lewis–Nielsen model that can act correctly, when Φ approaches towards Φ_m, and from the other side it is converted to equations derived for the Bruggeman model, when Φ_m is closed to 1 [239]. In addition, Pal model is used to calculate the effects of morphology of 3-D materials on permeability through the Φ_m parameter [239].

Detail of some of these models has been reviewed in Table 13.

All mentioned limitations reveal the importance of experimental studies to evaluate the parameters affecting the difference between experimental and theoretical values of permeability for 1-D and 2-D nanomaterials.

20.1.5 Modification on the Present Models

In accordance with the appearance of new type of MMMs based on CNTs, the necessity to apply new modification for prediction of the morphology and physical and/or chemical properties of 1-D and 2-D nanostructures is sensed [156]. The proposed modification on previously reported models for evaluation of chemical and physical properties of CNT-based MMMs is the combination of present models using adsorption percentages of gases onto CNT-based membranes [156]. For this purpose, effective parameters were automatically processed using experimental analysis through a program written in Visual Basic [156].

In this modification, initially, volume fraction (Φ) of each carbon nanostructures has been calculated using Eq. 1:

$$\phi = (w_f/\rho_f)/(w_f/\rho_f + w_P/\rho_P), \tag{1}$$

where W_f and W_P stand for the weights of filler and polymer, respectively. Whereas, ρ_f and ρ_p are the density of filler and polymer, respectively. Also, permeability (P_r) is defined as Eq. 2:

$$Pr_{\mathbf{Exp.}} = (w_{CNT} + w_P)/(w_G + w_P), \tag{2}$$

where, W_{CNT}, W_P and W_G are the amounts of gases diffused to the CNTs, polymer and graphite, respectively.

Table 13 Detail of models related to the performance of MMMs

Model	History	Predictions	Limitation	References
"Maxwell" model	Introduced by Maxwell" et al. in 1873	Predict the permittivity of a dielectric	This model is only suitable to evaluate correct amount of the permeability of 3-D MMMs, when Φ is less than 0.2, i.e. at condition at which $0 < \Phi < 0.2$	[210, 238]
"Bruggeman" model	Bruggeman et al.	This model was adapted to estimate the permeability of 3-D spherical materials	It has limitations similar to that of the Maxwell model, that is, it does not give the correct behavior at $\varphi \rightarrow \varphi_{\mathrm{m}}$. Also, it does not account for particle size distribution, particle shape, and aggregation of particles. Furthermore, the Bruggeman model is an implicit relationship that needs to be solved numerically for the permeability	[239]
"Lewis–Nielsen" model	Lewis–Nielsen	This model, besides covering a broad range of Φ, extending from zero to Φ_m, can solve some of limitations of "Maxwell" and "Bruggeman" models such as the effects of particle size distribution, the morphology of nanomaterial, and coagulation of materials through the Φ_m factor	This model has significant limitations that cannot precisely predict the physical or chemical properties of CNT-based MMMs	[240]

(continued)

Table 13 (continued)

Model	History	Predictions	Limitation	References
"Pal" model	Pal	Pal" model was originally developed for thermal conductivity	It is expected to exhibit significant deviation from the actual behavior at high values of φ, especially when $\varphi \rightarrow \varphi_m$, where φ_m is the maximum packing volume fraction of core–shell particles. Also the modified Maxwell model does not account for particle size distribution, particle shape, and aggregation of particles	[242]
Felske model	Felske	This model was developed an exact expression for the thermal conductivity of composites of core–shell particles (core particle covered with interfacial layer) – The Felske model gives almost the same predictions as the modified Maxwell model		[241]

The sequence of this modification is based on the use of Bruggeman, Maxwell, Lewis–Nielsen and Pal model, respectively. Scheme 1 shows the detail of the proposed modification for evaluation of the correctness of the previously reported models for the CNT-based MMMs [156]. As clearly revealed according to the Schem.1, the experimental permeability and volume fraction of each carbon nanostructure were experimentally determined using the adsorption of various gases on carbon nanostructures using Eqs. 1 and 2 [156].

These results were then used to evaluate λ_d and calculated permeability ($P_{r,Cal}$) using Bruggeman and Maxwell models. $P_{r,Cal}$ was then used to evaluate the quantity of Ψ function using Lewis–Nielsen model according to Eq. 3 [156]. After that, calculated Ψ function (Ψ_{cal}) was used to evaluate maximum volume fraction (Φ_m) using Lewis–Nielsen model. Finally, calculated volume fraction (Φ_{Cal}), evaluated by

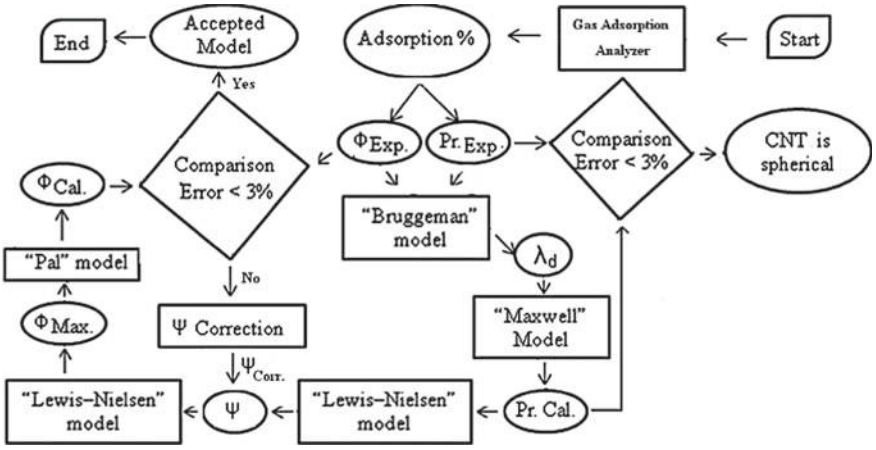

Scheme 1 Sequence of applied modifications to the present gas-permeation models [156]

Pal model was compared to the experimental volume fraction (Φ_{Exp}) to see whether, there is good conformity between the theoretical and experimental results. Otherwise, whether correction factors are needed for applying on Ψ function to approach calculated parameters to the experimental results. During evaluation of $P_{r,Exp}$ with $P_{r,Cal}$, it is concluded that, if deviation is small (e.g. less than 0.3%), the carbon nanostructures can be assumed spherical (3-D); hence the present models are acceptable without any modifications [156].

20.1.6 Detail of Modification Detail of Modification of the Present Models

Based on the limitations of existing models for prediction of MMMs [156], combination of the present models seems to be capable to affect the present limitations via studying the correction factors, applied on Ψ function to have good agreement between theoretical and experimental results [156]. This study also validates the accuracy of present models for evaluation of the $P_{r,Cal}$ of carbon nanomaterials to various gases such as H_2 and CO_2 [156]. In addition, the amount of gas adsorption of various gases has been considered as good probe for evaluation of the compatibility of theoretical model with carbon nanostructure-based membranes. Therefore, two aims are followed in this modification: (i) Estimation of P_r and Φ in both the experimental and theoretical studies to assess the accuracy of previously reported model for CNT-based MMMs and (ii) Wherever it is needed, to apply the correction factor to get the best prediction for the categories [156]. Difference between theoretical and experimental permeability of H_2 on CNTs based on A) Maxwell and Lewis model has been graphically shown in Fig. 5.

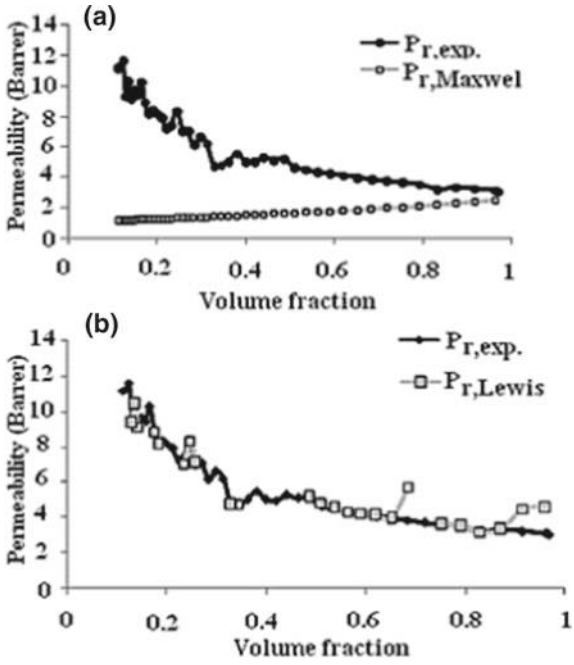

Fig. 5 Difference between theoretical and experimental permeability of H_2 on CNTs based on A) Maxwell and Lewis models[156]

According to the results (Fig. 5), significant difference was observed between $P_{r,Cal}$ and $P_{r,Exp}$ of various gases such as H_2 according to the Maxwell model, when studying the permeability of even simple carbon nanostructure-based membranes such as pure SWCNTs as shown in Fig. 5 [156].

21 Separation Properties of MMMs

During the last decade, membrane separation has been recognized as available and effective methodology from laboratory to the industrial scales [35, 156]. Compared to the conventional separation processes, improvement in the membrane separation performance as well as lower cost of the membrane technology has promoted their applications [35, 156]. Therefore, novel membrane technologies can potentially offer economic, environmental, and high performance benefits for separation process [136].

Up to date, several progresses have been made in the developing MMMs for separation process [144, 154, 155]. However maximum separation performance has been evaluated for MMMs via providing a variety of interfacial defects and non-idealities including leaky interface, aggregation of inorganic phase, and formation of defect and barriers in inorganic matrix [144, 154, 155]. To overcome the interfacial defects and nonidealities, most research has been focused on the modification of

surface based on the physiochemical properties of raw materials such as zeolite [153].

In the MMMs technology, the principal improvement in the separation properties is expected to capitalize on the positive effect induced often by the addition of inorganic phase. Therefore, selection of an appropriate inorganic phase for the desired separation is of great significance [241–245]. Typical inorganic fillers include various zeolites [83, 138–140, 163, 232, 245], carbon molecular sieves [145, 196, 246, 247], activated carbons [248], non-porous silica [157–159, 249], C_{60} [250], and graphite [251]. Such properties as filler types [97, 196, 251], pore size [172, 196, 197], Si/Al ratio [196], cations[173, 196], pore dimensions [173, 196], and activation temperatures [252] have been compared and confirmed to influence the resultant MMM performance.

21.1 Analytical Applications of MMMs

Separation process by selective transport mechanism is considered as an important practical technique for various applications in technology [64, 154]. In gas separation process by membranes, mixtures of gaseous species are separated due to their differential permeation through membranes [154]. Because of prevailing advantages of the MMMs including low energy requirements, simple operation, low capital and operating cost [5, 253], fabrication of various types of MMMs has been considered as an effective technology in laboratory and industrial scales [35]. Most of these reported advances have been made after 2000 [12]. For instance, a research reported by Li et al. [173] is an example on selective sorption. This group proposed a novel exchange treatment of zeolite with noble metal ions, such as Ag^+ and Cu^+ to change the physical and chemical adsorption properties of penetrants in the zeolite [12]. Examination and comparison of these studies reveal that the enhanced molecular sieving is still the major concern [196, 197, 247, 250, 254].

The latest approach to an old idea of compositing different materials in order to combine their desired optical, electrical, thermal and mechanical properties have persuaded researchers to develop MMMs by incorporating high separation performance molecular sieves in a proper polymer matrix [150, 155, 255, 256].

MMMs have been actively pursued in industry and academia for gas separation in the last 20 years [12]. Vast applications of MMMs are strongly due to the importance of effective factors such as selectivity and permeability of the membranes that significantly promote the efficiency of these membranes for gas separation and filtration process [156].

MMMs seem to be suitable for a number of applications such as gas separation [23, 24], micro filtration, ultra-filtration, nanofiltration and reverse osmosis [257]. Based on the literature, MMMs are applicable in the ethanol/water separation by pervaporation [153]. It has been reported that, the potential for MMMs has been examined for various gas separations, including air separation (e.g., O_2/N_2), natural gas separation (e.g., CO_2/CH_4), hydrogen recovery (e.g., H_2/CO_2, H_2/N_2, and H_2/CH_4),

and hydrocarbon separation (e.g., ethylene/ethane, cis/trans-butylene, i-pentane/n-pentane, and n-butane/CH_4) [12]. Also, activated carbon-based MMMs have been adopted for CO_2/CH_4 separation [12]. Detail of the applications of MMM in the gas separation process has been summarized in Table 14.

Consequently, the use of MMMs has generated an ever-increasing interest in the field of gas separation.

Table 14 Applications of MMM

Type of membrane	Detail	References
Rubbery polymer/microporous support layer	Recovery of VOCs for recovering hydrocarbons such as in the petrochemical refining and natural gas industries	[64]
Polyimide-zeolite MMMs	High selectivity and permeability towards pollutant gases	[12]
CNT-based MMM	Wide range of gas separation such as H_2, O_2, CH_4, N_2, and CO_2based on gas diffusion on pore surface and through the pore channel of CNT-MMM	[260]
Silicalite/cellulose acetate-based MMMs	Selective separation of O_2/N_2 and CO_2/H_2	[163]
Functionalized-MWCNTs blended PSF	Significant enhancement in permeability due to the increase in hydrophilicity and porosity	[222]
Ag-nanoparticles/carbon	O_2/N_2 separation	[46]
Pt/C or Pd/C composite membrane	Enhancement in the H_2 permeability	[258, 259]
SiO_2/C composite membranes	Enhancing gas separation performance	[260]
zeolite/C composite membranes by filling the microporous zeolite beta and KY into carbon matrix	Observation of a big improvement in selectivity	[148, 261]
Zeolite/C composite membranes	H_2 separation	[262]
Metal/C composite membranes	Gas separation	[30, 84, 263, 264]
Metal/C composite membranes. Using zeolite materials such as SAPO-34 and zeolite L	Gas separation	[265, 266]
Zeolites such as ZSM-5 and zeolite T into the carbon matrix	High gas permeability for H_2, CO_2, O_2 and selectivity for O_2/N_2, CO_2/CH_4 for both single gas and mixed-gas pairs	[267, 268]

22 Conclusions

This review suggests an important advances and modification related to the synthesis, fabrication, properties, models and analytical applications of MMMs. In this review, also behavior of MMMs has also compared to general membranes such as graphite-, silica, metal- polymer- and inorganic-based membranes in detail. In addition, the capability as a well as limitations of theoretical models during predication of the separation properties of MMMs is also discussed in detail. This study can be used in significant applications including gas sensors, membrane technology, electrochemical cell for hydrogen storage, separation of different gases and removal of impurities such as CO_2 from fuel and hydrogen sulfide from natural gases, hydrogen recovery and other industrial usages.

References

1. Zhang XY, Hu HQ, Zhu YD, Zhu SW (2007) 289, Carbon molecular sieve membranes derived from phenol formaldehyde novolac resin blended with poly(ethylene glycol). J Membr Sci 289:86–91
2. Mahajan R, Koros WJ (2002) Mixed matrix membrane materials with glassy polymers. Part 1. Polym Eng Sci 42:1420–1431
3. Sheffel JA, Tsapatsis M (2007) A model for the performance of microprous mixed matrix membranes with oriented selective flakes. J Membr Sci 295:50–70
4. Kim J, Bruggen B (2010) The use of nanoparticles in polymeric and ceramic membrane structures: review of manufacturing procedures and performance improvement for water treatment. Environ Pollut 158:2335–2349
5. Mahajan R, Koros WJ (2000) Factors controlling successful formation of mixed-matrix gas separation materials. Ind Eng Chem Res 39:2692–2696
6. Pal R (2008) Permeation models for mixed matrix membranes. J Colloid Interface Sci 317:191–198
7. Gonzo EE, Gottifredi JC (2006) Estimating models for predicting effective permeability of mixed matrix membranes. J Membr Sci 277:46–54
8. Pandey P, Chauhan RS (2001) Membrane for gas separation. Prog Polym Sci 26:853–893
9. Ngang HP, Ahmad AL, Low SC, Ooi BS (2012) Preparation of mixed-matrix membranes for micellar enhanced ultrafiltration based on response surface methodology. Desalination 293:7–20
10. Shao LB, Chung TS, Greenberg AR (2009) Polymeric membranes for the hydrogen economy: contemporary approaches and prospects for the future. J Membr Sci 327:18–31
11. Lu GQ, JC C, Duke M, Giessler S, Socolow R, Williams RH, Kreutz T (2007) Inorganic membranes for hydrogen production and purification: a critical review and perspective. J Colloid Interface Sci 314:589–601
12. Chung TS, Jiang LY, Li Y, Kulprathipanja S (2007) Mixed matrix membranes (MMMs) comprising organic polymers with dispersed inorganic fillers for gas separation. Prog Polym Sci 32:483–507
13. Li Y, Chung TS (2010) Molecular-level mixed matrix membranes comprising Pebax® and POSS for hydrogen purification via preferential CO_2 removal. Int J Hydrogen Energ 35:10560–10568
14. Chen HZh, Chung T-S (2012) CO_2-selective membranes for hydrogen purification and the effect of carbon monoxide (CO) on its gas separation performance. Int J Hydrogen Energy 37:6001–6011

15. Saufi MS, Fee CJ (2013) Mixed matrix membrane chromatography based on hydrophobic interaction for whey protein fractionation. J Membr Sci 444:157–163
16. Damle A (2014) Membranes for clean and renewable power applications. Techverse Inc., USA, pp 3–48
17. Schäfer A, Hughes G, Richard BS (2014) Renewable energy powered membrane technology: a leapfrog approach to rural water treatment in developing countries? Renew Sustain Energy Rev 40:542–556
18. Piacentini E, Drioli E, Giorno L (2014) Membrane emulsification technology: twenty-five years of inventions and research through patent survey. J Membr Sci 468:410–422
19. Caputo G, Giaconia A (2014) Membranes for clean and renewable power applications. Woodhead Publishing, pp 347–364
20. Khan AL, Gahlaut CK, Khan AU, Vankelecom IFJ (2013) Mixed matrix membranes comprising of Matrimid and $–SO_3H$ functionalized mesoporous MCM-41 for gas separation. J Membr Sci 447:73–79
21. Gugliuzza A, Capriccioli ABA (2014) Membranes for clean and renewable power applications. Woodhead Publishing, pp 365–378
22. Winston WS, Sirkar KK (1992) Membrane handbook. Chapman-Hall, New York, pp 725–885
23. Baker RW (2004) Chapter 1: overview of membrane science and technology, membrane technology and applications, 2nd edn. Wiley
24. Ismail AF, Goh PS, Sanip SM, Aziz M (2009) Transport and separation properties of carbon nanotube-mixed matrix membrane. J. Sep. Pur. Tech. 70:12–26
25. Scholes CA, Stevens GW, Kentish E (2012) Membrane gas separation applications in natural gas processing. Fuel 96:15–28
26. Earnst B, Haag S, Burgard M (2007) Permselectivity of a nickel/ceramic composite membrane at elevated temperatures: a new prospect in hydrogen separation? J Membr Sci 288:208–217
27. Li Y, Chung TS (2008) Highly selective sulfonated polyethersulfone (SPES)-based membranes with transition metal counterions for hydrogen recovery and natural gas separation. J Membr Sci 308:128–135
28. Morreale BD, Ciocco MV, Enick RM, Morsi BI, Howard BH, Cugini AV, Rothenberger KS (2003) The permeability of hydrogen in bulk palladium at elevated temperatures and pressure. J Membr Sci 212:87–97
29. Chen XY, Ghaffari Nik O, Rodrigue D, Kaliaguine S (2012) Mixed matrix membranes of aminosilanes grafted FAU/EMT zeolite and cross-linked polyimide for CO_2/CH_4 separation. Polymer 53:3269–3280
30. Zhang L, Chen X, Zeng C, Xu N (2006) Preparation and gas separation of nano-sized nickel particle-filled carbon membrane. J Membr Sci 281:429–434
31. Koros WJ, Fleming GK (1993) Membrane-based gas separation. J Membr Sci 83:1–80
32. Kesting RE, Fritzsche AK (1993) Polymeric gas separation membranes. Wiley, New York
33. Shahid S, Nijmeijer K (2014) Performance and plasticization behavior of polymer–MOF membranes for gas separation at elevated pressures. J Membr Sci 470:166–177
34. Coronas J, Santamaria J (1999) Separations using Zeolite membranes. J Sep Purif Method 28:127–177
35. Itta AK, Tseng HH, Wey MY (2010) Effect of dry/wet-phase inversion method on fabricating polyetherimide-derived CMS membrane for H_2/N_2 separation. Int J Hydrogen Energy 35:1650–1658
36. Stern SA (1994) Polymers for gas separations: the next decade. J Membr Sci 94:1–65
37. Robeson LM (1991) Correlation of separation factor versus permeability for polymeric membranes. J Membr Sci 62:165–185
38. Fuertes AB, Centeno TA (1998) Carbon molecular sievemembranes from polyetherimide. Microporous Mesoporous Mater 26:23–26
39. Yamamoto M, Kusakabe K, Hayashi J, Morooka S (1997) Carbon molecular sieve membrane formed by oxidative carbonization of a copolyimide film coated on a porous support tube. J Membr Sci 133:195–205

40. Japip S, Wang H, Xiao Y, Chung TS (2014) Highly permeable zeolitic imidazolate framework (ZIF)-71 nano-particles enhanced polyimide membranes for gas separation. J Membr Sci 467:162–174
41. Pabby AK, Sastre AM (2013) State-of-the-art review on hollow fibre contactor technology and membrane-based extraction processes. J Membr Sci 430:263–303
42. Yeong YF, Wang H, Pramoda KP, Chung TSh (2012) Thermal induced structural rearrangement of cardo-copolybenzoxazole membranes for enhanced gas transport properties. J Membr Sci 397–398:51–65
43. Ismail AF, David LIB (2001) A review on the latest development of carbon membranes for gas separation. J Membr Sci 193:1–18
44. Saufi SM, Ismail AF (2004) Fabrication of carbon membranes for gas separation—a review. Carbon 42:241–259
45. Park HB, Suh IY, Lee YM (2002) Novel pyrolytic carbon membranes containing silica: preparation and characterization. Chem Mater 14:3034–3046
46. Barsema JN, Balster J, Jordan V, Vegt NFA, Wessling M (2003) Functionalized carbon molecular sieve membranes containing Ag-nanoclusters. J Membr Sci 219:47–57
47. Kong Y, Du H, Yang J, Shi D, Wang Y, Zhang Y, Xin W (2002) Study on polyimide/TiO_2 nanocomposite membranes for gas separation. Desalination 146:49–55
48. Fritsch D, Peinemann KV (1995) Novel highly permselective 6Fpoly(amide-imide)s as membrane host for nano-sized catalysts. J Membr Sci 99:29–38
49. Wang HT, Holmberg BA, Yan Y (2002) Homogeneous polymer–zeolite nanocomposite membranes by incorporating dispersible template-removed zeolitenanocrystals. J Mater Chem 12:3640–3643
50. Süer MG, Baç N, Yilmaz L (1994) Gas permeation characteristics of polymer-zeolite mixed matrix membranes. J Membr Sci 91:77–86
51. Zimmerman CM, Singh A, Koros WJ (1997) Tailoring mixed matrix composite membranes for gas separations. J Membr Sci 137:145–154
52. Linkov VM, Sanderson RD, Jacobs EP (1994) Highly asymmetrical carbon membranes. J Membr Sci 95:93–99
53. Shao L, Low BT, Chung TS, Greenberg AR (2009) Polymeric membranes for the hydrogen economy: contemporary approaches and prospects for the future. J Membr Sci 327:18–31
54. Car A, Stropnik C, Yave W, Peinemann KV (2008) PEG modified poly(amide-b-ethylene oxide) membranes for CO_2 separation. J Membr Sci 307:88–95
55. Baker RW (2002) Membrane technology and applications. McGraw-Hill, New York, pp 301–392
56. Hsieh HP (1996) Inorganic membranes for separation and reaction, 1st edn. Elsevier
57. Rybak A, Grzywna ZJ, Sysel P (2013) Mixed matrix membranes composed of various polymer matrices and magnetic powder for air separation. J. Sep Purif Technol 118:424–431
58. Sircar S, Golden TC (2000) Purification of hydrogen by pressure swing adsorption. Separat Sci Tech 35:667–687
59. Karger J, Ruthven DM (1992) Diffusion in Zeolites and other microporous solids. Wiley, New York
60. Fain DE (1994) Membrane gas separation principles. MRS Bull 19:40–43
61. Sotirchos SV, Burganos VN (1999) Transport of gases in porous membranes. MRS Bull 40:41–45
62. Uhlhorn RJR, Keizer K, Burggraaf AJ (1992) Gas transport and separation with ceramic membranes. Part II. Synthesis and separation properties of microporous membranes. J Membr Sci 66:271–287
63. Giaconia A, Caputo G (2014) Membrane technologies for solar-hydrogen production. Woodhead Publishing Limited, pp 325–346
64. Javaid A (2005) Membranes for solubility-based gas separation applications. Chem Engineer J 112:219–226
65. Wang X, Fang D, Hsiao BS, Chu B (2014) Nanofiltration membranes based on thin-film nanofibrous composites. J Membr Sci 469:188–197

66. Moore TT, Koros WJ (2007) Gas sorption in polymers, molecular sieves, and mixed matrix membranes. J Appl Polym Sci 104:4053–4059
67. Musselman IH, Balkus KJ, Ferraris JP (2008) Mixed-matrix membranes for CO_2 and H_2 separations using metal-organic frameworks and mesoporous hybrid silicates. University of Texas at Dallas
68. Mahajan R, Koros WJ, Thundyil M (1999) Mixed matrix membranes: important and challenging! J Membrane Tech 105:6–8
69. Mahajan R, Burns R, Schaeffer M, Koros WJ (2002) Challenges in forming successful mixed matrix membranes with rigid polymeric materials. J Appl Polym Sci 86:881–890
70. Khosravi T, Mosleh S, Bakhtiari O, Mohammadi T (2012) Mixed matrix membranes of Matrimid 5218 loaded with zeolite 4A for pervaporation separation of water–isopropanol mixtures. Chem Eng Res Des 90:2353–2363
71. Bhat SD, Aminabhavi TM (2007) Zeolite K-LTL-loaded sodium alginate mixed matrix membranes for pervaporation dehydration of aqueous–organic mixtures. J Membr Sci 306:173–185
72. Sairam M, Patil MB, Veerapur RS, Patil SA, Aminabhavi TM (2006) Novel dense poly(vinyl alcohol)–TiO_2 mixed matrix membranes for pervaporation separation of water–isopropanol mixtures at 30 °C. J Membr Sci 281:95–102
73. Bos A, Pünt IGM, Wessling M, Strathmann H (1998) Plasticization-resistant glassy polyimide membranes for CO_2/CO_4 separations. J Sep Pur Tech 14:27–39
74. Qin JJ, Chung TS (2004) Effects of orientation relaxation and bore fluid chemistry on morphology and performance of polyethersulfone hollow fibers for gas separation. J Membr Sci 229:1–9
75. Clausi DT, Koros WJ (2000) Formation of defect-free polyimide hollow fiber membranes for gas separations. J Membr Sci 167:79–89
76. Qiao X, Chung TS, Rajagopalan R (2006) Zeolite filled P84 co-polyimide membranes for dehydration of isopropanol through pervaporation process. Chem Eng Sci 61:6816–6825
77. Balachandran U, Lee TH, Chen L, Song SJ, Picciolo JJ, Dorris SE (2006) Hydrogen separation by dense cermet membranes. Fuel 85:150–155
78. Gu Y, Oyama ST (2007) High molecular permeance in a poreless ceramic membrane. Adv Mater 19:1636–1640
79. Bastani D, Esmaeili N, Asadollahi M (2013) mixed matrix membranes containing zeolites as a filler for gas separation applications: a review. J Ind Eng Chem 19:375–393
80. Xiao Y, Dai Y, Chung TS, Guiver MD (2005) Effects of brominating matrimid polyimide on the physical and gas transport properties of derived carbon membranes. Macromolecules 38:10042–10049
81. Chua ML, Xiao YC, Chung TS (2013) Modifying the molecular structure and gas separation performance of thermally labile polyimide-based membranes for enhanced natural gas purification. J Chem Eng Sci 104:1056–1064
82. Wibisono Y, Cornelissen ER, Kemperman AJB, Meer WGJ, Nijmeijer K (2014) Two-phase flow in membrane processes: a technology with a future. J Membr Sci 453:566–602
83. Namboodiri VV, Vane LM (2007) High permeability membranes for the dehydration of low water content ethanol by pervaporation. J Membr Sci 306:209–215
84. Baker RW, Lokhandwala K (2008) Natural gas processing with membranes: an overview. Ind Eng Chem Res 47:2109–2121
85. Maindersma GW, Kuczynski M (1996) Implementing membrane technology in the process industry: problems and opportunities. J Membr Sci 113:285–292
86. Paul DR, Koros WJ (1976) Effect of partially immobilizing sorption on permeability and the diffusion time lag. J Polym Sci: Polym Phys 14:675–685
87. Song CW, Wang TH, Qiu YH, Qiu JSJ, Cheng HM (2009) Effect of carbonization atmosphere on the structure changes of PAN carbon membranes. J Porous Mater 16:197–203
88. Campo MC, Magalhães FD, Mendes A (2010) Carbon molecular sieve membranes from cellophane paper. J Membr Sci 350:180–188

89. Lie JA, Hagg MB (2006) Carbon membranes from cellulose: synthesis, performance and regeneration. J Membr Sci 284:79–86
90. Centeno TA, Fuertes AB (1999) Supported carbon molecular sieve membranes based on a phenolic resin. J Membr Sci 160:201–211
91. Fuertes AB, Menendez I (2002) Separation of hydrocarbon gas mixtures using phenolic resin-based carbon membranes. J Sep Purif Tech 28:29–41
92. Rao MB, Sircar S (1993) Nanoporous carbon membranes for separation of gas mixtures by selective surface flow. J Membr Sci 85:253–264
93. Teixeira M, Campo M, Tanaka DA, Tanco MA, Magen C, Mendes A (2012) Carbon-Al_2O_3-Ag composite molecular sieve membranes for gas separation. Chem Eng Res Des 90:2338–2345
94. Ismail AF, David LIB (2003) Future direction of R&D in carbon membranes for gas separation. J Membr Technol 2003:4–8
95. Koros WJ, Mahajan R (2000) Pushing the limits on possibilities for large scale gas separation: which strategies? J Mem Sci 175:181–196
96. Ozdemir SS, Buonomenna MG, Drioli E (2006) Catalytic polymeric membranes: preparation and application. Appl Catal: Gener 307:167–284
97. Verkerk AW, Male P, Vorstman MAG, Keurentjes JTF (2001) Properties of high flux ceramic pervaporation membranes for dehydration of alcohol/water mixtures. J Sep Purif Tech 22–23:689–695
98. Ockwig NW, Nenoff TM (2007) Membranes for hydrogen separation. Chem Rev 107:4078–4110
99. Cheng Z, Gao E, Wan H (2004) Novel synthesis of FAU-type zeolite membrane with high performance. Chem Commun 15:1718–1719
100. Vos RM, Verweij H (1998) High-selectivity, high-flux silica membranes for gas separation. Science 279:1710–1711
101. Sarrade S, Guizard C, Rios GM (2002) Membrane technology and supercritical fluids: chemical engineering for coupled processes. Desalinatio 144:137–142
102. Romero J, Gijiu C, Sanchez J, Rios GM (2004) A unified approach of gas, liquid and supercritical solvent transport through microporous membranes. Chem Eng Sci 59:1569–1576
103. Mortaheb HR, Ghaemmaghami F, Mokhtarani B (2012) Chem Eng Res Des 90:409–432
104. Yamamoto H, Mi Y, Stern SA, Clair AKSt. (1990) Structure/permeability relationships of polyimide membranes.II. J Polym Sci, Part B: Polym Phys 28:2291–2304
105. Tsapatsis M, Gavalas GR (1999) Synthesis of porous inorganic membranes. MRS Bull 24:30–35
106. Robeson LM, Burgoyne WF, Langsam M, Savoca AC, Tien CF (1994) High performance polymers for membrane separation. Polymer 35:4970–4978
107. Sohn W, Ryu D, Oh S, Koo J (2000) A study on the development of composite membranes for the separation of organic vapors. J Membr Sci 175:163–170
108. Moaddeb M, Koros WJ (1997) Gas transport properties of thin polymeric membranes in the presence of silicon dioxide particles. J Membr Sci 125:143–163
109. Hu Q, Marand E, Dhingra S, Fritsch D, Wen J, Wilkes G (1997) Poly(amide-imide)/TiO_2 nano-composite gas separation membranes: fabrication and characterization. J Membr Sci 135:65–79
110. Chandak MV, Lin YS, Ji W, Higgins RJ (1997) Sorption and diffusion of VOCs in DAY zeolite and silicalite-filled PDMS membranes. J Membr Sci 133:231–243
111. Smaïhi M, Jermoumi T, Marignan J, Nobel RD (1996) Organic-inorganic gas separation membranes: preparation and characterization. J Membr Sci 116:211–220
112. Joly C, Goizet S, Schrotter JC, Sanchez J, Escoubes M (1997) Sol-gel polyimide-silica composite membrane: gas transport properties. J Membr Sci 130:63–74
113. Vankelecom IFJ, Dotremont C, Morobé M, Uytterhoeven JB, Vandecasteele C (1997) Zeolite-filled PDMS membranes. 1. Sorption of halogenated hydrocarbons. J Phys Chem B 101:2154–2159
114. Vankelecom IFJ, Merckx E, Luts M, Uytterhoeven JB (1995) Incorporation of Zeolites in polyimide membranes. J Phys Chem 99:13187–13192

115. Lin L, Zhang Y, Kong Y (2009) Recent advances in sulfur removal from gasoline by pervaporation. Fuel 88:1799–1809
116. Smitha B, Suhanya D, Sridhar S (2004) Separation of organic–organic mixtures by pervaporation—a review. J Membr Sci 241:1–21
117. Hunger K, Schmeling N, Jeazet HBT, Janiak C, Staudt C, Kleinermanns K (2012) Investigation of cross-linked and additive containing polymer materials for membranes with improved performance in pervaporation and gas separation. Membranes 2:727–763
118. Shao P, Huang RYM (2007) Polymeric membrane pervaporation. J Membr Sci 287:162–179
119. Thompson JA, Vaughn JT, Brunelli NA, Koros WJ, Jones CW, Nair S (2014) Mixed-linker zeolitic imidazolate framework mixed-matrix membranes for aggressive CO_2 separation from natural gas. Microporous Mesoporous Mater 192:43–51
120. Bitter JGA (1984) Effect of crystallinity and swelling on the permeability and selectivity of polymer membranes. Desalination 51:19–35
121. Lin L, Wang G, Qu H, Yang J, Wang Y, Shi D, Kong Y (2006) Pervaporation performance of crosslinked polyethylene glycol membranes for deep desulfurization of FCC gasoline. J Membr Sci 280:651–658
122. Lin L, Kong Y, Zhang Y (2008) Sorption and transport behavior of gasoline components in polyethylene glycol membranes. J Membr Sci 325:438–445
123. Kong Y, Lin L, Zhang Y, Lu F, Xie K, Liu R, Guo L, Shao S, Yang J, Shi DD (2008) Studies on polyethylene glycol/polyethersulfone composite membranes for FCC gasoline desulphurization by pervaporation. Eur Polym J 44:3335–3343
124. Chen J, Li J, Chen J, Lin Y, Wang X (2009) Pervaporation separation of ethyl thioether/heptane mixtures by polyethylene glycol membranes. Sep Purif Tech 66:606–612
125. Lin L, Kong Y, Wang G (2006) Selection and crosslinking modification of membrane material for FCC gasoline desulfurization. J Membr Sci 285:144–151
126. Ji W, Sikdar S, Hwang S (1995) Sorption, diffusion and permeation of 1,1,1-trichloroethane through adsorbent-filled polymeric membranes. J Membr Sci 103:243–255
127. Zhang RR, Lu XS, Li SZ, Lin WS, Gu AZ (2005) Analysis on the heating performance of a gas engine driven air to water heat pump based on a steady-state model. Energy Convers Manage 46:1714–1730
128. Hernandez-Maldonado AJ, Yang FH, Qi G, Yang RT (2005) Desulfurization of transportation fuels by π-complexation sorbents: Cu(I)-, Ni(II)-, and Zn(II)-zeolites. Appl Catal B 56:111–126
129. Salem ABSH, Hamid HS (1997) Removal of sulfur compounds from naphtha solutions using solid adsorbents. Chem Eng Tech 20:342–347
130. Lu GQ, Costa JCD, Duke M, Giessler S, Socolow R, Williams RH, Kreutz T (2007) Inorganic membranes for hydrogen production and purification: a critical review and perspective. J Colloid Interface Sci 314:589–630
131. Li YS, Zhu H, Zhu GQ, Liu J, Yang WS (2007) Hydrothermal stability of LTA zeolite membranes in pervaporation. J Membr Sci 297:10–15
132. Caro J, Noack M (2008) Zeolite membranes—recent developments and progress. Microporous Mesoporous Mater 115:215–233
133. Weng TH, Tseng HH, Wey MY (2009) Preparation and characterization of multi-walled carbon nanotube/PBNPI nanocomposite membrane for H_2/CH_4 separation. Int J Hydrogen Energy 34:8707–8715
134. Hernández-Maldonado AJ, Yang RT (2004) Desulfurization of diesel fuels by adsorption via π-complexation with vapor-phase exchanged Cu(I)−Y Zeolites. J Am Chem Soc 126:992–993
135. Koops GH, Nolten JAM, Mulder MHV, Smolders CA (1994) Selectivity as a function of membrane thickness: gas separation and pervaporation. J Appl Polym Sci 53:1639–1651
136. Qu H, Kong Y, Lv H, Zhang Y, Yang J, Shi D (2010) Effect of crosslinking on sorption, diffusion and pervaporation of gasoline components in hydroxyethyl cellulose membranes. Chem Eng J 157:60–66

137. Herrera-Herrera Antonio V, González-Curbelo MÁ, Hernández-Borges J, Rodríguez-Delgado MÁ (2012) Carbon nanotubes applications in separation science: a review. Anal Chim Acta 734:1–30
138. Cong H, Radosz M, Towler BF, Shen Y (2007) Polymer–inorganic nanocomposite membranes for gas separation. Sep Purif Tech 55:281–291
139. Armor JN (1995) Membrane catalysis: where is it now, what needs to be done? Catal Today 25:199–207
140. Ciobanu G, Carja G, Ciobanu O (2008) Structure of mixed matrix membranes made with SAPO-5 zeolite in polyurethane matrix. Microporous Mesoporous Mater 115:61–66
141. Kim S, Chen L, Johnson JK, Marand E (2007) Polysulfone and functionalized carbon nanotube mixed matrix membranes for gas separation: theory and experiment. J Membr Sci 294:147–158
142. Hennepe HJCte, Boswerger WBF, Bargeman D, Mulder MHV, Smolders CA (1994) Zeolite-filled silicone rubber membranes experimental determination of concentration profiles. J Membr Sci 89:185–196
143. Duval J-M, Kemperman AJB, Folkers B, Mulder MHV, Desgrandchamps G, Smolders CA (1994) Preparation of zeolite filled glassy polymer membranes. J Appl Polym Sci 54:409–418
144. Kulprathipanja S (2002) Mixed matrix membrane development. Membrane Tech 2002:9–12
145. Koros WJ, Mahajan R (2002) Mixed matrix membrane materials with glassy polymers. Polymer Eng Sci 42:1432–1441
146. Goh PS, Ismail AF, Sanip SM, Ng BC, Aziz M (2011) Recent advances of inorganic fillers in mixed matrix membrane for gas separation. Sep Purif Tech 81:243–264
147. Ma Y, Shi F, Wang Z, Wu M, Ma J, Gao C (2012) Preparation and characterization of PSf/clay nanocomposite membranes with PEG 400 as a pore forming additive. Desalination 286:131–137
148. Li Y, Krantz W, Chung TS (2007) A novel primer to prevent nanoparticle agglomeration in mixed matrix membranes. AIChE J 53:2470–2475
149. Noble RD (2011) Perspectives on mixed matrix membranes. J Membr Sci 378:393–397
150. Vu DQ, Koros WJ, Miller SJ (2003) Mixed matrix membranes using carbon molecular sieves: I. Preparation and experimental results. J Membr Sci 211:335–348
151. Rafizah WAW, Ismail AF (2008) Effect of carbon molecular sieve sizing with poly(vinyl pyrrolidone) K-15 on carbon molecular sieve–polysulfone mixed matrix membrane. J Membr Sci 307:53–61
152. Widjojo N, Chung TS, Kulprathipanja S (2008) The fabrication of hollow fiber membranes with double-layer mixed-matrix materials for gas separation. J Membr Sci 325:326–335
153. Tin PS, Chung T-S, Jiang L, Kulprathipanja S (2005) Carbon-zeolite composite membranes for gas separation. Carbon 43:2025–2027
154. Ismail AF, Kusworo TD, Mustafa A (2008) Enhanced gas permeation performance of polyethersulfone mixed matrix hollow fiber membranes using novel Dynasylan Ameo silane agent. J Membr Sci 319:306–312
155. Ismail AF, Rahim RA, Rahman WA (2008) Characterization of polyethersulfone/Matrimid® 5218 miscible blend mixed matrix membranes for O_2/N_2 gas separation. Sep Purif Tech 63:200–206
156. Solaymani A, Doroodmand MM, Sabbaghi S (2014) Modification of theoretical models for the effective properties of mixed-matrix membranes fabricated with carbon nanotubes. J Comput Theoret Nanosci 11:80–90
157. Zhan X, Lu J, Tan T, Li J (2012) Mixed matrix membranes with HF acid etched ZSM-5 for ethanol/water separation: preparation and pervaporation performance. Appl Surf Sci 259:547–556
158. Hennepe HJCte, Bargeman D, Mulder MHV, Smolders CA (1987) Zeolite-filled silicone rubber membranes: part 1. Membrane preparation and pervaporation results. J Membr Sci 35:39–55
159. Zhan X, Li JD, Chen J, Huang J (2009) Pervaporation of ethanol/water mixtures with high flux by zeolite-filled PDMS/PVDF composite membranes. J Polym Sci 27:771–780

160. Gorgojo P, Gorgojo B, Uriel S, Téllez C, Coronas J (2008) Mixed matrix membranes from nanostructured materials for gas separation. Stud Surf Sci Catal 174 Part A:653–656
161. Wee S-L, Tye C-T, Bhatia S (2008) Membrane separation process—pervaporation through zeolite membrane. Sep Purif Tech 63:500–516
162. Merkel TC, He Z, Pinnau I, Freeman BD, Meakin P, Hill AJ (2008) Sorption and Transport in Poly(2,2-bis(trifluoromethyl)-4,5-difluoro-1,3-dioxole-co-tetrafluoroethylene) containing nanoscale fumed silica. Macromolecules 36:8406–8414
163. He Z, Pinnau I, Morisato A (2002) Nanostructured poly(4-methyl-2-pentyne)/silica hybrid membranes for gas separation. Desalination 146:11–15
164. Merkel TC, Freeman BD, Spontak RJ, He Z, Pinnau I, Meakin P, Hill AJ (2002) Ultrapermeable, reverse-selective nanocomposite membranes. Science 296:519–522
165. Moore TT, Mahajan R, Vu DQ, Koros WJ (2004) Hybrid membrane materials comprising organic polymers with rigid dispersed phases. AICHE J 50:311–321
166. Sircar S, Rao MB, Thaeron CMA (1999) Selective surface flow membrane for gas separation. Sep Sci Tech 34:2081–2093
167. Bouma RHB, Checchetti A, Chidichimo G, Drioli E (1997) Permeation through a heterogeneous membrane: the effect of the dispersed phase. J Membr Sci 128:141–149
168. Kulprathipanja S, Neuzil RW, Li NN (1986) Separation of fluids by means of mixed matrix membranes. US4740219A
169. Mahajan R (2000) Formation, characterization and modeling of mixed matrix membrane materials. Ph.D. Dessertation, The Univeristy of Texas at Austin, TX
170. Jia MD, Peinemann KV, Behling RD (1992) Preparation and characterization of thin-film zeolite–PDMS composite membranes. J Membr Sci 73:119–128
171. Wang D, Li K, Teo WK (1998) Preparation and characterization of polyetherimide asymmetric hollow fiber membranes for gas separation. J Membr Sci 138:193–201
172. Kim IC, Lee KH, Tak TM (2001) Preparation and characterization of integrally skinned uncharged polyetherimide asymmetric nanofiltration membrane. J Membr Sci 183:235–247
173. Li Y, Chung TS, Kulprathipanja S (2007) Novel Ag+-zeolite/polymer mixed matrix membranes with a high CO_2/CH_4 selectivity. AIChE J 53:610–616
174. Shiflet MB, Foley HC (1999) Ultrasonic deposition of high-selectivity nanoporous carbon membranes. Science 285:1902–1905
175. Hayashi J-I, Mizuta H, Yamamoto M, Kusakabe K, Morooka S (1997) Pore size control of carbonized BPDA-pp'ODA polyimide membrane by chemical vapor deposition of carbon. J Membr Sci 124:243–251
176. Xiao YC, Wang KY, Chung TS, Tan J (2006) Evolution of nano-particle distribution during the fabrication of mixed matrix -polyimide hollow fiber membranes. Chem Eng J 61:6228–6233
177. Yong HH, Park HC, Kang YS, Won J, Kim WN (2001) Zeolite-filled polyimide membrane containing 2,4,6-triaminopyrimidine. J membr Sci 188:151–163
178. Shiflett MB, Foley HC (2000) On the preparation of supported nanoporous carbon membranes. J Membr Sci 179:275–282
179. Caro J, Noack M, Kölsch P, Schäfer R (2000) Zeolite membranes—state of their development and perspective. Microporous Mesoporous Mater 38:3–24
180. Chung TS, Lin W-H, Vora RH (1994) Development of a defect-free 6FDA-durene asymmetric hollow fiber and its composite hollow fibers. J Membr Sci 88:21–36
181. Pinnau I, Koros W (1991) Structures and gas separation properties of asymmetric polysulfone membranes made by dry, wet, and dry/wet phase inversion. J Appl Polym Sci 43:1491–1502
182. Pesek SC, Koros W (1993) Aqueous quenched asymmetric polysulfone membranes prepared by dry/wet phase separation. J Membr Sci 81:71–88
183. Wang DL, Li K, Teo WK (1996) Polyethersulfone hollow fiber gas separation membranes prepared from NMP/alcohol solvent systems. J Membr Sci 115:85–108
184. Kesting RE, Fritzsche AK, Cruse CA, Moore MD (1990) The second-generation polysulfone gas-separation membrane. II. The relationship between sol properties, gel macrovoids, and fiber selectivity. J Appl Polym Sci 40:1575–1582

185. Husain S, Koros WJ (2005) Mixed matrix hollow fibers for gas separation. North American Membrane Society, Providence, RI
186. Jiang LY, Chung TS, Cao C, Huang Z, Kulprathipanja S (2005) Fundamental understanding of nano-sized zeolite distribution in the formation of the mixed matrix single- and dual-layer asymmetric hollow fiber membranes. J Membr Sci 252:89–100
187. Miller SJ, Munson CL, Kulkarni SS, Hasse DJ (2002) Purification of p-xylene using composite mixed matrix membranes. US patent 6,500,233
188. Lanying J (2006) Fabrication and characterization of composite membranes for gas separation. Ph.D. Thesis. Singapore: National University of Singapore
189. Li Y (2006) Development of mixed matrix membranes for gas separation application. Ph.D. Thesis. National University of Singapore, Singapore
190. Koros WJ, Wallace D, Wind JD, Miller SJ, Bickel CS, Vu DQ (2004) Crosslinked and crosslinkable hollow fiber mixed matrix membrane and method of making the same. US patent 6,755,900
191. Bernardo P, Drioli E, Golemme G (2009) Membrane gas separation: a review/state of the art. Ind Eng Chem Res 48:4638–4663
192. Wang H, Zhang L, Gavalas GR (2000) Preparation of supported carbon membranes from furfuryl alcohol by vapor deposition polymerization. J Membr Sci 177:25–31
193. Tseng HH, Kumar IA, Weng TH, Lu CY, Wey MY (2009) Preparation and characterization of carbon molecular sieve membranes for gas separation—the effect of incorporated multiwall carbon nanotubes. Desalination 240:40–45
194. Acharya M, Foley HC (1999) Spray-coating of nanoporous carbon membranes for air separation. J Membr Sci 161:1–5
195. Li Y, Guan H-M, Chung TS, Kulprathipanja S (2006) Effects of novel silane modification of zeolite surface on polymer chain rigidification and partial pore blockage in polyethersulfone (PES)–zeolite a mixed matrix membranes. J Membr Sci 275:17–28
196. Huang S, Dai L (2002) Plasma etching for purification and controlled opening of aligned carbon nanotubes. J Phys Chem B 106:3543–3545
197. Deng J, Zhang X, Wang K, Zou H, Zhang Q, Fu Q (2007) Synthesis and properties of poly(ether urethane) membranes filled with isophorone diisocyanate-grafted carbon nanotubes. J Membr Sci 288:261–267
198. Kalappa P, Lee J-H, Rashmi J, Venkatesha TV, Pai KV, Xing W (2008) Effect of polyaniline functionalized carbon nanotubes addition on the positive temperature coefficient behavior of carbon black/high-density polyethylene nanocomposites. IEEE Trans Nanotechnol 7:223–228
199. Jeon I-Y, Lee H-J, Choi Y-S, Tan L-S, Baek J-B (2008) Semimetallic transport in nanocomposites derived from grafting of linear and hyperbranched poly(phenylene sulfide)s onto the surface of functionalized multi-walled carbon nanotubes. Macromolecules 41:7423–7432
200. Zou W, Du Z-J, Liu Y-X, Yang X, Li H-Q, Zhang C (2008) Functionalization of MWNTs using polyacryloyl chloride and the properties of CNT–epoxy matrix nanocomposites. Compos Sci Tech 68:3259–3264
201. Duval JM (1995) Adsorbent filled polymeric membranes: applications to pervaporation and gas separation. Ph.D. Thesis. University of Twente, The Netherlands
202. Li Y, Chung TS, Cao C, Kulprathipanja S (2005) The effects of polymer chain rigidification, zeolite pore size and pore blockage on polyethersulfone (PES)-zeolite a mixed matrix membranes. J Membr Sci 260:45–55
203. Ma P-C, Siddiqui NA, Marom G, Kim J-K (2010) Dispersion and functionalization of carbon nanotubes for polymer-based nanocomposites: a review. Compos Part A—Appl Sci Manuf 41:1345–1367
204. Aroon MA, Ismail AF, Matsuur T, Montazer-Rahmatia MM (2010) Performance studies of mixed matrix membranes for gas separation: a review. Sep Purif Tech 75:229–242
205. Liu Y-H, Yi B, Shao ZG, Xing D, Zhang H (2006) Carbon nanotubes reinforced nafion composite membrane for fuel cell applications. Electrochemical and Solid State Letters 9:356–359

206. Solaymani A, Doroodmand MM, Sabbaghi S (2013) Effect of pressure on gas permeability and selectivity of carbon nanostructure/polyacrylonitrile mixed matrix membrane. Sci Adv Mater 5:656–662
207. Lin H, Freeman BD (2005) Materials selection guidelines for membranes that remove CO_2 from gas mixtures. J Mol Struct 739:57–74
208. McLeary EF, Jansen JC, Kapteijn F (2006) Zeolite based films, membranes and membrane reactors: progress and prospects. Microporous Mesoporous Mater 90:198–220
209. Hinds BJ, Chopra N, Rantell T, Andrews R, Gavalas V, Bachas LG (2004) Aligned multiwalled carbon nanotube membranes. Science 303:62–65
210. Liu T, Tong Y, Zhang W-D (2007) Preparation and characterization of carbon nanotube/polyetherimide nanocomposite films. Compos Sci Tech 67:406–412
211. Majumder M, Ajayan PM (2010) Carbon nanotube membranes: a new frontier in membrane science. Compr Membr Sci Eng 1:291–310
212. Ago H, Komatsu T, Ohshima S, Kuriki Y, Yumura Y (2000) Dispersion of metal nanoparticles for aligned carbon nanotube arrays. Appl Phys Lett 77:79–81
213. Kanzow H, Lenski C, Ding A (2001) Single-wall carbon nanotube diameter distributions calculated from experimental parameters. Phys Rev B 63:125402
214. Belin T, Epron F (2005) Mater Sci Eng: B 119:105–118
215. Shoulidas AI, Ackerman DM, Johnson JK, Sholl DS (2002) Rapid transport of gases in carbon nanotubes. Phys Rev Lett 89:185901
216. Ismail AF, Goh PS, Tee JC, Sanip SM, Aziz M (2008) A review of purification techniques for carbon nanotubes. NANO 3:127–143
217. Mi W, Lin YS, Li Y (2007) Vertically aligned carbon nanotube membranes on macroporous alumina supports. J Membr Sci 304:1–7
218. Klinke C, Bonard JM, Kern K (2005) Thermodynamic calculations on the catalytic growth of multiwall carbon nanotubes. Phys Rev: B 71:035403
219. Sholl DS (1999) Characterization of molecular cluster diffusion in AlPO4-5 using molecular dynamics. Phys Lett 305:269–275
220. Cervini R, Simon GP, Ginic-Markovic M, Matisons JG, Huynh C, Hawkins S (2008) Aligned silane-treated MWCNT/liquid crystal polymer films. Nanotechnology 19:175602
221. Chen W, Tao X (2005) Self-organizing alignment of carbon nanotubes in thermoplastic polyurethane. Macromol Rapid Commun 26:1763–1767
222. Peigney A, Laurent C, Flahaut E, Rousset A (2000) Carbon nanotubes in novel ceramic matrix nanocomposites. Ceram Int 26:677–683
223. Shirazi Y, Tofighy MA, Mohammadi T (2011) Synthesis and characterization of carbon nanotubes/poly vinyl alcohol nanocomposite membranes for dehydration of isopropanol. J Membr Sci 378:551–561
224. Qiu S, Wu L, Pan X, Zhang L, Chen H, Gao C (2009) Preparation and properties of functionalized carbon nanotube/PSF blend ultrafiltration membran. J Membr Sci 342:165–172
225. Shawky HA, Chae S-R, Lin S, Wiesner MR (2011) Synthesis and characterization of a carbon nanotube/polymer nanocomposite membrane for water treatment. Desalination 272:46–50
226. Matranga C, Bockrath B, Chopra N, Jinds BJ, Andrews R (2006) Raman spectroscopic investigation of gas interactions with an aligned multiwalled carbon nanotube membrane. Langmuir 22:1235–1240
227. Sears K, Dumée L, Schütz J, She M, Huynh C, Hawkins S, Duke M, Gray S (2010) Recent developments in carbon nanotube membranes for water purification and gas separation. Materials 3:127–149
228. Vatanpour V, Madaeni SS, Moradian R, Zinadini S, Astinchap B (2011) Fabrication and characterization of novel antifouling nanofiltration membrane prepared from oxidized multiwalled carbon nanotube/polyethersulfone nanocomposite. J Membr Sci 375:284–294
229. Celik E, Liu L, Choi H (2011) Protein fouling behavior of carbon nanotube/polyethersulfone composite membranes during water filtration. Water Res 45:5287–5294
230. Bazilevsky AV, Sun K, Yarin AL, Megaridis CM (2007) Selective intercalation of polymers in carbon nanotubes. Langmuir 23:7451–7455

231. Ismail AF, Rahim NH, Mustafa A, Matsuura T, Ng BC, Abdullah S, Hashemifard SA (2011) Gas separation performance of polyethersulfone/multi-walled carbon nanotubes mixed matrix membranes. Sep Purif Tech 80:20–31
232. Majumder M, Chopra N, Hinds BJ (2005) Effect of tip functionalization on transport through vertically oriented carbon nanotube membranes. J Am Chem Soc 127:9062–9070
233. Mondal S, Hu JL (2008) Microstructure and water vapor transport properties of functionalized carbon nanotube-reinforced dense-segmented polyurethane composite membranes. Polym Eng Sci 48:1718–1724
234. Narayan RJ, Brigmon CJ, Brigmon RL (2005) Structural and biological properties of carbon nanotube composite films. Mater Sci Eng B 123:123–129
235. Brunet L, Lyon DY, Zodrow K, Rouch J-C, Caussat B, Serp P, Remigy J-C, Wiesner MR, Alvarez PJJ (2008) Properties of membranes containing semi-dispersed carbon nanotubes. Environ Eng Sci 25:565–575
236. Chen H, Sholl DS (2006) Predictions of selectivity and flux for CH_4/H_2 separations using single walled carbon nanotubes as membranes. J Membr Sci 269:152–160
237. Kim S, Pechar TW, Marand E (2006) Poly(imide siloxane) and carbon nanotube mixed matrix membranes for gas separation. Desalination 192:330–339
238. Maxwell C (1873) Treatise on electricity and magnetism. Cambridge University Press, London
239. Bruggeman DAG (1935) Calculation of different physical constants of heterogeneous substances. Ann Phys 24:636–679
240. Lewis TB, Nielsen LE (1970) Dynamic mechanical properties of particulate-filled composites. J Appl Polymer Sci 14:1449–1471
241. Felske JD (2004) Effective thermal conductivity of composite spheres in a continuous medium with contact resistance. Int J Heat Mass Transfer 47:3453–3461
242. Pal R (2008) On the Lewis-Nielsen model for thermal/electrical conductivity of composites. Compos A 39:718–726
243. Sholl DS, Johnson JK (2006) Making high-flux membranes with carbon nanotubes. Science 312:1003–1004
244. Derakhshan AA, Rajabi L (2012) Review on applications of carboxylate–alumoxane nanostructures. Powder Tech 226:117–129
245. Chen W, Wu S, Lei Y, Liao Z, Guo B, Liang X, Jia D (2011) Interfacial structure and performance of rubber/boehmite nanocomposites modified by methacrylic acid. Polymer 52:4387–4395
246. Xu Y, Ray G, Abdel-Magid B (2006) Thermal behavior of single-walled carbon nanotube polymer–matrix composites. Compos A: Appl Sci Manuf 37:114–121
247. Hashemifard SA, Ismail AF, Matsuura T (2010) A new theoretical gas permeability model using resistance modeling for mixed matrix membrane systems. J Membr Sci 350:259–268
248. Petropoulos JH (1985) A comparative study of approaches applied to the permeability of binary composite polymeric materials. J Polym Sci: Polym Phys Ed 23:1309–1324
249. Halbach TS, Mülhaupt R (2008) Boehmite-based polyethylene nanocomposites prepared by in-situ polymerization. Polymer 49:867–876
250. Guiver MD, Robertson GP, Dai Y, Bilodeau F, Kang YS, Lee KJ, Jho JY, Won J (2002) Structural characterization and gas-transport properties of brominated matrimid polyimide. J Polym Sci: Polym Chem 40:4193–4204
251. Vu VQ, Koros WJ, Miller SJ (2003) Effect of condensable impurity in CO_2/CH_4 gas feeds on performance of mixed matrix membranes using carbon molecular sieves. J Membr Sci 221:233–239
252. Vu DQ, Koros WJ, Miller SJ (2003) Mixed matrix membranes using carbon molecular sieves: I. Preparation and experimental results. J Membr Sci 211:311–334
253. Anson M, Marchese J, Garis E, Ochoa N, Pagliero C (2004) ABS copolymer-activated carbon mixed matrix membranes for CO_2/CH_4 separatio. J Membr Sci 243:19–24
254. Merkel TC, He Z, Pinnau I, Freeman BD, Meakin P, Hill AJ (2003) Effect of nanoparticles on gas sorption and transport in Poly(1-trimethylsilyl-1-propyne). Macromolecules 36:6844–6855

255. Chung TS, Chan SS, Wang R, Lu Z, He C (2003) Characterization of permeability and sorption in Matrimid/C60 mixed matrix membranes. J Membr Sci 211:91–99
256. Jansen JC, Darvishmanesh S, Tasselli F, Bazzarelli F, Bernardo F, Tocci E, Friess K, Randova A, Drioli E, Bruggen B (2013) Influence of the blend composition on the properties and separation performance of novel solvent resistant polyphenylsulfone/polyimide nanofiltration membranes. J membr Sci 447:107–118
257. Rezakazemi M, Amooghin AE, Montazer-Rahmati MM, Ismail AF, Matsuura T (2014) State-of-the-art membrane based CO_2 separation using mixed matrix membranes (MMMs): an overview on current status and future directions. Prog Polym Sci 39:817–861
258. Huang Y, Merkel TC, Baker RW (2014) Pressure ratio and its impact on membrane gas separation processes. J membr Sci 463:33–40
259. Kang GD, Cao YM (2014) Application and modification of poly(vinylidene fluoride) (PVDF) membranes—a review. J Member Sci, pp 145–165
260. Jiang LY, Chung TS, Rajagopalan R (2007) Matrimid®/MgO mixed matrix membranes for pervaporation. AIChE J 53:1745–1757
261. Veerapur RS, Gudasi KB, Aminabhavi TM (2008) Sodium alginate–magnesium aluminum silicate mixed matrix membranes for pervaporation separation of water–isopropanol mixtures. Sep. and Purif. Tech. 59:221–230
262. Lee J, Rasmussen HK, Rasmussen KE, Pedersen-Bjergaard S (2008) Environmental and bioanalytical applications of hollow fiber membrane liquid-phase microextraction: a review. Anal Chim Acta 624:253–268
263. Cong H, Zhang J, Radosx M, Shen Y (2007) Carbon nanotube composite membranes of brominated poly(2,6-diphenyl-1,4-phenylene oxide) for gas separation. J Membr Sci 294:178–185
264. Yoda S, Hasegawa A, Suda H, Uchimaru Y, Haraya K, Tsuji T, Otake K (2004) Preparation of a platinum and Palladium/polyimide nanocomposite film as a precursor of metal-doped carbon molecular sieve membrane via supercritical impregnation. Chem Mater 16:2363–2368
265. Hu CC, Liu TC, Lee KR, Ruaan RC, Lai JY (2006) Zeolite-filled PMMA composite membranes: influence of coupling agent addition on gas separation properties. Desalination 193:14–24
266. Jiang LY, Chung T-S, Rajagopalan R (2007) Dual-layer hollow carbon fiber membranes for gas separation consisting of carbon and mixed matrix layers. Carbon 45:166–172
267. Tseng HH, Shiu P-T, Lin YS (2011) Effect of mesoporous silica modification on the structure of hybrid carbon membrane for hydrogen separation. Int J Hydrogen Energy 36:15352–15363
268. Yoshimune MFI, Suda H, Haraya K (2006) Gas transport properties of carbon molecular sieve membranes derived from metal containing sulfonated poly(phenylene oxide). Desalination 193:66–72

Carbon Nanotubes in Organic Catalysis

Angel Luis Corcho-Valdés, Claudia Iriarte-Mesa, Jesús Calzadilla-Maya, Yasser Matos-Peralta, Luis Felipe Desdín-García, and Manuel Antuch

Abstract Nanoscience and nanotechnology have revolutionized organic catalysis, increasing the efficiency of these reactions and reducing their environmental impact. Particularly, carbon nanotubes are widely used in many organic reactions such as C–C couplings, hydrogenations, alkane dehydrogenations, transesterifications and oxidations. Excellent results have been obtained in terms of the synthesis of the catalysts, reaction yields, selectivity, and reusability. In this review, we provide a general overview of the design, synthesis, and use of carbon nanotubes as catalysts and catalytic supports, along with the main strategies for their surface functionalization and doping with heteroatoms. Concluding considerations from the authors' perspective are provided, regarding the promising use of these materials and the challenges to be faced in the near future.

Keywords Organic catalysis · Carbon nanotubes · Catalyst · Catalyst support · Nanoparticles · Nitrogen doping

Abbreviations

ACN	6-Aminohexanenitrile
ADN	Adiponitrile

A. L. Corcho-Valdés · J. Calzadilla-Maya · L. F. Desdín-García · M. Antuch (✉)
Centro de Aplicaciones Tecnológicas Y Desarrollo Nuclear (CEADEN), No. 502, Calle 30 y 5ta Ave. Miramar, C.P. 11300 La Habana, Cuba
e-mail: antuch@ceaden.edu.cu; manuantcubi@yahoo.com

L. F. Desdín-García
e-mail: desdin@ceaden.edu.cu

C. Iriarte-Mesa
Department of Inorganic Chemistry-Functional Materials, Faculty of Chemistry, University of Vienna, Währinger Straße 42, 1090 Vienna, Austria

Y. Matos-Peralta
Laboratorio de Bioinorgánica. Facultad de Química, Universidad de La Habana. Zapata Y G. Vedado, C.P. 10400 La Habana, Cuba

M. Jawaid and A. Khan (eds.), *Carbon Composite Catalysts*, Composites Science and Technology, https://doi.org/10.1007/978-981-19-1750-9_7

AP	Acetophenone
BINO	1,1′-Bi-2-naphthol
BP	2-Phenyl-2-propanol
CAL	Cinnamaldehyde
CD	Cinchonidine
CDNS	Cyclodextrin nanosponges
CHP	And cumene hydroperoxide
CN	Carbon nitrides
CNF	Carbon nanofibers
CNTs	Carbon nanotubes
COL	Cinnamyl alcohol
CPA	2-Chloroethylphosphonic acid
CVD	Chemical vapor deposition
DME	Dimethyl ether
DMO	Dimethyl oxalate
EB	Ethylbenzene
EDA	Ethylenediamine
EIS	Electrochemical impedance spectroscopy
EL	Ethyl lactate
EOR	Electrooxidation reaction
EP	Ethyl pyruvate
FA	Formaldehyde
FTS	Fischer–tropsch synthesis
GO	Graphene oxide
HDA	1,6-Hexanediamine
HTC	Hydrothermal carbonization
LCST	Lower critical solution temperature
MTU	S-methylisothiourea
MWCNTs	Multiwalled carbon nanotubes
nB	N-butanol
NCNTs	Nitrogen-doped carbon nanotubes
NPs	Nanoparticles
ODH	Oxidative dehydrogenation reactions
PANI	Polyaniline
PC	Poly(citric acid) dendrimer
PCC	Pyridinium chlorochromate
PDA	Polydiacetylenes
PL	Photoluminescence
PMS	Peroxymonosulfate
PNIPAM	Poly(*N*-isopropylacrylamide)
PVP	Polyvinylpyrrolidone
RGO	Reduced graphene oxide
SDS	Sodium dodecylsulfate
SMTU	S-methylisothiourea hemisulfate
SPR	Surface plasmon resonance

SWCNT	Single walled carbon nanotubes
TBAB	Tetrabutylammonium bromide
TBHP	Tert-butyl hydroperoxide
TC	Tetracycline hydrochloride
TH	Transfer hydrogenation

1 Introduction

Nanoscience and nanotechnology have transformed the face of chemistry and hence the industry over the last years. One of the fields where the potentialities of the nanomaterials have been successfully demonstrated has been organic catalysis [1]. A large amount of nanosized materials with diverse catalytic properties have been designed and synthesized and some of them have even entered the market [2]. Before the rise of nanoscience in the development of new functional materials for catalysis, different nanometric metals (e.g., Pd and Pt) had already been used to catalyze numerous and diverse organic reactions [1]. Nanocatalysts allow the occurrence of selective chemical transformations in a short time; in many cases with ease in the separation procedures, recovery and reuse of the catalyst [3].

Carbon nanostructures are currently widely used to catalyze organic reactions [1]. In 1991 the carbon nanotubes (CNTs) were discovered by Ijima and nowadays is considered as an additional carbon allotrope [4]. CNTs are cylindrical-shaped nanostructures formed by a rolled one-atom-thick layer of carbon sp^2, known as Single-Wall Carbon Nanotubes (SWCNT). It is also possible to find several concentric nanotubes forming a multilayer nanotube, typically referred to as Multi-Wall Carbon Nanotubes (MWCNT). The electronic properties (i.e., their conducting or semiconducting characteristics) of CNTs are determined by how their cells and edges are arranged, being divided into three types according to the way in which they are rolled (i.e., armchair, zigzag and chiral) [1] (Fig. 1).

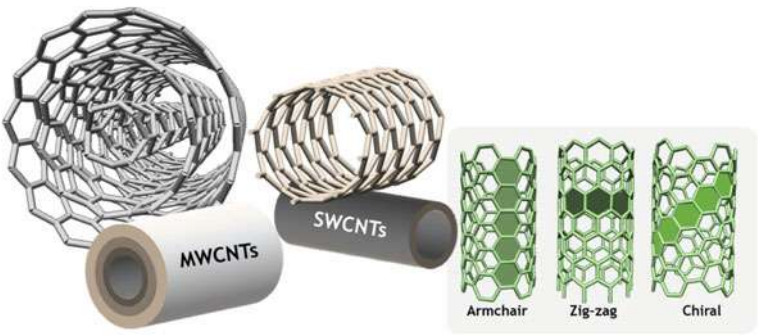

Fig. 1 Structure and lateral size of SWCNTs and MWCNTs

CNTs may work not only as catalysts in organic transformations, but also as support for other catalytic species, such as metal nanoparticles, for example. These applications arise especially for their high electrical conductivity, mechanical resistance, thermal stability, tolerance to catalyst poisoning, and the flexibility to modulate the specific surface area (e.g., from 55 to 495 $m^2 \cdot g^{-1}$ for MWNTs, it is worth noting that a high specific area is essential for a catalyst) and their small internal diameter from 5 to 100 nm [5]. To these excellent properties is added the flexibility to functionalize their surfaces as well as the possibilities of shaping the macroscopic morphology of the support, altering their chemical structure (e.g., doping with nitrogen or boron atoms) and tuning specific metal-support interactions [3]. A large number of transition metals and metal oxides have been coated on the surfaces of CNTs to obtain catalysts used in several organic reactions [6]. The catalytic performance of chemically modified CNTs have been widely reported, as well as the potential of these materials as supports for metal nanoparticles (NPs) or organometallic compounds [1], which has diversified their use in organic catalysis.

This contribution is devoted to highlighting the potential of CNTs in the catalysis of organic reactions. Herein, we focus on SWCNTs and MWCNTs used either as supports for catalytically active species or as metal-free catalysts, for which previous strategies for functionalization or heteroatom doping of carbon structures play a fundamental role. The purpose of this contribution is to provide examples of the countless possibilities offered by the chemical modification of CNTs to obtain functional catalysts, with an emphasis put on the organic reactions of industrial interest. The description of the design and the obtaining of these materials are described in the examples presented. We intended to cover the most recent advances reported in organic catalysis; consequently, 36% of the work reviewed here comes from the last three years (2019–2021), 63% from the last five years (2017–2021), and 92% from the last decade (2011–2021), thus showing a current view of the most recent progress in the field. This Chapter contains 2 main sections in addition to this Introduction. Section 2 focuses on the use of CNTs as catalytic supports. In Sect. 3 the main synthetic routes to obtain metal-free catalysts from CTNs are described, emphasizing nitrogen-doped CNTs catalysts, due to the attractive possibilities offered by these hybrid materials. Each section is organized by families of organic reactions where examples of nanocatalysts based on CNTs are described and demonstrate their unquestionable role in the enhanced catalytic efficiencies observed.

2 Carbon Nanotubes as Catalyst Supports

When nanotubes are used as catalytic supports, the previous decoration of the CNTs with metallic nanoparticles (NPs) as catalytic species are needed, being widely reported the modification both inside and outside the CNTs walls, as well as their previous functionalization with organic moieties to improve the subsequent interactions with NPs [7, 8].

Fig. 2 Carbon nanotubes as catalyst supports

In this section, several examples where CNTs have played an essential role as supports for catalytically active NPs in different organic reactions are described (Fig. 2). Special emphasis will be placed on cross-coupling reactions (e.g. Sonogashira, Heck, and Suzuki–Miyaura), hydrogenation reactions, and oxidation of alcohols, where the presence of CNTs in ethanol fuel cells and their role as catalytic supports in electro and photo-oxidation of alcohols will be described.

2.1 Cross-Coupling Reactions

Cross-coupling reactions are synthetic transformations that occur when mixing of an organometallic compound with an organic electrophile. This process is catalyzed by metals and allows the formation of C–C, C–H, C–N, C–O, C–S, C–P, or C–M bonds. Cross-coupling reactions were discovered in the 1970s by Kochi, Murahashi, Corriu, and Kumada and since then; several organometallic compounds have been used, including organoboron [9], organotin [10], organosilicon [11], and organozinc [12].

The reactions of several organometallic complexes and electrophiles have been proven successfully, forming a wide range of molecular unions [7], with applications ranging from the production of polymers [13] to natural products and pharmaceuticals [14, 15]. The cross-coupling reactions occur by a general catalytic cycle (Scheme 1), including initially an oxidative addition followed by a transmetallation and a reductive elimination as the final step [16].

2.1.1 Heck Reaction

In 1972, Mizoroki and Heck discovered the reaction of formation of a C–C bond when organohalides react with alkenes. From the addition of a palladium catalyst

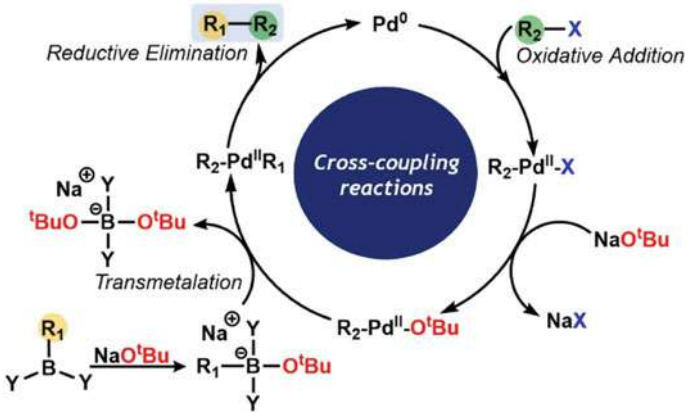

Scheme 1 Mechanism of cross-coupling reactions with Pd as catalyst

and a base, it is possible to obtain substituted alkenes (Scheme 2) [17]. This reaction is extensively used in biomedicine, industry and electronics because of its facility to generate organic compounds faster, effectively and at lower temperatures [18]. The palladium-catalyzed reaction proceeds with the formal loss of a molecule of hydrogen halide, producing a new C–C bond which involves an olefin and an aryl group. The Heck reaction occurs in relatively moderate conditions including a wide diversity of functional groups such as aldehydes [19], amines [20], esters [21], and nitro groups [22], allowing high conversions.

Not only palladium has been used as a catalyst in the Heck reaction. Synthetic procedures based on other metal and/or metal oxide nanoparticles supported in CNTs have been described with that purpose. Hajipour et al. reported the use of CNTs decorated with cobalt NPs as a catalyst for the Heck reaction [23]. The previous functionalization of CNTs with imidazolium was also described to improve the immobilization of the Co nanoparticles [24]. The nanoparticles encapsulated inside the walls of the nanotubes catalyzed the reactions at a higher rate, and the stability was enhanced after several reuse cycles. A hybrid material based on nanotubes decorated with RuO_2 NPs also proved to be a regioselective and chemoselective catalyst in this type of reaction [25].

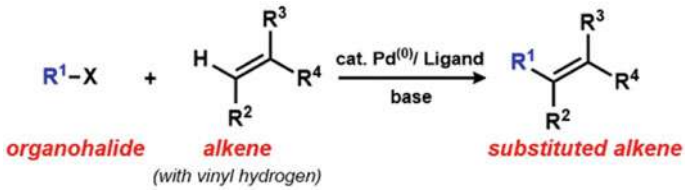

Scheme 2 Heck reactions between organohalides and alkenes

Magnetic CNTs have also been obtained by using Chemical Vapor Deposition (CVD) by adding Ni NPs to hydrolyzed CNTs for the subsequent decoration with Pd NPs. The magnetic properties of the hybrid material obtained allowed their separation and reutilization after being used in the Heck reaction [26].

Nanotubes decorated with polyaniline (PANI) were also used to achieve the immobilization of palladium nanoparticles. Different PANI/CNTs ratios were evaluated to corroborate the catalytic activity and stability of the grafted material in comparison with the same material without PANI. The nitrogen atoms of PANI interact with Pd providing an enhanced stability and reusability of the catalyst, which was also theoretically analyzed [27].

The interaction between nitrogen atoms and Pd NPs has been widely studied and nitrogen has even been included in the nanotube structure by doping strategies and CVD (N-CNTs), obtaining pyrrole, pyridine, and other nitrogenous derivatives that facilitate the immobilization of Pd in the nanotube structure [28]. Palladium-decorated nitrogen-doped carbon nanotubes (Pd/N-CNTs) were obtained from green and facile synthesis and the catalyst obtained was uses in the Heck reaction and selective oxidation of benzyl alcohol [29]. The N-CNTs were synthesized from CVD with ethylenediamine as precursor. Polyvinylpyrrolidone (PVP) and sodium dodecylsulfate (SDS) were used as stabilizers to reduce the palladium nanoparticles.

The catalytic efficiency and reusability of different composites based on CNTs have been evaluated using some aryl halides and olefins and tuning also the reaction conditions, i.e., temperature, base, solvents, reaction times, and amounts of catalyst. Some of these examples are presented in Table 1.

Ferromagnetic multi-walled carbon nanotubes (FMMWCNTs) were decorated with aminated 2-chloroethylphosphonic acid (CPA) and *S*-methylisothiourea (MTU) to immobilize Pd(II) NPs, forming a heterogeneous catalyst with a narrow size distribution between 20–30 nm (Table 1). The material obtained (FMMWCNTs@CPA@SMTU@PdII NPs) exhibited catalytic properties at room temperature and was used in some reactions involving alkenes, aryl halides, and arylboronic acids. Some of the advantages of this material were its easy separation with an external magnetic field and the possibility of its reuse more than four times without an abruptly decrease of the catalytic activity [30].

The surface of MWCNTs was decorated with (S)-methyl histidinate to immobilize palladium and obtain an effective and stable palladium-based catalyst. To bond the (S)-methyl histidinate on the nanotube surface, the MWCNTs were first chemically oxidized and then mixed with thionyl chloride. The (S)-methyl histidinate was subsequently added and finally, the Pd salt was incorporated to the hybrid. This new palladium catalyst presented a high catalytic activity and reusability in poly(ethylene glycol) and green solvents, using small amounts of palladium under mild conditions [31].

A Pd(II) complex anchored to MWCNTs showed also activity and durability for the Mizoroki–Heck cross-coupling of alkenes with aryl halides. To synthesize the catalytic composite, the use of MWCNTS functionalized with acid groups was reported, as well as their subsequent reaction with thionyl chloride forming a chlorine bond. The Pd(II) salt was then added to obtain the compound Pd-MWCNTs. In the

Table 1 The use of CNTs as catalysts supports in Heck reactions

Catalyst	Reactants	Reaction conditions	Time (min)	Yield (%)	Reusability (%/cycle)	Refs
Co-in-CNTs (I)	Iodobenzene and methylacrylate	Co (0.17 mol%) in PEG, 60 °C	300	47	–	[23]
Co-in-CNTs (II)		Co (3.4 mol%) in PEG, 60 °C	180	97	85/9	
Co-out-CNTs		Co (1.7 mol%) in PEG, 60 °C	300	84	73/5	
Co-IL-MWCNT		Co (5 mol%) in $NaHSO_4$, 100 °C	180	87	77/6	[24]
Pd/NiCNTs-OH		Pd/Ni (10 mg) in DMF, 100 °C	180	99.2	–	[25]
RuO_2/SWCNT	Iodobenzene and styrene	RuO_2 (0.9 mol%) in $(CH_3)_3COK$, 100 °C	10	91	86/8	[26]
PANI@CNT-0.5		Pd (0.15 mol%) in DMF, 110 °C	100	99	94/10	[27]
Pd/N-CNTs	Iodobenzene and ethylacrylate	Pd (8.6 mol%) in PVP/SDS, 130 °C	30	99.9	89/5	[29]
FMMWCNTs-CPA-SMTU-Pd (II) NPs		Pd (0.35 mol%) at r.t	15	98	80/7	[30]
Pd-(S)-methylhistidinate-MWCNT	Bromobenzene and phenylacethylene	Pd (1 mol%) in PEG, 50 °C	120	91	78/6	[31]

presence of this Pd-MWCNTs catalyst, both aryl bromides and aryl iodides could be coupled with different vinyl substrates in high yields (e.g., a yield of 95% was obtained for the reaction between iodobenzene and styrene). The catalyst obtained showed not only high catalytic activity, but also offered many practical advantages such as thermal stability and oxygen insensitivity. The catalyst Pd-MWCNTs (of heterogeneous nature) was reutilized for four cycles with consistent activity. Such material was recovered with ease in a simple and non-tedious manner. Furthermore, its easy preparation and excellent catalytic performance make it a good heterogeneous system, useful as an alternative to other heterogeneous palladium catalysts [32].

MWCNTs have also been functionalized with DNA to immobilize Pd nanoparticles for the Heck reaction [33]. The catalyst obtained (Pd-DNA-MWCNTs) allowed the regioselective catalysis between aryl iodides and 2,3-dihydrofuran in excellent yields (54%-83%) under mild conditions. Furthermore, the catalyst Pd-DNA-MWCNTs could be easily separated and reused nine times without losing its catalytic activity.

Several carbon nanomaterials (e.g., reduced graphene oxide (RGO), SWCNT, MWCNT, carbon nanofibers (CNF), graphene oxide (GO)) have been used as supports of palladium oxide (PdO) for Heck olefination of aryl halides [34]. With SWCNT and MWCNT, 72% and 63% reaction yields were obtained in 20 and 15 min at 150 and 120 °C, as well as, 78 and 65% yields were obtained in 1.15 and 1.30 h, respectively.

A hybrid catalyst $Pd_{50}Ni_{50}$/MWCNT was synthesized by the solvent reduction method of Pd NPs and Pd_Ni bimetallic NPs protected with polyvinylpyrrolidone and deposited onto MWCNT. The use of $Pd_{50}Ni_{50}$/MWCNTs in a Mizoroki–Heck strategy catalyzed the reaction between *p*-iodoanisole and vinylbenene producing the corresponding *p*-methoxystilbene with a yield of 99%. In the reaction studied, K_2CO_3 was used as base and tetrabutylammonium bromide (TBAB) as an additive [35].

Catalysts based on the combination of CNTs and cyclodextrin nanosponges (CDNS) have been used in Heck reactions [36]. The hybrid materials allowed the immobilization of Pd NPs. Different solvents, bases, temperatures, times and combinations of Pd NPs, CNTs and CDNS were tested, covering a range of yields between 85 and 94% in several C–C coupling reactions. The reusability of the hybrid catalysts were evaluated up to 6 times maintaining a yield of 83%.

2.1.2 Sonogashira Reaction

The Sonogashira-Hagihara reaction is based on the formation of a C–C bond between aryl or vinyl halides with terminal alkynes to form conjugated enynes and arylalkines. This reaction takes place using as catalyst Palladium (0), as cocatalyst a compound of copper (I), and an imine base (Scheme 3) [37]. It is also possible to carry out this reaction without the Cu(I) cocatalyst [38].

An example of the application of this reaction is the production of Tazorac for the treatment of acne, psoriasis and facial wrinkles [39], as well as in the preparation of

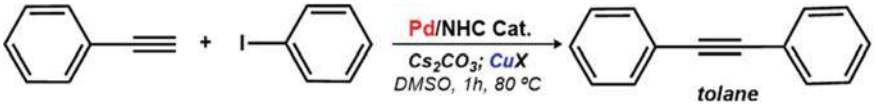

Scheme 3 Cross-coupling of aryl halides with terminal alkynes by Sonogashira reaction

Altinicline maleate, a drug which acts as an agonist at neural nicotinic acetylcholine receptors [40].

CNTs functionalized with polyaniline and decorated with Cu(I) for the Sonogashira reaction between phenyl iodide and 1-phenylethyne demonstrated excellent results and high reusability [41]. However, magnetic catalysts based on carbonaceous materials have shown the best benefits. In that sense, the CNTs surface have been first decorated with Fe NPs, and then functionalized with CPA for the subsequent grafting of *S*-methylisothiourea hemisulfate (SMTU). All these consecutive steps allowed the decoration with Pd NPs. The hybrid catalyst obtained was tested at different synthesis parameters obtaining high yields for a broad set of aryl halides and terminal alkynes [42].

Nanotubes have also been functionalized with drugs to immobilize Pd NPs for their subsequent use in the Sonogashira reactions. For example, Abbasi et al. [43] functionalized pramipexole on the surface of CNTs with that purpose. The authors tested different reaction parameters in order to find adequate conditions to maximize the catalytic power of the reaction between 1-phenylethyne and the aryl halide. Nazari et al. [44] also reported the immobilization of palladium nanoparticles onto CNTs previously decorated with the drug baclofen. In both cases, yields of 90% were reported when drugs were present in the catalyst structures. [43, 44].

Table 2 shows other examples of catalysts based on Pd or Cu(I) supported in CNTs for their use in the Sonogashira reaction.

A heterogeneous nanocatalyst based on Pd supported on MWCNTs functionalized with imino-pyridine was obtained by Adib et al. [45]. The synthetic procedure for the preparation of the nanosized catalyst (MWCNT- imino-pyridine/Pd) started with the oxidation of MWCNTs with HNO_3 with reflux for 12 h. The product (MWCNTs-COOH) was mixed with ethylenediamine (EDA) and imino-pyridine. The imino-pyridine functionalized MWCNTs and $PdCl_2$ were then mixed in acetonitrile and reduced with hydrazinium hydroxide to finally obtained the MWCNT- imino-pyridine/Pd. The ability of MWCNT-imino-pyridine/Pd to increase the rate of the Sonogashira reaction was tested, producing different derivatives of aryl alkynes and biaryls. Using pyrrolidine as base, *p*-iodoanisole reacted with 1-phenyletin under copper-free conditions. The catalyst could be reused up to 3 cycles, obtaining *p*-methoxytoluene quantitatively. The formation of the C–C bond between *p*-iodoanisole and 1-phenyletin was studied using water as solvent at 120 °C and pyrrolidine as base. No decrease in catalytic activity was observed after the catalyst was removed and used 6 consecutive times. The MWCNT-imino-pyridine/Pd catalyst proved to be commercially inexpensive since its synthesis was performed from accessible materials and convenient procedures.

Table 2 The use of CNTs as catalysts supports in Sonogashira reactions

Catalyst	Reactants	Reaction conditions	Time (min)	Yield (%)	Reusability (%/cycle)	Ref
pramipexole–MWCNTs/Pd	4-methylbromobenzene and phenylacetylene	Pd (0.002 mol%) in DMF, 80 °C	300	90	98/6	[43]
FMMWCNTs-CPA-SMTU-Pd (II) NPs	Iodobenzene and phenylacetylene	Pd (0.58 mol%) in Et_3N, 80 °C	17	98	97/5	[42]
Cu(I)-PANI-MWCNT		Cu(I) (10 mol%) in DMF, 135 °C	120	96	90/6	[41]
baclofen-MWCNTs-Pd		Pd (0.2 mol%) in DMF, 100 °C	300	90	98/5	[44]
MWCNTs-imino-pyridine-Pd		Pd (0.5 mol%) in DMF, 120 °C	30	98	–	[45]

CNTs-cyclodextrin hybrids were used to anchor metallic palladium nanoparticles (Pd@CDNS-CNT). This material was used in Sonogashira coupling using water as the solvent and moderate conditions [36]. The cyclodextrin nanosponges, i.e., CDNS, contributed to the catalysis by encapsulating the organic reagents within its hydrophobic cavitiy and therefore favoring the contact of the reagent with the catalytically active metallic palladium nanoparticles. Furthermore, the hydrophilic nature of the CDNS that is due to the exposure of OH groups of the sugars towards the outer shell of the cyclodextrin, allowed the chemical transformation to occur in H_2O as solvent. The catalytic activity of this composite was then compared to other known catalysts, including Pd@CDNS, and Pd@CNT, which confirmed the higher catalytic activity of the Pd@CDNS-CNT, thus suggesting a synergy between CDNS and CNT.

2.1.3 Suzuki–Miyaura Reaction

The Suzuki–Miyaura coupling consists in the reaction between an organic borane and an organic halide or tiflate, in basic medium. The chemical nature of the borane may be an aryl, alkynyl, and vinyl. This reaction is catalyzed by metals, typically Pd (Scheme 4) [46].

Suzuki–Miyaura coupling allows to form carbon–carbon simple bonds and hence produce conjugated systems. The use of organoboron brings not only a notable selectivity but also stability in this transformation. Outstandingly, this procedure is amenable to large scales since it is relatively cheap, thus allowing the preparation of a large variety of molecules relevant for multiple applications [47].

To improve the catalytic efficiencies of the Suzuki–Miyaura reactions and enhance the immobilization of Pd NPs, CNTs have been functionalized with different organic moieties, e.g., diethyltriamine [48], isoniazid [49] and thiol groups [50], which have allowed to obtain yields of 99%.

The synthesis of a catalyst for the Suzuki–Miyaura reaction based on palladium anchored at the surface of N-doped CNTs previously obtained from CVD has been reported [51]. The efficiency of the catalyst was tested with various aryl harulosides, solvents, bases, temperatures and times. It was compared with undoped nanotubes and it obtained a lower performance when compared the doped ones. Different preparation methodologies of immobilization of Pd NPs on CNTs have been compared,

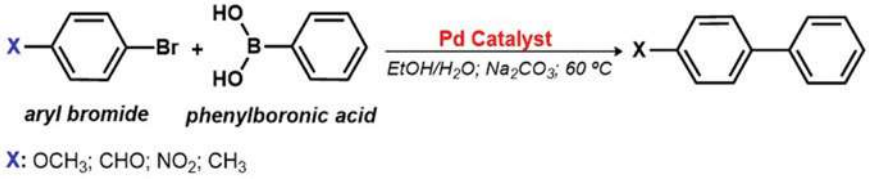

Scheme 4 The need of a palladium catalyst in Suzuki–Miyaura reaction

as well as the activity and selectivity of the catalyst obtained and the influence of CNTs used as supports [52]. The authors found that MWCNTs had the optimum performance above the SWCNTs, due to its higher catalytic activity and selectivity during the various cycles of use in the reaction and because a larger amount of NPs immobilized per unit area in their structure.

The CNTs decorated with bimetallic systems in the form of core–shell have been used in the Suzuki–Miyaura reaction. For example, Nan et al. [47] obtained core–shell Ni@Pd nanoparticles by a high-temperature aqueous phase process. By varying the initial masses of both metals, core–shell NPs with different compositions were obtained. These NPs were immobilized on CNTs previously functionalized with mercaptopropyl groups to catalyze the carbonylative reactions. Other examples of the use of CNTs as supports of Pd are presented in Table 3 with a direct application Suzuki–Miyaura reactions.

Under mild conditions and using green solvents, the reaction between a wide range of aryl halides and phenylboronic acid was tested with a complex catalyst formed by Pd and methyl histidinate grafted on the surface of a MWCNT (Pd-(S)-methyl histidinate@MWCNT) [31]. After using this catalyst 6 times, no significant difference was observed in its catalytic activity proving the potentialities of the Pd-(S)-methylhistidinate@MWCNTs for use in the chemical industry.

Veisi et al. [56] reported the synthesis of a recyclable catalyst based on the immobilization of Pd on biguanide(metformine)-functionalized SWCNTs (SWCNT-Met/Pd^{2+}). A series of biphenyl compounds were synthesized through the Suzuki–Miyaura reaction using SWCNT-Met/Pd^{2+} as the catalyst and the yields of the products were in the range from 80 to 95%. The catalyst could be readily recovered and reused for at least 5 consecutive cycles without significant loss of its catalytic activity.

2.2 Hydrogenation

Hydrogenation certainly is an ubiquitous chemical transformation, which is very utilized in industrial applications [57]. Hydrogenation reactions may proceed using two different strategies, namely (i) the transfer hydrogenation (TH) and (ii) the direct hydrogenation, where gaseous H_2 is put in contact with the reaction medium [58]. Hydrogenation is a type of chemical (redox) reaction involving the addition of hydrogen (H_2) to another compound (Scheme 5). The typical substrates of this reaction are alkenes [59], alkynes [60], ketones [61] and nitriles [62].

A Fe-based catalyst was used for the Fischer–Tropsch synthesis (FTS) to obtain directly low-molecular-weight olefins from syngas [63]. This composite showed a high selectivity of light olefins (45%) but low stability was observed due to the agglomeration of Fe NPs. An alternative material based on Fe NPs supported on CNTs was then also tested to overcome this drawback, obtaining 42% of selectivity and despicable agglomeration. From these results it was concluded that the nanotube walls played a protective role for Fe NPs and increased both the stability and the activity of the iron catalyst, even in harsh conditions.

Table 3 CNTs as catalysts supports in Suzuki–Miyaura reactions

Catalyst	Reactants	Reaction conditions	Time (min)	Yield (%)	Reusability (%/cycle)	Ref
Isoniazide-MWCNTs/Pd	4-metylbromobenzene and phenylboronic acid	Pd (0.2 mol%) in $EtOH/H_2O$, 60 °C	120	96	87/5	[49]
MWCNTs-CC-SH/Pd		Pd (0.2 mol%) in $EtOH/H_2O$, 80 °C	120	96	90/4	[53]
CNT-DANTA-PDADAMAC	4-nitroiodobenzene and 4-methoxyphenylboronic acid	Pd (1.2 mol%) in $EtOH/H_2O$, r.t	1440	0	–	[54]
PdCNT		Pd (1.2 mol%) in $EtOH/H_2O$, r.t	240	98	97/5	
Pd/CNTs	Iodobenzene and phenylboronic acid	Pd (0.02 mol%) in $EtOH/H_2O$, 60 °C	20	83	84/4	[29]
Pd/N-CNTs		Pd (0.02 mol%) in $EtOH/H_2O$, 60 °C	20	89	93/5	
Pd/N-CNTs-1%		Pd (0.02 mol%) in $EtOH/H_2O$, 60 °C	20	97	92/7	
FMMWCNTs-CPA-SMTU-Pd (II) NPs		Pd (0.55 mol%), r.t	10	98	83/7	[42]
SWCNT-DETA-Pd		Pd (0.2 mol%) in $EtOH/H_2O$, 60 °C	22	98	80/7	[48]
Ni@Pd/CNT		Pd (2 mol%) in methoxybenzene, 70 °C	30	98	96/10	[47]

(continued)

Table 3 (continued)

Catalyst	Reactants	Reaction conditions	Time (min)	Yield (%)	Reusability (%/cycle)	Ref
Pt–S-MWNT	4-iodomethoxybenzene and 4-methylphenylboronic acid	Pt (0.35 mol%) in THF, 70 °C	1440	99	82/12	[50]
Pd/PdO/WCNTs	4-methoxybromobenzene and phenylboronic acid	Pd (0.1 mol%) in H_2O, 90 °C	240	99	83/10	[55]
Pd-(S)-methylhistidinate-MWCNT	Bromobenzene and phenylboronic acid	Pd (0.0022 mol%) in EtOH/H_2O, r.t	60	96	–	[31]

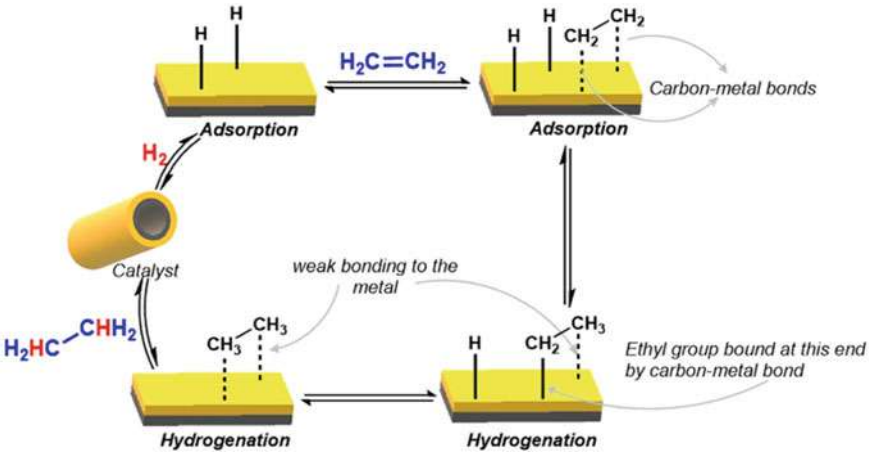

Scheme 5 Mechanism of hydrogenation in a solid catalyst surface

Cubic FeN NPs encapsulated inside CNTs channels have been used for CO hydrogenation via a FTS procedure [64]. The catalyst exhibited a 5–7 times higher activity than a reduced Fe catalyst, as well as a FeN catalyst grafted on SiO_2. The enhanced catalytic activity was related to the improvement of the resistance of FeN against oxidation when it was supported on CNTs.

Iron–potassium nanocatalysts supported on single- and multi-walled CNTs (i.e., FeK/SWNTs and FeK/MWNT) have been used for CO_2 hydrogenation to olefins. In these reactions, FeK/SWNTs and FeK/MWNTs catalysts showed a selectivity of 62.3% and 52.4%, respectively. FeK/MWNTs were found to be more selective to light olefins (C2-C4, 30.7%) and FeK/SWNTs, to heavy olefins (C5, 39.8%) [65].

Kangvansura et al. [66] synthesized different Fe-based catalysts incorporating potassium and manganese to N-doped nanotubes (e.g., Fe-NCNT; K-Fe-NCNT; Mn-Fe-NCNT; K-Mn-Fe-NCNT). The different catalysts obtained were used for CO_2 hydrogenation. The presence of *n*-alkanes was found in the products indicating the occurrence of the FTS reaction in 60 h. Ethanol production was also observed with K-Fe-NCNT and K-Mn-Fe-NCNT catalysts, where K appears to be a structural promoter in the hydrogenation of CO_2 mainly from alkenes and ethanol.

For the hydrogenation of nitroarenes a nanohybrid of CNTs decorated with cyclodextrin and imidazolium salt has been synthesized as support of Pd NPs [67]. This resulting hybrid composite exhibited an enhanced selectivity and catalytic activity towards nitro groups. Silica-decorated CNTs ensured an improved dispersion of Pd NPs and led smaller particle size. Furthermore, Pt and Pd NPs were introduced in modified MWCNT via co-impregnation method for hydrogenation of furfuraldehyde in liquid phase using ethylic alcohol as a solvent [68]. The obtaining of bimetallic compounds with these metals was also reported by adding different transition metals (e.g., Cr, Mn, Fe, Co and Ni) and the efficiency in the process of hydrogenation of furfural was compared. A synergistic effect was observed from the

increase in the rate of the reaction and perdurability when using the bimetallic catalysts. For example, the Pt-Fe/MWNT catalyst showed higher conversion to furfuryl alcohol and the Pd–Ni/MWNT to tetrahydrofurfuryl alcohol with a yield of 87.4% and 83.3%, respectively.

Asymmetric hydrogenation reactions using chirally modified Pt NPs supported on CNTs have been reported [69]. The activity and enantioselectivity of the hybrid nanocatalyst obtained were improved for the asymmetric hydrogenation of α-ketoesters using cinchonidine (CD) as the chiral converter, which was associated with the ultrahigh enrichment of the CD and reactants inside the channels of the CNTs.

Bimetallic Ni-ZrO_2 catalysts were obtained at the surface of CNT. The modification of CNTs was achieved using a repetitive impregnation and co-impregnation approach. Both materials showed catalytic activity in CO_2 methanization. The catalyst synthesized by the sequential impregnation method was more active and selective to CH_4 than the catalyst prepared by co-impregnation. This catalyst was based on core_shell structures (i.e., NiO NPs covered with ZrO_2) that grew up on CNTs, preventing the access of reactants to the nucleus and interface of Ni and Ni-ZrO_2. Furthermore, TEM analysis of the catalyst prepared by sequential impregnation showed that the NiO nanoparticles were deposited either on the surface or next to the ZrO_2 nanoparticles, increasing the Ni–ZrO_2 interface thus improving the catalytic performance. This arrangement of Ni and ZrO_2 on the surface of the CNTs was responsible for the better catalytic performance shown by the catalyst prepared by sequential impregnation. In this case, by increasing the proportion of these Ni–O–Zr exposed species, the interaction between hydrogen atoms (dissociated on Ni surface) and CO_2 molecule (activated by ZrO_2) could be improved, increasing then the reaction rate and selectivity towards CH_4 [70].

The doping of CNTs with heteroatoms is a promising strategy to tune their catalytic activity. Certainly, Cu catalysts decorating B-doped CNT (Cu/xB-CNT) have been prepared, aiming the reduction of dimethyl oxalate (DMO) with H_2 to yield ethanol [71]. B-doping allowed to introduce acid sites at the surface and was also shown to favor the anchoring of Cu species (both Cu^0 and Cu^+). It is worth to highlight that such Cu/xB-CNT catalyst exhibited 100% yield for the transformation of DMO with 78.1% of the selectivity for the formation of ethanol. Moreover, the selectivity of the B-doped catalyst was 1.7 times higher than that of the non-doped catalyst, thus demonstrating the role of doping in the catalytic activity.

The hydrogenation of adiponitrile (ADNA) was carried out with catalysts prepared from functionalized MWCNT decorated with Ni. Such catalyst had functional groups including NH_2-, COOH-, OH- at the surface of the MWCNTs. These groups provide nucleation sites for the further growth of Ni nanoparticles. The presence of nitrogen was reported to increase the Lewis basicity of the support, which increased the production of the primary amine 6-aminohexanonitrile (ACN) and 1,6-hexanediamine (HDA). Interestingly, the presence of the basic ionic liquid [Bmim]OH can change the selectivity by decreasing the nucleophilic addition of the primary amine to the α-carbon of the aldimine by stabilizing the -NH_2 groups in

the intermediates. Overall, the optimized Ni/N-MWCNTs exhibited a conversion of 95% to transform ADNA into ACN and HDA in the presence of [Bmim]OH [72].

MWNTs may also be used as a support for Fe_3O_4 NPs when prepared using a coprecipitation method in the presence of a dendrimer of poly-citric acid (PC). Such composite allowed the further deposition of Pt(II) and was employed in five cycles for the selective reduction of nitro and nitrile derivatives in the presence of $NaBH_4$. The magnetic properties of this catalyst offer clear advantages for its simple separation employing a magnet [73].

In a different study, CNTs were combined with poly (N-isopropylacrylamide) (PNIPAM), which then permitted the inclusion of Pd to yield a nanocatalyst active for the selective hydrogenation of cinnamaldehyde (CAL). This material presented a wettability that was dependent of temperature. At low temperatures (e.g., 25 °C) the surface of the composite is hydrophilic, which increases the dispersion of Pd nanoparticles; however, at higher temperatures (e.g., 80 °C) the surface is hydrophobic, thus allowing the adsorption of CAL, which improved the catalytic activity and kept the selectivity for the formation to cinnamyl alcohol (COL), as compared to a similar catalyst without PNIPAM [74].

2.3 Oxidation of Alcohols

Currently, oxidation reactions using transition metals or sulfoxides as stoichiometric oxidants are widely employed, although the large amount of by-products thereby formed. Typical oxidants include species (e.g., $BaMnO_4$, MnO_2, RuO_4, Ag_2CO_3) and organic molecules sensitive to moisture, such as carbodiimides [75, 76].

Recent trends for aerobic oxidations employing catalysts based on transition metals include Rh, Ir, Pt, Au, Fe, Cu, Pd or Ru, in addition to O_2 and H_2O_2 as oxidants. [77]. The use of O_2 for stoichiometric oxidations is particularly appealing since it is widely available and yield either H_2O or H_2O_2 as benign by-products [78].

Different metallic NPs (e.g., Au, Pd, Ni, Sn, Ag, Ru, Pt) have been used as catalysts for the oxidation reactions of different alcohol structures (i.e., benzyl alcohol, 1-phenyl alcohol, ethanol, 2-heptanol, isopropyl alcohol, 1-butanol, 2-methyl-1-propanol, 2-butanol, 2-methyl-2-propanol) [79]. Furthermore, bimetallic and ternary systems coupled to the CNTs surfaces or immobilized on an organic compound, previously grafted to the nanotube, have been obtained with the same purpose [80, 81]. For example, Kaboudin et al. [82] reported the oxidation of different types of alcohols using a new catalyst synthesized from MWCNTs decorated with Fe compounds to confer its magnetic properties and facilitate the separation of the catalyst. The magnetic MWCNT were then functionalized with pyridine groups to immobilize Au NPs. The oxidation reaction catalyzed by AuNPs@MWCNTs with K_2CO_3 as a base was selective to benzoic acid. Interestingly, no reaction occurred under an inert atmosphere of N_2 with both benzyl alcohol and 1-phenyl ethanol. From this result, it was suggested that the oxidation reaction needs molecular oxygen as an activator.

CNTs were also decorated with Au NPs for the effective and selective oxidation of alcohols to acids or aldehydes under aerobic conditions. Firstly, the CNTs were functionalized with a water-soluble polymer PDADMAC and then Au NPs were immobilized on the grafted material. More than 99% of conversion was obtained in 3 h. The primary alcohols reached acid and the secondary alcohols reached aldehydes, allowing to propose a mechanism to obtain acids from alcohols with gold nanoparticles [83].

Ionic liquids were also immobilized on MWCNTs decorated with zinc polyoxometalate. The hybrid material obtained was used given its catalytic activity for the oxidation of alcohols with hydrogen peroxide. The carboxylate MWCNTs (MWCNTs-COOH) reacted with $SOCl_2$ to form MWCNTs-Cl, then with 1-(3-aminopropyl) imidazole obtaining MWCNTs-API, subsequently functionalized with 1-bromobutane to produce MWCNTs-APIB. The imidazolium electrostatically interacted with the ZnPOM ($(n\text{-}C_4H_9)_{4\,N})_5[PZnMo_2W_9O_{39}]$) producing ZnPOM@APIB-MWCNT. The oxidation of benzyl alcohol with this catalyst was tested and a yield of 95% was obtained in 4 h [84].

2.3.1 Electro and Photo-Oxidation of Alcohols

Both the high price and the scarcity of noble metals has limited their incorporation in the anode and the cathode in ethanol fuel cells at a large scale, thus hindering its commercialization [85]. In that sense, a hydrothermal procedure has been used for the decoration of CNTs using glucose and urea as starting materials (Scheme 6).

The functionalized CNTs have been widely reported for the electro- and photo-oxidation of alcohols (Fig. 3).

Such hydrothermal procedure permits to deposit very small films of N-doped carbon layers. Hence, controlling the amount of glucose and urea, the amount of N-doping may be as high as 1.7% in weight. Interestingly, N-doped CNT with Pd nanoparticles supported at their surface presented an enhanced electrochemical activity towards EtOH oxidation, as compared to unmodified CNT [86].

Scheme 6 Hydrothermal carbonization for nitrogen doping of CNTs

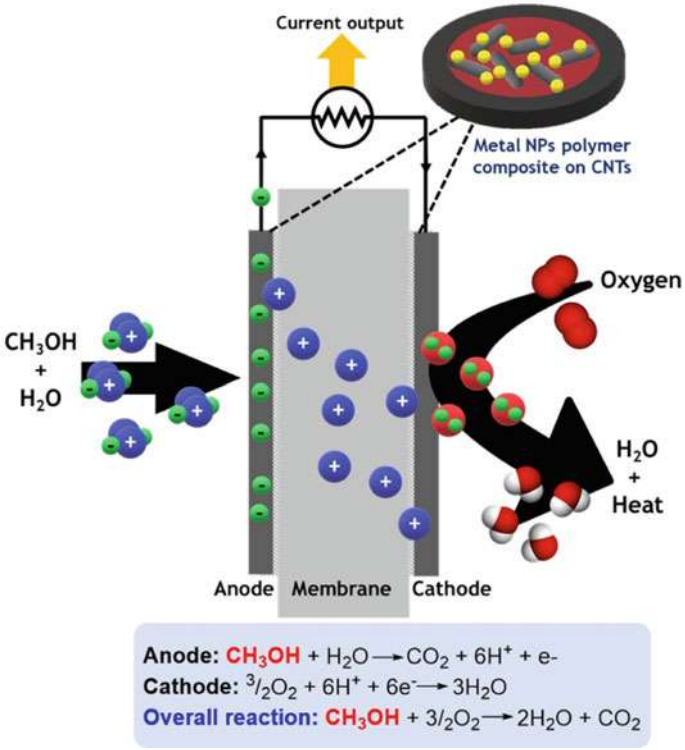

Fig. 3 Use of CNTs fuel cells for electro-oxidation of ethanol

Hiltrop et al. [87] reported the use of Pd in the anode of an EtOH fuel cell, by taking advantage of the interaction between Pd nanoparticles and N-doped CNTs. The performance of this electrocatalyst decreased over time, but remained for 80 h.

Several catalysts formed by two metals (Pt-Ru and Pt–Mo) were synthesized by chemical reduction; metal-carbonyls were the precursors and were prepared in-situ via the bubbling of carbon monoxide. The highest activity was observed in both cases for equal weight amounts of both metals. The ratio of current densities of Pt-Ru-SWCNT/Pt-SWCNT was at least 7, while the ration of current densities of Pt-Ru-SWCNT/Pt–Mo-SWCNT was at least 3. Moreover, the onset potential of the oxidation of ethanol shifted 200 mV towards negative values for the Pt-Ru-SWCNT, indicating the outstanding electrocatalytic power of this composite [88].

Additionally, ternary catalysts based on the combination of Pd-Au-P at the surface of CNT have been prepared for ethanol electrooxidation (EOR). This catalyst took advantage from the presence of an ionic liquid derived from perylene-3,4,9,10-tetracarboxylic acid, which enabled the uniform distribution of ultra-small Pd_4AuP nanoparticles. The performance of such catalyst was very high, and much more stable than other catalysts prepared for the EOR under alkaline conditions, which was attributed to a synergy between all components in the composite [89].

MWCNT modified with multiple hydroxyl groups and a nanobelt of carbon nitride was obtained by using a solvothermal approach and ultrasound. This allowed the simultaneous hydrogen evolution reaction and the degradation of tetracycline hydrochloride. These photocatalysts showed small fluorescence, high photocurrent density, and small interfacial resistance, as measured by electrochemical impedance spectroscopy. The best composition of the catalyst was 0.005% in weight of carbon nitride, located at the surface of hydroxylated MWCNT, which yielded a rate of production of hydrogen equal to 176 μmol/g·h [90].

A different approach was obtained by depositing nanosized Au at the surface of vanadium oxide. This composite was especially efficient for the degradation via photocatalysis of 2-naphtol and benzyl alcohol in the presence of H_2O_2. Interestingly, the photocatalytic transformation of 2-naphtol was dependent on the support. This work showed that the surface plasmon resonance associated to nanosized Au, anchored at the surface of vanadium oxide played a key role to increase the photocatalytic activity of this material. The transformation of both 2-naphtol and benzyl alcohol was believed to occur through the generation of a superoxide radical intermediate [91].

3 Carbon Nanotubes as Catalyst

In the previous section, several examples of organic reactions catalyzed by catalytically active species, mainly NPs, supported on CNTs were discussed. This section will also analyze the role of the CNTs as catalysts, not only as supports. Reactions such as oxidative dehydrogenations (e.g., phenylethane, ethyl lactate and ethanol oxidative dehydrogenations), the catalytic conversion of n-butanol, as well as selective oxidations will be addressed. Furthermore, additional depictions on the applications of CNTs doped with nitrogen, will also be described to demonstrate the effect of doping on the activity of the materials obtained.

3.1 Oxidative Dehydrogenation Reactions

3.1.1 Ethylbenzene Oxidative Dehydrogenation

The direct dehydrogenation of ethylbenzene (EB) to yield vinylbenzene is an essential transformation in the petrochemical industry. Nanocarbon materials, such as CNTs [92], graphene [93], mesoporous carbon [71], nanodiamonds [94], and metal–organic framework (MOF)-derived nanocarbon [95] are potential alternatives to conventional metal-based catalysts for the dehydrogenation of alkanes to meet the strict requirements of renewable and sustainable chemistry.

There are structural characteristics necessary to maintain stable redox catalytic activity of carbon compounds: surface oxygenated functional groups, large surface

area, and extensive ordered graphitic structure [96]. The oxygen groups (ketones with high of nucleophilicity) are the active sites for the reaction of the C-H bond that is used for oxidative dehydrogenation [97]. CNTs are one of the most economical carbon nanostructures to synthesize and use in catalytic reactions [98].

Liu et al. applied an analysis of reaction rates, active site titration, isotopic analysis and experiments varying the temperature to perform surface reactions and hence show the composition of the products of oxidative dehydrogenation reactions of alkanes catalyzed by nanometric carbon. The authors found that ketone functionalities on nanometric carbon work as active sites for oxidative dehydrogenation of alkanes (ODH). When performing the kinetic and isotopic analyses of the reactions, it was observed that the catalytic reaction mechanism involves at least five steps that include:

(1) dissociative chemical adsorption of EB
(2) hydrogen subtraction
(3) formation and desorption of reaction products
(4) dissociative adsorption of oxygen
(5) reoxidation of active sites.

Steps 2, 3, and 5 are kinetically combined and the subtraction of H (reduction of the nanocatalysts) is a determining step of the rate in the reaction conditions (Scheme 7). The proposed catalytic mechanism is different from the typical Mars-van-Krevelen or Langmuir–Hinshelwood [99] process thanks to the lack of crosslinked oxygen in the original structure of nanometric carbon catalysts [92].

Shi et al. modified CNTs with carbon nitrides (CN) for phenylethane dehydrogenation. The CN layers were produced in-situ and after heat treatment were spread

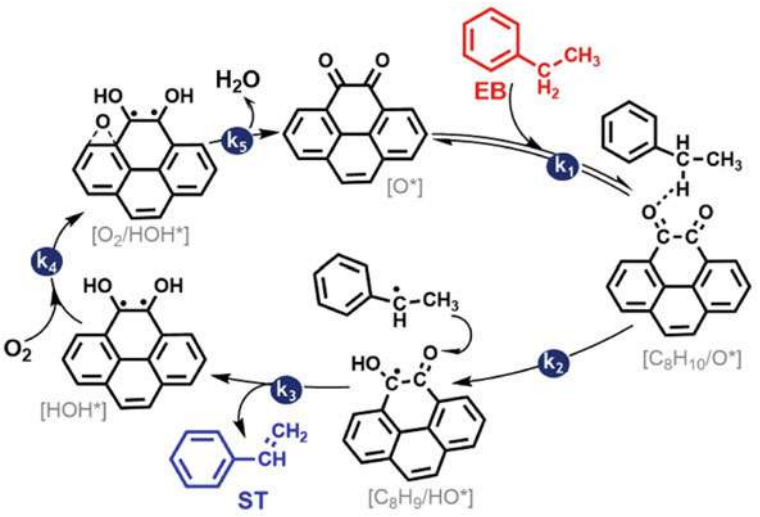

Scheme 7 Pathway of alkane oxidative dehydrogenation reactions catalyzed by nanocarbon materials. A representative portion of the nanometric carbon skeleton is shown here as four benzene rings

evenly over the oxidized CNT surface. Such transformation increased the surface area and the basicity of the nanometric carbon. CN sheets with a large number of electrons certainly increased the nucleophilicity and hence the activation capacity of the C-H bond of nanometric carbon catalysts. The nanometric carbon modified with CN showed a higher rate of its own reaction than the unmodified ones [100].

Tian et al. synthesized polydopamine-decorated CNT catalysts by a new synthetic route using in situ polymerization followed by heating. Combined metal-free catalysts have been found to show higher activity as compared to undoped or N-doped CNT compounds in phenylethane dehydrogenation reactions. This high activity could be due to the movement of electrons from the polydopamine to the nanometric carbon matrix [101].

Nanodiamonds codoped with nitrogen and oxygen and combined with CNT were reported recently. The authors synthesized a novel, metal-free nanocatalyst with a high performance and a high reaction rate for the synthesis of vinylbenzene in a clean and simple way through the direct dehydrogenation of phenylethane in the presence of steam and without oxidants. The hybrid N–O-ND-CNT-d catalyst allowed to obtain vinylbenzene with a yield of 16.8% and a selectivity of 98.7%. The rate of production of vinylbenzene was 5.2 mmol/g·h. The compound N–O-ND-CNT-d presented a stable reaction rate 4.7 times higher compared to the original oxidized CNTs [102].

3.1.2 Ethyl Lactate Oxidative Dehydrogenation

Pyruvic acid and pyruvate derivatives are important intermediates for the preparation at industrial scale of additives for pharmaceuticals, agricultural products, food, perfumery and cosmetics [103]. Pyruvic acid is normally synthesized by decarboxylation of 2,3-dihydroxybutanedioic acid. The main drawback of this route is the need for an excess of $KHSO_4$ as a dehydration agent [104]. Oxidative dehydrogenation (ODH) is a compelling route to replace this dehydrative decarboxylation approach which yields both lactic acid and ester compounds. An example of this is the selective catalytic transformation of ethyl lactate (EL) into ethyl pyruvate (EP) [105]. The ODH procedure is very promising because of its friendliness to the environment (Scheme 8) [106].

Wang et al. reported the first use of MWCNTs which had been oxidized previously, as interesting catalysts for the formation of EP using the ODH reaction. The

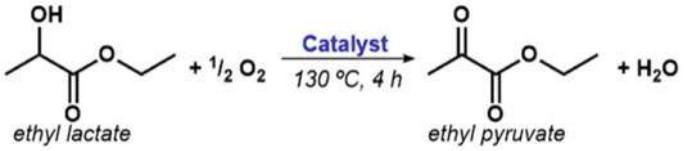

Scheme 8 Catalytic reaction of ethyl lactate in ethyl pyruvate

authors showed that nanometric carbon plays a role in the activation of O–H bonds. Chemical titration provided compelling evidence that ketone carbonyl groups within the nanometric carbon were the actual active sites to account for this transformation. [107].

Moreover, ODH reactions performed on pyruvate as substrate currently uses metal-based catalysts, such as mixed oxides (MoO_3) and liquid phase heteroatom-doped Pd–C [108]. Unfortunately, the use of metal-based catalysts has clear drawbacks including their scarcity and the associated environmental problems related to their toxicity. Therefore, the development of new nanometric carbon catalysts is essential, since carbon nanomaterials have proven their efficiency for a wide scope of C-H activation reactions [109] and the activation of O–H bonds [110].

3.1.3 Methanol Oxidative Dehydrogenation

The transformation of methanol to formaldehyde (FA) or the dehydration of methanol to yield dimethyl ether (DME) is also a highly important industrial process [111–114]. The most commonly used catalysts in the direct dehydrogenation of methanol to obtain FA are noble metals such as silver [115], platinum [116], Fe-MoO_x [117]. However, undesired observations have been made, including a low recyclability and stability of the catalyst, risks of explosion, safety issues, and the excessive oxidation of the precursor [118].

The dehydrogenation of alkanes has been long studied, and hence it is currently a model reaction in order to study the catalytic reactions occurring at the surface of carbon nanostructures (Scheme 9) [97].

The dehydrogenation of methanol to FA is more complex than the dehydrogenation of other alkanes because it involves breaking both the C-H bond and the O–H bond, generating multiple and different reaction routes [119].

Yan et al. have prepared an oxidized derivative of CNTs (o-CNTs) and have employed it for the conversion of methanol in the presence of oxygen. A conversion of 60% was observed under mild conditions, producing 65% of DME and 30% of FA. The process took 150 h, which was in the same order of actual industrial catalysts. As already discussed in this chapter, functional group titration suggested that carboxyl functional groups were the active sites to form DME [118].

3.1.4 Catalytic Conversion of n-butanol

The use of biomass as renewable energy source has prompted the scientific community to find novel conversion paths, and hence to develop innovative catalysts, aiming at protecting the environment [120]; n-Butanol (nB) may be obtained in large amounts by the fermentation of biomass; hence, it is an important chemical that may be converted into aldehydes, acids, alkenes and so on (Scheme 10) [121].

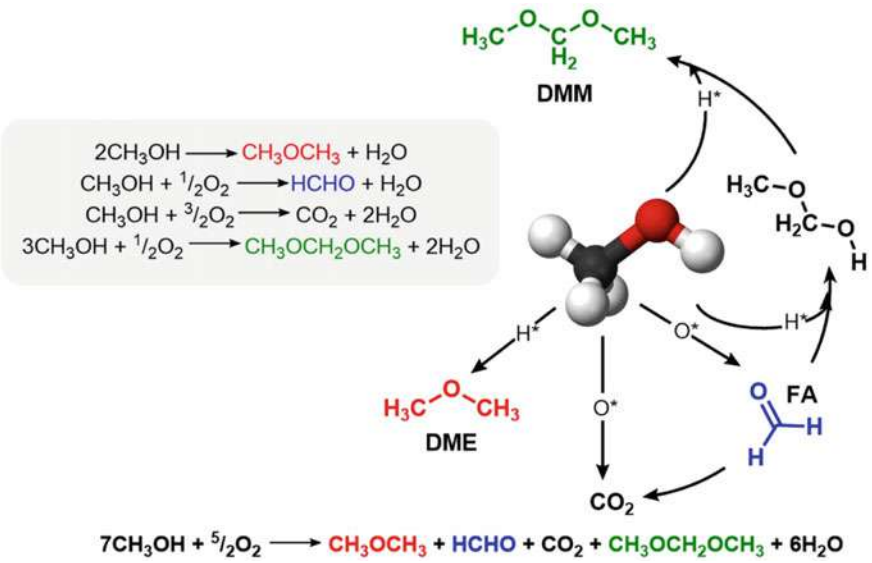

Scheme 9 Methanol dehydrogenation catalyzed by CNTs (O* and H* represent the redox sites and acid sites, respectively)

The transformation of nB has been undertaken with zeolites and with polyacidic compounds [122], including also noble metals such as gold, silver and ruthenium [123]; or systems containing molybdenum, vanadium and iron oxides [124].

In this context, the emergence in the use of nanocarbon materials is highly appealing, as an alternative to catalysts using metals. Carbonaceous materials offer a large flexibility to tune its redox properties, and its acid/base properties; moreover, these are compatible with organic compounds and are very abundant [125].

Li et al. [126] have presented a complete study on the application of MWCNTs for the transformation of nB. The ODH approach described before, and the dehydration of n-butanol at the surface of MWCNTs has shown impressive activity, beyond 50% conversion, and a stability around 120 h at mild industrial conditions, i.e., below 330 ºC. As discussed so far, COOH groups have been identified as the active sites for dehydration reactions, while the redox reactions occurring at these MWCNTs has been attributed to ketones. An interesting feature noted in this work is the fact that the ODH activity is related to the graphitization of the MWCNTs.

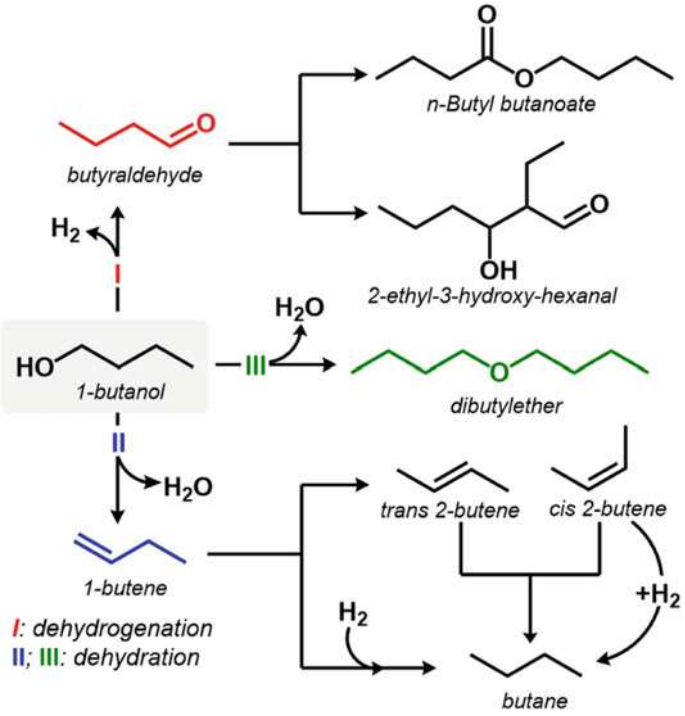

Scheme 10 Dehydration and dehydrogenation routes for catalytic conversion of n-butanol

3.2 Nitrogen-Doped Carbon Nanotubes Catalysts

The need for metal-free catalysis is growing as an imperative nowadays. Many processes have been catalyzed avoiding the use of metals, including alkane dehydrogenation [127], the reduction of nitrobenzene [128], the transesterification reaction [129], and the selective oxidation [130], owing to their high specific surface areas, versatile chemical properties, and environmental benignity. The structural characteristics of non-metal doped carbon nanostructures are presented in Fig. 4.

The doping of carbon nanostructures with N atoms introduces basic sites to the material, which brings interesting catalytic properties. In reference [131] a work is reported where carbon nanostructures doped with N are able to catalyze the hydrochlorination of acetylene. This material was obtained from polydiacetylenes (PDA) and SiC. The catalytic activity in this case has been attributed to the similar atomic radius between N and C, which enables an easier incorporation within the C matrix. This certainly increases the electron-donating properties of the carbonaceous surface and hence provides more activity for catalysis [132].

The following section presents more examples of N-CNTs used as catalysts for oxidation reactions of H_2S, organic amines and aryl alkanes, as well as the role of these materials in the hydrogenation of nitroarenes.

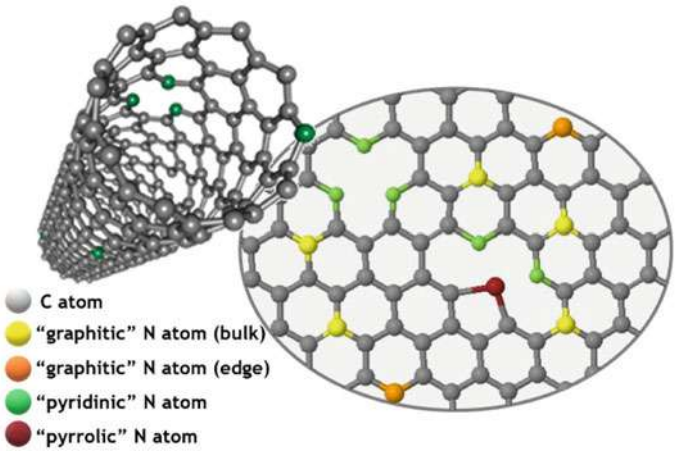

Fig. 4 CNTs doped with nitrogen

3.2.1 H_2S Catalytis Oxidation

The elimination of H_2S from natural gas, crude oil and coal is one of the most significant research lines in environmental catalysis. This compound is a toxic and putrid, responsible for the deterioration of pipes and the poisoning of catalysts [133].

The Claus process is widely employed to transform H_2S into S_n, via the following reaction: $\left(2H_2S + SO_2 \rightarrow \frac{3}{n}S_n + 2H_2O\right)$. Unfortunately, this reaction does not occur till completion, and hence additional procedures need to be implemented to remove H_2S traces (Scheme 11) [134].

N-doped carbon has shown amazing properties for the oxidation of H_2S. Such desulfurization reaction may be carried out in non-continuous conditions at temperatures below 180 °C or in continuous conditions at temperatures above 180 °C [135]. Reference [136] reports on the use of N-containing mesoporous carbon, which enables the selective oxidation of hydrogen sulfide, at temperatures close to the environment. This report is excellent, yielding 2.77 g of S_n per gram of catalyst. In addition to, reference [137] also presents N-doped carbon materials, supported on β-SiC and α-Al_2O_3. This catalyst presented conversions beyond 97% and selectivity for sulfur above 70%, operating at 210 °C.

A cutting-edge study is shown in reference [138], where the N-doped carbon with mesoporous structure, and supported onto CNTs did not present an additional inert host. This strategy maximized the availability of catalytic sites to contact hydrogen sulfide and hence to promote its selective oxidation. This catalyst displayed an amazing activity, with a rate of formation of sulfur equal to 449 g of sulfur per kg of catalyst per hour; a competitive stability above 120 h and a sulfur selectivity of 81.6%. These incredible results have been attributed to an interconnected structure and to the availability of active N sites.

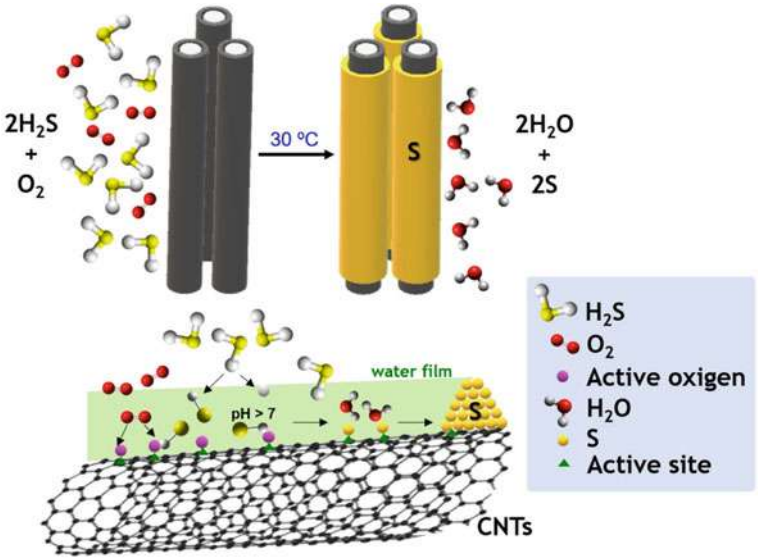

Scheme 11 Selective catalytic oxidation of H_2S

3.2.2 Benzylamine Oxidation

The modern pharmaceutical industry requires, among other compounds, the synthesis of organic imines using processes friendly to the environment [139]. A common manner to obtain organic imines involves the use of metallic catalysts for the coupling of organic amines, which has the drawbacks of a higher cost and pollution [140], besides, the presence of trace metals for pharmaceutical applications is intolerable [141], hence the need to find new catalysts to achieve this transformation.

Nanocarbon structures have also shown great potential to catalyze this transformation, as depicted in Scheme 12 [142].

As described before, the catalytic activity of carbon materials is effectively enhanced with the incorporation of heteroatoms to its structure. Such dopants provide additional functional groups that contribute to its catalytic activity [143]. Reference [144] describes an interesting approach, including the treatment of N-doped CNTs with O_3/H_2O, which introduces oxygen groups close to N atoms, to form groups resembling amides. Certainly, such amide-like moieties modify the reactivity of this

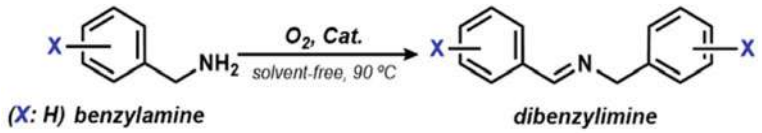

Scheme 12 Organic imine synthesis by catalytic benzylamine oxidation

catalyst towards the C-H activation, yielding an oxidative coupling of benzyl amine to produce an imine with 99% selectivity, under ambient conditions.

3.2.3 Aerobic Oxidation of Ethylbenzene

The oxidation of aryl-alkanes, for example toluene or cumene, to obtain the corresponding alcohols or ketones is currently a challenging transformation (Scheme 13).

Despite the fact that a large number of metal catalysts are available, the problems associated to them have been commented before in this Chapter. Nanocarbon structures offer also an alternative to carry out these transformations. Indeed, Luo et al. have shown that CNTs act as catalysts with outstanding activities for the aerobic oxidation of cumene and ethylbenzene. Certainly, this work shows a conversion for EB of 38.2 and 60.9% for AcPO [145].

As an alternative to dioxygen for the oxidation, tert-butyl hydroperoxide (TBHP) has also been reported as the oxidant for EB transformation, and N-doped CNTs as catalysts [146]. For example, N-doped sp^2 nanocarbon structures have been employed for EB oxidation with a threefold ration of TBHP. The catalytic activity in this case is supposed to be due to the hosting of reactive oxygen by the catalyst species during the oxidation reaction [147]. Moreover, reference [148] describes the pertinence of N-doped CNTs for EB oxidation, with dioxygen being the final oxidant. In this work, N-doping presented an unexpected feature, since it inhibited the catalytic activity, and providing a better catalytic efficiency (40% for EB and 72% for AcPO).

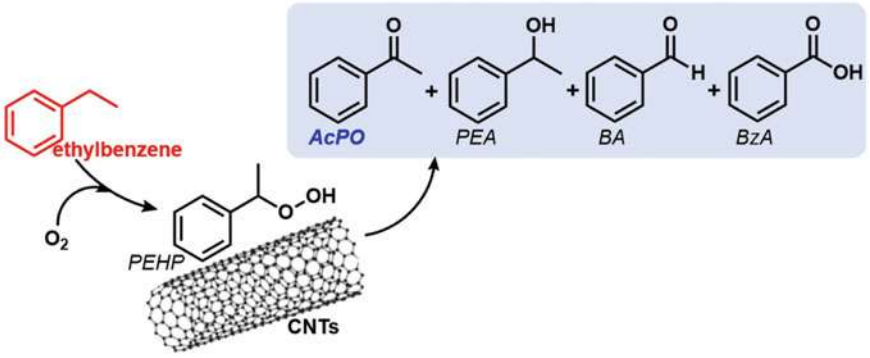

Scheme 13 Aerobic oxidation of ethylbenzene to AcPO (target product), 1-phenylethyl alcohol (PEA), 1-phenylethyl hydroperoxide (PEHP), benzaldehyde (BA) and benzoic acid (BzA)

3.2.4 Cyclohexene Allylic Oxidation

Carbon nanostructures doped with nitrogen have displayed an outstanding catalytic activity towards the allylic oxidation of cyclohexene, yielding with an amazing selectivity to 2-cyclohexene-1-none. Such impressive activity has been supposed to be due to the stabilization of peroxyl and cycloxyl radicals and the charge transfer to these radicals from N-CNTs, which is facilitated because of the sp^2 layers (Scheme 14) [149].

The effect of the solvent is highly important in this kind of reactions. Indeed, reference [150] describes special catalytic efficiency for the hydroxylation of benzene, which was catalyzed by graphene in water. This was due to the fact that the reaction products may be readily transferred to water, thus avoiding overoxidation. Another report on the influence of solvent in this reaction was provided by Cao et al. [151] in the specific case of α-pinene oxidation over CNTs. Though, a thorough comprehension of the effect of the solvent in the oxidation of alkenes is not complete yet, since the amount of solvents tested has been still very limited. The effect of solvent has also been studied in the allylic oxidation of cyclohexene, using N-doped CNTs as catalyst [152]. A number of factors including polarity, basicity and viscosity have been shown to have influence on the reaction outcome.

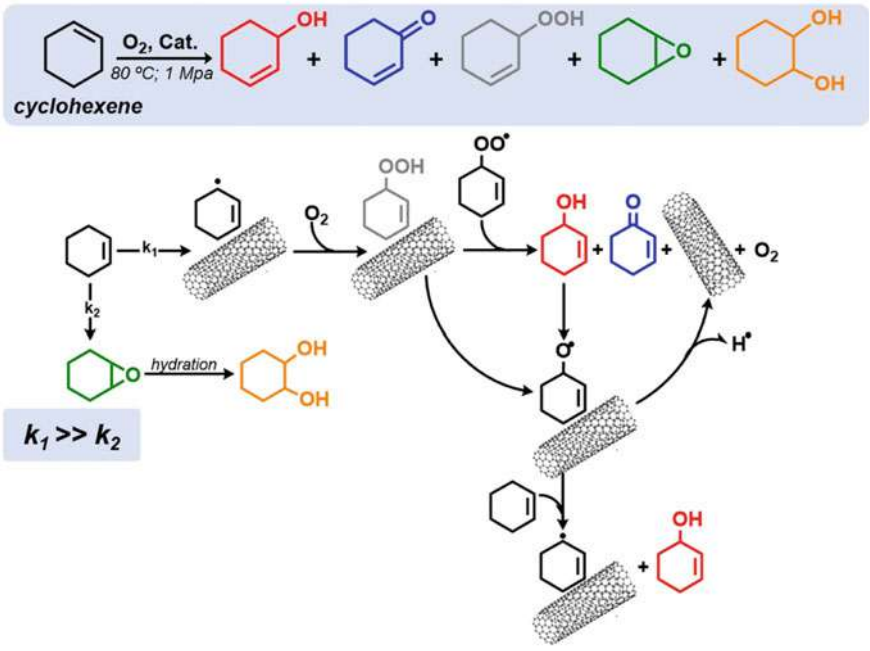

Scheme 14 Allylic oxidation of cyclohexene and suggested reaction mechanism of the N-CNT catalyst

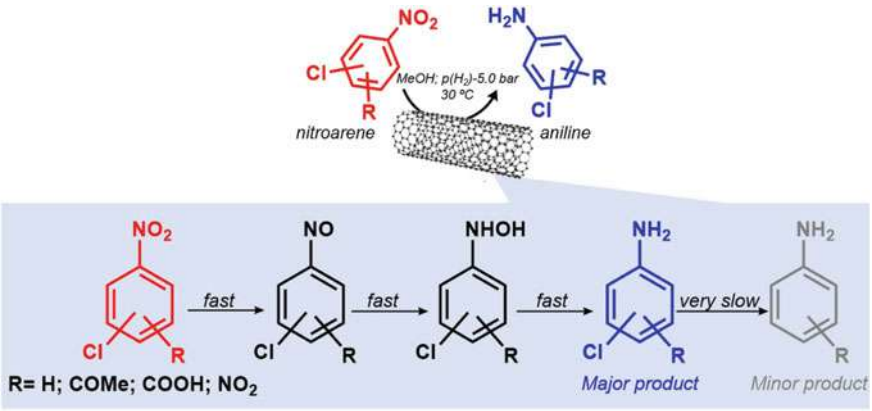

Scheme 15 Catalytic hydrogenation of nitroarenes to amines

3.2.5 Nitrobenzene Hydrogenation

Another useful and very important chemical reaction, which is very used in the commercial production of a large number of pigments, drugs or polymers is the hydrogenation of nitrobenzene. Metal catalysts play a crucial role in this reaction, but, the need to find alternatives to metal catalysts is mandatory nowadays (Scheme 15) [153]. The problems associated to metal catalysts include their scarcity, the instability of certain intermediates, ease of agglomeration, poisoning and the lack of adequate anchoring of the metallic species to the support [154].

A number of N-doped CNTs were prepared by a nitridation approach, as described in reference [128]. This approach allows to obtain a wide variety of N-doped CNTs with different amounts of N, and different defects as well. All these catalysts were employed for the hydrogenation of nitrobenzene. Interestingly, the abundance of pyrrolic N atoms accounts for high conversions of nitrobenzene, in the order of 60%, and a selectivity in the order of 90%. This study concluded that the presence of defects in the structure of N-doped CNT is secondary in the catalytic activity, being the presence of N doping the most influential feature to account for the catalytic activity.

3.3 Selective Oxidation Reactions

3.3.1 Benzyl Alcohol Oxidation

The synthesis of aldehydes or ketones from the oxidation of alcohols in a selective manner is of utmost importance for organic chemistry [155]. A large body of research

has been performed to achieve the oxidation of benzyl alcohol, which is an important intermediate in the production of many important chemicals (Scheme 16) [156].

A wide variety of metallic reagents have been employed for the oxidation of alcohols, including peroxides or high-valent Cr and Mn species [157]. These species may be pernicious to the environment, and are not safe for transportation, given their high oxidizing power. Additionally, these reagents are not selective. These catalysts may be substituted by others based on carbon nanostructures [158]; however, carbon nanocatalysts often need the inclusion of additional co-catalysts or the use of rather high temperatures for the reaction to proceed. A nice example of the oxidation of benzyl alcohol, using CNTs is described in reference [159]. Such study employs O_2 as the final oxidant and the reaction is promoted by HNO_3. Multiple factors were evaluated to account for the catalytic activity, yielding a maximum conversion of 96.2%, with selectivity for benzaldehyde of 88.3%. Six consecutive catalytic cycles were carried out, with excellent results.

Reference [160] reports that peroxymonosulfate (PMS, HSO_5^-) may be activated by carbon nanostructures, and possesses increased activity for oxidation reactions and for the degradation of aqueous contaminants. A number of carbon nanostructures provide activity in the degradation of phenol under mild reaction conditions, including nanodiamonds, reduced graphene oxide and CNTs. Certainly, the sp^2 sheets favor the electron transfer towards the species to be degraded. Unfortunately, a systematic evaluation of the role of PMS in generating reactive intermediates of radical nature, and the role of heteroatoms in carbon nanostructures is not established yet.

Reference [161] presents on the other hand a new procedure for the selective oxidation of benzyl alcohol. Such procedure comprised the use of activated CNTs and PMS as the oxidant. In this case, an electrophilic oxygen has been given the catalytic responsibility, since it may act as electron-receiving group, in order to activate PMS via the O–O bond breaking, thus forming highly reactive $SO_5^{-\bullet}$ and $SO_4^{-\bullet}$ radical species. Moreover, the presence of C = O groups may also participate in the generation of $^{\bullet}OH$ and $SO_4^{-\bullet}$ radicals in order to feed the redox cycle.

Scheme 16 Catalytic production of benzaldehyde

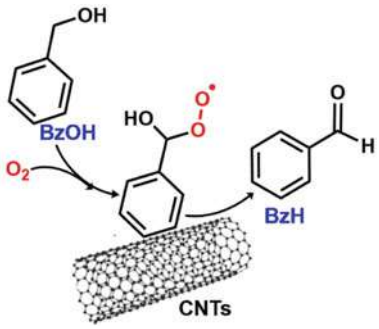

3.3.2 Cumene Oxidation

Cumene may yield important oxidation products, including 2-phenyl-2-propanol (BP), cumene hydroperoxide (CHP) and acetophenone (AP), as depicted in Scheme 17 [162, 163]. These products are important intermediates for the synthesis of other useful products, such as fragrances, drugs or polymers [163, 164].

C-based nanostructures may be active catalysts for this transformation as well, even superior to catalysts based on transition metals. As an example, reference [164] reports on the development of CNTs as outstanding catalyst for cumene oxidation, achieving a conversion of 24.1% and a selectivity of 88.4% for CHP. N-doping in this case is likely to activate oxygen molecules and to increase the rate of peroxide decomposition.

In a different work, reference [165] reports on the reaction between HCl and CNTs to activate the nanotubes, copper acetate was used as co-catalyst for the oxidation of cumene. This work suggests that the active site is associated to adsorbed chlorine at the surface of C. Such chlorine should have interacted with copper acetate to form a Cu-Cl intermediate, which should have contributed to the decomposition of

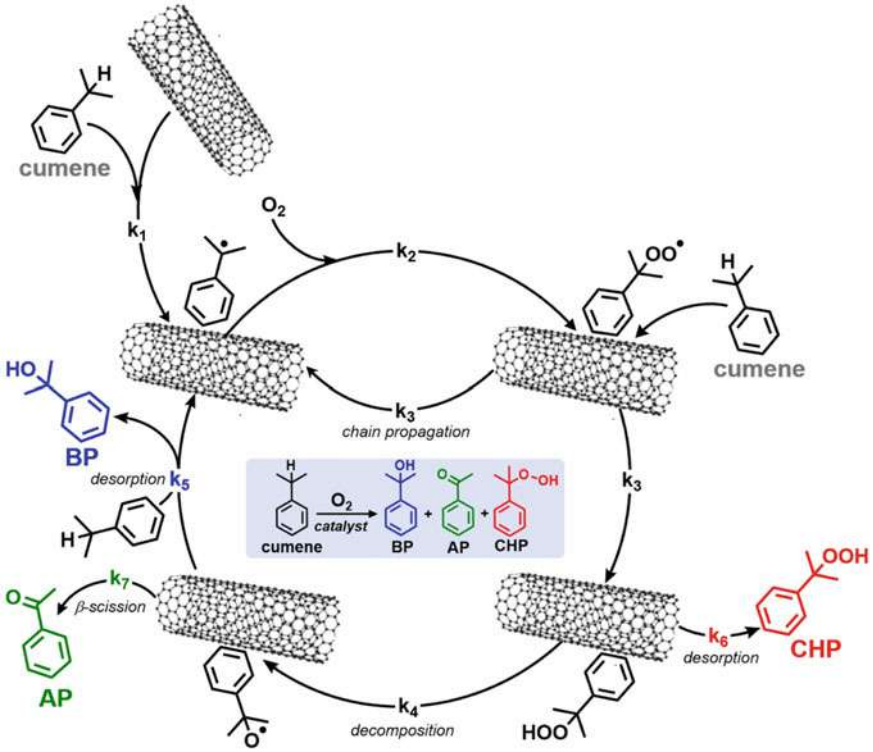

Scheme 17 Aerobic oxidation of cumene with CNTs as catalysts

peroxides and hence accelerating the rate of the reaction. It is worth to highlight that this contribution offers the path to pre-treat the carbon nanostructures, in order to enhance their catalytic activities.

4 Conclusions

This review was dedicated to carbon nanotubes and their main applications in organic catalysis. We have provided an overview of the multiple designs and architectures, along with experimental procedures to obtain functional materials with specific catalytic activities. A generalized view of the contents of this review shows that the prior functionalization of CNTs opens up countless possibilities for the immobilization of catalytic species, which constitutes one of the main advantages of carbon nanostructures as catalytic supports. The incredible performance of metallic, bimetallic, and metallic oxide nanoparticles as supported catalysts on CNTs have enhanced the efficiency of catalyzed organic reactions, increasing reaction ratios, yields, and selectivities in comparison to conventional catalytic methods. Furthermore, the use of these hybrid catalysts has played a fundamental role in reducing toxic pollutants emitted into the environment (one of the main disadvantage of organic reactions), making these reactions more profitable and environmentally friendly processes. CNTs doped with heteroatoms offers versatile chemical properties and excellent reusabilities as metal-free catalysts in several organic reactions.

It is worth highlighting also that, despite CNTs have demonstrated high efficiency in organic catalysis, a large amount of the current systems exists only at the laboratory scale. We envision the scaling-up as the main challenge to be faced by the scientific community, aiming to widen the presence of these materials in routine chemical processes in the industry.

References

1. Campisciano V, Gruttadauria M, Giacalone F (2019) Modified nanocarbons for catalysis. Chem Cat Chem 11:90–133. https://doi.org/10.1002/cctc.201801414
2. Li S, Zhao Z, Zhao J, Zhang Z, Li X, Zhang J (2020) Recent advances of Ferro-, Piezo-, and pyroelectric nanomaterials for catalytic applications. ACS Appl Nano Mater 3:1063–1079. https://doi.org/10.1021/acsanm.0c00039
3. Esteves LM, Oliveira HA, Passos FB (2018) Carbon nanotubes as catalyst support in chemical vapor deposition reaction: a review. J Ind Eng Chem 65:1–12. https://doi.org/10.1016/j.jiec.2018.04.012
4. Iijima S (1991) Helical microtubules of graphitic carbon. Nature 354:56–58
5. Serp P, Castillejos E (2010) Catalysis in carbon nanotubes. ChemCatChem 2:41–47. https://doi.org/10.1002/cctc.200900283
6. Yan Y, Miao J, Yang Z, Xiao FX, Bin YH, Liu B et al (2015) Carbon nanotube catalysts: recent advances in synthesis, characterization and applications. Chem Soc Rev 44:3295–3346. https://doi.org/10.1039/c4cs00492b

7. Pérez Sestelo J, Sarandeses LA (2020) Advances in cross-coupling reactions. Molecules 25:23–26. https://doi.org/10.3390/molecules25194500
8. Hong K, Sajjadi M, Suh JM, Zhang K, Nasrollahzadeh M, Jang HW et al (2020) Palladium nanoparticles on assorted nanostructured supports: applications for suzuki, heck, and sonogashira cross-coupling reactions. ACS Appl Nano Mater 3:2070–2103. https://doi.org/10.1021/acsanm.9b02017
9. Polášek J, Paciorek J, Stošek J, Semrád H, Munzarová M, Mazal C (2020) Stereoselective bromoboration of acetylene with boron tribromide: preparation and cross-coupling reactions of (Z)-bromovinylboronates. J Org Chem 85:6992–7000. https://doi.org/10.1021/acs.joc.0c00341
10. Huang X, Yao F, Wei T, Cai M (2017) A highly efficient and recyclable Pd(PPh3)4/PEG-400 system for Stille cross-coupling reactions of organostannanes with aryl bromides. J Chem Res 41:547–550. https://doi.org/10.3184/174751917X15045169836226
11. Xu W, Liu Y, Kato T, Maruoka K (2021) The formation of C-C or C-N bonds via the copper-catalyzed coupling of alkylsilyl peroxides and organosilicon compounds: a route to perfluoroalkylation. Org Lett 23:1809–1813. https://doi.org/10.1021/acs.orglett.1c00215
12. Menges-Flanagan G, Deitmann E, Gössl L, Hofmann C, Löb P (2021) Scalable continuous synthesis of organozinc reagents and their immediate subsequent coupling reactions. Org Process Res Dev 25:427–433. https://doi.org/10.1021/acs.oprd.0c00399
13. Gao X, Zhang Q, Hu J, Zhang H (2020) Ferrocene-containing cross-conjugated polymers synthesized by palladium-catalyzed cross-coupling polymerization. Polymer (Guildf) 207:122827. https://doi.org/10.1016/j.polymer.2020.122827
14. Buskes MJ (2020) Impact of cross-coupling reactions in drug discovery and development. Molecules 25:3493. https://doi.org/10.1089/gen.34.08.07
15. Ben-Lulu M, Gaster E, Libman A, Pappo D (2020) Synthesis of biaryl-bridged cyclic peptides via catalytic oxidative cross-coupling reactions. Angew Chemie - Int Ed 59:4835–4839. https://doi.org/10.1002/anie.201913305
16. Nolan SP, Navarro O (2007) C-C bond formation by cross-coupling, vol 11. Elsevier Inc. https://doi.org/10.1016/b0-08-045047-4/00143-6
17. Huang X, Teng S, Chi YR, Xu W, Pu M, Wu YD et al (2021) Enantioselective intermolecular heck and reductive heck reactions of aryl triflates, mesylates, and tosylates catalysed by nickel. Angew Chemie—Int Ed 60:2828–2832. https://doi.org/10.1002/anie.202011036
18. Xie JQ, Liang RX, Jia YX (2021) Recent advances of catalytic enantioselective heck reactions and reductive-heck reactions. Chinese J Chem 39:710–728. https://doi.org/10.1002/cjoc.202000464
19. Zheng YL, Newman SG (2021) Cross-coupling reactions with esters, aldehydes, and alcohols. Chem Commun 57:2591–2604. https://doi.org/10.1039/d0cc08389e
20. Moghaddam FM, Pourkaveh R, Karimi A (2017) Oxidative heck reaction as a tool for para-selective olefination of aniline: a DFT supported mechanism. J Org Chem 82:10635–10640. https://doi.org/10.1021/acs.joc.7b01570
21. Guo T, Ding Y, Zhou L, Xu H, Loh TP, Wu X (2020) Palladium-catalyzed anti-michael reductive heck reaction of α, β-unsaturated esters. ACS Catal 10:7262–7268. https://doi.org/10.1021/acscatal.0c02414
22. Zhou F, Zhou F, Su R, Yang Y, You J (2020) Build-up of double carbohelicenes using nitroarenes: dual role of the nitro functionality as an activating and leaving group. Chem Sci 11:7424–7428. https://doi.org/10.1039/d0sc02058c
23. Hajipour AR, Khorsandi Z, Farrokhpour H (2019) In situ synthesis of carbon nanotube-encapsulated cobalt nanoparticles by a novel and simple chemical treatment process: efficient and green catalysts for the heck reaction. New J Chem 43:8215–8219. https://doi.org/10.1039/c9nj00813f
24. Hajipour AR, Khorsandi Z, Karimi H (2015) Cobalt nanoparticles supported on ionic liquid-functionalized multiwall carbon nanotubes as an efficient and recyclable catalyst for Heck reaction. Appl Organomet Chem 29:805–808. https://doi.org/10.1002/aoc.3372

25. Gopiraman M, Karvembu R, Kim IS (2014) Highly active, selective, and reusable RuO2/SWCNT catalyst for heck olefination of aryl halides. ACS Catal 4:2118–2129. https://doi.org/10.1021/cs500460m
26. Wen X, Dai T, Zhao Z, Luo Z, Chen C, Sun W et al (2020) In situ preparation of magnetic nickel-containing functionalized carbon nanotubes to support palladium as a catalyst for the heck reaction. Appl Catal A Gen 591:117405. https://doi.org/10.1016/j.apcata.2019.117405
27. Yu R, Liu R, Deng J, Ran M, Wang N, Chu W et al (2018) Pd nanoparticles immobilized on carbon nanotubes with a polyaniline coaxial coating for the heck reaction: coating thickness as the key factor influencing the efficiency and stability of the catalyst. Catal Sci Technol 8:1423–1434. https://doi.org/10.1039/c7cy02588b
28. Ombaka LM, Ndungu PG, Kibet J, Nyamori VO (2017) The effect of pyridinic- and pyrrolic-nitrogen in nitrogen-doped carbon nanotubes used as support for Pd-catalyzed nitroarene reduction: an experimental and theoretical study. J Mater Sci 52:10751–10765. https://doi.org/10.1007/s10853-017-1241-0
29. Wang LL, Zhu LP, Bing NC, Wang LJ (2017) Facile green synthesis of Pd/N-doped carbon nanotubes catalysts and their application in Heck reaction and oxidation of benzyl alcohol. J Phys Chem Solids 107:125–130. https://doi.org/10.1016/j.jpcs.2017.03.025
30. Ghasemzadeh MS, Akhlaghinia B (2019) PdII immobilized on ferromagnetic multi-walled carbon nanotubes functionalized by aminated 2-chloroethylphosphonic acid with S -Methylisothiourea (FMMWCNTs@CPA@SMTU@PdII NPs) applied as a highly efficient and recyclable nanostructured catalyst for suzuki-. Aust J Chem 72:674–692. https://doi.org/10.1071/CH19117
31. Hajipour AR, Khorsandi Z (2016) Immobilized Pd on (S)-methyl histidinate-modified multi-walled carbon nanotubes: a powerful and recyclable catalyst for Mizoroki-Heck and Suzuki-Miyaura C-C cross-coupling reactions in green solvents and under mild conditions. Appl Organomet Chem 30:256–261. https://doi.org/10.1002/aoc.3425
32. Movassagh B, Parvis FS, Navidi M (2015) 40–44 Pd(II) salen complex covalently anchored to multi-walled carbon nanotubes as a heterogeneous and reusable precatalyst for Mizoroki-Heck and Hiyama cross-coupling reactions. Appl Organomet Chem 29:40–44. https://doi.org/10.1002/aoc.3246
33. Hajipour AR, Khorsandi Z, Farrokhpour H (2016) Regioselective Heck reaction catalyzed by Pd nanoparticles immobilized on DNA-modified MWCNTs. RSC Adv 6:59124–59130. https://doi.org/10.1039/c6ra11737f
34. Lakshminarayana B, Mahendar L, Ghosal P, Satyanarayana G, Subrahmanyam C (2017) Nano-sized recyclable PdO supported carbon nanostructures for Heck Reaction: influence of carbon materials. ChemistrySelect 2:2700–2707. https://doi.org/10.1002/slct.201602051
35. Ohtaka A, Sansano JM, Nájera C, Miguel-García I, Berenguer-Murcia Á, Cazorla-Amorõs D (2015) Palladium and bimetallic palladium-nickel nanoparticles supported on multi-walled carbon nanotubes: application to carbon-carbon bond-forming reactions in water. ChemCatChem 7:1841–1847. https://doi.org/10.1002/cctc.201500164
36. Sadjadi S, Heravi MM, Raja M (2018) Combination of carbon nanotube and cyclodextrin nanosponge chemistry to develop a heterogeneous Pd-based catalyst for ligand and copper free C-C coupling reactions. Carbohydr Polym 185:48–55. https://doi.org/10.1016/j.carbpol.2018.01.020
37. Eremin DB, Boiko DA, Kostyukovich AY, Burykina JV, Denisova EA, Anania M et al (2020) Mechanistic study of Pd/NHC-catalyzed Sonogashira reaction: discovery of NHC-Ethynyl coupling process. Chem—A Eur J 26:15672–15681. https://doi.org/10.1002/chem.202003533
38. Mohajer F, Heravi MM, Zadsirjan V, Poormohammad N (2021) Copper-free Sonogashira cross-coupling reactions: an overview. RSC Adv 11:6885–6925. https://doi.org/10.1039/d0ra10575a
39. Mansour AM (2016) Tazarotene copper complexes: Synthesis, crystal structure, DFT and biological activity evaluation. Polyhedron 109:99–106. https://doi.org/10.1016/j.poly.2016.01.041

40. Wagner FF, Comins DL (2006) Expedient five-step synthesis of SIB-1508Y from natural nicotine. J Org Chem 71:8673–8675. https://doi.org/10.1021/jo0616052
41. Hajipour AR, Jajarmi S (2018) A novel and highly efficient polyaniline-functionalized multi-wall carbon nanotube-supported cu(I) complex for Sonogashira coupling reactions of aryl halides with phenylacetylene. Appl Organomet Chem 32:1–7. https://doi.org/10.1002/aoc.3992
42. Ghasemzadeh MS, Akhlaghinia B (2019) FMMWCNTs@CPA@SMTU@PdII NPs: as a versatile ferromagnetic nanostructured catalyst for sonogashira-hagihara cross-coupling reaction in solvent-free conditions. ChemistrySelect 4:1542–1555. https://doi.org/10.1002/slct.201803453
43. Abbasi S, Hekmati M (2017) Functionalization of multi-walled carbon nanotubes with pramipexole for immobilization of palladium nanoparticles and investigation of catalytic activity in the Sonogashira coupling reaction. Appl Organomet Chem 31:1–8. https://doi.org/10.1002/aoc.3600
44. Nazari P, Hekmati M (2019) Functionalization of multi-walled carbon nanotubes by the baclofen drug to immobilize palladium nanoparticles and catalyze Sonogashira coupling reactions. Appl Organomet Chem 33:1–8. https://doi.org/10.1002/aoc.4729
45. Adib M, Karimi-Nami R, Veisi H (2016) Palladium NPs supported on novel imino-pyridine-functionalized MWCNTs: efficient and highly reusable catalysts for the Suzuki-Miyaura and Sonogashira coupling reactions. New J Chem 40:4945–4951. https://doi.org/10.1039/c5nj02842f
46. Kuchkina NV, Haskell AK, Sorokina SA, Torozova AS, Nikoshvili LZ, Sulman EM et al (2020) Pd catalyst based on hyperbranched polypyridylphenylene formed in situ on magnetic silica allows for excellent performance in Suzuki-Miyaura reaction. ACS Appl Mater Interfaces 12:22170–22178. https://doi.org/10.1021/acsami.0c04357
47. Nan L, Yalan C, Jixiang L, Dujuan O, Wenhui D, Rouhi J et al (2020) Carbonylative Suzuki-Miyaura cross-coupling by immobilized Ni@Pd NPs supported on carbon nanotubes. RSC Adv 10:27923–27931. https://doi.org/10.1039/d0ra03915b
48. Ghorbani-Vaghei R, Hemmati S, Hashemi M, Veisi H (2015) Diethylenetriamine-functionalized single-walled carbon nanotubes (SWCNTs) to immobilization palladium as a novel recyclable heterogeneous nanocatalyst for the Suzuki-Miyaura coupling reaction in aqueous media. Comptes Rendus Chim 18:636–643. https://doi.org/10.1016/j.crci.2014.10.010
49. Hajighorbani M, Hekmati M (2016) Pd nanoparticles deposited on Isoniazid grafted multi walled carbon nanotubes: synthesis, characterization and application for Suzuki reaction in aqueous media. RSC Adv 6:88916–88924. https://doi.org/10.1039/c6ra19934h
50. Lee EK, Park SA, Woo H, Hyun Park K, Kang DW, Lim H et al (2017) Platinum single atoms dispersed on carbon nanotubes as reusable catalyst for Suzuki coupling reaction. J Catal 352:388–393. https://doi.org/10.1016/j.jcat.2017.05.005
51. Labulo AH, Omondi B, Nyamori VO (2018) Suzuki-Miyaura reaction and solventfree oxidation of benzyl alcohol by Pd/nitrogen-doped CNTs catalyst. J Mater Sci 53:15817–15836. https://doi.org/10.1007/s10853-018-2748-8
52. Cornelio B, Rance GA, Laronze-Cochard M, Fontana A, Sapi J, Khlobystov AN (2013) Palladium nanoparticles on carbon nanotubes as catalysts of cross-coupling reactions. J Mater Chem A 1:8737–8744. https://doi.org/10.1039/c3ta11530e
53. Veisi H, Nikseresht A, Ahmadi N, Khosravi K, Saeidifar F (2019) Suzuki-Miyaura reaction by heterogeneously supported Pd nanoparticles on thio-modified multi walled carbon nanotubes as efficient nanocatalyst. Polyhedron 162:240–244. https://doi.org/10.1016/j.poly.2019.01.070
54. Jawale DV, Gravel E, Boudet C, Shah N, Geertsen V, Li H et al (2015) Room temperature Suzuki coupling of aryl iodides, bromides, and chlorides using a heterogeneous carbon nanotube-palladium nanohybrid catalyst. Catal Sci Technol 5:2388–2392. https://doi.org/10.1039/c4cy01680g

55. Yang F, Chi C, Dong S, Wang C, Jia X, Ren L et al (2015) Pd/PdO nanoparticles supported on carbon nanotubes: a highly effective catalyst for promoting Suzuki reaction in water. Catal Today 256:186–192. https://doi.org/10.1016/j.cattod.2015.02.026
56. Veisi H, Khazaei A, Safaei M, Kordestani D (2014) Synthesis of biguanide-functionalized single-walled carbon nanotubes (SWCNTs) hybrid materials to immobilized palladium as new recyclable heterogeneous nanocatalyst for Suzuki-Miyaura coupling reaction. J Mol Catal A Chem 382:106–113. https://doi.org/10.1016/j.molcata.2013.10.028
57. Cano M, Benito AM, Maser WK, Urriolabeitia EP (2013) High catalytic performance of palladium nanoparticles supported on multiwalled carbon nanotubes in alkene hydrogenation reactions. New J Chem 37:1968–1972. https://doi.org/10.1039/c3nj00183k
58. Wang D, Astruc D (2015) The golden age of transfer hydrogenation. Chem Rev 115:6621–6686. https://doi.org/10.1021/acs.chemrev.5b00203
59. Zhang XY, Du HZ, Zhai DD, Guan BT, Guan BT (2020) Combined KH/alkaline-earth metal amide catalysts for hydrogenation of alkenes. Org Chem Front 7:1991–1996. https://doi.org/10.1039/d0qo00383b
60. Bakuru VR, Samanta D, Maji TK, Kalidindi SB (2020) Transfer hydrogenation of alkynes into alkenes by ammonia borane over Pd-MOF catalysts. Dalt Trans 49:5024–5028. https://doi.org/10.1039/d0dt00472c
61. Weber S, Brünig J, Veiros LF, Kirchner K (2021) Manganese-catalyzed hydrogenation of ketones under mild and base-free conditions. Organometallics 40:1388–1394. https://doi.org/10.1021/acs.organomet.1c00161
62. Sarkar K, Das K, Kundu A, Adhikari D, Maji B (2021) Phosphine-free manganese catalyst enables selective transfer hydrogenation of nitriles to primary and secondary amines using ammonia-borane. ACS Catal 11:2786–2794. https://doi.org/10.1021/acscatal.0c05406
63. Chen X, Deng D, Pan X, Bao X (2015) Iron catalyst encapsulated in carbon nanotubes for CO hydrogenation to light olefins. Cuihua Xuebao/Chinese J Catal 36:1631–1637. https://doi.org/10.1016/S1872-2067(15)60882-8
64. Yang Z, Guo S, Pan X, Wang J, Bao X (2011) FeN nanoparticles confined in carbon nanotubes for CO hydrogenation. Energy Environ Sci 4:4500–4503. https://doi.org/10.1039/c1ee01428e
65. Wang S, Wu T, Lin J, Ji Y, Yan S, Pei Y et al (2020) Iron-potassium on single-walled carbon nanotubes as efficient Catalyst for CO_2 hydrogenation to heavy olefins. ACS Catal 10:6389–6401. https://doi.org/10.1021/acscatal.0c00810
66. Kangvansura P, Chew LM, Saengsui W, Santawaja P, Poo-arporn Y, Muhler M et al (2016) Product distribution of CO2 hydrogenation by K- and Mn-promoted Fe catalysts supported on N-functionalized carbon nanotubes. Catal Today 275:59–65. https://doi.org/10.1016/j.cattod.2016.02.045
67. Sadjadi S, Koohestani F (2020) Pd immobilized on polymeric network containing imidazolium salt, cyclodextrin and carbon nanotubes: efficient and recyclable catalyst for the hydrogenation of nitroarenes in aqueous media. J Mol Liq 301:112414. https://doi.org/10.1016/j.molliq.2019.112414
68. Liu L, Lou H, Chen M (2018) Selective hydrogenation of furfural over Pt based and Pd based bimetallic catalysts supported on modified multiwalled carbon nanotubes (MWNT). Appl Catal A Gen 550:1–10. https://doi.org/10.1016/j.apcata.2017.10.003
69. Chen Z, Guan Z, Li M, Yang Q, Li C (2011) Enhancement of the performance of a platinum nanocatalyst confined within carbon nanotubes for asymmetric hydrogenation. Angew Chemie 123:5015–5019. https://doi.org/10.1002/ange.201006870
70. Romero-Sáez M, Dongil AB, Benito N, Espinoza-González R, Escalona N, Gracia F (2018) CO2 methanation over nickel-ZrO2 catalyst supported on carbon nanotubes: a comparison between two impregnation strategies. Appl Catal B Environ 237:817–825. https://doi.org/10.1016/j.apcatb.2018.06.045
71. Ai P, Tan M, Yamane N, Liu G, Fan R, Yang G et al (2017) Synergistic effect of a boron-doped carbon-nanotube-supported Cu catalyst for selective hydrogenation of dimethyl oxalate to ethanol. Chem—A Eur J 23:8252–8261. https://doi.org/10.1002/chem.201700821

72. Lv Y, Cui H, Liu P, Hao F, Xiong W, Luo H (2019) Functionalized multi-walled carbon nanotubes supported Ni-based catalysts for adiponitrile selective hydrogenation to 6-aminohexanenitrile and 1,6-hexanediamine: switching selectivity with [Bmim]OH. J Catal 372:330–351. https://doi.org/10.1016/j.jcat.2019.03.023
73. Tabatabaei Rezaei SJ, Khorramabadi H, Hesami A, Ramazani A, Amani V, Ahmadi R (2017) Chemoselective reduction of nitro and nitrile compounds with magnetic carbon nanotubes-supported Pt(II) catalyst under mild conditions. Ind Eng Chem Res 56:12256–12266. https://doi.org/10.1021/acs.iecr.7b02795
74. Zhu J, Dou M, Lu M, Xiang X, Ding X, Liu W et al (2019) Thermo-responsive polymer grafted carbon nanotubes as the catalyst support for selective hydrogenation of cinnamaldehyde: Effects of surface chemistry on catalytic performance. Appl Catal A Gen 575:11–19. https://doi.org/10.1016/j.apcata.2019.02.009
75. Che CM, Cheng KW, Chan MCW, Lau TC, Mak CK (2000) Stoichiornetric and catalytic oxidations of alkanes and alcohols mediated by highly oxidizing ruthenium-oxo complexes bearing 6,6'-dichloro-2,2'-bipyridine. J Org Chem 65:7996–8000. https://doi.org/10.1021/jo0010126
76. Sheldon RA, Arends IWCE, Ten BGJ, Dijksman A (2002) Green, catalytic oxidations of alcohols. Acc Chem Res 35:774–781. https://doi.org/10.1021/ar010075n
77. Olenin AY, Mingalev PG, Lisichkin GV (2018) Partial catalytic oxidation of alcohols: catalysts based on metals and metal coordination compounds (a review). Pet Chem 58:577–592. https://doi.org/10.1134/S0965544118080182
78. Kopylovich MN, Ribeiro APC, Alegria ECBA, Martins NMR, Martins LMDRS, Pombeiro AJL (2015) Catalytic oxidation of alcohols: recent advances. Adv Organomet Chem 63:91–174. https://doi.org/10.1016/bs.adomc.2015.02.004
79. Davis SE, Ide MS, Davis RJ (2013) Selective oxidation of alcohols and aldehydes over supported metal nanoparticles. Green Chem 15:17–45. https://doi.org/10.1039/c2gc36441g
80. Alshammari HM, Alshammari AS, Humaidi JR, Alzahrani SA, Alhumaimess MS, Aldosari OF et al (2020) Au-Pd bimetallic nanocatalysts incorporated into carbon nanotubes (CNTs) for selective oxidation of alkenes and alcohol. Processes 8:1–11. https://doi.org/10.3390/pr8111380
81. Liu CH, Liu J, Zhou YY, Cai XL, Lu Y, Gao X et al (2015) Small and uniform Pd monometallic/bimetallic nanoparticles decorated on multi-walled carbon nanotubes for efficient reduction of 4-nitrophenol. Carbon N Y 94:295–300. https://doi.org/10.1016/j.carbon.2015.07.003
82. Kaboudin B, Saghatchi F, Kazemi F (2019) Synthesis of decorated carbon nanotubes with Fe3O4 and Au nanoparticles and their application in catalytic oxidation of alcohols in water. J Organomet Chem 882:64–69. https://doi.org/10.1016/j.jorganchem.2018.12.012
83. Kumar R, Gravel E, Hagège A, Li H, Jawale DV, Verma D et al (2013) Carbon nanotube-gold nanohybrids for selective catalytic oxidation of alcohols. Nanoscale 5:6491–6497. https://doi.org/10.1039/c3nr01432k
84. Hajian R, Alghour Z (2017) Selective oxidation of alcohols with H2O2 catalyzed by zinc polyoxometalate immobilized on multi-wall carbon nanotubes modified with ionic liquid. Chinese Chem Lett 28:971–975. https://doi.org/10.1016/j.cclet.2016.12.003
85. Zhang J, Lu S, Xiang Y, Jiang SP (2020) Intrinsic effect of carbon supports on the activity and stability of precious metal based catalysts for electrocatalytic alcohol oxidation in fuel cells: a review. Chemsuschem 13:2484–2502. https://doi.org/10.1002/cssc.202000048
86. Wei Y, Zhang X, Luo Z, Tang D, Chen C, Zhang T et al (2017) Nitrogen-doped carbon nanotube-supported pd catalyst for improved electrocatalytic performance toward ethanol electrooxidation. Nano-Micro Lett 9:1–9. https://doi.org/10.1007/s40820-017-0129-5
87. Hiltrop D, Masa J, Maljusch A, Xia W, Schuhmann W, Muhler M (2016) Pd deposited on functionalized carbon nanotubes for the electrooxidation of ethanol in alkaline media. Electrochem Commun 63:30–33. https://doi.org/10.1016/j.elecom.2015.11.010
88. Maya-Cornejo J, Garcia-Bernabé A, Compañ V (2018) Bimetallic Pt-M electrocatalysts supported on single-wall carbon nanotubes for hydrogen and methanol electrooxidation in

fuel cells applications. Int J Hydrogen Energy 43:872–884. https://doi.org/10.1016/j.ijhydene.2017.10.097
89. Yang H, Yu Z, Li S, Zhang Q, Jin J, Ma J (2017) Ultrafine palladium-gold-phosphorus ternary alloyed nanoparticles anchored on ionic liquids-noncovalently functionalized carbon nanotubes with excellent electrocatalytic property for ethanol oxidation reaction in alkaline media. J Catal 353:256–264. https://doi.org/10.1016/j.jcat.2017.07.025
90. Zhao H, Wang S, He F, Zhang J, Chen L, Dong P et al (2019) Hydroxylated carbon nanotube/carbon nitride nanobelt composites with enhanced photooxidation and H2 evolution efficiency. Carbon N Y 150:340–348. https://doi.org/10.1016/j.carbon.2019.05.020
91. Das B, Sharma M, Baruah MJ, Mounash BP, Karunakar GV, Bania KK (2020) Gold nanoparticle supported on mesoporous vanadium oxide for photo-oxidation of 2-naphthol with hydrogen peroxide and aerobic oxidation of benzyl alcohols. J Environ Chem Eng 8:104268. https://doi.org/10.1016/j.jece.2020.104268
92. Liu W, Wang C, Su D, Qi W (2018) Oxidative dehydrogenation of ethylbenzene on nanocarbon: kinetics and reaction mechanism. J Catal 368:1–7. https://doi.org/10.1016/j.jcat.2018.09.023
93. Hu X, Liu Y, Huang H, Huang B, Chai G, Xie Z (2020) Template-free synthesis of graphene-like carbons as efficient carbocatalysts for selective oxidation of alkanes. Green Chem 22:1291–1300. https://doi.org/10.1039/c9gc03781k
94. Feng L, Liu Y, Jiang Q, Liu W, Wu KH, Ba H et al (2020) Nanodiamonds @ N, P co-modified mesoporous carbon supported on macroscopic SiC foam for oxidative dehydrogenation of ethylbenzene. Catal Today 357:231–239. https://doi.org/10.1016/j.cattod.2019.02.046
95. Kharissova OV, Kharisov BI, Ulyand IE, García TH (2020) Catalysis using metal-organic framework-derived nanocarbons: recent trends. J Mater Res 35:2190–2207. https://doi.org/10.1557/jmr.2020.166
96. Schaetz A, Zeltner M, Stark WJ (2012) Carbon modifications and surfaces for catalytic organic transformations. ACS Catal 2:1267–1284. https://doi.org/10.1021/cs300014k
97. Qi W, Liu W, Guo X, Schlögl R, Su D (2015) Oxidative dehydrogenation on nanocarbon: intrinsic catalytic activity and structure-function relationships. Angew Chemie 127:13886–13889. https://doi.org/10.1002/ange.201505818
98. Maniecki T, Shtyka O, Mierczynski P, Ciesielski R, Czylkowska A, Leyko J et al (2018) Carbon Nanotubes: Properties, Synthesis, and Application. Fibre Chem 50:297–300. https://doi.org/10.1007/s10692-019-09979-2
99. Pereira MFR, Orfão JJM, Figueiredo JL (2000) Oxidative dehydrogenation of ethylbenzene on activated carbon catalysts 2 Kinetic modelling. Appl Catal A Gen 196:43–54. https://doi.org/10.1016/S0926-860X(99)00447-0
100. Shi L, Qi W, Liu W, Yan P, Li F, Sun J et al (2018) Carbon nitride modified nanocarbon materials as efficient non-metallic catalysts for alkane dehydrogenation. Catal Today 301:48–54. https://doi.org/10.1016/j.cattod.2017.03.047
101. Tian S, Yan P, Li F, Zhang X, Su D, Qi W (2019) Fabrication of polydopamine modified carbon nanotube hybrids and their catalytic activity in ethylbenzene dehydrogenation. ChemCatChem 11:2073–2078. https://doi.org/10.1002/cctc.201900146
102. Zhou Q, Guo X, Song C, Zhao Z, Defect-Enriched N (2019) O-codoped nanodiamond/carbon nanotube catalysts for styrene production via dehydrogenation of ethylbenzene. ACS Appl Nano Mater 2:2152–2159. https://doi.org/10.1021/acsanm.9b00124
103. Kładna A, Marchlewicz M, Piechowska T, Kruk I, Aboul-Enein HY (2015) Reactivity of pyruvic acid and its derivatives towards reactive oxygen species. Luminescence 30:1153–1158. https://doi.org/10.1002/bio.2879
104. Sugiyama S, Fukunaga S, Ito K, Ohigashi S, Hayashi H (1991) Catalysts for vapor-phase dehydration of ethylene glycol and their application to pyruvic acid synthesis. J Catal 129:12–18. https://doi.org/10.1016/0021-9517(91)90003-M
105. Hayashi H, Shigemoto N, Sugiyama S, Masaoka N, Saitoh K (1993) X-ray photoelectron spectra for the oxidation state of TeO2-MoO3 catalyst in the vapor-phase selective oxidation of ethyl lactate to pyruvate. Catal Letters 19:273–277. https://doi.org/10.1007/BF00771764

106. Schwartz TJ, O'Neill BJ, Shanks BH, Dumesic JA (2014) Bridging the chemical and biological catalysis gap: Challenges and outlooks for producing sustainable chemicals. ACS Catal 4:2060–2069. https://doi.org/10.1021/cs500364y
107. Wang D, Liu W, Xie Z, Tian S, Su D, Qi W (2020) Oxidative dehydrogenation of ethyl lactate over nanocarbon catalysts: Effect of oxygen functionalities and defects. Catal Today 347:96–101. https://doi.org/10.1016/j.cattod.2018.06.018
108. Zhao X, Zhang C, Xu C, Li H, Huang H, Song L et al (2016) Kinetics study for the oxidative dehydrogenation of ethyl lactate to ethyl pyruvate over MoVNbOx based catalysts. Chem Eng J 296:217–224. https://doi.org/10.1016/j.cej.2016.03.088
109. Liu W, Chen B, Duan X, Wu KH, Qi W, Guo X et al (2017) Molybdenum carbide modified nanocarbon catalysts for alkane dehydrogenation reactions. ACS Catal 7:5820–5827. https://doi.org/10.1021/acscatal.7b01905
110. Rinaldi A, Zhang J, Frank B, Su DS, Hamid SBA, Schlögl R (2010) Oxidative purification of carbon nanotubes and its impact on catalytic performance in oxidative dehydrogenation reactions. Chemsuschem 3:254–260. https://doi.org/10.1002/cssc.200900179
111. Raun KV, Lundegaard LF, Beato P, Appel CC, Nielsen K, Thorhauge M et al (2020) Stability of iron-molybdate catalysts for selective oxidation of methanol to formaldehyde: influence of preparation method. Catal Letters 150:1434–1444. https://doi.org/10.1007/s10562-019-03034-9
112. Yuan M, Che Y, Tang R, Li S, Zhang Y, Tian Y et al (2020) One-step synthesis of methylal via methanol oxidation by Mo:Fe(x)/HZSM-5 bifunctional catalyst. Fuel 261:116416. https://doi.org/10.1016/j.fuel.2019.116416
113. Shimoda K, Ishikawa S, Tashiro M, Kumaki M, Hiyoshi N, Ueda W (2020) Synthesis of high dimensionally structured Mo-Fe mixed metal oxide and its catalytic activity for selective oxidation of methanol. Inorg Chem 59:5252–5255. https://doi.org/10.1021/acs.inorgchem.9b03713
114. Barbarossa V, Viscardi R, Di Nardo A, Santagata A (2020) Kinetic parameter estimation for methanol dehydration to dimethyl ether over sulfonic and polymeric acid catalysts. J Chem Technol Biotechnol 95:1739–1747. https://doi.org/10.1002/jctb.6372
115. Said AEAA, El-Aal MA (2017) Direct dehydrogenation of methanol to anhydrous formaldehyde over Ag2O/γ-Al2O3 nanocatalysts at relatively low temperature. Res Chem Intermed 43:3205–3217. https://doi.org/10.1007/s11164-016-2820-4
116. Childers CL, Huang H, Korzeniewski C (1999) Formaldehyde yields from methanol electrochemical oxidation on carbon-supported platinum catalysts. Langmuir 15:786–789. https://doi.org/10.1021/la980798o
117. Routray K, Zhou W, Kiely CJ, Grünert W, Wachs IE (2010) Origin of the synergistic interaction between MoO3 and iron molybdate for the selective oxidation of methanol to formaldehyde. J Catal 275:84–98. https://doi.org/10.1016/j.jcat.2010.07.023
118. Yan P, Zhang X, Herold F, Li F, Dai X, Cao T et al (2020) Methanol oxidative dehydrogenation and dehydration on carbon nanotubes: active sites and basic reaction kinetics. Catal Sci Technol 10:4952–4959. https://doi.org/10.1039/d0cy00619j
119. Cheng W, Liu X, Li N, Han J, Li S, Yu S (2018) Boron-doped graphene as a metal-free catalyst for gas-phase oxidation of benzyl alcohol to benzaldehyde. RSC Adv 8:11222–11229. https://doi.org/10.1039/c8ra00290h
120. Bharathiraja B, Jayamuthunagai J, Sudharsanaa T, Bharghavi A, Praveenkumar R, Chakravarthy M et al (2017) Biobutanol – An impending biofuel for future: a review on upstream and downstream processing tecniques. Renew Sustain Energy Rev 68:788–807. https://doi.org/10.1016/j.rser.2016.10.017
121. Bagheri S, Muhd JN (2017) Mo3VOx catalyst in biomass conversion: a review in structural evolution and reaction pathways. Int J Hydrogen Energy 42:2116–2126. https://doi.org/10.1016/j.ijhydene.2016.09.173
122. Phung TK, Proietti Hernández L, Lagazzo A, Busca G (2015) Dehydration of ethanol over zeolites, silica alumina and alumina: Lewis acidity, Brønsted acidity and confinement effects. Appl Catal A Gen 493:77–89. https://doi.org/10.1016/j.apcata.2014.12.047

123. Khan Y, Marin M, Viinikainen T, Lehtonen J, Puurunen RL, Karinen R (2018) Structured microreactor with gold and palladium on titania: Active, regenerable and durable catalyst coatings for the gas-phase partial oxidation of 1-butanol. Appl Catal A Gen 562:173–183. https://doi.org/10.1016/j.apcata.2018.06.010
124. Lopez-Pedrajas S, Estevez R, Schnee J, Gaigneaux EM, Luna D, Bautista FM (2018) Study of the gas-phase glycerol oxidehydration on systems based on transition metals (Co, Fe, V) and aluminium phosphate. Mol Catal 455:68–77. https://doi.org/10.1016/j.mcat.2018.05.020
125. Gu Q, Ding Y, Liu Z, Lin Y, Schlögl R, Heumann S et al (2019) Probing the intrinsic catalytic activity of carbon nanotubes for the metal-free oxidation of aromatic thiophene compounds in ionic liquids. J Energy Chem 32:131–137. https://doi.org/10.1016/j.jechem.2018.07.004
126. Li F, Yan P, Herold F, Drochner A, Wang H, Cao T et al (2020) Oxygen assisted butanol conversion on bifunctional carbon nanotube catalysts: activity of oxygen functionalities. Carbon N Y 170:580–588. https://doi.org/10.1016/j.carbon.2020.08.053
127. Liu W, Wang C, Herold F, Etzold BJM, Su D, Qi W (2019) Oxidative dehydrogenation on nanocarbon: effect of heteroatom doping. Appl Catal B Environ 258. https://doi.org/10.1016/j.apcatb.2019.117982
128. Xiong W, Wang Z, He S, Hao F, Yang Y, Lv Y et al (2020) Nitrogen-doped carbon nanotubes as a highly active metal-free catalyst for nitrobenzene hydrogenation. Appl Catal B Environ 260:118105. https://doi.org/10.1016/j.apcatb.2019.118105
129. Shameli A, Ameri E (2017) Synthesis of cross-linked PVA membranes embedded with multi-wall carbon nanotubes and their application to esterification of acetic acid with methanol. Chem Eng J 309:381–396. https://doi.org/10.1016/j.cej.2016.10.039
130. Wang J, Huang R, Zhang Y, Diao J, Zhang J, Liu H et al (2017) Nitrogen-doped carbon nanotubes as bifunctional catalysts with enhanced catalytic performance for selective oxidation of ethanol. Carbon N Y 111:519–528. https://doi.org/10.1016/j.carbon.2016.10.038
131. Li X, Li P, Pan X, Ma H, Bao X (2017) Deactivation mechanism and regeneration of carbon nanocomposite catalyst for acetylene hydrochlorination. Appl Catal B Environ 210:116–120. https://doi.org/10.1016/j.apcatb.2017.03.046
132. Fu H, Huang K, Yang G, Cao Y, Wang H, Peng F et al (2020) Synergistic effect of nitrogen dopants on carbon nanotubes on the catalytic selective epoxidation of styrene. ACS Catal 10:129–137. https://doi.org/10.1021/acscatal.9b03584
133. Ba H, Duong-Viet C, Liu Y, Nhut JM, Granger P, Ledoux MJ et al (2016) Nitrogen-doped carbon nanotube spheres as metal-free catalysts for the partial oxidation of H2S. Comptes Rendus Chim 19:1303–1309. https://doi.org/10.1016/j.crci.2015.09.022
134. Garcia-Arriaga V, Alvarez-Ramirez J, Amaya M, Sosa E (2010) H2S and O2 influence on the corrosion of carbon steel immersed in a solution containing 3M diethanolamine. Corros Sci 52:2268–2279. https://doi.org/10.1016/j.corsci.2010.03.016
135. Zhang Z, Jiang W, Long D, Wang J, Qiao W, Ling L (2017) A general silica-templating synthesis of alkaline mesoporous carbon catalysts for highly efficient H2S oxidation at room temperature. ACS Appl Mater Interfaces 9:2477–2484. https://doi.org/10.1021/acsami.6b13597
136. Sun F, Liu J, Chen H, Zhang Z, Qiao W, Long D et al (2013) Nitrogen-rich mesoporous carbons: highly efficient, regenerable metal-free catalysts for low-temperature oxidation of H2S. ACS Catal 3:862–870. https://doi.org/10.1021/cs300791j
137. Ba H, Liu Y, Truong-Phuoc L, Duong-Viet C, Mu X, Doh WH et al (2015) A highly N-doped carbon phase "dressing" of macroscopic supports for catalytic applications. Chem Commun 51:14393–14396. https://doi.org/10.1039/c5cc05259a
138. Li S, Liu Y, Gong H, Wu KH, Ba H, Duong-Viet C et al (2019) N-doped 3D mesoporous carbon/carbon nanotubes monolithic catalyst for H2S selective oxidation. ACS Appl Nano Mater 2:3780–3792. https://doi.org/10.1021/acsanm.9b00654
139. Luo J, Wei H, Liu Y, Zhang D, Zhang B, Chu W et al (2017) Oxygenated group and structural defect enriched carbon nanotubes for immobilizing gold nanoparticles. Chem Commun 53:12750–12753. https://doi.org/10.1039/c7cc06594a

140. Yang J, Mou CY (2018) Ordered mesoporous Au/TiO2 nanospheres for solvent-free visible-light-driven plasmonic oxidative coupling reactions of amines. Appl Catal B Environ 231:283–291. https://doi.org/10.1016/j.apcatb.2018.02.054
141. Wen G, Gu Q, Liu Y, Schlögl R, Wang C, Tian Z et al (2018) Biomass-derived graphene-like carbon: efficient metal-free carbocatalysts for epoxidation. Angew Chemie - Int Ed 57:16898–16902. https://doi.org/10.1002/anie.201809970
142. Lin Y, Sun X, Su DS, Centi G, Perathoner S (2018) Catalysis by hybrid sp2/sp3 nanodiamonds and their role in the design of advanced nanocarbon materials. Chem Soc Rev 47:8438–8473. https://doi.org/10.1039/c8cs00684a
143. Wu KH, Wang DW, Zong X, Zhang B, Liu Y, Gentle IR et al (2017) Functions in cooperation for enhanced oxygen reduction reaction: the independent roles of oxygen and nitrogen sites in metal-free nanocarbon and their functional synergy. J Mater Chem A 5:3239–3248. https://doi.org/10.1039/c6ta10336g
144. Wei H, Ma Y, Luo J, Wu KH, Xie W, Wen G et al (2020) Creation of N-C=O active groups on N-doped CNT as an efficient CarboCatalyst for solvent-free aerobic coupling of benzylamine. Carbon N Y 170:338–346. https://doi.org/10.1016/j.carbon.2020.08.018
145. Luo J, Peng F, Yu H, Wang H, Zheng W (2013) Aerobic liquid-phase oxidation of ethylbenzene to acetophenone catalyzed by carbon nanotubes. ChemCatChem 5:1578–1586. https://doi.org/10.1002/cctc.201200603
146. Balasubramanyan S, Sugunan S, Narayanan BN (2018) Nitrogen-doped sulphonated 3-dimensional holey graphene nanoarchitecture for selective oxidation of ethylbenzene. J Mater Sci 53:12079–12090. https://doi.org/10.1007/s10853-018-2501-3
147. Tang P, Gao Y, Yang J, Li W, Zhao H, Ma D (2014) Growth mechanism of N-doped graphene materials and their catalytic behavior in the selective oxidation of ethylbenzene. Cuihua Xuebao/Chinese J Catal 35:922–928. https://doi.org/10.1016/s1872-2067(14)60150-9
148. Su Y, Li Y, Chen Z, Huang J, Wang H, Yu H et al (2021) New understanding of selective aerobic oxidation of ethylbenzene catalyzed by nitrogen-doped carbon nanotubes. ChemCatChem 13:646–655. https://doi.org/10.1002/cctc.202001503
149. Cao Y, Yu H, Peng F, Wang H (2014) Selective allylic oxidation of cyclohexene catalyzed by nitrogen-doped carbon nanotubes. ACS Catal 4:1617–1625. https://doi.org/10.1021/cs500187q
150. Yang JH, Sun G, Gao Y, Zhao H, Tang P, Tan J et al (2013) Direct catalytic oxidation of benzene to phenol over metal-free graphene-based catalyst. Energy Environ Sci 6:793–798. https://doi.org/10.1039/c3ee23623d
151. Cao Y, Li Y, Yu H, Peng F, Wang H (2015) Aerobic oxidation of α-pinene catalyzed by carbon nanotubes. Catal Sci Technol 5:3935–3944. https://doi.org/10.1039/c5cy00136f
152. Cao Y, Yu H, Wang H, Peng F (2017) Solvent effect on the allylic oxidation of cyclohexene catalyzed by nitrogen doped carbon nanotubes. Catal Commun 88:99–103. https://doi.org/10.1016/j.catcom.2016.10.002
153. Oberhauser W, Evangelisti C, Tiozzo C, Bartoli M, Frediani M, Passaglia E et al (2017) Platinum nanoparticles onto pegylated poly(lactic acid) stereocomplex for highly selective hydrogenation of aromatic nitrocompounds to anilines. Appl Catal A Gen 537:50–58. https://doi.org/10.1016/j.apcata.2017.03.003
154. Xiong W, Wang KJ, Liu XW, Hao F, Xiao HY, Le LP et al (2016) 1,5-Dinitronaphthalene hydrogenation to 1,5-diaminonaphthalene over carbon nanotube supported non-noble metal catalysts under mild conditions. Appl Catal A Gen 514:126–134. https://doi.org/10.1016/j.apcata.2016.01.018
155. Kuang Y, Rokubuichi H, Nabae Y, Hayakawa T, Kakimoto MA (2010) A nitric acid-assisted carbon-catalyzed oxidation system with nitroxide radical cocatalysts as an efficient and green protocol for selective aerobic oxidation of alcohols. Adv Synth Catal 352:2635–2642. https://doi.org/10.1002/adsc.201000366
156. Luo J, Yu H, Wang H, Wang H, Peng F (2014) Aerobic oxidation of benzyl alcohol to benzaldehyde catalyzed by carbon nanotubes without any promoter. Chem Eng J 240:434–442. https://doi.org/10.1016/j.cej.2013.11.093

157. Besson M, Gallezot P (2000) Selective oxidation of alcohols and aldehydes on metal catalysts. Catal Today 57:127–141. https://doi.org/10.1016/S0920-5861(99)00315-6
158. Long J, Xie X, Xu J, Gu Q, Chen L, Wang X (2012) Nitrogen-doped graphene nanosheets as metal-free catalysts for aerobic selective oxidation of benzylic alcohols. ACS Catal 2:622–631. https://doi.org/10.1021/cs3000396
159. Luo J, Peng F, Yu H, Wang H (2012) Selective liquid phase oxidation of benzyl alcohol catalyzed by carbon nanotubes. Chem Eng J 204–205:98–106. https://doi.org/10.1016/j.cej.2012.07.098
160. Duan X, Ao Z, Zhang H, Saunders M, Sun H, Shao Z et al (2018) Nanodiamonds in sp2/sp3 configuration for radical to nonradical oxidation: core-shell layer dependence. Appl Catal B Environ 222:176–181. https://doi.org/10.1016/j.apcatb.2017.10.007
161. Li J, Li M, Sun H, Ao Z, Wang S, Liu S (2020) Understanding of the oxidation behavior of benzyl alcohol by peroxymonosulfate via carbon nanotubes activation. ACS Catal 10:3516–3525. https://doi.org/10.1021/acscatal.9b05273
162. Su DS, Wen G, Wu S, Peng F, Schlögl R (2017) Carbocatalysis in liquid-phase reactions. Angew Chemie—Int Ed 56:936–964. https://doi.org/10.1002/anie.201600906
163. Liao S, Chi Y, Yu H, Wang H, Peng F (2014) Tuning the selectivity in the aerobic oxidation of cumene catalyzed by nitrogen-doped carbon nanotubes. ChemCatChem 6:555–560. https://doi.org/10.1002/cctc.201300909
164. Liao S, Peng F, Yu H, Wang H (2014) Carbon nanotubes as catalyst for the aerobic oxidation of cumene to cumene hydroperoxide. Appl Catal A Gen 478:1–8. https://doi.org/10.1016/j.apcata.2014.03.024
165. Deng J, Li Y, Cao Y, Wang H, Yu H, Zhang Q et al (2020) Trace amounts of Cu(OAc)2 boost the efficiency of cumene oxidation catalyzed by carbon nanotubes washed with HCl. Catal Sci Technol 10:2523–2530. https://doi.org/10.1039/c9cy02536g

Carbonaceous Supported Pt-Alloy Based Nanocomposite Electrocatalysts for Methanol Electrooxidation Reaction in Direct Methanol Fuel Cell: A Review

Mohamad Fahrul Radzi Hanifah, Juhana Jaafar, Mohd Hafiz Dzarfan Othman, Ahmad Fauzi Ismail, and Mukhlis A. Rahman

Abstract The DMFC commercialization and practical operations are still confronts several major challenges particularly in high cost, maintaining long-term stability and durability, deteriorating of anode electrocatalyst performance as well as the sluggish methanol oxidation kinetic reaction occurred at the anode due to the poisoning effect of the platinum (Pt) electrocatalyst. The selection of the appropriate anode electrocatalysts for methanol oxidation reaction (MOR) is quite limited, only the anode electrocatalysts that can enhance the MOR activity and minimize the poisoning effect by the carbonaceous intermediate species-like carbon monoxide (CO) can be considered to improve the DMFC performance. The strategy of coupling or alloying Pt with other noble or non-noble metals can prevent such mentioned problems above and able to upgrade the ability of anti-CO poisoning through the modification of the CO adsorption site. In general, the highly accessible of electrocatalytic active sites and dispersed are very important for the superior Pt-based alloy electrocatalyst performance through the utilization of the electrocatalyst support with the large specific surface areas. However, the commonly used carbon supporting materials for monometallic Pt and bimetallic Pt-based alloy electrocatalysts suffer from severe corrosion due to the electrooxidation on the surface under acidic condition at high operating voltages for prolonged times which resulting the dissolution, aggregation, migration and detachment of Pt NPs leading to a serious problem of stability. The most efficient strategy to overcome the limitations described above is through the embedding the monometallic Pt and bimetallic Pt-based alloy electrocatalyst on the metal oxides. This proposed strategy provides a medium to anchor the Pt-based alloy electrocatalyst securely onto the carbonaceous support materials and the electrocatalytic performance of the electrocatalyst also have been proven to be significantly improved in oxidizing the methanol in DMFC. Nevertheless, studies on

M. F. R. Hanifah · J. Jaafar (✉) · M. H. D. Othman · A. F. Ismail · M. A. Rahman
Advanced Membrane Technology Research Centre (AMTEC), School of Chemical and Energy Engineering, Faculty of Engineering, Universiti Teknologi Malaysia, 81310 UTM Skudai, Johor Bahru, Johor, Malaysia
e-mail: juhana@petroleum.utm.my

M. Jawaid and A. Khan (eds.), *Carbon Composite Catalysts*, Composites Science and Technology, https://doi.org/10.1007/978-981-19-1750-9_8

the possible combination of both supported Pt-based alloy electrocatalyst embedding metal oxides as the potential anode nanocomposite electrocatalyst with careful design still lacking and remains important challenge.

1 Introduction

The DMFC commercialization and practical operations are still confronts several major challenges particularly in high cost, maintaining long-term stability and durability, deteriorating of anode electrocatalyst performance as well as the slow or sluggish methanol oxidation kinetic reaction occurred at the anode due to the poisoning effect of the electrocatalyst [76, 97]. Many studies have been carried out to identify the suitable electrocatalyst with efficient functionality and cost for the enhancement of DMFC operation and commercialization as the promising alternative source of energy. Since the selection of the appropriate anode electrocatalysts for methanol oxidation reaction (MOR) is quite limited, only the anode electrocatalysts that can enhance the MOR activity and minimize the poisoning effect by the carbonaceous intermediate species-like carbon monoxide (CO) can be considered to improve the DMFC performance. In addition, the selected anode electrocatalyst should be active for MOR.

The production of anode electrocatalyst containing platinum (Pt) has been studied and investigated by many researchers in all over the world as the Pt possesses an excellent electrical conductivity, highly resistance against the corrosion and tend to promotes the high electrocatalytic efficiency with the most active for the methanol adsorption dissociation [135]. However, the use of pure Pt electrocatalyst leading to a serious drawback since it can be deactivated and easily poisoned by the carbonaceous intermediate species-like CO generated during the MOR at low operating temperature [94]. The adsorbed CO could degrade and reduce the lifetime of the Pt electrocatalyst when utilize in DMFC. On the other hands, due to the high cost of the noble and rare metal of Pt electrocatalyst in practical applications, recent studies have been directed towards the producing of the electrocatalyst containing reduced amount of Pt. The strategy of coupling or alloying Pt with other noble or non-noble metals such as ruthenium (Ru), palladium (Pd), nickel (Ni), iron (Fe) and cobalt (Co) demonstrate great expectation for MOR with enhanced the electrocatalyst performance [135]. The additional metals in Pt-based alloy electrocatalyst can prevent such mentioned problems above and able to upgrade the ability of anti-CO poisoning through the modification of the CO adsorption site [135]. The kinetics of MOR enhances significantly upon the alloying with a second metal for the formation of bimetallic alloy such as Pt-Ru [56], Pt–Pd [100], Pt–Rh [72] and others.

Besides that, the electrocatalytic activity of the Pt-based alloy electrocatalysts mostly depends on their specified size, shape and composition. Thus, the synthesis of nano-sized electrocatalysts has attracted considerable interest by researchers since it can increase the Pt density with more exposure of the electrocatalytic active sites and enhance the stability with less vulnerable to aggregation sufficiently [103]. In general,

the highly accessible of electrocatalytic active sites and dispersed are very important for the superior Pt-based alloy electrocatalyst performance. Therefore, the utilization of the electrocatalyst support with the large specific surface areas are necessary in order to obtain the high dispersion of active Pt-based alloy metals. Instead of carbon black [101], the other carbonaceous materials such as carbon nanotube (CNT) [27], carbon nanofiber [79] and graphene or reduced graphene oxide (RGO) [31] were also widely used as anode electrocatalyst support. The charge transfer efficiency and durability of the electrocatalyst can be enhanced through the interaction of electrocatalyst-support. The outstanding characteristics should be exhibited by the practical electrocatalyst support such as excellent electrical conductivity, large surface area, easy recovery or retrieval of electrocatalyst, mesoporous structure, good tolerance of corrosion and strong interaction of electrocatalyst-support [135].

Thus, the selection of the best supporting materials is very crucial in obtaining excellent efficiency, behaviour and stability of the electrocatalyst and all-inclusive DMFC. However, the commonly used carbon supporting materials for monometallic Pt and bimetallic Pt-based alloy electrocatalysts suffer from severe corrosion due to the electrooxidation on the surface under acidic condition at high operating voltages for prolonged times which resulting the dissolution, aggregation, migration and detachment of Pt NPs leading to a serious problem of stability [76, 89]. The most efficient strategy to overcome the limitations described above is through the embedding the monometallic Pt and bimetallic Pt-based alloy electrocatalyst on the metal oxides such as CeO_2 [111], IrO_2 [113], MnO_2 [134], RuO_2 [37], SnO_2 [93] and TiO_2 [115]. This proposed strategy provides a medium to anchor the Pt-based alloy electrocatalyst securely onto the carbonaceous support materials and the electrocatalytic performance of the electrocatalyst also have been proven to be significantly improved in oxidizing the methanol as well as the efficiency of DMFC [110]. Nevertheless, studies on the possible combination of both supported Pt-based alloy electrocatalyst embedding metal oxides as the potential anode nanocomposite electrocatalyst with careful design still lacking and remains important challenge.

In this chapter, the detailed discussion on the operating principles of DMFC, general mechanism of MOR, the DMFC advantages as well as the issues or challenges involved in DMFC developments have been reviewed accordingly. In addition, the focuses mainly on the exciting research progress of unsupported and supported monometallic Pt and bimetallic Pt-based alloy electrocatalysts for MOR occurring at the anode of DMFC from the previous reported works over the past few years. Besides that, an overview regarding the type of the carbonaceous supporting materials and the progress of the ternary nanocomposite electrocatalysts containing metal oxides preparation towards the electrocatalytic activity of MOR and the DMFC performance as well as the electrocatalyst synthesis methods employed have been thoroughly analyzed and discussed. Ultimately, the future perspectives in determining the most suitable and effective anode electrocatalysts toward MOR were briefly summarized.

2 Direct Methanol Fuel Cell

DMFC has been attracted considerable attention in academia and industry since it can be identified as a leading contender to compete with the conventional battery technology for powering portable electronic devices. In 1990, the Jet Propulsion Laboratory of NASA in collaboration with the University of Southern California have developed a DMFC with higher lifetime to replace the traditional batteries like lithium-ion battery [6]. In addition, many of top device companies like Panasonic, fujitsu, Sony and LG, Samsung from South Korea, Sanyo from Japan and others have invested in the research of DMFC prototype [18]. It is worth to note that the DMFC has a similar configuration with the PEMFC in which the anode and cathode compartments have separated by polymer electrolyte membrane. DMFC is actually a subcategory of PEMFC that use the methanol liquid as the fuel and can be distinguished from other type of commercial PEMFC in the aspect of fuel type utilization. In fundamental, technology of DMFC produces electrical energy directly from the high energy density of aqueous methanol fuel [42]. In general, the DMFC fuel delivery mode can be divided into two basic categories in the system which is active and passive modes [44, 87]. In an active fuel delivery mode of DMFC system, the recirculation process is involved for the outlet stream of DMFC stack through the feed of liquid methanol under the closed-loop control. The delivery of the methanol liquid to the anode compartment is usually carried out by a peristaltic pump while oxygen from the surrounding air or oxygen gas can be supplied to the cathode compartment by a fan or blower. Meanwhile, the liquid methanol is continuosly delivered or fed to the DMFC stack in the passive fuel delivery mode of DMFC system. The operation of the passive mode system is totally autonomously without requiring any external device for supplying the methanol fuel and blowing the surrounding air into the DMFC stack. The removal of the water and carbon dioxide occurred from the DMFC stack cell by passive means including the diffusion, capillary action, natural convection and others during MOR in the passive mode of DMFC system [43, 62]. The simpler, low cost and more compact design of the passive mode of DMFC system seems to be more advantageous compared to the active mode of DMFC system. However, the active mode of DMFC system is more appropriate to be employed in high-power system while the passive mode of the DMFC system is more preferable to be applied in low-power system for the aspect of practical uses [88]. Figure 1 displays the schematic diagram of the passive and active modes methanol fuel delivery of DMFC system.

2.1 Operating Principles of DMFC

Figure 2 illustrates the schematic diagram of the DMFC system displaying the basic operating principles that involve its reactant and product as well as the flow directions of hydrogen ions (proton) conduction from anode to cathode. In DMFC, the main

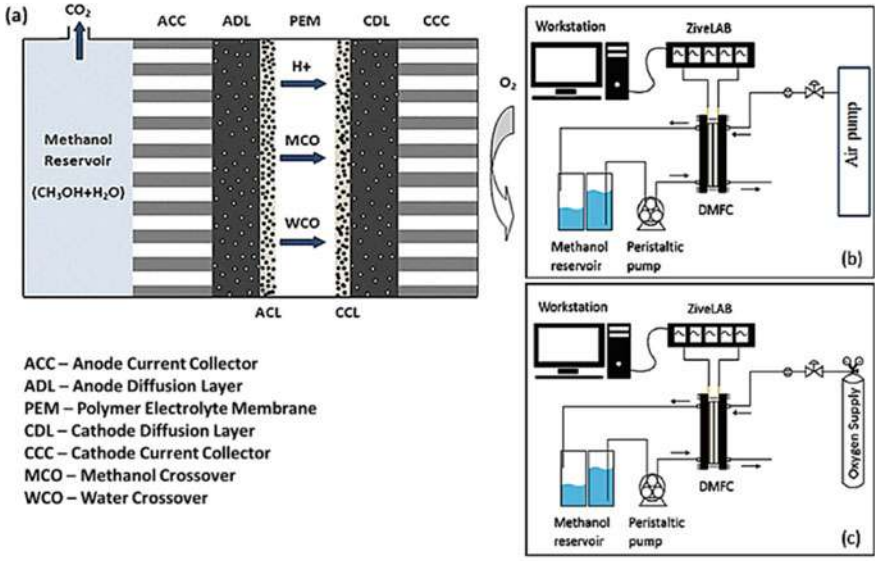

Fig. 1 Schematic diagram of **a** passive mode, **b** and **c** active mode of DMFC system [1, 96]

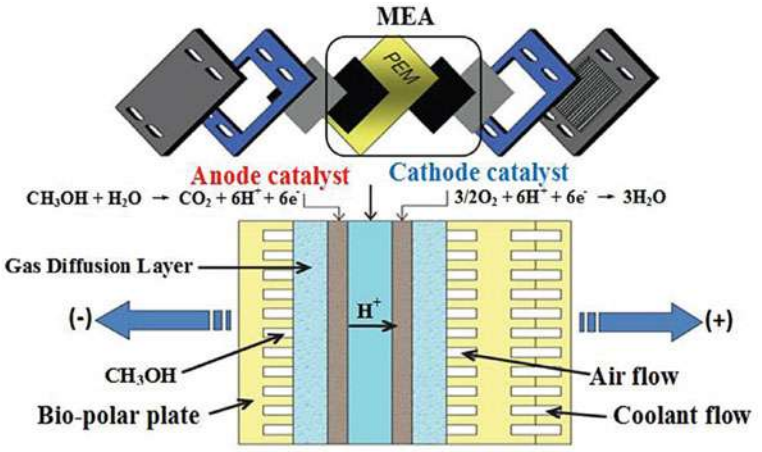

Fig. 2 Representative schematic diagram of DMFC system with the basic operating principle (Gong et al. 2018)

active components are the membrane electrode assembly (MEA) in which comprised of the proton electrolyte membrane, both anode and cathode of gas diffusion layer and catalyst layer where the MOR and ORR occur to generate the electrical energy from chemical energy directly. The commercial Nafion membrane is frequently used as a polymer electrolyte membrane (proton-conducting solid membrane) in MEA of

DMFC that can act as the electrolyte and separator between the anode and cathode compartments. The methanol solution is directly feed to the anode and the oxygen or surrounding air containing oxygen is feed to the cathode during the running of DMFC system. At the anode, methanol solution is directly oxidized on the electrocatalyst surface in the present of water to release the CO_2, protons and electrons (Eq. 2.1). The resulting CO_2 from MOR is removed by the acidic electrolyte solution. The protons pushed by electric field are free to migrate through the polymer electrolyte membrane and the produced electrons flow through the external load circuit from anode and reach an electrocatalyst NPs on the cathode. Meanwhile, at the cathode, the oxygen molecules react with the protons and electrons from anode and produce water (Eq. 2.2). The excess of generated electrons at the anode compared with the consumed electrons at the cathode causing an electric potential difference between the electrodes that can drives the load or current to work as real power sources. The common electrochemical reaction at the anode and cathode in acidic media-based DMFC are as follows [104]:

$$\textbf{Anode reaction} : CH_3OH + H_2O \rightarrow CO_2 + 6H^+ + 6e \tag{2.1}$$

$$\textbf{Cathode reaction} : 3/2O_2 + 6H^+ + 6e^- \rightarrow 3H_2O \tag{2.2}$$

$$\textbf{Overall reaction} : CH_3OH + 3/2O_2 \rightarrow CO_2 + 2H_2O \tag{2.3}$$

2.2 *General Mechanism of Methanol Oxidation Reaction (MOR)*

The MOR mechanism on pure Pt electrocatalysts in acidic electrolyte media have been commonly studied under well-controlled conditions by researchers from various research groups for over the past few decades. Based on the reported works in literature, the mechanism of MOR can be summarized as below:

(a) Methanol electrosorption
(b) Dissociation of methanol (activation of C-H bond)
(c) Adsorption of water and activation
(d) Addition of oxygen to the adsorbed carbonaceous intermediate species for the generation of carbon dioxide.

Notably, the carbonaceous intermediate-like CO_{ads} species is normally formed and strongly adsorbs onto the surface of Pt electrocatalyst during MOR in which can negatively effect on the DMFC performance. Up to date, the electrooxidation of methanol to CO_2 can be obtained through the two possible pathway namely indirect MOR mechanism that involves the carbonaceous intermediate-like CO_{ads} species and direct MOR mechanism in which the production of CO_2 from methanol without involving

the formation of CO_{ads} intermediate species [104]. Figure 3 represents the schematic illustration of the possible MOR mechanism along with the produced carbonaceous intermediate species by electrocatalyst. It is worth to note that the carbonaceous intermediate-like CO_{ads} is the most harmful intermediate species because of strongly adsorption onto the Pt surface. The produced carbonaceous intermediate-like CO_{ads} species with relatively higher stability after a series of adsorption and deprotonation on the anode electrocatalyst surface restricts the MOR rate at the anode [135]. As a result, the severe declines of electrocatalyst performance occur due to the inhibition of methanol chemisorption onto Pt active sites in which this phenomenon can be called as poisoning effect. In addition, the resulting CO_{ads} during MOR could blocks the electrocatalytic active sites of the anode electrocatalyst. As clearly shown in Eq. 2.7, the CO_{ads} formation can be obtained through indirect mechanism in which involve the dehydrogenation process of COH directly. Below are the possible reactions involve with the production of carbonaceous intermediate species in MOR based on the dehydrogenation of methanol (Gong et al. 2018):

$$CH_3OH + Pt \rightarrow Pt\,CH_2OH + H^+ + e^- \tag{2.4}$$

$$Pt{-}CH_2OH + Pt. \rightarrow Pt_2{-}CHOH + H^+ \tag{2.5}$$

$$Pt_2{-}CHOH + Pt \rightarrow Pt_3{-}COH + H^+ + e^- \tag{2.6}$$

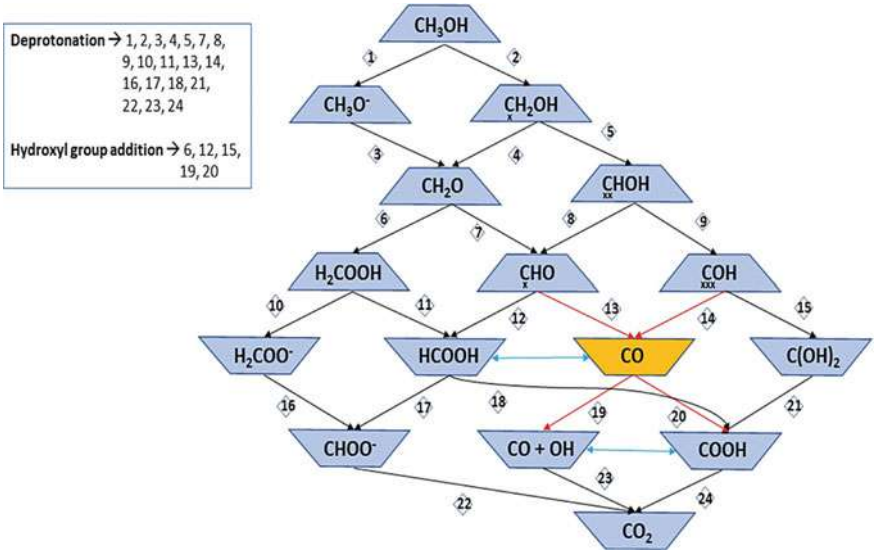

Fig. 3 Schematic representation of the possible MOR mechanism [135]

$$Pt_3{-}COH \rightarrow 2Pt + Pt{-}CO + H^+ + e^- \tag{2.7}$$

The oxygenated species is generated from the process of water degradation (Eq. 2.8) in which a pair of proton and electron is taken away by formaldehyde to form COH via hydrogen abstraction. The produced OH group will combine with the carbonaceous intermediate species (formaldehyde (CHOH), COH, CO) and the di-oxygenated species like formic acid (H-COOH, COOH) to be produced (see Eqs. 2.10a, 2.10b, 2.11a, 2.11b, 2.12a and 2.12b).

$$Pt + H_2O \rightarrow Pt{-}OH + H^+ + e^- \tag{2.8}$$

The liberation of Pt active sites occurs after removal of the carbonaceous intermediate species as demonstrated by the series of equations below:

$$Pt{-}CH_2OH \rightarrow Pt + HCHO + H^+ + e^- \tag{2.9}$$

$$Pt_2{-}CHOH + Pt{-}OH \rightarrow 3Pt + HCOOH + H^+ + e^- \tag{2.10a}$$

OR

$$Pt_2{-}CHOH + H_2O \rightarrow 2Pt + HCOOH + 2H^+ + 2e^- \tag{2.10b}$$

$$Pt_3{-}COH + Pt{-}OH \rightarrow 3Pt + Pt{-}COOH + H^+ + e^- \tag{2.11a}$$

OR

$$Pt_3{-}COH + H_2O \rightarrow 2Pt + Pt{-}COOH + 2H^+ + 2e^- \tag{2.11b}$$

$$Pt{-}CO + Pt{-}OH \rightarrow Pt + Pt{-}COOH \tag{2.12a}$$

OR

$$Pt{-}CO + H_2O \rightarrow Pt{-}COOH + H^+ + e^- \tag{2.12b}$$

The complete overall reaction is achieved with the formation of CO_2 through the reaction between the oxygenated species or water and carbonaceous intermediate-like CO_{ads} species or others. The removing possibility of CO_{ads} or other carbonaceous intermediates from the surface of electrocatalyst through the oxidizing process of the carbonaceous intermediate species together with the produced oxygenated species (water or OH^- ions) which can get adsorbed onto the electrocatalyst surface. Again, with applied the same concept as discussed above, the dissociation of water occurs separately to form the OH_{ads} species on the Pt electrocatalyst surface. Then, both the carbonaceous intermediate and oxygenated species can react together to produce

CO_2.

$$HCHO + H_2O \rightarrow CO_2 + 4H^+ + 4e^- \tag{2.13}$$

$$HCOOH \rightarrow CO_2 + 2H^+ + 2e^- \tag{2.14}$$

$$Pt{-}COOH \rightarrow Pt + CO_2 + H^+ + e^- \tag{2.15}$$

$$Pt{-}CO_{ads} + Pt{-}OH_{ads} \rightarrow 2Pt + CO_2 + H^+ + e^- \tag{2.16}$$

So far, many studies have been conducted with other alternative metals or Pt-based alloy nanocomposite electrocatalysts to enhance the electrocatalytic performance of MOR with superior resistance towards CO_{ads} poisoning effect. However, the process of MOR and its mechanism is still complicated and hard to establish eventhough the produced poisonous carbonaceous intermediate species during MOR is well identified.

2.3 Significant Advantages of DMFC

As a new power generation device with the production of clean energy, DMFC provide several significant advantages including high efficiency of energy conversion, low pollution, few safety concerns, easy and rapid start-up and shutdown, high reliability, low weight, low radiation, simplicity of the system, less complex configuration, no noise, suitability for small and portable applications (chargers for mobile phones, laptops and cameras), small size compared to rechargeable batteries, low operational temperature (vary up to 150 °C), flexible power ranges in applications and ease of recharging for portable applications [45, 71, 19].

In addition, DMFC use liquid and renewable fuels of dilute aqueous methanol solution as a feed to the system is relatively cheap or cost effective, available from a wide range of (sustainable) sources, facile transportation, safe and easily stored and handled as well as remarkably higher specific energy density that have huge potential to replace the rechargeable lithium-polymer and lithium-ion polymer batteries [76, 103]. In recent years, DMFC have received the intensive research interest due to its indisputable merits over PEMFC in which the fuel reforming and purification process can be eliminated conveniently that makes the DMFC system has high security and reliability as well as simpler in structural design [21]. Then, the existing of restricted problem regarding the hydrogen source in PEMFC can effectively solved.

Moreover, DMFC possesses an outstanding power transformer that directly and immediately convert the chemical energy from methanol into electrical energy without combustion [81, 97]. Unlike the conventional power sources of fossil fuel, DMFC is capable of generating electrical power from the methanol fuel and oxidant

streams without producing high amounts of undesirable environmental pollutants such as nitrogen oxides, sulfur oxides, and carbon monoxide. In fact, an environmentally favourable of DMFC produce the greenhouse gas of CO_2 and do not generate toxic by-products. However, small concentrations of side products such as carboxylic acids, ketones and aldehydes are generated. Nevertheless, through the effect of water_gas shift, the hydrogen gives CO_2 obliquely during resolving level. Furthermore, the CO_2 produced through DMFC process would yet be restored through the utilization of CO_2 during photosynthesis. Thus, the concerning energy would be sustainable without further contribute to the greenhouse effect. In addition, the tremendous DMFC performance offers the limited CO_2/kW as compared with the traditional or standard pathway.

2.4 Issues or Challenges in DMFC

Despite of possessing a lot of benefits regarding utilizing of DMFCs working in many applications purpose, the most significant obstacles are still remaining for DMFC debut. Some of the certain barriers incorporate the important materials employed based on the membrane electrode assembly (MEA) in DMFC system mainly the expensive price of Pt electrocatalysts, the methanol crossover through the electrolyte from anode to cathode and the lower conductivity as well as power density performance of DMFC in attributing to the PEMFC. Several severe obstacles need to overcome for achieving the large scale of DMFC commercialization as described below [104]:

i. The high cost and low electrocatalytic activity of the electrocatalysts at the anode and cathode give the greatest current concern.
ii. The poor kinetics of MOR at lower temperatures, making highly desirable for identification of enhanced electrocatalysts and higher operating temperatures.
iii. The slow oxygen reduction reaction (ORR) occurred at the cathode particularly serious problem with aqueous mineral acids. Even though research studies show this issue is not really serious as with acidic polymer membranes. In addition, the methanol vapor also exists in the cathode compartment where it should be removed.
iv. The massive price of currently employed commercial Nafion membrane (perfluoro sulfonic acid membrane) and its permeability condition that brought to methanol crossover from the anode region to the cathode region. The phenomena of methanol crossover led to the degradation of anode and cathode performance as the fuel utilization deterioration and mixed potential problems occurred, respectively.

Meanwhile, during MOR, numerous exterior intermediates species are produced mainly the CO, COH_{ads}, HCO_{ads}, $HCOO_{ads}$ then further oxidized to CO_2. Some of the certain intermediate's species are difficult to oxidize and remain powerfully adsorbed to the exterior of electrocatalyst. The adsorbing of new methanol units and supporting

new reaction have been prevented accordingly since the intermediates electrooxidation can be considered as the rate restricting level. Meanwhile, the electrocatalyst poisoning can be reduced severely through the oxidation reaction in which resulting an increasing of intermediates adsorbs onto electrocatalyst from oxidized into CO_2 and thus decreases the DMFC performance but still bearing within complete oxidation reaction. Consequently, it gives the highly significant hurdle to further expand electrocatalysts in improving the MOR that can slow down the contamination or poisoning effect.

2.5 Anode Electrocatalysts for MOR

Anode electrocatalyst is one of the most significant and important criteria that contribute to the DMFC reliability with an outstanding performance. The motivation to find out an efficient anodic electrocatalyst has currently become predominant among the researchers in all over the world for seeking the alternative materials to make some modifications that can provide more attractive features to enhance the traditional used of pure noble Pt metal electrocatalysts. The field of anode electrocatalysts specifically for DMFC application have attracted consideration interest to many of the researchers worldwide and can be well-reflected through the number of scientific publications which have a rapid increase over the years especially from 2010 until 2020, as indicated by Fig. 4a. Moreover, the total number of 3854 scientific publications have been published on the anode electrocatalysts area for the past five years from 2016 until 2020, implying that the anode electrocatalysts is presently an attractive research area in DMFC technology application. On the other hand, the highest number of the published articles on the anode electrocatalysts have been dominated by China (2795 publications) followed by USA (906 publications) and only 61 publications from Malaysia from 2010 until 2020 as demonstrated by Fig. 4b. All these analysis data obtained from web of science (WOS) revealed that the studies of anode electrocatalysts displays the growing interest among the research community and it is worth and significant to be carried out in Malaysia.

In addition, the electrocatalytic performance of the anode electrocatalysts towards MOR can be evaluated by various techniques the cyclic voltammetry, chronoamperometry and EIS analysis. In general, the electrocatalytic performance can be evaluated and analyzed based on the MOR peak current density at a specific potential through the cyclic voltammetry tool while the electrocatalytic stability performance can be identified by using the chronoamperometry tool. Meanwhile, the resistance value of the anode electrocatalyst during MOR, particularly the charge transfer resistance (R_{ct}) and solution or electrolyte resistance (R_s) can be determined by EIS technique. It is worth to note that the electrocatalytic activity of anode electrocatalyst can be expressed in terms of ECSA, onset potential (E_{onset}), the ratio of the forward peak current density (I_f) to the backward peak current density (I_b) (I_f/I_b ratio) and onset potential value. The larger I_f/I_b ratio value indicates the higher electrocatalyst stability towards carbonaceous intermediate-like CO_{ads} species poisoning effect

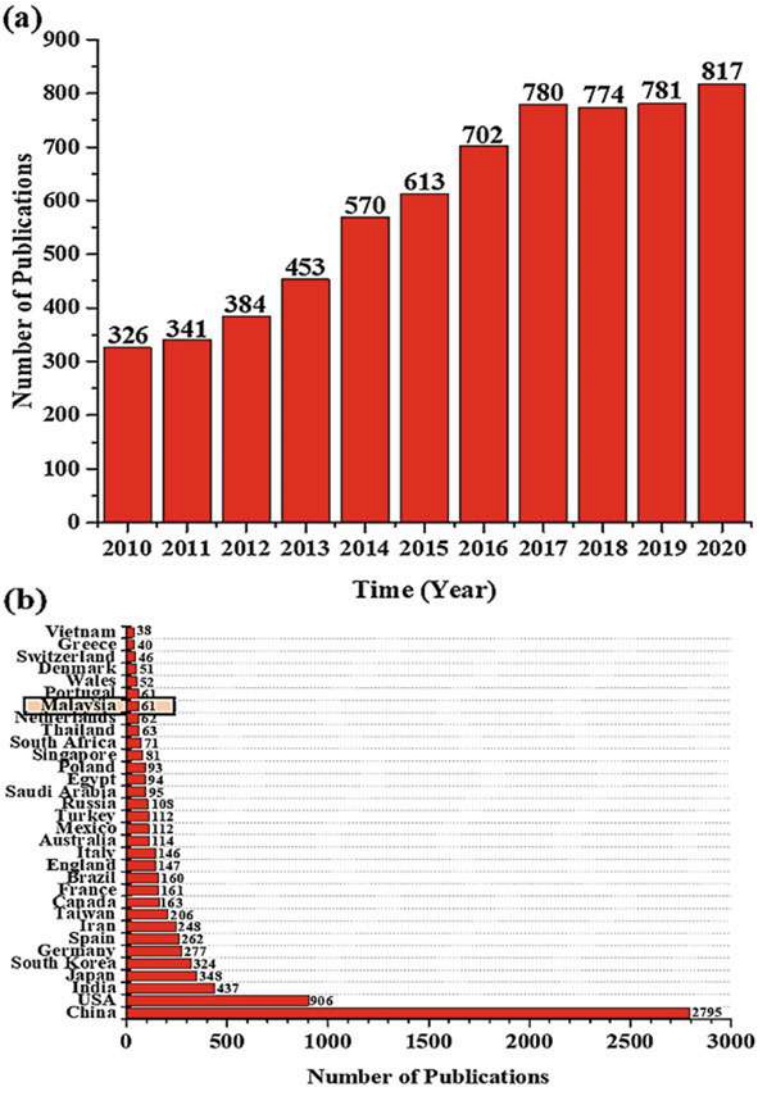

Fig. 4 Number of publications on anode electrocatalyst from the year 2010 to 2020, **a** by year and **b** by country. The data is obtained from the Web of Science mentioning 'catalyst for methanol oxidation reaction' as a keyword

during MOR. Furthermore, the greater electrocatalytic activity of electrocatalyst obtained during MOR will give the higher value of peak current density from the cyclic voltametric (CV) curve. Besides that, the morphological behaviour and chemical composition of the electrocatalyst are the important role of the characteristic

parameters in influencing the electrocatalytic performance of the anode electrocatalyst toward MOR. Therefore, all the characteristic parameters as mentioned above will thoroughly reviewed and presented in this section based on the previous studies [46, 135].

2.6 Unsupported Monometallic Pt Electrocatalysts for MOR

As mentioned before, the noble Pt metal electrocatalyst is still irreplaceable and indispensable as anode electrocatalyst for MOR in acidic electrolyte since from firstly studied in 1922 by E. Müller. Therefore, many research groups have conducted a very thorough investigation toward the MOR characteristics on the Pt surface. Basically, the electrocatalytic activity of Pt is straightly depends on the morphology, particle size, structure and surface state. In general, the electrocatalytic activity and percentage of utilization of Pt increase with the smaller size of PtNPs due to the exposed Pt atoms ratio to the surface boosts. However, Mailard et al., (2005) found out that the high loading of PtNPs with the size of higher than 3 nm tend to agglomerate. In addition, the exploration of Pt nanostructures with various dimensional morphologies like nanowires, nanosheets, nanotubes or porous structures instead of zero-dimensional NPs leading to increase the number of Pt active sites exposed and enhance the stability due to the inherent structure of anisotropic that less vulnerable to aggregation sufficiently, ripening and also dissolution compared with the zero-dimensional isotropic of PtNPs [103].

In another study, [80] reported the fabrication of the three-dimensional (3D) Pt needle-like nanoflowers (NFW) at the glassy carbon electrode (GCE) through a simple and facile one-step electrochemical approach. Figure 5A demonstrates the highly magnified SEM image with inset view clearly reveal the Pt flower-like morphology with porous nature and uniform size have been electrodeposited homogenously at the GCE. Basically, the higher ECSA implying the presence of more electrochemical active sites and the hydrogen adsorption/desorption peak region from CV curve is widely used to determine and estimate the ECSA value. The comparison study between the smooth Pt bulk (curve a), 3D PtNFW (curve b) and PtNPs (curve c) toward the ECSA values were demonstrated in the CV curves from Fig. 5B in the presence of 0.5 M H_2SO_4 solution. Basically, three well-defined hydrogen adsorption peaks at around -0.19 V, -0.11 V and -0.015 V were clearly observed for PtNFW catalyst, then a double layer region and subsequently a reduction peak of deposited PtNFW attributing to the polycrystalline structure of Pt surface. Besides that, a broad featureless hydrogen desorption peak still can be observed within the potential region from -0.28 V to 0.08 V for Pt bulk electrode with very lower adsorption/desorption current density than PtNFW and PtNPs catalysts. From the CV curve results in Fig. 5C, the 3D PtNFW exhibited the remarkable electrocatalytic activity and excellent poisoning tolerance against the carbonaceous oxidative intermediate species for MOR in acidic media. Meanwhile, the high I_f value of the 3D PtNFW was

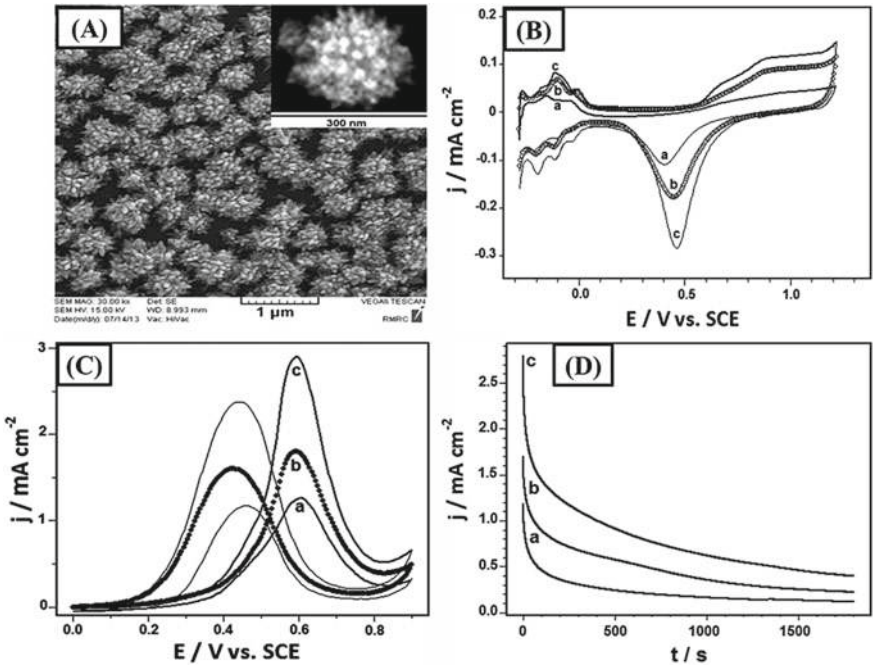

Fig. 5 **A** SEM image of 3D PtNFW, CV curves of the Pt bulk electrode **a**, Pt NPs/GCE **b** and 3D Pt NFW/GCE **c** in the **B** 0.5 M H_2SO_4 and **C** 0.5 M H_2SO_4 + 0.5 M CH_3OH solutions at the scan rate of 50 mVs^{-1}, **D** chronoamperometric curves of the Pt bulk electrode **a**, Pt NPs/GCE **b** and 3D Pt NFW/GCE **c** towards MOR in the 0.5 M H_2SO_4 + 0.5 M CH_3OH solutions at 0.6 V [80]

obtained in which about 1.65 and 2.33 times higher than the PtNPs and Pt bulk electrode that can be ascribed to the NFW morphology of Pt electrocatalyst with more carbonaceous intermediate species are effectively oxidized on the PtNFW electrocatalyst. Moreover, as can be clearly seen from the chronoamperometric curve in Fig. 5D, the PtNFW catalyst was obviously exhibited the lowest rate of the current density decay after the first 1000 s in comparison with the PtNPs and Pt bulk electrode. In addition, the PtNFW also demonstrate the higher current density during the whole stability testing time than the Pt NPs and Pt bulk electrode implying that the as-synthesized PtNFW possess the outstanding electrocatalytic activity and stability toward MOR.

In different study, Zhang and co-workers in 2012 prepared the highly homogenous of single-crystal ultrathin Pt nanowires (UTPtNWs) by using the sacrificial templates of insulin amyloid fibrils (INSAFs). The employ of INSAFs to construct the UTPtNWs provided the low-energy crystal facets preferential exposure that would be highly benefits for MOR. In addition, the existence of abundant UTPtNWs possess the range of tens to hundreds micrometers of lengths with a uniform diameter intertwisted with each other as demonstrated by TEM image in Fig. 6a, b. The TEM image of a typical single UTPtNW in Fig. 6c had a uniform diameter of 1.8 nm

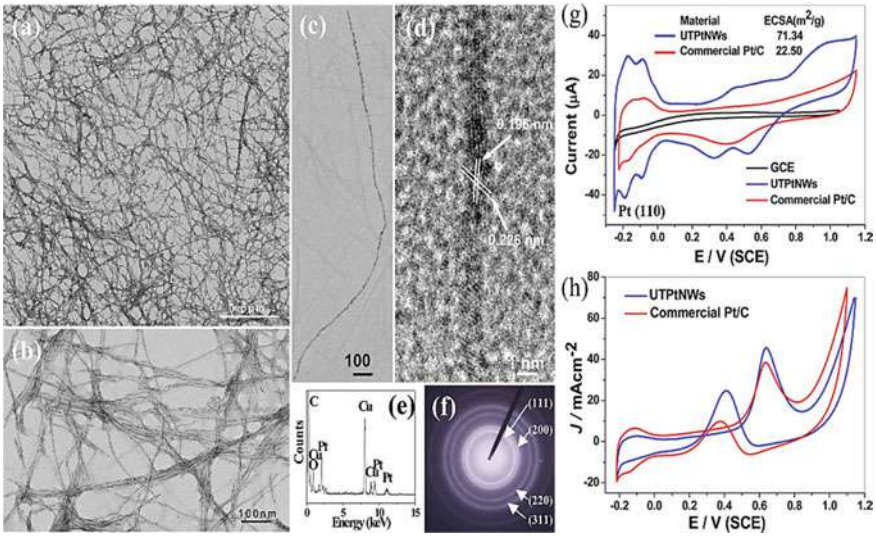

Fig. 6 **a** Low- and **b** high-magnification TEM images of UTPtNWs, **c** TEM image of a typical single UTPtNW, **d** Lattice fringes measurement for Pt (1 1 1) and Pt (2 0 0) planes, **e** EDX spectrum of UTPtNWs, **f** SAED pattern of UTPtNWs marked in different position, **g** and **h** CV curves of UTPtNWs, commercial C/Pt catalyst and GCE in 0.5 M H_2SO_4 and 0.5 $_M$ $H_2SO_4 +$ CH_3OH solutions, respectively [143]

with the length of 2.1 μm. In addition, the distance spacing of the visible crystal lattice fringes of an individual UTPtNW were measured to be 0.226 and 0.196 nm corresponded to the (111) and (200) planes, respectively as demonstrated in Fig. 6d. On the other hand, the EDX analysis of the UTPtNWs implying composed of only Pt element while the C and Cu elements arose from the TEM grid (Fig. 6e). Besides that, the high crystallinity of a few UTPtNWs were confirmed by the selected-area electron diffraction (SAED) that can be indexed to the (111), (200), (220) and (311) planes of the face centered cubic (FCC) structure (Fig. 6f). Meanwhile, from the CV curve in Fig. 6g, the as synthesized UTPtNWs displayed the larger ECSA value of 71.34 m^2/g, than commercial Pt/C catalyst (22.50 m^2/g) indicating that the UTPtNWs possess a huge number of electrochemical active sites leading to higher electrocatalytic activity of MOR. Accordingly, the two oxidation peaks of both UTPtNWs and the commercial Pt/C catalysts toward the MOR appear at 0.64 V and 0.40 V for forward and backward peaks, respectively as clearly shown in Fig. 6h. In addition, the UTPtNWs demonstrate the higher I_f value of 45.50 mA cm^{-2} than the commercial Pt/C catalyst (38.50 mA cm^{-2}), suggesting an excellent electrocatalytic activity of MOR that might be due to the preferential exposure of particular crystal facets and the existence of less surface defects on the UTPtNWs electrocatalyst.

As demonstrated from CV curves in Fig. 7a, the small hydrogen adsorption/desorption peaks were obtained for both the PtNPs-pineapple and PtNPs-banana compared with the PtNPs-sugarcane bagasse indicating the PtNPs active sites might

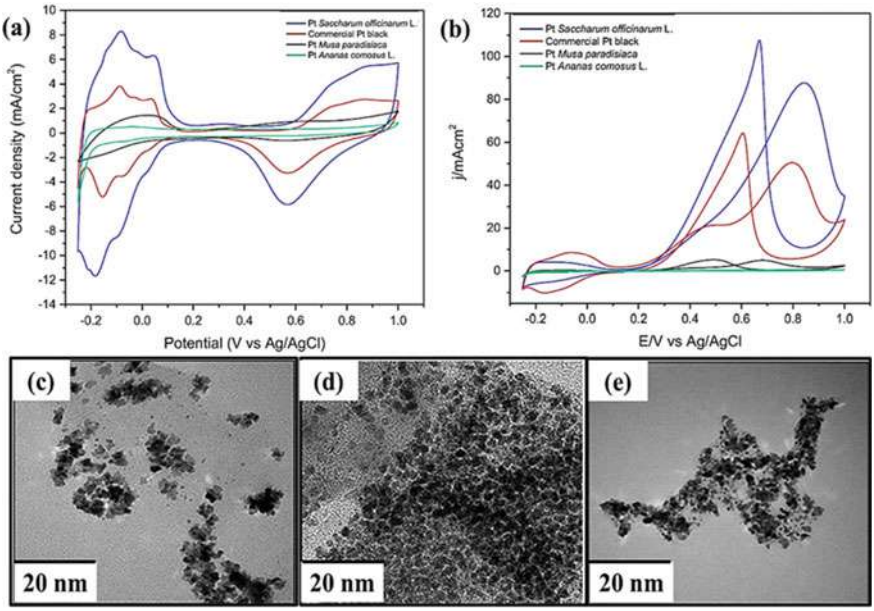

Fig. 7 **a** CV curves that represent the hydrogen adsorption and desorption of Pt catalyst in 0.5 M H_2SO_4 solution at the scan rate of 50 mV/s, **b** CV curve of electrocatalytic activity of Pt catalyst toward MOR in 0.5 M H_2SO_4 + 1 M CH_3OH solution at the scan rate of 50 mV/s, **c**, **d** and **e** TEM images of the produced PtNPs through plant extracts of sugarcane bagasse (*Saccharum officinarum*), pineapple peels (*Ananas comosus L.*) and banana peel (*Musa paradisiaca*), respectively [41]

blocked by some of the organic molecules. In addition, the ECSA value of PtNPs-sugarcane bagasse (94.58 m^2/g) was much higher than the PtNPs-banana peel extract (3.69 m^2/g), PtNPs-pineapple peel extract (1.69 m^2/g) and commercial Pt black (27.49 m^2/g) implying a significant enhanced electrochemical property and plenty of electrochemical active sites available for hydrogen adsorption/desorption process that leads to improve the MOR. Meanwhile, the highest forward peak current density of the PtNPs-sugarcane bagasse (87.68 mA/cm^2) was obtained from the CV curves as represented in Fig. 7b demonstrating an enhanced electrocatalytic activity of MOR which can be attributed to the existence of very fine PtNPs with spherical shape and well-dispersed homogenously as illustrated in the HRTEM image (Fig. 6c–e) [41].

Based on the above considerations, it is obvious that the strategy of structure construction provides the enhancement of the electrocatalytic activity and stability of unsupported Pt nanocatalysts against MOR as a result from the geometric advantages. Meanwhile, some of the research progress on unsupported monometallic Pt electrocatalyst with different nanostructures were compared for electrocatalytic performance in term of ECSA, onset potential, I_f and I_f/I_b ratio values toward MOR as listed and summarized in Table 1. Generally, it can be observed that the value of I_f and ECSA obtained are quite low and not really outstanding value. There are only two research works demonstrated the high value of ECSA and I_f as reported by

Table 1 Comparison in electrocatalytic performance of the as-prepared unsupported monometallic Pt electrocatalyst towards MOR from previous reported works

No	Electrocatalysts	Electrolytes	ECSA	Onset Potential (V)	Maximum forward peak current density/specific activity (I_f, mA cm^{-2})	I_f/I_b ratio	Scan rate (mV s^{-1})	References
1	Pt mesoflowers	0.1 M $HClO_4$ + 0.5 M CH_3OH solution	13.9 $m^2\ g^{-1}$	0.39	3.42	0.988	50	[154]
2	Monodisperse Pt nanocubes	0.1 M $HClO_4$ + 0.2 M CH_3OH solution	42.3 $m^2\ g^{-1}$	–	0.48	–	50	[98]
3	Porous Pt nanotubes	1.0 M CH_3OH + 0.5 M H_2SO_4 solution	23.9 $m^2\ g^{-1}$	–	1.62	–	5	[4]
4	Pt nanoflowers	0.5 M CH_3OH + 0.5 M H_2SO_4 solution	0.42 cm^2	–	2.80	1.22	50	[80]
5	Pt nanowires	1.0 M CH_3OH + 0.5 M H_2SO_4 solution	71.34 $m^2\ g^{-1}$	–	45.50	–	50	[143]

(continued)

Table 1 (continued)

No	Electrocatalysts	Electrolytes	ECSA	Onset Potential (V)	Maximum forward peak current density/specific activity (I_f, mA cm^{-2})	I_f/I_b ratio	Scan rate (mV s^{-1})	References
6	Porous Pt nanotubes	1.0 M CH_3OH + 1.0 M KOH solution	47.17 $m^2\ g^{-1}$	–	4.94	–	50	[70]
7	Pt nanowires	1.0 M CH_3OH + 0.5 M H_2SO_4 solution	40.5 $m^2\ g^{-1}$	–	0.98	1.15	50	[138]
8	Biogenic Pt NPs-sugarcane	1.0 M CH_3OH + 0.5 M H_2SO_4 solution	94.58 $m^2\ g^{-1}$	0.278	87.68	0.81	50	[41]
9	Sponge-like Pt	1.0 M CH_3OH + 0.5 M H_2SO_4 solution	31.73 $m^2\ g^{-1}$	–	1.51	–	50	[48]

[143] and [41]. However, the I_f/I_b ratio displayed by [41] shows the lowest value indicating the less stability towards carbonaceous intermediate-like CO_{ads} species poisoning effect during MOR. In addition, the sluggish reaction kinetics problem and the high cost of high Pt loading cannot be deserved for the commercialization of DMFC since the pure metal electrocatalysts are prone to the poisoning effect by carbonaceous intermediate species mainly CO_{ads}, thereby the electrocatalytic active sites will be blocked and occupied during MOR. Therefore, the presence drawback cannot be addressed through the shape or structure construction strategy only.

Consequently, the enhancement factor of electrocatalytic activity of MOR with the efficient approaches to tune the adsorption or desorption of carbonaceous intermediates species on the Pt electrocatalyst surface may be significant and promising from the effect of component. Thereby, the synthesis or composition with tuneable effect is increasing to proceed further electrocatalytic performance enhancement of electrocatalysts. The relatively less expensive and facile synthesis of the electrocatalysts with new modification that possesses an excellent electrocatalytic activity, anti-CO_{ads} poisoning ability and durability are more preferable for MOR catalyzation. Hence, the anode electrocatalysts containing smaller Pt noble metal amount and more other noble and non-noble metals are widely investigated and studied for operation in DMFC. A number of previous reported works will be discussed and examined thoroughly in the following section.

2.7 Unsupported Bimetallic Pt-Alloyed Based Electrocatalyst for MOR

The strategy of alloying the Pt electrocatalyst with the other transition metals either noble or non-noble metal category such as Ru, Pd, Rh, Ir, Ni, Co and Fe can sharply improve the Pt atoms utilization efficiency during MOR. Furthermore, the incorporation of the transition metals as mentioned above resulting an excellent dispersion in which displayed the outstanding DMFC performance test compared to employ the single Pt metal. More importantly, the improvement of the electrocatalytic activity and stability toward MOR in DMFC system can be considerately obtained through this strategy by modulating the strength of binding between Pt atoms and the adsorbed carbonaceous intermediate species due to the synergistic effects including ensemble, strain and ligand effects [103]. The ensemble effects occur when various surface atoms like Pt-Ru alloy represent different mechanism of reactions for MOR. As stated before, the noble of Pt electrocatalyst always known the best monometallic metal specifically for MOR which can oxidize the methanol to the poisoning carbonaceous intermediate species (CO_{ads}) easily but the strongly binding of CO_{ads} and Pt metal makes it very difficult to get rid CO_{ads} and clean the Pt active sites, whereas with incorporation of the Ru atom can activate the H_2O (OH_{ads}) readily at a lower potential. Therefore, the combination of the two metals provides ensemble effects where the removal process of CO_{ads} more easily and the electrocatalytic activity of MOR

can greatly enhanced simultaneously. In addition, the ligand effects occur when the adjacent atoms with different electronegativity cause inducing the transfer of electron between the atoms and thus, the alteration involve on their electronic structure occurred. On the other hand, the strain effect occurred due to the mismatched superficial atoms arrangement and may result in compressed or stretched on the strain surface. Based on the literature review, the compressive strain tends to be induced when the Pt based alloy possesses a smaller atomic radius in which cause the improvement of MOR activity due to weakened affinity between carbonaceous intermediate species and Pt atoms. Sometimes all the ensemble, ligand and strain effects are co-existed that brought to the synergistic effect that would determine the improvement of electrocatalytic activity of MOR for the Pt based alloy nanostructures.

2.7.1 Bimetallic Pt and Non-Noble Metals

The production of anode electrocatalysts with highly electrocatalytic activity and lower cost for DMFC application is a great challenge. The main approaches to reduce the Pt usage and enhancing the electrocatalytic performance are through the alloying Pt metal with other transition metals and controlling the shape and structure of Pt-based NPs. In addition, the Pt and non-noble metals combination can increase the electrocatalytic efficiency and decrease the cost of the electrocatalyst. Moreover, the Pt atoms utilization efficiency can sharply increase through the integration with other metals. Currently, a number of various non-noble metals are investigated and studied by researchers particularly for Pt-based alloy electrocatalysts such as Co, Ni, Fe, Cu, Mn and Zn. Basically, some of Pt-based alloy electrocatalysts including the Pt-Cu, Pt-Fe, Pt-Ni and Pt–Co alloy electrocatalysts have the lower cost and more remarkable electrocatalytic performance compared with the other non-noble metals as well as exhibit improved electrocatalytic activities of MOR in comparison with the monometallic counterparts [89]. Meanwhile, the electrodeposition of support-less 3D foam of Cu on a carbon paper containing microporous layer by using the template of hydrogen bubbles and then displaced with the Pt through the simple immersion as reported by Kim et al., (2017). The gained Pt-Cu alloy electrocatalyst exhibited outstanding durability. In addition, the top of Co atom is the most preferable site for methanol adsorption as proved by Orazi et al., (2017). In this study, the C-O and O–H bonds are found out to be weakened while the C-H bonds are strengthened and consequently, the as-synthesized Pt–Co electrocatalyst is proven to be a better option to avoid the poisoning effect during MOR. Moreover, the fabrication of Pt alloy electrocatalysts depend on the architectures design with the surface of highly active and optimized expensive element utilization. Normally, the highly active surface of Pt-based alloy with low cost of transition metals could be fabricated by controlling the atomic ratio, morphology and structure through the various synthesis methods to attain better electrocatalytic performance and superior durability [89].

In another study, Yue et al., (2017) reported the fabrication of Pt@Cu NPs with low amount of Pt by an electrochemical method which demonstrated remarkable electrocatalytic performance including stability and reusability. Meanwhile, in recent

study, [150] reported an efficient strategy to synthesis of the hollow structures for Pt-Cu alloy tetradecahedrons (Pt-Cu TNs) by using Cu_2O tetradecahedral as the starting template with the Pt/Cu atomic ratio and the shell thickness under controlled. The obtained Pt-Cu TNs electrocatalyst possesses enhanced electrocatalytic activity, stability and high CO_{ads} tolerance ability significantly towards MOR compared with the commercial Pt black electrocatalyst. The results obtained can be attributed to the synergistic effect between Pt and Cu, higher surface area, rough surfaces and easy access for methanol to the surface of the electrocatalyst. Meanwhile, the fabrication of concave PtCo nanocrosses (PtCo CNCs) through a facile and effective route with the assistance of iminodiacetic acid (IDA) as the structure-directing agent to control the cross-like structure have been reported by Li et al. [55]. As shown by TEM image in Fig. 8a, the PtCo CNCs have constructed by six arms in 3D space with the concave octahedra surface bounded by high-index facets for every protruding

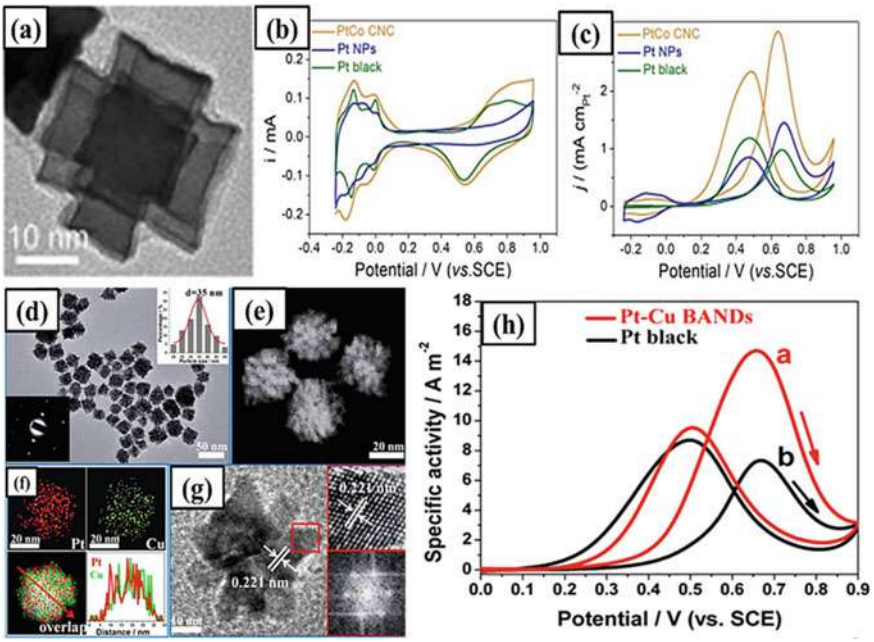

Fig. 8 **a** TEM image of PtCo nanocrystals, CV curves of PtCo CNC in 0.5 M H_2SO_4 solution **b**, 0.5 M H_2SO_4 + 1 M CH_3OH solution **c** at the scan rate of 50 mV/s (Li et al. [55]), **d** TEM image with low resolution of Pt-Cu BANDs; the inset located at the right top displays the corresponding Pt-Cu BANDs size distribution histogram and the inset on the left-bottom demonstrates the corresponding SAED pattern of Pt-Cu BANDs, **e** HAADF-STEM image of Pt-Cu BANDs, **f** EDX elemental mapping pattern of overlapping images and EDX line scanning profile for Pt-Cu BANDs, **g** HRTEM image of Pt-Cu BANDS with lattice fringe measurement; the inset at the right-top demonstrates magnified HRTEM images captured from the squares marked regions and the FFT pattern of crystalline grain in the inset was shown at the right-bottom, **h** CV curves of Pt-Cu BANDs **a** and commercial Pt black **b** in nitrogen saturated 0.5 M H_2SO_4 + 1 M CH_3OH solution at a scan rate of 50 mV/s [34, 66]

arm each protruding arm in which matching like theoretical models. In addition, the ECSA of PtCo CNCs obtained from the CV curves as shown in Fig. 8b was estimated to be 22.8 m^2 $g-1^{-1}$ in which slightly larger than PtNPs (18.2 m^2 $g-1^{-1}$) and Pt black (16.9 m^2 $g-1^{-1}$) indicating that the electrocatalytic active sites with large number were created through the surface of concave surrounded by high-index facets. Besides that, the as-synthesized PtCo CNCs exhibit more enhanced specific activity of 3.04 mA cm^{-2} in which 2.09 and 3.1 times higher than PtNPs (1.45 mA cm^{-2}) and commercial Pt black (0.98 mA cm^{-2}), respectively as indicated by the CV curves of MOR in Fig. 8c. Moreover, the E_{onset} of MOR for the PtCo CNCs shifted to negative direction around 140 mV compared with the PtNPs and commercial Pt black implying that the MOR more readily occur on the PtCo CNCs surface. Basically, the outstanding electrocatalytic performance of the PtCo CNCs electrocatalyst towards MOR can be related by the synergistic effect between the Pt and Co atoms in cross-like structure and the concave surface surrounded by high-index facets.

In different study, [34] reported the preparation of the bimetallic Pt-Cu alloy nanodendrites (Pt-Cu BANDs) through one-pot hydrothermal method without employ any template and seed in the existence of formaldehyde and poly (allylamine hydrochloride). In addition, the as-synthesized Pt-Cu BANDs exhibited a complete dendritic-like structure with well-dispersed and their average NPs size of about 35 nm suggesting the high-yield of nanodendrites formation as shown in TEM image from Fig. 8d. Besides that, the individual Pt-Cu BANDs also demonstrates the crystalline structure as indicated by SAED image located at the left-bottom in Fig. 8d. Every Pt-Cu BANDs comprise a 3D interconnected porous nanostructure which is possesses of smaller crystallites with the average diameters of around 3–6 nm as indicated by a high angle annular darkfield scanning TEM (HAADF-STEM) in Fig. 8e. Meanwhile, both Pt and Cu have uniform distribution in the shape of dendritic implying the formation of the Pt-Cu BANDs alloy as indicated by the patterns of elemental mapping and EDX line scanning profile from Fig. 8f. On the other hand, the huge number of crystalline grains correspond to their crystallographic orientations with the interplanar spacing of 0.221 nm was observed on the surface of Pt-Cu BANDs electrocatalyst as shown at the right-top in Fig. 8g in which smaller than the lattice spacing of FCC Pt crystal (0.226 nm) based on (111) plane, thereby indirectly approves the Pt-Cu alloy formation with perfectly (111) facets. Furthermore, the Pt-Cu BANDs was further confirmed to have (111) facets based on the six-fold rotational symmetry of the spots diffraction as indicated by the fast Fourier transform (FFT) pattern located at the right-bottom in Fig. 8g. In addition, the two obvious peaks that related to the typical feature of MOR from the CV curves in Fig. 8h were observed on both Pt-Cu BANDs and commercial Pt black electrocatalysts during the forward and backward scan directions. The Pt-Cu BANDs electrocatalyst have better electrocatalytic activity of MOR than the commercial Pt black since the specific current density value of 5.61 A m^{-2} was obtained by Pt-Cu BANDs in which 3.5 times higher than Pt black (1.62 A m^{-2}).

Therefore, according to the critical review on the previous of several reported works as discussed above, the optimization of Pt microstructure and lower amount of Pt for the binary Pt-based modified alloy electrocatalyst is basically necessary

to meet the requirement of the electrocatalytic performance and stability of DMFC. Meanwhile, the comparison study on the electrocatalytic performance of the previous reported anode binary Pt-based non-noble metal alloy electrocatalysts toward MOR in acidic media was tabulated in Table 2. The electrocatalyst performance of binary Pt-based alloy with non-noble metal electrocatalysts that listed in Table 2 showing an increasing trend in terms of ECSA and I_f/I_b ratio values as compared with the obtained results of unsupported monometallic electrocatalyst in Table 1 from the previous section. Thus, it is obviously proven that the alloying strategy of less amount Pt metal electrocatalyst with other non-noble metal provide the enhancement in Pt utilization efficiency in the addition of increasing electrocatalytic active sites and the poisoning effect tolerance during MOR.

2.7.2 Bimetallic Pt and Noble Metals

Conventionally, the Pt-Ru electrocatalysts are commonly employed at the anode of DMFC because of the capability of Ru metal in promoting the anti-poisoning properties of CO_{ads} for the nearby Pt atom [76]. The deposition of Ru atoms or clusters onto the Pt NPs would be an efficient approach to enhance both electrocatalytic activity and anti-poisoning ability. However, the stability is relatively poor under DMFC operating condition due to the exposed Ru metals on the surface tend to dissolve than embedded Ru in the crystal lattice. Furthermore, the Pt-Ru electrocatalyst cost is still relatively expensive for the DMFC commercialization since the Ru can be categorized as a noble metal (Gong et al. 2018). Meanwhile, the noble metal of Au also possesses high electrocatalytic activity for the oxidation of CO_{ads} at the nanoscale. The formed Pt-Au nanocatalysts exhibit the synergistic effects of electrocatalytic property in which the Pt electronic band's structure can be altered by changing the adsorption force surface. Thus, the significant improvement in both electrocatalytic activity and stability that could enhance the CO_{ads} tolerance on the Pt electrocatalysts are achieved as a result of the synergistic electrocatalytic effects. In addition, one of the most outstanding noble metal candidates for alloying with the Pt is Pd because of the similar lattice constant with identical facets allowing the formation of single crystallinity for bimetallic nanocrystals. Therefore, the addition of second noble metals like Ru, Au and Pd can reduce the Pt amount while enhancing and maintaining the high electrocatalytic activities and durability as well as increase the anti-poisoning of CO_{ads} properties.

Meanwhile, [73] reported and established the synthesis of Pt-Ru nanodendrites through one-pot co-reduction of Pt and Ru precursors in oleyamine by hydrogen gas. The TEM image in Fig. 9A demonstrates the high yield of Pt-Ru nanodendrites was produced with the shape uniformity. In addition, the HRTEM image of an individual Pt-Ru nanodendrite in Fig. 9B displays the morphology of dendritic obviously that assemble with staggered branches of around 6 nm in width as the building blocks. Furthermore, the Pt-Ru nanodendrites lattice fringes are extended across the arms without clear phase separation, displaying well mixing of Pt and Ru atoms. The Fourier filtered lattice fringe images of a single NP in Fig. 9C and D, can be assigned

Table 2 Comparison in electrocatalytic performance of MOR for unsupported bimetallic Pt alloy with non-noble metals electrocatalyst from previous studies

No	Electrocatalysts	Electrolytes	ECSA	Onset Potential (V)	Maximum forward peak current density/specific activity (I_f, mA cm^{-2})	I_f/I_b ratio	Scan rate (mV s^{-1})	References
1	$Pt_{71}Co_{29}$ LNFs	0.1 M $HClO_4$ + 0.5 M CH_3OH solution	29.79 $m^2\ g^{-1}$	0.48	2.51	–	50	[146]
2	PtCu	1.0 M CH_3OH + 0.5 M H_2SO_4 solution	53.7 $m^2\ g^{-1}$	–	0.32	1.13	50	[139]
3	1D aligned Pt-Ni	0.5 M CH_3OH + 0.5 M H_2SO_4 solution	100 $m^2\ g^{-1}$	–	0.89	1.40	50	[117]
4	Pt–Co nanowire	1.0 M CH_3OH + 0.5 M H_2SO_4 solution	81.1 $m^2\ g^{-1}$	–	1.07	–	50	[132]
5	Pt-Fe nanowire	1.0 M CH_3OH + 0.5 M H_2SO_4 solution	65.6 $m^2\ g^{-1}$	–	1.20	–	50	[133]
6	Pt-Ni	1.0 M CH_3OH + 0.5 M H_2SO_4 solution	–	0.22	55.4	1.14	10	[78]
7	Pt-Cu BANDs	0.5 M H_2SO_4 + 1 M CH_3OH solution	23.5 $m^2\ g^{-1}$	–	15.1 A m^{-2}	1.50	50	[34]
8	PtCo CNCs	0.5 M H_2SO_4 + 1 M CH_3OH solution	22.8 $m^2\ g^{-1}$	–	3.04	–	50	[66]
9	PtCu NFs	0.5 M H_2SO_4 + 0.5 M CH_3OH solution	63.7 $m^2\ g^{-1}$	0.465	25.8 A m^{-2}	1.43	50	[63]

(continued)

Table 2 (continued)

No	Electrocatalysts	Electrolytes	ECSA	Onset Potential (V)	Maximum forward peak current density/specific activity (I_f, mA cm^{-2})	I_f/I_b ratio	Scan rate (mV s^{-1})	References
10	PtCo MNs	0.5 M H_2SO_4 + 1.0 M CH_3OH solution	35.7 $m^2\ g^{-1}$	–	0.91	0.83	50	[112]
11	Pt–Cu TNs	1 M CH_3OH and 0.5 M H_2SO_4 solution	42.0 $m^2\ g^{-1}$	0.24	2.50	1.52	50	[150]
12	Octahedral PtCo NCs	0.5 M CH_3OH + 0.5 M H_2SO_4 solution	23.3 $m^2\ g^{-1}$	–	2.57	–	50	[21]
13	PtPb Concave nanocubes	0.1 M $HClO_4$ + 0.5 M CH_3OH solution	46.6 $m^2\ g^{-1}$	–	2.09	–	50	[37]
14	PtCu nanoframes	0.1 M $HClO_4$ + 1.0 M CH_3OH solution	41.3 $m^2\ g^{-1}$	–	2.35	–	20	[28]
15	HOH Pt-Ni NCs	0.5 M H_2SO_4 + 2 M CH_3OH solution	0.32 cm^2	–	1.71	–	50	[121]
16	Pt-Cu MONCs	0.5 M H_2SO_4 + 2 M CH_3OH solution	–	–	4.46	1.45	50	[77]
17	Nanotube-shaped PtFe intermetallics	0.5 M H_2SO_4 + 1 M CH_3OH solution	15.17 $m^2\ g^{-1}$	–	61.64 A m^{-2}	1.40	50	[147]
18	Radial Pt–Co NDs	0.5 M H_2SO_4 + 1.0 M CH_3OH solution	38.5 $m^2\ g^{-1}$	–	31.72	1.08	50	[38]
19	Pt-Ni HSNs	0.5 M H_2SO_4 + 1.0 M CH_3OH solution	44.5 $m^2\ g^{-1}$	–	45	–	50	[61]

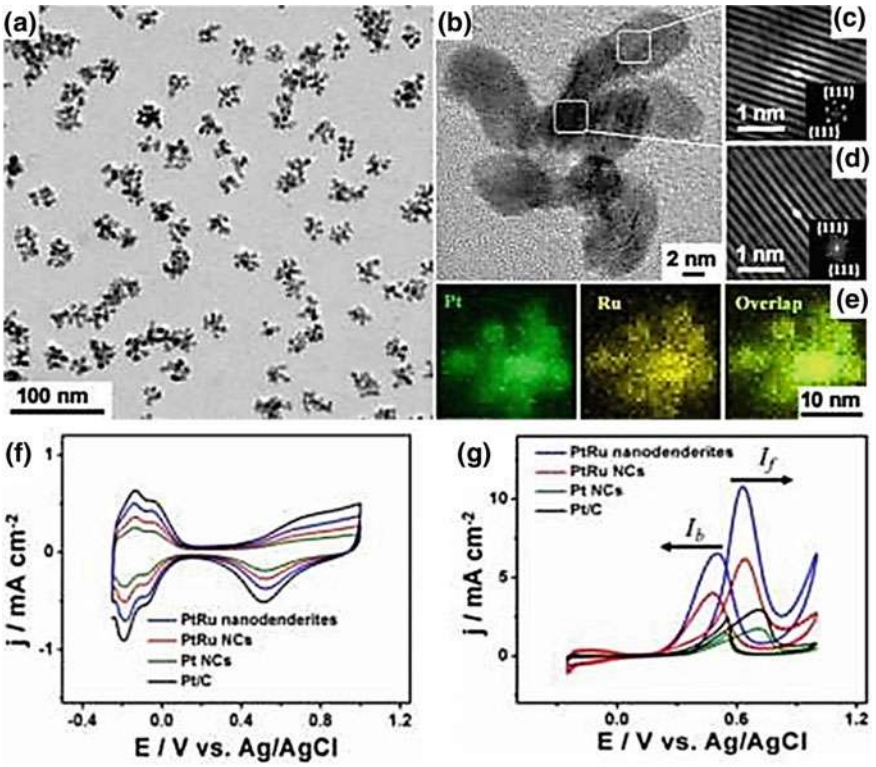

Fig. 9 **a** TEM image of PtRu nanodendrites, **b** TEM image with high magnification of a single PtRu nanodendrites; **c** and **d** The insets display the corresponding Fourier filtered lattice fringes patterns of the nanocrystal in the inner and outer area, respectively, **e** Elemental mapping images of a single PtRu nanodendrites, CV curves of the PtRu nanodendrites, PtRu NCs, Pt NCs and Pt/C catalysts measured in a saturated of **f** 0.1 M $CHClO_4$ solution, **g** 0.1 M $CHClO_4$ + 1 M CH_3OH solution at a scan rate of 50 mV/s [73]

to the (111) plane with the interlayer spacing of 0.23 nm for both outer and inner regions. In addition, the Pt-Ru alloy formation can be confirmed through the distribution of both Pt and Ru uniformly throughout the entire nanodendrites as displayed in Fig. 9E. On the other hand, the Pt-Ru nanodendrites possesses the high value of ECSA (40 m^2 g−1) in which larger than the PtRu nanocrystals (NCs) (29 m^2 g−1) and Pt NCs (16 m^2 g−1) as indicated from the CV curves in Fig. 9F that can be originated from the structure of multi-armed dendritic. Moreover, the as-synthesized P-Ru nanodendrites exhibit the remarkable electrocatalytic activity of MOR with the I_f value of 10.08 mA cm^{-2}, compared with the other Pt-Ru NCs, Pt NCs and commercial Pt/C electrocatalysts as illustrated by CV curves in Fig. 9G. The greater I_f/I_b ratio of Pt-Ru nanodendrites (1.66) was obtained compared with the PtRu NCs (1.5), Pt NCs (1.18) and Pt/C (1.2) indicating the excellent tolerance for poisoning species leading to facilitate the kinetics of MOR. The MOR more readily occurs on

the PtRu nanodendrites surface that results a great enhancement in the electrocatalytic performance can be attributted to the shape effect, high accessible surface area with porous structure, provide massive active electrocatalytic sites for the methanol molecules with facile diffusion into porous interior.

In another study, Zhang et al. [146] reported the synthesis of ultrafine PtRu dilute alloy nanodendrites (PtRu NDs) through the reduction of Ru^{III} ions induced by Pt metal. As demonstrated from TEM image in Fig. 10a, b, the PtRu NDs present good monodispersity with irregular dendritic nanostructure (4–7 branches) and a narrow size distribution (inset in Fig. 10a). From the results shown in Fig. 10c and d, both Pt and Ru element signals are uniformly distributed throughout the entire spatial range of PtRu NDs with much higher Pt content than Ru suggesting the homogeneous nanostructure. As exhibited from the CV curves of MOR results in Fig. 10e, PtRu

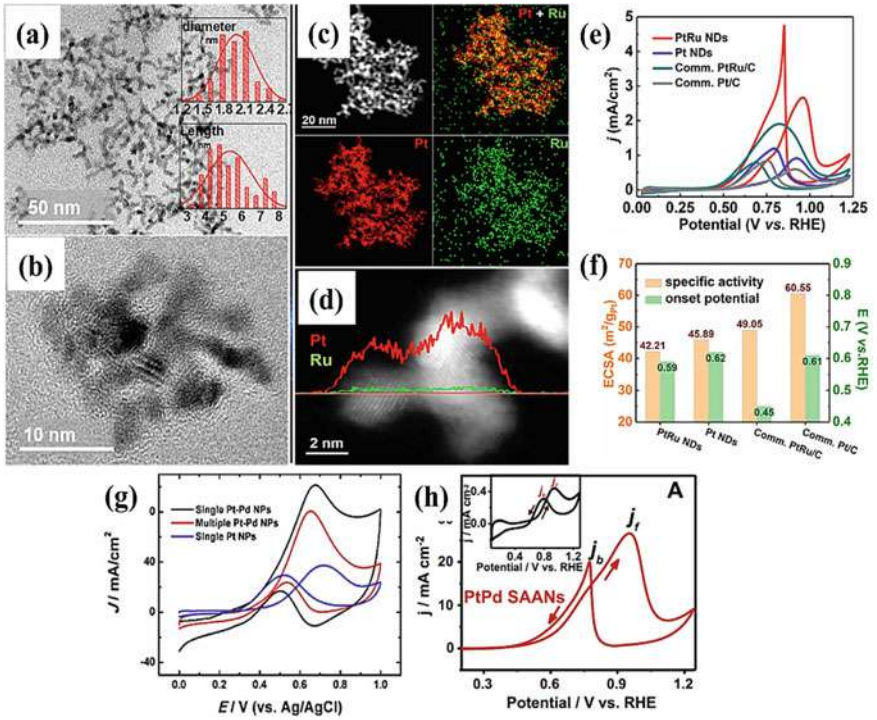

Fig. 10 **a** TEM image of PtRu NDs with included histograms demonstrate the distribution of the branches size in nanodendrites, **b** HRTEM image of PtRu NDs, **c** HAADF-STEM with EDX elemental mapping of the PtRu NDs, **d** EDX line-scanning profile of individual PtRu NDs, **e** CV curves of PtRu NDs, Pt NDs, commercial PtRu/C and commercial Pt/C toward MOR in 0.1 M $HClO_4$ + 0.5 M CH_3OH at a scan rate of 50 mV/s, **f** Histogram exhibit the specific activity, ECSA and onset potential value (versus RHE) of various catalysts, **g** CV curves of single Pt–Pd NPs, multiple Pt–Pd NPs and single Pt NPs responses toward MOR in 0.5 M CH_3OH + 0.5 M H_2SO_4 solution at a scan rate of 50 mV/s, **h** CV curves of PtPd SAANs and Pt black catalysts (inset) for MOR in 0.5 M H_2SO_4 + 0.5 M CH_3OH at a scan rate of 50 mV/s (Shi et al. 2017), [144, 100]

NDs displayed the highest I_f value of MOR (2.66 mA cm^{-2}) compared with the pure-Pt NDs (0.91 mA cm^2), commercial PtRu/C (1.90 mA cm^{-2}) and commercial Pt/C (0.60 mA cm^2) electrocatalysts. In addition, the ECSA value of the PtRu NDs, pure-Pt NDs, commercial PtRu/C electrocatalysts and commercial Pt/C are calculated to be 42.21 m^2/g, 45.89 m^2/g, 49.05 m^2/g and 60.55 m^2/g, respectively. The ECSA of pure Pt NDs is slightly higher than PtRu NDs as clearly shown in Fig. 10f, which can be attributed to the slightly higher length to diameter ratio in pure-Pt NDs and also the partial replacement of the active Pt sites by Ru atoms on the PtRu NDs surface. Additionally, the E_{onset} of PtRu NDs possesses negative shifted of around 0.03 V compared with the pure-Pt NDs, indicating the lower activation barrier of MOR on the PtRu NDs surface due to the effect of trace Ru atoms. However, the E_{onset} of PtRu NDs for MOR is higher than that of commercial PtRu/C.

Meanwhile, Tang and co-workers in 2019 reported the electrodeposition of single Pt–Pd NP by using single nanopore electrode as a template. Figure 10g shows the typical CV responses of MOR on the single Pt–Pd NPs (black curve), multiple Pt–Pd NPs (red curve) and single Pt NPs (blue curve). The I_f value of MOR is around 37.1, 81.2 and 102.0 mA·cm^{-2} for single Pt NPs, multiple Pt–Pd NPs and single Pt–Pd NPs, respectively. It can be observed obviously that the I_f value of the single Pt–Pd NPs is much larger than the single Pt NPs and multiple Pt–Pd NPs, indicating that the single PtPd NPs have remarkable electrocatalytic performance towards MOR. The excellent electrocatalytic activity of single Pt–Pd NPs towards MOR can also be obtained from its more negative E_{onset} (0.16 V) compared with the values using pure Pt NPs (0.32 V) and multiple Pt–Pd NPs (0.24 V). Besides that, Shi et al., (2017) reported the preparation of the bimetallic Pt–Pd sheet-assembled alloy networks (PtPd SAANs) through an eco-friendly one-pot aqueous approach using the l-glutamic acid as the green shape-director and weak-stabilizing agent at RT, without the involvement of any additive, seed, toxic or organic solvent. In addition, as indicated from CV curve results in Fig. 10h, the I_f value of PtPd SAANs (26.6 mA cm^{-2}) is much higher than Pt black (0.44 mA cm^{-2}), indicating the improved electrocatalytic activity of PtPd SAANs towards MOR which can be ascribed to the unique PtPd SAANs structures and the synergistic effects between Pt and Pd. Furthermore, the PtPd SAANs possesess the I_f/I_b ratios value of 1.43 in which higher than Pt black (1.41) reflecting the improved CO_{ads} poisoning tolerance of PtPd SAANs.

In 2017, Qiu and the teams reported the production of single crystalline mesoporous bimetallic PtPd NPs with a hollow interior and porous surface structure in the presence of Br^- and I^- ions through a facile hydrothermal one-pot synthesis method. The highly purity and uniform distribution of PtPd NPs with an average diameter of 31.5 nm was obtained successfully as displayed by SEM image (see Fig. 11a and inset). Besides that, in large view of SEM image, the PtPd NPs clearly exhibit a hollow interior with the porous surface structure (Fig. 11b, c). In addition, the mesoporous structure of the PtPd NPs can be clearly observed in TEM image shown in Fig. 11d. A typical HRTEM image recorded for the white square area marked on the single crystalline structure of PtPd NP in Fig. 11e clearly indicates the presence of continuous fringes with an orientation along the (100) zone axis and no obvious grain boundaries can be observed, indicating a good crystallinity of the PtPd NPs.

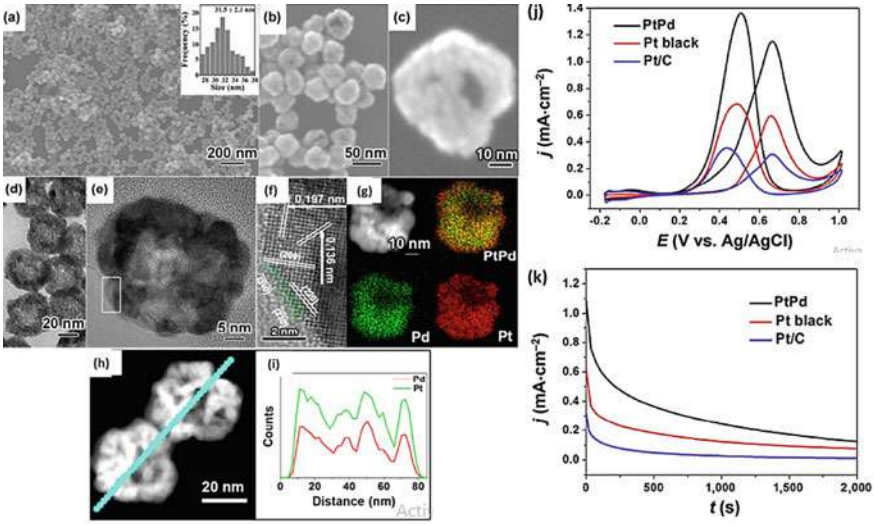

Fig. 11 **a–c** SEM images of the prepared mesoporous PtPd NPs with different resolutions; the inset in **a** displays the corresponding particle size distribution histrogram, **d** TEM image of the PtPd NPs, **e** HRTEM image of the single PtPd NPs, **f** Lattice fringes measurement for PtPd (2 0 0) and PtPd (2 2 0) planes, **g** HAADF-STEM-EDX mapping images of overlapping PtPd NPs, **h** HAADF-STEM image with the EDX cross-sectional compositional line profiles of the PtPd NPs, **j** CV curves of the as-synthesized PtPd NPs, commercial Pt black and Pt/C catalysts in a mixture of 0.5 M H_2SO_4 + 0.5 M CH_3OH solution at a scan rate of 50 mV/s, **k** Chronoamperometry curves of the PtPd NPs, commercial Pt black and Pt/C catalysts recorded at 0.65 V for 2000s in a mixture of 0.5 M H_2SO_4 + 0.5 M CH_3OH [85]

Moreover, the lattice fringes spacing of 0.197 and 0.136 nm can be indexed to the (200) and (220) planes of a fcc PtPd, respectively (Fig. 11f). Noticeably, the PtPd NPs are also enclosed by high index (340) and (230) planes in some surface atomic arrangement indicating a high number of low-coordinated surface sites, which might result in improved electrocatalytic activities of MOR.

Furthermore, the Pt and Pd are found to be homogeneously distributed on the mesoporous NPs as demonstrated by HAADF-STEM-EDS mapping image (Fig. 11g) and also the line scanning profile results in Fig. 11h confirm the formation of the PtPd alloy with hollow interiors. Based on the CV curves results in Fig. 11j, the highest calculated I_f value was obtained by the mesoporous PtPd NPs (1.15 mA cm^{-2}) compared with the commercial Pt black (0.59 mA cm^{-2}) and Pt/C (0.31 mA cm^{-2}). Meanwhile, from the chronoamperometric curves results in Fig. 11k, it can be seen that all the electrocatalysts undergo an initial rapid degradation of MOR current density, then continues to gradually decay because of the accumulation of toxic intermediates (CO_{ads}) on the Pt surface during MOR. The as-synthesized single crystalline mesoporous PtPd NPs exhibit the highest remaining MOR current density suggesting the enhanced electrocatalytic stability of MOR as compared with the commercial Pt black and Pt/C electrocatalysts.

Based on the several review of previous reported works above, it can be concluded that the use of unsupported bimetallic Pt-based alloy electrocatalysts with the addition of other noble metals provide a better choice for MOR than that of pure monometallic Pt electrocatalysts. Table 3 listed some of the previous research works on unsupported bimetallic Pt with noble metals electrocatalysts and their electrocatalytic performance towards MOR. It can be observed that all the electrocatalytic performance results in term of the ECSA, I_f and I_f/I_b ratio shows the significant improvement compared with the electrocatalytic performance results of the pure Pt monometallic electrocatalysts as listed in Table 1. The synergistic effect Pt-based alloy NPs contribute to the enhancement of electrocatalytic performance with a better poisoning-tolerance towards carbonaceous intermediate species (CO_{ads}) during MOR.

2.8 *Carbonaceous Materials as the Promising Pt Alloy-Based Electrocatalyst Supports for MOR*

In recent years, the development and optimization of new anode Pt alloy-based electrocatalysts for DMFC by using carbonaceous supports have been demonstrated a great progress. Some of the new nano/mesostructured carbonaceous materials play a vital role as the highly potential of electrocatalyst support materials. The combination of remarkable carbonaceous support material and Pt alloy-based electrocatalyst could display the breakthroughs in the research and development of a future new anode electrocatalyst for DMFC application. In addition, it is compulsory to reduce the Pt electrocatalyst amount since the Pt is an expensive noble metal. The major problems regarding the use of Pt electrocatalyst are including the poisoning effect by carbonaceous intermediate-like CO species during MOR and the poor of MOR kinetics could be overcome and prevented by utilizing the additional materials and various carbonaceous supports as stated by previously reported works. Meanwhile, a lot of studies on the reduction of Pt alloy-based electrocatalyst amount loading have been carried out in recent years to increase the efficiency of Pt electrocatalyst percentage utilization so that the electrocatalytic activity of Pt electrocatalyst toward MOR can be enhanced. The combination of Pt alloy-based electrocatalyst with various carbonaceous support materials could be a great anode electrocatalyst to be studied for future DMFC. There are various kind of carbon materials support sources like carbon black, carbon nanotubes, carbon nanofibers and graphene that have been employed together with Pt-based electrocatalysts to enhance the electrocatalytic performance of MOR and also play an important role in determining the degree of electrocatalyst dispersion, distribution, stabilization and the size of electrocatalyst nanoparticles. Therefore, the electrocatalyst support materials must possess some of the essential factors or characteristics such as large surface area for the electrocatalyst dispersion, high porosity, highly chemical stability at the relevant

Table 3 Comparison in electrocatalytic performance of MOR for unsupported bimetallic of Pt with nobel metals electrocatalyst from previous studies

No	Electrocatalysts	Electrolytes	ECSA	Onset Potential (V)	Maximum forward peak current density/specific activity (I_f, mA cm^{-2})	I_f/I_b ratio	Scan rate (mV s^{-1})	References
1	Pt–Pd NPs	0.5 M CH_3OH + 0.5 M H_2SO_4 solution	–	0.16	102	6.08	50	[100]
2	Pt–Ag DSNCs	0.5 M H_2SO_4 + 1.0 M CH_3OH solution	17.8 $m^2\ g^{-1}$	–	3.18	1.13	50	[128]
3	PtPd Hollow Nanocatalysts	0.1 M H_2SO_4 + 0.1 M CH_3OH solution	21.1 cm^2	–	0.19	1.31	50	[127]
4	PtRu nanoflowers	1.0 M CH_3OH + 0.5 M H_2SO_4 solution	18.9 $m^2\ g^{-1}$	–	1.62	1.03	50	[58]
5	PtRu nanodendrites	1.0 M CH_3OH + 0.1 M $HClO_4$ solution	40 $m^2\ g^{-1}$	–	10.08	1.66	50	[73]
6	$Pt_{48}Ag_{52}$ alloy nano-octahedra	1.0 M CH_3OH + 0.5 M H_2SO_4 solution	12 $m^2\ g^{-1}$	–	2.96	–	50	[33]

(continued)

Table 3 (continued)

No	Electrocatalysts	Electrolytes	ECSA	Onset Potential (V)	Maximum forward peak current density/specific activity (I_f, mA cm^{-2})	I_f/I_b ratio	Scan rate (mV s^{-1})	References
7	PtRu nanotubes	1.0 M CH_3OH + 0.1 M $HClO_4$ solution	9.4 ± 0.9 $m^2\ g^{-1}$	0.30	0.50	–	5	[152]
8	Pt–Ag nanourchin	0.5 M CH_3OH + 0.5 M H_2SO_4 solution	13.33 $m^2\ g^{-1}$	–	2.33	2.08	50	[140]
9	PtRh nanosponges	0.5 M H_2SO_4 + 1.0 M CH_3OH solution	32.9 $m^2\ g^{-1}$	–	1.23	1.20	50	[72]
10	PtRu nanowires	0.5 M CH_3OH + 0.1 M $HClO_4$ solution	72.1 $m^2\ g^{-1}$	–	1.16	–	50	[37]
11	PtPd NPs	0.5 M CH_3OH + 0.5 M H_2SO_4 solution	42.27 $m^2\ g^{-1}$	–	1.15	–	50	[85]
12	Pt–Ag hollow NCs	0.1 M $HClO_4$ + 1.0 M CH_3OH solution	52.1 $m^2\ g^{-1}$	–	1.15	1.53	50	[20]
13	3D Pt/Pd NSLs-WPAS	1.0 M CH_3OH + 0.5 M H_2SO_4 solution	46 $m^2\ g^{-1}$	–	2.08	–	100	[120]

(continued)

Table 3 (continued)

No	Electrocatalysts	Electrolytes	ECSA	Onset Potential (V)	Maximum forward peak current density/specific activity (I_f, mA cm^{-2})	I_f/I_b ratio	Scan rate (mV s^{-1})	References
14	Pt–Pd NPs	1.0 M CH_3OH + 0.5 M H_2SO_4 solution	31.59 $m^2\,g^{-1}$	–	0.67	1.32	50	[126]
15	Pd–Pt alloy concave nanocubes	1.0 M CH_3OH + 0.5 M H_2SO_4 solution	2.2 $m^2\,g^{-1}$	–	8.76	1.40	50	[137]
16	Pt–Ru nanowire network	1 M CH_3OH + 0.1 M $HClO_4$ solution	–	–	30.95	–	5	[54]
17	Pt–Ag	1.0 M CH_3OH + 0.1 M H_2SO_4 solution	27.88 $m^2\,g^{-1}$	0.44	0.80	1.40	50	[86]
18	PtRu nanodendrites	0.5 M CH_3OH + 0.1 M $HClO_4$ solution	42.21 $m^2\,g^{-1}$	–	2.66	–	50	[144]

temperatures, high electrochemical stability under operating conditions and excellent electrical conductivity and good water handling capability for easy recovery and to avoid flooding [92].

2.9 *Carbonaceous Materials Supported Bimetallic Pt Alloy Electrocatalyst*

The carbonaceous supported bimetallic Pt-based alloy NPs are widely investigated and extensively employed actively as anode electrocatalysts toward MOR in acidic media. The use of supports can enhance the dispersity, surface area, stability and reduce the cost, thereby providing a better candidate for MOR. The electrocatalytic performance of the carbonaceous supported bimetallic Pt-based alloy electrocatalyst relies mainly on the support material characteristics and the interaction between Pt-based alloy and carbonaceous support material. In addition, the carbonaceous supporting material give the impacts of particle size distribution that leads to further effect on the electrocatalytic activity of MOR. Furthermore, the carbonaceous supporting materials play a critical role in the process of electrocatalytic activity of MOR by providing the new active sites and enhance the physical and chemical properties of electrocatalyst. In this section, the effect of morphology, composition and structure of carbonaceous bimetallic Pt-based alloy electrocatalyst on the electrocatalytic activity and stability for MOR are thoroughly discussed. Moreover, a considerable number of literatures has focused and discussed on understanding the impact of carbonaceous-based materials as electrocatalyst support for DMFC application. Meanwhile, Table 4 summarises the previous research works regarding the comparison of electrocatalytic performance by various carbonaceous materials supported bimetallic Pt-based alloy electrocatalysts toward MOR. In general, it can be observed and noticed that the ECSA, I_f and I_f/I_b ratio value of the carbonaceous supported bimetallic Pt-based alloy electrocatalysts are significantly larger and outstanding compared with the value obtained by unsupported bimetallic alloy electrocatalysts as shown in Tables 2 and 3.

In previous study, Vinayan et al. (2016) reported the preparation of PtAu alloy NPs that dispersed over various chemically modified carbon supports by sodium-borohydride assisted modified polyol reduction method. The surface-modification of graphene nanosheets (f-G), multi-walled carbon nanotubes (f-MWNTs) and (graphene nanosheets-carbon nanotubes) hybrid support (f-GMWNTs) were synthesized by soft functionalization method using a cationic polyelectrolyte poly-(diallyldimethyl ammonium chloride). In addition, Fig. 12a depict the TEM image of f-G-MWNTs hybrid structure showing that the MWNTs are adjacent in between graphene sheets which can act as the spacers between graphene sheets to avoid agglomeration and improving the interconnectivity between the MWNTs and graphene sheets supports. On the other hand, the TEM images in Fig. 12b, c, exhibit the uniform dispersion of Pt and PtAu alloy NPs over f-G-MWNTs hybrid supports,

Table 4 Comparison in electrocatalytic performance of MOR for the carbonaceous materials-supported bimetallic Pt-based alloy electrocatalysts from the previous reported work

No	Electrocatalysts	Electrolytes	ECSA	Onset Potential (V)	Maximum forward peak current density/specific activity (I_f, mA cm^{-2})	I_f/I_b ratio	Scan rate (mV s^{-1})	References
1	Co@Pt/MWCNTs	0.2 M CH_3OH + 0.5 M KOH solution	69.2 m^2/g	–	26.5	–	50	[3]
2	Pt-Au-RGO	1.0 M $HClO_4$ + 1.0 M CH_3OH solution	57.7 m^2/g	–	14.0	2.23	50	[108]
3	PtCu/graphdiyne	1.0 M CH_3OH + 0.5 M H_2SO_4 solution	94.5 m^2/g	–	0.35	1.47	50	[139]
4	Pt/Co(1:9)/RGO	2.0 M CH_3OH + 1.0 M H_2SO_4 solution	320.38 cm^2/g	0.378	38.02	1.05	20	[11]
5	Au-Pt NPs/V	0.5 M CH_3OH + 1.0 M NaOH solution	29.67 m^2/g	– 0.65	5.68	–	100	[16]
6	PtOs-1/C	1.0 M CH_3OH + 0.5 M H_2SO_4 solution	52 m^2/g	–	0.98	1.50	20	[60]

(continued)

Table 4 (continued)

No	Electrocatalysts	Electrolytes	ECSA	Onset Potential (V)	Maximum forward peak current density/specific activity ($I_{f,}$ mA cm^{-2})	I_f/I_b ratio	Scan rate (mV s^{-1})	References
7	Au-Pt NPs/AETGO/GCE	0.5 M CH_3OH + 0.1 M $HClO_4$ solution	104.7 $m^2\ g^{-1}$	–	9.5 ± 0.09 A cm^{-2}	1.73	50	[129]
8	Pt-Fe/RGO	1.0 M CH_3OH + 0.5 M H_2SO_4 solution	18 m^2/g	–	4.67	3.00	20	[31]
9	RGO/PANI/Pt-Cu	1.0 M CH_3OH + 0.5 M KOH solution	35.7 m^2/g	−0.54	60.41	–	50	[53]
10	Pt/Co-coal-carbon nanofiber	0.5 M CH_3OH + 0.5 M H_2SO_4 solution	–	0.10	3.3 A m^{-2}	–	–	[79]
11	PtRu@WMC-F7	1.0 M CH_3OH + 0.5 M H_2SO_4 solution	–	–	36.4	–	50	[69]
12	PtRu/Nitrogen-doped Graphene	1.0 M CH_3OH + 0.5 M H_2SO_4 solution	82.5 m^2/g	0.29	6.2 A m^{-2}	–	50	[122]
13	PtRu/3D GF	1.0 M CH_3OH + 0.5 M H_2SO_4 solution	186.2 m^2/g	–	109.3	1.14	50	[51]
14	Pt–Sn/graphene	2.0 M CH_3OH + 0.5 M H_2SO_4 solution	57.89 m^2/g	0.378	1.703	1.341	20	[114]

(continued)

Table 4 (continued)

No	Electrocatalysts	Electrolytes	ECSA	Onset Potential (V)	Maximum forward peak current density/specific activity (I_f, mA cm^{-2})	I_f/I_b ratio	Scan rate (mV s^{-1})	References
15	PtSn(70:30)/C-PANI	1.0 M CH_3OH + 0.5 M H_2SO_4 solution	58.2 m^2/g	–	200	–	50	[5]
16	Pt-Fe/MWCNTs	1.0 M CH_3OH + 0.5 M H_2SO_4 solution	–	0.30	86	1.5	100	[90]
17	PtCo/graphene	2.0 M CH_3OH + 1.0 M H_2SO_4 solution	75.8 m^2/g	–	35.8	1.28	20	[36]
18	PtNi/ graphene	1.0 M CH_3OH + 0.5 M H_2SO_4 solution	70.2 m^2/g	0.3782	4.87	–	50	[125]
19	Ni_{50}/Pt/CNFs	1.0 M CH_3OH + 0.5 M H_2SO_4 solution	–	0.43	10.9	1.60	–	[22]

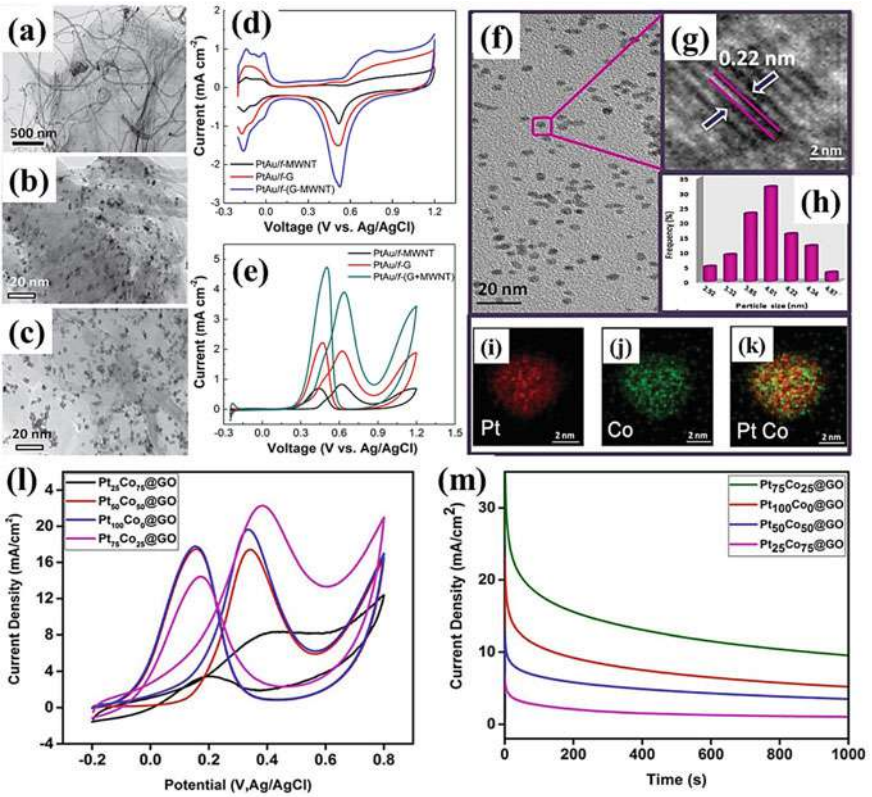

Fig. 12 TEM images of **a** f-G-MWNTs, **b** Pt/f-G-MWNTs and **c** PtAu/f-G-MWNTs, CV curves of PtAu/f-MWNTs, PtAu/f-G and PtAu/f-G-MWNT in **d** 0.5 M H_2SO_4 solution and **e** 0.5 M H_2SO_4 + 1 M CH_3OH solution at a scan rate of 20 mV/s, **f** TEM and **g** HRTEM images of $Pt_{75}Co_{25}$@GO NPs with lattice fringe measurement, **h** the particle size distribution histogram, **i, j** Elemental mapping analysis of **i** Pt, **j** Co and **k** overlapping $Pt_{75}Co_{25}$, **l** CV curves result during MOR of the $Pt_{100-x}Co_x$@GO catalysts conducted in a saturated nitrogen of 0.5 $_M$ H_2SO_4 + 0.5 M CH_3OH solution at 25 °C under a scan rate of 50 mV/s, **m** Chronoamperometry curves obtained during MOR of the $Pt_{100-x}Co_x$@GO catalysts in nitogen saturated of 0.5 $_M$ H_2SO_4 + 0.5 M CH_3OH solution at 25 °C under fixed voltage of 0.4 V (Vinayan et al., 2016; Burhan et al., 2020)

respectively. The f-G-MWNTs hybrid support possesses ordered mesoporous structure with 3D interconnected pores facilitate the reactants move to the deep interior portions of the carbonaceous support and electrocatalyst NPs, thereby increasing the three-phase boundary. Meanwhile, the ECSA values PtAu/f-MWNTs, PtAu/f-G and PtAu/f-G-MWNTs electrocatalysts were estimated from CV curves in Fig. 12d and found to be ~30 m^2 g^{-1}, ~63 m^2 g^{-1} and ~96 m^2 g^{-1}, respectively. Obviously, the ECSA values for PtAu electrocatalysts changed according to the morphology of carbonaceous electrocatalyst supports and the PtAu/f-G-MWNTs electrocatalyst achieve the highest ECSA value in which can produce a greater number of Pt active

sites. From the CV curves in Fig. 12e, the PtAu/f-G-MWNTs hybrids electrocatalyst obtain the highest I_f value of MOR as compared with the PtAu/f-MWNTs and PtAu/f-G. The carbonaceous supporting materials with large surface area offer better dispersion of the electrocatalysts and promotes the interaction of electrocatalyst NPs-carbon support that prevents the electrocatalysts NPs agglomeration. Therefore, both an active electrocatalyst and outstanding supporting material with strongly interaction are crucial and required to enhance the MOR activity.

In recent study, Burhan et al. (2020) reported the fabrication of the graphene oxide-based platinum-cobalt nanoparticles ($Pt_{100-x}Co_x$@GO NPs) with different Pt/Co ratio as an efficient electrocatalyst for MOR. From the HRTEM image of $Pt_{75}Co_{25}$@GO NPs in Fig. 12g, it can be observed that the particles are generally spherical shape and do not agglomerate. Furthermore, the atomic lattice fringes measurement of the monodisperse $Pt_{75}Co_{25}$ NPs as shown in Fig. 12h was determined in a range of 0.22 nm for Pt (111) plane and the mean particle size was found to be 4.01 ± 0.51 nm. Further, the TEM–EELS mapping of $Pt_{75}Co_{25}$@GO NPs in Fig. 12i–k, confirms the alloy composition of Pt and Co formation with evenly distributed throughout the entire electrocatalyst. Meanwhile, based on the CV curves results in Fig. 12l, the best electrocatalytic performance with the highest If value was obtained by the $Pt_{75}Co_{25}$@GO electrodes in which 1.27, 1.44 and 2.94 times higher than $Pt_{100}Co_0$@GO, $Pt_{50}Co_{50}$@GO and $Pt_{25}Co_{75}$@GO electrocatalysts, respectively. Besides that, excellent distribution of the Pt_Co alloy electrocatalyst on GO leads to an enhancement in the electrocatalytic performance of $Pt_{100-x}Co_x$@GO with the positive impact of GO utilization. On the other hand, it can be concluded that the peak current density decreases with the whole-time stability testing for all the prepared electrocatalysts, as demonstrated in Fig. 12m. However, the $Pt_{75}Co_{25}$@GO NPs electrocatalyst still exhibit the higher electrocatalytic activity and stability compared with other $Pt_{100-x}Co_x$@GO electrocatalysts after 3600 s.

In 2016, Vilian and the research teams reported the synthesis of Pt-AuNPs-RGO electrocatalyst through a simple strategy of chemical reduction reaction by using sodium borohydride as chemical reducing agent. The STEM image with EDX elemental mapping and the line profile of a single Pt-Au-RGO composite electrocatalyst (Fig. 13a) indicates that the Pt and Au NPs were finely dispersed on the RGO sheets surface. In addition, based on the desorption peaks from the CV curves in Fig. 13b, the Pt-Au-RGO electrocatalysts exhibited the higher ECSA value (57.7 m^2 g−1) than the Pt-RGO (40.5 m^2 g−1) and Pt/C electrocatalysts (10.9 m^2 g−1) because of the uniform structure and highly decorated rate of Pt on the Au-RGO electrocatalysts resulting the higher accessible surface area and conductivity to facilitates the transport of electron as well as increase the acceleration of the mass-transfer kinetics at the electrode surface which consequently enhance the electrocatalytic activity of the Pt-Au-RGO electrocatalysts. From the CV curves results as displayed in Fig. 13c, it can be noticed that the electrocatalytic activity of Pt-Au-RGO electrocatalyst towards MOR is more outstanding than the Pt-RGO and Pt/C electrocatalysts due to the excellent binding capability between the chemical functional groups on the RGO surface and the positively charged Au^{3+}. In addition, the highly loading of Pt NPs on Au-RGO can facilitate electron transport and result in higher electrocatalytic

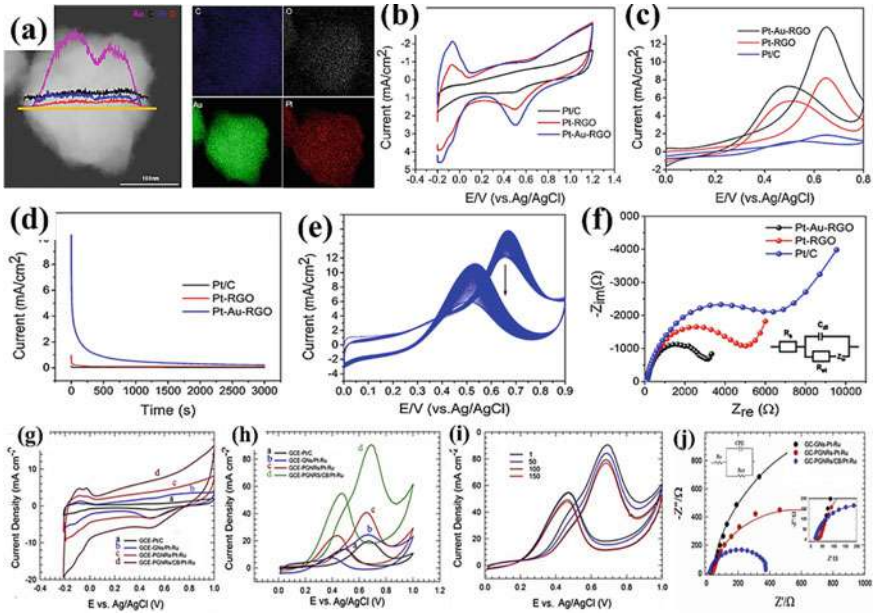

Fig. 13 **a** EDX line scanning profiles and mapping images analysis of Pt-Au-RGO catalyst, CV curves obtained for Pt/C, Pt-RGO and Pt-Au-RGO catalysts in a nitrogen saturated of **b** 1 M $HClO_4$ and 1 $_M$ $HClO_4$ + 1 M CH_3OH solutions at a scan rate of 50 mV/s, **d** Chronoamperometry curves of Pt/C, Pt-RGO and Pt-Au-RGO catalysts at 0.5 V in a 1 M $HClO_4$ + 1 M CH_3OH solution for 3000 s, **e** CV curves of Pt-Au-RGO catalyst modified electrode with 200 cycles in a nitrogen saturated of 1 M $HClO_4$ + 1 M CH_3OH solution at a scan rate of 50 mV/s, **f** Nyquist plots obtained from EIS for Pt/C, Pt-RGO and Pt-Au-RGO catalysts toward MOR in 1 M $HClO_4$ + 1 M CH_3OH solution at amplitude of 5 mV; inset is the Randles circuit, **g** CV curves obtained for GCE-Pt/C **a**, GCE-GNs-Ar/Pt-Ru **b**, GCE-GNs-Ar/Pt-Ru **c**, and GCE-PGNRs/CB/Pt-Ru **d** in Argon saturated of 0.5 M H_2SO_4 solution, **h** CV curves obtained toward MOR for GCE-Pt/C **a**, GCE-GNs-Ar/Pt-Ru **b**, GCE-GNs-Ar/Pt-Ru **c**, and GCE-PGNRs/CB/Pt-Ru **d** in Argon saturated of 0.5 M H_2SO_4 + 1 M CH_3OH solution, **i** Nyquist plots of GCE-Pt/C **a**, GCE-GNs-Ar/Pt-Ru **b**, GCE-GNs-Ar/Pt-Ru **c**, and GCE-PGNRs/CB/Pt-Ru **d** obtained from EIS at EDC = 0.4 V in the range of 10 kHz to 0.1 Hz with the amplitude of 5 mV; inset demonstrates the equivalent circuit model used, **j** The long-term stability of GCE-PGNRs/CB/Pt-Ru catalyst in 0.5 M H_2SO_4 + 1 M CH_3OH solution [108], Torabi et al., 2018

activity of MOR. From Fig. 13d, an initial rapid decrease in the decay current density for all of the Pt-RGO, Pt/C, and Pt-Au-RGO electrocatalysts occur due to the formation of poisoning carbonaceous reactive intermediate species like CO_{ads}, $COOH_{ads}$ and CHO_{ads} during MOR. The Pt-Au-RGO electrocatalyst remain the highest current density after complete testing duration of 3000 $_s$, indicating the superior electrocatalytic performance with good tolerance of the carbonaceous intermediate species-like CO_{ads} during MOR.

Besides that, it can be seen obviously that the I_f value increased with increasing the number of scans at the beginning and then drop gradually with further rising of the cycle number, as represented in Fig. 13e. The as-prepared Pt-Au-RGO electrocatalyst

remained as high of 88% of its initial peak current density value and possessed the higher electrocatalytic stability which can be ascribed to the strong interaction between Pt and RGO after the addition of Au, that leads to more resistance toward CO_{ads}-poisoning during MOR. Meanwhile, Fig. 13f displays the EIS Nyquist plots of the Pt-RGO, Pt/C and Pt-Au-RGO electrocatalysts that contain semicircle portion with fitted curves according to the equivalent circuit (inset in Fig. 13f) for MOR. It can be observed that the Pt-RGO electrocatalyst have a significant increase of Rct which can be attributed to the formation of a large amount of CO_{ads} and OH_{ads} on its surface. Therefore, the loading of Pt NPs on Au-RGO can improve the electron-transfer reaction, which indicates an excellent composite electrocatalyst for MOR on its surface.

In different study, Torabi et al., (2018) reported the preparation of GCE-PGNRs/CB/Pt-Ru alloy nanoclusters electrocatalyst via electrodeposition method. Based on the obtained CV curves in Fig. 13g, the ECSA values of 32.3, 41.6, 72.2 and 116.5 m^2 $g-1$ were estimated for the GCE-Pt/C, GCE-GNs-Ar/Pt-Ru, GCE-PGNRs/Pt-Ru, and GCE-PGNRs/CB/Pt-Ru, respectively. The large ECSA of GCE-PGNRs/CB/Pt-Ru obtained can be attributed to well distributed and interconnected nanocluster structures of the Pt-Ru, leading to a fast electrochemical accessibility of electrocatalytic regions on the surface of the electrode. As indicated by CV curves of MOR in Fig. 13h, the I_f value obtained on the modified electrodes demonstrates the order of GCE-PGNRs/CB/Pt-Ru > GCE-PGNRs/Pt-Ru > GCE-GNs-Ar/Pt-Ru > GCE-Pt/C. In addition, the E_{onset} value of MOR for the GCE-PGNRs/CB/Pt-Ru (+0.270 V) is more negative than the GCE-PGNRs/Pt-Ru (+0.360 V), GCE-GNs-Ar/Pt-Ru (+0.420 V) and GCE-Pt/C (+0.460 V), respectively. Meanwhile, the If/Ib ratio for GCE-PGNRs/CB/Pt-Ru is 2.10 indicating a better tolerant toward CO poisoning effect compared with the GCE-PGNRs/Pt-Ru (1.7) and GCE-Pt/C (1.5), respectively. In addition, the long-term stability of GCE-PGNRs/CB/Pt-Ru toward MOR was determined based on the chronoamperometric curves in Fig. 13I in which displaying the partially decreases of the electrocatalytic activity with the number of cycles up to 150 and then, maintains outstanding with further scans. The results of remarkable electrocatalytic activity and stability of the GCE-PGNRs/CB/Pt-Ru electrocatalyst can be related to several characteristics including the CB as electrocatalyst support that can improve the MOR activity of GCE-PGNRs/CB/Pt-Ru electrocatalyst by reducing the aggregation between PGNRs layers and provides the rapid operative routes for the electrolyte transport. Based on the Nyquist plots from EIS study that displayed as fitted curves according to equivalent circuit (inset) as demonstrated in Fig. 13j, both the R_s and R_{ct} are decreased upon addition of CB to PGNRs indicating the enhancement electrolyte transport that leads to increase the MOR rate. Besides that, the appearance of Ru could produce the OH^- species with the huge number at low overpotential and help the H^+ transport during MOR and thereby, reduce the poisoning effect of carbonaceous intermediate species mainly CO_{ads} on the Pt surface.

2.10 Carbonaceous Materials Supported Bimetallic Pt–Pd Alloy Nanocomposite Electrocatalyst

Recently, [124] reported one-step synthesis of the octahedral PtPd alloy/RGO (o-PtPd/RGO) nanocomposites through the plasma reduction method. The ECSA of the o-PtPd/rGO electrocatalyst (253.96 cm^2mg^{-1}) was estimated from the CV curves in Fig. 14a which is 2.9 times higher than the commercial Pt/C catalysts (87.74 cm^2mg^{-1}) that can be attributed to the increased loading of the PtPd NPs, the large defects, corners and edges number of the octahedral PtPd alloy structure, the synergistic effect of the PtPd alloy and the high stability of the RGO support. In addition, according to the results of CV curves in Fig. 14b, obviously, the higher I_f value of MOR for the o-PtPd/rGO electrocatalyst was obtained in comparison with the other

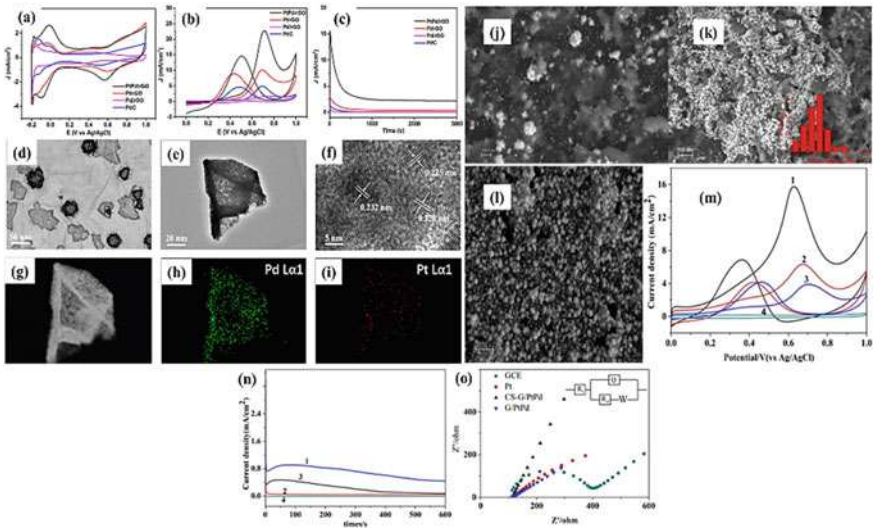

Fig. 14 CV curves obtained for PtPd/RGO, Pt/RGO, Pd/RGO and commercial Pt/C catalysts modified electrodes in **a** 0.5 M H_2SO_4 solution, **b** 0.5 M H_2SO_4 + 1 M H_2SO_4 solution at a scan rate of 50 mV/s, **c** Chronoamperometry curves obtained toward MOR for PtPd/RGO, Pt/RGO, Pd/RGO and commercial Pt/C catalysts modified electrodes at fixed of 0.6 V in 0.5 M H_2SO_4 + 1 M H_2SO_4 solution, **d**, **e** TEM with different magnification and **f** HRTEM images of the as-prepared o-PtPd/RGO nanocomposite catalyst; lattice fringes measurement of PtPd alloy correspond to (1 1 1) planes, **g** HAADF-STEM image and **h**, **i** EDX mapping of Pd and Pt in a single octahedral PtPd NP, **j–l** SEM images of Pt/CS-G/GCE, Pt–Pd/CS-G/GCE, and Pt–Pd/G/GCE catalysts, respectively **m** CV curves of MOR for Pt–Pd/CS-G/GCE (black, 1), Pt/CS-G/GCE (red, 2), Pt–Pd/G/GCE (blue, 3) and Pd/CS-G/GCE (pink, 4) in nitrogen-saturated 1 M H_2SO_4 + 1 M CH_3OH solution at a scan rate of 50 mV/s, **n** Chronoamperometric curves based on time-dependent current density for for Pt–Pd/CS-G/GCE, Pt/CS-G/GCE, Pt–Pd/G/GCE and Pd/CS-G/GCE in nitrogen-saturated 1 M H_2SO_4 + 1 M CH_3OH solution at a scan rate at 0.4 V, **o** Nyquist plots from EIS result for GCE, Pt/CS-G/GCE, Pt–Pd/G/GCE and Pt–Pd/CS-G/GCE electrodes in 0.1 M KCl + 0.005 M $[Fe(CN)_6]^{4-/3-}$ electrolyte solution [123, 124]

electrocatalysts. The E_{onset} of the o-PtPd/rGO electrocatalyst (0.31 V) with more negative value was achieved compared with the Pt/RGO (0.41 V), Pd/RGO (0.58 V) and commercial Pt/C (0.49 V). Moreover, the I_f/I_b ratio value of the o-PtPd/RGO catalyst was calculated to be 1.56, which is higher than the Pt/RGO (1.13), Pd/RGO (1.54) and Pt/C (1.05), revealing the enhancement of the CO_{ads} tolerance during MOR. All the I_f, E_{onset} and I_f/I_b results lead to the outstanding electrocatalytic performance of the o-PtPd/rGO electrocatalyst that mainly attributed to the synergistic effects of the PtPd alloy and the RGO support. Meanwhile, from the chronoamperometric results in Fig. 14c, the initial and final current densities of the o-PtPd/rGO electrocatalyst were obviously much higher, while the slower decline rate was achieved compared with the commercial Pt/C, indicating reliable stability for long-term operation.

Figure 14d displays the TEM image of o-PtPd/rGO electrocatalyst showing the uniformly decoration of the octahedral PtPd alloy NPs on the RGO surface. The available of large amount of oxygen containing functional groups on the GO serves the nucleation sites for the o-PtPd alloy NPs growth. The migrated and accumulated Pt and Pd nanocrystal nuclei form the nanoclusters with stacking faults around the octahedral PtPd alloy with a driving force provided to promote the growth and formation of the octahedral PtPd alloy. In addition, as shown by TEM image in Fig. 2–20e, the individual PtPd alloy NP had an octahedral-like structure with many surface defects, corners and edges that can enhance the electrocatalytic performance of MOR. In addition, Fig. 14f shows the dense lattice fringes with the measured lattice spacing were around 0.225 nm, 0.228 nm and 0.232 nm corresponded to the (111) planes of the fcc PtPd alloy. Figure 14g–l shows the HAADF-STEM images of an individual o-PtPd NP confirming the PtPd alloy formation with abundant Pd and a relatively less Pt amount that was uniformly distributed in the alloy

In another study, [123] developed a fast method of in-situ electrochemical reduction incorporated with the carbon radical reaction to synthesize highly dispersed Pt–Pd NPs on the functionalized graphene. It can be observed that spherical Pt–Pd co-loaded catalysts are obtained on the CS-G/GCE as represented by the SEM image of the resultant Pt–Pd/CS-G/GCE in Fig. 14j and the range size of the Pt–Pd co-loaded CS-G/GCE electrocatalysts are around 40 to 90 nm where the smaller in size as compared with the Pt–Pd catalysts on G/GCE (Fig. 14k). The smaller size of the Pt–Pd co-loaded electrocatalysts on the RGO surface could provide the binding sites for anchoring the Pd ions precursor through the coordination reaction, which is advantages to the metal NPs loading with controllable feature size. As can be seen from SEM images in Fig. 14l, the range size of the Pt spherical electrocatalysts are around 40 nm to 200 nm and show significant aggregation, as compared with the Pt–Pd electrocatalysts on CS-G/GCE. It means that well dispersed Pd electrocatalysts may act as dispersants for Pt and Pd NPs co-deposition. As observed from the CV curves in Fig. 14m, the I_f value of the Pt–Pd /CS-G/GCE electrocatalyst towards MOR is about 15.7 mA/cm^2, in which 4 and 2.5 times larger than that of Pt–Pd/G/GCE (3.91 mA/cm^2) and Pt/CS-G/GCE (6.34 mA/cm^2), respectively. This clearly demonstrates that the Pt–Pd/CS-G/GCE electrocatalyst exhibits outstanding electrocatalytic activity towards MOR. The higher electrocatalytic activity of Pt–Pd/CS-G/GCE than Pt/CS-G/GCE can be due to the synergetic effects between

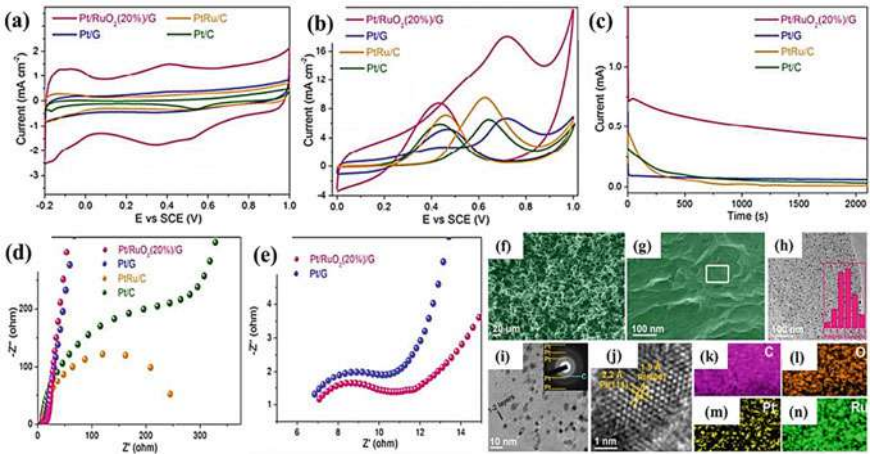

Fig. 15 CV curves of the Pt/RuO_2 (20%)/G, Pt/G, PtRu/G and Pt/C catalysts in **a** 1 M H_2SO_4 solution and **b** 1 M H_2SO_4 + 2 M CH_3OH solution at a scan rate of 20 mV/s, **c** Chronoamperometric curves of the Pt/RuO_2 (20%)/G, Pt/G, PtRu/G and Pt/C catalysts measured at 0.5 V in 1 M H_2SO_4 + 2 M CH_3OH solution for 2000s, **d** and **e** Nyquist plots from EIS studies for Pt/RuO_2 (20%)/G, Pt/G, PtRu/G and Pt/C catalysts in 1 $_M$ H_2SO_4 + 2 M CH_3OH solution, FESEM **f**, **g** and TEM images **h**, **i** of Pt/RuO_2 (20%)/G catalyst; inset in **h** demonstrate the particle size distribution histogram and inset in **i** shows the SAED pattern, **j** HRTEM image of Pt/RuO_2 (20%)/G catalyst reveal the lattice fringes for PtNPs, Elemental mapping images of C **k**, O **l**, Pt **m** and Ru **n** obtained from squared region marked in **g** [40]

the Pt and Pd electrocatalysts. In addition, the higher I_f/I_b value (2.27) of Pt–Pd/CS-G/GCE than Pt/CS-G/GCE (1.53), indicating more facile and effective MOR occurs on Pt–Pd/CS-G/GCE with less accumulation of carbonaceous intermediate CO_{ads}-like species on its surface. Meanwhile, based on the time-dependent current density curve in Fig. 14n, the remaining current density value of Pt–Pd/CS-G/GCE is about 2 and 24 times higher than the Pt–Pd/G/GCE and Pt/CS-G/GCE, respectively, further implying that the Pt–Pd/CS-G/GCE electrocatalyst have remarkable electrocatalytic activity towards MOR. In addition, the excellent long-term stability of Pt–Pd/CS-G/GCE, indicating good poisoning-tolerant towards carbonaceous intermediate species during MOR. Besides that, the sequence of Rct value based on semicircle diameter of Nyquist plot from EIS study (Fig. 14o) within the frequency range of 100 kHz to 0.1 Hz can be inferred as Pt–Pd/CS-G < Pt–Pd/G < Pt/CS-G < GCE. This result means that Pt–Pd/CS-G has the lowest R_{ct} value due to the synergistic effect between Pd NPs and Pt NPs.

From the review of several previous research works above, it can be concluded that the employ of the carbonaceous supporting material plays a vital role in stabilizing and provides good dispersion of the bimetallic alloy NPs, improving the electrocatalytic performance of MOR by increasing the ECSA, thus leads to improve the DMFC efficiency. In addition, as can be seen in Table 5, the overall electrocatalytic performance of the carbonaceous supported Pt–Pd electrocatalysts from

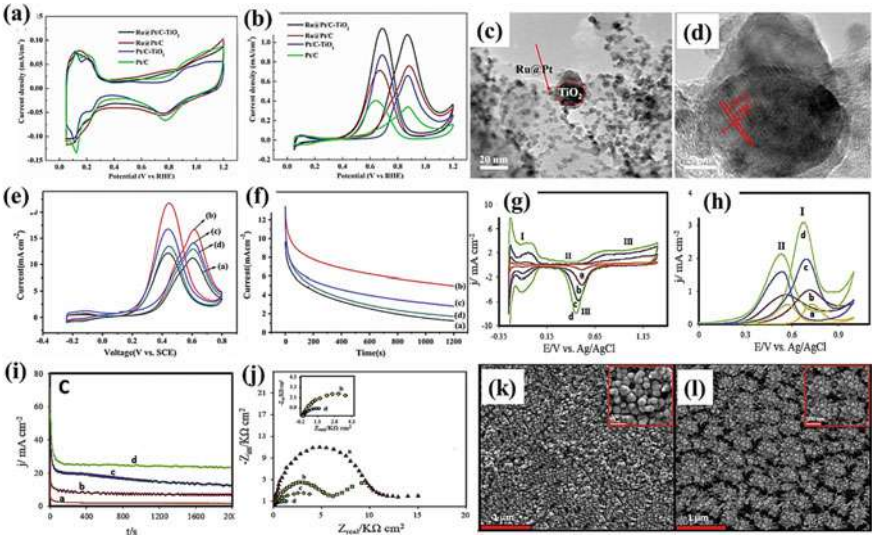

Fig. 16 CV curves of Ru@Pt/C-TiO_2, Ru@Pt/C, Pt/C-TiO_2 and Pt/C electrocatalysts in Ar-saturated of **a** 0.5 M H_2SO_4 solution and **b** 0.5 M H_2SO_4 + 0.5 M CH_3OH solution at a scan rate of 50 mV/s, **c** TEM image of Ru@Pt/C-TiO_2 electrocatalyst, **d** Lattice fringe measurement of TiO_2 corresponding to (1 0 1) plane, **e** CV curves of MOR for the PtRu/C **a**, PtRu/5%WO_3-C **b**, PtRu/10%WO_3-C **c** and PtRu/20%WO_3-C **d** catalysts in 0.5 M H_2SO_4 + 0.5 M CH_3OH solution at a scan rate of 20 mV/s, **f** Chronoamperometry curves of MOR on the PtRu/C **a**, PtRu/5%WO_3-C **b**, PtRu/10%WO_3-C **c** and PtRu/20%WO_3-C **d** catalysts in 0.5 M H_2SO_4 + 0.5 M CH_3OH solution at 0.6 V, CV curves of the PtPd-NPs/RGO **a**, PtPd-NFs/RGO **b**, PtPd-NPs/Cu_2O-NPs/RGO **c** PtPd-NFs/Cu_2O-NSs/RGO **d** in **g** 0.5 M H_2SO_4 solution and **h** 0.5 M H_2SO_4 + 0.5 M CH_3OH solution at a scan rate of 50 mV/s, **i** Chronoamperometry curves of the PtPd-NPs/RGO **a**, PtPd-NFs/RGO **b**, PtPd-NPs/Cu_2O-NPs/RGO **c** PtPd-NFs/Cu_2O-NSs/RGO **d** in 0.5 M H_2SO_4 + 0.5 M CH_3OH solution at a peak potential value, **j** Nyquist plots from EIS study toward MOR in 0.5 M H_2SO_4 + 0.5 M CH_3OH solution for PtPd-NPs/RGO **a**, PtPd-NFs/RGO **b**, PtPd-NPs/Cu_2O-NPs/RGO **c** PtPd-NFs/Cu_2O-NSs/RGO **d** at the electrode potential of 0.3 V, **k** and **l** SEM images of PtPd-NPs/Cu_2O-NPs/RGO/GCE and PtPd-NFs/Cu_2O-NSs/RGO/GCE [68, 95, 115]

previous reported works is generally enhance and even higher than some of the listed electrocatalysts in Table 4 towards MOR indicating the beneficial of using the Pt–Pd alloy NPs compared with other bimetallic alloy NPs. Meanwhile, although the carbonaceous supporting materials provide some advantages to the bimetallic alloy electrocatalyst that leads to the increase MOR performance and offer new perspective in the synthesis of nanocomposite electrocatalysts, yet various degrees of carbon corrosion problem still happen either for oxidized or functionalized carbonaceous supports. In addition, metal NPs with high surface energy have a tendency of severe aggregation under reaction condition which can reduce the electrocatalytic performance toward MOR [110]. Therefore, the modification should be taken to increase the stability of carbonaceous support materials in order to prevent their degradation under DMFC operating conditions [46]. The introduction of inorganic materials such as metal oxides can assist to immobilize the metal NPs and to anchor the bimetallic

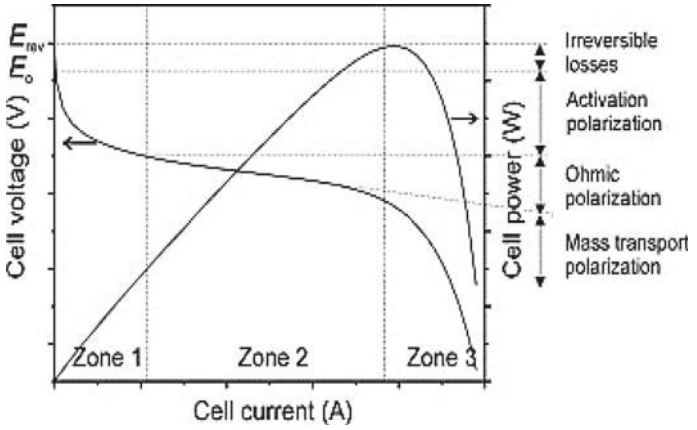

Fig. 17 The representative schematic diagram of polarization curve and power plots [109]

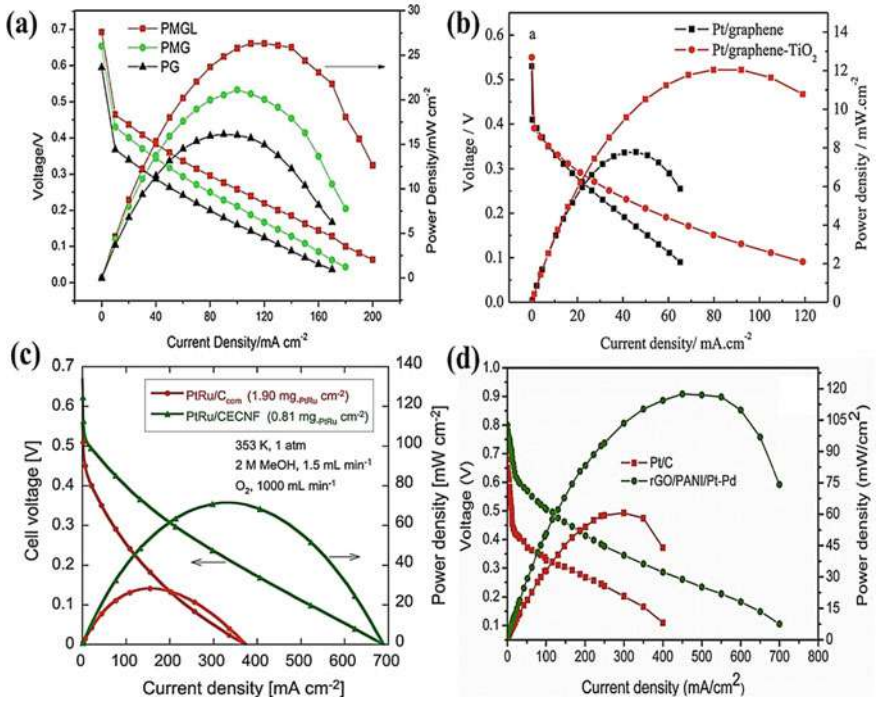

Fig. 18 DMFC polarization curves of **a** Pt-MnO_2/rGO (PMG), Pt-MnO_2/rGO-L (PMGL) and Pt/rGO (PG) [134], **b** Pt/graphene and Pt/graphene-TiO_2 [149], **c** PtRu/CECNF and PtRu/C_{com}Pt/C/CC [52], **d** rGO/PANI/Pt–Pd/CC and Pt/C at 70 °C [9]

Table 5 Comparison in electrocatalytic performance of the carbonaceous support supported Pt–Pd electrocatalysts based electrode towards MOR from the previous studies

No	Electrocatalysts	Electrolytes	ECSA	Onset Potential (V)	Maximum forward peak current density/specific activity (I_f, mA cm^{-2})	I_f/I_b ratio	Scan rate (mV s^{-1})	References
1	RGO/Pt–Pd HNS	1.0 M CH_3OH + 1.0 M NaOH solution	18.5 $m^2 g^{-1}$	0.423	28.2	–	50	[57]
2	RGO/Pt–Pd	1.0 M CH_3OH + 1.0 M KOH solution	–	–	57.46	–	50	[9]
3	CS-Graphene/Pt–Pd bimetallic NPs	1.0 M CH_3OH + 1.0 M H_2SO_4 solution	–	–	15.70	2.27	50	[123]
4	PtPd/RGO-CNT	1.0 M CH_3OH + 0.1 M $HClO_4$ solution	40.10 $m^2 g^{-1}$	0.33	5.25	–	50	[131]
5	Pd@Pt DNC/RGO	0.5 M CH_3OH + 0.5 M KOH solution	114.15 $m^2 g^{-1}$	0.37	90.17	–	50	[68]
6	RGO-PtPd	1.0 M CH_3OH + 0.5 M H_2SO_4 solution	81.2 $m^2 g^{-1}$	–	0.54	1.72	50	[30]

(continued)

Table 5 (continued)

No	Electrocatalysts	Electrolytes	ECSA	Onset Potential (V)	Maximum forward peak current density/specific activity (I_f, mA cm^{-2})	I_f/I_b ratio	Scan rate ($mV\ s^{-1}$)	References
7	PtPd nanocubes/RGO	1.0 M CH_3OH + 0.1 M $HClO_4$ solution	197 $cm^2\ g^{-1}$	–	1.31	1.61	50	[74]
8	GO/Pd–Pt	1.0 M CH_3OH + 0.1 M $HClO_4$ solution	55.89 $m^2\ g^{-1}$	0.5	4.35	–	50	[47]
9	Porous Pt–Pd NSs/RGO	1.0 M CH_3OH + 1.0 M NaOH solution	681 $cm^2\ mg^{-1}$	–	180	1.50	50	[59]
10	PtPd-RGO	1.0 M CH_3OH + 0.5 M H_2SO_4 solution	83.4 $m^2\ g^{-1}$	–	0.449	2.12	50	[50]
11	Pt-PdNPs/Graphene	0.5 M CH_3OH + 1.0 M NaOH solution	23.34 $m^2\ g^{-1}$	–	2.727	–	100	[148]
12	$Pt_{30}Pd_{70}$/C	1.0 M CH_3OH + 1.0 M KOH solution	–	0.154	32.53	6.39	10	[24]
13	Pd–Pt ANFs/RGO	0.5 M CH_3OH + 1.0 M NaOH solution	200.32 $cm^2\ mg^{-1}$	–	2.16	3.29	50	[116]

(continued)

Table 5 (continued)

No	Electrocatalysts	Electrolytes	ECSA	Onset Potential (V)	Maximum forward peak current density/specific activity (I_f, mA cm^{-2})	I_f/I_b ratio	Scan rate (mV s^{-1})	References
14	Pt–Pd-gCN-CB	1.0 M CH_3OH + 1.0 M NaOH solution	84.3 $m^2\,g^{-1}$	–	5.24	–	50	[84]
15	5Pt1Pd/GP	0.5 M CH_3OH + 0.5 M H_2SO_4 solution	199.16 $m^2\,g^{-1}$	0.41	0.35	1.20	50	[82]
16	PtPd/RGO	0.5 M CH_3OH + 1.0 M H_2SO_4 solution	253.96 $cm^2\,mg^{-1}$	0.31	22.76	1.56	50	[124]
17	Pd-PtNPs/S-NS-Graphene	0.5 M CH_3OH + 1.0 M NaOH solution	467.72 $m^2\,g^{-1}$	–	35.13	7.20	50	[142]
18	Graphene-PtPd nanodendrites	1.0 M CH_3OH + 0.5 M H_2SO_4 solution	–	0.45	1.61	1.23	50	[15]
19	Pt_1Pd_1/GNS	0.5 M CH_3OH + 0.1 M H_2SO_4 solution	46.11 $m^2\,g^{-1}$	–	0.44	0.82	50	[127]

NPs securely onto carbonaceous support specifically graphene as well as enhancing the electrocatalytic performance through the bifunctional mechanism.

2.10.1 Carbonaceous Materials Supported Pt-Based Electrocatalysts Integration with Transition Metal Oxides

As mentioned in the previous section, one of the critical issues that should be addressed is the carbon corrosion problem occur during MOR resulting a serious loss of Pt electrocatalytic performance towards MOR and the drastic decay of DMFC performance. Therefore, plenty of studies have been reported and highlighted the preparation of ternary Pt-based electrocatalysts including the use of bimetallic alloy and metal oxides for catalyzing the MOR. Some of the metal oxides such as MnO_2, SnO_2, TiO_2, WO_3, Fe_2O_3 and CeO_2 have been widely employed to take benefit of their inertness properties to maintain the stability of carbonaceous supporting materials for anode electrocatalyst in electrocatalytic activity of MOR [89]. The metal oxides can be an excellent electrocatalyst support or act as co-electrocatalyst in DMFC because of the excellent corrosion resistant and electrocatalytic properties [7, 76]. For instance, Huang et al. [39] reported the synthesis of 3D porous Pt/RuO_2/graphene aerogel electrocatalysts through a facile self-assembly approach. Based on CV curves obtained as depicted in Fig. 15a, the Pt/RuO_2 (20%)/G possesses the largest ECSA of 122.7 m^2 $g-1$ which is the most outstanding compared with the Pt/G (35.1 m^2 $g-1$), PtRu/C (46.9 m^2 $g-1$) and Pt/C (26.6 m^2 $g-1$) electrocatalysts. These results can be related to the small Pt sizes and the 3D interconnected porous structure of Pt/RuO_2 (20%)/G, threby leading to a rapid electrochemical accessibility of the electrocatalytic regions on the surface of electrode. Meanwhile, from the CV curve results in Fig. 15b, the highest If value of Pt/RuO_2 (20%)/G electrocatalyst (18.2 mA cm^{-2}) was obtained in which 2.7, 1.9 and 2.8 times higher than Pt/G (6.8 mA cm^{-2}), PtRu/C (9.4 mA cm^{-2}) and Pt/C (6.4 mA cm^{-2}) electrocatalysts, respectively indicating a very high electrocatalytic activity of MOR for the Pt/RuO_2 (20%)/G electrocatalyst. This result should be ascribed to the introduction of RuO_2 component in the ternary electrocatalyst, which could offer the large amount of hydroxyl species for oxidative removal of the carbonaceous intermediate species and thus keep clear of the Pt active sites during MOR.

Based on the chronoamperometric curves depicted in Fig. 15c, the current densities for all the electrodes gradually declined with time due to the poisoning intermediates species accumulation and the partial conversion of metal Pt to Pt oxides. The selected Pt/RuO_2 (20%)/G electrocatalyst demonstrated a significantly slower current density decay in comparison with the Pt/G, Pt/C and PtRu/C electrocatalyst, resulting am excellent electrocatalytic durability and strong anti-poisoning ability toward MOR. The attractive electrocatalytic properties of the Pt/RuO_2/G electrocatalyst with synergistically structural characteristics can be attributed to the uniform dispersion of Pt NPs on the ultrathin graphene, enabling a fast kinetics of electrocatalytic activity of MOR. The presence of RuO_2 could produce abundant of OH^-

species at low potentials, and concurrently assist the protons transport during electrocatalytic process of MOR resulting the strong synergetic coupling effects for the 3D Pt/RuO_2/G electrocatalyst. In addition, the interconnected 3D porous graphene frameworks provide a rapid and efficient pathway for the electrolyte transport and ensure a fast rate of charge-transfer in the hybrid of 3D Pt/RuO_2/G electrocatalyst. Meanwhile, from Nyquist plot as shown in Fig. 15d, e, it can be observed that the lowest R_{ct} for the Pt/RuO_2/G (4.5 Ω) and Pt/G (4.3 Ω) electrocatalysts were obtained compared with the Pt/C (493.5 Ω) and PtRu/C (259.7 Ω) electrocatalysts, indicating the remarkable electrical conductivity of graphene-based electrocatalysts.

In addition, the FESEM image of Pt/RuO_2/G architecture shows a well-defined 3D framework with multilevel porous structure (Fig. 15f, g). In addition, the flexible with thin graphene layers are decorated uniformly by both RuO_2 and Pt NPs with an average diameter of 3.3 nm as represented from HRTEM image in Fig. 15h. Considering that the RuO_2 NPs deposited on graphene sheets usually have larger sizes than those of Pt NPs, the actual Pt average size of Pt/RuO_2/G architecture should be even smaller than 3.3 nm. Moreover, the distinguishable lattice fringes with inter-planar distance of 2.2 and 1.9 Å, corresponded to the (111) and (200) planes of cubic Pt crystals, respectively were revealed as shown by HRTEM image in Fig. 15j and consistent with the results from the SAED (inset of Fig. 15i). In addition, element mapping analysis as depicted in Fig. 15k–n, unravel that the 3D Pt/RuO_2/G electrocatalyst mainly consists of C, O, Pt and Ru elements with homogenously dispersed across the entire graphene sheet.

In another study, [115] reported the preparation of Ru@Pt/C-TiO_2 electrocatalyst through two-step of ethanol reduction method. Based on the desorption peak from the CV curves in Fig. 16a, the estimated ECSA value of Ru@Pt/C-TiO_2 (69.6 m^2/g) was larger than the Ru@Pt/C (67.8 m^2/g), Pt/C-TiO_2 (61.5 m^2/g) and Pt/C (60.0 m^2/g) suggested that the deposited TiO_2 and Ru core on carbon support contribute to the increase of ECSA for Ru@Pt/C-TiO_2. Meanwhile, from Fig. 16b, the Ru@Pt/C-TiO_2 shows enhanced electrocatalytic activity of MOR with the I_f value of 1.08 mA/cm^2, in which significantly larger than the Ru@Pt/C (0.76 mA/cm^2), Pt/C-TiO_2 (0.66 mA/cm^2) and Pt/C (0.34 mA/cm^2) attributing to the bifunctional mechanism derived from TiO_2 and strong electronic interaction between Pt and Ru, C-TiO_2, that leads to weakening the binding energy of CO_{ads} on Pt. The HRTEM images of Ru@Pt/C-TiO_2 displayed in Fig. 16c, d, demonstrated the large size of TiO_2 (18 nm) that pointed out by ellipse with the lattice fringe measurement of 3.52 Å corresponded to (1 0 1) plane of TiO_2 and some smaller size of Ru@Pt NPs around 4.2 nm indicated by arrow were clearly observed.

Meanwhile, the hybrid PtRu/WO_3-C electrocatalyst was prepared through the microwave-assisted polyol process by [68]. Based on the CV curves of MOR in Fig. 16e, the forward peaks of PtRu/WO_3-C electrocatalysts were lower than backward peaks indicating the poor stability of the electrocatalysts. The I_f value obtained for PtRu/C, PtRu/5% WO_3-C, PtRu/10% WO_3-C and PtRu/20% WO_3-C electrocatalysts during MOR were around 11.24, 16.8, 14.2 and 13.0 mA cm^{-2}, respectively. It can be observed that the electrocatalytic performance was enhanced after the addition of WO_3 into carbon black and the PtRu/5% WO_3-C electrocatalyst demonstrated the

best electrocatalytic activity of MOR. However, the electrocatalytic activity become reduced with the excessive of WO_3 that give the negative effect on the formation of PtRu alloy. Besides that, according to the slopes of the decay currents density as indicated by chronoamperometric curves in Fig. 16f, the stability performance of the electrocatalysts followed the order of PtRu/5% WO_3-C > PtRu/10% WO_3-C > PtRu/20% WO_3-C > PtRu/C, which have the same trend for the electrocatalytic activity of MOR results. Therefore, the existance of WO_3 and more available of Pt active sites on the electrocatalyst surface play a vital role in the enhancement of MOR activity.

On the other hand, [95] reported a simple electrochemical approach for the fabrication of the PtPd-NFW/Cu_2O-NSs/rGO nanocomposite electrocatalyst. As illustrated by the CV curves in Fig. 16g, the ECSA values followed the order for these electrocatalysts: PtPd-NFW/Cu_2O-NSs/rGO (2.40 cm^2) > PtPd-NPs/Cu_2O-NPs/rGO (1.57 cm^2) > PtPd-NFW/rGO (0.84 cm^2) > PtPd-NPs/rGO (0.34 cm^2). The existance of Cu_2O has a positive effect on the enhancing the electrical conductivity and uniform electrodeposition of PtPd-NFW and PtPd-NPs with highly efficient utilization and thus, increasing the ECSA value of PtPd electrocatalysts accordingly. In addition, the I_f value of MOR as demonstrated in Fig. 16h increase in the order of PtPd-NFW/Cu_2O-NSs/rGO > PtPd-NPs/Cu_2O-NPs/rGO > PtPd-NFW/rGO > PtPd-NPs/rGO as the changes in morphology from NPs to the NFW indicating that the addition of Cu_2O NSs and the synergistic effect between the PtPd, Cu_2O and rGO contribute to the improvement of the electrocatalytic activity of MOR which can be related to the higher surface-active area of the NSs compared with Cu_2O NPs. Meanwhile, the I_f/I_b ratio was found to be in the order of PtPd-NFW/Cu_2O-NSs/rGO > PtPd-NPs/Cu_2O-NPs/rGO > PtPd-NFW/rGO > PtPd-NPs/rGO revealing the enhanced poisoning tolerance capability and efficient MOR on the surface of PtPd-NFW/Cu_2O-NSs/rGO. Besides that, the PtPd-NFW/Cu_2O-NSs/rGO shows a negative shifting of E_{onset} suggesting that the methanol molecules are more easily oxidized on its surface. On the other hand, the utilization of the Cu_2O NSs and RGO as the electrocatalyst support prevent the unfavorable agglomeration of the electrocatalyst active sites. Moreover, the oxophilic nature of the Cu_2O facilitates the formation of OH_{ads} and spillover to PtPd surface that can react with the carbonaceous intermediate species (CO_{ads}) effectively to produce CO_2, thus releasing the active sites on PtPd for continuing the MOR.

As can be seen from the chronoamperometric curves in Fig. 16i, the PtPd-NFW/Cu_2O-NSs/rGO electrocatalyst (23.30 mA cm^{-2}) remain the highest current density of MOR after 2000s compared with the PtPd-NPs/rGO (1.72 mA cm^{-2}), PtPd-NFW/rGO (6.21 mA cm^{-2}) and PtPd-NPs/Cu_2O-NPs/rGO (12.13 mA cm^{-2}) implying that the PtPd-NFW/Cu_2O-NSs/rGO has the superior electrocatalytic performance and high level of poisoning tolerance toward MOR in acidic media. According to the Nyquist plots from EIS study as shown in Fig. 16j, the semicircle diameters that related to R_{ct} showed to decrease in the order of PtPd-NPs/rGO > PtPd-NFW/rGO > PtPd-NPs/Cu_2O-NPs/rGO > PtPd-NFW/Cu_2O-NSs/rGO implying that the existence of Cu_2O contribute to the higher electrocatalytic activities with lowering the R_{ct} by donating their surface oxygen atoms to the CO_{ads} to form CO_2 through bi-functional

mechanism and thus, leads to the enhancement of MOR rate. In addition, from the SEM image with inset in Fig. 16k, it can be observed that the PtPd-NPs has been consisting of dense and homogeneous discrete spherical shapes, while the SEM image with inset in Fig. 16l demonstrated the PtPd needle-like NFW with visible and clear pricks totally covered the Cu_2O-NSs/rGO surface. The comparison study from previous reported work on the electrocatalytic performance of several ternary electrocatalysts with the incorporation of various kind of metal oxides towards MOR are summarized in Table 6. It is worth notice that all the ECSA, E_{onset}, I_f and I_f/I_b ratio value of the obtained ternary electrocatalysts demonstrated a significantly enhance and remarkable electrocatalytic performance towards MOR as compared with the value obtained by the electrocatalysts in the previous sections. The combination of carbonaceous supporting materials, bimetallic Pt-based alloy electrocatalyst and the metal oxides to form the ternary nanocomposite electrocatalyst provide the most outstanding performance of electrocatalytic towards MOR in DMFC.

2.11 DMFC Performance Based on the Advanced Anode Nanocomposite Electrocatalysts

A lot of works remains to be completed to accelerate the commercialization process even though the great progress has been achieved. Meanwhile, it is worth notice that results of electrocatalytic performance derived from the conventional three-electrodes systems like CV, chronoamperometry and EIS test still not reflect the exact information for anode electrocatalysts in the real practical of DMFC and only provide the intrinsic activity of the electrocatalysts while excluding many adverse factors involved with the practical DMFC. Therefore, the evaluation of the electrocatalyst performance in the practical DMFC should be carried out. Basically, the polarization curve is a common performance data or information that can be represented by the cell voltage versus current density to evaluate the overall DMFC performance and the various voltage losses in the DMFC system are identified and briefly described. In general, the various limiting factors (losses) can be determined and investigated from the polarization curve including the mass transport, ohmic and activation losses which can be illustrated in Fig. 17.

The mass transport loss occurs when the mass transport rate of a species to or from the electrode limits the current production. The loss is remarkably notable at high values of current density due to limited mass transfer of reactants by diffusion to the electrode that cause the lack of reactants present near the electrocatalyst sites and product accumulation [49]. Meanwhile, the ohmic losses involve the loss of potential due to the resistance in the flow of electric charges (ions or electrons) through the electrode material and various interconnection. In DMFC, this type of loss mostly originates from the resistance to the flow of ions (H^+) through the membrane layers and electrolyte. Last but not least, the activation loss occurs in DMFC during the transfer of electrons from or to a compound reacting at the electrode surface in

Table 6 Comparison in electrocatalytic performance of MOR for the ternary nanocomposite electrocatalysts from previous studies

No	Electrocatalysts	Electrolytes	ECSA	Onset Potential (V)	Maximum forward peak current density/specific activity (I_f, mA cm^{-2})	I_f/I_b ratio	Scan rate (mV s^{-1})	References
1	Pt/CeO_2-ZnO	1.0 M CH_3OH + 0.5 M H_2SO_4 solution	2.11 cm^2	0.22	0.919	1.23	50	[153]
2	Pt/RGO-CeO_2 NWS	0.5 M CH_3OH + 0.5 M H_2SO_4 solution	78.6 $m^2\ g^{-1}$	−0.336	9.36 A m^{-2}	–	50	[111]
3	PtRu/C@$Mo_xTi_{1-x}O_{2-\delta}$-FI	0.5 M CH_3OH + 0.5 M H_2SO_4 solution	74.7 $m^2\ g^{-1}$	–	13.7 A m^{-2}	–	50	[66]
4	Pt-MnO_2/RGO	2.0 M CH_3OH + 1.0 M H_2SO_4 solution	79.4 $m^2\ g^{-1}$	0.16	24.7	1.12	50	[99]
5	Pt/C-Au@CeO_2-Pt	0.5 M CH_3OH + 0.5 M H_2SO_4 solution	77.8 $m^2\ g^{-1}$	0.26	162	1.16	50	[25]
6	PtPd-Nanoflowers/Cu_2O-NSs/RGO	0.5 M CH_3OH + 0.5 M H_2SO_4 solution	2.40 cm^2	0.17	3.08	1.47	50	[95]
7	PtRu/WO_3–C	0.5 M CH_3OH + 0.5 M H_2SO_4 solution	–	0.20	16.8	–	20	[68]

(continued)

Table 6 (continued)

No	Electrocatalysts	Electrolytes	ECSA	Onset Potential (V)	Maximum forward peak current density/specific activity (I_f, mA cm^{-2})	I_f/I_b ratio	Scan rate (mV s^{-1})	References
8	Pt/RuO_2/Graphene	2.0 M CH_3OH + 1.0 M H_2SO_4 solution	122.7 $m^2\ g^{-1}$	–	18.2	–	20	[39]
9	Pt–CoOOH-CDs/C	1.0 M CH_3OH + 1.0 M KOH solution	63.64 $m^2\ g^{-1}$	–	48.26	4.52	50	[106]
10	Pt/TiO_2–C	0.5 M CH_3OH + 0.5 M H_2SO_4 solution	66.1 $m^2\ g^{-1}$	–	> 0.50	–	10	[64]
11	Pt/graphene-TiO_2	0.5 M CH_3OH + 0.5 M H_2SO_4 solution	74.7 $m^2\ g^{-1}$	–	0.57	–	50	[149]
12	Pt-C/TiO_2	1.0 M CH_3OH + 0.5 M H_2SO_4 solution	23.8 $m^2\ g^{-1}$	–	1.22	1.29	50	[118]
13	Ru@Pt/C-TiO_2	0.5 M CH_3OH + 0.5 M H_2SO_4 solution	69.6 $m^2\ g^{-1}$	–	1.08	–	50	[115]
14	Pt/TiO_2@Ru–C	0.5 M CH_3OH + 0.5 M H_2SO_4 solution	82.9 $m^2\ g^{-1}$	0.28	0.587	–	20	[65]

(continued)

Table 6 (continued)

No	Electrocatalysts	Electrolytes	ECSA	Onset Potential (V)	Maximum forward peak current density/specific activity (I_f, mA cm^{-2})	I_f/I_b ratio	Scan rate (mV s^{-1})	References
15	Pt–V_2O_5/C	1.0 M CH_3OH + 1.0 M H_2SO_4 solution	–	0.21	17.40	1.06	50	[75]
16	Pt-MnO_2/RGO	0.5 M CH_3OH + 0.5 M H_2SO_4 solution	52.16 $m^2\ g^{-1}$	–	23.21	1.02	50	[134]
17	Pt/CeO_2-MC	2.0 M CH_3OH + 1.0 M H_2SO_4 solution	–	–	47.00	–	25	[136]
18	Pt/CeO_2–RGO	0.5 M CH_3OH + 0.5 M H_2SO_4 solution	53.78 $m^2\ g^{-1}$	0.28	~ 30.00	1.12	50	[35]

which contribute to the loss of cell voltage at lower values of current density due to the activation energy needed for MOR/ORR. However, the low activation losses can be achieved in anode by increasing the surface area of electrode, improving electrocatalysis and increasing the temperature.

Meanwhile, [134] reported the synthesis of carbon riveted Pt-MnO_2/RGO (PMGL) electrocatalyst through in situ carbonization using l-ascorbic acid as carbon source. In the assembled DMFC, PMGL, Pt-MnO_2/RGO (PMG) and Pt/RGO (PG) were used as anode catalyst, with the commercial catalyst Pt/C serving as cathode catalyst by using 2 M of methanol concentration with the operation temperature of 60 °C. The PMGL as anode electrocatalyst shows the best performance with a maximum power density of 26.31 mW cm^{-2}, followed by PMG (21.11 mW cm^{-2}) and PG (16.13 mW cm^{-2}) as indicated by the polarization and power density curves in Fig. 18a. The output performance of DMFC depends on the loading of electrode catalyst, the type of proton exchange membrane, current collectors, assembly conditions, methanol concentration and operating temperature conditions.

In another study, [149] reported the synthesis of Pt/graphene-TiO_2 hybrid catalysts via a facile one-pot solvothermal method. Based on the polarization and power density curves shown in Fig. 18b, the obtained maximum power density of the DMFC using Pt/graphene-TiO_2 electrocatalyst is around 12.04 mW cm^{-2}, with an increment of 55% compared with that using Pt/graphene electrocatalyst (7.78 mW cm^{-2}) at the same operating conditions. However, the performance of DMFC test using Pt/graphene as anode electrocatalyst is quite poor since the graphene sheets tend to horizontally stack during MEA fabrication due to the intensive van der waals force, thereby, resulting in a decrease of active sites at superimposed plane between graphene sheets. In different study, [52] reported the preparation of different CeO_2 contents embedded carbon nanofibers (CECNFs) through an electrospinning technique, followed by the deposition of 15 wt% PtRu NPs on the CECNFs to form PtRu/CECNF electrocatalyst. Figure 18c demonstrate the DMFC performance of PtRu/CECNF with the maximum power density of 71 mW cm^{-2} in which 2.5 times higher than that of PtRu/C_{com} (28 mW cm^{-2}). The significantly enhancement of the PtRu utilization in the DMFC containing PtRu/CECNF electrocatalyst and the interaction between Pt, CeO_2 and the bulky nanofiber electrocatalyst layer are the significant reasons for the high DMFC performance obtained.

In 2019, Arakula and the teams reported a wet reflux strategy for the synthesis of rGO/polyaniline (PANI)/Pt–Pd composite as a potential anode electrocatalyst with enhanced MOR for DMFC. The DMFC containing rGO/PANI/Pt–Pd electrocatalyst exhibited the remarkable maximum power density with enhanced performance (117.45 mW /cm^2 at a load current density of 450 mA/cm^2) at 70 $^{°C}$ compared with the Pt/C (59.16 mW/cm^2 at a load current density of 241.5 mA/cm^2) as demonstrated by resulting polarization and power density curves in Fig. 18d. The MOR ability of rGO/PANI/Pt–Pd electrocatalyst is significantly higher than the Pt/C because of the larger ECSA. Since the rGO/PANI/Pt–Pd electrocatalyst increases the ECSA and MOR, the methanol molecules can easily decompose on the surface of rGO/PANI/Pt–Pd electrocatalyst. The compatibility between rGO, PANI and Pt–Pd has also played a critical role in achieving excellent maximum power density.

Table 7 summarises the comparison in DMFC performance in term of maximum power density and OCV value with the operating conditions like methanol concentration and temperature for the anode nanocomposite electrocatalysts from the previous reported research works. It can be concluded that most of the reported anode electrocatalysts listed in Table 2–7 possesses the maximum power density value of less than 100 mW/cm^2 which can further improve by producing the ternary nanocomposite electrocatalyst based on the combination of carbonaceous support material (the most preferable is RGO), bimetallic Pt-based alloy electrocatalyst (Pt–Pd alloy NPs) and the metal oxide (CeO_2) through an efficient production method.

3 Conclusion and Future Prospects

The anode electrocatalyst production through the simple and efficient method with the remarkable and satisfactory electrocatalytic performance to catalyze the MOR effectively is very significant interest is very significant interest for realize the wider DMFC commercialization. Various factors must be considered by researchers for future research in terms of determination the ideal new anode electrocatalysts. Based on the previous research works, it has found that the pure metal of Pt electrocatalysts are prone to the poisoning effect by carbonaceous intermediate species mainly CO_{ads}, thereby the electrocatalytic active sites will be blocked and occupied during MOR. Therefore, the presence drawback cannot be addressed through the shape or structure construction strategy only. The composition of anode electrocatalysts with tunable effect is highly precious for the electrocatalytic performance enhancement towards MOR catalyzation. Hence, the anode electrocatalysts containing smaller Pt noble metal amount and more other noble and non-noble metals are widely investigated and provide a better choice for MOR than that of pure monometallic Pt electrocatalysts. The synergistic effects resulted from such combination could promotes the electrocatalytic performance of the present electrocatalyst materials and help new types synthesis progress with optimum quality of performance. In addition, the nanostructured morphology of carbonaceous supporting materials should be introduced that can plays a vital role in stabilizing and provides good dispersion of bimetallic alloy NPs, improving the electrocatalytic performance of MOR by increasing the ECSA, thus leads to improve the DMFC efficiency. Moreover, the durability of the produced nanocomposite electrocatalyst containing support and metals could be enhanced that possible to be practically employed for future DMFC applications. Although, the carbonaceous supporting materials provide some advantages to the bimetallic alloy electrocatalyst that leads to the increase of MOR performance yet various degrees of carbon corrosion problem still happen either for oxidized of functionalized carbonaceous supports. Meanwhile, the introduction of inorganic materials such as metal oxides can assist to immobilize the metal NPs and to anchor the bimetallic NPs securely onto carbonaceous support specifically graphene as well as enhancing the electrocatalytic performance through bifunctional mechanism. From the previous reported work on the electrocatalytic performance of several ternary electrocatalysts

Table 7 Comparison in DMFC performance and operating conditions for the nanocomposite electrocatalysts from the previous studies

No	Electrocatalysts	Temperature (° C)	Methanol concentration (M)	OCV (V)	Current density	Power density (mW cm^{-2})	References
1	Pt–Ru/C-TiO_2	80	1	0.65	2500 A m^{-2}	709.32 W/m^2	[29]
2	PtRu/FWCNTs	30	1	> 0.50	110 mA cm^{-2}	20	[13]
3	Pt-Ru/Carbon nanocage	RT	2	0.35	35 mA cm^{-2}	> 6	[87]
4	Carbon aerogel/PtRu	70	2	0.80	450 mA cm^{-2}	> 100	[12]
5	C/Pt	80	10	0.51	400 mA cm^{-2}	61.50	[32]
6	PtRu/TiO_2-CNF	RT	3	0.49	22.50 mA cm^{-2}	3.80	[2]
7	PtCo/C	60	1	0.67	0.14 A cm^{-2}	40	[10]
8	Pt + Pd/C	90	2	0.55	0.55 A cm^{-2}	90	[8]
9	Pt nanowire catalyst layer	120	–	0.70	170 mA cm^{-2}	63.90	[67]
10	rGO/PANI/Pt–Pd	70	1	0.79	450 mA cm^{-2}	117.45	[9]
11	PtRu/CB@N_xC	80	2	0.80	250 mA cm^{-2}	60	[145]
12	Pt/TiO_2–C	80	2	0.66	281.25 mA cm^{-2}	83.20	[64]
13	Pt/graphene-TiO_2	80	2	0.55	90 mA cm^{-2}	12.04	[149]
14	Carbon riveted Pt-MnO_2/RGO	60	2	0.70	120 mA cm^{-2}	23.61	[134]
15	PtRu-Vulcan	30	1	0.37	–	3.5	[13]
16	Pt/MO-CNTs	60	2	0.60	250 mA cm^{-2}	48	[119]
17	Pt/Co (1:9)/RGO	100	2	0.71	–	118.4	[11]

(continued)

Table 7 (continued)

No	Electrocatalysts	Temperature (° C)	Methanol concentration (M)	OCV (V)	Current density	Power density (mW cm^{-2})	References
18	Pt-WO_3/C	40	2	~ 0.45	0.08 A cm^{-2}	7.8	[23]
19	PtRu/CeO_2-C	80	2	< 0.70	325 mA cm^{-2}	71.0	[52]
20	Pt/MWCNT	25	2	0.80	140 mA cm^{-2}	28.5	[83]
21	Pt-CeO_2/C	60	1	0.443	50 mA cm^{-2}	7.1	[130]
22	Pt/$Ce_{0.7}$-$Mo_{0.3}O_2$–δC	60	1	1.0	300 mA cm^{-2}	69.4	[141]
23	Pt-RuO_x/C	70	2	0.53	160 mA cm^{-2}	27.6	[91]
24	Pt–Sn/Vulcan carbon	70	2	~ 0.45	0.25 A/cm^2	38.0	[107]
25	Pt–Ru/Al_2O_3–C	RT	2	0.75	220.1 mA cm^{-2}	44.02	[26]
26	90 wt.% PtRu/C	25	1	0.70	40 mA cm^{-2}	10.5	[22]
27	PtRu/C-SA	80	1	0.80	250 mA cm^{-2}	105	[17]
28	PtRu18/TECNF	80	2	0.575	420 mA cm^{-2}	80.6	[105]
29	PtRu/C	80	1	0.80	375 mA cm^{-2}	78.0	[102]
30	PtRu/MC	60	1	0.65	290 mA cm^{-2}	67.0	[14]
31	N-GA/PtRu	90	0.5	0.67	426 mA cm^{-2}	93.0	[151]
32	Pt@RFC	60	1	0.78	~ 187.5 mA cm^{-2}	58.5	[56]

with the incorporation of various kind of metal oxides towards MOR demonstrated a significantly enhance and remarkable electrocatalytic performance towards MOR as compared with the value obtained by the electrocatalysts in the previous sections. The combination of carbonaceous supporting materials, bimetallic Pt-based alloy electrocatalyst and the metal oxides to form the ternary nanocomposite electrocatalyst provide the most outstanding performance of electrocatalytic towards MOR in DMFC. It is expected a great demand in the system of portable power with huge power density become a trend in future since the portable electronic devices market is growing fast. There has good possibility to contribute in the market significantly since a few numbers of studies have been performed on the technology of DMFC due to some of the advantages that have been discussed before. However, the progress is still needed to address the technical barriers explained earlier in the previous sections. Herein, several considerations for the production of anode electrocatalyst in this review:

- Alloying Pt with other transition metals specifically Pd could help destabilizing the CO_{ads} intermediate during MOR, thus increasing the life-cycle of the electrocatalysts.
- Utilizing the electrocatalysts support particularly graphene have shown to be highly active for MOR by providing dispersed active sites and high conductivity.
- The utilization of inorganic materials specifically metal oxides can be considered to immobilize the bimetallic Pt alloy NPs and help to anchor the bimetallic NPs securely onto carbonaceous support specifically graphene as well as enhancing the catalytic performance due to bifunctional mechanism. A combination of metal oxides and graphene has shown to improve the MOR current density and CO resistivity owing to enhanced diffusion of ions, large active surface area and reduced methanol crossover.

Overall, the knowledge presented in this review, including the recent progress on different materials for anode electrocatalysts and the effects of different parameters, is expected to provide a guidance on the production of anode electrocatalyst with outstanding electrocatalytic performance toward MOR for DMFC applications.

References

1. Abdullah FA, Kamarudin SK, Zainoodin AM, Masdar MS (2020) Parametric studies of direct methanol fuel cell under different modes of operation. Jurnal Kejuruteraan 32(1):159–164
2. Abdullah N, Kamarudin SK, Shyuan LK, Karim NA (2019) Synthesis and optimization of PtRu/TiO_2-CNF anodic catalyst for direct methanol fuel cell. Int J Hydrogen Energy 44(58):30543–30552
3. Ali S, Ahmed R, Sohail M, Khan SA, Ansari MS (2015) Co@Pt core–shell nanoparticles supported on carbon nanotubes as promising catalyst for methanol electro-oxidation. J Ind Eng Chem 28:344–350
4. Alia SM, Zhang G, Kisailus D, Li D, Gu S, Jensen K, Yan Y (2010) Porous platinum nanotubes for oxygen reduction and methanol oxidation reactions. Adv Funct Mater 20:3742–3746

5. Amani M, Kazemeini M, Hamedanian M, Pahlavanzadeh H, Gharibi H (2015) Investigation of methanol oxidation on a highly active and stable Pt–Sn electrocatalyst supported on carbon–polyaniline composite for application in a passive direct methanol fuel cell. Mater Res Bull 68:166–178
6. Andújar JM, Segura F (2009) Fuel cells: history and updating. A walk along two centuries. Renew Sustain Energy Rev 13(9):2309–2322
7. Antolini E, Gonzalez ER (2009) Ceramic materials as supports for low-temperature fuel cell catalysts. Solid State Ionics 180:746–763
8. Arikan T, Kannan AM, Kadirgan F (2013) Binary Pt–Pd and ternary Pt–Pd–Ru nanoelectrocatalysts for direct methanol fuel cells. Int J Hydrogen Energy 38(6):2900–2907
9. Arukula R, Vinothkannan M, Kim AR, Yoo DJ (2019) Cumulative effect of bimetallic alloy, conductive polymer and graphene toward electrooxidation of methanol: an efficient anode catalyst for direct methanol fuel cells. J Alloy Compd 771:477–488
10. Baglio V, 'Urso CD, Sebastián D, Stassi A, Aricò AS (2014) PtCo catalyst with modulated surface characteristics for the cathode of direct methanol fuel cells. Int J Hydrogen Energy 39(10):5399–5405
11. Baronia R, Goel J, Tiwari S, Singh P, Singh D, Singh SP, Singhal SK (2017) Efficient electrooxidation of methanol using PtCo nanocatalysts supported reduced graphene oxide matrix as anode for DMFC. Int J Hydrogen Energy 42(15):10238–10247
12. Bong S, Han D (2020) Mesopore-controllable carbon aerogel and their highly loaded PtRu anode electrocatalyst for DMFC applications. Electroanalysis 32(1):104–111
13. Borghei M, Scotti G, Kanninen P, Weckman T, Anoshkin IV, Nasibulin AG, Franssila S, Kauppinen EI, Kallio T, Ruiz V (2014) Enhanced performance of a silicon microfabricated direct methanol fuel cell with PtRu catalysts supported on few-walled carbon nanotubes. Energy 65:612–620
14. Bruno MM, Petruccelli MA, Viva FA, Corti HR (2013) Mesoporous carbon supported PtRu as anode catalyst for direct methanol fuel cell: polarization measurements and electrochemical impedance analysis of mass transport. Int J Hydrogen Energy 38(10):4116–4123
15. Cai Z-X, Liu C-C, Wu G-H, Chen X-M, Chen X (2014) Green synthesis of Pt-on-Pd bimetallic nanodendrites on graphene via in situ reduction, and their enhanced electrocatalytic activity for methanol oxidation. Electrochim Acta 127:377–383
16. Cao R, Xia T, Zhu R, Liu Z, Guo J, Chang G, Zhang Z, Liu X, He Y (2018) Novel synthesis of core-shell Au-Pt dendritic nanoparticles supportedon carbon black for enhanced methanol electro-oxidation. Appl Surf Sci 433:840–846
17. Carmo M, Brandalise M, Neto AO, Spinacé EV, Taylor AD, Linardi M, Poçoc JGR (2011) Enhanced activity observed for sulfuric acid and chlorosulfuric acid functionalized carbon black as PtRu and PtSn electrocatalyst support for DMFC and DEFC application. Int J Hydrogen Energy 36(22):14659–14667
18. Chen JY, Niu Q, Chen GK, Nie J, Ma G (2017) Electrooxidation of methanol on Pt @Ni bimetallic catalyst supported on porous carbon nanofibers. J Phys Chem C 121(3):1463–1471
19. Chen Q, Cao Z, Du G, Kuang Q, Huang J, Xie Z, Zheng L (2017) Excavated octahedral Pt-Co alloy nanocrystals built with ultrathin nanosheets as superior multifunctional electrocatalysts for energy conversion applications. Nano Energy 39:582–589
20. Chen S, Thota S, Wang X, Zhao J (2016) From solid to core@shell to hollow Pt–Ag nanocrystals: thermally controlled surface segregation to enhance catalytic activity and durability. J. Mater. Chem. A. 4:9038–9043
21. Chen W, Yuan W, Ye G, Han F, Tang Y (2017) Utilization and positive effects of produced CO_2 on the performance of a passive direct methanol fuel cell with a composite anode structure. Int J Hydrogen Energy 42(23):15613–15622
22. Chen X, Li T, Shen J, Hu Z (2017) From structures, packaging to application: a system-level review for micro direct methanol fuel cell. Renew Sustain Energy Rev 80:669–678
23. Cíntora-Juárez D, Ocampo-Flores AL, Ordóñez LC, Roquero P (2017) The promoting role of tungsten oxides in the anodic oxidation of methanol on platinum-based catalysts. Electrocatalysis 8:261–269

24. Cruz-Cruz JJDL, Domínguez-Crespo MA, Ramírez-Meneses E, Torres-Huerta AM, Brachetti-Sibaja SB, Cayetano-Castro N, Dorantes-Rosales HJ (2020) Int J Hydrogen Energy 45(7):4570–4586
25. Dao DV, Adilbish G, Le TD, Nguyen TTD, Lee I-H, Yu Y-T (2019) Au@CeO_2 nanoparticles supported Pt/C electrocatalyst to improve the removal of CO in methanol oxidation reaction. J Catal 377:589–599
26. Das S, Kundu PP (2015) Pt–Ru/Al_2O_3–C nanocomposites as direct methanol fuel cell catalysts for electrooxidation of methanol in acidic medium. RSC Adv 5:93539
27. Dinesh MM, Huang T, Yao S, Sun G, Mao S (2019) Hafnium sulphide-carbon nanotube composite as Pt support and active site-enriched catalyst for high performance methanol and ethanol oxidations in alkaline electrolytes. J Power Sources 410–411:204–212
28. Ding J, Zhu X, Bu L, Yao J, Guo J, Guo S, Huang X (2015) Highly open rhombic dodecahedral PtCu nanoframes. Chem Commun 51:9722
29. Ercelik M, Ozden A, Seker E, Colpan CO (2017) Characterization and performance evaluation of Pt-Ru/$CeTiO_2$ anode electrocatalyst for DMFC applications. Int J Hydrogen Energy 42:21518–21529
30. Esabattina S, Posa VR, Zhanglian H, Godlaveeti SK, Reddy RRN, Somala AR (2018) Fabrication of bimetallic PtPd alloy nanospheres supported on rGO sheets for superior methanol electro-oxidation. Int J Hydrogen Energy 43:4115–4124
31. Eshghi A, Kheirmand M, Sabzehmeidani MM (2018) Platinum-Iron nanoparticles supported on reduced graphene oxide as an improved catalyst for methanol electro oxidation. Int J Hydrogen Energy 43(12):6107–6116
32. Feng Y, Liu H, Yang J (2017) A selective electrocatalyst–based direct methanol fuel cell operated at high concentrations of methanol. Sci Adv 3(6):1700580
33. Fu G-T, Ma R-G, Gao X-Q, Chen Y, Tang Y-W, Lu T-H, Lee J-M (2014) Hydrothermal synthesis of Pt–Ag alloy nanooctahedra and their enhanced electrocatalytic activity for the methanol oxidation reaction. Nanoscale 6:12310
34. Gong L, Yang Z, Li K, Xing W, Liu C, Ge J (2018) Recent development of methanol electrooxidation catalysts for direct methanol fuel cell. J Energy Chem 27:1618–1628
35. Han T, Zhang TZ (2015) Novel hydrolyzing synthesis of CeO_2-RGO support for Pt electrocatalyst in direct methanol fuel cells. Mater Lett 154:177–179
36. Huang HJ, Sun DP, Wang X (2012) PtCo alloy nanoparticles supported on graphene nanosheets with high performance for methanol oxidation. Chin Sci Bull 57:3071–3079
37. Huang H, Zhu J, Li D, Shen C, Li M, Zhang X, Jiang Q, Zhang J, Wu Y (2017) Pt nanoparticles grown on 3D RuO_2-modified graphene architectures for highly efficient methanol oxidation. J Mater Chem A 5:4560–4567
38. Huang L, Jiang Z, Gong W, Shen PK (2018) Facile fabrication of radial PtCo nanodendrites for enhanced methanol oxidation electrocatalysis. ACS Appl Nano Mater 1(9):5019–5026
39. Huang L, Zhang X, Han Y, Wang Q, Fang Y, Dong S (2017) High-index facets bounded platinum-lead concave nanocubes with enhanced electrocatalytic properties. Chem Mater 29(10):4557–4562
40. Huang L, Zhang X, Wang Q, Han Y, Fang Y, Dong S (2018) Shape-control of Pt-Ru nanocrystals: tuning surface structure for enhanced electrocatalytic methanol oxidation. J Am Chem Soc 140(3):1142–1147
41. Ishak NAIM, Kamarudin SK, Timmiati SN, Karim NA, Basri S (2021) Biogenic platinum from agricultural wastes extract for improved methanol oxidation reaction in direct methanol fuel cell. J Adv Res 28:63–75
42. Joghee P, Malik JN, Pylypenko S, O'Hayre R (2015) A review on direct methanol fuel cells–In the perspective of energy and sustainability. MRS Energy Sustain 2(3)
43. Kamaruddin MZF, Kamarudin SK, Daud WRW, Masdar MS (2013) An overview of fuel management in direct methanol fuel cells. Renew Sustain Energy Rev 24:557–565
44. Kamarudin SK, Achmad F, Daud WRW (2009) Overview on the application of direct methanol fuel cell (DMFC) for portable electronic devices. Int J Hydrogen Energy 34(16):6902–6916

45. Kamarudin SK, Hashim N (2012) Materials, morphologies and structures of MEAs in DMFCs. Renew Sustain Energy Rev 16(5):2494–2515
46. Kaur A, Kaur G, Singh PP, Kaushal S (2021) Supported bimetallic nanoparticles as anode catalysts for direct methanol fuel cells: a review. Int Hydrogen Energy 46:15820–15849
47. Khan M, Yousaf AB, Chen M, Wei C, Wu X, Huang N, Qi Z, Li L (2015) Mixed-phase Pd–Pt bimetallic alloy on graphene oxide with high activity for electrocatalytic applications. J Power Sources 282:520–528
48. Kong X, Cao H, Li C, Chen X (2017) One step photochemical synthesis of clean surfaced sponge-like porous platinum with high catalytic performances. J Colloid Interface Sci 487:60–67
49. Koroglu EO, Yoruklu HC, Demir A, Ozkaya B (2019) Chapter 3.9—scale-up and commercialization issues of the mfcs: challenges and implications. Microbial Electrochem Technol: Sustain Platform Fuels Chem Remediation Biomass Biofuels Biochem 565–583
50. Kumar GS, Reddy NR, Sravani B, Sarma LS, Reddy TV, Madhavi V, Reddy SA (2021) Ultra-range bimetallic Pt–Pd nanospheres deposited on reduced graphene sheet as efficient electrocatalyst towards electrooxidation of methanol. J Cluster Sci 32:27–36
51. Kung C-C, Lin P-Y, Xue Y, Akolkar R, Dai L, Yu X, Liu C-C (2014) Three-dimensional graphene foam supported platinum ruthenium bimetallic nanocatalysts for direct methanol and direct ethanol fuel cell applications. J Power Sources 256:329–335
52. Kunitomo H, Ishitobi H, Nakagawa N (2015) Optimized CeO_2 content of the carbon nanofiber support of PtRu catalyst for direct methanol fuel cells. J Power Sources 297:400–407
53. Lashkenari MS, Ghasemi AK, Ghorbani M, Rezaei S (2021) Fabrication of RGO/PANI-supported Pt/Cu nanoparticles as robust electrocatalyst for alkaline methanol electrooxidation. J Mater Sci: Mater Electron 32:4833–4845
54. Li B, Higgins DC, Zhu S, Li H, Wang H, Ma J, Chen Z (2012) Highly active Pt–Ru nanowire network catalysts for the methanol oxidation reaction. Catal Commun 18:51–54
55. Li J, Zhao L, Li X, Hao S, Wang Z (2020) Fabrication of C@MoxTi$_{1-x}O_2-\delta$ nanocrystalline with functionalized interface as efficient and robust PtRu catalyst support for methanol electrooxidation. J Energy Chem 40:7–14
56. Li K, Jin Z, Ge J, Liu C, Xing W (2017) Platinum nanoparticles partially-embedded into carbon sphere surface: a low metal-loading anode catalyst with superior performance for direct methanol fuel cells. J Mater Chem A 5:19857–19865
57. Li M, Han G, Yang B, Chang Y, Xiao Y, Li Y (2014) Using formic acid vapor as reducer to prepare Pt nanoparticles supported on carbon nanofiber mats for methanol electrooxidation. Catal Commun 51:86–89
58. Li M, Zheng H, Han G, Xiao Y, Li Y (2017) Facile synthesis of binary PtRu nanoflowers for advanced electrocatalysts toward methanol oxidation. Catal Commun 92:95–99
59. Li S-S, Lv J-J, Hu Y-Y, Zheng J-N, Chen J-R, Wang A-J, Feng JJ (2014) Facile synthesis of porous Pt-Pd nanospheres supported on reduced graphene oxide nanosheets for enhanced methanol electrooxidation. J Power Sources 247:213–218
60. Li S-S, Yu J, Hu Y-Y, Wang A-J, Chen J-R, Feng J-J (2014) Simple synthesis of hollow Pt-Pd nanospheres supported on reduced graphene oxide for enhanced methanol electrooxidation. J Power Sources 254:119–125
61. Li S, Tian ZQ, Liu Y, Jang Z, Hasan SW, Chen, Tsiakaras P, Shen PK (2021) Hierarchically skeletal multi-layered Pt-Ni nanocrystals for highly efficient oxygen reduction and methanol oxidation reactions. Chinese J Catalysis 42(4):648–657
62. Li X, Faghri A (2013) Review and advances of direct methanol fuel cells (DMFCs) part I: design, fabrication, and testing with high concentration methanol solutions. J Power Sources 226:223–240
63. Li X, Zhou Y, Du Y, Xu J, Wang W, Chen Z, Cao J (2019) PtCu nanoframes as ultra-high performance electrocatalysts for methanol oxidation. Int J Hydrogen Energy 44:18050–18057
64. Li Y, Liu C, Liu Y, Feng B, Li L, Pan H, Kellogg W, Higgins D, Wu G (2015) Sn-doped TiO_2 modified carbon to support Pt anode catalysts for direct methanol fuel cells. J Power Sources 286:354–361

65. Li Z, Guo Y, Liu Z, Wu X, Zeng J, Hou Z, Zhou W, Liao S (2016) Highly stable and efficient platinum nanoparticles supported on TiO_2@Ru-C: investigations on the promoting effects of the interpenetrated TiO_2. Electrochim Acta 216:8–15
66. Li Z, Jiang X, Wang X, Hu J, Liu Y, Fu G, Tang Y (2020) Concave PtCo nanocrosses for methanol oxidation reaction. Appl Catalysis B: Environ 277:119135
67. Lin K, Lu Y, Du S, Li X, Dong H (2016) The effect of active screen plasma treatment conditions on the growth and performance of Pt nanowire catalyst layer in DMFCs. Int J Hydrogen Energy 41(18):7622–7630
68. Liu W, Qin X, Zhang X, Shao Z, Yi B (2016) Preparation of PtRu/WO_3–C by intermittent microwave method with enhanced catalytic activity of methanol oxidation. J Appl Electrochem 46:887–893
69. Liu W, Qin X, Zhang X, Shao Z, Yi B (2017) Wormholelike mesoporous carbon supported PtRu catalysts toward methanol electrooxidation. J Energy Chem 26(1):200–206
70. Lou Y, Li C, Gao X, Bai T, Chen C, Huang H, Liang C, Shi Z, Feng S (2016) Porous Pt nanotubes with high methanol oxidation electrocatalytic activity based on original bamboo-shaped Te nanotubes. ACS Appl Mater Interfaces 8:16147–16153
71. Lu J, Li Y, Li S, Jiang SP (2016) Self-assembled platinum nanoparticles on sulfonic acid-grafted graphene as effective electrocatalysts for methanol oxidation in direct methanol fuel cells. Sci Rep 6:21530
72. Lu Q, Huang J, Han C, Sun L, Yang X (2018) Facile synthesis of composition-tunable PtRh nanosponges for methanol oxidation reaction. Electrochim Acta 266:305–311
73. Lu S, Eid K, Ge D, Guo J, Wang L, Wang H, Gu H (2017) One-pot synthesis of PtRu nanodendrites as efficient catalyst for methanol oxidation reaction. Nanoscale 9:1033–1039
74. Lu Y, Jiang Y, Wu H, Chen W (2013) Nano-PtPd cubes on graphene exhibit enhanced activity and durability in methanol electrooxidation after CO stripping-cleaning. J Phys Chem C 117(6):2926–2938
75. Maiyalagan T, Khan FN (2009) Electrochemical oxidation of methanol on Pt/V2O5–C composite catalysts. Catal Commun 10(5):433–436
76. Mansor M, Timmiati SN, Lim KL, Wong WY, Kamarudin SK, Kamarudin NHN (2019) Recent progress of anode catalysts and their support materials for methanol electrooxidation reaction. Int J Hydrogen Energy 44:14744–14769
77. Mao J, Chen Y, Pei J, Wang D, Li Y (2016) Pt-M (M = Cu, Fe, Zn, etc) bimetallic nanomaterials with abundant surface defects and robust catalytic properties. Chem Commun 52:5985–5988
78. Mathe NR, Scriba MR, Coville NJ (2014) Methanol oxidation reaction activity of microwaveirradiated and heat-treated Pt/Co and Pt/Ni nano-electrocatalysts. Int J Hydrogen Energy 39:18871–18881
79. Mu X, Xu Z, Xie Y, Mi H, Ma J (2017) Pt nanoparticles supported on Co embedded coal-based carbon nanofiber for enhanced electrocatalytic activity towards methanol electro-oxidation. J Alloy Compd 711:374–380
80. Ojani R, Hasheminejad E, Raoof JB (2015) Direct growth of 3D flower-like Pt nanostructures by a template-free electrochemical route as an efficient electrocatalyst for methanol oxidation reaction. Energy 90:1122–1131
81. Paik Y, Kim S-S, Han OH (2008) Methanol behavior in direct methanol fuel cells. Angew Chem Int Ed 47(1):94–96
82. Pinithchaisakula A, Ounnunkada K, Themsirimongkon S, Promsawana N, Waenkaewa P, Saipanya S (2017) Efficiency of bimetallic PtPd on polydopamine modified on various carbon supports for alcohol oxidations. Chem Phys 483–484:56–67
83. Pu L, Zou L, Zhou Y, Zou Z, Yang H (2017) High performance MWCNT–Pt nanocomposite based cathode for passive direct methanol fuel cells. RSC Adv 7:12329
84. Qian H, Chen S, Fu Y, Wang X (2015) Platinum–palladium bimetallic nanoparticles on graphitic carbon nitride modified carbon black: a highly electroactive and durable catalyst for electrooxidation of alcohols. J Power Sources 300:41–48
85. Qiu P, Lian S, Yang G, Yang S (2017) Halide ion-induced formation of single crystalline mesoporous PtPd bimetallic nanoparticles with hollow interiors for electrochemical methanol and ethanol oxidation reaction. Nano Res 10(3):1064–1077

86. Radhakrishnan T, Sandhyarani N (2019) Pt-Ag nanostructured 3D architectures: a tunable catalyst for methanol oxidation reaction. Electrochim Acta 298:835–843
87. Ramli ZAC, Kamarudin SK, Zainoodin AM, Basri S (2019) Synthesis, characterization and potential of Pt-Ru supported carbon nanocage (CNC) electrocatalyst for future DMFC. Int J Integr Eng 11(7):190–200
88. Rashidi R, Dincer I, Naterer GF, Berg P (2009) Performance evaluation of direct methanol fuel cells for portable applications. J Power Sources 187:509–516
89. Ren X, Lv Q, Liu L, Liu B, Wang Y, Liu A, Wu G (2020) Current progress of Pt and Pt-based electrocatalysts used for fuel cells. Sustain Energy Fuels 4:15
90. Rodriguez JR, Félix RM, Reynoso EA, Gochi-Ponce Y, VerdeGómez Y, Moyado SF, Alonso-Núñez G (2014) Synthesis of Pt and Pt-Fe nanoparticles supported on MWCNTs used as electrocatalysts in the methanol oxidation reaction. J Energy Chem 23(4):483–490
91. Rufino ECG, Purgato FLS, Olivi P (2012) Influence of modifications to the pechini method on the electroactivity and stability of Pt-RuOx/C catalysts. J Electrochem Soc 159:F393–F397
92. Sahoo NG, Pan Y, Li L, Chan SH (2012) Graphene-Based Materials for Energy Conversion. Adv Mater 24(30):4203–4210
93. Sha R, Badhulika S (2018) Facile synthesis of three-dimensional platinum nanoflowers on reduced graphene oxide—tin oxide composite: an ultra-high performance catalyst for methanol electro-oxidation. J Electroanal Chem 820:9–17
94. Sha R, Jones SS, Badhulika S (2019) Controlled synthesis of platinum nanoflowers supported on carbon quantum dots as a highly effective catalyst for methanol electro-oxidation. Surf Coat Technol 360:400–408
95. Shahrokhian S, Rezaee S (2018) Vertically standing Cu_2O nanosheets promoted flower-like PtPd nanostructures supported on reduced graphene oxide for methanol electro-oxidation. Electrochim Acta 259:36–47
96. Shrivastava NK, Thombre SB, Chadge RB (2016) Liquid feed passive direct methanol fuel cell: challenges and recent advances. Ionics 22:1–23
97. Siwal SS, Thakur S, Zhang QB, Thakur VK (2019) Electrocatalysts for electrooxidation of direct alcohol fuel cell: chemistry and applications. Mater Today Chem 14:100182
98. Sun Q, Park S-J, Kim S (2015) Preparation and electrocatalytic oxidation performance of Pt/MnO_2-graphene oxide nanocomposites. J Ind Eng Chem 26:265–269
99. Sun X, Zhu X, Zhang N, Guo J, Guo S, Huang X (2015) Controlling and self assembling of monodisperse platinum nanocubes as efficient methanol oxidation electrocatalysts. Chem Commun 51:3529
100. Tang H, Hao H, Zhu J, Guan X, Qiu B, Li Y (2019) Single Pt–Pd bimetallic nanoparticle electrode: controllable fabrication and unique electrocatalytic performance for the methanol oxidation reaction. Chem A Euro J 25(19):4935–4940
101. Themsirimongkon S, Pongpichayakul N, Fang L, Jakmunee J, Saipanya S (2020) New catalytic designs of Pt on carbon nanotube-nickel-carbon black for enhancement of methanol and formic acid oxidation. J Electroanal Chem 876:114518
102. Tian M, Shi S, Shen Y, Yin H (2019) PtRu alloy nanoparticles supported on nanoporous gold as an efficient anode catalyst for direct methanol fuel cell. Electrochim Acta 293:390–398
103. Tian XL, Wang L, Deng P, Chen Y, Xia BY (2017) Research advances in unsupported Pt-based catalysts for electrochemical methanol oxidation. J Energy Chem 26:1067–1076
104. Tiwari JN, Tiwari RN, Singh G, Kim KS (2013) Recent progress in the development of anode and cathode catalysts for direct methanol fuel cells. Nano Energy 2:553–578
105. Tsukagoshi Y, Ishitobi H, Nakagawa N (2018) Improved performance of direct methanol fuel cells with the porous catalyst layer using highly-active nanofiber catalyst. Carbon Resources Convers 1(1):61–72
106. Tu W, Sun Y, Wu D, Wang H, Huang H, Shao M, Liu Y, Kang Z (2019) Cobalt oxyhydroxide and carbon dots modified by platinum as superior electrocatalyst for methanol oxidation. Mater Chem Phys 225:64–71
107. Veizaga NS, Rodriguez VI, Rocha TA, Bruno M, Scelza OA, de Miguel SR, Gonzalez ER (2015) Promoting effect of tin in platinum electrocatalysts for direct methanol fuel cells (DMFC). J Electrochem Soc 162:F243–F249

108. Vilian ATE, Hwang S-K, Kwak CH, Oh SY, Kim C-Y, Lee G-W, Lee JB, Huh YS, Han Y-K (2016) Pt-Au bimetallic nanoparticles decorated on reduced graphene oxide as an excellent electrocatalysts for methanol oxidation. Synth Met 219:52–59
109. Viva FA (2020) Platinum-based cathode catalyst systems for direct methanol fuel cells. Chapter 9. Direct Methanol Fuel Cell Technol 257–287
110. Vu THT, Tran TTT, Le HNT, Tran LT, Nguyen PHT, Nguyen HT, Bui NQ (2015) Solvothermal synthesis of P-SiO_2/graphene nanocomposites as efficient electrocatalyst for methanol oxidation. Electrochim Acta 161:335–342
111. Wang H, Xue Y, Zhu B, Yang J, Wang L, Tan X, Wang Z, Chu Y (2017) CeO_2 nanowires stretch-embedded in reduced graphite oxide nanocomposite support for Pt nanoparticles as potential electrocatalyst for methanol oxidation reaction. Int J Hydrogen Energy 42:20549–20559
112. Wang H, Yu H, Li Y, Yin S, Xue H, Li X, Xu Y, Wang L (2018) Direct synthesis of bimetallic PtCo mesoporous nanospheres as efficient bifuctional electroctalysts for both oxygen reduction reaction and methanol oxidation reaction. Nanotechnology 29:175403
113. Wang H, Zheng J, Peng F, Yu H (2013) Pt/IrO_2/CNT anode catalyst with high performance for direct methanol fuel cells. Catal Commun 33:34–37
114. Wang X, Lian J, Wang Y (2014) The effect of Sn on platinum dispersion in Pt/graphene catalysts for the methanol oxidation reaction. Int J Hydrogen Energy 39(26):14288–14295
115. Wang Y, Wang J, Han G, Du C, Sun Y, Du L, An M, Yin G, Gao Y, Song Y (2019) Superior catalytic performance and CO tolerance of Ru@Pt/C-TiO_2 electrocatalyst toward methanol oxidation reaction. Appl Surf Sci 473:943–950
116. Wu K, Zhang Q, Sun D, Zhu X, Chen Y, Lu T, Tang Y (2015) Graphene-supported Pd-Pt alloy nanoflowers: In situ growth and their enhanced electrocatalysis towards methanol oxidation. Int J Hydrogen Energy 40:6530–6537
117. Wu P, Zhang H, Qian Y, Hu Y, Zhang H, Cai C (2013) Composition- and aspect-ratio-dependent electrocatalytic performances of one-dimensional aligned pt–ni nanostructures. J Phys Chem C 117(37):19091–19100
118. Wu X, Zhuang W, Lu L, Li L, Zhu J, Mu L, Li W, Zhu Y, Lu X (2017) Excellent performance of Pt-C/TiO_2 for methanol oxidation: Contribution of mesopores and partially coated carbon. Appl Surf Sci 426:890–896
119. Xiao M, Zhu J, Ge J, Liu C, Xing W (2015) The enhanced electrocatalytic activity and stability of supported Pt nanopartciles for methanol electro-oxidation through the optimized oxidation degree of carbon nanotubes. J Power Sources 281:34–43
120. Xu G, Si R, Liu J, Zhang L, Gong X, Gao R, Liu B, Zhang J (2018) Directed self-assembly pathways of three-dimensional Pt/Pd nanocrystal superlattice electrocatalysts for enhanced methanol oxidation reaction. J Mater Chem A 2018(6):12759–12767
121. Xu X, Zhang X, Sun H, Yang Y, Dai X, Gao J, Li X, Zhang P, Wang H-H, Yu N-F, Sun S-G (2014) Synthesis of Pt–Ni alloy nanocrystals with high-index facets and enhanced electrocatalytic properties. Angew Chem 126:12730–12735
122. Xu X, Zhou Y, Lu J, Tian X, Zhu H, Liu J (2014) Single-step synthesis of PtRu/N-doped graphene for methanol electrocatalytic oxidation. Electrochim Acta 120:439–451
123. Yan X, Liu T, Jin J, Devaramani S, Qin D, Lu X (2016) Well dispersed Pt–Pd bimetallic nanoparticles on functionalized graphene as excellent electro-catalyst towards electro-oxidation of methanol. J Electroanal Chem 770:33–38
124. Yang C, Zhang D, Zhao W, Cui M, Liang R, Ou Q, Zhang S (2020) Plasma-synthesized octahedral PtPd alloy/reduced graphene oxide nanocomposites with boosted electrocatalytic activity for methanol oxidation. J Alloys Compounds 835:155334
125. Yang L, Li G, Ma R, Hou S, Chang J, Ruan M, Cai W, Jin Z, Xu W, Wang G, Ge J, Liu C, Xing W (2021) Nanocluster PtNiP supported on graphene as an efficient electrocatalyst for methanol oxidation reaction. Nano Res 14:2853–2860
126. Yang Y, Cao Y, Yang L, Huang Z, Long NV (2018) Synthesis of Pt–Pd bimetallic porous nanostructures as electrocatalysts for the methanol oxidation reaction. Nanomaterials 8(4):208

127. Yang Y, Luo L-M, Guo Y-F, Dai Z-X, Zhang R-H, Sun C, Zhou X-W (2016) In situ synthesis of PtPd bimetallic nanocatalysts supported on graphene nanosheets for methanol oxidation using triblock copolymer as reducer and stabilizer. J Electroanal Chem 783:132–139
128. Yao W, Jiang X, Li M, Li Y, Liu Y, Zhan X, Fu G, Tang Y (2021) Engineering hollow porous platinum-silver double-shelled nanocages for efficient electro-oxidation of methanol. Appl Catalysis B: Environ 282:119595
129. Yola ML, Eren T, Atar N, Saral H, Ermiş I (2015) Direct-methanol fuel cell based on functionalized graphene oxide with mono-metallic and bi-metallic nanoparticles: electrochemical performances of nanomaterials for methanol oxidation. Electroanalysis 28(3):570–579
130. You E, Guzmán-Blas R, Nicolau E, Scibioh MA, Karanikas CF, Watkins JJ, Cabrera CR (2012) Co-deposition of Pt and ceria anode catalyst in supercritical carbon dioxide for direct methanol fuel cell applications. Electrochim Acta 75:191–200
131. Yousaf AB, Imran M, Zaidi SJ, Kasak P (2019) Engineering and understanding of synergistic effects in the interfaces of rGO-CNTs/PtPd nanocomposite revealed fast electro-oxidation of methanol. J Electroanal Chem 832:343–352
132. Yu S, Liu Q, Yang W, Han K, Wang Z, Zhu H (2013) Graphene–CeO_2 hybrid support for Pt nanoparticles as potential electrocatalyst for direct methanol fuel cells. Electrochim Acta 94:245–251
133. Yu X, Wang D, Peng Q, Li Y (2013) PtM (M=Cu Co, Ni, Fe) nanocrystals: from small nanoparticles to wormlike nanowires by oriented attachment. Chem Eur J 19:233–239
134. Yuan W, Zhang Y, Zhang N, Yin C, Zhang X, Liu X (2017) Carbon riveted Pt-MnO_2/reduced graphene oxide anode catalyst for DMFC. Catal Commun 100:66–70
135. Yuda A, Ashok A, Kumar A (2020) A comprehensive and critical review on recent progress in anode catalyst for methanol oxidation reaction. Catalysis Rev https://doi.org/10.1080/01614940.2020.1802811
136. Zaidi SJ, Bello M, Al-Ahmed A, Yousaf AB, Imran M (2017) Mesoporous carbon supported Pt/MO_2 (M = Ce, Pr, Nd, Sm) heteronanostructure: promising non-Ru methanol oxidation reaction catalysts for direct methanol fuel cell application. J Electroanal Chem 794:86–92
137. Zhan F, Bian T, Zhao W, Zhang H, Jin M, Yang D (2014) Facile synthesis of Pd–Pt alloy concave nanocubes with high-index facets as electrocatalysts for methanol oxidation. CrystEngComm 16:2411
138. Zhang C, Xu L, Yan Y, Chen J (2016) Controlled synthesis of Pt nanowires with ordered large mesopores for methanol oxidation reaction. Sci Rep 6:31440
139. Zhang C, Zhang Y, Xiao H, Zhang J, Li L, Wang L, Bai Q, Liu M, Wang Z, Sui N (2021) Superior catalytic performance and CO tolerance of PtCu/graphdiyne electrocatalyst toward methanol oxidation reaction. Colloids Surfaces A: Physicochem Eng Aspects 612:125960
140. Zhang G, Yang Z, Zhang W, Wang Y (2017) Nanosized Mo-doped CeO_2 enhances the electrocatalytic properties of the Pt anode catalyst in direct methanol fuel cells. J Mater Chem A 5:1481–1487
141. Zhang H, Chen M, Xu L, Hou W, Liu X, Chen F (2017) Laser irradiation-induced construction of Pt/Ag bimetallic nanourchins with improved electrocatalytic properties. RSC Adv 7:52165
142. Zhang K, Chen X, Wang L, Zhang D, Xue Z, Zhou X, Lu X (2018) Pt-Pd nanoparticles supported on sulfonated nitrogen sulfur co-doped graphene for methanol electro-oxidation. Int J Hydrogen Energy 43:15931–15940
143. Zhang L, Li N, Gao F, Hou L, Xu Z (2012) Insulin amyloid fibrils: an excellent platform for controlled synthesis of ultrathin superlong platinum nanowires with high electrocatalytic activity. J Am Chem Soc 134:11326–11329
144. Zhang L, Zhang X-F, Chen X-L, Wang A-J, Han D-M, Wang ZG, Feng J-J (2019) Facile solvothermal synthesis of $Pt_{71}Co_{29}$ lamellar nanoflowers as an efficient catalyst for oxygen reduction and methanol oxidation reactions. J Colloid Interface Sci 536:556–562
145. Zhang Q, Yang Z, Ling Y, Yu X, Zhang Y, Cheng H (2018) Improvement in stability of PtRu electrocatalyst by carbonization of in-situ polymerized polyaniline. Int J Hydrogen Energy 43(28):12730–12738

146. Zhang S, Rong H, Yang T, Bai B, Zhang J (2019) Ultrafine PtRu dilute alloy nanodendrites for enhanced electrocatalytic methanol oxidation. Chem Eur J 25:1–8
147. Zhang X, Tian S, Yu W, Lu B, Shen T, Xu L, Sun D, Zhang S, Tang Y (2018) Nanotube-shaped PtFe intermetallics: Control synthesis, crystal structure and their improved electrocatalytic activities. CrystEngComm 20:4277–4282
148. Zhang Y, Chang G, Shu H, Oyama M, Liu X, He Y (2014) Synthesis of Pt-Pd bimetallic nanoparticles anchored on graphene for highly active methanol electro-oxidation. J Power Sources 262:279–285
149. Zhao L, Wang Z-B, Liu J, Zhang J-J, Sui X-L, Zhang L-M, Gu DM (2015) Facile one-pot synthesis of Pt/graphene-TiO_2 hybrid catalyst with enhanced methanol electrooxidation performance. J Power Sources 279:210–217
150. Zhao R, Fu G, Chen Z, Tang Y, Wang Y, Huang S (2019) A novel strategy for the synthesis of hollow Pt–Cu tetradecahedrons as an efficient electrocatalyst toward methanol oxidation. CrystEngComm 21:1903–1909
151. Zhao S, Yin H, Du L, Yin G, Tang Z, Liu S (2014) Three dimensional N-doped graphene/PtRu nanoparticle hybrids as high performance anode for direct methanol fuel cells. J Mater Chem A 2:3719
152. Zheng J, Cullen DA, Forest RV, Wittkopf J, Zhuang Z, Sheng W, Chen JG, Yan Y (2015) Platinum-ruthenium nanotubes and platinum-ruthenium coated copper nanowires as efficient catalysts for electro-oxidation of methanol. ACS Catal 5(3):1468–1474
153. Zheng Y, Zhang X, Zhang Z, Li Y, Sun Y, Lou Y, Li X, Lu Y (2018) Preparation and application of ZnO doped Pt-CeO_2 nanofibers as electrocatalyst for methanol electro-oxidation. J Rare Earths 36:974–980
154. Zhuang L, Wang W, Hong F, Yang S, You H, Fang J, Ding B (2012) Porous platinum mesoflowers with enhanced activity for methanol oxidation reaction. J Solid State Chem 191:239–245

Carbon Composites and Catalysts for Decomposition of Organic Pollutants

Siara Silvestri and Mayara Gabriela Gonçalves

Abstract This chapter discusses hybrid composites, which comprise a carbonaceous matrix material (amorphous carbon, activated carbon, biochar, hydrochar, polymeric carbon, graphene, graphene oxide, reduced graphene oxide, carbon nanotubes, and fullerenes) that serve as a support and/or or anchor of a photocatalyst. Each composite component contributes to the catalytic performance and the mechanism for these good effects is the key point, and these effects can be: Single support effect, stabilization of microstructure or active components, dual function effect on pollutant degradation reactions, influence in the speed of adsorption/desorption and diffusion of molecules, influences the migration or transfer of active free radical species (O_2-•, h^+, •OH, $1O_2$), improves mechanics, thermomechanics, electronics or other physical and chemical properties, especially for catalyst polymer matrix composites. Factors such as carbonaceous matrix preparation temperature, origin of this matrix or biomass, pH and synthesis conditions can positively or negatively affect the electron transfer process in the composite, making the composite efficient or not in the degradation of organic pollutants in aqueous media. The application of a carbonaceous matrix in the formation of photocatalytic composites has numerous advantages, as will be seen throughout the chapter. The presence of a carbonaceous matrix facilitates the process of removing the photocatalyst from the medium, facilitates the electron transfer process, requiring less energy to activate the photocatalyst. It is also possible to use carbon from organic waste, such as biomass, reducing the cost of producing composites. These and other advantages will be discussed throughout the chapter, as well as the influence of the synthesis process to obtain a composite with very high photocatalytic efficiency to be applied in the degradation of emerging pollutants.

Keywords Carbon materials · Heterostructures · Supported photocatalysts · Treatment of contaminants

S. Silvestri (✉) · M. G. Gonçalves
Federal University of Santa Maria, Av. Roraima 1000, Santa Maria, Brazil
e-mail: siarasilvestri@gmail.com

M. Jawaid and A. Khan (eds.), *Carbon Composite Catalysts*, Composites Science and Technology, https://doi.org/10.1007/978-981-19-1750-9_9

Abbreviations and Acronyms

AOP	Advanced oxidative processes
BC	Conduction band
BV	Valence band
CNT	Carbon nanotube
EPFR	Environmental persistent free radicals
GAC	Granular activated carbon
GO	Graphene oxide
HTC	Hydrothermal carbonization
rGO	Reduced graphene oxide
ROS	Reactive oxidative species
SAC	Spherical activated carbon
UV	Ultraviolet irradiation

1 General Introduction: Photocatalysts for Treatment of Contaminants

In the past, water and its capacity for self-purification were seen as infinite properties. However, the increase in the number of inhabitants on the planet and the increase in the consumption of chemicals that end up in aquatic environments have raised concerns about the quality and availability of water for human consumption, due to the rapid degradation of wastewater [1, 2].

For contaminants resistant to conventional water and effluent treatments, the use of advanced technologies based on chemical oxidation, such as Advanced Oxidative Processes (AOP), is one of the most viable options for effective and non-selective degradation of contaminants. AOP can be defined as treatment methods that promote the formation of highly oxidizing species, such as hydroxyl radicals ($E^0 = 2.8$ V), capable of reacting with a wide variety of organic and inorganic contaminants, causing their degradation [3, 4].

A common way of classifying AOPs is between homogeneous and heterogeneous processes, based on how catalysts are found in the reaction medium. Being fully dissolved in homogeneous processes and forming suspended particulate colloids in heterogeneous processes [4].

The difficulty in removing catalysts after treatment has limited the widespread use not only of homogeneous treatments, but also of heterogeneous ones, which generally use nanometric catalysts [5, 6].

Among the homogeneous processes that require additional steps to remove similar catalysts, Fenton and like-Fenton, are among the most studied. The Fenton reaction involves a complex sequence of reactions catalyzed by ferrous ions (Fe^{2+}) in an acidic environment, which lead to the decomposition of hydrogen peroxide (H_2O_2) and the formation of hydroxyl radicals [7–9].

The Fenton process has a high pH restriction, requiring adjustment between 2 and 3, because in the pH range above 3 occurs the formation of colloidal precipitates of iron hydroxides, which cease the reaction [10]. To remove the large amount of iron from the treated solution, it is necessary to precipitate it, which generates a large amount of sludge. Thus, the use of immobilized iron on carbon supports is an alternative so that Fenton processes can be carried out by solid catalysts and that preferably the variations of the reaction medium are more stable, since originally the Fenton process is highly dependent on pH [7, 10].

As for heterogeneous AOPs, such as photocatalysis with semiconductor nanoparticles (ex: TiO_2, ZnO, ZnS, WO_3), the main bottleneck in the process is the high dependence on an artificial source of ultraviolet radiation, a high rate of recombination of the electron–hole pair and low photon utilization efficiency. Since the association between semiconductors and carbon materials also generated an important improvement in photocatalytic activity, allowing the degradation of various contaminants such as medicines [11–14], dyes [15–17], pesticides [14, 18, 19], and synthetic hormones [20].

In this chapter, various aspects of composite carbon catalysts applied to the degradation of contaminants will be covered, such as the different types of carbon materials used, the methods of preparation and some fundamental characterizations for these materials. The relationships between the synthesis variables and the composition and properties of the catalysts will also be discussed critically. Ways to improve photocatalytic activity and some mechanisms of charge generation proposed in different studies will also be addressed.

1.1 Photocatalysis for Treatment of Contaminants

AOPs can be defined as processes in which highly oxidizing and non-selective transient species are generated, the main one being the hydroxyl radical (•OH), whose reduction potential is approximately +2.8 V at 25 °C, which allows to transform several toxic contaminants quickly [4, 21].

There are three basic mechanisms of oxidation of organic compounds through the hydroxyl radical: proton abstraction, electron transfer and addition of radicals [22]. Equations 1, 2 and 3 represent, respectively, the three mechanisms:

$$^{\bullet}OH + RH \rightarrow R^{\bullet} + H_2O \quad (1)$$

$$^{\bullet}OH + RX \rightarrow RX^{\bullet} + {}^{-}OH \quad (2)$$

$$^{\bullet}OH + PhX \rightarrow OH\,PhX^{\bullet} \quad (3)$$

Due to their instability, such radicals must be generated in situ, continuously, through chemical or photochemical processes.

In chemical processes, the formation of radicals occurs through the combination of oxidizing agents, the main methods being: O_3/H_2O_2, Fenton (Fe^{2+}/H_2O_2) and like-Fenton (other metallic cations, in addition to Fe^{2+}/H_2O_2). The photochemical processes, in turn, occur through the action of ultraviolet radiation combined with the chemical oxidants already mentioned, or even semiconductors, such as titanium dioxide (TiO_2) and zinc oxide (ZnO). The main photochemical AOPs are O_3/UV, H_2O_2/UV, TiO_2/UV, TiO_2/H_2O_2/UV, ZnO/UV and photo-Fenton (Fe^{2+}/H_2O_2/UV or visible light) [4, 11, 23, 24].

In 1894, Henry J. Fenton demonstrated that hydrogen peroxide could be activated by ferrous salts to intensify the oxidation of malic acid. Subsequently, other studies have shown that a combination of hydrogen peroxide and ferrous ions promotes the generation of hydroxyl radicals, (Eq. 4). In parallel, the hydroxyl radical can oxidize another ferrous ion (Eq. 5), or even react with hydrogen peroxide (Eq. 6) [23, 25]. When the reagents are in excess, these secondary reactions are favored and there is an important loss in the efficiency of the process, since, in these cases, the ferrous ion and hydrogen peroxide act as scavengers of hydroxyl radicals [10].

$$Fe^{2+} + H_2O_2 \rightarrow Fe^{3+} + OH^- + {}^{\bullet}OH \tag{4}$$

$$Fe^{2+} + {}^{\bullet}OH \rightarrow Fe^{3+} + OH^- \tag{5}$$

$$H_2O_2 + {}^{\bullet}OH \rightarrow H_2O + HO_2^{\bullet} \tag{6}$$

The pH of the reaction medium is a factor that strongly influences the Fenton process. As can be seen in Eq. 4, during the reaction between Fe^{2+} and H_2O_2 one of the products formed is the hydroxyl ion (OH^-), which can precipitate Fe^{3+} ions in the form of hydroxides (Eq. 7), as well as decomposing the peroxide of hydrogen in water and molecular oxygen, ceasing the production of radicals (Eq. 8). To avoid this problem, protons are added to the medium to form water and ferric ions (Eq. 9) [10, 23].

$$Fe^{3+}\,(aq) + 3OH^-\,(aq) \rightarrow Fe(OH)_3\,(s) \tag{7}$$

$$H_2O_2 + HO^- \rightarrow 2H_2O + O_2 \tag{8}$$

$$2Fe^{2+} + H_2O_2 + 2H^+ \rightarrow 2Fe^{3+} + 2H_2O \tag{9}$$

These equations indicate the need for an acidic environment so that the maximum production of hydroxyl radicals is achieved. Studies have shown that the Fenton reaction is favored at a pH close to 3, because in an aqueous solution the iron ions exist in the form of different complexes depending on the pH range $(Fe(H_2O_2)_6)^{3+}$ at pH = 1–2; $Fe(OH)(H_2O_2)_5{}^{2+}$ at pH = 2–3; $Fe(OH)(H_2O_2)^{4+}$ at pH = 3–4 and $Fe(OH)_3$ at pH > 5) [26], and $Fe(OH)(H_2O)_5{}^{2+}$, or simply, $Fe(OH)^{2+}$ predominant in

pH 3 is the one with the highest catalytic activity. Its maximum absorbance occurs at a wavelength of 300 nm, and can extend up to approximately 400 nm [27].

Another relevant aspect is that the ferric ions generated can catalyze the decomposition of hydrogen peroxide through the process known as like-Fenton (Eqs. 10 and 11), in which Fe^{2+} is regenerated and hydroperoxide radicals ($HO_2^{\bullet}$) are formed.

$$Fe^{3+} + H_2O_2 \rightarrow FeOOH_2^+ + H^+ \tag{10}$$

$$FeOOH_2^+ \rightarrow HO_2^{\bullet} + Fe^{2+} \tag{11}$$

The rate of removal of organic pollutants by reagent Fe^{3+}/H_2O_2 ($k = 3.1 \times 10^{-3\ s-1}$) is less than that of reagent Fe^{2+}/H_2O_2 ($k = 76$ mol L^{-1} s^{-1}), possibly due to the lower reactivity of Fe^{3+} towards H_2O_2 and because the hydroperoxide radicals have a very low oxidation potential when compared to the hydroxyl radials. Also called Fenton-like systems are those in which hydrogen peroxide is combined with other metallic cations, such as copper, manganese, chromium or any form of iron other than ferrous ions. The degradation efficiency of substances by the Fenton process can be increased when it occurs in the presence of an irradiation source, a system known as photo-Fenton [23, 27].

Several studies have already used the Fenton and photo-Fenton processes to treat water containing pesticides [10], medicines [8, 28], dyes [25], among many other examples. However, the large generation of sludge after the precipitation of metals to remove the treated solution remains the main problem associated with Fenton's processes, hence the need for the use of supports.

Heterogeneous photocatalysis is another type of AOP whose catalysts have shown good performance in several studies when combined with carbon materials. The performance of carbon materials will be covered in detail later.

In the original process, heterogeneous photocatalysis is initiated when UV light, with energy equal to or greater than the band gap of a semiconductor, promotes an electron from the valence band (BV) to the conduction band (BC), creating a reducer of local BC (e^-) and an oxidation site in BV (h^+) [3, 23]. In this way the so-called electron–hole pair (e^-/h^+) is formed, which allows the semiconductor to act both as an electron acceptor and as a donor, triggering various oxidation reactions [5, 29, 30] (Fig. 1).

The positive hole can promote the oxidation of water and OH-ions, generating radicals $^{\bullet}OH$, as shown below. The excited electron, in turn, reduces O molecules to form the superoxide radical anion ($O_2^{\bullet -}$), which can generate other reactive species, such as the hydroperoxide radical $^{\bullet}OOH$ and hydrogen peroxide H_2O_2 [5, 29, 30].

$$2H_2O + 4e^- \rightarrow O_2 + 4H^+ \tag{12}$$

$$e^- + O_2 \rightarrow O_2^{-\bullet} \tag{13}$$

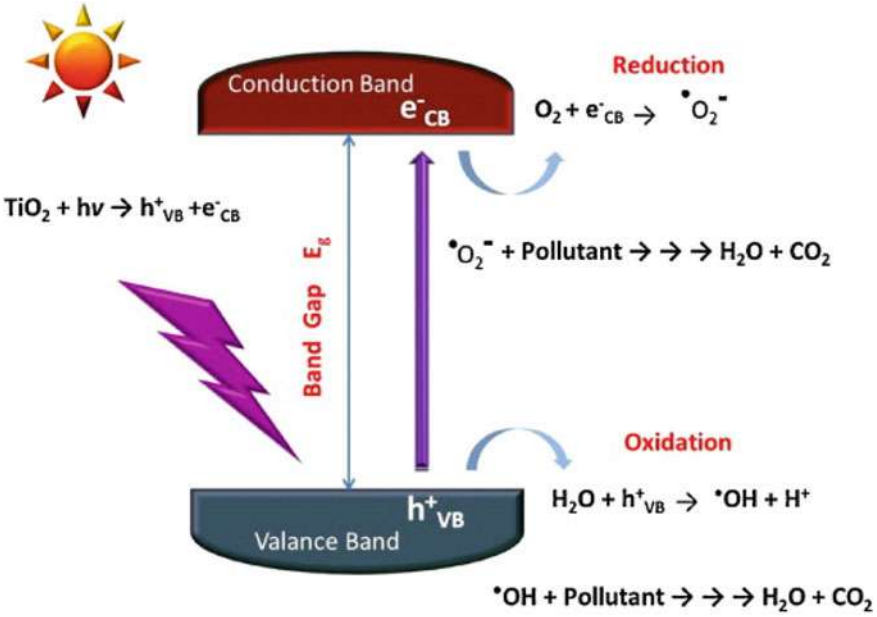

Fig. 1 Scheme of the photocatalytic process on the surface of a semiconductor in an aqueous medium after radiation absorption. Reproduced with permission from Ref. [29]

$$2O_2^{\bullet -} + 2H_2O \rightarrow H_2O_2 + 2HO^- + O_2 \tag{14}$$

$$H_2O_2 + e^- \rightarrow HO^- + {}^{\bullet}OH \tag{15}$$

All species produced in the photocatalysis, including the hole (h^+), can react directly with the target contaminant, chemically converting it into intermediate molecules or completely mineralizing, as is more desirable.

Among the semiconductors used in photocatalysis, TiO_2 appears as a major highlight, due to characteristics such as high photocatalytic efficiency, stability, low cost and less toxicity compared to other photocatalysts [31, 32]. The most photoactive phase of TiO_2, anatase, presents a band gap around 3.2 eV, corresponding to the energy of the UV-A fraction (380 nm) which is equivalent to only 5% of the solar spectrum [32]. Another semiconductor widely used in photocatalysis is zinc oxide. ZnO has a 3.37 eV band gap and violet absorption at room temperature [33]. Although ZnO absorbs a larger fraction of the solar spectrum, which reduces the need for artificial sources of energy, its photocatalytic efficiency is lower than that of TiO_2 because it is a direct semiconductor, so it is often necessary to use an agent electron scavenger, in order to avoid recombination of the electron–hole pair [5, 6, 30, 31].

The great utility of these processes is centered on the treatment of effluents resistant to conventional treatments, however many of these processes can also be used

for the air decontamination [34], soil remediation [35] and disinfection of water by inactivating bacteria and viruses [36].

2 Photocatalysts Supported on Carbon Materials

In recent years, notable efforts have been made to allow the implementation of photocatalytic processes on a large scale. To this end, studies have already reported the use of the most diverse types of associations between conventional catalysts and other materials, which can serve as a support, to facilitate the recycling of the catalyst, or to form composites with exclusive physical and chemical properties.

For the Fenton process, the use of iron immobilized in clays and zeolites or iron minerals, such as goethite, hematite, magnetite and ferridrite, instead of iron salts were some alternatives evaluated by the researchers, but which have low efficiency in relation to the process homogeneous [23, 37]. The use of carbon-based supports, however, has generated greater interest for their high specific surface areas and high absorption of visible light.

A considerable increase in the generation of hydroxyl radicals can be achieved when the Fenton reaction is photocatalyzed by ultraviolet light or visible light, a process known as photo-Fenton [7], therefore, the high absorption of light by the carbon support can assist and increase the reactions of degradation of contaminants on the surface [38].

The positive effect of using carbon supports is due to two main factors: (I) it increases the rate of the peroxide direct photolysis reaction, which produces additional amounts of $^{\bullet}OH$; (II) participates in the photo-reduction of Fe^{3+}, regenerating from Fe^{2+}, which will be able to react with more H_2O_2 molecules [39].

In the case of heterogeneous photocatalysis, it is widely reported in the literature that, in order to decrease the costs of implantation in large-scale systems, it is also necessary to reduce the need for artificial sources of radiation and electron sequestrating agents (such as O_2) [5, 30, 31] therefore it is of interest that the supports can also assist in these functions.

Doping with metallic nanoparticles, heterojunctions between semiconductors, sensitization by dyes and doping with N, S and C are some strategies used to achieve this goal. In this line, we highlight the associations of conventional catalysts, such as TiO_2 and ZnO, with carbon materials, which can allow an important improvement in the photocatalytic activity of the system and serve as support for the anchoring of NP [16, 17, 40–42]. Carbon supports have shown great advantages over others already evaluated, such as glass, silica gel, metals, ceramics, polymers, optical fibers, alumina clays, cellulose and many others [31, 43]. A large majority of supports, despite facilitating recycling, lead to a loss of catalytic efficiency due to the decrease in the active surface of the catalyst.

Carbon compounds, on the other hand, provide a high density of adsorption sites for the contaminant and bring it closer to the active surface of the semiconductor. The benefits of these composites compared to pure semiconductors are generally

attributed to: (i) increased light absorption in the visible region, (ii) favoring the charge separation process, decreasing the recombination of the electron–hole pair due to the matrix of allow the flow of electrons, and (iii) the approximation between the radicals generated and the target compounds, due to the previous adsorption of contaminants in the porous structures of the carbonaceous surface [5, 32, 44]. More details on these mechanisms will be included in Sect. 8 of this chapter.

3 Composites Prepared from Different Carbon Materials

Among the various existing carbon materials, the most used in the formation of composites for the degradation of contaminants are graphene and its derivatives, carbon nanotubes, in addition to materials produced from alternative carbon sources, such as amorphous coal, activated carbon, biochar and hydrocarbon [28, 40, 42, 43, 45, 46].

Nanometric forms of carbon (for example, polymeric carbon, graphene, graphene oxide, reduced graphene oxide, carbon nanotubes and fullerenes) have different characteristics than carbon mass materials. Among the main ones, we can mention the high surface area/volume ratio and the large amount of surface defects (many atoms with incomplete coordination), as characteristics that provide high reactivity and excellent catalytic performances [6, 47, 48].

Carbon nanotubes are attractive for the formation of composites with the semiconductors used in heterogeneous photocatalysis, as they have high electrical conductivity, mechanical resistance and high specific surface area and, in addition, their tubular shape provides a long distance for electron transport (Fig. 2), and an important factor to avoid electron recombination with the gaps and increase the photoefficiency of the catalysts.

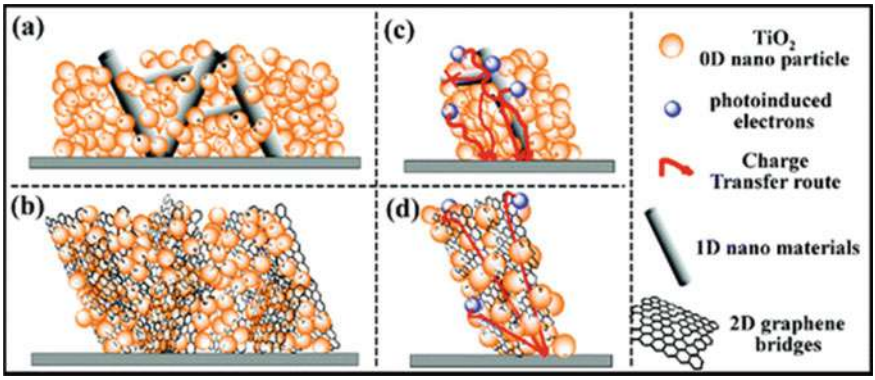

Fig. 2 Transport of electrons photogenerated by TiO_2 through **a** and **b** carbon nanotubes (1D nanomaterial) or **c** and **d** graphene (2D nanomaterial). Reproduced with permission from Ref. [49]

Graphene also has high electrical conductivity ($\sigma = 64$ mS cm^{-1}) due to π semi-filled orbitals perpendicular to the plane, which allow for electron transport [50]. Another very important characteristic is that the greater the crystallinity of graphene, the greater the electronic mobility, reaching values greater than 15,000 m^2 V^{-1} s^{-1}, which favors the flow of electrons [51] the electrons photogenerated by the semiconductor oxide are transferred to carbonaceous materials, which have greater electronics of affinity. The electron transport by graphene (2D nanomaterial) is greater than that of carbon nanotubes (1D nanomaterial), not only due to the excellent electronic mobility of graphene, but also due to the greater contact with the semiconductor [49].

One of its derivatives, graphene oxide (GO) has oxygenated functional groups on its surface and has insulating behavior. To restore part of the conductivity and maintain some oxygenated groups, which help in the interaction with some contaminants, the GO can be subjected to reduction, forming the reduced graphene oxide, rGO, an intermediate material between graphene and graphene oxide.

The presence of functional groups on the surface facilitates electrostatic interactions and hydrogen bonds with contaminants, while the electrons of the p orbitals and defects at the edges of the graphene sheets allow the π-π and Van der Waals interactions [52]. Thus, rGO has greater versatility, since it can interact with different types of contaminants, and these interactions bring contaminants closer to the surface of the catalysts (Fig. 3).

Ebrahimi et al. [19] synthesized the Mn-doped ZnO/Graphene composite and evaluated the photodegradation of the herbicide 2,4-Dichlorophenoxyacetic Acid under various conditions. They identified that by increasing the catalyst dose from 0.5 to 3 g L^{-1}, there was an improvement in the degradation efficiency until reaching the dose of 2 g L^{-1} of the composite. Above the optimum dose, the excess of catalyst was harmful, as it increased the turbidity of the solution and decreased the penetration of ultraviolet radiation. The authors also evaluated the effect of the concentration of the herbicide, from 10 to 100 mg^{-1}, and the results showed that above 50 mg L^{-1} there is a great decrease in the percentage of degradation. This was attributed to the high adsorption of 2,4-D that occupied the active surface of the catalyst, reducing the sites of adsorption of hydroxyl ions and the formation of the radical $^{\bullet}OH$.

Ng et al. [53] degraded 2,4-dichlorophenoxyacetic acid using photoelectrodes containing TiO_2 and rGO and reported a significant increase (~90%) in photocurrent generation when using the composite.

Satisfactory results have also been achieved by Lon et al. [54] which synthesized TiO_2 nanocomposites with graphene oxide and degraded more than 95% of AO7 in 20 min under optimized conditions (10 mg L^{-1} of AO7 and 163 mg L^{-1} of photocatalyst), also under UV radiation.

Table 1 presents a brief review of the literature on carbon nanomaterials composites with TiO_2 and ZnO applied to photodegradation of contaminants such as drugs, phenols, pesticides and dyes.

To further improve the feasibility of using advanced methods of degrading contaminants, many researchers are betting on the use of lower-cost carbon sources or that present simpler methods of preparation, such as biomasses. The interest in the use

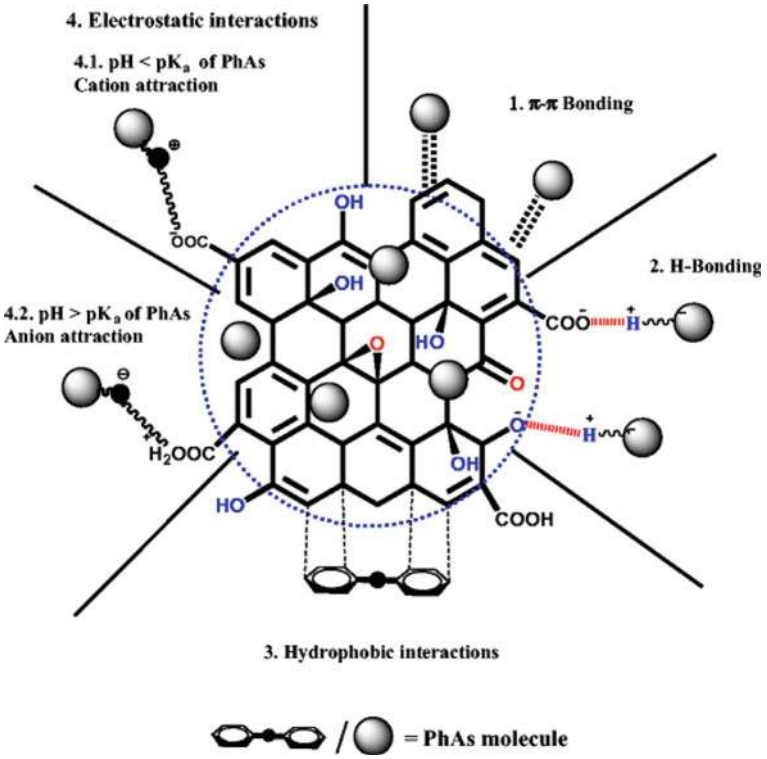

Fig. 3 Mechanisms of interaction between drugs and graphene oxides and their derivatives. Reproduced from Khan et al. [52], with permission from Springer Nature

of renewable matrices has been growing, since they are cheap and are available in large quantities, such as agro-industrial waste.

Chen et al. [59] synthesized ZnO compounds with amorphous carbon (C@ZnO), generated by the hydrothermal carbonization of glucose. In comparison to pure ZnO, the intensity of the photoluminescence of the C@ZnO nanostructures decreased in the regions of visible light, due to the effective absorption by amorphous carbon. In addition, C@ZnO showed greater adsorption and degradation capacity for the methyl orange dye than for the pure semiconductor. The study also showed that the efficiency of the composite was maintained even after five cycles, indicating good stability.

Among the materials that use alternative sources, biochar and hydrochar deserve to be highlighted, due to their low cost and for being viable alternatives for the use of the most diverse forest, agricultural and urban residues [60, 61].

The biochar is a solid from the biomass pyrolysis, under limited oxygen conditions, and the hydrochar is the main product formed when the wet biomass is heated under high pressure, so that the water behaves like a subcritical fluid. Under these conditions, the polarity of the water is reduced considerably, becoming practically

Table 1 TiO_2- and ZnO-carbon nanocomposites and their photocatalytic degradations of pollutants

Composites	Pollutant	Pollutant (concentration)	Cat. dosage	Light source	Efficiency	Time	Reference
Bi-doped TiO_2 nanotubes/graphene	MB and dinoseb (phenolic herbicide)	10 mg L^{-1}	50 mg in 180 mL	500 W linear halogen lamp	72% (dinoseb) and 95% (MB)	110 min (dinoseb) and 15 min (MB)	[18]
TiO_2/rGO	MB	10 mg L^{-1}	1 mg in 100 mL	50 W xenon lamps (λ = 400–700 nm)	96%	150 min	[55]
Mn-doped ZnO/Graphene	2,4-Dichlorophenoxyacetic Acid	25 mg L	2 g L^{-1}	LED lamp	66.2%	120 min	[19]
Ti^{3+} self-doped TiO_2/rGO	bisphenol A (BPA), phenol, acetaminophen (AAP), and sulfamethoxazole (SMX)	10 mg L^{-1}	100 mg in 100 mL	300 W Xenon lamp (λ > 420 nm)	Degradation: ~100% BPA and AAP, 77% Phenol, and 52% SMX Mineralization: 80% BPA, 53% AAP, 60% Phenol and 26% SMX	BPA 15 min; AAP 40 min; Phenol and SMX 60 min	[56]
ZnO/GO	simazine	25 ppm	10–40 mg in 4 mL	100 W metal halide lamp	64% for 10 mg and 94% for 40 mg of catalyst	60 min	[57]
ZnO/CNTs	Rhodamine B	20 mg L^{-1}	30 mg in 30 mL	Sunlight	46% decolorization and 92% COD removal	60 min	[58]

non-polar, which facilitates the volatilization of organic compounds from biomass [61, 62].

An interesting feature of biochar is the presence of organic radicals formed by the hemolytic breakdown of chemical bonds during pyrolysis. These radicals are usually centered on oxygen or carbon atoms. One of the types of radicals centered on oxygen atoms is the semiquinone, studies show that this radical contributes to the catalytic capacity of the biochar, as it can promote the generation of ^{-}OH in water [63] and transformation of $O_2^{\bullet-}$ into $^{\bullet}OH$ [17, 64]. The formation of these radicals occurs preferably at moderate temperatures and decreases at high temperatures, due to the loss of phenolic groups [65]. In addition, it plays an important role in redox reactions since the semiquinone radical tends to stabilize by oxidation (forming quinones) or reduction (forming hydroquinone). The action of the semiquinone radical as an electron acceptor in the biochar has been demonstrated in studies carried out by Chen, Kappler, Gonçalves, Silvestri and their collaborators [66–69].

Like-quinone structures were detected by EPR and IV spectroscopy in TiO_2/biochar composites and were identified as the main electron acceptor responsible for decreasing e^{-}/h^{+} recombination. The composite was used for degradation of the orange acid dye 7 (AO7) and removed 46.5% by adsorption and 57.6% by photocatalysis at 4 h [69].

Matos and collaborators [44] found that the Au-TiO_2/biochar composite performed much better than the commercial catalyst (P25 TiO_2) in degrading the methylene blue dye, reaching 30 times higher when sulfur doped and 5 times higher when nitrogen doped. The explanation for the increase in photoactivity due to the presence of sulfur is still not entirely clear, but there is a strong correlation with the increase in the volume of microcores in the biochar, which the author suggests can act as micro-reactors for the degradation of the dye. The same research group also demonstrated great efficacy of ZnO/biochar in the degradation of methylene blue, the photocatalytic activity of the composite in relation to ZnO was 2.5 times greater [70].

Recently, Zhou et al. [71] developed catalysts of three-dimensional magnetic microspheres (3D) doped with N@TiO_2 with porous architecture (MCMs doped with N@TiO_2), the microspheres were prepared from chitin biomass. Under the optimized conditions, the material adsorbed 40.15% of the methyl orange under absence of light after 40 min, and degraded 74.37% in 2 h of treatment under UV irradiation.

Activated coals have also been widely used as carbon supports. These materials are obtained by the carbonization of different types of materials, followed by an activation step, which can be physical or chemical. The consequence of activation is the formation of a support with a high specific surface area, large pore volume, good chemical stability and functional groups on the surface, which results in high adsorption capacity and a high degree of reactivity [72–74].

Another type of coal that can be used as a photocatalyst support is spherical activated carbon (SAC), also called granular activated carbon (GAC), which is produced from the carbonization of ion exchange resins. The original resins are spherical polymers that promote the replacement of cations or anions on their surface, according to

the functional groups incorporated in it. After its carbonization, the spherical shape is maintained, therefore, the SAC can act as a guiding agent for the size, dispersion and shape of the nanostructures [43, 75]. In addition, this material has high mechanical stability and has a surface area and adsorption capacity superior to that of the polymeric matrix.

Baek et al. [43] evaluated the removal of humic acids in water using the TiO_2 catalyst supported by SAC. The degradation promoted by the catalyst developed in the study was similar to that of the commercial catalyst, about 77% after 5 h of irradiation. The advantages of using SAC described by the authors were: the ease of removing the catalyst, the duration of its photoactivity for a greater number of cycles and the adsorption of the reaction intermediates by the coal.

In a study with ZnO supported on granular activated carbon, there was mineralization of 83% of the dye and 91% of discoloration after 60 min of treatment, the concentrations of contaminant and catalyst were 50 mg L^{-1} and 0.5 L^{-1}, respectively [16]. These results confirm the great advantage of using semiconductors doped or associated with other materials, especially carbonaceous.

Some studies using carbon support for TiO_2, ZnO or ferrites and applied to the degradation of aqueous pollutants are summarized in Table 2.

4 Synthesis of Heterostructures

The anchoring of photocatalysts in carbon-based materials can be accomplished using various processes, such as sol–gel, coprecipitation, hydrothermal, mechanical mixing and chemical vapor deposition [31]. The most used method for the immobilization of TiO_2 in different matrices is the sol–gel. As its name suggests, this process refers to any synthesis in which there is a transition from the "sol" state, formed by solid particles dispersed in a liquid, to the "gel" state, a continuous network of particles with filled pores by a liquid [32, 81].

The process begins with the hydrolysis of the precursors, followed by the condensation or formation of particles from the sol, which subsequently connect and form a gelatinous network and, finally, the drying or calcination stage occurs. By evaporation of the liquid it is possible to obtain powders, films, monolithic solids, aerogels and zeolites, for example. Its use is particularly useful for the synthesis of metal oxides, although some sulfides, borides and nitrides can also be produced by this route [82].

The sol–gel method has been known since the time when Elbelmen first used it in 1845 to obtain ceramics, but only in 1939 did it have its first industrial application. In the last three decades, there has been an increase in interest in this method, both in the scientific and industrial fields, as it is capable of generating high-purity and well-controlled materials. In addition, it can be an economical route, as long as the reagents are not too expensive and the pyrolysis temperature (when this step is necessary) is not too high [81, 82].

Table 2 Photocatalysts-carbon composites and their photocatalytic degradations of pollutants

Composites	Pollutant (mg L^{-1})	Dosage (g L^{-1})	Process	Efficiency (%)	Time (min)	Reference
Activated carbon/TiO_2	Diclofenac (50)	1.2	Sunlight (30 W m^2)	85	180	[76]
TiO_2/hydrothermal carbon	Diclofenac (10)	1	UV (125 W)	93	300	[13]
Coffee biochar/TiO_2	Diclofenac (10)	1	UV (125 W)	90	120	[77]
TiO_2/pBC	Sulfamethoxazole (10)	1.25	UV (50 W)	91.97	53	[78]
Biochar-based Zn-TiO_2/pBC	Sulfamethoxazole (10)	1.25	Visible light (50 W)	81.21	180	[79]
ZnO-GAC	Acid orange 7 (50)	0.5	Ultrasound (60 W)	91.2	60	[16]
biochar@$ZnFe_2O_4$/BiOBr	Ciprofloxacin (15)	0.5	Photocatalysis visible light	84	60	[80]
biochar@$CoFe_2O_4$/Ag_3PO_4	Bisphenol (20)	0.5	Photocatalysis visible light	91.12	60	[81]
$MnFe_2O_4$/biochar	Tetracycline (40)	0.5	Photo-Fenton visible light	95	120	[82]
$CuFe_2O_4$/biochar	Rhodamine B (10)	1	Photo-Fenton	88	60	[83]

For zinc oxide, the chemical precipitation method is the most common. Precipitation is the formation of a solid in an aqueous medium when it exceeds its solubility limit. The salt that presents the cation of interest is initially dissolved and will react with a precipitating agent (such as NaOH) so that it instantly forms suspended solid particles, called colloids. The interesting thing about this method is that depending on the conditions of the synthesis it is possible to control the size and shape of the particles. However, they need to have their surfaces passivated to avoid agglomeration and formation of larger particles, as colloids tend to coagulate, due to the existing forces of attraction. Therefore, it is necessary to create a hysterical impediment with molecules that can coat the surfaces of the nanoparticles preventing their growth, but that do not react with the particles themselves [83, 84].

Sol–gel and co-precipitation are methods that can be used to obtain pure oxides, or even associated with other materials. In the latter case, these methods also compete with other routes, such as mechanical mixing, chemical deposition, electrodeposition. Mechanical mixing, the simplest method, occurs by mixing the carbon material (or its precursor) with the semiconductor particles in solution, after the contact time, drying or pyrolysis is carried out. This method often requires the functionalization of the carbonaceous surface to increase its dispersion in water, if this is the solvent used. This synthesis presented results considered satisfactory by some authors [85–87], especially if the simplicity of the method is taken into account. However, a low interaction between the carbonaceous matrix and the catalyst can occur, which can make it difficult to establish a chemical bond [32].

In the case of carbon composites with semiconductors such as TiO_2 and ZnO, its can be prepared from different types of precursors, which are the initial chemical substances that present the cation from which the oxide must be obtained. For the sol–gel it is necessary that they have a tendency to form gels. The most common are alkoxides, carboxylates and some ionic salts [81]. Some examples of TiO_2 precursors are titanium trichloride, titanium tetrafluoride, titanium tetrabutoxide, titanium tetraisopropoxide and titanium oxysulfate [88]. In the case of ZnO, any zinc salt, organic or inorganic, can be used as a precursor, as long as it is initially soluble and tends to decrease its solubility with the addition of the precipitating agent. Some common examples are zinc chloride, zinc nitrate, zinc acetate and zinc citrate.

Another important variable in the synthesis of these composites is the thermal treatment, necessary both for the crystallization of the semiconductor particles and for the carbonic structure. The influences of this synthesis variable will be reported in the later sections of this chapter. For now, it is important to mention that heat treatment is usually done in muffle-type ovens, tubular oven, autoclave and under different types of environments, usually reducing or with limited amounts of oxygen to prevent ash formation.

The thermal treatment allows manipulating the physical properties of the catalyst, such as porosity, proportion of the anatase/rutile phases and surface area through the process temperature control [31, 32].

When it occurs in the presence of moisture, usually in an autoclave, it is called a hydrothermal method. This has been widely used in association with sol–gel to prepare semiconductor composites with carbon nanomaterials and hydrocarbons. If

the solvent used is non-aqueous, which allows higher temperatures to be reached, the process is called solvothermal [32].

5 Main Characterizations of Carbon Supported Photocatalysts

The physical interaction between the photocatalyst and the carbonaceous support is quite difficult to characterize using conventional techniques (FTIR, XRD, thermal analysis, etc.) because there is a considerable discrepancy between the photocatalyst/support mass ratio. On the other hand, fluorescence and UV–Vis spectroscopic analyzes for solid and microscopic characterization (SEM, TEM, AFM) are useful for this task. An example is the use of scanning electron microscopy (SEM) to visualize the formation of the composite, as presented by Lee and collaborators [89] in Fig. 4.

Microscopic characterization is mandatory to examine relevant aspects such as the distribution of the photocatalyst by the support and the general morphology of the catalytic system. As an example, we can observe (Fig. 5) the variation in the topography of the polypyrrole (support) when anchoring the $SnFe_2O_4$ photocatalyst, presented by Leichtweis and collaborators [9] and the variation in the topography of the polymethylmethacrylate (PMMA) when it supports 1% of TiO_2, presented by Gautam and collaborators [90].

In addition, due to the possibility of leaching, it is prudent to re-characterize the catalyst after the photocatalytic reactions and then compare the data with those collected for the prepared material to identify any structural or morphological changes and loss of the photocatalyst. In the case of metallic photocatalysts, EDX and XPS analyzes can be useful to investigate metal leaching and changes in its oxidation state.

In the case of polymeric carbon supports, due to functional chemical reactions or copolymerization, NMR and mass spectroscopy analyzes can also be useful [9].

It is known that when carbon matrices, such as activated carbon, biochar and hydrocarbons serve as support for a photocatalyst, the energy band of the band is reduced. This reduction is attributed to the ease of charge transfer between the energy levels (HOMO, LUMO, valence band and conduction band) of the support and the photocatalyst [91–95], as previously described. This ease of charge transfer contributes positively to the generation of electron-gap pairs, which sequentially will lead to the formation of reactive oxidative species (ROS) [96–99]. The determination of this band energy interval is fundamental for a better understanding of the functioning and activation of the composite. This parameter can be determined by solid-state diffuse reflectance spectroscopy and calculated using the Kubelka-Mulk function ($F(R) = (1 - R)^2/2R$) [69, 77, 100] or Tauc method ($\alpha h\nu = A(h\nu - E_g)^n$) [9, 101, 102], where R is reflectance, α is the absorption coefficient, $n = 2$, for permitted

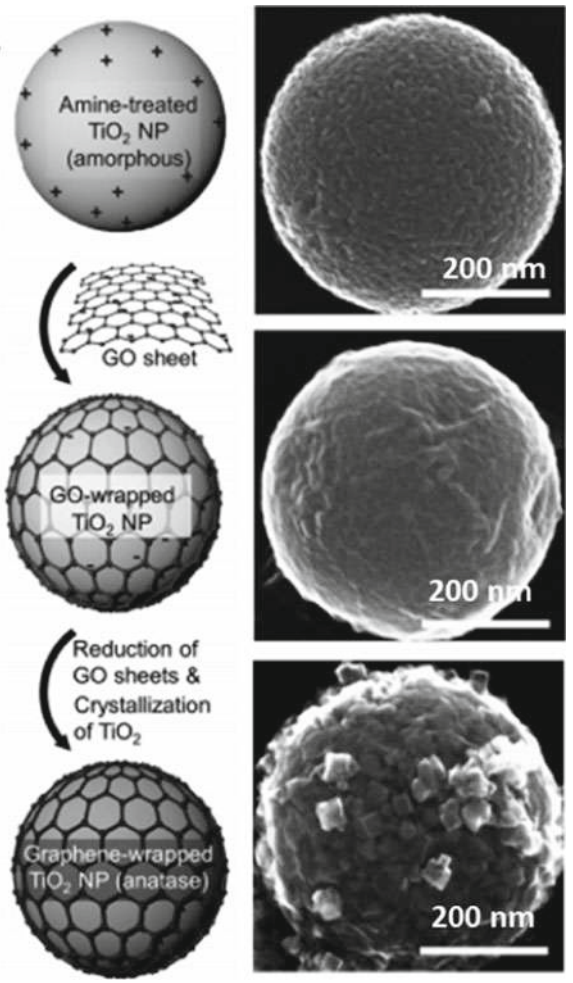

Fig. 4 SEM images of synthesis steps of graphene-wrapped TiO_2. Adapted with permission from [89]

direct transitions, and A is the characteristic parameter for the respective transitions, regardless of the photon energy hν.

Photogenerated ROS can be identified through EPR analysis with the aid of spin adducts, such as DMPO and TEMPO [64, 69, 103], or by adding scavengers to the test solution. The most used scavengers are benzoquinone (as $O_2^{-\bullet}$ trap), ammonium oxalate, ethylenediamine tetraacetic acid and triethanolamine (hole: h^+), isopropanol, tert-butyl alcohol ($^\bullet OH$), and sodium azide ($^1O_2$ singlet).

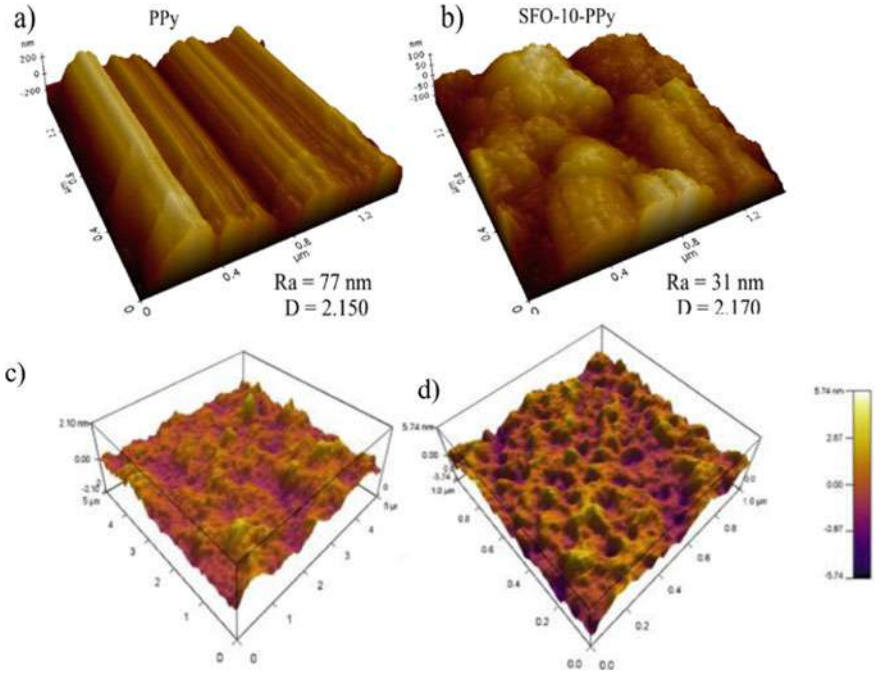

Fig. 5 AFM topography for **a** PPy and **b** SFO-10-PPy, and the surface roughness of the membranes **c** PMMA and **d** 1%TiO_2/PMM. Adapted with permission from Ref. [9, 90]

6 Correlation Between Synthesis, Composition and Material Properties

Each component of the carbonaceous matrix component contributes to catalytic performance. The mechanism for these good effects is the key point, and these effects can be:

- Simple support effect
- Stabilization of the microstructure or active components
- Dual function effect on pollutant degradation reactions
- Influence on the speed of adsorption/desorption and diffusion of molecules
- Influence on the migration or transfer of active species as $O_2^{-\bullet}$, h^+, $^\bullet OH$, $^1O_2$, etc.
- Improve mechanical, thermomechanical, electronic or other physical and chemical properties.

Biochars are carbon-rich materials with characteristics of high surface area and porous nature. Pyrolysis, gasification and hydrothermal carbonization (HTC) are used to produce biochar and hydrochar, respectively. However, several studies have reported that not all biochar has these characteristics [68, 69, 73, 77, 104–106]. Activated charcoal is available in the form of powder, grains or fibers. Powdered

activated carbons have a particle size of less than 100 μm, with an average diameter between 15 and 25 μm.

The biochar can be modified with photocatalytic materials, not only to degrade pollutant but also for regeneration of photocatalyst, to perform the dual functions of pollutant adsorption and degradation. Sol–gel [107], ultrasound [108], solvothermal [54, 109], thermal poly-condensation [72], and hydrolysis [109, 110] are some of the methods adopted to produce biochar anchored with nanoparticles that have photocatalytic activity.

The fullerene and graphene have recently emerged as promising candidates for photocatalysis. They can be seen as a "hot topic" and will certainly induce major changes in the fields of photocatalysis and water treatment [111].

The bonding modes between the carbon support and the photocatalyst vary between covalent bonding, hydrogen bonding, hydrophobic interactions, physical entrapment, and electrostatic interactions. Bonding groups such as carboxyl and phosphonate-esters retain their stability under certain pH conditions in aqueous media. Anchoring groups existing on the surface carbon matrix, that show high affinity by the OH groups that occupy the surface of photocatalyst it can establish a chemical and robust covalent bond in strongly acidic and alkaline media.

Table 3 lists the carbon support, the method of preparing the composite and the temperature, and the functional groups on the surface of the prepared composite. Nawaz et al. [7] stated that the anchoring of $NiFe_2O_4$ nanoparticles in the MWCNTs occurs through strong electrostatic interactions with the functional groups produced on the surface of the MWCNTs after synthesis [7].

The photoactivity of composites depends on several properties, such as porosity, surface area, pore size, surface chemistry, band gap energy, crystallite size, synthesis temperature, among others, which are not always related to each other.

6.1 Temperature

Carbon supports, such as biochar and activated carbon, produced at temperatures above 500 °C have a reduced number of functional groups containing oxygen on their surface. Therefore, only a small number of electrons can be excited in high temperature biochars due to the relatively lower content of functional groups containing oxygen (Table 3). Ie, the increase of pyrolysis and HTC temperature resulted in the sequentially decreased O contents and increased C contents in biochars and hydrochar, this can be observed by the atomic ratio of O/C [116, 117].

Fast pyrolysis was employed to produce biochar using switchgrass and pinewood lignocellulose [118], and walnut shell [119]. It was found that the number and cross-linking of aromatic rings increased with an increase in temperature. It is also found that activated carbon materials are capable of photocatalytic degradation by generating reactive oxygen species [44] upon exposure to UV irradiation [103, 120, 121]. According to Azzaz and collaborators, HTC leads to a decrease in esters and hydroxyl groups in hydrochar compared to crude biomass [116].

Table 3 Correlation between the functional groups on the surface with the different temperatures of preparation of the carbonaceous material

Carbonaceous material	Preparation method	Functional group	Temperature (°C)	Reference
Amorphous carbon nanotubes + ZnS	Teflon-lined stainless steel autoclave	Carbonyl and carboxyl	>200	[112]
Pecan Nutshells Biochar-ZnO	Mechanical mixing and pyrolysis	Phenolic	350	[113]
Food wastes hidrochar	HTC	Phenols, alcohols, or carboxylic acid	≥300	[114]
Food wastes biochar	Pyrolysis in tubular reactor under N_2 atmosphere	Nonpolar aliphatic fractions	<400	[114]
Bamboo charcoal–TiO_2	Pyrolysis under the flowing N_2 gas	Aromatic	800	[106]
TiO_2/graphene	Solvothermal (autoclave) synthesis	Carbonyl, hydroxyl, aromatic ring,	180	[34]
$NiFe_2O_4$–MWCNTs	Hydrothermal reaction	Hydroxyl, carbonyl, carboxylate	180	[7]
$SnFe_2O_4$/polypyrrole	Polymerization in acidic medium	Positively charged functional groups	Room temperature	[9]
ZnO/PPy	Polymerization in acidic medium	Alkyl amine (C–N–), primary, secondary, and tertiary amine, and Aromatic groups	Room temperature	[115]

The biochar's photocatalytic activity is mainly contributed by the oxygen-containing functional groups present on the surface of it and the condensed aromatic rings [103]. In a study by Wang and collaborators [122], the various reaction mechanism that leads to formation of reactive oxygen species by biochar in the presence of daylight irradiation.

6.2 Composition

Animal waste, such as pig manure, poultry litter, dairy waste, is generally characterized by low amounts of fixed carbon and an important volatile matter content

[116]. Dung-based hydrochars have low porosities, usually attributed to the low HTC temperatures applied (>350 °C). The high content of volatile matter initially present in the raw material can negatively affect the development of micro and mesoporosity due to its possible recombination with the aromatic structure [123]. An elevated specific surface area provides more active sites for the photochemical reaction and, thus, photocatalytic activity is increased [112].

Residues of compounds with a high lignocellulose content show the development of carbon microspheres on the surface, related to the dehydration of polymers (mainly cellulose and polysaccharides) when submitted to HTC [116].

Dairy residues have a macroporous and tubular structure. These variations in structures and porosity are believed to be more related to the origin of biomass than to heat treatment [124].

Biomass from agricultural residues is composed of cellulose (40–60%, % by weight), hemicellulose (20–40%, % by weight) and lignin (10–25%, % by weight) together with other lipid extracts [125]. The biomass of agricultural residues presents a high concentration of hydroxyl, carboxylic and phenolic functional groups together with the low initial content of C explain the high content of volatile compounds and a low percentage of fixed carbon [126].

Graphene is a two-dimensional network constituted of a single layer of sp^2-bound carbon atoms. It possesses a wide range of valuable properties. Those include mainly the large specific surface area, out-standing optical transmittance and outstanding electron conductivity [111].

The polymers used as support are dispersions of macromolecular structure, with various types of defects, configurations and conformations, terminal groups, which may have functional groups in side chains, in addition to crystalline and amorphous regions. These characteristics give rise to the accumulation of surface charge, making some polymers conductive and other insulating materials (without charges) [90, 102, 127].

Thus, the origin of the support gives the composite unique characteristics.

6.3 Composite pH

The pH of the biochar increases with increasing pyrolysis temperature, which is attributed to the increase in ash content after pyrolysis. The increase in pH is due to the increase in carbonates and functional groups such as –COO– and –O–. This pH change contributes to the change in the biochar's surface load, which significantly influences the anchoring of the catalyst [113, 128–130].

The existence of heteroatoms on the surface, such as oxygen, carbon, hydrogen, contributes to a certain pH. These heteroatoms form organic functional groups, such as phenol (found in lignin, in phenolic substances and tannins), carboxyl (found in pectin), lactone (found in hemicellulose by proton exchange: protonation). All of these groupings can control the surface to be acidic ($CO–OH^{2+}$), neutral (R–CO–OH, R–OCO, Ar–OH), or alkaline (CO–O–, Ar–O–) [128, 129, 131].

6.4 Optimal Catalyst Quantity

The higher content of carbon (as support) may affect the photonic process (less number of photo-generated electrons) due to the less content of photocatalyst, taking into account the mass of the photocatalyst added to the solution. On the other hand, the high content of carbon may block the irradiation of photocatalyst particles [132].

Evidence of the decrease in the intensity of the photoluminescence peaks indicates that the biochar is capable of inhibiting the recombination of photoelectrons and holes or at least reducing the rate of recombination [133].

When biochar is added to form a composite, it can promote light absorption [133]. However, there is an ideal biochar/photocatalyst ratio, and this varies according to the source of the biochar. An excess of biochar leads to a reduction in photocatalytic efficiency because it blocks the light that reaches the surface of the catalyst [113, 133]. A very low biochar/photocatalyst ratio is not enough to prevent electron/gap recombination, also leading to a reduction in the photocatalytic efficiency of the composite [9, 100].

Table 4 shows the proportion of carbon support/photocatalyst used as the best performance in some studies.

7 Improvement of Catalytic Photoactivity

Oxygen-containing structures are rich on the surface of carbonaceous supports and involved in the acceptance and donation of electrons during interactions between the support and organic contaminants.

Defects in the C structure can also participate in the photodegradation of pollutants, since they can promote electron transfer. Electron-rich defect sites and persistent free radical (EPFR) sites on biochar can react with O_2 to produce reactive oxygen species, which degrade organic pollutants via the free radical pathway [21, 134, 135]. Carbon composites can also acquire electrons from electron donors or supply electrons to receptors [112]. At the same time, biochars, hydrochars, polymers, GO, rGO, carbon matrices in general can act as an electron launcher or electron conductor to degrade organic pollutants because of carbon structures for electronic conductivity [64, 69, 102].

The improvement in the photocatalytic activity of the composite when it is supported on activated carbon, hydrochar, or biochar, is also attributable to the porosity of the support, providing high adsorption capacity and rapid passage of reactive species to the photocatalyst particles [21, 74, 76, 136–140].

It is more likely that the reactivity of the carbon supports is contributed by the coupling of the redox potential, environmentally persistent free radicals and transition metals. Reactivity can also be linked to the pH of the medium. In alkaline systems, the abundant H^+ in the system can react with free electrons, promote the separation of electrons and H^+, and accelerate emerging pollutant degradation under UV-light

Table 4 Proportion of carbon support/photocatalyst with better performance against pollutants in aqueous media

Composite	Best aspect ratio	Pollutant	Experimental conditions	Reference
MDF biochar/TiO_2	10% TiO_2	Methylene blue dye	Composite dosage: 1 g L^{-1} Volume: 100 mL Pollutant concentration: 10 mg L^{-1} Source: UV irradiation	[100]
$SnFe_2O_4$/polypyrrole	10 wt% $SnFe_2O_4$	Tartrazine dye	Composite dosage: 1 g L^{-1} Volume: 100 mL Pollutant concentration: 20 mg L^{-1} Source: UV–visible light irradiation H_2O_2: 3.4×10^{-5} mol L^{-1}	[9]
PPy/TiO_2	1:100 PPy/TiO_2	RhB dye	Composite dosage: 0.15 g Volume: 150 mL Pollutant concentration: 10 mg L^{-1} Source: tungsten-halogen lamp	[91]
Walnut shells biochar/TiO_2	0.2:1 wt biochar/TiO_2	Methyl orange dye	Composite dosage: 10 mg Volume: 40 mL Pollutant concentration: 20 mg L^{-1} Source: mercury lamp	[133]

or Vis-light. On the other hand, most of H^+ are consumed under alkaline conditions, thereby inhibiting photodegradation [9, 68].

When using fullerene as carbonaceous support for photocatalysts, photocatalytic activity can be improved due to the generation of singlet oxygen by fullerene (band gap = 1.7 eV) when activated by UV radiation. However, fullerene powder has high hydrophobicity, making it difficult to disperse the material in the aqueous reaction medium and leading to the formation of aggregates [111].

Xia and collaborators [141] conclued that the use of reduced graphene oxide with BiOCOOH enhanced photocatalytic activity in Rhodamine B dye degradation under simulated sunlight irradiation, which could be ascribed to enhanced adsorption

capacity, narrower band gap and lower recombination rate of photogenerated electron–hole pairs. Li and collaborators [28], when using graphene oxide nanosheets as support for TiO_2–Fe_3O_4, attributed that graphene oxide nanosheets can ensure easier charge transport and promote catalytic performance and stability, due to the high conductivity. This conclusion was also reported by Rokhsat and Akhavan [142], when supporting ZnO in graphene oxide. Several authors report that the interfacial charge transfer could be the main contribution of graphene oxide and reduced graphene oxide [7, 143–146].

8 Charge Photogeneration Mechanisms

Under UV-light irradiation, the abundant electrons in the low-temperature biochars and hydrochars could be excited and react with dissolved oxygen on the reaction medium to generate serials oxygen-containing free radicals, which can degrade emerging pollutants effectively [68, 77, 100, 113]. Fullerene (C_{60}) is a trap-rich conductor, and acts as an electron acceptor (as showed in Fig. 6a) [6, 136, 147], whereas graphene, graphene oxide, and carbon nanotubes are used mainly as electron mediators in photocatalytic systems (as simplify in Fig. 6b) [7, 46, 111, 141, 146, 148].

Recent research utilizes the properties of environmental persistent free radicals (EPFR) on biochar to catalyze different oxidants for generating ROS for organic contaminant degradation. Fang and colaborators proposed a mechanism for the formation of EPFR in biochars from biomass pyrolysis [64], as shown in Fig. 7,

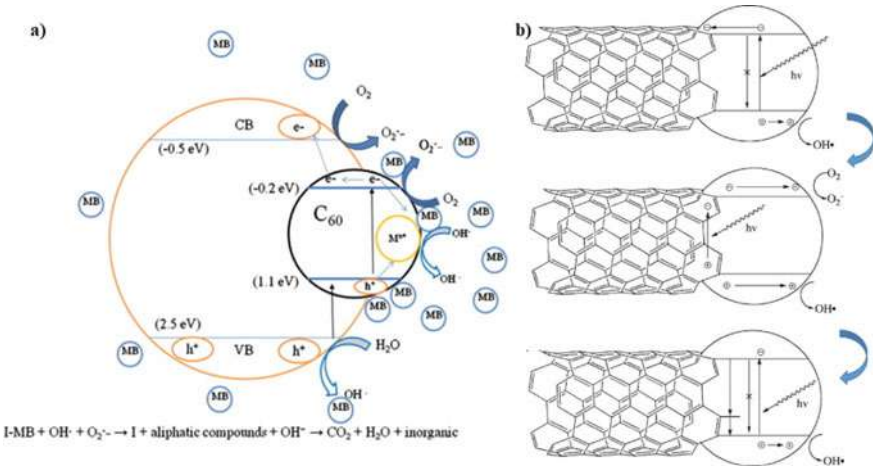

Fig. 6 **a** Separation of generated electrons and holes on the interface of M-fullerene/TiO_2 compounds [147]. **b** Mechanisms of synergistic enhancement in TiO_2–CNT composites [6]. Reprinted with the permission from [147] and [6]

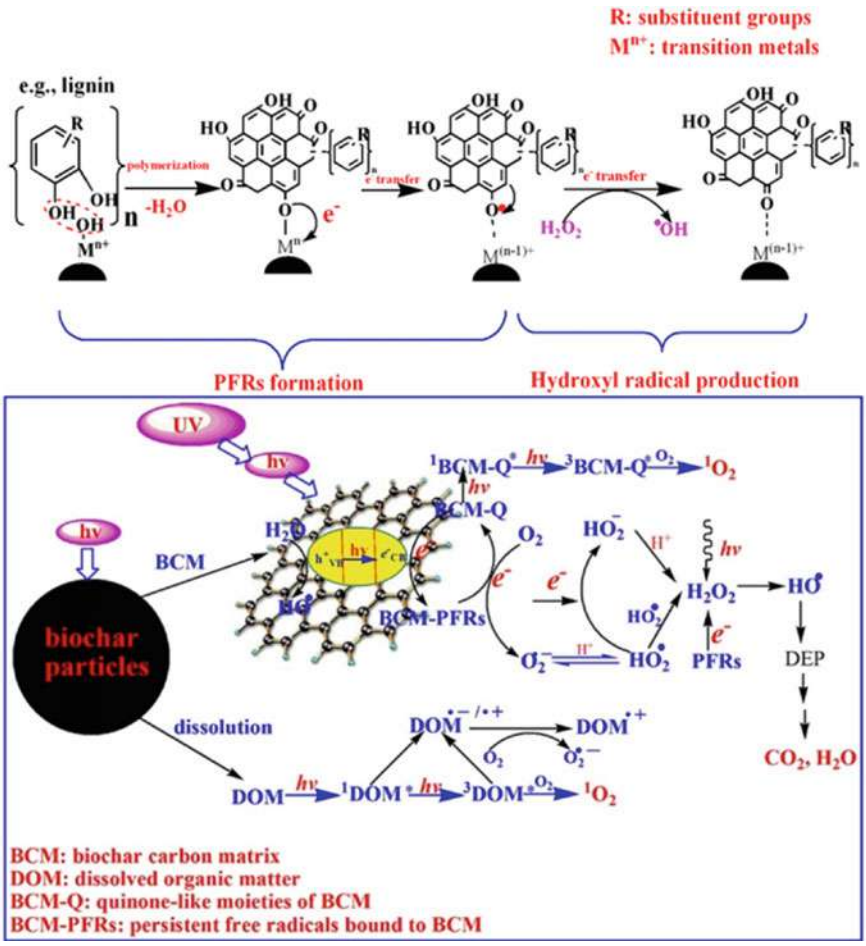

Fig. 7 Mechanism of formation of •OH from biochar proposed by Fang and collaborators. Reproduced with permission from Ref. [64, 103]

condensed structures transfer electrons to transition metals accompanied by the formation of surface-bonded EPFRs on the biochar. In this work, the authors reported that EPFRs of the semiquinone type could activate H_2O_2 effectively to form •OH, through the reaction of EPFRs in the biochar with H_2O_2 by transferring a single electron and reducing it to •OH. Both the biochar produced by Fang and collaborators [64] and the hydrochar produced by Ruan and collaborators [117] contain Fe (III) ions in the structure. The carbon-centred radicals with an adjacent oxygen atom and oxygen-centred radicals were formed by the interaction between phenolic hydroxyl groups and Fe(III) cations in both researchs [64, 117].

In another study, Fang and colleagues concluded that biochar and EPFRs played important roles in the production of singlet oxygen ($^1O_2$) and •OH for degradation

of diethylphthalate [103]. The mechanisms were proposed as follows (Fig. 7): (i) formation of $^1O_2$ and $^{\bullet}OH$ from the biochar due to the incidence of UV radiation and electron transfer; (ii) excitation of the quinone-like structure in the triplet state under UV irradiation stimulating the formation of singlet oxygen; (iii) formation of EPFRs promoted by UV transferring electrons to O_2 with the formation of $O_2^{\bullet-}$ and additional H_2O_2 yield; and (iv) $^{\bullet}OH$ production mainly by pathways involved with H_2O_2, including activation of EPFRs and photo-Fenton reaction. It is important to note that EPFRs can be generated under UV irradiation.

A very similar mechanism can be found in the work of Silvestri and collaborators in supporting TiO_2 in polypyrrole (PPy) [14]. When the TiO_2 and PPy are in contact it is possible that a transfer of photo-generated electron occurs from the TiO_2 to PPy, avoiding the recombination of the photo-generated charge carries in TiO_2. Similar findings were observed by Sangareswari [149] and Gao and collaborators [91]. The reason is that apart from outstanding mechanical property and large surface area, polypyrrole has electrical and electronic properties, in order to conjugated polymers are efficient electron donors and good hole transporters upon visible light excitation.

9 Conclusion

An interconnected structure is potentially superior in photocatalysis, not only for the mobility of loads, but also from a practical point of view for the removal of the photocatalyst from the environment. The effect of the support material (mainly those on a macro and micro scale) promotes the photocatalyst's ability to absorb electromagnetic radiation, due to the increase in the surface area, in a given support / photocatalyst ratio. As noted, the effect of the support material on the quantum efficiency of the supported photocatalyst is poorly addressed by studies published in the literature and requires further studies.

As advantages of the support stand out: (i) Stabilization of the microstructure and active components, (ii) Effect of double function in pollutant degradation reactions, (iii) Influence on the speed of adsorption/desorption and diffusion of molecules, (iv) Influence on migration or transfer of active species such as $O_2^{-\bullet}$, h^+, $^{\bullet}OH$, $^1O_2$, (v) Improvement of mechanical, thermomechanical, electronic or other physical and chemical properties, (vi) use of a smaller amount of photocatalyst.

References

1. Taheran M, Naghdi M, Brar SK, Verma M, Surampalli RY (2018) Emerging contaminants: here today, there tomorrow! Environ Nanotechnol Monit Manag 10(February):122–126
2. Martín-Pozo L, de Alarcón-Gómez B, Rodríguez-Gómez R, García-Córcoles MT, Çipa M, Zafra-Gómez A (2019) Analytical methods for the determination of emerging contaminants in sewage sludge samples. A review. Talanta 192(June 2018):508–533

3. Wetchakun K, Wetchakun N, Sakulsermsuk S (2019) An overview of solar/visible light-driven heterogeneous photocatalysis for water purification: TiO_2- and ZnO-based photocatalysts used in suspension photoreactors. J Ind Eng Chem 71:19–49
4. Deng Y, Zhao R (2015) Advanced oxidation processes (AOPs) in wastewater treatment. Curr Pollut Rep 1(3):167–176
5. Fagan R, Mccormack DE, Dionysiou DD, Pillai SC (2016) A review of solar and visible light active TiO_2 photocatalysis for treating bacteria, cyanotoxins and contaminants of emerging concern. Mater Sci Semicond Process 42:2–14
6. Leary R, Westwood A (2011) Carbonaceous nanomaterials for the enhancement of TiO_2 photocatalysis. Carbon N Y 49(3):741–772
7. Nawaz M et al (2020) Photo-Fenton reaction for the degradation of sulfamethoxazole using a multi-walled carbon nanotube-$NiFe_2O_4$ composite. Chem Eng J 382:123053
8. Gomis J et al (2015) Determination of photostability, biocompatibility and efficiency as photo-Fenton auxiliaries of three different types of soluble bio-based substances (SBO). Catal Today 252:177–183
9. Leichtweis J, Silvestri S, Vieira Y, De Lima TA, Foletto EL (2021) A novel tin ferrite/polymer composite use in photo–Fenton reactions. Int J Environ Sci Technol 18:1537–1548
10. Chen S, Sun D, Chung J-S (2007) Treatment of pesticide wastewater by moving-bed biofilm reactor combined with Fenton-coagulation pretreatment. J Hazard Mater 144(1–2):577–584
11. Makropoulou T, Kortidis I, Davididou K, Motaung DE, Chatzisymeon E (2020) Photocatalytic facile ZnO nanostructures for the elimination of the antibiotic sulfamethoxazole in water. J Water Process Eng 36(April):101299
12. Kim JR, Kan E (2016) Heterogeneous photocatalytic degradation of sulfamethoxazole in water using a biochar-supported TiO_2 photocatalyst. J Environ Manage 180:94–101
13. Maletić M et al (2019) Hydrothermal synthesis of TiO_2/carbon composites and their application for removal of organic pollutants. Arab J Chem 12(8):4388–4397
14. Silvestri S, Burgo TAL, Dias-Ferreira C, Labrincha JA, Tobaldi DM (2020) Polypyrrole-TiO_2 composite for removal of 4-chlorophenol and diclofenac. React Funct Polym 146(October 2019):104401
15. Hitkari G, Singh S, Pandey G (2017) Structural, optical and photocatalytic study of ZnO and ZnO–ZnS synthesized by chemical method. Nano-Struct Nano-Objects 12:1–9
16. Liu F, Yi P, Wang X, Gao H, Zhang H (2015) Degradation of Acid Orange 7 by an ultrasound/ZnO-GAC/persulfate process. Sep Purif Technol 194(July 2017):181–187
17. Guan K, Zhou P, Zhang J, Zhu L (2020) Synthesis and characterization of ZnO@RSDBC composites and their Photo-Oxidative degradation of Acid Orange 7 in water. J Mol Struct 1203:127425
18. Alam U, Fleisch M, Kretschmer I, Bahnemann D, Muneer M (2017) One-step hydrothermal synthesis of Bi-TiO_2 nanotube/graphene composites: an efficient photocatalyst for spectacular degradation of organic pollutants under visible light irradiation. Appl Catal B Environ 218:758–769
19. Ebrahimi R et al (2020) Photocatalytic degradation of 2,4-dichlorophenoxyacetic acid in aqueous solution using Mn-doped ZnO/graphene nanocomposite under LED radiation. J Inorg Organomet Polym Mater 30(3):923–934
20. Rosa SMC, Nossol ABS, Nossol E, Zarbin AJG, Peralta-Zamora PG (2017) Non-synergistic UV-A photocatalytic degradation of estrogens by nano-TiO_2 supported on activated carbon. J Braz Chem Soc 28(4):582–588
21. Faheem, Du J, Kim SH, Hassan MA, Irshad S, Bao J (2020) Application of biochar in advanced oxidation processes: supportive, adsorptive, and catalytic role. Environ Sci Pollut Res
22. Calvosa L, Monteverdi A, Rindone B, Riva G (1991) Ozone oxidation of compounds resistant to biological degradation. Water Res 25(8):985–993
23. Malato S, Blanco J, Vidal A, Richter C (2002) Photocatalysis with solar energy at a pilot-plant scale : an overview. Appl Catal B Environ 37:1–15
24. Klavarioti M, Mantzavinos D, Kassinos D (2009) Removal of residual pharmaceuticals from aqueous systems by advanced oxidation processes. Environ Int 35(2):402–417

25. Meili L, Pimentel WRO, Tonholo J, Zanta CLPS (2020) Removal of reactive dyes from aqueous solution by Fenton reaction : kinetic study and phytotoxicity tests
26. Catrinescu C, Teodosiu C, Macoveanu M, Miehe-brendl J (2003) Catalytic wet peroxide oxidation of phenol over Fe-exchanged pillared beidellite. Water Res 37:1154–1160
27. Pignatello JJ, Oliveros E, MacKay A (2006) Advanced oxidation processes for organic contaminant destruction based on the Fenton reaction and related chemistry. Crit Rev Environ Sci Technol 36(1):1–84
28. Li Q, Kong H, Li P, Shao J, He Y (2019) Photo-Fenton degradation of amoxicillin via magnetic TiO_2-graphene oxide-Fe_3O_4 composite with a submerged magnetic separation membrane photocatalytic reactor (SMSMPR). J Hazard Mater 373(March):437–446
29. Banerjee S, Dionysiou DD, Pillai SC (2015) Self-cleaning applications of TiO_2 by photo-induced hydrophilicity and photocatalysis. BAppl Catal B Environ 176–177:396–428
30. Nakata K, Fujishima A (2012) TiO_2 photocatalysis : design and applications. J Photochem Photobiol C : Photochem Rev 13:169–189
31. Shan AY, Idaty T, Ghazi M, Rashid SA (2010) Immobilisation of titanium dioxide onto supporting materials in heterogeneous photocatalysis: a review. Appl Catal A Gen 389(1–2):1–8
32. Leary R, Westwood A (2010) Carbonaceous nanomaterials for the enhancement of TiO_2 photocatalysis. Carbon 9
33. Choi K, Kang T, Oh SG (2012) Preparation of disk shaped ZnO particles using surfactant and their PL properties. Mater Lett 75:240–243
34. Trapalis A et al (2016) TiO_2/graphene composite photocatalysts for NO_x removal: a comparison of surfactant-stabilized graphene and reduced graphene oxide. Appl Catal B Environ 180:637–647
35. Zhou Z et al (2019) Persulfate-based advanced oxidation processes (AOPs) for organic-contaminated soil remediation: a review. Chem Eng J 372(January):836–851
36. Benabbou AK, Derriche Z, Felix C, Lejeune P, Guillard C (2007) Photocatalytic inactivation of *Escherischia coli*. Effect of concentration of TiO_2 and microorganism, nature, and intensity of UV irradiation. Appl Catal B Environ 76(3–4):257–263
37. Miao W, Liu Y, Chen X, Zhao Y, Mao S (2020) Tuning layered Fe-doped g-C_3N_4 structure through pyrolysis for enhanced Fenton and photo-Fenton activities. Carbon N Y 159:461–470
38. Wang Y, Liu R (2017) Comparison of characteristics of twenty-one types of biochar and their ability to remove multi-heavy metals and methylene blue in solution. Fuel Process Technol 160:55–63
39. Xu L, Shen C, Hu C, Liu W, Wen Y (2018) Fe–N-graphene wrapped Al_2O_3/pentlandite from microalgae: high Fenton catalytic efficiency from enhanced Fe^{3+} reduction. Environ Sci Technol, 3–9
40. Da Costa E, Zarbin AJG, Peralta-Zamora P (2013) Multivariate optimisation of TiO_2/carbon nanocomposites for photocatalytic degradation of a reactive textile dye. Mater Res Bull 48(2):581–586
41. Yu S, Wang Y, Sun F, Wang R, Zhou Y (2018) Novel mpg-C_3N_4/TiO_2 nanocomposite photocatalytic membrane reactor for sulfamethoxazole photodegradation. Chem Eng J 337(December 2017):183–192
42. Wang S et al (2018) Carboxymethyl cellulose stabilized ZnO/biochar nanocomposites: enhanced adsorption and inhibited photocatalytic degradation of methylene blue. Chemosphere 197:20–25
43. Baek M-H, Yoon J-W, Hong J-S, Suh J-K (2013) Application of TiO_2-containing mesoporous spherical activated carbon in a fluidized bed photoreactor—adsorption and photocatalytic activity. Appl Catal A Gen 450:222–229
44. Matos J (2015) Eco-friendly heterogeneous photocatalysis on biochar-based materials under solar irradiation. Top Catal 59(2–4):394–402
45. Falla PH et al (2014) Optimization the efficiency photovoltaic solar cells using synthesized TiO_2 semiconductor nanomaterials and functionalized carbon nanotubes. Energy Procedia 57:1860–1867

46. Sampaio MJ et al (2015) Synergistic effect between carbon nanomaterials and ZnO for photocatalytic water decontamination. J Catal 331:172–180
47. Rane AV, Kanny K, Abitha VK, Thomas S (2018) Methods for synthesis of nanoparticles and fabrication of nanocomposites. In: Synthesis of inorganic nanomaterials. Elsevier, pp 121–139
48. Brindha A, Sivakumar T (2017) Visible active N, S co-doped TiO_2/graphene photocatalysts for the degradation of hazardous dyes. J Photochem Photobiol A Chem 340:146–156
49. Yang N, Zhai J, Wang D, Chen Y, Jiang L (2010) Two-dimensional graphene bridges enhanced photoinduced charge transport in dye-sensitized solar cells. ACS Nano 4(2):887–894
50. Granadeiro CM et al (2012) Photoluminescent bimetallic-3-hydroxypicolinate/graphene oxide nanocomposite. RSC Adv 2(25):9443–9447
51. Zhao D, Sheng G, Chen C, Wang X (2012) Enhanced photocatalytic degradation of methylene blue under visible irradiation on graphene@ TiO_2 dyade structure. Appl Catal B Environ 111:303–308
52. Khan A et al (2017) The role of graphene oxide and graphene oxide-based nanomaterials in the removal of pharmaceuticals from aqueous media: a review. Environ Sci Pollut Res 24(9):7938–7958
53. Kamat PV (2010) To what extent do graphene scaffolds improve the photovoltaic and photocatalytic response of TiO_2 nanostructured films? J Phys Chem Lett, 2222–2227
54. Chen M, Bao C, Hu D, Jin X, Huang Q (2019) Facile and low-cost fabrication of ZnO/biochar nanocomposites from jute fibers for efficient and stable photodegradation of methylene blue dye. J Anal Appl Pyrolysis 139(November 2018):319–332
55. Yang Y, Xu L, Wang H, Wang W, Zhang L (2016) TiO_2/graphene porous composite and its photocatalytic degradation of methylene blue. Mater Des 108:632–639
56. Yang L, Xu L, Bai X, Jin P (2019) Enhanced visible-light activation of persulfate by Ti^{3+} self-doped TiO_2/graphene nanocomposite for the rapid and efficient degradation of micropollutants in water. J Hazard Mater 365:107–117
57. Flores K et al (2020) The effect of hybrid zinc oxide/graphene oxide (ZnO/GO) nano-catalysts on the photocatalytic degradation of simazine. Chemosphere 259:127414
58. Ahmad M, Ahmed E, Hong ZL, Ahmed W, Elhissi A, Khalid NR (2014) Ultrasonics sonochemistry photocatalytic, sonocatalytic and sonophotocatalytic degradation of rhodamine B using ZnO/CNTs composites photocatalysts. Ultrason Sonochem 21(2):761–773
59. Chen T et al (2016) Enhanced photocatalytic activity of C@ ZnO core-shell nanostructures and its photoluminescence property. Appl Surf Sci 389:303–310
60. Ahmad M et al (2014) Biochar as a sorbent for contaminant management in soil and water: a review. Chemosphere 99:19–33
61. Novotny EH, de F. Maia CMB, de M. Carvalho MT, Madari BE (2015) Biochar: pyrogenic carbon for agricultural use—a critical review. Rev Bras Ciência do Solo 39(2):321–344
62. Lehmann J, Joseph S (2012) Biochar for environmental management: science and technology. Routledge
63. Liao S, Pan B, Li H, Zhang D, Xing B (2014) Detecting free radicals in biochars and determining their ability to inhibit the germination and growth of corn, wheat and rice seedlings. Environ Sci Technol 48(15):8581–8587
64. Fang G, Gao J, Liu C, Dionysiou DD, Wang Y, Zhou D (2014) Key role of persistent free radicals in hydrogen peroxide activation by biochar: implications to organic contaminant degradation. Environ Sci Technol 48(3):1902–1910
65. Bährle C, Custodis V, Jeschke G, van Bokhoven JA, Vogel F (2014) In situ observation of radicals and molecular products during lignin pyrolysis. Chemsuschem 7(7):2022–2029
66. Chen G, Zhang Z, Zhang Z, Zhang R (2018) Redox-active reactions in denitri fi cation provided by biochars pyrolyzed at different temperatures. Sci Total Environ 615:1547–1556
67. Kappler A, Wuestner ML, Ruecker A, Harter J, Halama M, Behrens S (2014) Biochar as an electron shuttle between bacteria and Fe(III) minerals. Environ Sci Technol Lett 1(8):339–344
68. Gonçalves MG et al (2020) Relationship of the physicochemical properties of novel ZnO/biochar composites to their efficiencies in the degradation of sulfamethoxazole and methyl orange. Sci Total Environ 748:141381

69. Silvestri S, Gonçalves MG, Veiga PAS, Matos TTS, Zamora PP, Mangrich AS (2019) TiO_2 supported on *Salvinia molesta* biochar for heterogeneous photocatalytic degradation of Acid Orange 7 dye. J Environ Chem Eng 7:102879
70. Matos J, Montaña R, Rivero E, Velasco J, Ledezma G (2014) Photocatalytic activity of ZnO-biochar hybrid composites. Eurasian Chemico—Technol J 16:293–297
71. Zhou Y et al (2021) N-doped magnetic three-dimensional carbon microspheres@ TiO_2 with a porous architecture for enhanced degradation of tetracycline and methyl orange via adsorption/photocatalysis synergy. Chem Eng J 411:128615
72. Colmenares JC, Varma RS, Lisowski P (2016) Sustainable hybrid photocatalysts: titania immobilized on carbon materials derived from renewable and biodegradable resources. Green Chem 18(21):5736–5750
73. Khalid NR, Majid A, Tahir MB, Niaz NA, Khalid S (2017) Carbonaceous-TiO_2 nanomaterials for photocatalytic degradation of pollutants: a review. Ceram Int 43(17):14552–14571
74. El Mouchtari EM et al (2019) TiO_2 and activated carbon of *Argania spinosa* tree nutshells composites for the adsorption photocatalysis removal of pharmaceuticals from aqueous solution. J Photochem Photobiol A Chem 388(October):2020
75. Holtz RD, de Oliveira SB, Fraga MA, do C. Rangel M (2008) Synthesis and characterization of polymeric activated carbon-supported vanadium and magnesium catalysts for ethylbenzene dehydrogenation. Appl Catal A Gen 350(1):79–85
76. Gar Alalm M, Tawfik A, Ookawara S (2016) Enhancement of photocatalytic activity of TiO_2 by immobilization on activated carbon for degradation of pharmaceuticals. J Environ Chem Eng 4(2):1929–1937
77. Sarmento J, Vitória L, Brombilla DL (2020) Conversion of spent coffee grounds to biochar as promising TiO_2 support for effective degradation of diclofenac in water. Appl Organomet Chem 34:1–11
78. Zhang H et al (2017) TiO_2 supported on reed straw biochar as an adsorptive and photocatalytic composite for the efficient degradation of sulfamethoxazole in aqueous matrices. Chemosphere 185:351–360
79. Xie X, Li S, Zhang H, Wang Z, Huang H (2019) Promoting charge separation of biochar-based Zn-TiO_2/pBC in the presence of ZnO for efficient sulfamethoxazole photodegradation under visible light irradiation. Sci Total Environ 659:529–539
80. Chen M, Dai Y, Guo J, Yang H, Liu D, Zhai Y (2019) Solvothermal synthesis of biochar@$ZnFe_2O_4$/BiOBr Z-scheme heterojunction for efficient photocatalytic ciprofloxacin degradation under visible light. Appl Surf Sci 493(May):1361–1367
81. Pierre AC (2020) Introduction to sol-gel processing. Springer Nature
82. Livage J, Henry M, Sanchez C (1988) Sol-gel chemistry of transition metal oxides. Prog solid state Chem 18(4):259–341
83. Sahai A, Goswami N (2014) Structural and vibrational properties of ZnO nanoparticles synthesized by the chemical precipitation method. Phys E Low-Dimens Syst Nanostruct 58:130–137
84. Khomchenko V, Sopinskyy M, Mazin M, Dan'ko V, Lytvyn O, Piryatinskii Y (2019) The violet luminescence band in ZnO and ZnO-Ag thin films. J Lumin 213:519–524
85. Lin L, Wang H, Xu P (2017) Immobilized TiO_2-reduced graphene oxide nanocomposites on optical fibers as high performance photocatalysts for degradation of pharmaceuticals. Chem Eng J 310:389–398
86. Silvestri S, Gonçalves MG, Da Silva Veiga PA, Matos TTDS, Peralta-Zamora P, Mangrich AS (2019) TiO_2 supported on *Salvinia molesta* biochar for heterogeneous photocatalytic degradation of Acid Orange 7 dye. J Environ Chem Eng 7(1):102879
87. Morawski AW et al (2017) Photocatalytic degradation of acetic acid in the presence of visible light-active TiO_2-reduced graphene oxide photocatalysts. Catal Today 280:108–113
88. Li T, Wang T, Qu G, Liang D, Hu S (2017) Synthesis and photocatalytic performance of reduced graphene oxide–TiO_2 nanocomposites for orange II degradation under UV light irradiation. Environ Sci Pollut Res 24(13):12416–12425

89. Lee JS, You KH, Park CB (2012) Highly photoactive, low bandgap TiO_2 nanoparticles wrapped by graphene. Adv Mater 24(8):1084–1088
90. Gautam A, Kshirsagar AS, Banerjee S, Dhapte VV, Khanna PK (2016) UVC-shielding by nano-TiO_2/PMMA composite: a chemical approach. J Mater Sci Nanotechnol 4(1):1–14
91. Gao F et al (2016) Preparation of polypyrrole/TiO_2 nanocomposites with enhanced photocatalytic performance. Particuology 26:73–78
92. Thandu M, Comuzzi C, Goi D (2015) Phototreatment of water by organic photosensitizers and comparison with inorganic semiconductors. Int J Photoenergy 2015:10–12
93. Arshadnia I, Movahedi M, Rasouli N (2017) $SnFe_2O_4$/SnO_2/PANI magnetically separable photocatalyst for decolorization of two dye mixture in aqueous solution. Surf Interf 8(May):91–96
94. Deng F, Li Y, Luo X, Yang L, Tu X (2012) Preparation of conductive polypyrrole/TiO_2nanocomposite via surface molecular imprinting technique and its photocatalytic activity under simulated solar light irradiation. Colloids Surf A Phys Eng Asp 395:183–189
95. Zhang W, Zhou L, Shi J, Deng H (2018) Synthesis of Ag_3PO_4/G-C_3N_4 composite with enhanced photocatalytic performance for the photodegradation of diclofenac under visible light irradiation. Catalysts 8(2):45
96. Kovacic M et al (2016) Solar-driven photocatalytic treatment of diclofenac using immobilized TiO_2-based zeolite composites. Environ Sci Pollut Res 23(18):17982–17994
97. Yang X et al (2020) Recent advances in photodegradation of antibiotic residues in water. Chem Eng J 405(June 2020):126806
98. Shen J, Ma G, Zhang J, Quan W, Li L (2015) Facile fabrication of magnetic reduced graphene oxide-$ZnFe_2O_4$ composites with enhanced adsorption and photocatalytic activity. Appl Surf Sci 359:455–468
99. Martínez C, Canle L. M, Fernández MI, Santaballa JA, Faria J (2011) Aqueous degradation of diclofenac by heterogeneous photocatalysis using nanostructured materials. Appl Catal B Environ 107(1–2):110–118
100. Silvestri S, Stefanello N, Sulkovski AA, Foletto EL (2020) Preparation of TiO_2 supported on MDF biochar for simultaneous removal of methylene blue by adsorption and photocatalysis. J Chem Technol Biotechnol 95:2723–2729
101. Ceretta MB, Vieira Y, Wolski EA, Foletto EL, Silvestri S (2020) Biological degradation coupled to photocatalysis by ZnO/polypyrrole composite for the treatment of real textile wastewater. J Water Process Eng 35(January):101230
102. Silvestri S, Ferreira CD, Oliveira V, Varejão JMTB, Labrincha JA, Tobaldi DM (2019) Synthesis of PPy-ZnO composite used as photocatalyst for the degradation of diclofenac under simulated solar irradiation. J Photochem Photobiol A Chem 375(February):261–269
103. Fang G, Liu C, Wang Y, Dionysiou DD, Zhou D (2017) Photogeneration of reactive oxygen species from biochar suspension for diethyl phthalate degradation. Appl Catal B Environ 214:34–45
104. Ruan X et al (2019) Formation, characteristics, and applications of environmentally persistent free radicals in biochars: a review. Bioresour Technol 281(February):457–468
105. Sun T et al (2018) Simultaneous quantification of electron transfer by carbon matrices and functional groups in pyrogenic carbon. Environ Sci Technol 52(15):8538–8547
106. Wang B, Liu B, Ji XX, Ma MG (2018) Synthesis, characterization, and photocatalytic properties of Bamboo charcoal/TiO_2 composites using four sizes powder. Materials (Basel) 11(5):670
107. Akay S, Kalderis D, Khataee A, Gholami P, Kayan B (2017) Sonocatalytic degradation of an anthraquinone dye using TiO_2-biochar nanocomposite. Ultrason Sonochem 39(August 2018):120–128
108. Hu Y et al (2019) An efficient adsorbent: simultaneous activated and magnetic ZnO doped biochar derived from camphor leaves for ciprofloxacin adsorption. Bioresour Technol 288(April):1–8

109. Hu H et al (2020) Synthesis of ZnO nanoparticle-anchored biochar composites for the selective removal of perrhenate, a surrogate for pertechnetate, from radioactive effluents. J Hazard Mater 387(November):121670
110. Siqueira G, Bras J, Dufresne A (2010) *Luffa cylindrica* as a lignocellulosic source of fiber, microfibrillated cellulose, and cellulose nanocrystals. BioResources 5(2):727–740
111. Youssef Z et al (2018) Dye-sensitized nanoparticles for heterogeneous photocatalysis: cases studies with TiO_2, ZnO, fullerene and graphene for water purification. Dye Pigment 159(May):49–71
112. Fang Z, Fan Y, Liu Y (2011) Photochemical synthesis and photocatalysis application of ZnS/amorphous carbon nanotubes composites. Front Optoelectron China 4(1):121–127
113. Leichtweis J, Silvestri S, Carissimi E (2020) New composite of pecan nutshells biochar-ZnO for sequential removal of Acid Red 97 by adsorption and photocatalysis. Biomass and Bioenergy 140(June):105648
114. Fu M, Mo C, Li H, Zhang Y, Huang W (2019) Comparison of physicochemical properties of biochars and hydrochars produced from food wastes. J Clean Prod 236:117637
115. Belén M, Vieira Y, Wolski EA, Foletto EL, Silvestri S (2020) Biological degradation coupled to photocatalysis by ZnO/polypyrrole composite for the treatment of real textile wastewater. J Water Process Eng 35(March):101230
116. Azzaz AA, Khiari B, Jellali S, Ghimbeu CM, Jeguirim M (2020) Hydrochars production, characterization and application for wastewater treatment: a review. Renew Sustain Energy Rev 127(May) (2020)
117. Ruan X, Liu Y, Wang G, Frost RL, Qian G, Tsang DCW (2018) Transformation of functional groups and environmentally persistent free radicals in hydrothermal carbonisation of lignin. Bioresour Technol 270(September):223–229
118. Kim P et al (2011) Surface functionality and carbon structures in lignocellulosic-derived biochars produced by fast pyrolysis. Energy Fuels 25(10):4693–4703
119. Yuan T, He W, Yin G, Xu S (2019) Comparison of bio-chars formation derived from fast and slow pyrolysis of walnut shell. Fuel 261(August 2019):116450
120. Velasco LF, Fonseca IM, Parra JB, Lima JC, Ania CO (2012) Photochemical behaviour of activated carbons under UV irradiation. Carbon N Y 50(1):249–258
121. Cui J, Zhang F, Li H, Cui J, Ren Y, Yu X (2020) Recent progress in biochar-based photocatalysts for wastewater treatment: synthesis, mechanisms, and applications. Appl Sci 10(3)
122. Wang RZ et al (2019) Recent advances in biochar-based catalysts: properties, applications and mechanisms for pollution remediation. Chem Eng J 371:380–403
123. Lang Q et al (2019) Properties of hydrochars derived from swine manure by CaO assisted hydrothermal carbonization. J Environ Manage 233(November 2018):440–446
124. Wu K et al (2017) Characterization of dairy manure hydrochar and aqueous phase products generated by hydrothermal carbonization at different temperatures. J Anal Appl Pyrolysis 127(July):335–342
125. McKendry P (2002) Energy production from biomass (part 1): overview of biomass. Bioresour Technol 83(1):37–46
126. Kambo HS, Dutta A (2015) A comparative review of biochar and hydrochar in terms of production, physico-chemical properties and applications. Renew Sustain Energy Rev 45:359–378
127. Zhang Y-J, Xue J-Q, Li F, Dai J-Z, Zhang X-Z-Y (2019) Preparation of polypyrrole/chitosan/carbon nanotube composite nano-electrode and application to capacitive deionization process for removing Cu^{2+}. Chem Eng Process 139:121–129
128. Li H, Dong X, Evandro B, De Oliveira LM, Chen Y, Ma LQ (2017) Mechanisms of metal sorption by biochars: biochar characteristics and modifications. Chemosphere 178:466–478
129. Singh B, Camps-Arbestain M, Lehmann J, CSIRO (Australia) (2017) Biochar: a guide to analytical methods. CSIRO, Australia and New Zealand
130. Yuan P, Wang J, Pan Y, Shen B, Wu C (2019) Review of biochar for the management of contaminated soil: preparation, application and prospect. Sci Total Environ 659:473–490

131. Trager MH, Lavian J, Lee EY, Gary D (2020) Experimental design via NaOH activation process and statistical analysis for activated sugarcane bagasse hydrochar for removal of dye and antibiotic. J Environ Chem Eng, 101631 (2020)
132. Djellabi R et al (2019) Unravelling the mechanistic role of Ti–O–C bonding bridge at titania/lignocellulosic biomass interface for Cr(VI) photoreduction under visible light. J Colloid Interface Sci 553:409–417
133. Lu L, Shan R, Shi Y, Wang S, Yuan H (2019) A novel TiO_2/biochar composite catalysts for photocatalytic degradation of methyl orange. Chemosphere 222:391–398
134. Lee JE, Park YK (2020) Applications of modified biochar-based materials for the removal of environment pollutants: a mini review. Sustainability 12(15)
135. Chen N, Huang Y, Hou X, Ai Z, Zhang L (2017) Photochemistry of hydrochar: reactive oxygen species generation and sulfadimidine degradation. Environ Sci Technol 51(19):11278–11287
136. Dong C, Xing M, Lei J, Zhang J (2020) TiO_2/carbon composite nanomaterials for photocatalysis. Elsevier
137. Vinayagam M, Ramachandran S, Ramya V, Sivasamy A (2018) Photocatalytic degradation of orange G dye using ZnO/biomass activated carbon nanocomposite. J Environ Chem Eng 6(3):3726–3734
138. Oruç Z, Ergüt M, Uzunoğlu D, Özer A (2019) Green synthesis of biomass-derived activated carbon/Fe-Zn bimetallic nanoparticles from lemon (*Citrus limon* (L.) Burm. f.) wastes for heterogeneous Fenton-like decolorization of Reactive Red 2. J Environ Chem Eng 7(4), 103231
139. Rai P, Gautam RK, Banerjee S, Rawat V, Chattopadhyaya MC (2015) Synthesis and characterization of a novel $SnFe_2O_4$@activated carbon magnetic nanocomposite and its effectiveness in the removal of crystal violet from aqueous solution. J Environ Chem Eng 3(4):2281–2291
140. Nasseh N, Arghavan FS, Rodriguez-Couto S, Hossein Panahi A, Esmati M, A-Musawi TJ (2020) Preparation of activated carbon@ZnO composite and its application as a novel catalyst in catalytic ozonation process for metronidazole degradation. Adv Powder Technol 31(2):875–885
141. Xia SH et al (2015) Reduced graphene oxide modified flower-like BiOCOOH architectures with enhanced photocatalytic activity. Mater Lett 156:36–38
142. Rokhsat E, Akhavan O (2016) Improving the photocatalytic activity of graphene oxide/ZnO nanorod films by UV irradiation. Appl Surf Sci 371:590–595
143. Liu J, Wang Z, Liu L, Chen W (2011) Reduced graphene oxide as capturer of dyes and electrons during photocatalysis: surface wrapping and capture promoted efficiency. Phys Chem Chem Phys 13(29):13216–13221
144. Guo H et al (2019) Enhanced catalytic performance of graphene-TiO_2 nanocomposites for synergetic degradation of fluoroquinolone antibiotic in pulsed discharge plasma system. Appl Catal B Environ 248(October 2018):552–566
145. Yang Y et al (2013) Preparation of reduced graphene oxide/poly(acrylamide) nanocomposite and its adsorption of Pb(II) and methylene blue. Langmuir 29(34):10727–10736
146. Bai S et al (2013) The influence of wrinkling in reduced graphene oxide on their adsorption and catalytic properties. Carbon N Y 60:157–168
147. Da Meng Z et al (2012) Synthesis and characterization of M-fullerene/TiO_2 photocatalysts designed for degradation azo dye. Mater Sci Eng C 32(8):2175–2182
148. Rajaji U et al (2019) Graphene oxide encapsulated 3D porous chalcopyrite ($CuFeS_2$) nanocomposite as an emerging electrocatalyst for agro-hazardous (methyl paraoxon) detection in vegetables. Compos Part B Eng 160(August 2018):268–276
149. Sangareswari M, Meenakshi Sundaram M, Meenakshi M (2015) Development of efficiency improved polymer-modified TiO_2 for the photocatalytic degradation of an organic dye from wastewater environment. Appl Water Sci 7(4):1781–1790

Electrocatalysis Based on Carbon Composite Catalysts

Berdan Ulas, Sefika Kaya, Aykut Caglar, Omrüye Ozok, Kawa Hama Sharif, Emrah Kavak, Arif Kivrak, Anish Khan, and Hilal Kivrak

Abstract Electrocatalysis can be defined as the heterogeneous catalysis of electrochemical reactions, occuring at the electrode–electrolyte interface and where the electrode plays both the role of electron donor/acceptor and of catalyst. Fuel cells, batteries and capacitors, hydrogen peroxide sensors, glucose sensors, and heavy metal sensors are the electrochemical sensors catalyzed via electrocatalysts such as Pt, Pd, and other metallic catalysts. These noble materials are expensive and thus should be replaced non noble and unexpensive ones. In this context, carbon composite catalysts are promising candidates. In this chapter, carbon composite catalysts and their applications as fuel cell anode and cathode catalysts, sensor materials for hydrogen peroxide sensors, glucose sensors, and heavy metal sensors, and materials for batteries and capacitor are investigated.

Keywords Carbon composite catalysts · Fuel cell · Batteries · Capacitors · Sensors

B. Ulas · A. Caglar
Department of Mining Engineering, Faculty of Engineering, Van Yuzuncu Yil University, Van, Turkey

S. Kaya · A. Caglar · H. Kivrak (✉)
Department of Chemical Engineering, Faculty of Engineering and Architectural Sciences, Eskisehir Osmangazi University, Eskişehir, Turkey
e-mail: hilalkivrak@gmail.com

O. Ozok · K. H. Sharif · E. Kavak · A. Kivrak
Department of Chemistry, Faculty of Science and Arts, Eskisehir Osmangazi University, Eskişehir, Turkey

K. H. Sharif · E. Kavak
Department of Chemical Engineering, Faculty of Engineering, Van Yüzüncü Yil University, Van, Turkey

A. Khan
Center of Excellence for Advanced Materials Research, King Abdulaziz University, Jeddah 21589, Saudi Arabia

M. Jawaid and A. Khan (eds.), *Carbon Composite Catalysts*, Composites Science and Technology, https://doi.org/10.1007/978-981-19-1750-9_10

1 Introduction

The need for energy has increased rapidly due to the acceleration of industrialization and the increasing population [1]. Currently, this energy need is met by fossil fuel-based energy systems. The fact that fossil fuels will be depleted in the near future has led researchers to alternative energy sources [2]. In addition, the fact that fossil fuels are one of the main causes of environmental pollution and political tensions arising from fossil fuel reserves have accelerated the commercialization of alternative energy conversion systems [3]. Metal-based catalysts are generally used for the occurred reaction in these systems. The use of precious metals such as Pd, Pt, and Ru as electrocatalyst makes fuel cell, battery and sensor applications more expensive. Another disadvantage of these metals is that they are exposed to CO poisoning during the electrochemical reaction [4]. An alloying strategy with second and third metals is commonly used to improve CO poisoning tolerance, but a significant reduction in the cost of the catalyst system can rarely be achieved [5]. Recently, carbon-based materials have been used as catalysts in the mentioned systems due to their advantages namely high surface area [6], high conductivity [7], easy availability [8], and low cost [9]. Carbon-based materials have been used as support materials for many years and there is a detailed literature on this subject. It prevents agglomeration of metal particles and indirectly increases electrochemical activity due to its electron conductivity [10]. Recently, the use of carbon-based composites as catalysts in electrochemical applications has become widespread. Carbon-based composite materials have been used as electrocatalysts in fuel cells, capacitors, batteries and various sensors, and their performance compared to precious metals is found to be promising. In this chapter, the use and advantages of carbon-based composites in fuel cells, capacitors, batteries and sensor applications are examined.

2 Carbon Composite Catalysts for Fuel Cells

Fuel cells, which convert chemical energy into electrical energy through electrochemical reactions, are environmentally friendly and clean alternative technology. The energy conversion efficiency of fuel cells is higher than 40–50% compared to a coal-fired power plant. Fuel cells do not harm the environment as only water is formed as a by-product [11].

Platinum is generally used as a catalyst in fuel cell cells. Platinum is a valuable metal with the high cost and causes problems such as performance decrease of the fuel cell due to CO poisoning [12]. Therefore, studies in recent years have focused on developing new catalyst support materials to improve the catalytic activity of the fuel cell and minimize CO poisoning. Carbon composites are ideal catalyst support materials that overcome carbon corrosion with their superior physical and chemical properties [13]. Carbon composites frequently used as catalyst support materials can be listed as carbon nanotubes (CNTs), carbon nanofibers (CNFs), graphene, and

graphene oxide. These carbon based materials improve the catalytic activity and stability of the catalyst with properties such as porous structure, large surface area, and high electrical conductivity. Carbon composites generally exhibit high oxygen reduction reaction (ORR) activity in an alkaline environment [14–16]. In this section, recent studies with carbon composites as a support material in fuel cells are included.

2.1 Carbon Nanotube Composites

Discovered by Iijima in 1991, CNTs come to the fore with their properties such as large surface areas, superior mechanical and chemical properties, and high electronic conductivity. In recent studies, CNTs have attracted great attention as support material of fuel cell catalyst for improving the thermal stability and electrocatalytic activity of catalysts [17, 18]. CNTs could be classified into multi-walled carbon nanotube (MWCNT) and single-walled carbon nanotube (SWCNT). While SWCNT consists of a single rounded graphene sheet, MWCNT consists of concentric cylindrical graphene sheets intertwined [19].

Prasanna et al. [20] have developed ternary hexafluoroisopropylidenedianiline/ cyclophosphazene/benzidine-disulfonic acid-CNTs (HFPA/CP/BZD-CNT) composite as new support for direct alcohol fuel cell applications. The catalysts coated on the composite by the chemical reduction method were used as anode material for ethylene glycol electrooxidation. The results reveal that compared to Pt/CNT and Pt/C, Pt/HFPA/CP/BZD-CNT and Pt-Sn/HFPA/CP/BZD-CNT catalysts have higher specific activity and low initial potential for ethylene glycol electrooxidation in alkaline medium. The oxidation currents of Pt/HFPA/CP/BZD-CNT and Pt-Sn/HFPA/CP/BZD-CNT catalysts were obtained as 22.23 and 36.42 mA/mg, respectively.

Lilloja et al. [21] have used nitrogen-doped carbide-derived carbon/carbon nanotube (CDC/CNT) composites as a cathode catalyst for the anion exchange membrane fuel cell. The composites were synthesized with different nitrogen precursors (dicyandiamide, cyanamide, urea, or melamine) via high-temperature pyrolysis. The results revealed that surface area and total pore volume of the CDC/CNT catalyst increased with doping nitrogen. It was reported that N-CDC/CNT-urea has the highest surface area (470 m^2/g) and total pore volume (0.54 cm^3/g) compared to pristine CDC and CNT. In electrochemical measurements, all prepared nitrogen-doped composites showed similar results with a single reduction peak in terms of oxygen reduction reaction activity. Additional tests for N-CDC/CNT-mel catalysts reveal that the composite exhibits good stability after 10,000 potential cycles. The peak power density of N-CDC/CNT-mel composite was attained as 310 mW/cm^2 in an anion exchange membrane fuel cell.

Lilloja et al. [22] have developed transition-metal and nitrogen doped carbide-derived carbon/CNT composites (M-N-CDC/CNT) in another study. The composites were prepared by using metal (iron, cobalt, and iron/cobalt combination) and nitrogen

(1,10-phenanthroline) through high-temperature pyrolysis. They reported that M-N-CDC/CNT composite had a good electrocatalytic performance in anion-exchange membrane fuel cells. The good electrocatalytic performance of M-N-CDC/CNT composites was explained by the presence of M-Nx and pyridinic-N fragments and also micro and mesoporous structures. According to the experimental results, the current density and the peak power density of the CoFe-N-CDC/CNT composite were reported as 470 mA/cm^2 at 0.75 V and 1120 mW/cm^2, respectively.

Wang et al. [13] have investigated the performance of nano-molybdenum carbide (Mo_2C)/CNT composite as an anode catalyst in the microbial fuel cell. The Mo_2C/CNTs composites, which contain different amounts of molybdenum hexacarbonyl as 8.4, 15, 16.7, 20, 30 and 70 wt%, were prepared by using the microwave-assisted method as platinum-free catalyst. It was emphasized that the composite containing 16.7 wt% Mo compared to platinum, exhibits the best performance for fuel cells and will be an good alternative to platinum. The maximum current density of the composite was achieved as 1.12 mA/cm^2. They said that CNT with properties such as electronic conductivity and biocompatibility formed biofilm that facilitates electron transfer from type c cytochrome to electrodes and this biofilm supported hydrogen oxidation.

Cao et al. [12] have improved a new nanocomposite ($Pt/RuO_2{\cdot}xH_2O$/CNT) for direct methanol fuel cells as a solution to problems such as the cost of platinum catalyst, weak kinetics, and CO poisoning tendency of Pt. The catalyst was prepared with 14.8 wt% Pt loading on the CNT at Pt: Ru ratio of 1:1. The TEM analysis results revealed that the catalyst was in the adjacent lattice plane structure and the distance between the two cages was ~0.233 nm. The current density of the $Pt/RuO_2{\cdot}0.56H_2O$/CNT catalyst was obtained to be 1.5 times higher compared to the PtRu/Vulcan catalyst. They stated that $Pt/RuO_2{\cdot}0.56H_2O$/CNT catalyst exhibited very good performance for methanol electrooxidation.

Higgins et al. [23] have synthesized titanium nitride-CNT (TiN-CNT) nanocomposites by a simplistic fabrication procedure. These nanocomposites were used as support material for the platinum electrocatalyst toward methanol oxidation reaction and oxygen reduction reaction. CV analysis was carried out in nitrogen environment (0.1 M $HClO_4$ + 1 M methanol) at a scan rate of 50 mV/s. CV curves emphasized that the peak current density of Pt/TiN–CNTs as 22.9 mA/cm^2 was higher than that of commercial Pt/C as 15.8 mA/cm^2. The electrochemically active surface areas of Pt/TiN–CNT and Pt/C were obtained as 109.75 m^2/g_{Pt} and 104.37 m^2/g_{Pt}, respectively. It is reported that TiN-CNT nanocomposites are promising as support materials for electrocatalysts.

The cobalt-polypyrrole-MWCNT composite was developed as a cathode electrocatalyst for polymer electrolyte fuel cells, direct methanol fuel cells, and direct ethanol fuel cells by Reddy et al. [24] Pt-Ru/MWCNT and Pt-Sn/MWCNT were investigated as anode electrocatalyst. They observed that Co-PPy/MWCNT catalyst showed excellent stability for 50 h at high current density and high voltage (0.7 V) in polymer electrolyte fuel cells. The high oxygen reduction reaction activity and its good performance even at long operating times of Co-PPy/MWCNT catalyst revealed that the MWVNT was suitable as a support material.

Sahoo et al. [25] have synthesized a novel electrocatalyst support material in a proton exchange membrane fuel cell. Few-layer graphene-MWNTs sandwiches (GCSs) were prepared with a catalysis-assisted chemical vapor deposition method. The electrocatalytic activity of the prepared Pt/GCS was compared with commercial Pt/C. The experimental results confirmed that Pt/GCS had a current density and maximum power density at 0.6 V were 613 mA/cm^2 and 495 mW/cm^2, respectively. They emphasized that the Pt/GCS electrocatalyst showed high performance approximately 71% higher than the Pt/C. 3D GO/CNT was used as support material for electrocatalyst in direct methanol fuel cells by Wang et al. [26]. PtPd-GO + e-CNT electrocatalyst was prepared with PtPd nanocrystals and carbon composite via chemical reduction method. It is reported that the electrochemically active surface area and mass activity of PtPd-GO + e-CNT were acquired as 164 m^2/g_{Pt} and 690 mA/mg, respectively.

Xu et al. [27] reported that antimony-doped tin oxide on MWCNT composite was improved as a support material for platinum catalysts. Electrochemical properties of Pt-ATO/MWCNT electrocatalyst were investigated and compared to Pt-SnO_2/MWCNT and commercial Pt/Cs. According to CV results, the onset potential of Pt-ATO/MWCNT, Pt-SnO_2/MWCNT, and Pt/C was obtained 0.38, 0.45, and 0.50 V, respectively. They said that the Pt-ATO/MWCNT electrocatalyst exhibited higher current density and lower onset potential. They also emphasized that the Pt-ATO/MWCNT electrocatalyst showed high catalytic activity and stability for methanol electrooxidation when compared to Pt-SnO_2/MWCNT and commercial Pt/Cs.

2.2 Mesoporous Carbon Composites

According to IUPAC, pores with a pore diameter of less than 2 nm are classified as micropores, those between 2 and 50 nm as mesopores, and those larger than 50 nm as macropores Any silica and alumina that have identical size mesopore are typically mesoporous materials. Oxides of niobium, tantalum, titanium, zirconium, cerium, and tin are also known to be mesoporous. However, mesoporous carbon, often used in energy storage systems, is the flagship of mesoporous materials [28].

Mesoporous carbon, with its outstanding chemical/thermal stability, is well suited for use as a catalyst support material [29]. Mesoporous carbon with uniform pore distribution improves the performance of the catalyst by facilitating mass transfer on the catalyst surface. In addition to pore size distribution, pore volume and shape also significantly affect the performance of anode/cathode catalysts for fuel cells [30]. Both the surface and pores of mesoporous carbon can be modified to increase the efficiency of the catalyst. For surface and pore modifications, typically polymer coating, oxidation, and grinding are applied to increase the number of functional groups on the surface. It is usually treated with nitric acid, sulfuric acid, and phosphoric acid to functionalize mesoporous carbon [31]. The acid treatment process creates additional binding sites for the metal nanoparticles to bind, thus allowing a

high metal loading to the carbon support. However, the aforementioned acid treatment may also have disadvantages such as reducing the surface area, changing the pore structure, reducing the conductivity, and negatively affecting the corrosion resistance. Therefore, light surface functionalization methods are more preferred for the functionalization of mesoporous carbon structures [32].

Mesoporous silica–carbon composite (MSC) materials can be synthesized by hydrothermal carbonization technique, which provides a homogeneous and thickness-controlled carbon coating, and the carbon layer can be deposited on the regular and irregular mesoporous silica surface. Electrical interactions between amino-modified silica and hydro-thermal carbon are utilized to obtain a homogeneous carbon coating on the silica surface. The researchers reported that the composites they obtained had a high degree of graphitization, controlled geographic information system (shape and particle size), and adjustable pores. The application results showed that a thin carbon layer had a high adsorbability capacity for the dyes. It was also emphasized that the silica–carbon column could provide chromatographic fundamental separation of oligosaccharide isomers. The results show that silica–carbon composites are promising functional materials, such as adsorption and chromatographic separation for large-molecule processes [32] (Fig. 1).

Carbon-based materials, ranging from carbon and one-dimensional CNTs to two-Dimensional graphene, are commonly used as functional materials for many critical fields, such as catalysis, separation, and energy storage [34]. Till now various methods for the synthesis of carbon-based materials including carbon precursor's pyrolysis, chemical vapor deposition, template methods, and hydrothermal carbonization have been developed. In the hydrothermal carbonization method, inexpensive materials such as carbohydrates and various biomass are used as precursors. This synthesis

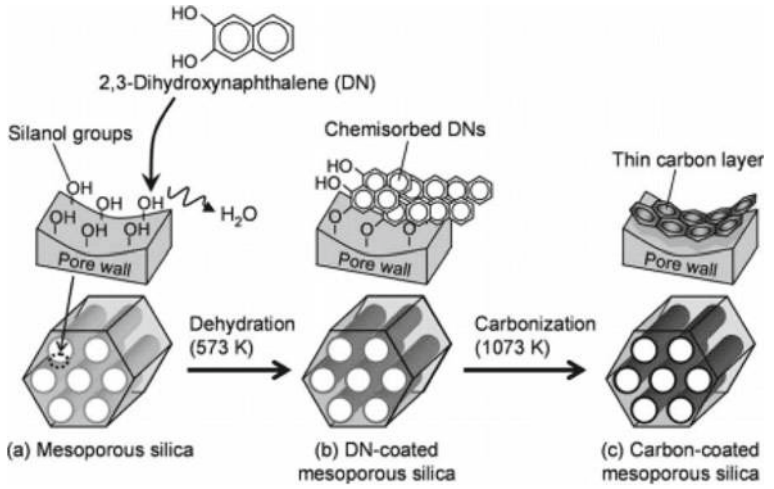

Fig. 1 Schematic representation of the synthesis of the mesoporous silica–carbon composite materials [33]. Reprinted with permission, Elsevier, 2010

method takes place in the aquatic environment and on the surface rich in oxygen compounds under 200 °C [35]. However, the hydrothermal carbonization products have a small surface area and porosity. In order to obtain pores by removing small organic compounds, heat treatment of the precursor in an inert environment is an important strategy. Thermally treated hydrothermal carbonization materials generally provide micropore formation and are not very suitable for processes with macroscale reactants [36]. In other words, carbon structures smaller than 10 mm can be synthesized by hydrothermal synthesis. Therefore, as a result of hydrothermal synthesis, the morphological structures and porosity of carbon materials are insufficient [37]. Nitrogen-modified carbon composite could be obtained by pyrolysis of cobalt, iron-ethylene diamine chelate complexes on silica. The catalytic activity and stability of nitrogen-modified carbon composites are highly dependent on the pyrolysis temperature, pyrolysis time, composite content, form, and distribution of nitrogen functional groups. It was prepared by the aforementioned nitrogen-modified carbon-supported Pt by impregnation method and was reported to show high catalytic activity with a good Pt dispersion [38].

Ordered mesoporous carbon materials have a high potential for catalyst, adsorbent, and electrode modification applications due to their low densities, high surface area (more than 1000 m^2/g), good chemical stability, large pore volume, and adjustable pore sizes (2–20 nm). is an alternative [39]. In-line mesoporous carbon has properties such as fast adsorption kinetics, high adsorption capacity, and high affinity for many adsorbates compared to other carbon-based materials, and thus it is widely used in water pollution control, gas storage, and bioadsorption applications. High-performance innovative carbon materials for specific applications have been prepared by various synthesis strategies. These are (1) physical or physically combined with carbon activation at high temperatures [40]; (2) carbonization of carbon precursor composed of one component thermally stable and one component thermally unstable [34]; (3) Self-assembly by co-condensation and carbonization using soft templates [41]; and (4) replication synthesis by impregnation, carbonization, and removal of the template with pre-synthesized hard templates [42].

2.3 Graphene and Graphene Oxide Composites

Graphene is a two-dimensional single sheet of sp^2 carbon in a hexagonal structure [43], and it has unique properties, such as high charge-carrier mobility, superconductivity, quantum Hall effects, high mechanical strength (130 GPa), and high surface area (2630 m^2/g) [44]. Graphene can synthesize various ways such as; chemical exfoliation, mechanical exfoliation, chemical vapor deposition (CVD), and epitaxial growth [45–47]. Graphene is used as a support material for metal catalysts, and the distribution of metal nanoparticles on graphene significantly affects the electrooxidation performance. The properties are given in Table 1 ideal as electrode support for catalysts in electrochemical energy systems [48].

Table 1 Applications of graphene and graphene oxide in fuel cells

Applications	Materials and conditions	References
Catalyst support	Functionalized graphene reduction of H_2PtCl_6 and GO by $NaBH_4$ functionalized graphene with Perfluorosulfonic acid	[49–51]
	Nitrogen-doped graphene using melamine	[52]
	Microwave-heating of graphene in an NH_3 atmosphere	[53]
	Pd–N doped-graphene/indium tin oxide (ITO) via CVD	[48]
	Pt-graphene/ITO and Au-graphene/ITO via CVD	[54]
	Functionalized graphene sheet (Mn, Ni, Cu, Co/N doped-graphene for lithium-ion battery) by a modified Hummers method	[55]
Metal-free catalyst	CVD in the presence of NH_3 (N-doped graphene)	[56]
	Direct annealing of graphene oxide and benzyl disulfide in argon (S-doped graphene)	[57]
	Thermal annealing GO in the presence of B_2O_3 (B-doped graphene)	[58]
	Sulfonic acid-functionalized GO (ionomer)	[59]
	Hybrid supports composed of functionalized GO	[60]
	Hybrid supports composed of functionalized GO	[50]
	Growing graphene via CVD	[61]

Graphene has been widely used as catalyst support in fuel cells (FCs). FCs, which convert chemical energy into electrical energy, are shown as a potential device in closing the future energy gap thanks to their environmental friendliness and high efficiency [62, 63]. Synthesized graphene-based nanoparticles such as Pt, Pd, TiO_2, nitrogen (N)-doped, sulfur (S)-doped, boron (B)-doped graphene, application and synthesize condition was given in Table 1. The versatility of the surface modifications and their unique defect behavior has resulted in the presence of functional groups that increase activity.

Since graphene is not electrochemically active, it was emphasized in the literature that graphene should be functionalized by various pretreatments. Graphene functionalization is categorized into five types namely (i) basal plane functionalization, (ii) edge functionalization, (iii) noncovalent adsorption on the basal plane, (iv) self-assembling of functionalized graphene nanosheets (GNS), and (v) asymmetrical functionalization. Graphene sheets attached with oxygen as epoxy, carboxylic acid, ketone, and hydroxyl are called graphene oxide (GO) [64, 65]. Hummer's method is mostly used for preparing GO and can be easily modified to functionalized graphene [47]. GO most attractive and the most promising material for fuel cell application. GO is an outstanding material to use with a different type of polymers to enhance the processibility, chemical, electro-chemical, and mechanical properties of membranes. For reduction of GO, various reduction agents were reported such as $NaBH_4$, NH_4BH_4, HI, Hydrazine, L-ascorbic acid/NH_3, and L-cysteine (Table 2).

Table 2 Organic and inorganic compounds as a reduction agent

Reduction agent	References
$NaBH_4$	[66]
NH_4BH_4	[67]
HI	[68]
Hydrazine	[69]
Urea/NH_3	[70]
Ethanol	[71]
L-ascorbic acid/NH_3	[72]
$NaHSO_3$	[73]
Zn-H_2SO_4	[74]
L-cysteine	[75]
Green tea	[76]
Leaf extract	[77]

Graphene-based electrodes are good conductors due to their graphene layers. In particular, the functionalization of graphene leads to increased charge transfer capability and higher electrocatalytic activity can be obtained [78]. PEMFC performance of graphene nanopellet and graphene oxide supported Pt catalyst reported by Devrim et al. [79]. The researchers reported that the current densities for Pt/GNP, Pt/C and Pt/GO were 0.28, 0.17 and 0.22 A/cm^2, respectively, while the maximum power density for Pt/GNP was 0.46 W/cm^2 at 190 °C. The researchers attributed the enhanced performance of Pt/GNP to the uniform distribution of Pt on the support and the very good electron conduction of GNP. Seger et al. [80] on the other hand, used carbon black supported Pt as the anode catalyst and Pt/GO as the cathode catalyst in a PEMFC. The pristine Pt showed a power density of 96 mW/cm^2, while Pt/GO exhibited a power density of 161 mW/cm^2. It has been reported that the increased performance is due to the charge exchange between the support and the metal catalyst. Microbial fuel cell anode catalysts were designed by Chen et al. The researchers reported the power densities of as-prepared GB/O-rGO/PAM, GB/rGO/PAM, GB, GB/GO/PAM, and CC as 782, 758, 605, 580, and 350 mW/cm^2, respectively. This increase in performance relative to bare carbon is attributed to the presence of functionalized graphene in the composite structure [81]. An extensive literature on the use of carbon-based composites as electrocatalysts is given in Table 3. As can be seen from Table 3, graphene-based materials are generally used for the oxygen reduction reaction in PEMFC. In all these studies, it has been reported that the catalyst performance in fuel cells is increased because functionalized graphene led to electron conductivity and higher affinity with metal catalysts.

Table 3 Literature on graphene based anode and cathode material for fuel cell

Fuel cell type	Anode catalyst	Cathode catalyst	Current density (mA/cm^2)	Maximum power density (mW/cm^2)	References
PEMFC	Pt/GNP	Pt/C	280	460	[79]
DMFC	Co/Graphene	Pt/C	62	1.1	[82]
PEMFC	Pt/CB carbon black	GO-Pt	–	161	[80]
MFCs	GB/rGO/PAM	Pt-PTC	–	758	[81]
PEMFC	–	Co_2C/rGO	2.21	–	[83]
MFC	–	3D-GNS	2.32	0.206	[84]
DEFC	PdNiO/EGO	Pt/C	19.9	16.6	[85]
PEMFC	Pt/rGO/Vulcan XC-72	Pt/rGO/Vulcan XC-72	–	645	[86]
MFC	Carbon cloth	GO-Zn/Co	4.34	773	[87]
MFC	Graphite	GP-HG	–	220	[88]
PEMFC	Pt/C	FeGNT	500	200	[89]
PEMFC	Pt	CF/PANI/rGO	−3.46	92	[90]

2.4 CNFs Composites

CNFs are frequently used as support materials by researchers due to the advantages they provide in fuel cell applications among carbon-based materials. CNFs are widely used as catalyst support and photoanode material for occurred reactions in applications such as sensors, batteries, supercapacitors and fuel cells. The main reason why CNFs are preferred in these applications is their high electrical conductivity and surface area. CNFs were first synthesized by Thomas Edison and Hughes by carbonization of cotton yarns and gas pyrolysis methods, respectively. Researchers predicted that CNFs could be a good component of composite materials for energy storage systems and sensors [91]. CNFs are more widely used in electronic devices because they show higher electrical and thermal stability than carbon fibers. Nanotubes, nanowires and nanorods have been used as support materials for anode or cathode catalyst in fuel cells. But CNFs have better kinetic properties due to modifiable surface properties and high charge transfer with metal catalysts [92]. CNFs are also prominent because they are predominantly mesoporous and possesses good crystallinity. CNFs can be produced by cheaper production methods than CNTs with high electronic conductivity [93].

Production methods and conditions are the primary cause of both the morphological and electronic properties of CNFs. CNFs can be defined morphologically as long and fibrous carbon sheets. The lengths of up to micrometers and the diameters of 50–200 nm are strongly dependent on the preparation conditions of the CNF. Although the mechanical and chemical properties of CNFs are close to those of other carbon

derivatives, they do not present any difficulties in terms of machinability. In addition, CNFs are suitable for aviation applications due to the low weight and high corrosion resistance. The tensile strength of CNFs is proportional to the diameter of the fiber. As the diameter of CNFs increases, the number of defects decreases and the tensile strength decreases. CNFs are also used as additives in fuel cell membranes due to their high surface area and flexibility.

Electrocatalytic activities of CNF supported metals for ethanol [94], urea [95], glycerol [96] and methanol [97] electrooxidation have been reported in the literature. Researchers have reported that even in conventional synthesis methods, nanoparticles are well dispersed on the support material. In addition to these anode catalysts, many CNF supported cathode catalysts have been reported in the literature namely Fe–N/CNF [98], N-CNF [99], Pd/Y-CNF [100], FeN4/CNF [101], Fe_3Co/CNF [102], and Co_3O_4/CNF [103]. CNFs could be easily functionalized with functional groups due to their reactive carbon edge [104]. In other words, the compatibility of CNFs with polymer matrices is very good. These properties have led to the widespread use of CNFs in proton-conducting membranes. Liu et al. investigated the performance of the SPEEK/CNF composite as a proton exchange membrane. Researchers reported that CNF increased the water uptake capacity, proton conductivity, and mechanical strength of the composite membrane. It was also emphasized that CNF would facilitate the commercialization of composite membranes due to its tunable surface properties [105]. In addition, due to these unique properties of CNF, Herrera et al. [106] reported the flexural strength and corrosion current of the PP/MWCNT/CNF composite to be used as a bipolar plate for fuel cells as 45.3 MPa and 0.0046 $\mu A/cm^2$, respectively.

3 Capacitors and Batteries

3.1 Capacitors

Devices that store electrical energy as an electrostatic charge are called capacitors [107]. When voltage is applied to two plates with an air gap between them, the plates transition to a static charged state [108]. When the applied potential is removed, the static charge will be maintained. The electric field created by the applied voltage is balanced by the static charges on the plates. The main function of capacitors is to store electrostatic charge, and the amount of charge stored by capacitors is an important parameter to evaluate their performance. The capacitance (C) of a capacitor is defined as the ratio of the positive charge (Q) stored on the electrodes to the potential difference (ΔV) between the electrodes [109].

$$C = \frac{Q}{\Delta V} \tag{1}$$

The amount of charge the capacitor will store can be increased with a dielectric material placed between the plates [110]. For example, oxide layers with a very large surface area are formed as dielectric material in electrolytic capacitors [111]. This layer forms a plate of the capacitor. Because the oxide layer is very rough, a liquid or dry gel is used as the second electrode [112]. In terms of working principle, it is almost the same as the capacitors consisting of two plates and dielectric material. Electrochemical capacitors use electrodes that act like plates and are immersed in an ionic electrolyte [113]. There is also a membrane inside this electrolyte that separates the electrodes. In electrochemical capacitors, ions separated from the electrolyte by applying voltage are neutralized in the Helmotz layer [114]. Therefore, a double-layer structure with high charge holding capacity is formed on the electrodes.

Capacitors are generally classified according to the material they contain. According to this criterion, common types of capacitors are vacuum capacitors [115], air capacitors [116], plastic film capacitors [117], mica capacitors [118], paper capacitors [119], glass capacitors [120], ceramic capacitors [121], aluminum electrolytic capacitors [122], tantalum electrolytic capacitors [123], os-con capacitors [124], and supercapacitors [125].

Supercapacitors offer high energy and power density [126]. There are no dielectric materials among the components of supercapacitors. There is a very thin insulating separator between the plates placed in the electrolyte. As a result of this structure, supercapacitors have very high capacitances compared to conventional capacitors. The main factors that provide this high capacitance are that the separator is very thin and the electrodes are covered with porous materials with a very high surface area. Since charge accumulates on the electrode surface, the surface area of the electrode is crucial to the performance of supercapacitors [127]. While activated carbon is widely used to increase the surface area of the electrode, other forms of carbon are also used, such as graphene, carbon aerogel, and CNT. Electrolytes in supercapacitors are composed of anion and cation forming substances and a solvent. Although water is the most common solvent for supercapacitors, organic solvents have also been reported, although low conductivity, in some studies [128].

Supercapacitors are divided into three groups according to the material used, namely electric double-layer capacitors (EDLC), pseudocapacitor, and hybrid capacitors [129]. Sudocapacitors are supercapacitors with a higher energy density compared to EDLC, although the charge–discharge circulation is weak [130]. EDLCs contain conductive polymers and metal oxides as active ingredients [131]. The most commonly reported metal oxides are manganese oxide and ruthenium oxide, which can allow reversible reactions [132]. Other metal oxides used apart from these are Fe_3O_4 [133], $Ni(OH)_2$ [134], and V_2O_5 [135]. Despite the high capacitance value provided by these metal oxides, their high cost is a significant disadvantage. Hybrid capacitors, on the other hand, are high capacitance capacitors formed by combining electrodes containing carbon and transition metal oxides. Hybrid capacitors, which have higher energy and power density than EDLCs, are more stable than pseudocapacitor [136] (Fig. 2).

EDLCs consist of an electrolyte, separator and two carbon-based electrodes. Charges that dissociate at the electrode/electrolyte interface under applied voltage

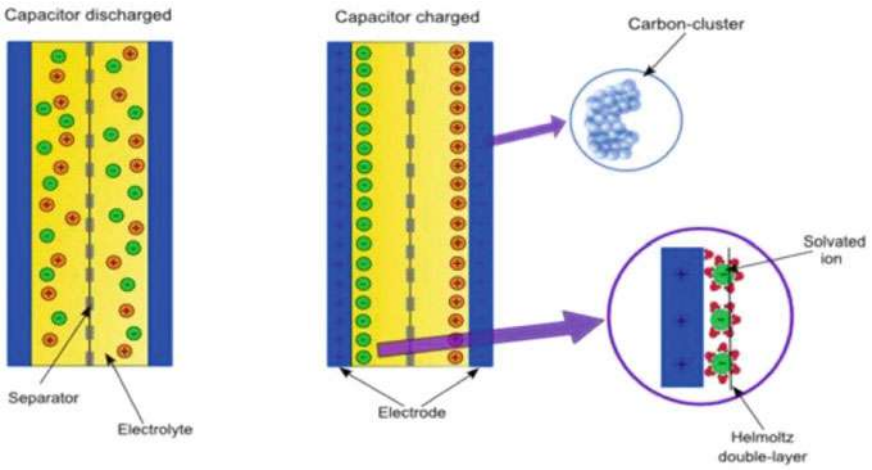

Fig. 2 Components of supercapacitor [137]

accumulate on the surface of the electrodes. Faradaic reactions do not occur because charges are electrostatically stored. Solutions such as H_2SO_4, KOH, propylene carbonate and acetonitrile are used as electrolytes [138]. The development of the electrode material constitutes a large part of the research on supercapacitors. The main motivation of this research is that the electrode has a great influence on the power density and capacitance of the supercapacitor. The used electrode materials are classified into three categories: carbon-based, transition metal oxide and conductive polymers [139]. Only carbon-based materials will be discussed in this chapter. CNF, carbon aerogel, graphite, activated carbon, and reduced graphene are the main carbon-based materials used as electrode materials for supercapacitor. Researchers' interest in carbon-based materials stems from the advantages of these materials such as thermal stability, chemical stability, mechanical strength, low cost, non-toxicity and easy availability.

Activated carbon is frequently used as electrode material in capacitors because it has average electrical conductivity and provides fast and easy synthesis at low cost [140]. However, the difficulty of accessing electrolyte ions to the micropores it contains is the most important disadvantage of this material. However, for the preparation of mesoporous and high surface area structures, methods in which these parameters are well controlled have been reported many times in the literature [141]. In a study conducted by Chen et al., electrodes with activated carbon, carbon black, CNT, and CNFs were developed for supercapacitors. The researchers have been reported that the cycle life, capacitance, energy density, power density and packing density of the obtained nanocomposite electrodes were 91.4%, 66.1 F/cm^3, 29.6 W h/L, 101.7 kW/L and 0.63 g/cm^3, respectively. The researchers emphasized that this performance of the electrodes is far above the current technology [142]. In another study, composite material consists of activated carbon, CNT, and reduced

graphene oxide was prepared in film form. It has been reported that CNT increases the conductivity of the electrode, while AC prevents agglomeration of other forms of carbon. It has been reported that the AG/CNT/RGO composite shows a capacitance of 101 F/g and a maximum energy density of 30 W h/kg at a current density of 0.2 A/g. The enhanced performance was attributed to the synergistic effect between AG, CNT and RGO [143].

Single-walled CNTs with sp^2 hybridization can be characterized as a coiled form of graphene sheets in the form of tubes. CNTs have an amplitude on the nanometric scale and a length measured in micrometers. They are synthesized by methods such as carbon arc discharge, pyrolysis of hydrocarbons, laser evaporation and chemical vapor deposition. Electrical conductivity, thermal conductivity, tensile strength and specific surface area of CNTs have been reported in the literature as 5000 S/cm, 6000 W/mK, 45 billion Pa, and 1315 m^2/g, respectively. These properties have made CNTs an interesting material for supercapacitors and are considered an important component for carbon composite systems. CNT-based composite materials for supercapacitors are often designed with other forms of carbon or metal oxides. Zhou et al. [144] synthesized the CNT/CNF composite by the CVD method and reported that it had a capacitance of 207 F/g at a charge/discharge rate of 1 A/g. It has also been reported that the composite material shows a very good cycle stability of 95.6% after 5000 charge/discharge cycles at a current density of 20 A/g and energy density of 63.7 Wh/kg. Wang et al. [145] prepared the CNT/MnO_2 composite electrode by hydrothermal methods and reported that this composite showed a very high energy density up to 27.14 Wh/kg at a power density of 571.3 W/kg. It has been reported to CNT/MnO_2 maintain this performance even after 8000 galvanostatic charge_discharge cycles. Composite material consisting of CNT, Fe_3O_4 and PANI was reported by Li et al. [146]. High specific energy density of 8.0 Wh/kg, a high specific power density of 5.3 kW/kg, and a specific capacitance of 201 F/g at a scan rate of 20 mV/s has been reported for CNT/PANI/Fe_3O_4. In addition, it was emphasized that the CNT/PANI/Fe_3O_4 supercapacitor had 3.6% capacitance loss after 10,000 charge–discharge cycles.

The high cost of mass production of CNT has made alternative electrode materials popular, one of which is graphene. Graphene is a carbon allotrope with 2D and hexagonal lattice. Graphene is one of the main types of carbon used as electrode material in supercapacitors due to its very large surface area of 2630 m^2/g [147]. The mechanical strength of graphene is also suitable for use in supercapacitors and can compete with CNTs. The layering of graphene prevents agglomeration and provides a higher surface area. In addition, graphene is a very good candidate for use as a supercapacitor electrode material with a thermal conductivity of 5000 W/mK and young module of 1 TPa [148]. Graphene used in supercapacitors was synthesized by the most common methods of mechanical exfoliation, arc discharge, chemical vapor deposition and epitaxial growth [149]. Composite materials consisting of different carbon derivatives have been frequently investigated as electrode materials. Tian et al. prepared the composite material consisting of graphene oxide and graphene using the liquid-shear-exfoliation method. It was emphasized by the researchers that the graphene exfoliated with the help of graphene oxide. The gravimetric capacitance of the obtained

graphene/graphene oxide composite was reported as 483 F/g at a current density of 1 A/g. In addition, graphene/graphene oxide nanosheets have an energy density of 17.9 Wh/kg at a power density of 500/kg [150]. Manjakkal et al. prepared three-dimensional graphene foam electrodes and claimed that the form of graphene affects supercapacitors performance depending on the surface area. They reported that the 3D graphene foam showed 38 mF/cm^2 capacitance at 0.67 mA/cm^2 current density. They also emphasized that graphene foam performs much higher than carbon-based supercapacitors in terms of capacitance, power density, and energy density [151]. A detailed literature on use of carbon composite materials for capacitors is given in Table 4.

3.2 Battery

A battery is defined as a series of electrochemical cells which are connected to each other in order to provide voltage and capacity. Each electrochemical cell in a battery consists of two electrodes namely, cathode and anode, and an electrolyte that enables the transfer of ions between cathode and anode. An external source is required to initiate the chemical reaction and to obtain the current. It is the chemistry of the battery that defines the capacity of the cell and the electrical energy given by the battery [165].

Invented by Yoshino, lithium-ion battery is the currently used rechargeable, high capacity, and light-weight power source of portable electronic devices and recently, electric vehicles. There are two different classifications for batteries which are disposable/rechargeable batteries and aqueous electrolyte/nonaqueous electrolyte batteries. The inherent limitation of aqueous electrolyte batteries is that their maximum available voltage is 1.5 V per cell, due to the electrolysis of water in the electrolyte around this voltage. Being the most commercially used example of nonaqueous-electrolyte batteries, lithium-ion (Li-ion) batteries harvest higher electromotive force per cell by employing transition-metal oxides containing lithium ion as a positive electrode, carbonaceous materials as a negative electrode, and a nonaqueous electrolyte. They also provide greater stability and enables the production of smaller, lighter and cheaper battery storage. From 1998s till now, there is expanding use of Li-ion batteries both for consumer use and electric vehicles and efforts are being focused on enhancing performance by adopting technological advances into the production of the Li-ion battery [166]. Additionally, the use of Li-ion batteries for energy storage is a recently emerging industrial application [167].

The working principle of Li-ion batteries is simply the recurring transfer of Li stored in anode to the cathode by an electrolyte. The electrolyte of Li-ion batteries is the lithium salt; lithium hexafluorophosphate ($LiPF_6$), in organic carbonate solvents such as ethylene carbonate, dimethyl, diethyl, and ethyl-methyl carbonates which have high polarity and provides good conductivity. The final hydrolysis products of $LiPF_6$ namely HF and PF_3O are known to be highly react, and on both cathode and anode sides [168–170] (Fig. 3).

Table 4 Literature on carbon based composites for capacitors

Material	Cycle life	Electrolyte	Energy density	Power density	Capacitance	References
CCS	87.0% after 6000 cycles	KOH	38.4 W h kg^{-1}	750 W kg^{-1}	606.7 F g^{-1}	[152]
Co–Co_3O_4@CNT–NC//rGO	93.6% after 10,000 cycles	KOH	46.7 Wh kg^{-1}	1601.1 W kg^{-1}	823.4 F g^{-1}	[153]
MnO_2/CNT	96.4% after 2000 cycles	CMC/Na_2SO_4	36.4 μWh·cm $^{-2}$	15.6 mW·cm^{-2}	386 mF·cm^{-2}	[154]
MoS_2@CNTs/Ni	no decay after 2000 cycles	Na_2SO_4	63 Wh kg^{-1}	25.5 kW kg^{-1}	512 F g^{-1}	[155]
PPy/RGO/CNT/BC	86.85% after 5000 cycles	$NaNO_3$	0.0328 mWh cm^{-2}	12 mW cm^{-2}	715 mF cm^{-2}	[156]
Activated carbon	96.66% after 16,000 cycles	Na_2SO_4	33,500 Wh kg^{-1}	23,000 W kg^{-1}	167 F g^{-1}	[157]
Activated carbon	no decay after 9,000 cycles	KOH	2.26 Wh kg^{-1}	51 W kg^{-1}	148 F·g^{-1}	[158]
Activated carbon	94% after 5000 cycles	Na_2SO_4	23 W h kg^{-1}	10 000 W kg^{-1}	394 F g^{-1}	[159]
N doped AC	95.5% after 15,000 cycles	EMIM BF_4/PC	60.3 Wh kg^{-1}	379.13 W kg^{-1}	268 F g^{-1}	[160]
3D graphene	94.6% after 20,000 cycles	$TBAPF_6$	24.1 mWh L^{-1}	711 W L^{-1}	27.5 mF L^{-1}	[161]
MX-rHGO film	93% after 10,000 cycles	H_2SO_4	38.6 Wh L − 1	62.4 W kg^{-1}	1445 F cm^{-3}	[162]
Co_3O_4/Graphene	99.3% after 20 000 cycles	KOH	43.1 Wh kg^{-1}	4000 W kg^{-1}	978.1 F g^{-1}	[163]
3DPC/Co_3O_4	83% after 2000 cycles	KOH	21.1 Wh kg^{-1}	790 W kg^{-1}	423 F g^{-1}	[164]

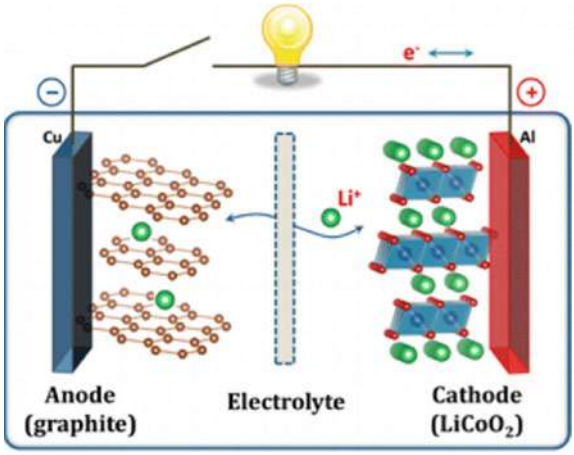

Fig. 3 Working principle of Li-ion battery mechanism [171]. Reprinted with permission from Copyright (2021) American Chemical Society

In Li-ion batteries, Li ions are released from cathode to the anode during the charge process and Li ions are suppled by anode to cathode during the discharge process. Therefore, a material to used as a cathode in Li-ion battery should contain elemental lithium. Layered structured lithium metal oxides are used as the cathode material of commercially produced Li-ion batteries. Among them, lithium cobalt oxide ($LiCoO_2$) is the most widely used while it suffers from cost and capacity efficiencies. $LiNiO_2$ provides higher capacity but has low thermal stability. There are studies showing the superiority of the combined use of Ni and Co in terms of stable cyclability and environmental compatibility [172].

The role of the anode material in a Li-ion battery is to accept Li ions during the charge process and to release the Lio ions during the discharge process. The standard anode material of a Li-ion battery is defined to be graphitic carbons which has low cost and provides operation at low valtages [173]. Lithium titanate ($Li_4Ti_5O_{12}$) and niobium pentoxide (Nb_2O_5) are some of the anode materials. Currently, gravimetric and volumetric energy density values are reported to be < 250 Wh/kg and < 650 Wh/L for the commercial Li-ion technology while the described need is around ~500 Wh/kg and > 1000 Wh/L. Manthiram et al. [174] emphasized that the steps that have been taken to increase the energy densities have mostly deal with the fabrication engineering point of view while the electrode materials remained the same.

The limited theoretical capacity of a commercialized graphite anode in a Li-ion battery is reported to be 372 mAh/ g. It was emphasized that providing an increase approximately two times of the current specific capacity of the anode will result in a 2 times increase of total battery capacity [175, 176]. Zhong et al. [177] were synthesized using nitrogen-rich CNT by template method. The structure of CNT caused rapid ion and electron transfer and high Li+/Na+ storage capacity. The presence of N in the structure led to the formation of defects that increased the electrochemical activity. Researchers reported that NCNT showed a reversible capacity of 132 mAh/g for SIBs after 5000 cycles at 4000 mA/g and 170 mAh/g for LIBs after 2000 cycles at the same current. Li et al. [178] were benefited from the high electrochemically active

surface area of activated carbon and reported that the activated carbon obtained from corn stalk showed a reversible capacity of 504 mAh/g after 100 cycles at 0.2 °C. It has been stated that the easy control of the pore size of activated carbon is the primary reason for the increased reversible capacity. In another stduy, An et al. [179] investigated the performance of a composite of carbon and silicon for Li-ion batteries. Researchers reported the specific activity of 1 wt% carbon-Si composite as 16.6 mAh/g. For the 10.0 wt% carbon-Si modified anode, the specific activity and initial discharge efficiency were reported as 513.1 mAh/g and 83.79%, respectively. This high performance is attributed to the fact that the defects formed by the addition of Si provide more lithium ions. Although carbon-based materials have very good surface properties, they must contain activated sites on their surface for high specific activity. Most researchers have increased the performance of batteries by creating defects on the surface with composite materials. The relevant literature is summarized in the Table 5.

Incorporation of lithium into metal oxides is performed either by insertion reaction which is the intercalation of Li into the host material and not causing any structural change in the host or by conversion reaction which is the reduction of metal oxide to pure metal. The latter, i.e. conversion reaction, is known to cause significant changes in volume and result in local stress. Subsequent to recurring charge–discharge cycles, this local stress causes the pulverization problem which is the cracking and degradation of the primary structures. The creation of carbon composites for the metal oxides is proposed as a solution to the pulverization problem. Improvement and conservation of the mechanical flexibility and the electronic contiguity of the active material are the two main advantages offered by carbon. There are several approaches developed to incorporate carbon into metal oxide anode materials [193–196]. Gao et al. [197] reported the synthesis of multi-wall Sn/SnO_2@carbon composite hollow nanofibers

Table 5 Literature on carbon based composites as anode material for battery

Anode materials	Cycle number	Spesific capacity (mA h/g)	References
Si–C-Graphite	100	448	[180]
Hard Carbon	100	318	[181]
SiO_x@G	1000	780	[182]
SnS_2/Graphene	50	559	[183]
LVO/$Ti_3C_2T_x$	1000	146	[184]
SnS_2/Graphene/SnS_2	200	1357	[185]
CC@CN@MoS_2	1000	265	[186]
SiO_x–TiO_2@C	600	700	[187]
Fe_3O_4@PrGO	100	2136	[188]
Si/C-HF	300	710	[189]
TCPSi-CNT	110	1150	[190]
CoSe/RGO	100	769.6	[191]
OPDHC-A	3000	210	[192]

with a solid wire core wrapped by a double-wall-tube. They have employed electrospinning and carbonization reduction methods to prepare anode materials to be used in Li-ion batteries. The synthesizd structures has provided more area for electrolyte to contact with electrode materials as well as more active sites for redox reaction. The reported high specific capacity for Sn/SnO_2@CNFs was 986.3 mAh/g at 1 A/g current density with high cycling performance for about two thousand cycles. In the recent article of Li et al. [198], the relation between the magnetism of transition metal electrodes and the electron transfer during charge storage process was emphasized. In situ magnetometry was employed to monitor the evolution of internal electronic structure in a Fe_3O_4/Li model battery cell. They have determined a significant change in the interface magnetization and described this fact as an explanation for the large excess capacity during low-voltage discharge which was provided by the ability of electrochemically reduced Fe nanoparticles to store large number of spin-polarized electrons. Ding et al. [199] have reported the use of pristine MoO_3 as an anode material in Li-ion batteries. In their study, two steps method comprised of converting MoO_3 powder into nanorods to enhance the kinetics and than the carbon coating of MoO_3 nanorods to prevent their aggregation and increase their conductivity. The specific capacity value was 856 mAh/g at a current density of 0.1 °C which was 373 mAh/g after four hundred cycles at 0.75 °C. Tu et al. [200] have reported the synthesis of mesoporous carbon buble composite containing ZnO quantum dots at its surface. This composite structure was designed to take the Advantages of both high electrochemical activity of quantum dots and the flexibility provided by carbon skeleton. The reported capacity was 930 mAh/g at a current density of 100 mA/g for about eight-five cycles.

Being more abundant and cheaper than lithium, there is an increasing interest on the use of sodium-ion batteries which employs a similar working mechanism with Li-ion batteries. Among NiS, Ni_3S_2, and NiS_2, NiS is a widely used anode material both in Na-ion and Li-ion batteries. However, it suffers from pulverization problem. The hybridization of NiS with carbonaceous materials reported to increase mechanical flexibility against large volume changes and enhance ionic conductivity and reduce the charge transfer resistance [201–204]. Wang et al. have reviewed the use of graphene incorporated metal oxides at nano-size as anode material in sodium-ion batteries. As a conclusion, the poor electron conductivity and still ion kinetics as well as the low tolerance of this transition metal oxide materials to the volumetric changes were found resposible for the inefficient electrochemical energy storage performance of sodium-ion batteries. Therefore, it has been stated that incorporating graphene into the structure will enhance the performance and cycle stability thanks to its high surface area and flexibility [205].

4 Carbon Catalysts for Electrochemical Sensors

The world is fighting new types of diseases and health disorders from factors such as environmental pollution, food genetic modification. Therefore, there is a need

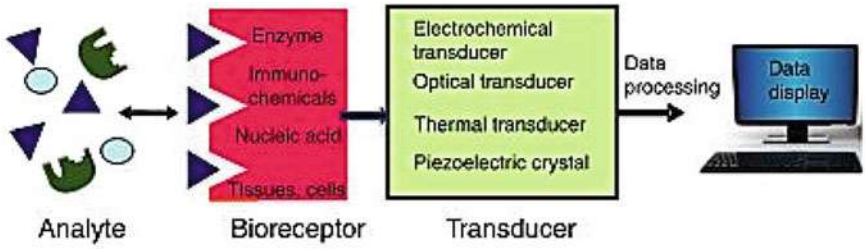

Fig. 4 The working principle of a biosensor [213]. Reprinted with permission, Elsevier, 2017

to develop new, efficient, and rapid diagnostic devices for health intended. Among the many diagnostic tools obtained, testing blood in clinical and biomedical fields is becoming a fast solution, convenient and user-friendly device [206]. The conventional analysis methods are not user-friendly technologies that take a long time, require laboratory experience, require a lot of expertise, and the limits of detection and accuracy need to be improved. The biosensors stand out with the fast, cheaper, user-friendly, and improved performance of diagnostic tests [207]. The biosensor which was introduced by Cammann [208] and later interpreted "It is an integrated transceiver device with biochemical reactions using biological recognition elements such as enzymes, tissues isolated by electrical, thermal, and optical signals to detect chemical compounds" by IUPAC, the biosensor is an analytical device that converts a biological perception into an electrical signal [209]. Figure 4 illustrates the working principle of the biosensors. The analyte is a substance that needs to be detected. The bioreceptor can be any substance containing any biological element such as organelle, antibody, DNA. A transducer is used to convert the biological signal into an electronic signal. Biosensors are classified according to the type of biological element and/or device mode; (I) Electrochemical, (II) calorimetric/thermal, (III) piezoelectric, (IV) optical, and (V) resonance [210].

Electrochemical biosensors can be listed as follows; "amperometric biosensor" to the current measured during the oxidation of the reactant, "potentiometric biosensor" that measures the potential of the biosensor electrode connected to the reference electrode, and "conductometric biosensor" that measures the conductivity change resulting from the reaction [211]. Electrochemical biosensors generally use a three-electrode system such as working electrode, reference electrode, and counter electrode. Different analytical methods such as fluorescence, spectrophotometer, and titrimetric are being improved for hydrogen peroxide (H_2O_2) quantification. These methods, which have disadvantages such as too much time loss and automation difficulty, are not preferred much. Electrochemical biosensors are the most suitable devices for the identification of sensors, thanks to their many advantages such as sensitivity, selectivity, lower detection limit, linear concentration range. In addition, the sensitivity of these analyzes is very good and most of these analyzes can be performed with small sample quantities in a microliter, even at nanoliter levels [212].

4.1 Hydrogen Peroxide Sensors

H_2O_2 is made up of water and oxygen and it breaks down into water and oxygen again after use, environmentally friendly. H_2O_2 exists in the biochemical processes and atmosphere events. Furthermore, it is a compound with a wide range of uses in the food, pharmaceutical, textile industry, etc. thanks to its powerful oxidizing feature. Biological sources of H_2O_2 include the catalytic decomposition of superoxide anions (O^{2-}) generated by partial reduction of oxygen during aerobic respiration by exposure to various biological, chemical, and physical agents within a cell [214]. It depends on both H_2O_2 and O^{2-} reactive oxygen species (ROS). The determination of low amounts of this compound, which is thermodynamically unstable, has become very important due to the fact that it is the product of the reactions catalyzed by oxidase enzymes [215, 216]. Many methods improved by now for the definition of H_2O_2 are based on enzymes. Enzyme-based H_2O_2 sensors have been utilized to determine byproducts of oxidases for glucose, D-amino acid, lysine, lactate, etc. Furthermore, H_2O_2 is a substrate for other enzymes [217]. Environmental parameters (such as pH) determine whether H_2O_2 reacts as an oxidant or a reductant, and also can gain or lose electrons depending on the type of reaction [218]. The enzyme-based H_2O_2 biosensor determines the anodic reaction shown in Eq. (2), which includes the oxidation of the H_2O_2 product.

$$H_2O_2 \rightarrow O_2 + 2H^+ + 2e^- \tag{2}$$

This type of biosensors provided good accuracy and precision in 100 μl blood samples [219]. In many studies in the literature, there are studies enzymes and non-enzymatic for the precise and rapid detection of H_2O_2. In electrochemical sensors where high sensitivity and selectivity are important, enzymatic and non-enzymatic sensors have advantages and disadvantages. For this reason, there are many electrochemical sensor studies with different materials and enzymatic and non-enzymatic in the literature [220]. Kivrak et al. [221] investigated the non-enzymatic H_2O_2 detection ability of graphene oxide obtained from graphite by electrochemical oxidation method with an electrochemical sensor. They reported that the electrochemical sensor showed rapid and selective responses to different concentration of H_2O_2. Caglar et al. [222] reported the analysis of H_2O_2 sensor detection by coating the pen-graphite with 3-Acrylamido propyl-trimethyl ammonium chloride hydrogel. ElKaoutit et al. [223] reported that they produced nafion-sonagel-carbon composite Horseradish Peroxidase enzyme immobilized to monitor H_2O_2 biosensor via electron transfer process. They emphasized that the biosensor showed high sensitivity, good stability, and reproducibility.

4.2 Glucose Sensors

Nowadays, it is important to diagnose many diseases, especially to start treatment by monitoring blood (glucose, etc.) levels. Glucose detection has a great importance in human life and metabolism. The glucose sensor is used to measure a patient's blood concentration, and is important for rapid detection of diabetes mellitus, food analysis, clinical diagnostics [224]. Normal blood glucose levels can range from 80 to 120 mg/dL (which can reach 250 mg/dL after a meal). The glucose conceration can be detected in a limited detection range of 10^{-3} to 10^{-6} M using chemical receptor or enzymatic techniques [225, 226]. Therefore, there are many practical requirements for a fast, inexpensive and most importantly very sensitive glucose sensor with a detection limit in the μm range [227]. Clark and Lyons [228] have been going on for sixty years since their first report on developing and improving glucose sensors in 1962. The glucose biosensor operates in an oxygen-dependent manner according to Eq. (3), which is catalyzed by the glucose oxidase enzyme [229].

$$C_6H_{12}O_6 + H_2O + O_2 \xrightarrow{\text{Glucose oxidase}} C_6H_{12}O_7 + H_2O_2 \tag{3}$$

As with other sensors, the most fundamental ingredients in the development of the glucose sensor are excellent conductivity, high mechanical strength, and most importantly, the selection of a suitable enzyme immobilization matrix [230]. Kamyabi et al. [231] reported that they developed a highly sensitive glucose biosensor by immobilization of glucose oxidase on poly(2,6-DP)/MWCNT/GCE (Fig. 5). They emphasized that the obtained bioelectrode is promising for sensitive detection of glucose with its high sensitivity, reproducibility, and long-term stability. Chen et al. [226] reported that they attached glucose oxidase to the hybrid surface prepared the graphene-gold nanoparticles by in situ method for glucose electrochemical biosensing. They emphasized that the hybrid they obtained could be used as an effective candidate for the determination of blood glucose concentration in clinical diagnoses with its good stability.

4.3 Heavy Metal Sensors

Industrialization and increasing population have increased water use and created clean water problems. Industrial activities (mining, metallurgy, cosmetics, chemistry, petroleum, textile, etc.), domestic wastewater, and agricultural products are the main sources of water pollution. The rapid increase in water pollution poses a danger to both human health and the ecosystem [232]. Heavy metals, which are among the most important pollutants in water, are metals with an atomic density of approximately 5 g/cm^3. Heavy metals such as mercury (Hg), cadmium (Cd), lead (Pb), chromium (Cr), arsenic (As), nickel (Ni), aluminum (Al) are extremely toxic and even low quantities of these in water are extremely dangerous [233, 234].

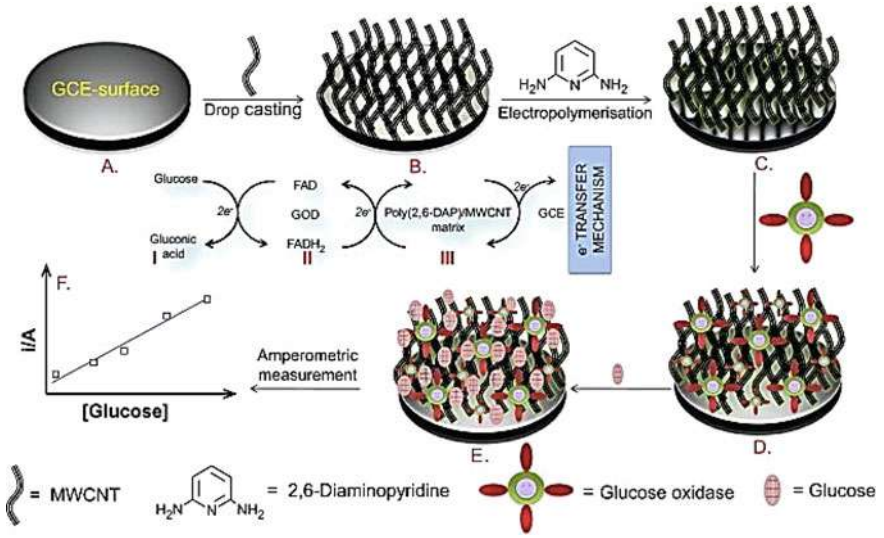

Fig. 5 Schematic representation of the production, biosensing, and electron transfer mechanism of an ultra-sensitive glucose biosensor of GOx/poly(2,6-DAP)/MWCNT/GCE electrode [231]. Reprinted with permission, Elsevier, 2013

Heavy metals which are not biodegradable enter living organisms through air, food, and water [235]. For this reason, it is very important to detect heavy metals in these environments. Heavy metals can be detected with being developed modern sensors. In recent years, many studies have been carried out for the electrochemical detection of heavy metals (Table 6). Various materials such as CNT, graphene and graphene oxide, CNF, mesoporous composite, and polymer have been used as the interface material for heavy metal detection [236, 237].

CNTs are used as sensors for heavy metal detection due to their large surface area, chemical stability, and high electrical conductivity. With various surface modifications of these materials, the electron transfer speed and detection sensitivity can be increased [238].

Alizadeh et al. [235] have investigated the detection of Pb(II) with ion-imprinted polymer (IIP) and MWCNT. The experimental results reveal that the sensor provides very good results regarding detection limit, selectivity, and sensitivity. Wu et al. [238] have synthesized Fe_3O_4 nanoparticles, Fe_3O_4/MWCNTs, and Fe_3O_4/F-MWCNTs composites as Cd(II), Pb(II), Cu(II), and Hg(II) sensitive electrodes and compared the performances of these composites. They reported that the Fe_3O_4/F-MWCNTs sensor exhibited excellent performances in recovery, selectivity, reproducibility, and stability.

Graphene consists of sp^2 carbon atoms arranged in a hexagonal pattern. Graphene and graphene derivatives such as graphene oxide (GO) and reduced graphene oxide

Table 6 Carbon-based sensors for detection of heavy metals

Sensor configuration	Heavy metal	Detection limit	References
IIP/MWCNT	Pb(II)	3.8 pmol/L	[235]
Fe_3O_4/F-MWCNTs	Cd(II) Pb(II) Cu(II) Hg(II)	0.05 nM 0.08 nM 0.02 nM 0.05 nM	[238]
GO/DTT	Cd(II) Pb(II) Cu(II) Hg(II)	1.9 ± 0.4 ng/mL 2.8 ± 0.6 ng/mL 0.8 ± 0.2 ng/mL 2.6 ± 0.9 ng/mL	[240]
DWCNTs/Gr	As(V)	0.287 ppb	[241]
rGO/IIP	Hg(II)	0.02 μg/L	[239]
GO/MWCNTs	Pb(II) Cd(II)	0.2 μg/L 0.1 μg/L	[243]
rGO/CNT	Pb(II) Cd(II)	0.2 ppb 0.6 ppb	[244]
Fe_2O_3/G	Zn(II) Cd(II) Pb(II)	0.11 μg/L 0.08 μg/L 0.07 μg/L	[245]
MCM/CQDs	Hg(II)	0.02 μmol/L	[242]

(rGO) have superior properties such as large surface area, excellent electrical conductivity, high electron transfer rate, and high electrocatalytic. Due to their unique electrochemical properties, they are widely used as electrodes for detecting heavy metals [237, 239]. Choi et al. [240] have studied the detection of Cd(II), Pb(II), Cu(II), and Hg(II) by using diaminoterthiophene electrode with graphene oxide doped (GO/DTT). They also emphasized that modified with graphene oxide increased selectivity and sensitivity of electrode. Duoc et al. [241] have prepared hybrid thin films based on double-walled CNTs and graphene (DWCNTs/Gr) for As(V) detection. The results were assigned that the sensor had a superior performance for heavy metals detection with a low detection limit.

Mesoporous composites are materials with pore sizes in the range of 2–50 nm. Wang et al. have used the mesoporous silica/carbon quantum dots (MCM/CQDs) as an electrode for Hg(II) detection. They combined the fluorescent properties of carbon quantum dots with the superior properties of mesoporous silica, which is known for its large surface area and porous structure. They reported that the synthesized composite provided high sensitivity and selectivity in detecting heavy metals [242].

5 Conclusions and Outlook

This chapter has summarized the use of carbon-based composite materials as electrocatalysts. Electrocatalysts are widely used for reactions in batteries, supercapacitors, sensors, and fuel cells. The conductivity and large surface area of carbon composites allow their use as both photoanode and electrode material in batteries and supercapacitors. Carbon-based composite materials have performances that can compete with the Pt catalyst, especially for ORR, which occurs on the cathode side of fuel cells. However, carbon-based composites exhibit lower current densities as anode catalysts than precious metals and are often used only as support materials. By functionalizing of carbon derivatives, its positive contribution to the electrooxidation reaction at the anode can be increased. Carbon based composites are an important solution for all these energy conversion and storage systems to be more commercially economical and more carbon-based innovative materials are needed. By changing the morphological properties of carbon derivatives, the number of active sites on their surfaces can be increased and superior performance can be obtained for electrochemical reactions.

References

1. Arbag H et al (2020) Effect of preparation technique on the performance of Ni and Ce incorporated modified Alumina catalysts in CO_2 reforming of Methane. Catal Lett 150(11):3256–3268
2. Cali A et al (2020) Highly durable phosphonated graphene oxide doped polyvinylidene fluoride (PVDF) composite membranes. Int J Hydrogen Energy 45(60):35171–35179
3. Yagizatli Y et al (2020) Improved fuel cell properties of Nano-TiO_2 doped Poly(Vinylidene fluoride) and phosphonated Poly(Vinyl alcohol) composite blend membranes for PEM fuel cells. Int J Hydrogen Energy 45(60):35130–35138
4. Eid K et al (2017) Rational one-step synthesis of porous PtPdRu nanodendrites for ethanol oxidation reaction with a superior tolerance for CO-poisoning. Nanoscale 9(47):18881–18889
5. Zhang G et al (2011) Preparation of Pd–Au/C catalysts with different alloying degree and their electrocatalytic performance for formic acid oxidation. Appl Catal B 102(3–4):614–619
6. Otowa T, Tanibata R, Itoh M (1993) Production and adsorption characteristics of MAXSORB: high-surface-area active carbon. Gas Sep Purif 7(4):241–245
7. Hecht DS et al (2011) High conductivity transparent carbon nanotube films deposited from superacid. Nanotechnology 22(7):075201
8. Bi Z et al (2019) Biomass-derived porous carbon materials with different dimensions for supercapacitor electrodes: a review. J Mater Chem A 7(27):16028–16045
9. Singh KP et al (2003) Color removal from wastewater using low-cost activated carbon derived from agricultural waste material. Ind Eng Chem Res 42(9):1965–1976
10. Wu G et al (2008) Enhanced methanol electro-oxidation activity of PtRu catalysts supported on heteroatom-doped carbon. Electrochim Acta 53(26):7622–7629
11. Sopian K, Daud WRW (2006) Challenges and future developments in proton exchange membrane fuel cells. Renewable Energy 31(5):719–727
12. Cao L et al (2006) Novel nanocomposite Pt/RuO_2 center dot xH(2)O/carbon nanotube catalysts for direct methanol fuel cells. Angew Chem Int Ed 45(32):5315–5319
13. Wang YQ et al (2014) Nano-molybdenum carbide/carbon nanotubes composite as bifunctional anode catalyst for high-performance Escherichia coli-based microbial fuel cell. Biosens Bioelectron 51:349–355

14. Maiyalagan T (2009) Silicotungstic acid stabilized Pt-Ru nanoparticles supported on carbon nanofibers electrodes for methanol oxidation. Int J Hydrogen Energy 34(7):2874–2879
15. Ma M et al (2015) Silver/iron oxide/graphitic carbon composites as bacteriostatic catalysts for enhancing oxygen reduction in microbial fuel cells. J Power Sources 283:74–83
16. Chen MJ et al (2018) Nanocarbon/oxide composite catalysts for bifunctional oxygen reduction and evolution in reversible alkaline fuel cells: a mini review. J Power Sources 375:277–290
17. Liu JL et al (2012) Carbon nanotube-based materials for fuel cell applications. Aust J Chem 65(9):1213–1222
18. Cheng Y et al (2014) Effect of nitrogen-containing functionalization on the electrocatalytic activity of PtRu nanoparticles supported on carbon nanotubes for direct methanol fuel cells. Appl Catal B 158:140–149
19. Saha MS, Kundu A (2010) Functionalizing carbon nanotubes for proton exchange membrane fuel cells electrode. J Power Sources 195(19):6255–6261
20. Prasanna D, Selvaraj V (2016) Development of ternary hexafluoroisopropylidenedianiline/cyclophosphazene/benzidine-disulfonic acid-carbon nanotubes (HFPA/CP/BZD-CNT) composite as a catalyst support for high performance alcohol fuel cell applications. Electrochim Acta 190:668–677
21. Lilloja J et al (2020) Nitrogen-doped carbide-derived carbon/carbon nanotube composites as cathode catalysts for anion exchange membrane fuel cell application. Appl Catal B 272
22. Lilloja J et al (2021) Transition-metal- and nitrogen-doped carbide-derived carbon/carbon nanotube composites as cathode catalysts for anion-exchange membrane fuel cells. ACS Catal 11(4):1920–1931
23. Higgins DC et al (2012) Titanium nitride-carbon nanotube core-shell composites as effective electrocatalyst supports for low temperature fuel cells. J Mater Chem 22(9):3727–3732
24. Reddy ALM, Rajalakshmi N, Ramaprabhu S (2008) Cobalt-polypyrrole-multiwalled carbon nanotube catalysts for hydrogen and alcohol fuel cells. Carbon 46(1):2–11
25. Sahoo M, Vinayan BP, Ramaprabhu S (2014) Platinum-decorated chemically modified reduced graphene oxide-multiwalled carbon nanotube sandwich composite as cathode catalyst for a proton exchange membrane fuel cell. RSC Adv 4(50):26140–26148
26. Wang HL et al (2014) Synthesis of 3D graphite oxide-exfoliated carbon nanotube carbon composite and its application as catalyst support for fuel cells. J Power Sources 260:338–348
27. Xu PP et al (2014) One-step synthesis of antimony-doped tin oxide/multi-walled carbon nanotube composites: a promising support for platinum catalysts in a direct methanol fuel cell. J Nanopart Res 16(10)
28. Eftekhari A, Fan Z (2017) Ordered mesoporous carbon and its applications for electrochemical energy storage and conversion. Mater Chem Front 1(6):1001–1027
29. Zhou H et al (2003) Lithium storage in ordered mesoporous carbon (CMK-3) with high reversible specific energy capacity and good cycling performance. Adv Mater 15(24):2107–2111
30. Fang B et al (2008) Hollow macroporous core/mesoporous shell carbon with a tailored structure as a cathode electrocatalyst support for proton exchange membrane fuel cells. J Phys Chem C 112(2):639–645
31. Pradhan BK, Sandle N (1999) Effect of different oxidizing agent treatments on the surface properties of activated carbons. Carbon 37(8):1323–1332
32. Lee HI et al (2009) Ultrastable Pt nanoparticles supported on sulfur-containing ordered mesoporous carbon via strong metal-support interaction. J Mater Chem 19(33):5934–5939
33. Kwon T et al (2010) Carbon-coated mesoporous silica as an electrode material. Microporous Mesoporous Mater 132(3):421–427
34. Liang C, Li Z, Dai S (2008) Mesoporous carbon materials: synthesis and modification. Angew Chem Int Ed 47(20):3696–3717
35. Wang Q et al (2001) Monodispersed hard carbon spherules with uniform nanopores. Carbon 39(14):2211–2214
36. Sevilla M, Fuertes AB, Mokaya R (2011) High density hydrogen storage in superactivated carbons from hydrothermally carbonized renewable organic materials. Energy Environ Sci 4(4):1400–1410

37. Lee J, Kim J, Hyeon T (2006) Recent progress in the synthesis of porous carbon materials. Adv Mater 18(16):2073–2094
38. Tintula K et al (2010) Mesoporous carbon and poly (3, 4-ethylenedioxythiophene) composite as catalyst support for polymer electrolyte fuel cells. J Electrochem Soc 157(11):B1679
39. Ryoo R et al (2001) Ordered mesoporous carbons. Adv Mater 13(9):677–681
40. Marsh H, Rodriguez-Reinonso F (2006) Activated carbon. Elsevier Science & Technology Books, Amsterdam, pp 89–100
41. Ghimbeu CM et al (2014) Catalyst-free soft-template synthesis of ordered mesoporous carbon tailored using phloroglucinol/glyoxylic acid environmentally friendly precursors. Green Chem 16(6):3079–3088
42. Jun S et al (2000) Synthesis of new, nanoporous carbon with hexagonally ordered mesostructure. J Am Chem Soc 122(43):10712–10713
43. Novoselov K et al (2004) Electric field effect in atomically thin carbon films. Science 306(5696):666–669
44. Stankovich S et al (2006) Graphene-based composite materials. Nature 442(7100):282–286
45. Jiang L, Fan Z (2014) Design of advanced porous graphene materials: from graphene nanomesh to 3D architectures. Nanoscale 6(4):1922–1945
46. Thomas D et al (2018) Synthesis of graphene nanosheets through spontaneous sodiation process. C J Carbon Res 4(3)
47. Hummers Jr WS, Offeman RE (1958) Preparation of graphitic oxide. J Am Chem Soc 80(6):1339
48. Caglar A et al (2021) A novel experimental and density functional theory study on palladium and nitrogen doped few layer graphene surface towards glucose adsorption and electrooxidation. J Phys Chem Solids 150
49. Kou R et al (2009) Enhanced activity and stability of Pt catalysts on functionalized graphene sheets for electrocatalytic oxygen reduction. Electrochem Commun 11(5):954–957
50. Li Y et al (2009) Cr(VI) reduction at rutile-catalyzed cathode in microbial fuel cells. Electrochem Commun 11(7):1496–1499
51. He D et al (2012) Highly active Platinum nanoparticles on graphene nanosheets with a significant improvement in stability and CO tolerance. Langmuir 28(8):3979–3986
52. Sheng Z et al (2011) Catalyst-free synthesis of nitrogen-doped graphene via thermal annealing graphite oxide with melamine and its excellent electrocatalysis. ACS Nano 5(6):4350–4358
53. Xin Y et al (2012) Preparation and electrochemical characterization of nitrogen doped graphene by microwave as supporting materials for fuel cell catalysts. Electrochim Acta 60:354–358
54. Caglar A et al (2020) A comparative experimental and density functional study of glucose adsorption and electrooxidation on the Au-graphene and Pt-graphene electrodes. Int J Hydrogen Energy 45(1):490–500
55. Zhang W et al (2019) A general approach for fabricating 3D MFe_2O_4 (M = Mn, Ni, Cu, Co)/graphitic carbon nitride covalently functionalized nitrogen-doped graphene nanocomposites as advanced anodes for lithium-ion batteries. Nano Energy 57:48–56
56. Qu L et al (2010) Nitrogen-doped graphene as efficient metal-free electrocatalyst for oxygen reduction in fuel cells. ACS Nano 4(3):1321–1326
57. Yang Z et al (2012) Sulfur-doped graphene as an efficient metal-free cathode catalyst for oxygen reduction. ACS Nano 6(1):205–211
58. Sheng Z et al (2012) Synthesis of boron doped graphene for oxygen reduction reaction in fuel cells. J Mater Chem 22(2):390–395
59. Zarrin H et al (2011) Functionalized graphene oxide nanocomposite membrane for low humidity and high temperature proton exchange membrane fuel cells. J Phys Chem C 115(42):20774–20781
60. Jha N et al (2011) Graphene-multi walled carbon nanotube hybrid electrocatalyst support material for direct methanol fuel cell. Int J Hydrogen Energy 36(12):7284–7290
61. Caglar A et al (2019) Few-layer graphene coated on indium tin oxide electrodes prepared by chemical vapor deposition and their enhanced glucose electrooxidation activity. Energy Storage 1(4):e73

62. Ulas B et al (2018) Composition dependent activity of PdAgNi alloy catalysts for formic acid electrooxidation. J Colloid Interface Sci 532:47–57
63. Caglar A et al (2018) A novel central composite design based response surface methodology optimization study for the synthesis of Pd/CNT direct formic acid fuel cell anode catalyst. Int J Hydrogen Energy 43(24):11002–11011
64. Staudenmaier L (1898) Verfahren zur darstellung der graphitsäure. Ber Dtsch Chem Ges 31(2):1481–1487
65. Brodie BC (1859) XIII. On the atomic weight of graphite. Philos Trans Roy Soc Lond 149:249–259
66. Gao W et al (2009) New insights into the structure and reduction of graphite oxide. Nat Chem 1(5):403–408
67. Pham V et al (2013) Highly efficient reduction of graphene oxide using ammonia borane. Chem Commun 49(59):6665–6667
68. Pei S et al (2010) Direct reduction of graphene oxide films into highly conductive and flexible graphene films by hydrohalic acids. Carbon 48(15):4466–4474
69. Stankovich S et al (2007) Synthesis of graphene-based nanosheets via chemical reduction of exfoliated graphite oxide. Carbon 45(7):1558–1565
70. Lei Z, Lu L, Zhao X (2012) The electrocapacitive properties of graphene oxide reduced by urea. Energy Environ Sci 5(4):6391–6399
71. Dreyer D et al (2011) Reduction of graphite oxide using alcohols. J Mater Chem 21(10):3443–3447
72. Fernandez-Merino M et al (2010) Vitamin C is an ideal substitute for hydrazine in the reduction of graphene oxide suspensions. J Phys Chem C 114(14):6426–6432
73. Chen W, Yan L, Bangal P (2010) Chemical reduction of graphene oxide to graphene by sulfur-containing compounds. J Phys Chem C 114(47):19885–19890
74. Dey R et al (2012) A rapid room temperature chemical route for the synthesis of graphene: metal-mediated reduction of graphene oxide. Chem Commun 48(12):1787–1789
75. Chen D, Li L, Guo L (2011) An environment-friendly preparation of reduced graphene oxide nanosheets via amino acid. Nanotechnology 22(32)
76. Wang Y, Shi Z, Yin J (2011) Facile synthesis of soluble graphene via a green reduction of graphene oxide in tea solution and its biocomposites. ACS Appl Mater Interfaces 3(4):1127–1133
77. Thakur S, Karak N (2012) Green reduction of graphene oxide by aqueous phytoextracts. Carbon 50(14):5331–5339
78. Hou J et al (2011) Graphene-based electrochemical energy conversion and storage: fuel cells, supercapacitors and lithium ion batteries. Phys Chem Chem Phys 13(34):15384–15402
79. Devrim Y, Arıca ED, Albostan A (2018) Graphene based catalyst supports for high temperature PEM fuel cell application. Int J Hydrogen Energy 43(26):11820–11829
80. Seger B, Kamat PV (2009) Electrocatalytically active graphene-platinum nanocomposites. Role of 2-D carbon support in PEM fuel cells. J Phys Chem C 113(19):7990–7995
81. Chen JY, Xie P, Zhang ZP (2019) Reduced graphene oxide/polyacrylamide composite hydrogel scaffold as biocompatible anode for microbial fuel cell. Chem Eng J 361:615–624
82. Sayed ET et al (2020) Facile and low-cost synthesis route for graphene deposition over cobalt dendrites for direct methanol fuel cell applications. J Taiwan Inst Chem Eng 115:321–330
83. Meganathan MD et al (2017) Reduced graphene oxide intercalated Co_2C or Co_4N nanoparticles as an efficient and durable fuel cell catalyst for oxygen reduction. J Mater Chem A 5(6):2972–2980
84. Santoro C et al (2017) Three-dimensional graphene nanosheets as cathode catalysts in standard and supercapacitive microbial fuel cell. J Power Sources 356:371–380
85. Tan JL et al (2017) Preparation and characterization of palladium-nickel on graphene oxide support as anode catalyst for alkaline direct ethanol fuel cell. Appl Catal A 531:29–35
86. Işıkel Şanlı L et al (2017) Engineered catalyst layer design with graphene-carbon black hybrid supports for enhanced platinum utilization in PEM fuel cell. Int J Hydrogen Energy 42(2):1085–1092

87. Yang W et al (2019) Graphene oxide-supported zinc cobalt oxides as effective cathode catalysts for microbial fuel cell: High catalytic activity and inhibition of biofilm formation. Nano Energy 57:811–819
88. Mashkour M et al (2017) Catalytic performance of nano-hybrid graphene and titanium dioxide modified cathodes fabricated with facile and green technique in microbial fuel cell. Prog Nat Sci: Mater Int 27(6):647–651
89. Unni SM et al (2015) Carbon nanohorn-derived graphene nanotubes as a platinum-free fuel cell cathode. ACS Appl Mater Interfaces 7(43):24256–24264
90. Mohanraju K et al (2015) Enhanced electrocatalytic activity of PANI and $CoFe_2O_4$/PANI composite supported on graphene for fuel cell applications. J Power Sources 284:383–391
91. Huang X (2009) Fabrication and properties of carbon fibers. Materials 2(4):2369–2403
92. Cavaliere S et al (2011) Electrospinning: designed architectures for energy conversion and storage devices. Energy Environ Sci 4(12):4761–4785
93. Sebastián D et al (2012) The influence of carbon nanofiber support properties on the oxygen reduction behavior in proton conducting electrolyte-based direct methanol fuel cells. Int J Hydrogen Energy 37(7):6253–6260
94. Geng D et al (2020) Pd x Fe y alloy nanoparticles decorated on carbon nanofibers with improved electrocatalytic activity for ethanol electrooxidation in alkaline media. New J Chem 44(13):5023–5032
95. Luong QT et al (2021) An effective strategy for preparing nickel nanoparticles encapsulated in polymer matrix-derived carbon shell with high catalytic activity and long-term durability toward urea electro-oxidation. Mater Chem Front
96. Gliserol PE (2017) Preliminary study on Pd-based binary catalysts supported with carbon nanofiber for the electrooxidation of glycerol. Malays J Anal Sci 21(3):700–708
97. Elbasri M et al (2019) Synthesis of carbon nanofibers/poly (para-phenylenediamine)/nickel particles nanocomposite for enhanced methanol electrooxidation. Int J Hydrogen Energy 44(45):24534–24545
98. Hu B-C et al (2018) SiO 2-protected shell mediated templating synthesis of Fe–N-doped carbon nanofibers and their enhanced oxygen reduction reaction performance. Energy Environ Sci 11(8):2208–2215
99. Kaur P et al (2021) Facile and scalable functionalization of carbon nanofibers for oxygen reduction reaction: role of nitrogen precursor and non-ionic dispersant. J Ind Eng Chem 96:307–314
100. Lee C-H et al (2019) Palladium on yttrium-embedded carbon nanofibers as electrocatalyst for oxygen reduction reaction in acidic media. Electrochem Commun 106:106516
101. Zhong R et al (2020) Atomic Fe-N_4 sites on electrospun hierarchical porous carbon nanofibers as an efficient electrocatalyst for oxygen reduction reaction. Chin Chem Lett 31(6):1588–1592
102. An G-H, Lee Y-G, Ahn H-J (2018) Multi-active sites of iron carbide nanoparticles on nitrogen@ cobalt-doped carbon for a highly efficient oxygen reduction reaction. J Alloy Compd 746:177–184
103. Selvakumar K et al (2019) Electrospun carbon nanofiber sprinkled with Co_3O_4 as an efficient electrocatalyst for oxygen reduction reaction in alkaline medium. ChemistrySelect 4(17):5160–5167
104. Jheng L-C et al (2021) Nanocomposite membranes of polybenzimidazole and amine-functionalized carbon nanofibers for high temperature proton exchange membrane fuel cells. RSC Adv 11(17):9964–9976
105. Liu X et al (2017) Electrospun multifunctional sulfonated carbon nanofibers for design and fabrication of SPEEK composite proton exchange membranes for direct methanol fuel cell application. Int J Hydrogen Energy 42(15):10275–10284
106. Ramírez-Herrera CA et al (2021) Enhanced mechanical properties and corrosion behavior of polypropylene/multi-walled carbon nanotubes/carbon nanofibers nanocomposites for application in bipolar plates of proton exchange membrane fuel cells. Int J Hydrogen Energy 46(51):26110–26125

107. Shukla A et al (2012) Electrochemical capacitors: technical challenges and prognosis for future markets. Electrochim Acta 84:165–173
108. Pandolfo T et al (2013) General properties of electrochemical capacitors. Wiley
109. Choi HS, Park CR (2014) Theoretical guidelines to designing high performance energy storage device based on hybridization of lithium-ion battery and supercapacitor. J Power Sources 259:1–14
110. Halper MS, Ellenbogen JC (2006) Supercapacitors: a brief overview. The MITRE Corporation, McLean, Virginia, USA, p 1
111. Park S-S, Lee B-T (2004) Anodizing properties of high dielectric oxide films coated on aluminum by sol-gel method. J Electroceram 13(1):111–116
112. Costa CU et al (2012) Electrochromic properties of inkjet printed vanadium oxide gel on flexible polyethylene terephthalate/indium tin oxide electrodes. ACS Appl Mater Interfaces 4(10):5266–5275
113. Lewandowski A, Świderska A (2003) Electrochemical capacitors with polymer electrolytes based on ionic liquids. Solid State Ionics 161(3–4):243–249
114. Kötz R, Carlen M (2000) Principles and applications of electrochemical capacitors. Electrochim Acta 45(15–16):2483–2498
115. Cicak K et al (2009) Vacuum-gap capacitors for low-loss superconducting resonant circuits. IEEE Trans Appl Supercond 19(3):948–952
116. Barakou F et al (2018) Merits and challenges of a differentiating-integrating measurement methodology with air capacitors for high-frequency transients. In Cigre Session 47
117. Kaiser CJ (1993) Plastic film capacitors. The capacitor handbook. Springer, pp 41–49
118. Saleem M, Ansari M, Saxena A (2013) Study of standard mica capacitors with respect to time and temperature. Mapan 28(1):25–29
119. Epstein B, Brooks H (1948) The theory of extreme values and its implications in the study of the dielectric strength of paper capacitors. J Appl Phys 19(6):544–550
120. Manoharan MP et al (2013) Flexible glass for high temperature energy storage capacitors. Energ Technol 1(5–6):313–318
121. Sakabe Y (1997) Multilayer ceramic capacitors. Curr Opin Solid State Mater Sci 2(5):584–587
122. Romero J, Azarian MH, Pecht M (2020) Reliability analysis of multilayer polymer aluminum electrolytic capacitors. Microelectron Reliab 112:113725
123. Dehbi A et al (2002) High temperature reliability testing of aluminum and tantalum electrolytic capacitors. Microelectron Reliab 42(6):835–840
124. Chen J-J et al (2021) A new improved V-square-controlled buck converter with Rail-to-Rail OTA-based current-sensing circuits. IEEE Trans Very Large Scale Integ VLSI Syst
125. Wang J et al (2020) Recent progress of biomass-derived carbon materials for supercapacitors. J Power Sources 451:227794
126. Yadav N, Yadav N, Hashmi S (2020) Ionic liquid incorporated, redox-active blend polymer electrolyte for high energy density quasi-solid-state carbon supercapacitor. J Power Sources 451:227771
127. Volfkovich YM (2021) Electrochemical supercapacitors (a review). Russ J Electrochem 57(4):311–347
128. Chatterjee DP, Nandi AK (2021) A review on the recent advances in hybrid supercapacitors. J Mater Chem A 9(29):15880–15918
129. Kar KK (2020) Handbook of nanocomposite supercapacitor materials II. Springer
130. Shi Z et al (2021) Boosting capacitance and energy density by construction $NiCoO_2/CoS_2$ nanocomposites arrays as pseudocapacitor. J Alloys Compd 160627
131. Siwal SS et al (2020) Carbon-based polymer nanocomposite for high-performance energy storage applications. Polymers 12(3):505
132. Sarif M et al (2021) Enhanced capacitive performance of manganese oxide/mesoporous carbon composite film electrodes. J Electron Mater 50(2):419–431
133. Arun T et al (2021) Role of electrolytes on the electrochemical characteristics of Fe_3O_4/MXene/RGO composites for supercapacitor applications. Electrochim Acta 367:137473

134. Ranjithkumar R et al (2020) Investigations and fabrication of $Ni(OH)_2$ encapsulated carbon nanotubes nanocomposites based asymmetrical hybrid electrochemical supercapacitor. J Energy Storage 32:101934
135. Kanth S et al (2021) Investigations on performance of PEDOT:PSS/V_2O_5 hybrid symmetric supercapacitor with redox electrolyte. J Appl Polym Sci 138(34):50838
136. Soltani M, Beheshti SH (2021) A comprehensive review of lithium ion capacitor: development, modelling, thermal management and applications. Journal of Energy Storage 34:102019
137. Pozo B et al (2018) Supercapacitor electro-mathematical and machine learning modelling for low power applications. Electronics 7(4):44
138. Scibioh MA Viswanathan B (eds) Electrolyte materials for supercapacitors. In: Materials for supercapacitor applications. Elsevier, pp 205–314
139. Fernando J (2021) Electrical double-layer capacitors. In: Kularatna N, Gunawardane K (eds) Energy storage devices for renewable energy-based systems, 2nd edn. Academic Press, Boston, pp 199–237
140. Dubey P et al (2020) Recent advances in biomass derived activated carbon electrodes for hybrid electrochemical capacitor applications: challenges and opportunities. Carbon 170:1–29
141. An G-H (2020) Ultrafast long-life zinc-ion hybrid supercapacitors constructed from mesoporous structured activated carbon. Appl Surf Sci 530:147220
142. Cheng F et al (2020) Boosting the supercapacitor performances of activated carbon with carbon nanomaterials. J Power Sources 450:227678
143. Li X et al (2018) Self-supporting activated carbon/carbon nanotube/reduced graphene oxide flexible electrode for high performance supercapacitor. Carbon 129:236–244
144. Zhou Y et al (2019) Branched carbon nanotube/carbon nanofiber composite for supercapacitor electrodes. Mater Lett 246:174–177
145. Wang Q et al (2019) Flexible supercapacitors based on carbon nanotube-MnO_2 nanocomposite film electrode. Chem Eng J 371:145–153
146. Li J et al (2017) High performance solid-state flexible supercapacitor based on Fe_3O_4/carbon nanotube/polyaniline ternary films. J Mater Chem A 5(22):11271–11277
147. Stoller MD et al (2008) Graphene-based ultracapacitors. Nano Lett 8(10):3498–3502
148. Yang Z et al (2012) The prospective two-dimensional graphene nanosheets: preparation, functionalization and applications. Nano-Micro Lett 4(1):1–9
149. Li J et al (2012) Review of electrochemical capacitors based on carbon nanotubes and graphene. Graphene 1(1):13
150. Tian J et al (2019) Novel preparation of hydrophilic graphene/graphene oxide nanosheets for supercapacitor electrode. Appl Surf Sci 496:143696
151. Manjakkal L et al (2018) Flexible self-charging supercapacitor based on graphene-Ag-3D graphene foam electrodes. Nano Energy 51:604–612
152. Niu H et al (2020) In-situ embedding MOFs-derived copper sulfide polyhedrons in carbon nanotube networks for hybrid supercapacitor with superior energy density. Electrochim Acta 329:135130
153. Zou Y et al (2018) Simple synthesis of core-shell structure of Co–Co_3O_4 @ carbon-nanotube-incorporated nitrogen-doped carbon for high-performance supercapacitor. Electrochim Acta 261:537–547
154. Huang G et al (2017) Fiber-based MnO_2/carbon nanotube/polyimide asymmetric supercapacitor. Carbon 125:595–604
155. Sun P et al (2019) Uniform MoS_2 nanolayer with sulfur vacancy on carbon nanotube networks as binder-free electrodes for asymmetrical supercapacitor. Appl Surf Sci 475:793–802
156. Bai Y et al (2019) Graphene/Carbon nanotube/bacterial cellulose assisted supporting for polypyrrole towards flexible supercapacitor applications. J Alloy Compd 777:524–530
157. Song X et al (2019) Tea waste derived microporous active carbon with enhanced double-layer supercapacitor behaviors. Appl Surf Sci 487:189–197
158. Chen H et al (2017) An activated carbon derived from tobacco waste for use as a supercapacitor electrode material. New Carbon Mater 32(6):592–599

159. Phiri J et al (2019) Highly porous willow wood-derived activated carbon for high-performance supercapacitor electrodes. ACS Omega 4(19):18108–18117
160. Zhang S et al (2019) Low-cost nitrogen-doped activated carbon prepared by polyethylenimine (PEI) with a convenient method for supercapacitor application. Electrochim Acta 294:183–191
161. Strauss V et al (2018) A simple route to porous graphene from carbon nanodots for supercapacitor applications. Adv Mater 30(8):1704449
162. Fan Z et al (2018) Modified MXene/Holey graphene films for advanced supercapacitor electrodes with superior energy storage. Adv Sci 5(10):1800750
163. Yang S et al (2018) Oxygen-vacancy abundant ultrafine Co_3O_4/graphene composites for high-rate supercapacitor electrodes. Adv Sci 5(4):1700659
164. Li S et al (2020) Three-dimensional porous carbon/Co_3O_4 composites derived from graphene/Co-MOF for high performance supercapacitor electrodes. Appl Surf Sci 503:144090
165. Winter M, Brodd RJ (2004) What are batteries, fuel cells, and supercapacitors? Chem Rev 104(10):4245–4270
166. Yoshino A (2012) The birth of the lithium-ion battery. Angew Chem Int Ed 51(24):5798–5800
167. Horiba T (2014) Lithium-ion battery systems. Proc IEEE 102(6):939–950
168. Levi MD et al (2000) Evidence for slow droplet formation during cubic-to-tetragonal phase transition in $Li_xMn_2O_4$ spinel. J Electrochem Soc 147(1):25
169. Tarascon JM, Armand M (2001) Issues and challenges facing rechargeable lithium batteries. Nature 414(6861):359–367
170. Aurbach D et al (2004) Design of electrolyte solutions for Li and Li-ion batteries: a review. Electrochim Acta 50(2–3):247–254
171. Goodenough JB, Park K-S (2013) The Li-Ion rechargeable battery: a perspective. J Am Chem Soc 135(4):1167–1176
172. Ohzuku T, Ueda A, Yamamoto N (1995) Zero-strain insertion material of Li[Li_1/3Ti_5/3]O_4 for rechargeable lithium cells. J Electrochem Soc 142(5):1431–1435
173. Megahed S, Scrosati B (1994) Lithium-ion rechargeable batteries. J Power Sources 51(1):79–104
174. Manthiram A (2017) An outlook on lithium ion battery technology. ACS Cent Sci 3(10):1063–1069
175. Landi BJ et al (2009) Carbon nanotubes for lithium ion batteries. Energy Environ Sci 2(6):638–654
176. Kasavajjula U, Wang C, Appleby AJ (2007) Nano-and bulk-silicon-based insertion anodes for lithium-ion secondary cells. J Power Sources 163(2):1003–1039
177. Zhong S et al (2020) Long-aspect-ratio N-rich carbon nanotubes as anode material for sodium and lithium ion batteries. Chem Eng J 395:125054
178. Li Y et al (2018) Mesoporous activated carbon from corn stalk core for lithium ion batteries. Chem Phys 506:10–16
179. An Y-B et al (2019) Improving anode performances of lithium-ion capacitors employing carbon–Si composites. Rare Met 38(12):1113–1123
180. Parekh MH et al (2020) In situ mechanistic elucidation of superior Si-C-Graphite Li-Ion battery anode formation with thermal safety aspects. Adv Energy Mater 10(2):1902799
181. Xiao L et al (2018) Low-defect and low-porosity hard carbon with high coulombic efficiency and high capacity for practical sodium ion battery anode. Adv Energy Mater 8(20):1703238
182. Xu Q et al (2018) SiO_x encapsulated in graphene bubble film: an ultrastable Li-ion battery anode. Adv Mater 30(25):1707430
183. Bin D-S et al (2019) Structural engineering of SnS_2/Graphene nanocomposite for high-performance K-ion battery anode. Nano Energy 60:912–918
184. Huang Y et al (2019) A safe and fast-charging lithium-ion battery anode using MXene supported Li_3VO_4. J Mater Chem A 7(18):11250–11256
185. Jiang Y et al (2019) Sandwich-like SnS_2/Graphene/SnS_2 with expanded interlayer distance as high-rate lithium/sodium-ion battery anode materials. ACS Nano 13(8):9100–9111

186. Ren W et al (2017) Ultrathin MoS_2 nanosheets@metal organic framework-derived N-doped carbon nanowall arrays as sodium ion battery anode with superior cycling life and rate capability. Adv Func Mater 27(32):1702116
187. Li Z et al (2018) Watermelon-like structured SiOx–TiO_2@C nanocomposite as a high-performance Lithium-ion battery anode. Adv Func Mater 28(31):1605711
188. Bulut Kopuklu B et al (2021) High stability graphene oxide aerogel supported ultrafine Fe_3O_4 particles with superior performance as a Li-ion battery anode. Carbon 174:158–172
189. Zuo X et al (2019) Silicon/carbon lithium-ion battery anode with 3D hierarchical macro-/mesoporous silicon network: Self-templating synthesis via magnesiothermic reduction of silica/carbon composite. J Power Sources 412:93–104
190. Ikonen T et al (2020) Conjugation with carbon nanotubes improves the performance of mesoporous silicon as Li-ion battery anode. Sci Rep 10(1):5589
191. Li Y et al (2018) Stable carbon-selenium bonds for enhanced performance in Tremella-like 2D chalcogenide battery anode. Adv Energy Mater 8(23):1800927
192. Xiang J et al (2017) Activated hard carbon from orange peel for lithium/sodium ion battery anode with long cycle life. J Alloy Compd 701:870–874
193. Kim I-S, Blomgren GE, Kumta PN (2005) Study of electrochemical inactivity of nanocomposites generated using high-energy mechanical milling. J Electrochem Soc 152(1):A248
194. Read J et al (2001) SnO_2-carbon composites for lithium-ion battery anodes. J Power Sources 96(2):277–281
195. Balan L et al (2006) Tin–graphite materials prepared by reduction of $SnCl_4$ in organic medium: synthesis, characterization and electrochemical lithiation. J Power Sources 161(1):587–593
196. Yang Z, Shen J, Archer LA (2011) An in situ method of creating metal oxide–carbon composites and their application as anode materials for lithium-ion batteries. J Mater Chem 21(30):11092–11097
197. Gao S et al (2020) A multi-wall Sn/SnO_2@carbon hollow nanofiber anode material for high-rate and long-life lithium-ion batteries. Angew Chem Int Ed 59(6):2465–2472
198. Li Q et al (2021) Extra storage capacity in transition metal oxide lithium-ion batteries revealed by in situ magnetometry. Nat Mater 20(1):76–83
199. Ding J et al (2017) Facile synthesis of carbon/MoO_3 nanocomposites as stable battery anodes. J Power Sources 348:270–280
200. Tu Z et al (2017) Amorphous ZnO quantum dot/mesoporous carbon bubble composites for a high-performance lithium-ion battery anode. ACS Appl Mater Interfaces 9(1):439–446
201. Wang Y-X et al (2015) Uniform yolk-shell iron sulfide–carbon nanospheres for superior sodium–iron sulfide batteries. Nat Commun 6(1):8689
202. Sun R et al (2015) Vanadium sulfide on reduced graphene oxide layer as a promising anode for sodium ion battery. ACS Appl Mater Interfaces 7(37):20902–20908
203. Choi SH et al (2015) 3D MoS_2–graphene microspheres consisting of multiple nanospheres with superior sodium ion storage properties. Adv Func Mater 25(12):1780–1788
204. Wang J et al (2017) Synthesis of NiS/carbon composites as anodes for high-performance sodium-ion batteries. J Solid State Electrochem 21(10):3047–3055
205. Wang L et al (2019) Metal oxide/graphene composite anode materials for sodium-ion batteries. Energy Storage Mater 16:434–454
206. Kirsch J et al (2013) Biosensor technology: recent advances in threat agent detection and medicine. Chem Soc Rev 42(22):8733–8768
207. Shukla SK, Govender PP, Tiwari A (2016) Polymeric micellar structures for biosensor technology. In: Iglič A, Kulkarni CV, Rappolt M (eds) Advances in biomembranes and lipid self-assembly. Academic Press, pp 143–161
208. Cammann K (1977) Bio-Sensors based on ion-selective electrodes. Fresenius J Anal Chem 287:1–9
209. Mehrotra P (2016) Biosensors and their applications—a review. J Oral Biol Craniofacial Res 6(2):153–159
210. Pejcic B, De Marco R, Parkinson G (2006) The role of biosensors in the detection of emerging infectious diseases. Analyst 131(10):1079–1090

211. Ronkainen NJ, Halsall HB, Heineman WR (2010) Electrochemical biosensors. Chem Soc Rev 39(5):1747–1763
212. Wang L, Wang E (2004) A novel hydrogen peroxide sensor based on horseradish peroxidase immobilized on colloidal Au modified ITO electrode. Electrochem Commun 6(2):225–229
213. Sawant SN (2017) Development of biosensors from biopolymer composites. In: Sadasivuni KK et al (eds) Biopolymer composites in electronics. Elsevier, pp 353–383
214. Geiszt M, Leto TL (2004) The Nox family of NAD(P)H oxidases: host defense and beyond. J Biol Chem 279(50):51715–51718
215. Çelik Kazıcı H et al (2018) Microstructured prealloyed Titanium-Nickel powder as a novel nonenzymatic hydrogen peroxide sensor. J Colloid Interface Sci 530:353–360
216. Kazici HC et al (2018) Synthesis, characterization, and voltammetric hydrogen peroxide sensing on novel monometallic (Ag, Co/MWCNT) and bimetallic (AgCo/MWCNT) alloy nanoparticles. Fullerenes, Nanotubes, Carbon Nanostruct 26(3):145–151
217. Li J et al (2017) Recent developments in electrochemical sensors based on nanomaterials for determining glucose and its byproduct H_2O_2. J Mater Sci 52(17):10455–10469
218. Jacob C, Winyard PG (2009) Redox signaling and regulation in biology and medicine. Wiley
219. Posch HE, Wolfbeis OS (1989) Optical sensor for hydrogen peroxide. Microchim Acta 97(1):41–50
220. He S et al (2014) Non-enzymatic hydrogen peroxide electrochemical sensor based on a three-dimensional MnO_2 nanosheets/carbon foam composite. RSC Adv 4(90):49315–49323
221. Demir Kivrak H, Aktaş N, Caglar A (2019) Electrochemical production of graphene oxide and its application as a novel hydrogen peroxide sensor. Int J Nano Dimension 10(3):252–259
222. Caglar A et al (2019) 3-Acrylamidopropyl-trimethylammoniumchloride cationic hydrogel modified graphite electrode and its superior sensitivity to hydrogen peroxide. Fullerenes, Nanotubes, Carbon Nanostruct 27(9):736–745
223. ElKaoutit M et al (2008) A third-generation hydrogen peroxide biosensor based on Horseradish Peroxidase (HRP) enzyme immobilized in a Nafion–Sonogel–Carbon composite. Electrochim Acta 53(24):7131–7137
224. Zhang JXJ, Hoshino K (2014) Chapter 4—Electrical transducers: electrochemical sensors and semiconductor molecular sensors. In: Zhang JXJ, Hoshino K (eds) Molecular sensors and nanodevices. William Andrew Publishing, Oxford, pp 169–232
225. Murphy-Pérez E, Arya SK, Bhansali S (2011) Vapor–liquid–solid grown silica nanowire based electrochemical glucose biosensor. Analyst 136(8):1686–1689
226. Chen Y et al (2011) Fabrication of gold nanoparticles on bilayer graphene for glucose electrochemical biosensing. J Mater Chem 21(21):7604–7611
227. Wang J (2008) In vivo glucose monitoring: towards 'Sense and Act' feedback-loop individualized medical systems. Talanta 75(3):636–641
228. Clark LC Jr, Lyons C (1962) Electrode systems for continuous monitoring in cardiovascular surgery. Ann N Y Acad Sci 102:29–45
229. Mehta A et al (2007) A novel multivalent nanomaterial based hydrogen peroxide sensor. Sens Actuators, A 134(1):146–151
230. Rahman MM et al (2010) A comprehensive review of glucose biosensors based on nanostructured metal-oxides. Sensors 10(5):4855–4886
231. Ali Kamyabi M et al (2013) A high-performance glucose biosensor using covalently immobilised glucose oxidase on a poly(2,6-diaminopyridine)/carbon nanotube electrode. Talanta 116:801–808
232. Min KJ, Kim JH, Park KY (2021) Characteristics of heavy metal separation and determination of limiting current density in a pilot-scale electrodialysis process for plating wastewater treatment. Sci Total Environ 757
233. Mukherjee S et al (2021) Sensory development for heavy metal detection: a review on translation from conventional analysis to field-portable sensor. Trends Food Sci Technol 109:674–689
234. Srivastava M, Srivastava A, Pandey SK (2020) Suitability of graphene monolayer as sensor for carcinogenic heavy metals in water: a DFT investigation. Appl Surf Sci 517

235. Alizadeh T et al (2017) An extraordinarily sensitive voltammetric sensor with picomolar detection limit for Pb2+ determination based on carbon paste electrode impregnated with nano-sized imprinted polymer and multi-walled carbon nanotubes. J Environ Chem Eng 5(5):4327–4336
236. Bansod B et al (2017) A review on various electrochemical techniques for heavy metal ions detection with different sensing platforms. Biosens Bioelectron 94:443–455
237. Akhtar M et al (2020) Ternary hybrid of polyaniline-alanine-reduced graphene oxide for electrochemical sensing of heavy metal ions. Synth Metals 265
238. Wu WQ et al (2019) Sensitive, selective and simultaneous electrochemical detection of multiple heavy metals in environment and food using a lowcost Fe_3O_4 nanoparticles/fluorinated multi-walled carbon nanotubes sensor. Ecotoxicol Environ Saf 175:243–250
239. Ghanei-Motlagh M et al (2016) A novel voltammetric sensor for sensitive detection of mercury(II) ions using glassy carbon electrode modified with graphene-based ion imprinted polymer. Mater Sci Eng C Mater Biol Appl 63:367–375
240. Choi SM et al (2015) A disposable chronocoulometric sensor for heavy metal ions using a diaminoterthiophene-modified electrode doped with graphene oxide. Anal Chim Acta 892:77–84
241. Duoc PND et al (2020) A novel electrochemical sensor based on double-walled carbon nanotubes and graphene hybrid thin film for arsenic(V) detection. J Hazard Mater 400
242. Wang MY et al (2019) Preparation of mesoporous silica/carbon quantum dots composite and its application in selective and sensitive Hg2+ detection. Microporous Mesoporous Mater 284:378–384
243. Huang H et al (2014) Ultrasensitive and simultaneous detection of heavy metal ions based on three-dimensional graphene-carbon nanotubes hybrid electrode materials. Anal Chim Acta 852:45–54
244. Xuan X, Park JY (2018) A miniaturized and flexible cadmium and lead ion detection sensor based on micro-patterned reduced graphene oxide/carbon nanotube/bismuth composite electrodes. Sensors Actuators, B 255:1220–1227
245. Lee S et al (2016) A sensitive electrochemical sensor using an iron oxide/graphene composite for the simultaneous detection of heavy metal ions. Talanta 160:528–536

An Overview of Textile Industry Wastewater Treatment Using Activated Carbon Catalysts Derived from Agricultural Waste

Mohammad Mujahid Ali Khan, Kashif Faheem, Saba Anas, Manoj Kumar, Anish Khan, and Abdullah M. Asiri

Abstract The Industrial wastewater particularly from Textile industry has caused effect of pollution on the environment. This study contain an overview of the production of activated carbon (AC) from bio-waste material. The methods for treatment of Industrial wastewater focussed on textile industry dye removal are discussed in this paper. This review presents a detailed explanation of the development, preparation, characterization and properties of activated carbon derived from agricultural waste. The application of the derived activated carbon in textile industry in general and dye removal (Methylene blue and Methyl orange) in textile industry specifically is discussed. The currently available Dye removal technique is summarized and their benefits and drawback are compared. Therefore, it is proven that we can use relatively inexpensive and renewable sources of the bio-waste to be very effective in terms of cost and adsorbent capacity and it can fruitfully replace the available but expensive material.

M. M. A. Khan (✉)
Applied Science and Humanities Section, Faculty of Engineering and Technology, University Polytechnic, Aligarh Muslim University, Aligarh 202002, India

K. Faheem
Department of Civil Engineering, Faculty of Engineering and Technology, Aligarh Muslim University, Aligarh 202002, India

S. Anas
Department of Mechanical Engineering, Faculty of Engineering and Technology, Aligarh Muslim University, Aligarh 202002, India

M. Kumar
Department of Chemistry, Hansraj College, University of Delhi, Delhi, India

A. Khan · A. M. Asiri
Center of Excellence for Advanced Materials Research, King Abdulaziz University, Jeddah 21589, Saudi Arabia
e-mail: akrkhan@kau.edu.sa

Chemistry Department, Faculty of Science, King Abdulaziz University, Jeddah 21589, Saudi Arabia

M. Jawaid and A. Khan (eds.), *Carbon Composite Catalysts*, Composites Science and Technology, https://doi.org/10.1007/978-981-19-1750-9_11

Keywords Industrial wastewater · Textile industry · Activated carbon · Agricultural waste

1 Textile Industrial Wastewater

The water that contains the surplus substances affecting its quality and making it unsuitable for use is the wastewater. It is produced from various sources such as Commercial areas, Industrial properties, residential areas, agriculture lands etc. The wastewater composition varies broadly and it is mainly dependent on the source from which it is generated. The wastewater constitute of many inorganic substances such as metal ions, heavy metals, solutes, ammonia alongside with gases, complex organic compounds such as plant material, food, nitrate, natural organic matter, excreta, protein, and also some other contaminants present in ground water, Industrial water and/or surface water [1]. When the wastewater components are not treated in proper manner it may cause serious environmental hazards and can affect the living beings and that is why it is very important and essential to treat wastewater before disposing it [2]. The sources of that surplus substance which are released to wastewater as industrial effluent are illustrated in Table 1.

The wastewater can be treated using wastewater process including biological, physical and chemical treatment process which is exploited to handle them. The Industrial wastewater particularly from Textile industry has caused effect of pollution on the environment [4]. As the textile industry is one industry sector which grows in line with increasing demand for the textile to improve the nation's economy [5]. The pollution caused by this occurs when water quality of industrial waste discharged into nearby drainage areas or streams. This activity creates an imbalance to the ecosystem. The Textile industry consumes large quantities of water and produces a lot of wastewater. The wastewater released from the textile industry contains many dyes and chemicals, which will affect the natural environment of planet [6]. The source of pollutant mainly originates from wet process, which includes the use of chemicals, and it is commonly used in cleaning, rising, dyeing and finishing. The process in textile industry use a lot of reactive dyes and dark coloured wastewater fumes can increases the turbidity of water. If the wastewater of textile is treated before it is discharged then it influences the natural environment specially the aquatic ecological system [7]. The methods for the treatment of wastewater are provided in Table 2. Which illustrate the primary, secondary and Tertiary techniques currently available for the wastewater treatment.

In terms of raw materials, product and equipment and process Textile industry is a very diverse sector and it has a very complicated industrial chain. The industry covers the textile product in various processing stages including bleaching, dyeing, printing and stiffening. For some time the impact on the ecosystem and the living being by textile industry has been recognised both in terms of consumption of water energy and discharge of pollutants. For instance, presence of high concentration of heavy metal in water can cause harmful effect to the environment. Heavy metal normally

Table 1 Sources of Surplus substance released to wastewater [3]

Substance	Released to wastewater from
Copper	Copper plating, Copper pickling
Chromium	Plating, Alum anodizing, Chrome tanning
Cadmium	Plating
Nickel	Plating
Zinc	Galvanize zinc plating, Rubber process
Metals, Acids and Salts	Mining industries
Acetic acid	Acetate rayon, Beet root manufacturing
Alkalis	Cotton and Straw kiering, Wool scouring
Acids	Chem. Manufactures, Mines, Textile manufactures
Cyanides	Gas manufacturing, Plating, Metal cleaning
Hydrocarbons, mineral oils, Phenols and Chromium	Petrochemical and Rubber factories
Phenols, heavy metals and cyanide	Gas and Coke manufacture, Chemicals plant
Chlorinated organic compounds	Pulp and paper industry
Organic chemicals	Microelectronics
Fluorine	Non-ferrous metals
Starch	Food processing, Textile industries
Sulphides, Sulphates and Chromium	Textile industries, Tanneries, Gas, Gas manufacture
Free chlorine	Non-ferrous metals
Tartaric acid	Dyeing, Leather, Chemicals manufacture

added to wastewater from industrial and commercial activities has to be removed if the wastewater is to reuse further.

2 Textile Process and Textile Wastewater Characteristic

Textile industry process consist of many establishment of a compartment group to produce textiles with products such as fibres, yarns and fabrics. Textile industry has

Table 2 Methods for the treatment of wastewater

Techniques for treatment of wastewater		
Primary	Secondary	Tertiary
Screening	Aerobic and Anaerobic treatment	Membrane technologies microfiltration, nanofilration and reverse osmosis
Sedimentation	Aerated lagoons	Adsorption: silica, clays, granular, activated carbon, natural and synthetic bio adsorbents
Homogenization	Activated sludge	Oxidation techniques: Fenton-reagent, photo catalysis, advanced oxidation process etc
Neutralization	Trickling filtration	Electrolytic precipitation and foam fractionation
Mechanical flocculation Chemical flocculation	Oxidation ditch and pond	Electrochemical process
		Ion exchange process
		Photo catalytic degradation Thermal evaporation

created awareness of environmental issues around the world due to recent increase in manufacturing and the key activities of the textile industry that integument spinning, polymerization, weaving, knitting and wet processing [8]. Figure 1 demonstrates the procedure of making fibres into textile goods as shown below [9].

Due to this fact, textile industry uses gallons of water and produces a high amount wastewater from the process bleaching, desizing and scouring. Textile industry characteristics is shown in Table 3.

3 Dye in Textile Wastewater Treatment

As we know, dye is an important process in textile industry. A dye is a coloured compound that binds chemically to the substrate to which it is added. This make thedyes distinguished from pigment, which do not chemically bind to the substance that they strain chemically. In general, the dye is added in an aqueous solution and can require mordant to increase the dyefastness on the fibre. It is classified depending upon the chemical structure and their application. The dye is made up of group of atoms which are responsible for the dye colour, called chromophores, as well as the electron donating or withdrawing substituent which causes or intensify the colour of the chromophores, called auxosphore [11]. The characteristic of dye make it such that even very low concentration of dyes in effluent is highly visible and degradation products of these textile dyes are carcinogenic. Also, the adsorption of light by these textile dyes creates problems for algae and photosynthesis aquatic plants. We are here concerned with Textile wastewater treatment of dye problem using Activated

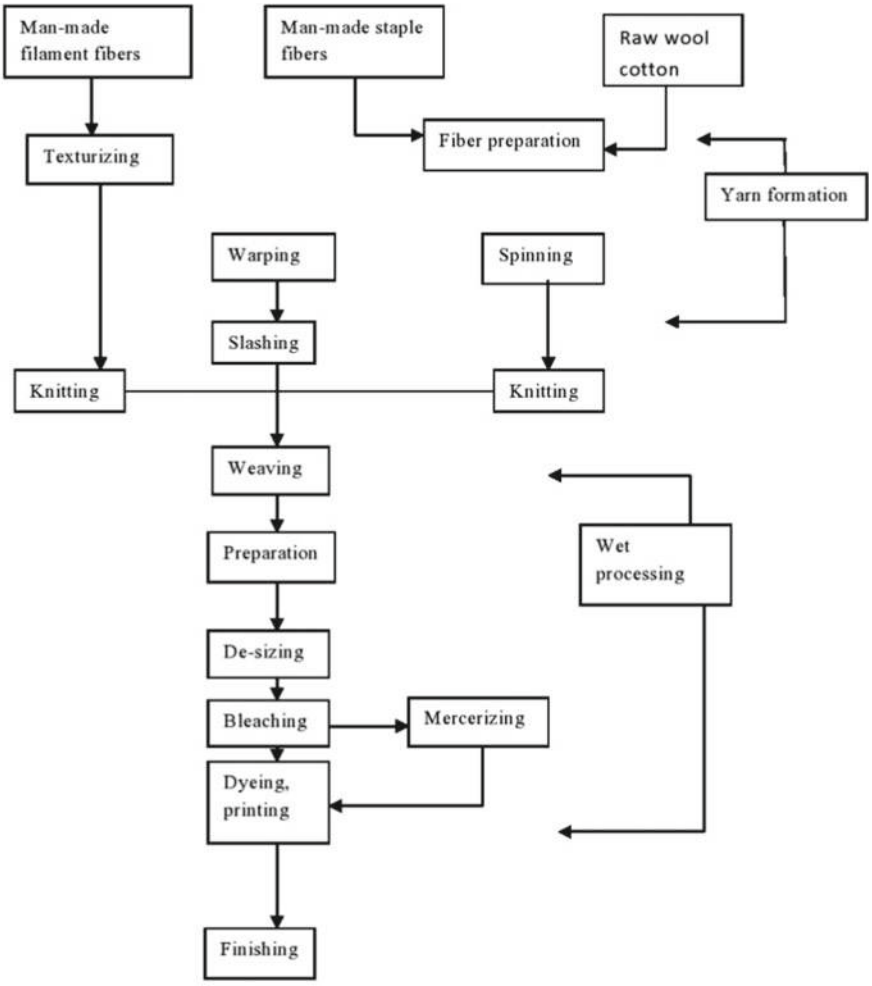

Fig. 1 A flow chart consisting of various steps involved in processing textile in a cotton mill

Table 3 Textile industry wastewater characteristics [10]

Parameters	Values
Biochemical oxygen demand (BOD)	80–6000 mg/l
Chemical oxygen demand (COD)	150–12,000 mg/l
Total suspended solids (TSS)	15–8000 mg/l
Total dissolved solids (TDS)	2900–3100 mg/l
Chloride	1000–1600 mg/l
Total kjeldahl nitrogen (TKN)	70–80 mg/l
pH	7.0–9.0

Carbon technique. So, as the dyeing process is an important part of textile industry which aims to change woven fabric or cloth to the coloured cloth or fabric. Dyeing process beautifies the textiles using various varieties of colours onto the fabric [11]. Dyeing process done to the fabric until the fabric set design produce the desired colour. In order to get the high quality woven fabric, the process of dyeing needs high temperature of more than 100 °C. Generally, while selecting the colour factors to be considered are the types of fibres being dyed, desired shade, dying fastness and its uniformity [12]. The major dyes classes, fixation rates, type of fibres for which they have affinity are listed in the Table 4.

To eliminate the dyes in textile effluent are very challenging as they are stable to heat, light and oxidizing agent and are non-biodegradable. Additionally, they are very toxic and affect the aquatic and mammalian life and inhibit growth of microorganism as well as contribute to imbalance ecosystem. Reactive dyes are carcinogenic in nature and hence can cause intestinal cancer and cerebral abnormalities in oetuses [13]. Additionally, acute exposure to the coloured effluent of dye can increase the heart rate, Heinz body formation, shock, cyanosis, tissue necrosis, dermatitis, allergy, quadriplegia, jaundice, and skin or eye infection on the human being [14].

Table 4 Available methods for dye removal illustrating the advantages and disadvantages [17, 18]

Physical/Chemical methods	Description of methods	Benefits	Drawbacks
Electrochemical destruction	Oxidation reaction using electricity	Breakdown compounds are non-hazardous	High cost of electricity
Electrokinetic coagulation	Addition of ferrous sulphate and ferric chloride	Economically feasible	High sludge production
Ion exchange	Ion exchange resin	Regeneration: no adsorbent loss	Not effective for all dyes
Photochemical	Oxidation reaction using H_2O_2-UV	No sludge production	Formation of by-products
Ozonation	Oxidation reaction using ozone gas	Application in gaseous state: no alteration of volume	Short half-life (20 min)
Fenton reagents	Oxidation reaction using mainly H_2O_2-Fe(II)	Effective decolourization	Sludge generation
NaOCl	Oxidation reaction using Cl^+ to attack the amino group	Initial and acceleration of azobond cleavage	Release of aromatic amines
Membrane filtration	Physical separation	Removal of all dye types	Concentrated sludge production
Activated carbon	Dye removal by adsorption	Good removal of a wide variety of dyes	Regeneration difficulties

3.1 Dye Removal Technologies

A wide range of traditional treatment technologies for the dye removal has been investigated extensively in recent decades. The traditional method of dye removal include membrane technologies (Nano filtration, dialysis and reverse osmosis), coagulation-flocculation, sedimentation, cloud point extraction, microbiological decomposition, anaerobic and aerobic degradation electrochemical treatment and adsorbent utilization (activated carbon, inorganic adsorbents such as clays or silica, exchange resin, synthetic ion, chitin-based adsorbents). Table 4 illustrates the critical study of the most common method used for dye removal containing industrial effluents [15, 16].

The Adsorption using activated carbon found to be more versatile and superior among these processes for wastewater treatment in terms of simplicity of design, initial cost, insensitivity to toxic substances, ease of operation and complete removal even from dilute solution of dyes [19]. Therefore using activated carbon we can remove the dye effluent in textile industry with superior and versatile way as discussed below.

3.2 Activated Carbon

Activated carbon could be defined as a material containing carbon having amorphous structure, with large internal surface area made by the pyrolysis of much inexpensive material [20]. Usually, the activated carbons are made from petroleum residue, woody materials, coal, lignite, peat [21]. The activated carbon can be proved very efficient for textile dye removal as an adsorbent because of its high degree of porosity, high carbon content, high physiochemical stability and low inorganic content. It can be characterised depending upon the chemical and physical properties of the materials [22]. The physical properties include the moisture content, volatile matter and ash content, pore structure and surface area. While the chemical properties of material include the surface chemistry activated carbon [23]. There are numerous types of AC that can be produced and it can be applied in industries based upon the type of problem to be resolved for example dye removal in wastewater treatment in textile industry is a widely discussed issue which can be solved using this technique/method [24–26]. The types of activated carbon applied in industries include granular activated carbon (GAC); pellet activated carbon and powdered activated carbon (PAC) [25–27].

The activated carbon mainly consists of carbon elements because of their electronic configuration ($1s^2$, $2s^2$, $2p^2$) that has unique bonding probability with other elements with carbon itself [28]. The hybridization development make the interaction bond with other carbon atoms result in three major allotropic forms of carbon namely; fullerenes, cubic diamond and hexagonal graphite. It is categorised from group substances of non-graphite form and microcrystalline of black carbon material with porous structure [29]. The non-graphite referred as a matter, which consist of much number of oxygen and number of hydrogen in their structure [30]. Now, based

on the atomic scale, the carbons indicate graphite allotropic forms as compared to the fullerene and diamond carbon and it can be classified into non-graphite carbon (without any measurable crystallographic order) and graphite carbon (with measurable crystallographic order) [31]. The non-graphitizable carbon known as non-graphite carbon, which can be transformed into graphite carbon while graphitizable carbon is a non-graphitic carbon, which can be transformed into graphitic carbon using methods of heat treatment. Apparently, the graphitizable structure is non-porous, soft and it has a very high density. In addition, the arrangement of carbon microstructure is in preferential direction [32]. In contrast, the non-graphitizable carbon structure are having low density, are porous and are mostly hard. Along with this, the microstructure arrangement is also very disordered [33]. This is the reason that activated carbon classified into non-graphitizable carbon because of their porous structure and low density [34].

3.3 Activated Carbon (AC) from Agricultural Wastes

The waste from agricultural practise (by-products) has the benefits as they are renewable additional sources of activated carbon and are very inexpensive when compared to other sources. The generation of activated carbon can be occurred either both naturally and synthetic of solid precursor containing carbon. That is why the precursor plays an important role in affecting the characteristics, quality and properties of activated carbon resulted. The precursor structure also could affect the activated carbon properties. Additionally the characteristic, performance and properties of the activated carbon will also depends on the type of time consumption, activating reagent, impregnation condition, inorganic impurities and carbonization techniques [35]. Variety of raw materials such as animals, minerals and plants can be used to produce activated carbon. The selection of activated carbon from the raw materials depends on the factors such as its purity, price, and stability of its supply and potential extent of its activation [24]. Those activated carbons, which are produced from raw materials, are inherent filterability high carbon content and porosity. Because of these properties it give rise to developments in producing activated carbons while parallel utilizing the agricultural bio-waste (lignocellulose materials) so as to production cost, providing readily available and sustaining long term usage [33].

Under controlled condition, the activated carbon can be produced through conversion of raw material using pyrolysis with or without additional chemical activating agents. Normally, any material having low cost which only contain high amount of carbon and relatively low inorganic content can be best utilized as a precursor agent for activated carbon processes [30]. In addition, any agricultural waste (lignocellulose) can be used for the production of activated carbon purpose because of the reasons discussed above.

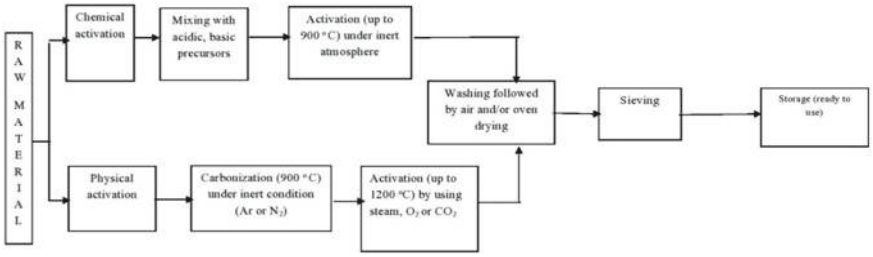

Fig. 2 Development/Production of activated carbon [35]

3.4 Preparation of Activated Carbon (AC)

The activated carbon development mainly consist of two steps including the carbonization of raw materials containing carbon and activation of char. With a variety of surface functional group the activated carbon are thermally and chemically stable. Figure 2 illustrates the routes for preparation of activated carbon [29, 30].

The activated carbon prepared in two different ways, which are chemical and physical treatment. In case of physical treatment the carbonaceous raw material are first carbonized the organic matter which is then followed by activation process step by step or carbon dioxide under specified pressure to raise the surface area and increase the porosity [36]. While, in case of chemical treatment, an activating regent impregnates the raw material which is then followed by a heating process under specified temperature under an inert atmosphere. It was reported that the activating regent purposes could dissolve the cellulose components of the raw material and promising the crosslink formation [34]. In addition, the chemical treatment found to be more advantageous compared to the physical treatment. The chemical treatment result in higher yield, lower temperature required, has high surface area, reduction of mineral matter content and well developed micro porosities in comparison with the physical treatment [37].

3.5 Carbonization

It is the thermal decomposition and elimination of species, which are having non-carbon content in raw material. The carbonization process consist of a pyrolysis methodology where entire volatile compound are released because of various consecutive, complex and rival reaction resulting in formation of fixed carbon in the absence of oxygen meaning an inert atmosphere and at a temperature of at least 800 °C [38]. The process of carbonization reduces the volatile matter content and it allows production of charcoal with fixed high content of carbon content by breaking down the raw material cross-linkage. After this the decomposition of tars take place in which the

low molecular weight volatile matter are diffused followed by light of hydrogen and aromatic gas. Simultaneously, the pore structure also begin to form and the produced tars fill the pore structure [20, 23, 36]. The classification of carbonization consist of four phase mainly based on the temperature required which is presented in Table 5.

Table 5 Activation methods of the agricultural residue while producing the activated carbon

Activation method	Raw material	Activating agents	Reference
Physical	Cocoa shell	Carbon dioxide	[39]
	Avocado peel	Carbon dioxide	[29]
	Pumpkin seed	Steam	[40]
	Thevetiaperuviana	Carbon dioxide	[41]
	Esparto grass	Steam	[42]
	Rice husk	Carbon dioxide	[25]
	Esparto grass	Steam	[21]
Chemical	Pineapple	Zinc chloride	[30]
	Olive cores	Phosphoric acid	[28]
	Fox nutshell	Zinc chloride	[26]
	Bamboo	Sodium hydroxide	[23]
	Grape waste	Zinc chloride	[21]
	Bamboo	Potassium hydroxide	[23]
	Bamboo	Hydrochloric acid	[23]
	Macore fruit	Sodium hydroxide	[27]
	Orange peel	Phosphoric acid	[43]
	Date palm leaflets	Potassium dioxide	[36]
	Buriti shell	Zinc chloride	[34]
	Deloxiaregia fruit pod	Potassium hydroxide	[44]
	Corncob	Phosphoric acid	[37]
	Spent coffee grounds	Potassium dioxide	[31]
	Tomato waste	Zinc chloride	[38]
	Thevetiaperuviana	Phosphoric acid	[41]
	Thevetiaperuviana	Zinc chloride	[41]
	Thevetiaperuviana	Potassium hydroxide	[41]
	Thevetiaperuviana	Sodium sulphate	[41]
	Apple pulp	Phosphoric acid	[45]
	Apple peel	Phosphoric acid	[45]
Physiochemical	Seeds	Steam	[33]
	Elaegnusangustifolia	Zinc chloride	[33]

3.6 Activation Process

This process mainly affect the properties of activated carbon produced. There are different factors involved in the activation process which impact the development of suitable activated carbon prepared for specified application in the industry wastewater treatment like for example dye removal. In the initial stage or preliminary stage, the tarry substances, which make the pore clogging, are remove in order to facilitate the surface of elementary carbon crystal with the activating agent for reaction [46]. During the secondary stage, those elementary crystal will burn followed by final stage involving the carbon particles oxidation. Let us say for example, there will be reduction in the total micropore volume of activated carbon by the burning of walls between the adjacent pores [35]. Mainly, there are two distinguished way for activation process to be performed, which are chemical and physical method. The activation condition of the agricultural residue while producing the activated carbon is illustrated in Table 5.

3.6.1 Physical Activation Process

The physical activation process consist of two main steps. After the carbonaceous material undergone, the carbonization the charcoal is produced. The activation of char is carried out in the presence of activating agents (oxidizing gas) such as carbon dioxide (CO_2), steam or mixture of CO_2 and stream at temperature reaching above 700 °C [29]. The main reason of using carbon dioxide as physical activation due to its characteristics like cleanliness, easy to be handled and the activation process can be easily controlled at temperature around 800 °C. Therefore, high uniformity of pore also can be obtained with the activation of CO_2 as compared to steam [42]. The oxidizing agent like CO_2 will remove the reactive carbon elements in activation process, which forming pores and vessels. Hence, high porosity of AC will be produced. There are three stages involving pore formation by activating agents; Opening of previously inaccessible pores, new pore development by selective activation and widening of the existing pores [41, 42].

3.6.2 Chemical Activation Process

Coming to the chemical activation process consisting of carbonization and activation. The first step of chemical activation process involve the impregnation of carbonaceous raw material with predefined ratio of chemical activating agents for dehydrating process [34]. This involve a relatively lower temperature depending upon the inorganic additive action to dehydrate and degrade the cellulose materials, Using the chemical activation process prevent the formation of ash or tar which develop the carbon yield [30, 35].

The activating agents which use phosphoric acid, potassium hydroxide, zinc chloride, nitric acid, sodium hydroxide and HCl. The reaction between the carbon residue and chemical degrade the cellulosic formation. This activation affect the improvement of pore development in the carbon structure because of the effect of various types of chemicals that is by oxidation reaction and dehydration of the chemicals, When reacting with the activating agents the surface oxygen functional groups can be initiate to the carbon yields of the raw materials [23, 28].

Final stage is the washing stage in which the AC washed with acids or alkali, mainly depending upon the regents used in the preparation and then followed by washing with water this step eliminate the chemical components present in the AC. The washing step is one of the most important steps in the chemical activation as the chemicals in the carbon structure occupy the porosity of producing AC to develop porosity in the activated carbon [47].

3.7 Characterization and Properties of Activated Carbon (AC)

The high adsorptive capacities of AC is strongly related to the porous characteristics like pre volume, pore size distribution, surface area, which the presence of functional groups on pore surface play a significant role in the adsorptive capacities of AC. The surface area of activated carbon is a significant characteristic whose value typically lies in the range of 500–1000 m^2/g. The activated carbon structure with high micropore is widely used for adsorption of small molecule pollutants and highly developed mesoporous AC that is used for the adsorption of larger molecules such as dyes. The porous structure is the main physical property, which characterized the activated carbon, and they are mainly classified into three major groups illustrated in Table 6 [29].

The pore shape of AC seems to be rectangular or cylindrical or it can be irregular in cross-sectional view. The surface area and pore volume consist in pore structure is one of the important property of AC. Therefore the application in industries is influenced the pore size requirement of AC [29].

Table 6 Classification of porous structure characterizing the activated carbon [22, 29]

Micropores	Pore width less than 2.0×10^{-9} m
Mesopores	Pore width range from 2.0×10^{-9} to 50.0×10^{-9} m
Macropores	Pore width larger than 50.0×10^{-9} m

4 Application of Activated Carbon for Wastewater Treatment

The application on activated carbon vary from liquid phase to gaseous phase such as in industrial, domestic and commercial wastewater treatment. Activated carbon physiochemical characterization give advantages for the elimination for wastewater. In case of textile and food industries, activated carbon can be used for deodorization, taste removal and decolourization purposes. Meanwhile, in healthcare industries, activated carbon from bio-waste can be applied for harmful chemical and drug adsorption [48]. The best application of activated carbon is determined by its physical property. Hardness or abrasion resistance properties are very important for AC during application, which frequent back washing. Apart from this, the chemical nature of AC also influence the adsorptive, catalytic and electrochemical properties significantly. For instance, for basic surface chemical properties are optimum in acidic surface like sulphur dioxide if the AC with acidic surface chemical properties are favourable for basic surface such as methylene blue and gas ammonia. Therefore, the AC has been very beneficial in adsorption process from liquid to gaseous phase application [49].

4.1 Dye Removal from Wastewater Using Activated Carbon (AC) Derived from Agricultural Waste (Lignocellulose) Material

As the discharge of dye-bearing wastewater from textile industry into natural river or stream poses various serious problems as the dyes imparts toxicity to the life of aquatic life and it lead to damages to the aesthetic nature of the environment. Now if effluent combustion and volume-discharged are both considered then, the textile industry rated as one of the most polluting among any other industrial sector. The basic dyes are the brightest class of soluble dyes used by the textile industry. The problem of dye removal in wastewater treatment is a serious issue to be resolved. The tinctorial value of basic dye in textile industry is very high. In fact less than 1 ppm of dye produces a certain coloration [49]. As discussed above about the activated carbon and how it can be prepared, activated using physical and chemical process. The application of activated carbon derived from agricultural waste develop a technology, which is low cost, efficient and capable of removing various dyes/colouring materials from textile industry [50]. Singh et al. described novel adsorbent for removal and recovery of inorganic and organic pollutants and have derived a new low-cost AC from coconut shell fibre which is bio-waste for the removal of dye components particularly methyl orange (MO) and methylene blue (MB) from wastewater. It was revealed that the adsorption for two dyes increases with an increase in the temperature, which indicate that, the process to be endothermic. Both the dye is removed at 100% at low concentration while the same decrease as increase in

Table 7 Currently available Low cost dye and its adsorption capacity

Name of the dye	Low-cost adsorbents	Adsorption capacity	Reference
MB	Fly ash	1.44×10^{-5}	[52]
MB	Perlite (EP)	$4.65 \times 10^{-5} - 8.21 \times 10^{-5}$	[53]
MB	Activated carbon derived from coconut shell fibers	5.24×10^{-5}	[51]
MO	Activated carbon derived from coconut shell fibres	2.88×10^{-5}	[51]
Crystal violet	Wollastonite	2.17×10^{-6}	[54]
Malachite green	Blast furnace slag	10.52×10^{-5}	[55]
Malachite green	Activated carbon derived from fertilizer waste	12.50×10^{-5}	[55]
Rosaline hydrochloride or basic fuchsin	Fly ash	1.35×10^{-5}	[56]
Crystal violet	Fly ash	9.76×10^{-5}	[56]

the concentration. The absorption capacity of the activated carbon derived from bio-waste (coconut shell) is very good as it is found to be quite cheaper than other available adsorbents illustrated in Table 7. It was also found that the derived activated carbon from agricultural waste can be successfully and fruitfully employed as an adsorbent for the dye removal [51].

5 Conclusion

The industrial wastewater treatment has always been concerning problem as it pose serious threat to the life of human being, natural plants and the environment as a whole. The detailed study of type of methods for treatment of wastewater summarized. In the study, it was found that activated carbon application in textile industry for removal of dye effluent is very superior and versatile than other methods. The activated carbon derived from agricultural waste its preparation and application has revealed that it can be very efficient technology which can be developed and quite low cost than other method for treatment of colourized water in textile. The AC adsorbent capacity is better than other available adsorbent. For carbonaceous raw material or bio-waste we can easily derive the activated carbon and apply it in the dye removal in textile industry as discussed in this work. Therefore, it is concluded-form the previous work and current research that activated carbon from agricultural waste can be fruitful to be employed as an adsorbent for dye removal.

References

1. Tchobanoglous G, Burton FL (1991) Wastewater engineering: treatment, disposal, and reuse. Metcalf & Eddy Inc., p 1334
2. Savant DV, Abdul-Rahman R, Ranade DR (2006) Anaerobic degradation of adsorbable organic halides (AOX) from pulp and paper industry wastewater. Biores Technol 97(9):1092–1104
3. Abdelbasir SM, Shalan AE (2019) An overview of nanomaterials for industrial wastewater treatment. Korean J Chem Eng 36(8):1209–1225
4. Venceslau MC, Tom S, Simon JJ (1994) Characterization of textile wastewaters-a review. Environ Technol 15(9):17–29
5. Kumar P, Bansal V, Kim K-H, Kwon EE (2018) J Ind Eng Chem 62:130
6. Pal P (2014) Industrial water treatment process technology. Butter-worth-Heinemann-Eksevier Inc. ISBN: 9780080999685
7. Kalhapure RS, Sonwane SJ, Sikwal DR, Jadhav M, Rambharose S, Mocktar C, Govender T (2015) Colloids Surf B: Biointerfaces 136:651
8. Parande AK, Babu BR, Raghu S, Prem Kumar T (2007) Textile technology. Cotton textile processing: waste generation and effluent treatment. J Cotton Sci 11:141–153
9. Somasiri W, Ruan W, Xiufen L, Jian C (2006) Decolourization of textile wastewater containing acid dyes in a UASB reactor system under mixed anaerobic granular sludge. Electron J Environ Agric Food Chem 5(1). ISSN 1579-4377
10. Al-Kdasi A, Idris LC, Abdullah KS (2005) Formulation of process treatment options for textile wastewater. Malays J Chem Eng 1:11–28
11. Yan H, Pan G (2004) Increase in biodegradation of dimethyl phthalate by Closterium lunula using inorganic carbon. Chemosphere 55:1281–1285
12. Guo JB, Zhou JT, Wang D, Tian CP, Wang P, Uddin MS, Yu H (2007) Biocatalyst effects of immobilized anthraquinone on the anaerobic reduction of Azo dyes by the salt-tolerant Bacteria. Water Res 41:426–432
13. Abdul Wahab NS (2009) Decolouration of textile wastewater using bioparticle. Thesis, UniversitiTeknologi Malaysia
14. Sen S, Demirer GN (2003) Anaerobic treatment of synthetic textile wastewater containing a reactive azo dye. J Environ Eng 129(7)
15. Birnhack L, Fridman N, Lahav O (2009) Potential application of quarry dolomite for post treatment of desalinated water. Desalin Water Treat 1:58–67
16. Badani Z, Cabassud C, Ait-Amar H (2009) Membrane separation process for the treatment and reuse of bath dye effluents. Desalin Water Treat 9:105–111
17. Robinson T, McMullan G, Marchant R, Nigman P (2001) Remediation on dyes in textile effluent: a critical review on current treatment technologies with a proposed alteration. Biores Technol 77:247–255
18. Dos Santos AB, Cervantes FJ, van Lier JB (2007) Review paper on current technologies for decolourisation of textile wastewaters: perspectives for anaerobic biotechnology. Biores Technol 98:2369–2385
19. Foo KY, Hameed BH (2009) An overview of landfill leachate treatment via activated carbon adsorption process. J Hazard Mater 171:54–60
20. Djebri N, Boutahala M, Chelali NE, Boukhalfa N, Zeroual L (2016) Enhanced removal of cationic dye by Calcium Alginate/Organo bentonite beads: modelling, kinetics, equilibrium, thermodynamic and reusability studies. Int J Biol Macromol 92:1277–1287
21. Cardoso JC, Natalia I, Zanoni MVB (2015) Bubble annular photoclectrocatalytic reactor with TiO_2 nanotubes array applied in the textile wastewater. J Environ Chem Eng 3(2):1177–1184
22. Yahya MA, Mansor MH, Zolkarnaini WAAW, Rusli NS, Aminuddin A, Mohamad K, Sabhan FAM, Atik AAA, Ozair LN (2018) A brief review on activated carbon derived from agricultural by-product. AIP Conf Proc 1972:1–9
23. Xia H, Wu J, Srinivasakannan C, Peng J, Zhang L (2015) The effect of activating agent on the preparation of bamboo-based high surface area activated carbon by microwave heating. High Temp Mater Processes (London) 35(6):1–7

24. Ong YK, Chung TS, Li FY, Sun SP, Liang CZ (2014) Treatment of highly concentrated wastewater containing multiple synthetic by a combined process of coagulation/flocculation and nano filtration. J Membr Sci 469:306–315
25. Saeed S, Khan K, Saeed S, Khan R (2015) Removal of dyes from textile wastewater using adsorption by activated carbon of rice husk. Int J Innov Sci Res 17(1):191–196
26. Kumar A, Jena HM (2016) Removal of methylene blue and phenol onto prepared activated carbon from fox nutshell by chemical activation in batch and fixed-bed column. J Clean Prod 137:1246–1259
27. Aboua KN, Yobouet YA, Yao KB, Gone DL, Trokourey A (2015) Investigation of dye adsorption onto activated carbon from the shells of Macore fruit. J Environ Manage 156:10–14
28. Kaouah F, Boumaza S, Berrama T, Trari M, Bendjama Z (2013) Preparation and characterization of activated carbon from wild olive cores (Oleaster) by H_3PO_4 for the removal of basic red 46. J Clean Prod 54:296–306
29. Palma C, Lloret L, Puen A, Tobar M, Contreras E (2016) Production of carbonaceous material from avocado peel for its application as alternative adsorbent for dyes removal. Chin J Chem Eng 24(4):521–528
30. Mahamad MN, Zaini MAA, Zakaria ZA (2015) Preparation and characterization of activated carbon from pineapple waste biomass for dye removal. Int Biodeterior Biodegradation 102:274–280
31. Jung KW, Choi BH, Hwang MJ, Jeong TU, Ahn KH (2016) Fabrication of granular activated Carbons derived from spent coffee grounds by entrapment in Calcium Alginate beads for adsorption of acid Orange 7 and Methylene Blue. Biores Technol 219:185–195
32. Yagub MT, Sen TK, Afroze S, Ang HM (2014) Dye and its removal from aqueous solution by adsorption: a review. Adv Coll Interface Sci 209:172–184
33. Sahin O, Baytar O, Saka C (2013) Surface and porous characterization of activated carbon prepared from pyrolysis of biomass by two-stage procedure at low activation temperature and it's the adsorption of Iodine. J Anal Appl Pyrol 104:378–383
34. Pezoti O Jr, Cazetta AL, Souza IPAF, Bedin KC, Martins AC, Silva TL, Almeida VC (2014) Adsorption studies of methylene blue onto $ZnCl_2$-activated carbon produced from Buriti shells (Mauritia flexuosa L). J Ind Eng Chem 20(6):4401–4407
35. Oganov AR, Hemley RJ, Hazen RM, Jones AP (2013) Structure, bonding and mineralogy of Carbon at extreme conditions. Rev Mineral Geochem 75:47–77
36. El-Shafey EI, Ali SNF, Al-Busafi S, Al-Lawati HAJ (2016) Preparation and characterization of surface funcationalized activated carbons from date palm leaflets and application for methylene blue removal. J Environ Chem Eng 4:2713–2724
37. Altintig E, Arabaci G, Altundag H (2016) Preparation and characterization of the antibacterial efficiency of silver loaded activated carbon from Corncobs. Surf Coat Technol 304:63–67
38. Saygili H, Guzel F (2016) High surface area mesoporous activated carbon from tomato processing solid waste by Zinc Chloride activation: process optimization, characterization and dyes adsorption. J Clean Prod 113:995–1004
39. Fisal A, Wan Daud WMA, Ahmad MA, Radzi R (2012) Cocoa (Theobroma Cacao) shell-based activated carbon by CO_2 activation in removing of cationic dye from aqueous solution: kinetics and equilibrium studies. Chem Eng Res Des 90(10):1480–1490
40. Njoku VO, Foo KY, Hameed BH (2014) Microwave-assisted preparation of pumpkin seed hull activated carbon and its application for the adsorptive removal of 2,4-Dichlorophenoxyacetic acid. J Chem Eng 215–216(38):3–8
41. Baseri JR, Palanisamy PN, Sivakumar P (2012) Preparation and characterization of activated carbon from Thevetia Peruviana for the removal of dyes from textile wastewater. Adv Appl Sci Res 3(1):377–383
42. Nabais JV, Laginhas C, Carrott MMLR, Carrott PJM, Amoros JEC, Gisbert AVN (2013) Surface and porous characterization of activated carbon made from a novel biomass precursor, the Esparto Grass. Appl Surf Sci 265:919–924
43. Fernandez ME, Nunell GV, Bonelli PR, Cuklerman AL (2014) Activated carbons develop from orange peels: batch and dynamic competitive adsorption of basic dyes. Ind Crops Prod 62:437–445

44. Sugumaran P, Susan VP, Ravichandran P, Seshadri S (2012) Production and characterization of activated carbon from banana empty fruit bunch and deloxic regia fruit pod. J Sustain Energy Environ 3(3):125–132
45. Hesas RH, Arami-niya A, Wan Daud WMA, Sahu JN (2013) Preparation and characterization of activated carbon from apple waste by micorwave-assisted phosphoric acid activation: application in methylene blue adsorption. BioResources 8(2):2950–2966
46. Heibati B, Couto SR, Al-Ghouti MA, Asif M, Tyagi I, Agarwal S, Gupta VK (2015) Kinetics and thermodynamics of enhanced adosrption of the dye AR 18 using activated carbons prepared from Walnut and Poplar Woods. J Mol Liq 208:99–105
47. Zhu GZ, Deng XL, Hou M, Sun K, Zhang YP, Li P, Liang FM (2016) Comparative study on characterization and adsorption properties of activated carbons by phosphoric acid activation from Corncob and its acid and alkaline hydrolysis residues. Fuel Process Technol 144:255–261
48. Adani KG, Barley RW, Pascoe RD (2005) Silver recovery from synthetic photographic and medical X-ray process effluents using activated carbon. Miner Eng 18(13–14):1269–1276
49. Yazidi A, Sellaoui L, Dotto GL, Bonilla-Petriciolet A, Frohlich AC, Lamine AB (2019) Monolayer and multilayer adsorption of pharmaceuticals on activated carbon: application of advanced statistical physics models. J Mol Liq 283:276–286
50. McKay G, Otterburn MS, Sweeney AG (1981) Surface mass transfer processes during colour removal from effluent using Silica. Water Resource 115:327
51. Singh KP, Mohan D, Sinha S, Tondon GS, Gosh D (2003) Color removal from wastewater using low-cost activated carbon derived from agricultural waste material. Ind Eng Chem Res 42(9):1965–1976
52. Weber TW, Chackravorti RK (1974) Pore and solid diffusion models for fixed bed adsorbers. J Am Inst Chem Eng 20:228
53. Dogan M, Mahir A, Onganer Y (2000) Adsorption of methylene blue from aqueous solution onto perlite. Water Air Soil Pollut 120:229
54. Khare SK, Srivastava RM, Panday KK, Singh VN (1988) Removal of basic dye (crystal violet) from water using wollastoniteas adsorbent. Environ Technol Lett 9:1163
55. Gupta VK, Srivastava SK, Mohan D (1997) Equilibrium uptake, sorption dynamics, process optimization and column operation for the removal and recovery of malachite green from wastewater using activated carbon and activated slag. Ind Eng Chem Res 36(6):2207
56. Mohan D, Singh KP, Singh G, Kumar K (2002) Removal of dyes from wastewater using fly ash-a low cost adsorbent. Ind Eng Chem Res 41:3688–3695